BIMEVOX Catalyst Systems for Low Temperature Steam Reforming of Ethanol with the Aim of Hydrogen Production

THESIS

Submitted in partial fulfillment
of the requirements for the degree of

DOCTOR OF PHILOSOPHY

by

SHWETA SHARMA

ID No. 2014PHXF0002P

Under the Supervision of

Prof. Banasri Roy

and

Co-Supervision of

Prof. Hare Krishna Mohanta

BITS Pilani
Pilani Dubai Goa Hyderabad

BIRLA INSTITUTE OF TECHNOLOGY AND SCIENCE, PILANI

2020

BITS Pilani
Pilani Dubai Goa Hyderabad

BIRLA INSTITUTE OF TECHNOLOGY AND SCIENCE, PILANI

CERTIFICATE

This is to certify that the thesis titled **"BIMEVOX Catalyst Systems for Low Temperature Steam Reforming of Ethanol with the Aim of Hydrogen Production"** submitted by **Shweta Sharma**, ID No **2014PHXF0002P** for award of Ph.D. of the Institute embodies original work done by him/her under my supervision.

Signature of the Supervisor

Prof. BANASRI ROY

Associate Professor,

Department of Chemical Engineering,

BITS-Pilani, Pilani Campus

Date: 02/03/2020

Signature of the Co-Supervisor

Prof. HARE KRISHNA MOHANTA

Associate Professor,

Department of Chemical Engineering,

BITS-Pilani, Pilani Campus

Date: 02.03.2020

DEDICATED
TO

MY PARENTS

&

MY HUSBAND

ACKNOWLEDGEMENTS

Word research consists of search, and search of anything is impossible without a mentor. Hence, I would like to express my sincere gratitude to my guide Prof. Banasri Roy, Associate Professor, Department of Chemical Engineering, BITS Pilani for continuous support during this whole journey of my research work, for her patience, constant motivation and knowledge. Her consideration of my work as a contribution towards science and society, even on minuscule level, has given me strength to complete it and has always filled me with a sense of pride. During my tenure, she contributed to a rewarding doctorate experience by giving me intellectual freedom in my work, supporting my attendance at various conferences, engaging me in new ideas, and demanding a high quality of work in all my endeavors.

My sincere gratitude is reserved for my Co-Supervisior, Prof. Hare Krishna Mohanta, Associate Professor & Head, Department of Chemical Engineering, BITS-Pilani, Pilani Campus for his invaluable insights and suggestions. I am very grateful for his patience, motivation, enthusiasm, and immense knowledge, which make him a great mentor.

I would like to thank the members of Doctoral Advisory Committee, Prof. Bharti Khungar, Associate Professor, Department of Chemistry, BITS-Pilani, Pilani campus and Dr. Srinivas Appari, Assistant Professor, Department of Chemical Engineering, BITS-Pilani, Pilani Campus, not only for their insightful comments and encouragement.

I extend my sincere thanks to Prof. Souvik Bhattacharyya, Vice-Chancellor, BITS-Pilani for giving me the opportunity to carry out the Ph.D. work in BITS-Pilani, Pilani Campus. My sincere thanks go to former Director Prof. A. K. Sarkar and present Director S. K. Barai , BITS-Pilani, Pilani Campus for providing the necessary infrastructure to carry out this research work. I am indebted to Dean, and Associate Dean, Academic - Graduate Studies & Research Division (AGSRD) (Ph.D programme), BITS-Pilani, Pilani Campus for providing the necessary research facilities required for my work.

I would like to thank Dr. Pratik N. Sheth, Assistant Professor, Department of Chemical, Engineering, BITS-Pilani, Pilani campus for giving me valuable inputs for GC equipment utilization and suggestions which were helpful in improving the quality of my research work. I am thankful to Prof. Arvind Kumar Sharma, Dr. Pradipta Chattopadhyay, Dr. Ajaya Kumar Pani, Prof. Suresh Gupta, Dr. Amit Jain, Prof. Smita Raghuvanshi, Dr. Raman Sharma, Dr. (Ms.) Priya C. Sande, Dr. Bhanu Vardhan Reddy Kuncharam, and Dr. Krishna C Etika, for their support throughout the work.

The greatest gift of life is friendship and I have received it in the form of Ms. Prachi Venkat and my sister Indu Sharma, and their constant physical and mental support. I thank my fellow lab-mates Ms. Bhagyesha Patil, Mr. Yashwanth, and Ms. Akanksha Pathak, for the stimulating discussions. I would also like to thank Ms. Rimzhim Gupta, Mr. Arun Karthik, Mr. Somesh Mishra and my juniors Ms. Sampda, and Mr. Hitesh for their support during thesis writing.

I thank to Department of Science & Technology (DST) for providing INSPIRE fellowships and necessary support to carry out research at department laboratories.

I would like to express my special thanks to Mr. Ashok Saini for his help and support throughout the experimental work and time to time technical assistance. I would like to thank Mr. Subodh Kumar Azad, Demonstrator for his help in handling various analytical equipments. Thanks are also due to Mr. Babulal Saini, Mr. Jeevan Lal Verma and Mr. Jangvir Sheron for their help and co-operation during this work. I would also like to acknowledge the support of Ms. Shailee Gaur, Abhishek, Tapas and all the fellow research scholars of the Department of Chemical Engineering, BITS, Pilani.

I owe a lot to my parents, and my brother, who encouraged and helped me at every stage of my personal and academic life, and longed to see this achievement come true. I am very much indebted to my husband Ankur Upadhyay, and my in-laws, who supported me in every possible way to see the completion of this work.

Above all, I thank the Almighty for giving me the strength and patience to work through all these years and to undertake this research task right up to its completion.

SHWETA SHARMA

ABSTRACT

Low temperature (≤500°C) steam reforming offers significant advantages for the production of hydrogen compared to the conventional process. The milder operating conditions lead to lower operation cost and might save on the cost of construction materials. Additionally, no CO shift reactor might be required due to favorable temperature condition for the water-gas shift reaction (WGSR). The present work deals with the catalytic performance of Cobalt (10 at.%) doped bismuth vanadate, $Bi_4(V_{0.90}Co_{0.10})_2O_{11-\delta}$ (BICOVOX), Nickel (10 at.%) doped bismuth vanadate, $Bi_4(V_{0.90}Ni_{0.10})_2O_{11-\delta}$ (BINIVOX), and Copper (10 at.%) doped bismuth vanadate, $Bi_4(V_{0.90}Cu_{0.10})_2O_{11-\delta}$ (BICUVOX) catalysts, known to have higher oxygen ion conduction in the low temperature range (300–600°C), for their application in steam reforming of ethanol operating at low temperature (200-400°C). Small grain size may be important in stabilizing the highly conductive and disordered γ-phase. Therefore, BICOVOX, BINIVOX and BICUVOX catalysts are synthesized by a solution combustion technique. The effects of post-combustion heat treatment temperature (400, 600 and 800°C) on the phase content and microstructure of the powders, which can alter the catalytic activity, are investigated.

The performance of the catalysts is assessed in different operating conditions in ethanol steam reforming (temperature (200–400°C), water to ethanol (H_2O: EtOH=2.5:1 and 23:1) molar ratio and feed flow rate (0.1 and 0.35 cc min^{-1}) and all catalysts are found active in the reforming reactions. Stability tests are conducted up to 150 h on stream (at 400°C, 0.35 cc min^{-1} flow rate and 23:1 H_2O: EtOH molar ratio) and the tendency toward carbon formation is investigated. At a reaction temperature of 400°C, 23:1 H_2O: EtOH molar ratio and 0.35 cc min^{-1} flow rate, the BICOVOX-600, BINIVOX-600 and BICUVOX-600 catalysts exhibit the highest selectivity of H_2 (~80%) and CO_2 (~70%) with almost 100% EtOH conversion, while the BIMEVOX-400 catalysts show the highest selectivity of CH_4 (~ 36%). No CO_2 is observed below 250°C and for 2.5:1 H_2O: EtOH molar ratio, making 250°C a crossover temperature at which all gaseous products are formed. Based on the product distribution, the proposed reaction pathway is a mixture of dehydrogenation of EtOH to CH_3CHO followed by C-C bond breaking to produce CO and CH_4. CH_4 also can be formed via Fischer-Tropsch reactions of CO/CO_2 with H_2. The CH_4 reacts to form H_2 and CO through steam reforming, while CO converts to CO_2 mostly through the WGSR.

Stability tests over the period of 150 hs show complete deactivation of BIMEVOX-400 (0% H_2 selectivity) and BIMEVOX-800 (0% H_2 selectivity) catalysts compared to BIMEVOX-600 (8-11% H_2 selectivity).

Thermo Gravimetric Analysis (TGA) & Differential thermal analysis (DTA) infers the purity and thermal stability of BIMEVOX_F catalysts compared to the parent compound BIVOX. The XRD (X-ray powder diffraction) and FESEM (Field emission scanning electron microscopy) analysis show that the crystallinity as well as particle size increases with the increasing heat treatment temperature in the fresh catalysts. Just prepared catalysts are revealed to be a mixture of Bi_2O_3, $BiVO_4$, and γ-BIMEVOX phases that are converted to phase pure γ-BIMEVOX during heat treatment. Phase purity and crystallinity of the catalyst is retained till 30 hrs of activity study with increased scale of particle agglomeration and little amorphous carbon is formed. Breaking of pure γ-phase and deposition of whisker and graphite with amorphous carbon is noticed after 150 hrs of catalytic activity.

Raman spectroscopy confirms the maximum oxygen mobility in BIMEVOX-600 catalysts as it shows the maximum V^{4+}:V^{5+} ratio for BIMEVOX-600 catalysts. The X-ray photoelectron spectroscopy (XPS) analysis reveal the lowest amount of coke deposited and maximum value of V^{4+}:V^{5+} ratio for BIMEVOX-600 sample with respect to the other samples, which could explain the best performance of BIMEVOX-600 catalysts.

Keywords: *BICOVOX, BINIVOX, BICUVOX catalysts; Low temperature steam reforming; Ethanol; Solution combustion synthesis; Calcination; Hydrogen production; Catalytic activity, Catalyst deactivation; Phase transition; Reaction pathway; Carbon deposition.*

Table of Contents

.List of Figures

List of Tables

NOMENCLATURE

GHSV	Gas hourly space velocity	h^{-1}
LHSV	Liquid hourly space velocity	h^{-1}
D_{Ni}	Diameter of Ni	Å
D_{Cu}	Diameter of Cu	Å
D_{Co}	Diameter of Co	Å
D_p	Particle diameter	nm
V_p	Particle volume	$cm^3\ g^{-1}$
S/E	Steam to Ethanol molar ratio	
H_2O/EtOH	Water to Ethanol molar ratio	
S_{BET}	BET surface area	m^2/g
%S	Percentage selectivity	
%Y	Percentage yield	
D_{pore}	Pore diameter	nm
V_{pore}	Pore volume	$cm^3\ g^{-1}$
O/F	Oxidizer ratio- fuel ratio	
x	Fraction of Metal	at%
ΔE	Activation energy	eV
T_{ig}	Ignition temperature	°C
T_m	Maximum temperature	°C
R_{exp}	Expected Profile Factor	
R_B	Bragg Factor	
R_{wp}	Weighted Profile Factor	
R_p	Profile Factor	
R_F	Crytallographic Factor	
x_i	Mole fraction of any species CO_2, CO, CH_4, H_2	
C	Carbon	
R	V–O bond length	Å
ν	Raman shift	cm^{-1}
s	Bond valence	
Sum:	Calculated total valence	
P	Pressure	atm
T	Temperature	°C
t	Time	

Greek Symbols

α-BIVOX	Face-centered orthorhombic phase
β-BIVOX	Orthorhombic phase
γ-BIVOX	Tetragonal phase
α	Monoclinic Bi_2O_3 or $BiVO_4$ phase
β	Tetragonal Bi_2O_3 or $BiVO_4$ phase
δ	Intrinsic oxygen ion vacancies
χ^2	Chi-Square; Refining parameter

Abbreviations

LTSR	Low temperature steam reforming
BIMEVOX	Metal doped bismuth vanadate
BIVOX	Parent compound $Bi_4V_2O_{11}$
BICOVOX	Cobalt doped bismuth vanadate,
BINIVOX	Nickel doped bismuth vanadate,
BICUVOX	Cupper doped bismuth vanadate,
BICOVOX_F	BICOVOX-fresh catalysts after calcination
BICUVOX_F	BINIVOX-fresh catalysts after calcination
BICUVOX_F	BICUVOX-fresh catalysts after calcination
BICOVOX_30HRS_U	BICOVOX catalysts after 30 hrs of catalytic activity
BICUVOX_30HRS_U	BINIVOX catalysts after 30 hrs of catalytic activity
BICUVOX_30HRS_U	BICUVOX catalysts after 30 hrs of catalytic activity
BICOVOX_U	BICOVOX catalysts after 150 hrs of catalytic activity
BICUVOX_U	BINIVOX catalysts after 150 hrs of catalytic activity
BICUVOX_U	BICUVOX catalysts after 150 hrs of catalytic activity
BICOVOX_Wash	BICOVOX catalyst just after preparation
BICUVOX_Wash	BINIVOX catalyst just after preparation
BICUVOX_Wash	BICUVOX catalyst just after preparation
SCS	Solution combustion synthesis
ATR	Attenuated total reflectance
POX	Partial oxidation
CPOX	Catalytic partial oxidation
APR	Aqueous phase reforming
COD	Crystallography Open Database
TGA	Thermo Gravimetric Analysis
DTA	Differential Thermal Analysis
XRD	X-ray Diffraction

SCWG	Supercritical water gasification
FTIR	Fourier Transform Infrared Spectroscopy
XPS	X-ray photoelectron spectroscopy
FESEM	Field Emission Scanning Electron Microscope
EDX	Energy Dispersive X-Ray
TCD	Thermal conductivity detector
GC	Gas chromatography
FID	Flame ionization detector
HSGC	Head space gas chromatograph
WGSR	Water gas shift reaction
IM	Impregnation
CP	Co-precipitation method
HT	Hydro-thermal method
SG	Sol-Gel method
TOS	Time-on-Stream
SSCS	Solid state combustion synthesis
DI	De-ionized
FWHM	Full width at half maximum
CI	Co-impregnation method
IWI	Incipient wetness impregnation method
RM	Reverse micro-emulsion;
IEO	International Energy Outlook
IEA	International Energy Agency

Chapter 1: Introduction

1.1 Background

Energy is a vital ingredient for all living organisms for their growth and sustainable development and also for human society as it plays a major role in the majority of economic activities. The contribution of energy industry towards economic growth can be explained in two ways (Kahia, Aïssa et al. 2017). First, it provides jobs and values by extracting, revolutionizing and distributing energy products and services and hence it works as an investor, employer and purchaser of goods into economies. Second, energy is a constituent of nearly all goods and services and is one of the most capital-consuming industries in the world (Stern 2010; Bekhet, Matar et al. 2017). Energy also contributes a reasonable share towards GDP (Gross domestic product) in most countries. In 2014, energy industries accounted for about 24.2% of GDP in India, 19.1% in Norway, 30% in Nigeria, 35% in Venezuela, and 57% in Kuwait as their economy depends on the energy export, while in the United States it was 5.9% as shown in Figure 1.1 (CERA 2012; StatisticsTimes 2017).

Indian economy is divided into three sectors; agricultural or primary sector (agriculture proper & livestock, forestry & logging, fishing and related activities), energy or secondary sector (mining & quarrying, construction, water supply, electricity, gas, and manufacturing), and services or tertiary sector (transport, trade, hotels, financial, communication and services related to broadcasting, public administration, defense, real estate, and other services). Natural resources are being utilized in the primary sector and it produces raw materials and basic goods for industries or the end-users. Therefore, it could be concluded that the primary sector recognizes as a basic sector facilitating the growth of the secondary and tertiary sectors. In the early period of civilization, excessive reliance on the primary sector is observed. However, with extreme commotion in food production, people started to turn towards industries. This led to the industrial revolution during the 19th century and rapid industrialization saw the development of the support system in the form of the service sector. Thus, the economy evolved from the primary sector to the tertiary sector gradually in phases (Prabhu 2016). The contribution of agricultural sector towards Indian GDP has decreased from 51.81 to 17.9% during 1950 to 2014 because technological advancements have led to increased dependence on energy sector by 71.4% (14 share% in 1950-51 and 24 share% in 2013-14) as shown in Figure 1.2 (StatisticsTimes 2017). In 2011, International Energy Agency (IEA 2014) had predicted that a cumulative global energy investment of US$ 38 trillion will be required by 2035 to meet the world's growing energy demand. In countries

with available energy resources, the industries can be an engine of economic recovery and development (Stern 2010; Tiba and Omri 2017).

Each energy source has its own characteristics, applications, advantages and disadvantages. The fundamental distinction among these is that few are finite whereas some are effectively perpetual or everlasting on any human scale which leads to categorization of energy resources into two groups: finite (e.g. fossil fuels and nuclear energy) and perpetual (renewable resources) as shown in Figure 1.3 (Inhaber 1979; Herzog, Lipman et al. 2001). Most of the world's energy resources are derived from the sun's rays hitting the earth's surface. Total energy balance of earth is explained in terms of energy coming in from sun and earth radiating back into space after having been distributed throughout the five components of Earth's climate system which is shown in Figure 1.4 (Jones and Nobel 2010; Stocker, Qin et al. 2013; Lindsey January 14, 2009). The total amount of energy received per second at the top of Earth's atmosphere is ~340 W/m^2. Out of that, an average of ~100 W/m^2 is reflected back to space by clouds and the atmosphere, leaving ~240 W/m^2 of solar energy input to the Earth's energy budget. Photosynthetic efficiency turns up to 2% of incoming sunlight into biomass as photosynthesis pigments absorbed ~17.5 W/m^2 solar radiation. Global mean downward and upward thermal radiations are determined to be 340.3 W/m^2 and 398.2 W/m^2 respectively. From this, it is concluded that a small amount (0.6 Wm^{-2}) is going into the subsurface, predominantly into the oceans, since the planet is not in equilibrium (Wild, Folini et al. 2013). Sun's energy has been preserved by prehistoric plants in their leaves, branches and roots. During ~650 millions of years, these plants got buried slowly under the sediments of volcanoes, river flow and ocean sources and the weight of those sediments compressed the dead plants and organisms, eventually converting them to fossil fuels by anaerobic decomposition. These fossil fuels release energy upon burning (Hubbert 1949; Morris 2015). The finite resources involve numerous organically-based fossil fuels such as coal, crude oil, oil shale, natural gas, natural bitumen & extra heavy oil, together with the non-solar nuclear energy sources such as uranium and thorium. These accessible reserves are being exhausted at a much faster rate as compared to the formation of new reserves (Scienceclarified 2017). The principal perpetual resources comprise of solar energy, wind energy, bio-energy and various forms of marine energy (tidal energy, wave energy and ocean thermal energy conversion (OTEC)) (Caillé, Al-Moneef et al. 2007).

International Energy Outlook (IEO 2016) has predicted that the world's energy demand will rise from 549 quadrillions BTU in 2012 to 815.0 quadrillion BTU in 2040, as the world population is projected to increase by 24.3% by 2040 (as the projection for world population

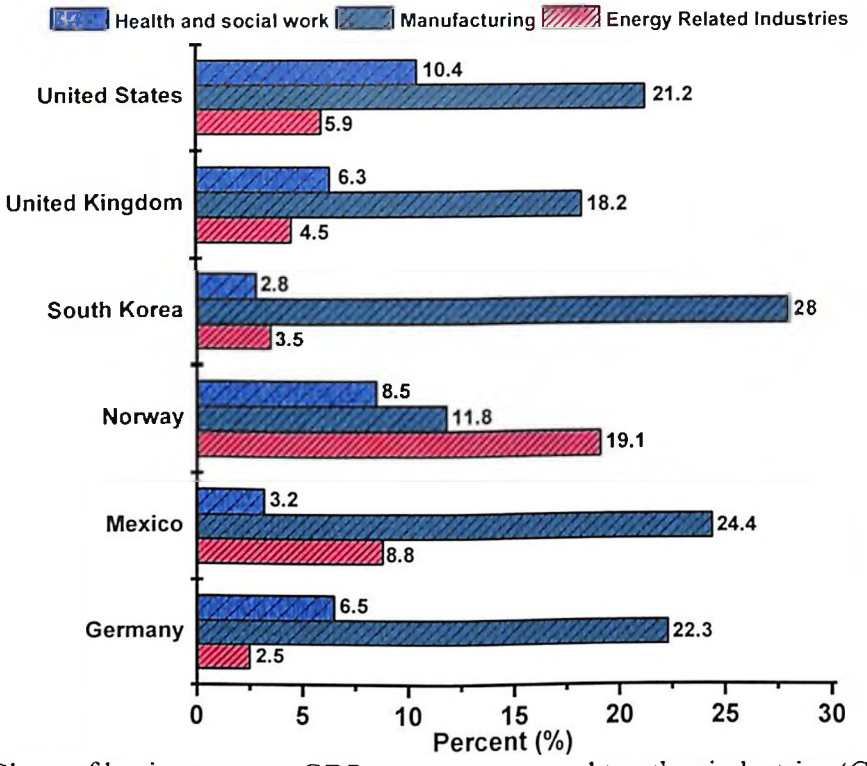

Figure 1-1: Share of business sector GDP, energy compared to other industries (CERA 2012)

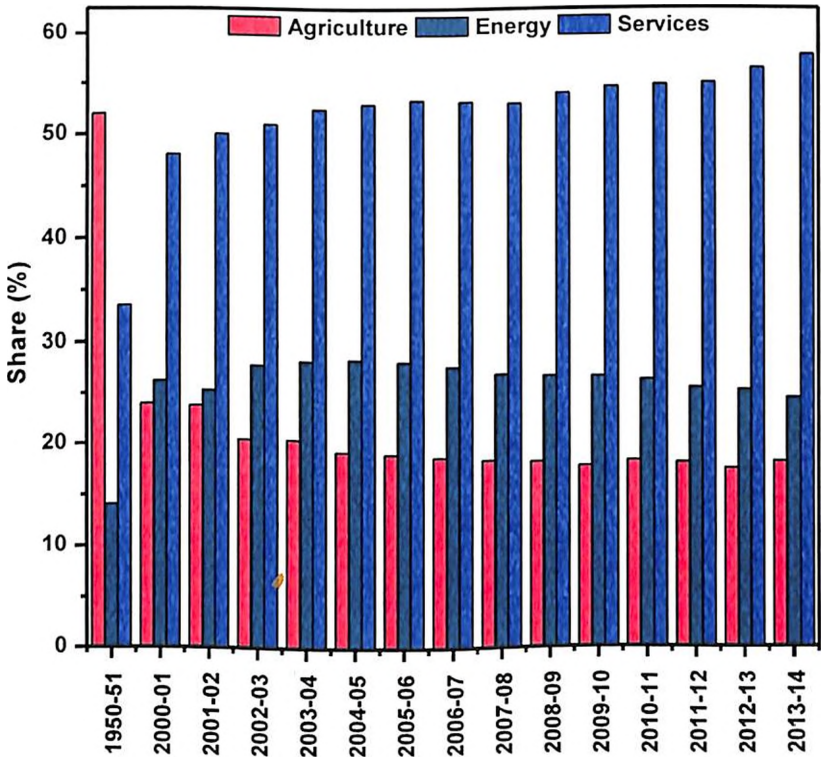

Figure 1-2: Sector wise GDP (% share) in India (Jones and Nobel 2010; Stocker, Qin et al. 2013; StatisticsTimes 2017)

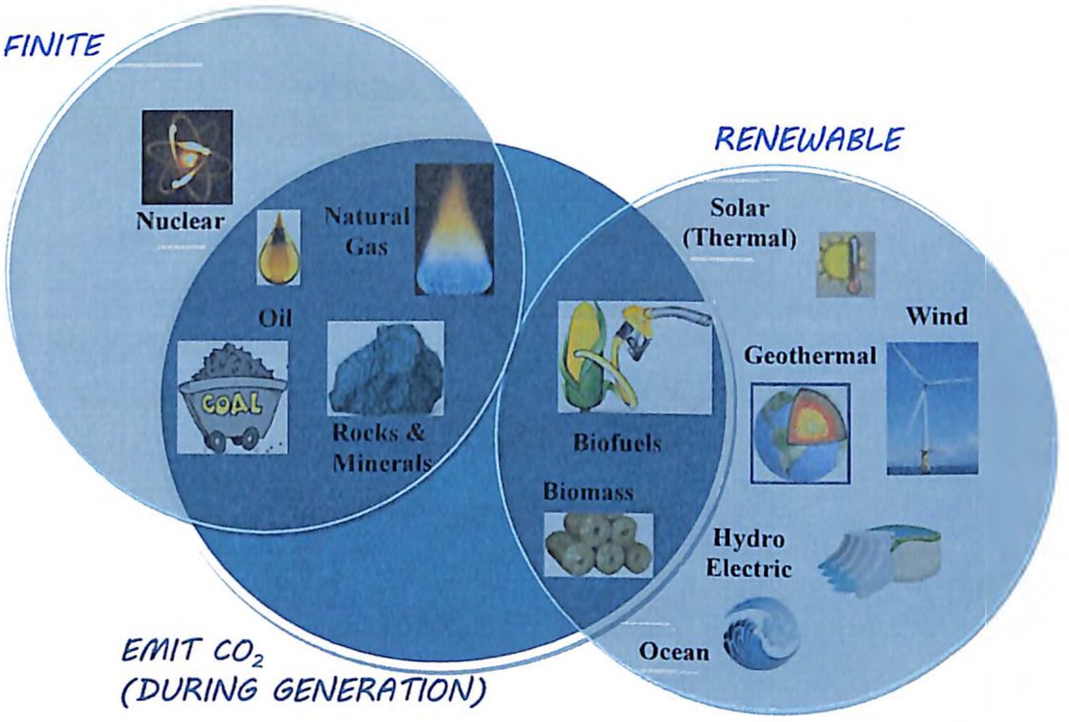

Figure 1-3: Distribution of energy resources (Inhaber 1979; Herzog, Lipman et al. 2001)

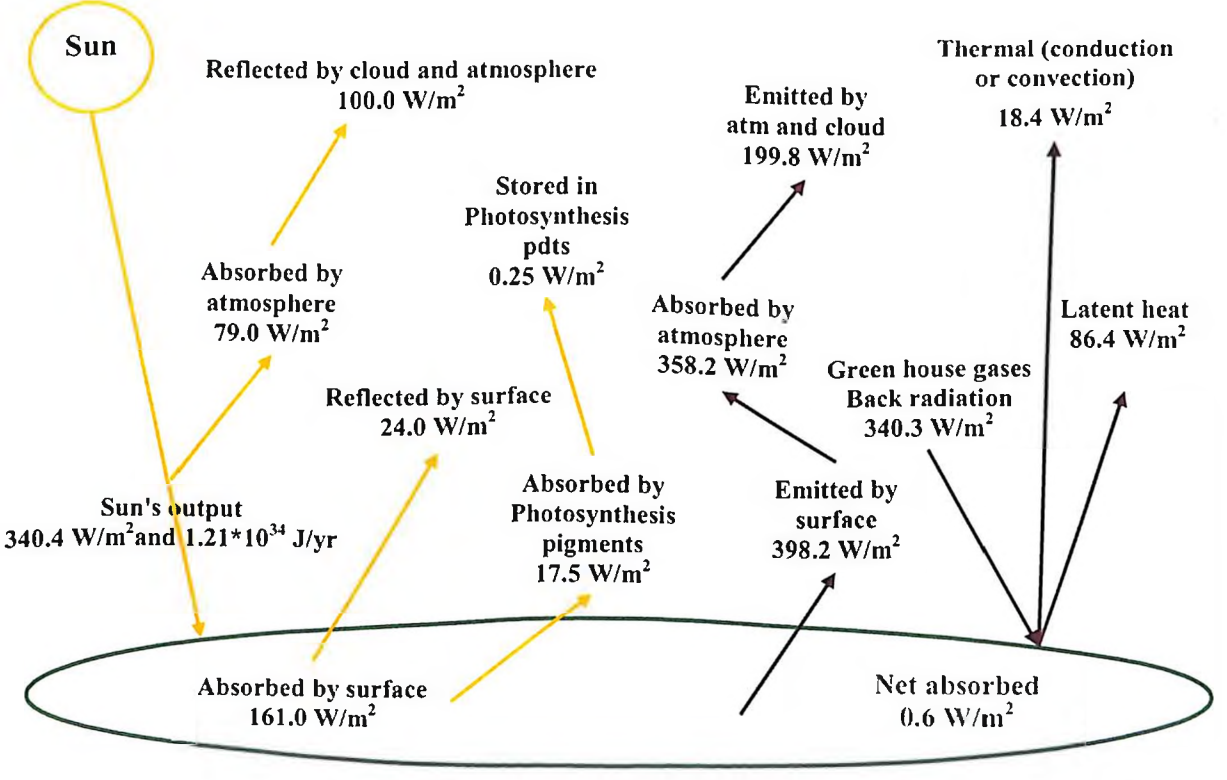

Figure 1-4: Earth's energy flow (Jones and Nobel 2010; Stocker, Qin et al. 2013; Lindsey January 14, 2009)

indicates that the 9 billion markers will be reached in 2040). In 2013, the total energy requirement for India was 185,000 MW, which is projected to increase by 53.75% by 2030. According to IEA 2015 report, India imports about 12% of the world's coal (140 million tons of coal equivalents (Mtce)). During the last 15 years, the dependence on coal has increased by ~60% which will further rise to ~100% by 2020. In 2016, India ranked third and eighth in the world in terms of primary energy consumption and production respectively; at the level of 884 Mtoe (million tonnes of oil equivalent), more than 75% of which is supplied by fossil fuels. However, India has only 0.9% of the world's oil reserves as against 5% for China, 15% for the USA and 59% for the Middle East. Hence, we have to pay a huge amount in foreign exchange to oil exporting countries (mostly the Middle East countries). Increase by merely 1US$ per barrel crude oil in the international market leads to an additional burden on India, worth Rupees 3000 crores (Conti, Holtberg et al. 2016; Sarkar, Mukhi et al. 2016). In 2014-15 India paid US$ 112.7 billion and US$ 10 billion to import 189.4 million tons of crude oil and 28.3 million tons of petroleum products, respectively. Figure 1.5 reveals India's fossil fuel distribution scenario in terms of (a) Total production-consumption and export-import data of conventional energy sources in 2014, (b) Production & consumption rate of petroleum products over 25 years from 1990 to 2015, and (c)% of petroleum products import from different countries (IEA 2015; Teske, Sawyer et al. 2015). Similar data, total energy production and consumption in India, from each source of energy is shown in Figure 1.6. It depicts that consumption rate is increasing rapidly in comparison with the production rate.

Besides becoming an economic burden, conventional energy sources, in addition to their non-renewable nature, directly lead to the huge increase in the amount of emission of the dangerous air pollutants (CO_2, SO_2, NO_x, chlorofluorocarbon, etc.) in our day to day life. A survey by the Central Pollution Control Board, India (CPCB, 2013) showed that 13 metropolitan cities in India produce 1409 kilotonnes/year of NO_x, 1.45 tons/capita of CO_2. According to WHO annual mean guidelines air quality standards are 20 $\mu g/m^3$ for the total particulate matter, and 20 $\mu g/m^3$ for SO_2 and 40 $\mu g/m^3$ for NO_2 (World Development Indicators, 2016). The total urban air pollution of SO_2 and NO_x from major cities in India are 35.4 $\mu g/m^3$ and 75 $\mu g/m^3$ in 2010 (World Development Report, 2012). The World Bank finds that environmental degradation costs India $80 billion per year or 5.7% of its economy. The acid precipitation, stratospheric ozone depletion, and global climate change are few of the horrific but direct results of the environmental pollution. Their effects on human health, agriculture, economy, and society are detrimental. The emission and harmful effects of various pollutants from fossil fuels are shown in Table 1.1. On a national scale, cotton

suffered the highest loss of 5.3 ± 3.1% followed by wheat (5.0 ± 1.2%), soybean (2.7 ± 1.9%), and rice (2.1 ± 0.9%) (Ghude, Jena et al. 2014). Estimation of economic loss for different crops due to air pollution in India is mentioned in Table 1.2. According to a health metrics and evaluation related study conducted (2016) by World Bank and Institute, health cost of air pollution in India is ~3% of its GDP. However, adding costs of lost labor due to air pollution and welfare costs puts India's GDP loss at more than 8.5%. Particulate pollution causes 109,000 premature deaths among adults, 7,500 deaths among children, 48,000 new cases of chronic bronchitis each year. Total damage to India because of environmental degradation is the US $ 80 billion (Mani, Markandya et al. 2016). Moreover, concerns about the depletion of fossil fuel reserves push the whole situation towards a worse direction.

Serious impacts of the comprehensive use of fossil fuels on human health drive the governments to modify their energy policies and also force the world scientists to think about the alternative sources of energy (Ferreira-Aparicio, Benito et al. 2005). In order to handle the energy situation, the Indian government policy is to utilize renewable energy resources like hydrogen (H_2) energy, wind, solar, nuclear, and conversion of municipal waste. Clean, domestic and renewable energy is commonly accepted as the key for future life. The renewable sources collectively provide ~18% of the world's total energy demand. Traditional biomass constitutes the major part of it and hydropower stations also play a major role as they provide ~20% of the global electricity (Global energy statistical yearbook, 2017). Nuclear energy shares 11% of the total energy and other renewable energy sources (modern bio-energy, geothermal energy, solar energy, small hydropower, and wind energy) are currently contributing ~2% (Herzog, Lipman et al. 2001). The World Energy Council (London, UK) expects the world primary energy consumption to have grown by 50-75% (from 546 EJ in 2010) in 2050, depending on different scenarios. The renewable energy sources are expected to provide 20–40% of the primary energy in 2050 and 30–80% in 2100. The industrial potential of the renewable sources has been estimated at 7600 EJ/year, which is certainly sufficiently high enough to meet future world's energy requirements (Fridleifsson 2003). Bioenergy shares 10% of the global energy supply that makes it the largest contributor to the renewable energy resources (Conti, Holtberg et al. 2016).

1.2 Motivation

Biomass energy offers a promising alternative to fossil fuels and contributes to accomplishing global energy demand by providing environmental benefits, opportunities for

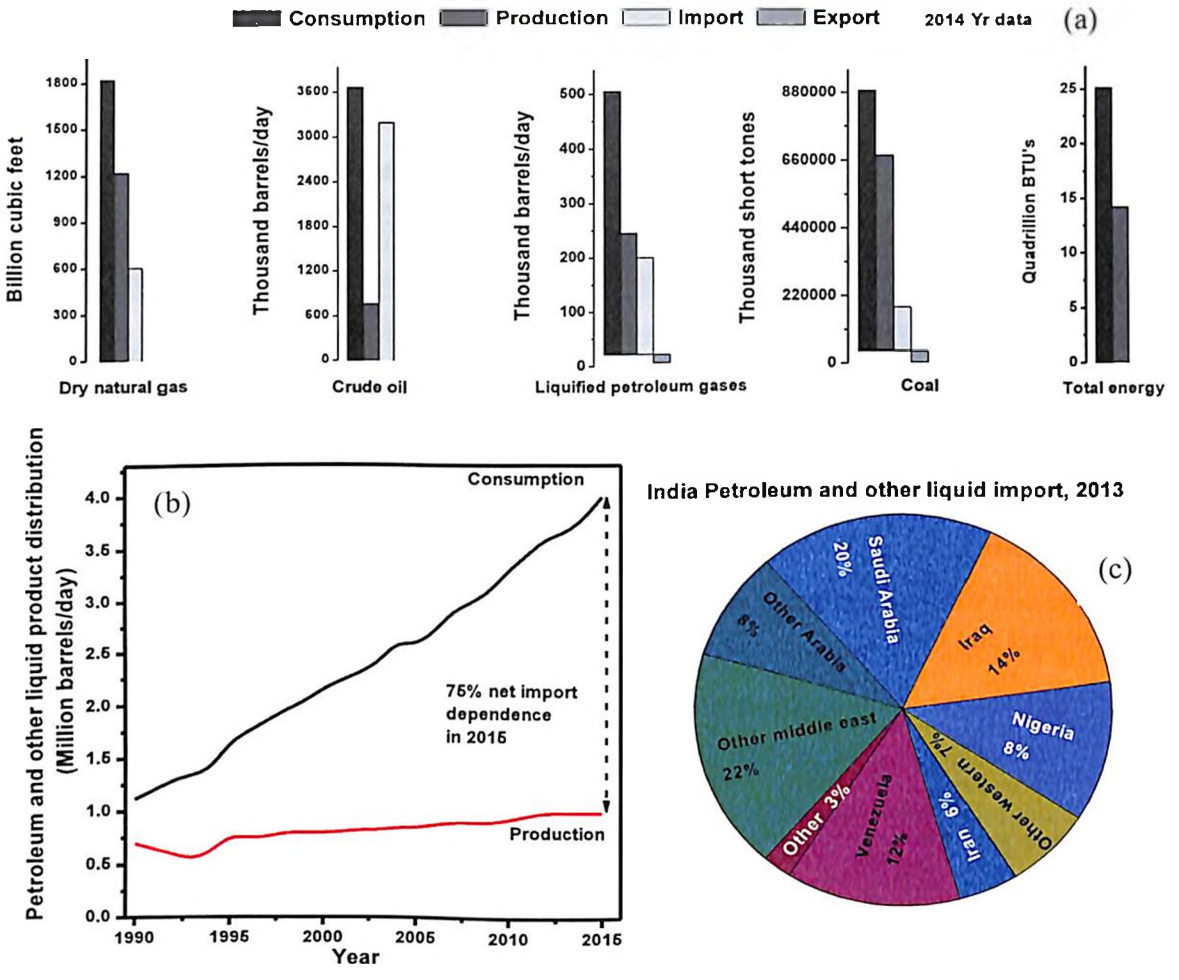

Figure 1-5 : India's fossil fuel distribution scenario in terms of (a) Total production-consumption and export-import data of conventional energy sources in 2014, (b) Production & consumption rate of petroleum products over 25 years from 1990 to 2015, and (c)% of petroleum products import from different countries (IEA 2015; Teske, Sawyer et al. 2015)

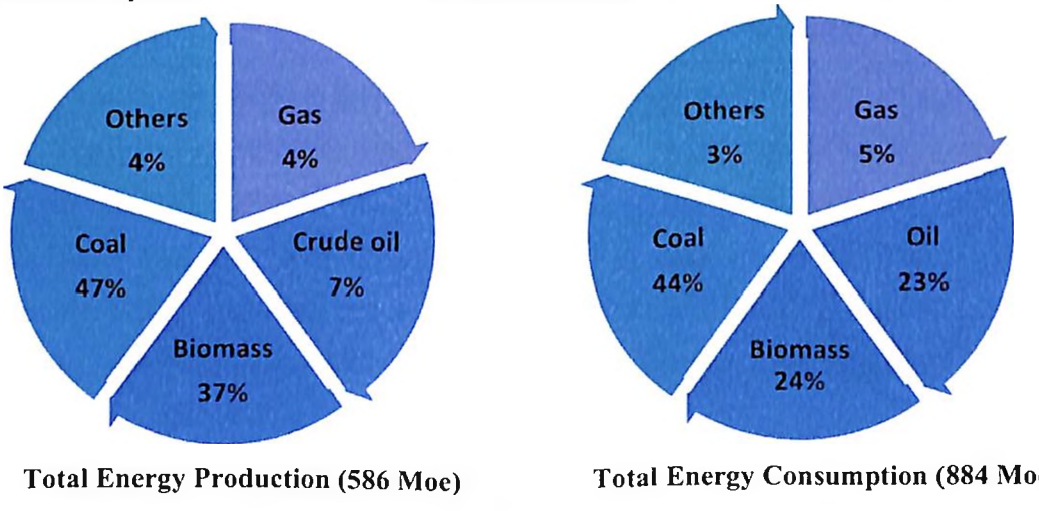

Figure 1-6 : Source-wise energy production and consumption in India, 2016 (Teske, Sawyer et al. 2015)

Table 1-1: The emission and harmful effects of various pollutants from fossil fuels (Sieminski 2014)

Fuel	Pounds of CO_2 emitted per million Btu of fuel	Emission of other pollutants (Pounds per Billion Btu of fuel)	Harmful effects
Coal (anthracite)	228.6	2591 - SO_2, 457 - NO_x, 2744-particulate 0.016 -murcury, 220 tons VOC's, 225 pounds arsenic, and 114 pounds of lead	Acid rain, Respiratory illnesses, lung disease, neurological and developmental damage
Coal (bituminous)	205.7		
Coal (lignite)	215.4		
Coal (subbituminous)	214.3		
Diesel fuel and heating oil	161.3	448- NO_x, 1122-SO2, 84- particulate	Respiratory diseases, such as emphysema or bronchitis, heart disease
Natural gas	117.0	92- NO_x, 1-SO_2, 7- particulate	Asthma, bronchitis, lung cancer, and heart disease

Table 1-2: Estimates of economic loss for different crops due to air pollution in India (Ghude, Jena et al. 2014)

Commodities	Production (million tone)	Loss (million tone)	Fraction loss (%)	Economic damage (billion USD)
Soyabean	8.6	0.23 (±0.16)	2.7 (±1.9)	0.06 (±0.12)
Cotton	3.3	0.1 (±0.10)	5.3 (±3.1)	0.07 (±0.04)
Wheat	71	3.5 (±0.8)	5.0 (±1.2)	0.62 (±0.15)
Rice	95.1	2.1(±0.8)	2.1(±0.9)	0.54 (±23)

social and economic development in rural and urban communities, along with the improved management of resources and wastes (Bioenergy 2009). Presently, biomass is a one of the major contributors to renewable energy which primarily is derived from the carbonaceous waste of various human and natural activities and includes agricultural crops, raw materials from forest, paper and wood mills sawdust, animal dung, sewage waste, grasses, municipal solid waste, food processing industries, landfill disposals and major parts of household waste and food (Demirbas 2009; Stern 2010; Conti, Holtberg et al. 2016; Milbrandt, Bush et al. 2016; Timmons, Buchholz et al. 2016).

Biomass is a versatile energy source that can be used for the production of heat, power, and transport fuels, apart from making a significant contribution to climate change mitigation (Berndes, Abt et al. 2016). The biomass to bioenergy network can be considered as the management of the flow of solar-generated materials, food, and fibre in our society. These interrelationships are depicted in Figure 1.7, which shows the numerous resource types and their applications, showing the flow of their harvest and residues to bioenergy applications (Yue, You et al. 2014; Zhang 2014). All biomass cannot directly be used to generate energy but rather they are converted into some intermediate energy carriers, called biofuels (ethanol, producer-gas, charcoal, etc.).

One of the most important characteristics of biomass is carbon neutrality i.e. CO_2 produced during biomass combustion is balanced by the CO_2 removed from the atmosphere via photosynthesis to grow biomass and thus, carbon dioxide is not accumulated as long as biomass is reproduced. This clears up space, reduces dumping issues associated with trash and more importantly, this is a part of a continuous recycling chain (Muradov and Veziroğlu 2011).

The net energy produce from biomass after combustion falls in the range from ~ 8 MJ/kg for green wood to 20 MJ/kg for dry plant matter, while it is ~27 MJ/kg in case of coal (Demirbas 2002). Alternative World Energy Outlook has calculated that biomass production rises from 1032 Mtoe in 2005 to 1650 Mtoe in 2013. In 2016, 10,233 trillion Btu of renewable energy was produced, out of which 4,829 trillion Btu was produced from biomass. The total consumption was 10,164 trillion Btu, out of which 4,760 trillion Btu was consumed from biomass energy.

Currently, the predominant use of biomass is for non-commercial applications (eg. domestic heating and cooking) in developing countries. Worldwide, ~70%, 10% and 4% of the primary energy are supplied by woody biomass (branches and twigs, wood chip and

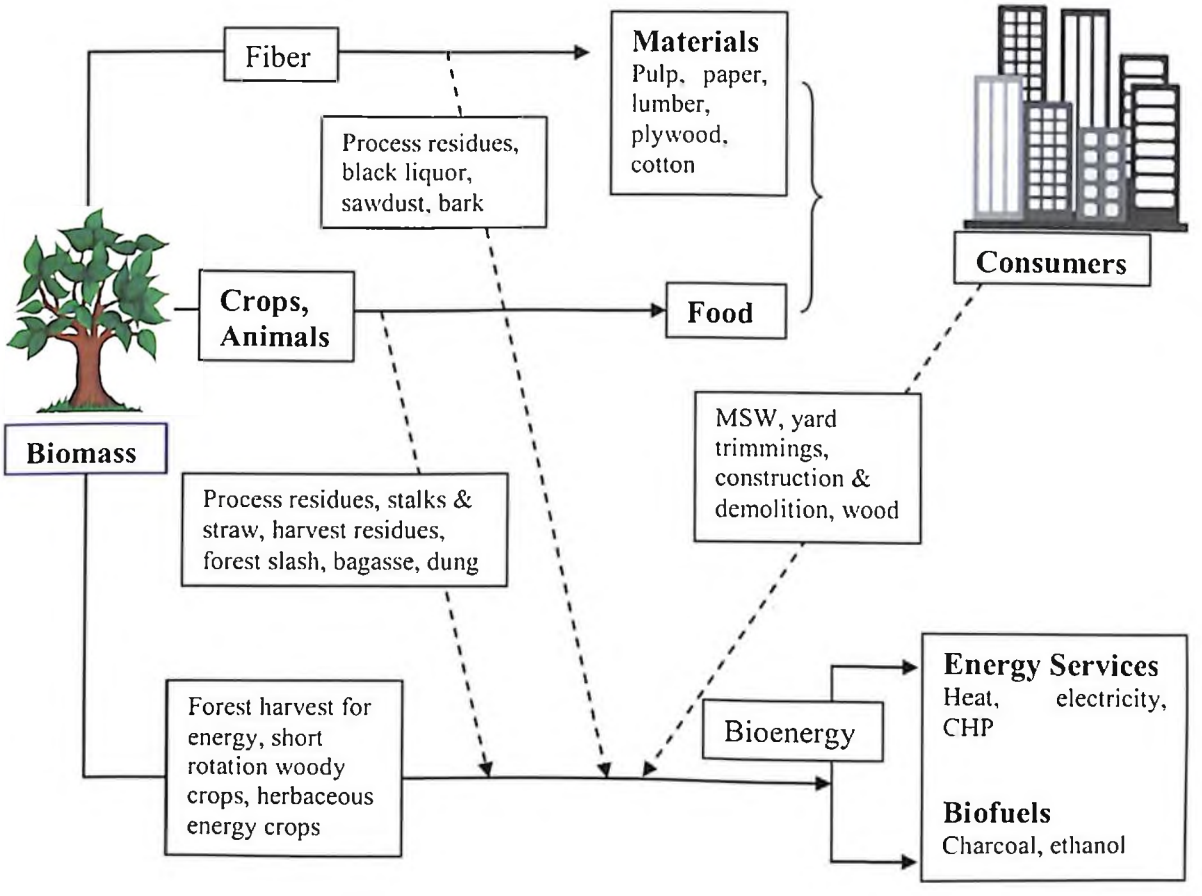

Figure 1-7: Biomass and bioenergy flow chart (Herzog, Lipman et al. 2001)

bark), charcoal and bioethanol respectively, as shown in Figure 1.8. USA and Brazil lead the world in terms of production and consumption of liquid biofuels. In Europe and American continents, 70% consumption of biomass is for the electricity production. In 2013, 462 TWh of electricity was produced globally from biomass (Owusu and Asumadu-Sarkodie 2016).

Biomass fuels in India account for about one-third of the total fuel used in the country. India produces about 450-500 million tons of biofuel every year. EIA, 2013 report estimates that 18000 MW of electricity was produced from biomass in India. However, a big portion of biomass (~ 70%) is used directly for household cooking and heating. The current share of biofuels in total fuel consumption is extremely low and is confined mainly to 5% blending of ethanol in gasoline (Fridleifsson 2003; Meier, Vagliasindi et al. 2014; Conti, Holtberg et al. 2016). Currently, Indian fuel market is not selling the bio-diesel, but the government is planning to meet 20% of the country's diesel requirements by 2020 using biodiesel. Energy from biomass needs to be increased to fulfil the future requirements.

Another factor in terms of industrial application is that biomass energy technology is inherently flexible; as it could be applied at a small, localized scale primarily for heat generation, or some could be used in much larger base-load power generation capacity. Biomass generation can thus be tailored to rural or urban environments, and utilized in domestic, industrial applications, or commercial (Davda, Shabaker et al. 2005). The original form of biomass can be used directly as a fuel or it can be refined in gas, solid and liquid biofuels like biogas, bioethanol, halomethane, sorbitol, glucose, hydroxymethylfurfural, gasoline, hydrogen or hydrocarbon fuels etc, according to the required applications. Hydrogen produced from biomass is carbon neutral unlike hydrogen produced from fossil fuel conversion (Huber, Iborra et al. 2006). Different biomass materials used for hydrogen production are mentioned in Table 1.3.

1.3 Scope of the work

Hydrogen, produced from renewable biomass instead of non-renewable fossil fuel sources, is an alternative source or carrier of environmentally clean renewable energy (Zerta, Schmidt et al. 2008). Currently, most of the hydrogen (>90%), is harvested from fossil fuels like petroleum oil, coal and natural gas. Only 4% and 1% is generated from water using electricity and biomass, respectively (Kathe, Empfield et al. 2016; Bailera, Kezibri et al. 2017). In 2017, expected production of the total hydrogen is 115.25 Billion US$ and is forecasted to be 154.74 Billion US$ by 2022, with a growth rate of 6.07% per year.

Worldwide ~ 65 M metric tons of hydrogen is produced annually, out of which ~31.2 and 27.95 M metric tons are consumed by petroleum refining and chemical sector, respectively (Satyapal, Petrovic et al. 2007; Demirbas 2009). Hydrogen production from diverse sustainable resources (wind, solar, biomass) is ~ 1 M metric tons/year and is expected to reach >150 M metric tons/year by 2040 (Milbrandt, Bush et al. 2016; Randolph, Miller et al. 2017).

In India, ~ 95% of the hydrogen produced presently comes from natural gas and coal and the rest is produced from biomass and electrolysis of water (Sieminski 2014). ~66000 tons of hydrogen was produced as a by-product from different oil refineries in 2014 (Wu, Chung et al. 2015). Consumption of hydrogen in India is dominated by the chemical sector to produce ammonia and methanol and that accounts for ~90% of hydrogen consumption. Only a small fraction of total H_2 production (~8%) is consumed as the primary energy source with an estimated growth of 5-10% per year (Mohan, Bhaskar et al. 2007; Wu, Chung et al. 2015). Hydrogen market in India is forecast to reach 365 million US$ by 2022, which was 200 million US$ in 2016 (TechSciResearch 2018).

Hydrogen is being explored for use in combustion engines, turbines, fuel cell electric vehicles, rocket fuel, treating metals, petrochemical industries, producing fertilizer, processing foods, hydrogen-powered submarines and ships. It can be considered the most environment friendly potential fuel to generate electricity with no pollutants and CO_2 emission although it produces water which can be released and recycled as shown in Figure 1.9 (Nath and Das 2003; Nath and Das 2004). It has the highest energy content (34 kcal/gm) per unit weight of all the fuels; three times the energy of the same mass of gasoline (~10.3 kcal/gm) (Cortright, Davda et al. 2002; Davda, Shabaker et al. 2005). Hydrogen can be produced from a vast range of conventional and alternative energy resources such as natural gas, coal, biomass, etc. using various production technologies.

Hydrogen as a fuel can be used directly in an internal combustion engine not much different from the engines used with gasoline (Balat and Kırtay 2010). It has extensive limits of flammability in air (4%–75% by volume) than gasoline (1%–7.6% by volume) and methane (5.3%–15% by volume), higher specific heat at constant pressure (14.89 J/kg.K) than gasoline (1.20 J/kg.K) and methane (2.22 J/kg.K), higher flammable temperature (585°C) than gasoline (228-471°C) and methane (540°C), lower flame temperature in air (2045 °C) than gasoline (2197°C) and higher diffusion coefficient in air (0.610 cm^2/sec) than gasoline (0.05 cm^2/sec) and methane (0.16 cm^2/sec) (Momirlan and Veziroglu 2005; Balat and Kırtay 2010; Nicoletti, Arcuri et al. 2015). Thus, one can consider H_2 as a good fuel for

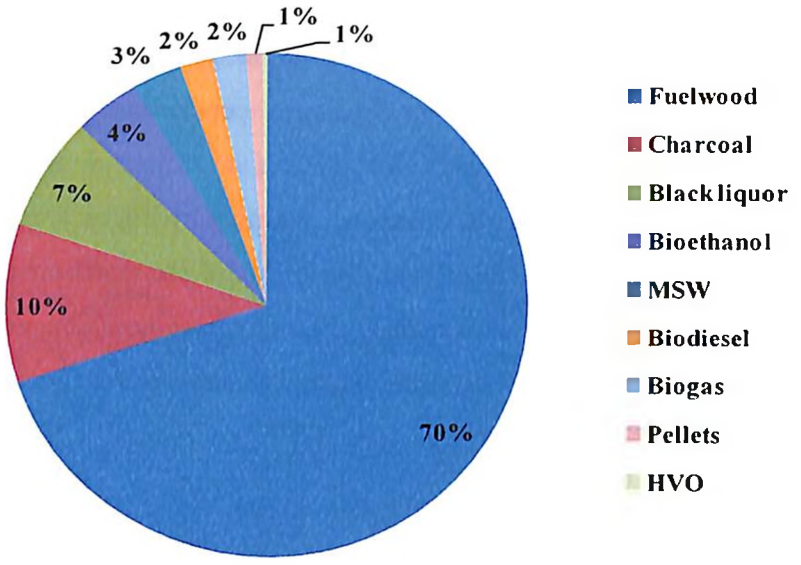

Figure 1-8 : Primary energy supply of biomass resources (Owusu and Asumadu-Sarkodie 2016)

Table 1-3 : Hydrogen production from ethanol studies incorporating different catalysts (examples: Fe_2O_3, dolomite, nickel based catalyst, etc. at low temperature range (Comberbach and Bu'Lock 1982; Bimbela, Chen et al. 2012; Elbaba and Williams 2013)

Biomass Species	Conversion process
Bio-nut shell	Steam gasification
Crop straw	Pyrolysis
Olive husk	Pyrolysis
Municipal solid waste	Supercritical water extraction
Oxygenated biomass (alcohols)	Reforming
Pulp and paper waste	Microbiol fermentation
Tea waste	Pyrolysis
Crop grain residue	Supercritical water extraction

applications. Properties of hydrogen are mentioned in Table 1.4.

The contribution of hydrogen energy to the world energy economy needs to grow which requires the technological innovations for hydrogen production from biomass; so that biomass can be converted to usable energy in ways that are more efficient, more economical and less polluting as today's practices. Challenges regarding hydrogen production technology are lowering the cost of production at least by a factor of 3-4 and improving production rates. A large number of technological processes are there to produce hydrogen including chemical, biological, electrolytic, photolytic and thermo-chemical and we are discussing them in the following subsections.

1.3.1 Overviews of hydrogen production technologies

Hydrogen can be produced from the vast range of feedstocks, including fossil fuels and biomass. Biomass can be converted to various forms of energy mainly by two types of processes: 1) Thermo-chemical and 2) Biochemical. In thermo-chemical conversion processes, biomass breaks down into its constituents like bio-fuels, gases and chemicals by applying heat and pressure (Hua, Ahluwalia et al. 2014). Combustion, gasification, pyrolysis, liquefaction, steam reforming and aqueous phase reforming, etc. processes are the different types of thermo-chemical processes. In biochemical processes living organisms decompose the biomass into biofuels and other side products. Fermentation, photosynthesis, biological water gas shift reaction, enzymatic processes are the main types of biochemical processes as shown in Figure 1.10 (Dunn 2002; Stein, Edwards et al. 2009; Balat and Kırtay 2010).

Biological processes for hydrogen productions are established to be more environments friendly and less energy intensive in comparison with the other techniques. Bio-hydrogen as a side-product from microorganism metabolism is emerging as an exciting developing area of technology advancement that suggests the generation of usable hydrogen from a variety of renewable resources (Balat and Kırtay 2010). There are three types of microorganisms of bio-hydrogen generation: cyano-bacteria, anaerobic bacteria, and fermentative bacteria. The production of hydrogen from biomass by fermentation is one of the routes that can contribute to a future sustainable hydrogen economy. The amount of hydrogen produced from glucose is affected by fermentation pathways and liquid end-products (Ren, Li et al. 2006). Theoretically, 4 mol of hydrogen is produced from 1 mol of glucose in acetate type fermentation; however, only 2 mol of hydrogen is produced when butyrate is the main fermentation product. Many studies have been performed on fermentative hydrogen generation from feedstocks, such as byproducts from the food industry, and agricultural

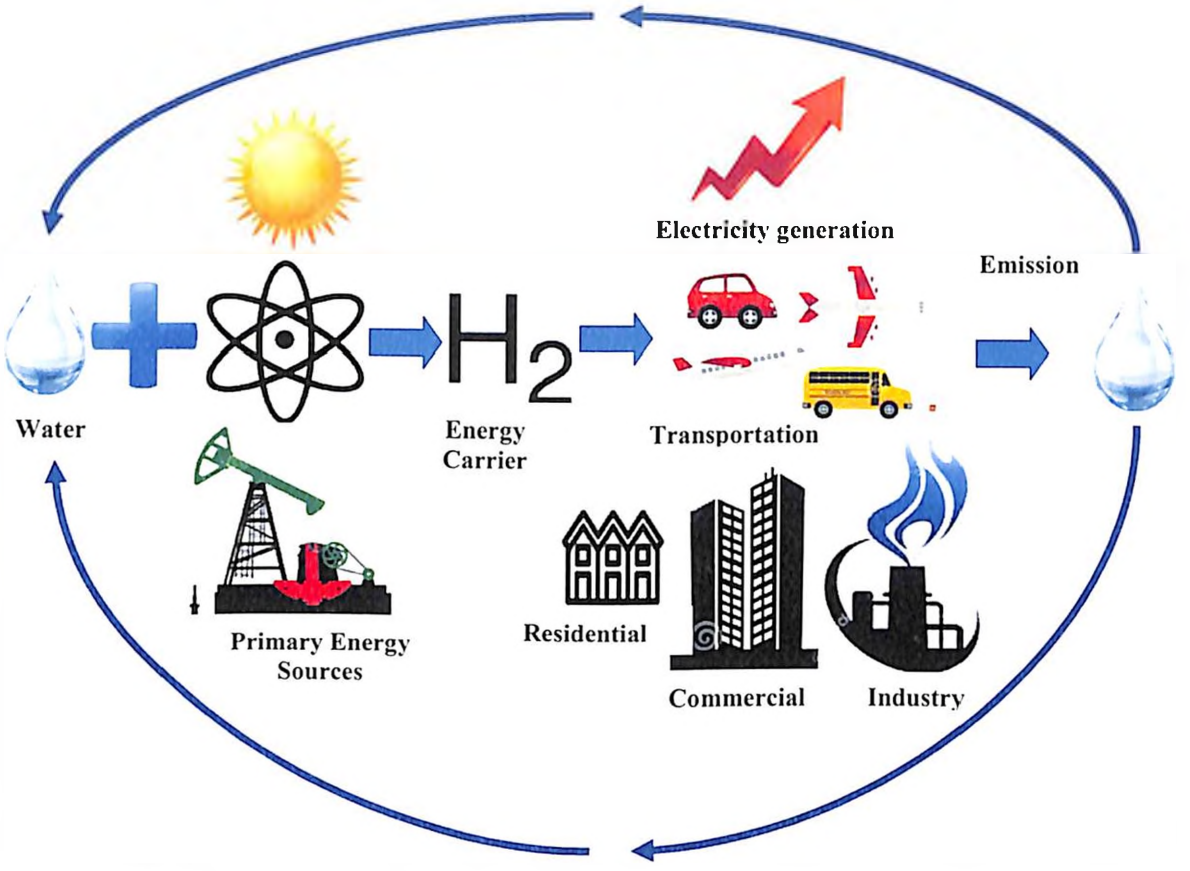

Figure 1-9 : Hydrogen energy system cycle (Nath and Das 2003; Momirlan and Veziroglu 2005; Stocker, Qin et al. 2013)

Table 1-4: Properties of Hydrogen

Property	Characterstics
Melting point	-259.16°C
Boiling point	-252.879°C
Density	0.000082 g /cm^3 (The lowest of any chemical element)
Appearance	Colorless in nature
Miscibility	Slightly soluble in water, alcohol and some other common liquids
Phase	Gaseous form Hydrogen changes from a gas to a liquid at a temperature of -252.77°C(-422.99°F) It changes from a liquid to a solid at a temperature of -259.2°C (-434.6°F)
Odor	Odorless
Reactivity with non-metals	It combines readily with non-metals, such as sulfur and phosphorus It combines readily with the halogens which include fluorine, chlorine, bromine, iodine, and astatine
Flammability	Highly Flammable, a highly combustible diatomic gas
Combustion	When mixed with air and with chlorine it can spontaneously explode by spark, heat or sunlight.

municipal waste, or wastewaters and from pure sugars (Nath and Das 2003). Anaerobic digestion of solid organic waste such as agricultural and municipal wastes and wastewater sludge is one of the renewable sources for H_2 production. However, perpetual hydrogen generation form this process has few limitations, one of them is the low yields of hydrogen and another one is that they are very slow kinetic processes. In addition, fermentative hydrogen production processes generate some fatty acids (lactic acid, acetic acid, butyric acid, etc). Separation of these acids is required to avoid water pollution problems (Das and Veziroğlu 2001). Reduced production rate per unit of capital investment is the major challenge with aerobic digestion for hydrogen generation (Dincer 2012). All these factors make them less attractive for industries as compared to the thermo-chemical processes. Different thermo-chemical methods are discussed in the following subsections.

1.3.1.1 *Biomass gasification*

It is a process of converting the organic or fossil-based carbonaceous material into a gaseous fuel mixture called producer gas (H_2, CO, CO_2, CH_4), char and tar by partial oxidation at high temperature (700 -1000°C) in the presence of a gasifying agent (oxidizing agent- air, steam, CO_2 or a combination of these). Gasification of biomass is generally observed to follow the reaction:

$$\text{Biomass} + O_2 \text{ (or } H_2O) \rightarrow CO, CO_2, H_2O, H_2, CH_4 + \text{other hydrocarbons} + \text{tar} + \text{char} + \text{ash} \quad (1.1)$$

The gaseous products obtained at the outlet of the gasifier can be reformed in a second reactor to produce fuels such as methanol and hydrogen. Obtained hydrogen could then be applied directly in fuel cells for production of electricity (Balat and Kırtay 2010). Gasification involves drying, pyrolysis, oxidation and reduction reactions. Gasification of biomass combined with water-gas shift reaction in the same reactor is the most common and widely used technology for hydrogen production. Here, by applying heat under pressure in the presence of steam and a controlled amount of oxygen, biomass can be converted into primarily a gaseous mixture of CO, CO_2, and H_2. The carbon monoxide then reacts with water to form carbon dioxide and produce more hydrogen by water-gas shift reaction. Absorbers or special membranes are used to separate the hydrogen from this gas stream.

However, one major issue with biomass gasification is to deal with the tar formed during the process. Tar is a complex mixture of condensable aromatic compounds which condenses at reduced temperature in exit pipes, heat exchangers or on particulate filters, and thus causes blocking and fouling of process equipment such as engines and turbines

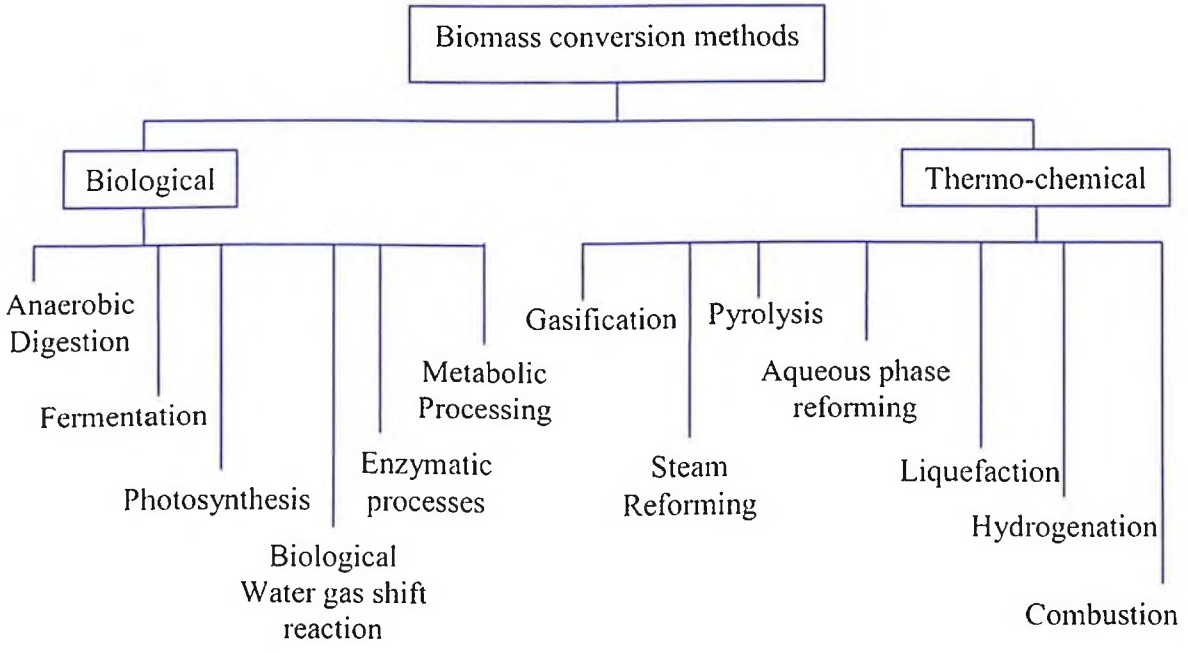

Figure 1-10 : Biomass conversion processes

(Devi, Ptasinski et al. 2003). This can lead to a decrease in total efficiency and an increase in the cost of the process (Świerczyński, Libs et al. 2007). Tar reduction can be done by heat treating it at high temperature (1200°C) and using catalysts (Ni-based catalysts Ni/MgO, alkaline metal oxides, Fe oxide, $Rh/CeO_2/M$ (M = SiO_2, Al_2O_3, and ZrO_2 etc.) or additives (dolomite, olivine, char etc.) (Holladay, Hu et al. 2009; Nordgreen, Nemanova et al. 2012). Catalysts not only reduce the tar content but also improve the gas product quality and conversion efficiency (Ni, Leung et al. 2006; Ni, Leung et al. 2007). Another problem of biomass gasification is the formation of ash that may cause deposition, sintering, slagging, fouling and agglomeration of catalysts (Asadullah, Ito et al. ; Ni, Leung et al. 2006; Balat and Kırtay 2010). The heating value of producer gas during gasification of solid biomass is in the range of 4.5-6.34 MJ/Nm^3 (Hollingdale, Breag et al. 1988; Zainal, Rifau et al. 2002; Sheth and Babu 2009). The gasification reaction of toluene with water gas shift reaction can be written as (Świerczyński, Libs et al. 2007):

$$C_7H_8 + 7H_2O \rightarrow 7CO + 11H_2; \quad \Delta H_{900°C} = 876\ KJ/mol \tag{1.2}$$

$$CO + H_2O \rightarrow CO_2 + H_2; \quad \Delta H_{900°C} = -33\ KJ/mol \tag{1.3}$$

1.3.1.2 *Pyrolysis*

The thermal decomposition of biomass in the absence of oxygen is known as pyrolysis of biomass. In pyrolysis, generally, we see three kinds of end products: solid (charcoal), liquid (tar and other organic liquid like bio-oil, methanol) and gases (CO, CO_2, some hydrocarbons, and H_2). Pyrolysis generally starts at 300°C and continues up to 500–800°C and the heating value of the producer gas during the process is in the range of 3.5 -8.9 MJ/m^3 (Ni, Leung et al. 2006). Pyrolysis is divided into two categories; the first one is slow or conventional pyrolysis and the other one is fast pyrolysis. Slow pyrolysis maximizes the char (35%) with the relatively smaller amount of fuel gas (40%) resulting from biomass and operates at low temperature (400-600°C), low heating rate, short gas residence time. On the other side, the fast pyrolysis maximizes the yield of fuel gas (70%) with the production of the small amount of char (20%) and operates at high temperature (650-800°C) (Demirbas 2007; Liu, Wang et al. 2014). The general Equation for fast pyrolysis is:

$$\text{Biomass} + \text{heat} \rightarrow H_2 + CO + CH_4 + \text{other products} \tag{1.4}$$

However, the major issue with the pyrolysis unit is the lack of consistency and long-term stability of the bio-oil (ageing reactions can happen e.g., polymerization, esterification,

acetalization, oxidization, and dimerization) which tends to degrade over time which further creates the economic and technical issues around quality (Bioenergy 2009).

1.3.1.3 *Partial oxidation*

Partial oxidation (POX) and catalytic partial oxidation (CPOX) have been suggested for hydrogen production (Krummenacher, West et al. 2003). POX is a non-catalytic thermo-chemical process for the conversion of raw material (methane, biogas, heating oil etc.) to syngas in the presence of oxygen and steam at temperatures and pressure in the range of 1300–1500°C and 3–8 MPa, respectively. Reactions taking place during partial oxidation of methane are (Kalamaras and Efstathiou 2013):

$$CH_4 + O_2 \rightarrow CO + 2H_2; \qquad \Delta H_{298°C} = -35.7\ KJ/mol \tag{1.5}$$

$$CH_4 + 2O_2 \rightarrow CO_2 + 2H_2O; \qquad \Delta H_{298°C} = -890.3\ KJ/mol \tag{1.6}$$

$$CH_4 + H_2O \rightarrow CO + 3H_2; \qquad \Delta H_{298°C} = 205.9\ \text{KJ/mol} \tag{1.7}$$

The obtained gaseous product is a mixture of CO, CO_2, H_2O, H_2 and CH_4. From an economic point of view, partial oxidation is more expensive than steam reforming (Lutz, Bradshaw et al. 2004). The catalyst can be added in the partial oxidation to lower the operating temperature (700–1000°C). Catalytic partial oxidation (CPOX) is a relatively inexpensive alternative to syngas generation. The exothermic nature of the reactions makes it difficult to control temperature (Kim, Kim et al. 2004). It leads to coke deposition and hot spot formation, which as a consequence deactivate the catalysts in long run. Some other critical challenges with partial oxidation of fuels are control of fuel combustion in the vaporizer/pre-heater section due to lower auto-ignition temperatures and creation of a homogeneous mixture of air and fuel after vaporization of the liquid (Cheekatamarla and Finnerty 2008).

1.3.1.4 *Aqueous phase reforming*

Aqueous phase reforming (APR) is one of the catalytic methods for hydrogen production from oxygenated hydrocarbons or aqueous carbohydrates. It operates at relatively high pressure (25-30 MPa) and low temperature (220 to 270°C) where the feed is in the condensed phase. APR has shown reduced energy consumption as it eliminates the energy-intensive vaporization (for water at its normal boiling point of 100°C, the heat of vaporization is ~ 2260 J/g) of biomass-water mixtures (Davda, Shabaker et al. 2003; Davda, Shabaker et al.

2005). Additionally, the typical operating pressure and low-temperature conditions for APR prove to be helpful for the separation of H_2 and CO_2 from other products that are volatile at atmospheric pressure. Additionally, APR is beneficial for producing H_2 for a fuel cell with a very small amount of CO in a single reactor as a consequence of the water gas shift (WGS) reaction is thermodynamically approved at lower temperature reaction condition (Huber, Iborra et al. 2006). However, methanation and Fischer-Tropsch reactions are also favoured under the moderate temperature and pressurized APR conditions which results in the formation of alkanes as by-product (Li, Li et al. 2016). The reforming reaction of glycerin can be written as (Luo, Fu et al. 2008):

$$C_3H_5(OH)_3 + 3H_2O \rightarrow 3CO_2 + 7H_2\,; \quad \Delta H_{298°C} = 205.29\ KJ/mol \tag{1.8}$$

1.3.1.5 *Steam reforming*

Steam reforming is one of the most extensively used and at the same time least expensive methods for hydrogen production from a vast range of feedstock like coal, natural gas, bio-ethanol, methanol, glycerol, ethylene glycol, methane, biodiesel, etc. The obtained product is a mixture of H_2, CO, CO_2 and CH_4. In the current scenario, feedstock more often used for steam reforming are aqueous oxygenated hydrocarbons and hydrocarbons (Haryanto, Fernando et al. 2005; Balat and Kırtay 2010; Moretti, Storaro et al. 2015).

$$C_nH_mO_k + (2n-k)H_2O \rightarrow nCO_2 + \left(2n + \left(\frac{m}{2}\right) - k\right)H_2 \tag{1.9}$$

$$C_nH_m + (2n)H_2O \rightarrow nCO_2 + \left(2n + \frac{m}{2}\right)H_2 \tag{1.10}$$

Its advantage arises from the high efficiency in terms of hydrogen production, and high conversion of feed but produces more amount of CO (Ebshish, Yaakob et al. 2012; El Doukkali, Iriondo et al. 2014). In steam reforming reaction, hydrogen evolves at a high temperature (600-1200°C) and these industrial reaction conditions increase the production cost and not feasible for energetic purposes (Ebshish, Yaakob et al. 2012; Xu, Liu et al. 2013; Trane-Restrup, Dahl et al. 2014). This process comprises of two stages. In the first stage, the hydrocarbon raw material is mixed with steam and passes over the catalyst which is placed inside the tubular reactor where the production of syngas takes place with low content of CO_2 (Song, Zhang et al. 2007). Later in the second stage, the cooled product gas is inserted into the CO catalytic converter, where conversion of carbon monoxide into carbon dioxide and hydrogen to a large extent takes place by means of steam (Muradov and Veziroğlu 2005).

From past 20 years, researchers are working on low-temperature steam reforming to produce H_2 from biomass at mild operating condition ($\leq$ 500°C), with significant advantages such as low operational, material cost and a small amount of CO in comparison with the high-temperature steam reforming. Marino et al. (1998), first time report the low-temperature steam reforming of ethanol for hydrogen production over Cu-Ni supported catalyst (Mariño, Cerrella et al. 1998). Furthermore, the temperature condition applied favours the water gas shift reaction and no extra step to separate CO from H_2 is required which also reduces the capital cost (Dan, Mihet et al. 2011; Giaconia, Turchetti et al. 2013; Dan, Mihet et al. 2015).

1.4 Catalysts for hydrogen from steam reforming of ethanol

The rates of several reactions are affected due to an additional substance which is neither reactant nor product; such materials are known as catalysts. They can speed up the reaction rate by a factor of a million or more and sometimes they may slow the reaction rates. The most important role of catalyst is its selectivity; as it can alter the rates of certain reactions, or a single reaction leaving the rest unaffected. Catalyst is involved in most of the industries for chemicals production (petroleum refining for alkylation, catalytic cracking, naphtha reforming, steam reforming, gasification etc.), in food processing (hydrogenation of fats), etc (Grenoble, Estadt et al. 1981; Ferreira-Aparicio, Benito et al. 2005; Eswaramoorthi, Sundaramurthy et al. 2006; Basagiannis and Verykios 2007; Dias and Assaf 2008; Angeli, Turchetti et al. 2016). Catalyst reduces the potential energy barrier over which the reactants must pass to form products as shown in Figures 1.11 and 1.12. Considering the conversion of CO to CO_2, the non-catalytic reaction is controlled by the dissociation of O_2 molecule to O atoms, which is a rate-limiting step. Required temperature for this dissociation is > 700°C and when it reaches, reaction rapidly goes to completion with a net release of energy. E_{nc} in Figure 1.11 shows the activation energy of CO to CO_2 conversion. When the same reaction is carried out in presence of Pt catalyst, gaseous O_2 and CO get adsorbed on separate Pt sites, called chemisorption. Later, the dissociation of chemisorbed O_2 to O atoms occurs at room temperature and then adsorbed O atoms react with CO on adjacent Pt sites producing CO_2. Further, CO_2 get desorbed from Pt catalyst. The presence of Pt catalyst facilitates the dissociation of O, which is slow energy intensive step associated with non-catalytic oxidation of CO. Activation energy for Pt catalyzed reaction (E_c) is considerably smaller than that for the non-catalyzed reaction. This indicates that the catalyst provides a new reaction pathway to alter the rate-limiting step at a significantly lower temperature and hence enhances the rate of

reaction (Farrauto, Dorazio et al. 2016). Figure 1.12 shows the calculated potential energy changes for the water gas shift reaction on Cu catalyst surface. The reaction pathway with the minimum energy barriers involves the following steps:

$$CO_{(g)} + * \leftrightarrow CO*_{(ads)} \quad (1.11)$$

$$H_2O_{(g)} + * \leftrightarrow H_2O*_{(ads)} \quad (1.12)$$

$$H_2O* + * \leftrightarrow HO* + H* \quad (1.13)$$

$$CO* + HO* \leftrightarrow HOOC* \quad (1.14)$$

$$HOOC* \leftrightarrow H* + CO_2 \quad (1.15)$$

$$2H* \leftrightarrow H_2 \quad (1.16)$$

Here '*' represent the surface site and therefore 'X*' shows the adsorbate bonded to site. The adsorption of CO ($\Delta E_{(1.11)}$=−1.10eV) and H_2O (with reaction energy $\Delta E_{(1.12)}$=−0.47 eV) on the Cu_{29} catalyst surface are exothermic as shown in Figure 1.12 (step-1 and 2 of reaction path). The main energy barrier in WGS reaction is the dissociation of water into adsorbed OH and H (step-3). The presence of Cu-nanocatalyst facilitates the water dissociation and reduces the energy barrier to +0.93ev which is >1.76ev in the absence of a catalyst. Then, the reaction of OH and CO produces a HOOC species. The final important energy barrier is for the decomposition of the OCOH intermediate into CO_2 gas and adsorbed H, which eventually yields H_2 gas. Overall, the WGS follows different mechanisms over the systems in terms of energy barrier (Liu and Rodriguez 2007; Rodriguez, Liu et al. 2007). Catalysis investigation is an important field in applied science and it associates many areas of materials science, chemistry and notably organometallic chemistry. Catalysis also involves many transition metals and transition metal complexes.

Catalysts play an important role in the activity towards ethanol conversion and selectivity of hydrogen and carbon-containing products during steam reforming of ethanol. Simplified reaction pathway for ethanol steam reforming involves the following reactions (Bej, Pradhan et al. 2014):

(i) Dehydrogenation of the ethanol and producing acetaldehyde

$$C_2H_5OH \rightarrow CH_3CHO + H_2; \quad \Delta H_{298°C} = 68.4\ KJ/mol \quad (1.17)$$

(ii) C-C bond cleavage to CH_4 and CO.

$$CH_3CHO \rightarrow CH_4 + CO; \quad \Delta H_{298°C} = -18.8\ KJ/mol \quad (1.18)$$

(iii) Which is followed by the water gas shift reaction (WGS) and methane reforming reactions:

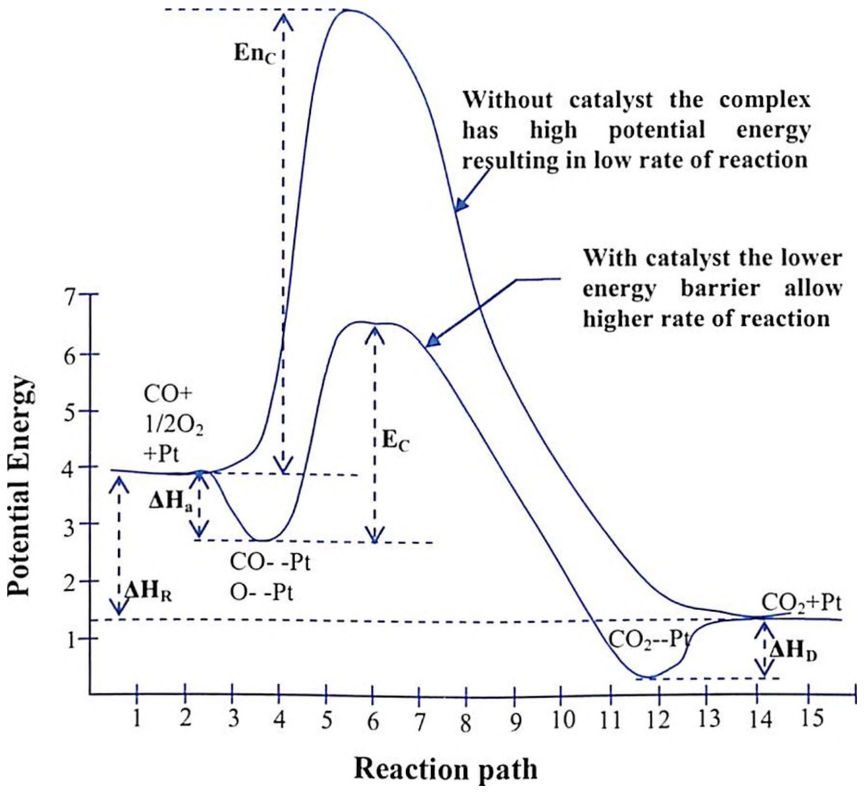

Figure 1-11 : Representation of the action of a Pt catalyst for thermal reaction of CO and O_2 (Farrauto, Dorazio et al. 2016)

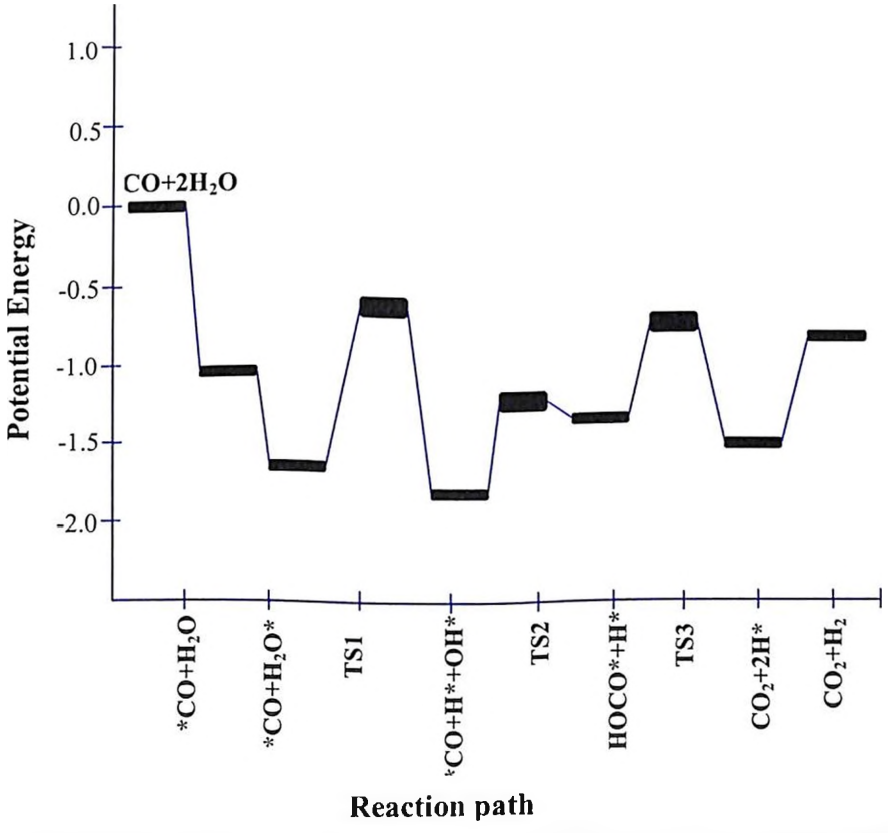

Figure 1-12: Potential energy diagram for the WGS on the Cu_{29} surface. "TS" represents the transition state (Liu and Rodriguez 2007)

$$CO + H_2O \rightarrow CO_2 + H_2; \qquad \Delta H_{298°C} = -41.1\ KJ/mol \tag{1.19}$$

$$CH_4 + H_2O \rightarrow CO + 3H_2: \qquad \Delta H_{298°C} = 205.9\ KJ/mol \tag{1.20}$$

Simplified pathway does not include the real adsorbed intermediates and side reactions, which are more likely to form on the catalyst surface. Temperatures also alter the reaction pathways as low temperature (200-500°C) favours the methanation while the methane reforming occurs at high temperature (700-1000°C) (Kourtelesis, Panagiotopoulou et al. 2015).

Undesired products are also formed during reforming along with coke formation, which lowers the catalytic activity. Two most frequent deactivation modes are exposure to poisoning from feed and sintering of the catalytic molecules due to high temperature and prolonged use. Catalysts are prepared with the maximum accessibility of the reactants to the active sites as they are well dispersed (i.e. high surface to volume ratio). As reactions proceed, the sites undergo coalescence or particle growth induced thermally, results in decreasing surface to volume ratio with fewer sites participating in the reaction. This phenomenon is known as sintering which is a thermodynamically unstable state that occurs to minimize the free energy. As sintering occurs, pore openings become progressively smaller, introducing greater pore diffusion resistance. Thus, a chemically controlled reaction may gradually become limited by pore diffusion. Another cause of catalyst deactivation results from contaminants present in the feedstock or from process equipment depositing onto catalyst surface, known as the poisoning of catalyst. Poisoning occurs by two basic mechanisms, first is selective poisoning in which an undesirable contaminant directly reacts with the active site, and decrease catalyst's activity and selectivity for a given reaction. Some poisons present in the feed (like Pb, Hg and Cd) chemically react with the catalytic component and result in inactive alloys. For example, the activity of Pt is reduced when it reacts with Pd (present in gasoline) and forms a Pt-Pb alloy. Some poisons like SO_2 chemisorbs onto metal sites and block them from further reactions. Second is non-selective poisoning in which deposition of fouling agents onto catalysts sites takes place, making sites and pores resulting in a loss in performance due to a decrease in accessibility of reactants to active sites. Reactor scale, that is, Fe, Ni, Cr, silica- and alumina-containing dust, phosphorous from lubricating oils are frequently found in catalysts. A very special type of fouling is coking in which a carbon-rich hydrogen deficient material is formed on and in the porous network. These mechanisms are non-discriminating as they deposit physically on the outer surface of catalysts which results in surface area loss that impacts the bulk mass

transfer. Thus, the slope of conversion versus temperature plot is decreased (Shabaker, Huber et al. 2003; Davda and Dumesic 2004; Farrauto, Dorazio et al. 2016).

At first, oxide catalysts are used for ethanol steam reforming, which lowers the CO concentration. Al_2O_3, MgO, La_2O_3, SiO_2, TiO_2, CeO_2 metal oxides are used as a catalyst and the results show that ethanol conversion increases with increase in temperature for all the catalysts but significant change is observed in the product selectivities and catalyst activities. With Al_2O_3 high conversion of ethanol is obtained but simultaneously ethylene concentration is high which then lowers the lifetime of catalysts. With CeO_2 system higher catalytic activity is found due to higher O^{2-} ion mobility through CeO_2. MgO shows low ethanol conversion but acetaldehyde concentration is high as it is basic in nature. ZnO shows high hydrogen selectivity and deactivation is more with Sm_2O_3 catalyst. The major disadvantage with the oxide catalyst is the large yield of by-products as they show the poor capacity for C-C breaking, which lowers the hydrogen concentration (Llorca, Piscina et al. 2001; Llorca, Homs et al. 2002; Llorca, de la Piscina et al. 2004).

Supported metal catalysts are observed to provide a better activity for H_2 production than pure oxide catalysts. The role of support is to activate primarily ethanol and water and helps in forming the C_2 intermediates and mobile surface OH groups. Metal phase helps in breaking the C-C bond cleavage to form C_1 intermediates (Casanovas, de Leitenburg et al. 2009).

A large number of different types of inorganic catalytic materials have been developed for steam reforming of ethanol; single or multimetallic (Pt, Ni, Ru, Rh, Pd , Ir, Co, Cu, Zn, Fe etc, used as single or alloy form) active phase on ceramic support (Al_2O_3, MgO, La_2O_3, SiO_2, TiO_2, CeO_2, activated C, ZrO_2, ZnO, etc), or metallic catalysts without any support (Shabaker, Davda et al. 2003; Davda, Shabaker et al. 2005; Huber, Iborra et al. 2006; Vagia and Lemonidou 2010; Chiou, Siang et al. 2012; Bimbela, Oliva et al. 2013; Kourtelesis, Panagiotopoulou et al. 2015; Angeli, Turchetti et al. 2016). The noble metal (such as Pt, Ru etc.) based catalysts, depending on the support, demonstrate high H_2 selectivity. But the very high cost of Pt (USD 934/Oz; the world spot price 16/6/2018) coupled with the limited availability makes it economically unfeasible to use. Davda et al. (2003, 2005), report that in terms of overall catalytic activity of ethylene glycol (as measured by the rate of CO_2 production per active surface metal site) over silica supported metallic catalysts, performance of Ni is comparable to Pt, and better than Ru, Rh, Pd, and Ir (Davda, Shabaker et al. 2003; Davda, Shabaker et al. 2005). Compared to Co, Pt, Pd, Fe, Ir, and Rh catalysts, Ni has a higher rate of C-C bond breakage rate, reasonably good water gas shift activity, and moderate

transfer. Thus, the slope of conversion versus temperature plot is decreased (Shabaker, Huber et al. 2003; Davda and Dumesic 2004; Farrauto, Dorazio et al. 2016).

At first, oxide catalysts are used for ethanol steam reforming, which lowers the CO concentration. Al_2O_3, MgO, La_2O_3, SiO_2, TiO_2, CeO_2 metal oxides are used as a catalyst and the results show that ethanol conversion increases with increase in temperature for all the catalysts but significant change is observed in the product selectivities and catalyst activities. With Al_2O_3 high conversion of ethanol is obtained but simultaneously ethylene concentration is high which then lowers the lifetime of catalysts. With CeO_2 system higher catalytic activity is found due to higher O^{2-} ion mobility through CeO_2. MgO shows low ethanol conversion but acetaldehyde concentration is high as it is basic in nature. ZnO shows high hydrogen selectivity and deactivation is more with Sm_2O_3 catalyst. The major disadvantage with the oxide catalyst is the large yield of by-products as they show the poor capacity for C-C breaking, which lowers the hydrogen concentration (Llorca, Piscina et al. 2001; Llorca, Homs et al. 2002; Llorca, de la Piscina et al. 2004).

Supported metal catalysts are observed to provide a better activity for H_2 production than pure oxide catalysts. The role of support is to activate primarily ethanol and water and helps in forming the C_2 intermediates and mobile surface OH groups. Metal phase helps in breaking the C-C bond cleavage to form C_1 intermediates (Casanovas, de Leitenburg et al. 2009).

A large number of different types of inorganic catalytic materials have been developed for steam reforming of ethanol; single or multimetallic (Pt, Ni, Ru, Rh, Pd , Ir, Co, Cu, Zn, Fe etc, used as single or alloy form) active phase on ceramic support (Al_2O_3, MgO, La_2O_3, SiO_2, TiO_2, CeO_2, activated C, ZrO_2, ZnO, etc), or metallic catalysts without any support (Shabaker, Davda et al. 2003; Davda, Shabaker et al. 2005; Huber, Iborra et al. 2006; Vagia and Lemonidou 2010; Chiou, Siang et al. 2012; Bimbela, Oliva et al. 2013; Kourtelesis, Panagiotopoulou et al. 2015; Angeli, Turchetti et al. 2016). The noble metal (such as Pt, Ru etc.) based catalysts, depending on the support, demonstrate high H_2 selectivity. But the very high cost of Pt (USD 934/Oz; the world spot price 16/6/2018) coupled with the limited availability makes it economically unfeasible to use. Davda et al. (2003, 2005), report that in terms of overall catalytic activity of ethylene glycol (as measured by the rate of CO_2 production per active surface metal site) over silica supported metallic catalysts, performance of Ni is comparable to Pt, and better than Ru, Rh, Pd, and Ir (Davda, Shabaker et al. 2003; Davda, Shabaker et al. 2005). Compared to Co, Pt, Pd, Fe, Ir, and Rh catalysts, Ni has a higher rate of C-C bond breakage rate, reasonably good water gas shift activity, and moderate

methanation reaction capacity. Thus inexpensive Co (USD 24.95/lb), Ni (USD 5.09/lb), Zn (USD 1.15/lb), Cu (USD 2.77/lb; the world spot price 16/8/2018) could be considered as a potential catalysts (Bimbela, Oliva et al. 2013).

Clearly, the development of efficient and stable catalysts, which will lead to high hydrogen yield, is a critical step for general catalyst based reforming of biomass (Chiou, Siang et al. 2012). In addition to oxide catalysts (Llorca, Piscina et al. 2001; Fatsikostas and Verykios 2004; Haryanto, Fernando et al. 2005), Ni-based catalysts (Garbarino, Sanchez Escribano et al. 2012; Elias, Lucrédio et al. 2013; Han, Bang et al. 2013; Vicente, Ereña et al. 2014), Co-based catalysts (Maia, Assaf et al. 2012; Soykal, Bayram et al. 2012; Varga, Ferencz et al. 2015), and noble metal catalysts (Martínez T, Araque et al. 2013; Kourtelesis, Panagiotopoulou et al. 2015) have been widely investigated for the purpose. It is evident from the literature that the supports with higher O^{2-} ion conductivity may play a very important role in the reforming. A recent comparative study showed the higher activity of the Ni/CeO_2 system over Ni/Al_2O_3 for n-BuOH and explained this behaviour on the basis of higher O^{2-} ion mobility through the CeO_2 lattice (Roy, Sullivan et al. 2011; Roy, Sullivan et al. 2014). CeO_2 is a non-stoichiometric oxide support with a fluorite structure known for its interesting redox property, giving high oxygen mobility through the lattice.

$$2CeO_2 \leftrightarrow Ce_2O_3 + V_O^{\bullet\bullet} + O_O^X + 2e'' \quad (1.21)$$

Ceria is able to change reversibly from Ce^{IV} under oxidizing conditions to Ce^{III} under reducing conditions. Oxygen atoms in CeO_2 are very mobile and leave the ceria lattice easily, giving rise to a large variety of non-stoichiometric oxides with the two limiting cases CeO_2 and Ce_2O_3. Ni doping in CeO_2 can increase the creation of oxygen vacancies as follows (Roy, Sullivan et al. 2011)

$$NiO \overset{CeO_2}{\Longleftrightarrow} Ni''_{Ce} + V_O^{\bullet\bullet} + O_O^X \quad (1.22)$$

Others researchers also discussed the importance of oxygen mobility through ceria and ceria related catalysts for accelerated surface oxidation reactions of carbon and high carbon resistance of the samples (Zhu and Flytzani-Stephanopoulos 2001; Chettibi, Wojcieszak et al. 2006; Kambolis, Matralis et al. 2010). The metal-doped bismuth vanadate (BIMEVOX) systems could be potential supports or catalysts for H_2 production due to high O^{2-} ion conductivity.

BIMEVOX is derived from the parent compound $Bi_4V_2O_{11}$ (BIVOX) by partially substituting V^{5+} with iso- and/or aliovalent metallic ions (Me = Li^+, Cu^{2+}, Co^{2+}, Ni^{2+}, Zn^{2+}, Fe^{3+}, Al^{3+}, Ti^{4+}, Zr^{4+}, Ge^{4+}, Sn^{4+}, Pb^{4+}, Nb^{5+} etc.). The subvalent substitutions may create

additional oxygen vacancies in the highly distorted vanadate octahedral layers, giving rise to oxygen mobility. BIVOX shows three main polymorphs, α (face-centered orthorhombic, a ≅ 5.533, b ≅ 5.611, and c ≅ 15.288Å), β (orthorhombic, a ≅ 11.06, b ≅ 5.61, c ≅ 15.28Å), and γ (tetragonal, space group I4/mmm, a ≅ 3.92 and c ≅ 15.5 Å) with sequential phase transition temperatures shown below (Abraham, Debreuille-Gresse et al. 1988).

$$\alpha \xrightarrow{\approx 450°C} \beta \xrightarrow{\approx 570°C} \gamma \xrightarrow{\approx 890°C} Liquid \qquad (1.23)$$

Among these three, the higher temperature γ phase shows the highest O^{2-} ion conductivity due to higher oxygen vacancy disorder in O-V polyhedra. The γ-BIMEVOX phase has an Aurivillius type crystal structure: alternate stacking of $(Bi_2O_2)^{2+}$ layers and $[(V/ME)O_{3.5}\square_{0.5})]^{2-}$ perovskite sheets. In order to stabilize the highly conductive γ phase of BIMEVOX at room temperature, the amount of metal substitution should be about 10-20 atomic percent (Abraham, Debreuille-Gresse et al. 1988; Muller, Chateigner et al. 1996; Steil, Fouletier et al. 1999; Mairesse, Roussel et al. 2003).

In this work, ethanol present in water is used at relatively low temperature to make process more economical.

1.5 Ethanol as a feedstock for Hydrogen production

The renewable feedstock for hydrogen production from steam reforming is usually oxygenated hydrocarbons (alcohols, bio-oils, organic acids), and lighter hydrocarbons (methane, natural gas) out of which ethanol has proven its value. There are various biochemical processes of producing ethanol from biomass. Acid hydrolysis of cellulosic biomass such as bagasse (waste product after the extraction and refining of sugar from sugar cane and agro-industrial wastes) is a quite often used technique of converting biomass into sugar and then to ethanol (Abelló, Bolshak et al. 2013; Bej, Pradhan et al. 2014; Chitsazan, Sepehri et al. 2016; Cifuentes, Hernández et al. 2016; Bilal and Jackson 2017). Ethanol from cellulosic biomass is produced by following steps: at first, the reduction of size takes place which then breaks down the hemicelluloses into sugar and opens up the structure of the cellulose component. The cellulose portion is broken down or hydrolyzed by dilute sulfuric acid into glucose sugar which is later converted to ethanol by fermentation. The sugars from the hemicellulose are also fermented to ethanol as shown in Figure 1.13 (Sukumaran, Singhania et al. 2009). Ethanol is a preferred feedstock for producing hydrogen via steam reforming for various reasons which are listed below:

(i) Literature shows that hydrogen production from steam reforming of natural gas as a feedstock, occurs at a temperature range of 725-1100°C, while with ethanol as a feedstock temperature range is 400-700°C (Seo, Youn et al. 2009; Mattos, Jacobs et al. 2012; Conti, Holtberg et al. 2016).

(ii) India is the 5th largest producer of ethanol in the world shows wide availability.

(iii) Ethanol is less toxic than methanol and is easy to transport and store.

(iv) Ethanol is free from sulfur, which works as a poison for metallic catalysts and therefore ethanol is beneficial for the lifetime of the catalysts (Garbarino, Finocchio et al. 2014).

(v) Total theoretical process energy (Energy needs during processing + Energy needed to vaporize and heat feed) needed during steam reforming of ethanol is 60 kJ/mol of usable H_2 which is less than the energy needed for gasoline (90 kJ/mol of usable H_2), methane (76 kJ/mol of usable H_2) and diesel fuel (89 kJ/mol of usable H_2) (F. Brown 2001).

1.6 Research Objectives

Thus, the following objectives of the present study are formulated based on the background of this subject till date

1. To prepare BIMEVOX {$Bi_4Me_{0.2}V_{1.8}O_{11-\delta}$; Me = Co, Ni, Cu) catalyst powders by solution combustion synthesis and perform physico-chemical characterization (to analyze phase content, microstructure, and surface chemistry) of the fresh and used catalysts.
2. To study catalytic activity at low temperature ($\leq$ 400°C), atmospheric pressure steam reforming for hydrogen production, using Ethanol.
3. To correlate the catalysts' microstructure chemistry with the catalytic activity results.

1.7 Thesis organization

The objectives are achieved by initially carrying out the detailed literature review on catalysts used for hydrogen production from steam reforming, which is given in chapter 2. The details of the materials used, catalyst preparation, catalyst characterization techniques, catalytic activity and product analysis techniques are described in chapter 3. The results pertaining to catalytic activity measurement, micro-structural analysis, surface chemistry analysis, reaction pathway, the effect of heat treatment on the catalysts, are elaborated in chapter 4. Chapter 5 deals with the summary of the work and important conclusions drawn from the present study.

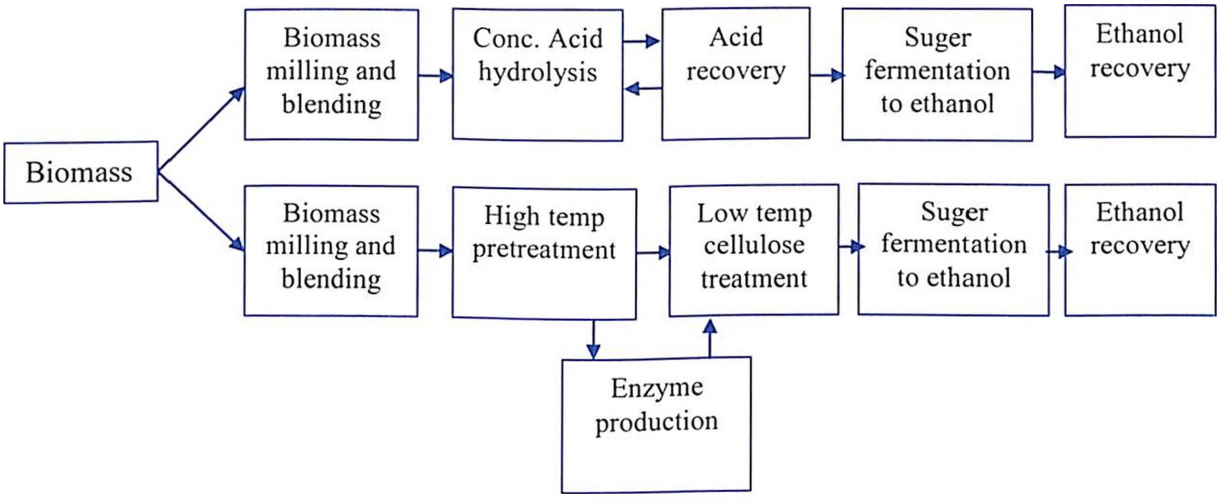

Figure 1-13 : Simplified diagram showing possible processes for ethanol production. The process depicted along the top of the Figure is the concentrated acid process that uses sulfuric acid to hydrolyze the biomass prior to fermentation to ethanol (Mielenz 2001)

Chapter 2: Literature Review

In the past decades, worldwide exhaustive studies have been carried out for the development of ceramic supports (single or in combination; Al_2O_3, MgO, La_2O_3, SiO_2, TiO_2, CeO_2, activated C, ZrO_2, ZnO, etc) based metallic (Pt, Ni, Ru, Rh, Pd , Ir, Co, Cu, Zn, Fe etc, used as single or alloy form) catalysts or metallic catalysts without any support for the reforming of biomass to produce H_2 (Sinfelt and Yates 1967; Vannice 1977; Grenoble, Estadt et al. 1981; Davda, Shabaker et al. 2003; Davda, Shabaker et al. 2005; Huber and Dumesic 2006).

India has prosperous history on catalysts related research. From 1993 to 2004 period total number of Indian origin research articles published in catalysts related journals are close to 1300 (B.Viswanathan 2005), while from 2003 to present, according to science direct database, this number has increased to 2200. Most of these articles are on selective chemical synthesis (Shah, Prathap et al. 2014; Yadav and Sharma 2014; Yadav and Sharma 2014), CO oxidation (Sudarsanam, Mallesham et al. 2014), and fuel cell applications (Shinde and Madras 2012; Singh and Chandra 2013), etc. All over the world, from 2003 onwards ~12,000 research articles are published on hydrogen production using various technologies and feeds in catalysts related journals (Das and Veziroğlu 2001; Devi, Ptasinski et al. 2003; Kim, Kim et al. 2004; Rioche, Kulkarni et al. 2005; Świerczyński, Libs et al. 2007; Roy and Leclerc 2015), ~2500 of these are on steam reforming (Świerczyński, Libs et al. 2007; Dan, Mihet et al. 2011; Bobadilla, Palma et al. 2013) and, out of that ~700 research articles are on low temperature steam reforming (Matsumura and Nakamori 2004; Wenju and Q. 2008; Lima da Silva, Malfatti et al. 2009; Ebshish, Yaakob et al. 2012).

Prasad el al. (2010) have studied thermo-catalytic synthesis of H_2 by decomposing pure CH_4 in the presence of activated carbon supported Pd catalysts (Prasad, Dhand et al. 2010). The production of H_2 by thermo catalytic decomposition of pure CH_4 using a nano-size Ni-Cu-Zn/MCM-22 catalyst has been investigated by Saraswat and Pant (2013) (Saraswat and Pant 2013). Sharma et al. (2012) have explored Jatropha-oil to liquid hydrocarbon fuels conversion using mesoporous titanosilicate supported sulfide catalysts (Sharma, Anand et al. 2012). Li et al. (2011) apply Ni-M/Al_2O_3 (M= Cu, Co, and Sn) catalysts, prepared by a co-impregnation method, for H_2 production by supercritical water gasification (SCWG) of glucose. H_2 yields and selectivity are significantly enhanced for the bimetallic catalysts compared to no catalyst reaction (Li, Lu et al. 2011).

Shabakar et al. (2003) have studied APR of 10 wt% ethylene glycol-water solution at temperatures of 210 and 225°C over Pt-black and Pt supported on TiO_2, Al_2O_3, carbon, SiO_2,

of 150–400°C and at atmospheric pressure. Catalysts have been prepared by co-precipitation technique. Cu/Al has been reported to be the most efficient catalyst as it demonstrates the lowest activation temperature (at which H_2 starts to produce) of 230°C with highest amount of H_2 yield (78 mol%) at 400°C. Whereas, in case of Ni/Al and Co/Al catalysts the highest H_2 yield are 65 and 72 mol%, respectively, at 400°C and activation temperature is 300°C. No activity is observed for Mg/Al catalyst (Segal, Anderson et al. 2002).

Shen et al. (2002) investigate steam reforming of methanol over Cu/Zn-based catalyst at a temperature of 230°C and atmospheric pressure (Shen and Song 2002). Reported results show almost complete methanol conversion (99–100%) and high H_2 (71–76%) with very low CO (0.05–0.15%) production.

Effects of different supports like silica and zirconia for nickel (20 wt%) based catalysts are investigated by Matsumura et al. (2004) for reforming of methane at 500°C. The catalysts are prepared by an impregnation technique. The maximum and minimum BET surface areas obtain for nickel supported over silica and zirconia catalysts are 244 and 38 m^2/gm, respectively. Results show maximum methane conversion (21.8%) and CO_2 selectivity (90.3%) for silica catalyst after 0.5 hrs. While, methane conversion and CO_2 selectivity for zirconia supported catalyst is 14.1% and 86.9%, respectively (Matsumura and Nakamori 2004).

Low temperature steam reforming of glycerol over Ni-based catalyst has been performed by Dou et al. (2009) in the temperature range of 400–700°C and atmospheric pressure in a continuous flow fixed-bed reactor (Dou, Dupont et al. 2009). Best results are obtained at 500°C with 95% glycerol conversion and 3.6 mol/m^3 H_2 yield.

Sekine et al. (2011) study the low temperature steam reforming of methane over metals (Pt, Rh and Ni) catalyst supported on $Ce_xZr_{1-x}O_2$ (x = 1, 0.75, 0.5, 0.25, 0) ceramics. Supports are prepared by co-precipitation method which is followed by impregnation method for metal loading and experiments are performed in the temperature range of 150–300°C at atmospheric pressure. According to the BET results the maximum and minimum surface areas are obtained for $Ce_{0.25}Zr_{0.75}O_2$ (55 m^2/gm) and CeO_2 (7.2 m^2/gm) support, respectively. The methane conversion increases with increasing zirconium content and Pt/ $Ce_{0.25}Zr_{0.75}O_2$ exhibited the highest methane conversion of 39.1% at 300°C (Sekine, Haraguchi et al. 2011).

Bobadilla et al. (2013) report H_2 production from methanol steam reforming at 350°C temperature over Ni and Ni-Sn (atomic ratio Ni/Sn = 3) nanoparticles-supported over CeO_2(15 wt%)-MgO(10 wt%)-Al_2O_3 catalysts prepared by two different techniques; polyol method and impregnation. Maximum methanol conversion (75%) and H_2 selectivity (80%)

with 4.3 mol/mol H_2 yield, 25% CH_4, 11% CO, and 64% CO_2 selectivity's are achieved for $Rh/Ce_{0.8}Zr_{0.2}O_2$, while 95% ethanol conversion with 3.6 mol/mol H_2 yield, 28% CH_4, 21% CO, and 50% CO_2 selectivity's are obtained in case of $Rh/Ce_{0.2}Zr_{0.8}O_2$ catalyst (Roh, Platon et al. 2006).

Kunzru group from IIT-Kanpur (2007) study steam reforming (SR) of ethanol for H_2 production over $Ni/Ce_{1-x}Zr_xO_2$ (x=0, 0.26, 0.59, 0.84 and 1) catalyst is prepared by co-precipitation and incipient wetness impregnation technique at temperature range of 400 to 650°C. Interest is to investigate the effect of support composition and metal loading on H_2 production. The best results in terms of EtOH conversion (almost 100%) and H_2 selectivity (97%) are obtained for 30% metal loaded $Ni/Ce_{0.74}Zr_{0.26}O_2$ catalyst at 600°C. At this temperature the selectivity of CO, CH_4, and CO_2 are reported to be 23.5, 17.5, and 57.5%, respectively (Biswas and Kunzru 2007).

Zhang et al, (2007) report the ethanol steam reforming over ceria-supported metal (Ni, Co) catalysts at 250-600°C, under atmospheric pressure, with water to ethanol molar ratio 9:1. Catalysts are prepared by deposition–precipitation method. Ethanol conversion increases with increase in temperature and 100% conversion is obtained at T ≥300°C. Maximum H_2 (87%) selectivity is obtained for Co/CeO_2 catalyst at 450°C, which is 80% in case of Ni/CeO_2 catalyst at 450°C. Minimum amount of CO is obtained at 400°C which is 2.5% for Co/CeO_2 and 1% for Ni/CeO_2 catalyst (Zhang, Tang et al. 2007).

Ciambelli et al, (2010) have performed the steam reforming of ethanol over Pt/CeO_2 catalysts (1, 3 & 5 wt% metal loaded) at 300-450°C range, water/ethanol molar ratio in the range 1.5–6.0, and space–time from 0.1 to 17 mg-min/μmol. Catalysts synthesis is done by wet impregnation method. Calculations of products selectivity is on the basis of molar% of each product evolved (excluding water) with respect to the feed consumed. 100% ethanol conversion is obtained at T ≥ 300°C. At 300°C and water/ethanol molar ratio 3, H_2 yield for 1, 3 and 5 wt% Pt loaded catalysts are 29, 39 and 38%, respectively with 32, 44, and 40% CH_4 selectivity, 21, 2 and 0% CO selectivity and 26, 56 and 59% CO_2 selectivity, respectively including C_3H_6O as a side product. Reported results show that for 5 wt% Pt/CeO_2 catalyst, H_2 yield increases from 39 to 62% with increase in temperature from 300 to 450°C at atmospheric pressure and water/ethanol molar ratio 3. However CO selectivity has been found to be 0% for 300 and 350°C and it is 7% at 450°C. On the basis of obtained product distribution over different Pt content for steam reforming of ethanol, they propose a reaction mechanism which comprises of ethanol adsorption, then acetaldehyde intermediate formation, followed by an intermediate C–C bond rupture to produce H_2, carbon oxides, and

are obtained for the catalyst prepared by the polyol method, while these values in case of impregnated catalysts are observed to be 59% and 56% respectively. They have explained that the nanoparticles produced by polyol method (surface area of Ni = 75 m^2/gm and Ni-Sn = 86 m^2/gm) showed better initial activity for steam reforming of methanol than impregnated (surface area of Ni = 78 m^2/gm and Ni-Sn = 75 m^2/gm) catalysts, due to the higher availability of metallic surface (Bobadilla, Palma et al. 2013).

Angeli et al. (2016) demonstrate methane reforming using Ni and Rh catalysts supported on La_2O_3–ZrO_2 and La_2O_3–CeO_2–ZrO_2 at the temperature range of 400-550°C and under atmospheric pressure (Angeli, Turchetti et al. 2016). Composition of the product outlet gas is reported to be H_2 (47-63%), CO (1-3%), CH_4 (20-41%) and CO_2 (9-14%). It is suggested that no CO shift reactor would be required due to favorable thermodynamic condition for the WGS reaction.

H_2 can be produced from different other biomasses (such as cellulose, glucose, catechol etc). Ethanol is chosen for the present study because in India, ethanol is produced from bagasse or molasses, which is the waste product after the extraction and refining of sugar from sugar cane. Therefore, ethanol produced in India is not only leaving sugar economy unaffected, but also could potentially be a good source of inexpensive H_2 production. More details of considering ethanol as feed is already discussed in Chapter 1 (section 1.6).

2.1.1 Low temperature steam reforming of ethanol

Homs et al. (2006) explore the low temperature ethanol steam reforming over ZnO-supported Ni and Cu catalysts. Catalysts are prepared by co-precipitation method and then tested at 250-450°C under atmospheric pressure. Reported BET surface areas are 47.9 and 46.8 m^2/gm for Ni/ZnO and Cu/ZnO, respectively. 100% ethanol conversion is achieved for Ni/ZnO at $T \geq 350$°C. Calculations of products selectivity is on the basis of molar% of each product evolved (excluding water) with respect to the total moles of product formed. The optimum results for Ni/ZnO is obtained at 400°C at which H_2 selectivity is 65.1%, with 0% CO, 25% CO_2 and 9.9% CH_4 selectivity's. However, in case of Cu/ZnO, maximum ethanol conversion is 84.1% at 450°C with 58.6% H_2, 9% CO_2, 1.2% CH_4 selectivity's and some other products (C_2H_4, C_3H_6, CH_3CHO) (Homs, Llorca et al. 2006).

Roh et al, (2006) perform steam reforming of ethanol over Rh (2 wt%)/CeO_2–ZrO_2 catalysts at 450°C. Catalysts are prepared by co-precipitation method and BET results show the maximum and minimum surface area 98 and 61 m^2/gm for Rh/$Ce_{0.2}Zr_{0.8}O_2$ and Rh/$Ce_{0.8}Zr_{0.2}O_2$ catalysts, respectively. Activity results show that 100% ethanol conversion

CH_4. Thereafter water gas shift reaction (WGSR) occurs, in which CO is converted to CO_2 (Ciambelli, Palma et al. 2010).

Chen et al, (2010) investigate the ethanol steam reforming over Rh(1 wt%)-Fe(10 wt%)/Ca(2 wt%)-Al_2O_3 catalyst which is prepared by a sequential incipient wetness impregnation method. Catalytic activity is carried out at 300-400°C, water to ethanol molar ratio 3:1, under atmospheric pressure. At 300°C, 99.3% ethanol conversion with 43% CO_2, 12.3% CO, and 40% CH_4 selectivity's and 3.5 mole H_2 yield are achieved. However, 100% ethanol conversion is obtained for 400°C with 63.8% CO_2, 0% CO, and 36.2% CH_4 selectivity's, and H_2 yield as high as 4.1 mole respectively. Experiments are also performed over Rh(1 wt%)/ Ca(2 wt%)-Al_2O_3 catalyst. Reported results show that presence of iron oxide enhances the water gas shift reaction (Chen, Choong et al. 2010).

Panagiotopoulou et al, (2012) investigate the steam reforming of ethanol over 0.5 wt% metal loaded Pt/Al_2O_3, Pt/CeO_2, and Pt/ZrO_2 catalysts at 300-400°C and atmospheric pressure. Catalysts are prepared by wet impregnation method and surface areas, as obtain by BET, are reported to be 83, 3.3, and 51 m^2/gm for Pt/Al_2O_3, Pt/CeO_2, and Pt/ ZrO_2, respectively. Pt/ ZrO_2 and Pt/Al_2O_3 catalysts exhibit higher ethanol conversion and 100% conversion obtained at 360°C, whereas for Pt/CeO_2 catalyst, >90% ethanol conversion occur at a temperature > 380°C. Activity results show the maximum CO (selectivity-21%) formation for Pt/CeO_2 catalyst in comparison with Pt/ZrO_2 (5% CO selectivity) and Pt/Al_2O_3 (6.5% CO selectivity) catalysts, at 400°C (Panagiotopoulou and Verykios 2012).

Pant group from IIT Delhi (2007) executes steam reforming of ethanol over (10-20 wt%) Co/Al_2O_3 catalysts to investigate the effect of reaction temperature (400-600°C), contact-time (3–17 sec/(mol of ethanol fed/ kg cat.)), and steam to ethanol molar ratio (1–8) on H_2 production. Catalysts are prepared by wet impregnation of commercial alumina pellets and surface areas, as obtain by BET, are reported to be 159, 158, and 138 m^2/gm for $Co(10\%)/Al_2O_3$, $Co(15\%)/Al_2O_3$, and $Co(20\%)/Al_2O_3$, respectively. The 15 wt% metal loaded Co/Al_2O_3 catalyst is found to be the most effective for the production of H_2. 500°C reaction temperature, 13-15 sec/(mol of ethanol fed/ kg cat.) contact-time (catalyst weight to total flow rate= W/F) and S/E molar ratio = 3–5 are revel to be the optimum operating conditions in order to achieve H_2 rich (~ 78%) product stream with minimum CO (~ 5%) and CH_4 (~ 2%) (Sahoo, Vajpai et al. 2007).

The performance of a bimetallic sample, Pt(3 wt.%)-Ni(10 wt.%) supported on CeO_2 powder, is investigated by Palma et al., (2014) for H_2 production by steam reforming of biomass-derived ethanol. Experiments are performed in the temperature range of 250–550°C,

with a water/ethanol molar ratio 3:1. The ethanol is completely converted at a T ≥ 300°C. Selectivity calculations are same as discussed for Ciambelli et al, (2010). Hydrogen selectivity increases from 20 to 56% with increasing temperature from 250 to 550°C. However, minimum CO selectivity is disclosed to be 3% with CH_4 (61%) and CO_2 (36%) selectivity, at 350°C (Palma, Castaldo et al. 2014).

Dan et al. (2015) from Romania study atmospheric pressure ethanol steam reforming at the range of 150-350°C and water to ethanol molar ratios 3:1-30:1 on Ni (8 wt%) catalysts deposited on CeO_2 (6 wt%) or La_2O_3 (6 wt%) promoted Al_2O_3 and ZrO_2 supports. Catalysts are prepared by wet impregnation method and surface areas for Ni/Al_2O_3, $Ni/La_2O_3–Al_2O_3$, $Ni/CeO_2–Al_2O_3$, Ni/ZrO_2, $Ni/La_2O_3–ZrO_2$, and $Ni/CeO_2–ZrO_2$ are reveal to be 102, 99, 100, 52.5, 50.7 and 59 m^2/gm, respectively. Based on experimental results, they conclude that the promotion of both Al_2O_3 and ZrO_2 by CeO_2 and La_2O_3, leads to better dispersion and stabilization of the Ni nanoparticles on the powder surface. For La_2O_3 promoted catalysts, 100% ethanol conversion is obtained at 300°C. However, ethanol conversion has been found to improve by the addition of CeO_2 to ZrO_2 supported catalyst, but is not significantly changed by the addition of CeO_2 to Al_2O_3 supported one. Among all, the best H_2 yield (55%) is obtained for $Ni/La_2O_3–ZrO_2$ catalyst. The increasing order for H2 production is like Ni/ZrO_2 (29%)<Ni/Al_2O_3 (35%)<$Ni/La_2O_3–Al_2O_3$ (36%)<$Ni/CeO_2–Al_2O_3$ (38%)<$Ni/CeO_2–ZrO_2$ (42%)< $Ni/La_2O_3–ZrO_2$ (55%) (Dan, Mihet et al. 2015).

Kourtelesis et al, (2015) report the low temperature steam reforming of ethanol over (2 wt%)Pt/Al_2O_3 catalyst within the temperature range of 300-400°C. Catalyst is prepared by employing the impregnation method and then calcined at 650 and 700°C. Obtained surface areas for Pt/Al_2O_3, Pt/Al_2O_3-650, and Pt/Al_2O_3-700 are observed to be 78.9, 71.9 and 71.7 m^2/gm, respectively. Selectivity of products containing carbon is defined as the concentration of each product at reactor effluent to the concentration of all carbon containing products. The maximum ethanol conversion (50%) is obtained at 400°C with 20 and 22% selectivity of CH_4 and CO with other side products (CH_3CHO, C_2H_4) for Pt/Al_2O_3 catalyst. Results are explained by the proposed mechanism, in which ethanol-dehydrogenation is considered to be the key step and it is found in the literature that Cu crystallite favor the dehydrogenation of ethanol to acetaldehyde on Pt surface. This step is followed by decomposition of acetaldehyde to CH_4 and CO (Kourtelesis, Panagiotopoulou et al. 2015).

H_2 production from ethanol steam reforming is evaluated by Dancini-Pontes *et al*, (2015) over the Cu(1 wt%)-Ni(5 wt%)/CeO_2 and CuNi/ Nb_2O_5–Na(0.1 wt%) catalysts with and

without nitrogen as the carrier gas. Catalysts are synthesized by wet impregnation method and surface area for $CuNi/CeO_2$ and $CuNi/ Nb_2O_5$–Na catalysts are found to be 48.4 and 21.1 m^2/gm, respectively. Catalysts performances are evaluated at 450°C, under atmospheric pressure and with steam to ethanol ratio 10:1. For $CuNi/CeO_2$ catalyst ethanol conversion increases from 53 (without N_2) to 60% (with N_2) and H_2 selectivity reduces from 72 (without N_2) to 65% (with N_2). But, for $CuNi/ Nb_2O_5$–Na catalyst, ethanol conversion decreases from 95 (without N_2) to 75% (with N_2) with increase in H_2 selectivity from 54 (without N_2) to 60% (without N_2). Coke formation is observed for both catalysts, and the carrier gas can favor the selectivity of H_2 and the ethanol steam reforming reaction, depending on the support used (Dancini-Pontes, DeSouza et al. 2015).

Mondal et al, (2015) from IIT-Delhi examine the H_2 production by LTSR of bio-ethanol over Ni(15, 30 wt%)/CeO_2-ZrO_2(weight ratio of Ce:Zr=1:1) and Rh(1 wt%)-Ni(30 wt%)/CeO_2-ZrO_2 catalysts at atmospheric pressure. The supports are prepared by a co-precipitation method and an impregnation method is used for metal loading and the effects of temperature (300-700°C) and water to ethanol molar ratio (3:1 -9:1) on ethanol conversion are studied. Complete ethanol conversion is achieved at 600°C with a maximum H_2 yield of 4.6 mol/mol on the 1wt% Rh-30 wt% Ni/ CeO_2-ZrO_2 catalyst (Mondal, Pant et al. 2015).

Arslan et al, (2016) investigate the LTSR (Reaction temperature 450°C) of ethanol over Ni impregnated CeO_2-ZrO_2 catalysts. Supports are synthesized by co-precipitation method. The surface areas for the Ni/CeO_2-ZrO_2 catalysts calcined at 450 and 650°C are revealed to be 82.8 and 12.8 m^2/gm, respectively. Activity results for Ni/CeO_2-ZrO_2-calcined at 450°C shows 72 mole% H_2 and 17.8 mole% CO_2. However H_2 mole% found to be less (61 mole%) with 18.7 mole% CO_2 in case of Ni/CeO_2-ZrO_2-calcined at 650°C. Results also show negligible coke formation in case of Ni/CeO_2-ZrO_2-calcined at 450°C catalyst (Arslan and Doğu 2016).

Bepari et al, (2017) explore the ethanol steam reforming over (5 and 10 wt%) cerium-promoted Ni-Mg-Al hydrotalcite catalysts for H_2 production in temperature range of 450-600°C, steam to ethanol ratio range 3:1–10:, and space-time range 11.02–44.08 h/(kmol of ethanol fed/ kg catalyst). Catalysts preparation is done by simultaneous co-precipitation and wet impregnation methods and BET results show that the surface area of 5% Ce/Ni-Mg-Al (8.15 m^2/gm) is higher than that of the 10% Ce/Ni-Mg-Al (5.64 m^2/gm). 99% ethanol conversion is obtained at 600°C, steam/EtOH molar ratio of 6 and space-time of 22.04 h/(kmol of ethanol fed/ kg catalyst) whereas, H_2, CO, CH_4, and CO_2 yields are 3.6, 1.3, 0.2 and 0.4 mol/mol ethanol, respectively for 10% Ce/Ni-Mg-Al catalyst. The maximum H_2

yield, 4.13 is achieved at 540°C, steam/EtOH molar ratio of 9 and space-time of 22.04 h/(kmol of ethanol fed/ kg catalyst) with 97% ethanol conversion for 10% Ce/Ni-Mg-Al (Bepari, Basu et al. 2017).

The ideal reaction pathway in ethanol reforming is the one that maximizes H_2 production. However, other undesirable side reactions may occur such as ethanol dehydrogenation, dehydration and decomposition. The reaction mechanism depends on the catalyst and operating conditions (temperature, water to ethanol molar ratio, flow rate, and pressure). The thermodynamic analysis becomes an important tool in the search of better or optimum conditions for high production rate and selectivity of hydrogen. It allows the prediction of what would be the best operating conditions to minimize the undesirable reactions which is independent of the catalyst used in the reforming. The literature review on thermodynamic analysis of ethanol steam reforming is discussed in the following section.

2.2 Thermodynamic aspects of low temperature steam reforming of Ethanol

Ethanol steam reforming includes convoluted sets of desirable and undesirable reactions for H_2 production, out of which undesirable side reactions may accounTable for the reduction in H_2 yield. To maximize the H_2 yield, the effect of the different parameters should be determined by thermodynamic analysis of ethanol steam reforming. The stoichiometric or the non-stoichiometric thermodynamic approaches can be studied by applying numerical methods to investigate the effect of parameters (D. and W. 1985). In the non-stoichiometric approach, minimization of Gibbs free energy is done while in the stoichiometric approach, set of stoichiometrically independent reactions are used to describe the system.

Garcia and Laborde (1990) have carried out the first thermodynamic analysis of gaseous products in ethanol steam reforming using the non-stoichiometric formulation over the following ranges: temperature 127 -527°C, pressure 1-9 atm, and H_2O: EtOH molar ratio 0: 1-10: 1 (Garcia and Laborde 1991). For all temperatures, pressures and feed molar ratios, the ethanol conversion is found to be 99.9%. Results show that for any pressure value within the range, at a constant H_2O: EtOH ratio, H_2 production increases and CH_4 production decreases with an increase in temperature, while at a constant temperature and pressure, both H_2 and CH_4 production rises with an increase in H_2O: EtOH ratio. With an increase in pressure for all temperatures (keeping H_2O: EtOH ratio constant) and H_2O: EtOH ranges (at constant temperature), H_2 production decreases and CH_4 production increases. Methane molar fraction for pure ethanol at T = 230°C and P = 1 atm is calculated to be 0.75 and it is 0.15 for H_2O:

EtOH=10: 1 at same temperature and pressure. A significant amount of H_2 production starts and CH_4 production falls at T > 270°C and atmospheric pressure. The dependency of CO production on temperature and H_2O: EtOH has also been reported, and it has been found that CO production increases with temperature, and decreases with increase in H_2O: EtOH ratio. They also report the dependency of C formation on H_2O: EtOH molar ratio. For H_2O: EtOH <1:1, (at any temperature) substantial amount of C deposition occurs, and in case of H_2O: EtOH = 10:1 no C is found (at any temperature). However, very small amount of C appears for H_2O: EtOH ≥ 2:1 and T>330°C.

Non-stoichiometric formulation for the thermodynamics of gaseous products in the ethanol steam reforming is investigated by the Vasudeva et al, (1996) with the following variable conditions: temperature range 400-927°C, pressure 1, 2, and 5 atm, and H_2O: EtOH molar ratio 0: 1-80: 1 and report that for these ranges the ethanol conversion is 99.9% (Vasudeva, Mitra et al. 1996). They reported that H_2 yield at 400°C, 1 atm, and H_2O: EtOH = 10 is 4.41 and it increases to 5.56 as the H_2O: EtOH increases to 20 for the same temperature and pressure and it increases further as water content increases in the feed. CH_4 and CO decreases with increase in H_2O: EtOH from 10 to 20 and for H_2O: EtOH =20 with an increase in temperature from 400 to 927°C, CH_4 and CO_2 yield decrease.

Fishtik et al, (2000) propose a non-stoichiometric thermodynamic analysis for ethanol steam reforming for the reaction conditions: temperature range 127-727°C, pressure 1 atm, and H_2O: EtOH molar ratio 1:1-10:1 (Fishtik, Alexander et al. 2000). At lower temperatures ethanol Figure out to decomposes into CH_4, but at the range of 427-527°C with high water content in the feed the water gas shift and methane reforming reactions occur predominantly which result in decrease in CH_4 and CO. Optimum results is obtained at 450°C and H_2O: EtOH = 4:1, where the mole fractions of H_2, CH_4, CO_2 and CO found to be 0.57, 0.17, 0.22 and 0.04, respectively.

Wenju et al, (2008) report the thermodynamic analysis of ethanol steam reforming by Gibbs free energy minimization method within the temperature limit 127-1727°C, pressure limit 1-60 atm, and H_2O: EtOH molar ratio limit 1:1-20:1 (Wenju and Q. 2008). Their study shows that the yield of H_2 increases with temperature and H_2O: EtOH ratio. At a given H_2O: EtOH ratio, the yield of H_2 initially increases sharply with increase in temperature and reaches to its maximum value (~95.5% yield) at ~730°C and then decreases slightly, while at a fixed temperature, the yield of H_2 keep on increasing with the increase of H_2O: EtOH ratios due to the WGSR. CO yield decreases with increase in H_2O: EtOH ratio while it keeps on increasing with increase in temperature at a fixed H_2O: EtOH ratio for all pressure ranges as

there is no appreciable effect of pressure on CO yield. Ethanol conversion is unaffected by pressure as it already reached to 100% at temperature ranges from 127-1727°C and H_2O: EtOH ratio = 3. However, H_2 yield decreases with increase in pressure at temperature <1000°C because the increase in pressure, shifts the equilibrium toward reactants in the hydrogen-forming reactions. The coke is reported not to form in the temperature range of 300–1727°C and H_2O: EtOH ratio range of 3–20 at 1 atm. There is slight increment in the coke formation with increase in pressure from 1 to 60 atm at a fixed temperature and H_2O: EtOH ratio= 1:1-3:1. The optimum results (H_2 selectivity: 61.48-71.49%, CO selectivity: 9.64-24.85% and CH_4 selectivity: 0-6.92%) are obtained in the range of 630-930°C, atmospheric pressure and H_2O: EtOH ratio= 3:1-6:1.

Rabenstein et al, (2008) report the thermodynamic analysis of ethanol steam reforming by Gibbs energy minimization method at temperature range 200-1000°C, H_2O: EtOH molar ratio 0:1-10:1 and under atmospheric pressure (Rabenstein and Hacker 2008). Results depict that the H_2 content (0.7 mole fraction) in the effluent is maximum at 600°C and increases very slightly with rising H_2O: EtOH ratio. The CO content has a maximum at low H_2O: EtOH ratios and high temperatures. The CO_2 content is almost constant at high level, for temperatures below 600°C and H_2O: EtOH ratios above 4.

Rossi et al, (2009) investigate the thermodynamics of ethanol steam reforming via minimizing Gibbs free energy method with operating parameters temperature in the range of 100-900°C, H_2O: EtOH molar ratio 1:1-10:1, and under atmospheric pressure (Rossi, Alonso et al. 2009). Results explain that for low H_2O: EtOH molar ratios, it is possible to increase H_2 production only at high temperatures. The maximum H_2 yield acquirs 90% at 500°C and 10:1 H_2O: EtOH molar ratio. The carbon formation occurs at H_2O: EtOH molar ratio of 3:1 and 1:1.

Silva et al, (2009) investigate on the thermodynamic analysis of ethanol steam reforming using Gibbs energy minimization method in the temperature range of 127-927°C, under atmospheric pressure, and H_2O: EtOH ratio of 1:1-10:1 (Lima da Silva, Malfatti et al. 2009). Reported results show that ethanol conversion is > 99% at T > 227°C for all H_2O: EtOH ratio, however at low temperatures the ethanol conversion dependents on H_2O: EtOH ratio. H_2 production increases with increase in temperatures and H_2O: EtOH ratio, while CH_4 shows exactly the opposite trend of H_2; decreases with increased temperature and H_2O: EtOH ratio. CO formation increases with increase in temperature while it decreases with H_2O: EtOH ratio. According to the calculation with H_2O: EtOH = 3:1 and T > 277°C, no C-

deposition is found, while for H_2O: EtOH = 5:1, predicted C-deposition is zero for all temperatures.

Non-stoichiometric formulation for the thermodynamics analysis of gaseous products in the ethanol steam reforming is investigated by Alvarado et al, (2010) with in the following conditions: temperature range 200-1000°C, pressure 1 atm, and H_2O: EtOH molar ratio range 0: 1-10: 1 (Díaz Alvarado and Gracia 2010). Reported results show the similar trend as observed in above mentioned thermodynamic studies of ethanol steam reforming. H_2 yield increases with temperature and H_2O: EtOH molar ratio. The predicted optimum reaction parameters are 550°C, H_2O: EtOH molar ratio 3:1 and atmospheric pressure at which H_2 yield is calculated to be 4.7 mol H_2/ mol EtOH reacted, with CO_2, CO and CH_4 yield 1.25, 0.4 and 0.25 mol/ mol EtOH reacted, respectively. Carbon deposition is occurred at H_2O: EtOH ratios < 4.0 for all temperatures. At temperature <400°C, mainly graphite carbon is present, whereas at higher reaction temperatures and at a H_2O: EtOH ratio < 3, the graphite carbon species completely disappear to give rise to carbon nano-tube structures that remain present even at temperatures as high as 1000°C for H_2O: EtOH equal to 0.

Silva et al, (2011) have performed the thermodynamic analysis of ethanol steam reforming by adopting non-stoichiometric Gibbs energy minimization method at temperature range 227-1177°C, pressure range 1-5 atm, and H_2O: EtOH molar ratio range 1:1-14:1. Reported results show that at temperature < 250°C, very small amount of H_2 is formed with CO_2, CH_4, and CO. The highest CH_4 production occurs at the lowest operating temperature, 227°C, due to the exothermic methanation reactions. However estimated CO_2 content is ~25% at temperature < 400°C and H_2O: EtOH molar ratio > 3:1. For H_2O: EtOH molar ratio < 3:1, CO_2 content decreases because of the carbon formation. Concentration of H_2 increases with increase in temperature till 550°C and after that no prominent change on H_2 concentration is observed because of the inhibition of the exothermic WGS reaction. Maximum calculated H_2 concentration is ~ 84 mole% at 550°C and it slightly increases with increase in H_2O: EtOH ratio. CO concentration also increases with increase in temperature and maximum CO concentration is 30 mole% at a temperature > 700°C and for H_2O: EtOH molar ratio 1:1-1.5:1. This behavior of CO production at high temperatures and very low H_2O: EtOH ratios could be attributed to the reverse WGS reaction. Besides, for T > 550°C, the concentration of methane is greatly decreased, and CO_2 concentration decreases gradually (Lima da Silva and Müller 2011).

The thermodynamic analysis of H_2 production from ethanol steam reforming at 300-900°C, 1-10 atm pressure, and H_2O: EtOH = 2.5:1-8:1 molar ratio is studied by Casas et al,

(2012) (Casas-Led, #243 et al. 2012). 100% ethanol conversion is obtained for all the temperature and H_2O: EtOH ratios. Results explain that H_2 and CO_2 production increases with increase in temperature, however for T > 550°C, CO_2 production starts decreasing and CH_4 shows exactly opposite behavior of H_2. Maximum H_2 yield is obtained at 700°C, under atmospheric pressure, and H_2O: EtOH molar ratio = 3.5:1.

Most research articles, found in the literature, discusses the thermodynamic analysis of ethanol steam reforming show great concern regarding the operating conditions for H_2 production using justifiable complex qualitative and quantitative techniques. Table 2.1 summarizes the operating parameters and product distribution obtained from thermodynamics analysis related articles of ethanol steam reforming using Gibbs free energy minimization method. From a thermodynamic point of view, as discussed above, the low temperature steam reforming of ethanol is considered to be entirely feasible.

So far, limited works have been reported on low temperature & atmospheric pressure steam reforming of ethanol (Sun, Qiu et al. 2005; Lee, Han et al. 2012; Ma, Zhang et al. 2012; Palma, Castaldo et al. 2014; Kourtelesis, Panagiotopoulou et al. 2015). Most of these are used unary (Al_2O_3, Y_2O_3, La_2O_3, CeO_2) or mixed ceramic oxide support based Ni, Co, Cu, Pt or mixed metal catalysts at the reaction temperature range of 250-600°C as shown in Table 2.2. The national and international working status on energy related catalysts is truly rich; however, according to the knowledge of this investigator no national level works have been reported on the development of metal doped bismuth vanadate (BIMEVOX) systems and study these as catalytic for H_2 production from ethanol, especially by LTSR. However, it is already discussed in the introduction that BIMEVOX systems show high O^{2-} ion conductivity due to higher oxygen vacancy disorder in O-V polyhedral and it is a well known fact that supports with higher O^{2-} ion conductivity help reforming of biomass more effectively. This shows the necessity of through study on BIMEVOX catalyst for LTSR of ethanol in Indian context.

Synthesis of nanoscale γ-BIMEVOX powder in one single step is of interest. Solution combustion synthesis (SCS) is a simple technique that has been used for the preparation of relatively pure, porous, and nanosized oxides used as catalysts, phosphors, pigments, etc (Sekar and Patil 1992; Patil 1993; Patil, Aruna et al. 2002; Bosze, McKittrick et al. 2003; Jacobsohn, Blair et al. 2008). Synthesis of $Bi_4V_2O_{11}$, BICOVOX, or any of the related BIMEVOX compounds by SCS was first used by Roy et al, (2009) (Roy and Fuierer 2009). One of the limiting factors could be that the vanadium nitrate precursor is not readily available. A possible variation on the SCS process is to include finely milled (vanadium)

oxide powder mixed in with the other metal nitrates and fuels. This approach has been used on a couple of occasions to produce silicate phosphors, where silicon nitrate is not commercially available (Bosze, McKittrick et al. 2003; Jacobsohn, Blair et al. 2008). The SCS powder could be helpful in obtaining highly dense, smaller grain, but crack-free microstructure in the final bulk material by lowering the sintering temperature. In addition, this porous and nano/submicron particle powder of high surface area (SA) can enhance the performance of the fixed/ fluidized bed reactor, where catalyst is used in the powder form (Chetouani, Taouk et al. 2003). Few catalysts those are prepared by SCS for ethanol steam reforming are discussed in the following section.

2.3 Catalysts prepared by SCS for ethanol steam reforming

Kumar et al, (2011) prepare Ni-Fe-Cu(molar ratio =1:1:0.5,1:0.5:1,0.5:1:1 and 1:1:1) multi-component catalysts by SCS for hydrogen production from ethanol reforming (Kumar, Mukasyan et al. 2011). The catalyst precursors include metal nitrates as oxidizers and glycine as fuel. BET surface areas are found to be 10.9, 13.6, 14.4 and 15.9 m^2/g for Ni-Fe-Cu(1:1:1), Ni-Fe-Cu(0.5:1:1), Ni-Fe-Cu(1:1:0.5), and Ni-Fe-Cu(1:0.5:1) respectively. Activity of the catalysts is measured at the temperature range 120-450°C and under atmospheric pressure. Ethanol conversion and H_2 selectivity is found to increase with reactor temperature and 100% conversion obtained at 400°C with maximum H_2 selectivity (42%) for Ni-Fe-Cu(1:0.5:1) catalyst.

Wenju et al, (2011) have prepared Ni(5-20 wt%)/MgO catalyst by using a single pot SCS method for ethanol steam reforming (Wenju, Yaquan et al. 2011). Magnesium nitrate ($Mg(NO_3)_3 \cdot 6H_2O$), nickel nitrate ($Ni(NO_3)_2 \cdot 3H_2O$), as oxidizers and urea ($CO(NH_2)_2$) as fuel are used as catalyst precursors. BET surface area and pore size of Ni(10 wt%)/MgO catalyst is 70 m^2/g and 5.9 nm respectively. Catalytic activity is performed at 600°C, atmospheric pressure and H_2O: EtOH molar ratio 10:1. 100% Ethanol conversion is found for Ni(10 wt%)/MgO, Ni(15 wt%)/MgO and Ni(20 wt%)/MgO with 75,75 and 76% H_2, 21, 23 and 25% CO, 69, 68 and 68% CO_2 and 9, 8 and 7% CH_4 yield, respectively. While, in case of Ni(5 wt%)/MgO catalyst only 63% ethanol conversion is reported with 36% H_2, 17% CO, 27% CO_2 and 19% CH_4 yield.

Cross et al, (2012) prepare a Ni(1-3 wt%) catalysts supported on γ-Al_2O_3 pellets by SCS for ethanol steam reforming (Cross, Kumar et al. 2012). Nickel nitrate and glycine are used as catalyst precursors. The BET surface area, pore volume of the γ-Al_2O_3 pellet is 158 m^2 /g and

Table 2-1: Operating parameters and obtained product distribution from thermodynamics of ethanol steam reforming using Gibbs free energy minimization method

Operating Parameters	Product Distribution	Coke formation	Remark	Ref.
P(atm):1 (constant) **T(°C):**200-1000 **H_2O:EtOH**:3: 1 (constant)	H_2:1-5.1 yield CO_2:0.9-1 CO:0-0.5 CH_4:1.1-0.01	- Maximum C forms H_2O:EtOH<4 and 600-800°C	Optimum parameters: T=550°C H_2O:EtOH=3:1 H_2=4.7 yield, but Coke% is less at 400°C	(Díaz Alvarado and Gracia 2010)
P(atm):1 (constant) **T(°C):**700 (constant) **H_2O:EtOH**:0-10	H_2:1-5.1			
P(atm):1-10 **T(°C):**500 (constant) **H_2O:EtOH**:3.5 (constant)	H_2:2.8-0.8 yield CO_2:0.9-0.6 CO:0.2-0.1 CH_4:1-1.5	Maximum C forms at 500-600°C	Optimum parameters: T=400°C H_2O:EtOH=3.5 P=1 atm H_2=2.8 yield	(Casas-Led. #243 et al. 2012)
P(atm):1 (constant) **T(°C):**300-900 **H_2O:EtOH**:3.5 (constant)	H_2:0.2-4.6 yield CO_2:0.6-0.4 CO:0.1-1.8 CH_4:1.4-0			
P(atm):1 (constant) **T(°C):**500 (constant) **H_2O:EtOH**:2.5-8	H_2:1.6-3 yield CO_2:0.8-1.1 CO: 0.1 CH_4:1.1-0.6			
P(atm): 1-5 **T(°C):** 550 (constant) **H_2O:EtOH**:4 (constant)	H_2:86-80 mol%	Maximum C forms H_2O:EtOH<3 and 550-800°C	Optimum parameters: T=450°C H_2O:EtOH=4 P=1 atm H_2=86 mol%	(Lima da Silva and Müller 2011)
P(atm): 1 (constant) **T(°C):** 227-1177 **H_2O:EtOH**:4 (constant)	H_2:50-88 mol% CH_4:52-8			
P(atm): 1 (constant) **T(°C):** 550 (constant) **H_2O:EtOH**:1-14	H_2:62-70 mol% CH_4:38-5			
P(atm):1 (constant) **T(°C):**200-1000 **H_2O:EtOH**: 9 (constant)	H_2:0.2-0.75 mole fraction CO_2:0.26-0.19 CO:0.01-0.1 CH_4:0.53-0.01	-	Optimum parameters: T=600°C H_2O:EtOH=6 H_2=0.7 mole fraction	(Hernández and Kafarov 2009)
P(atm):1 (constant) **T(°C):**700 (constant) **H_2O:EtOH**:3-9	H_2:0.2-0.75 mole fraction CO_2:0.1-0.19 CO:0.2-0.1 CH_4:0.02-0.01			
P(atm):1 (constant) **T(°C):**200-1000 **H_2O:EtOH**:6 (constant)	H_2:0.01-0.7 mole fraction CO_2:0.25-0.1 CO:0-0.19 CH_4:0.8-0	Maximum C forms H_2O:EtOH<3 and T> 400°C	Optimum parameters: T=550°C H_2O:EtOH=4 H_2=0.58 mole fraction	(Rabenstein and Hacker 2008)
P(atm):1 (constant) **T(°C):**800 (constant) **H_2O:EtOH**:1-10	H_2:0.65-0.7 mole fraction CO_2:0.08-0.12 CO:0.22-0.15 CH_4:0.02-0.01			
P(atm):1-60 **T(°C):** 600 (constant) **H_2O:EtOH**:3 (constant)	H_2:70-40% yield	Maximum C forms H_2O:EtOH<4 and T>350°C	Optimum parameters: T=600-900°C H_2O:EtOH=3-6 P=1 atm H_2=60-83% yield	(Wenju and Q. 2008)
P(atm):1 (constant) **T(°C):** 127-1727 **H_2O:EtOH**:3 (constant)	H_2:20-83% yield			
P(atm):1 (constant) **T(°C):** 500 (constant) **H_2O:EtOH**:1-20	H_2:20-90% yield			

P(atm):1 (constant) **T(°C):**100-900 **H_2O:EtOH**:5(constant)	H_2:20-90% selectivity CO_2:22-11% CO:1-25% CH_4:20-1%	Maximum C forms H_2O:EtOH<3 and T>500°C	Optimum parameters: T=400-800°C H_2O:EtOH=4-6 P=1 atm H_2=65-90% selectivity	(Rossi, Alonso et al. 2009)
P(atm):1 (constant) **T(°C):**600 (constant) **H_2O:EtOH**:1-10	H_2:31-90%			
P(atm):1 (constant) **T(°C):**400-927 **H_2O:EtOH**:10 (constant)	At 10 H_2O:EtOH & 1 atm H_2:4.41-5.37 yield CO_2:1.45-0.8 CO:0.2-1.17 CH_4:0.34-0.001	Maximum C forms H_2O:EtOH<2 and T>600°C	Optimum parameters: T=600-800°C H_2O:EtOH=2-10 P=1 atm H_2=3-4.8	(Vasudeva, Mitra et al. 1996)
P(atm):1 (constant) **T(°C):**500 (constant) **H_2O:EtOH**:0-20	At 500°C& 1 atm H_2:1.05-4.41 yield CO_2:0.58-1.45 CO: 0.25-0.2 CH_4:1.18-0.35			

Table 2-2 : Summery of ethanol steam reforming over different catalysts

S. No	Catalyst	Preparation method	Catalyst Properties	Operating parameters	Reaction condition	EtOH (Con)	H_2	CO	CH_4	Ref
1.	$Ni(16)/Al_2O_3$ $Ni(8)/Al_2O_3$	IM, DT: 125°C/ON, CT: 550°C /3h	S_{BET} = 182, V_{pore}=0.57 S_{BET} = 194, V_{pore}=0.78	T (°C)= 600	TOS (h) 0-6 0-6		%Mol 32-20 62.5-15	%Mol 4-1 10-6	%Mol 2-0 2.5-1	(Alberton, Souza et al. 2007)
2.	$Ni(10)/Al_2O_3$ $Ni(10)/Al_{0.99}La_{0.01}O_{1.5}$ $Ni(10)/Al_{0.97}La_{0.03}O_{1.5}$ $Ni(10)/Al_{0.95}La_{0.05}O_{1.5}$	Support: SG, DT: 110°C/10h, CT: 650°C/4h Catalyst: IWI, DT: 70°C /12h, CT: 450°C /3h	S_{BET} = 191, V_p = 0.25, D_p = 5.4 S_{BET} = 321, V_p = 0.47, D_p = 5.8 S_{BET} = 298, V_p = 0.34, D_p = 4.6 S_{BET} = 291, V_p = 0.29, D_p = 4.0		T (°C) 500 500 500 500	 80 83 86 75	%Mol 48 60 61 62	%Mol 5 5.5 6 6.5	%Mol 2 2 2 2	(Melchor-Hernández, Gómez-Cortés et al. 2013)
3.	$Ni(16)/Al_2O_3$ $Ni(15)/La_2O_3$ $Ni(20)/Y_2O_3$	IWI, DT: 110°C /12h, CT: 450°C /4h	S_{BET} = 84 S_{BET} = 78 S_{BET} = 78		T (°C) 200-700 200-700 200-700	30-100 40-100 40-100	Y 1-4.6 0.6-4.9 0.5-4	Y 0.9-1.2 0.2-1.1 0.2-0.4	Y 0.7-0 0.5-0 0.2-0.1	(Sun, Qiu et al. 2005)
4.	Ni/Al_2O_3 $Ni_{0.99}Rh_{0.01}/Al_2O_3$	IWI, DT: 27°C /24h, CT:600°C /2h.	D_{Ni} = 20 D_{Ni} = 13	GHSV = 9000, S/C = 2	T (°C) 200-700 200-700		%Mol 35-70 0-72	%Mol 8-0 0-0	%Mol 12-4 45-0	(González-Gil, Chamorro-Burgos et al. 2015)
5.	$Ni(8)/Ce_{0.8}Zr_{0.2}O_2$	Support: CP, DT: 120°C, CT: 600°C /5h Catalyst: IM, DT: 120°C /ON, CT: 600°C /5	S_{BET} = 85,	H_2O/EtOH=5 T= 600°C,	T (°C) 300-600 TOS (h) 0-10	30-100 100-92	% S 14 -91 77-72	% S 9 -36 20-19	% S 5-0.5 9	(Carbajal-Ramos, Gomez et al. 2016)
6.	$Ni(7)/Zr_{0.85}Mg_{0.15}O_{1.85}$	Support: CP, DT: 120°C /12 h, CT: 550°C /4h Catalyst: IWI, RT: 600°C	S_{BET} = 28.21, D_p = 10-15	H_2O/EtOH = 6, S/C = 3, GHSV = 4895 T = 600°C	T (°C) 400-600 TOS (h) 0-18	67-100 100	% S 61-70 70	% S 12-10 9 -10	% S 12.5-4 4	(Biswas and Kunzru 2008)

		/1 h								
7.	$Cu(35)/Al_{0.76}Mg_{0.24}O_{1.38}$ $Cu(35)/Al_{0.86}Zn_{0.14}O_{1.43}$ $Cu(35)/Al_{0.94}Si_{0.06}O_{1.53}$	IM, DT:120°C /ON, CT: 650°C /6 h.	D_{CuO} = 6.9 D_{Cu} =5.1, D_{CuO} = 20.1 D_{Cu} = 8.6 D_{CuO} =7.2, D_{Cu} = 18		T (°C) 250-600 250-600 400-600	50-100 100 100	%S 42.5-95.2 49.5-95.2 61.2-92.0	%S 15-30 41-36.5 29.6-32	%S 15-10 49.5-10 42.7-7.2	(Zhang, Liu et al. 2009)
8.	$Cu(30)/Ce_{0.42}Zr_{0.58}O_2$	Support: CP, DT: 110°C, CT: 750°C /6h, Catalyst: WI, DT: 110°C, CT: 550°C /4h	S_{BET} = 24.5, D_{pore} = 15.9, V_{pore} = 0.109		T(°C) 600-700	95-100	%S 68-75	%S 5-7.5	%S 3-0	(Patel, Jindal et al. 2013)
9.	$CuO\ (15)/Ce_{0.7}Pr_{0.3}O_2$	PT, DT: 80°C /24h, CT: 750°C /4h		GHSV = 10000, H_2O/EtOH = 3	T (°C) 350-650	80-100	%S 68-55	%S 1-32	%S 19-0	(de Lima, da Silva et al. 2012)
10.	$Cu_{0.91}Rh_{0.09}(6)/CeO_2$	IWI, DT:100°C /6-8 h, CT:450°C /3 h	S_{BET} = 154, V_{pore}=0.119, D_{pore} =3.7	H_2O/EtOH=4, O_2/EtOH=0.4, GHSV=244,000	T (°C) 350-600	100-100	%Mol 40-55	%Mol 1-11	%Mol 27-10	(Biswas and Kunzru 2007)
11.	$Cu_{0.77}K_{0.23}(12)/CeO_2$ $Cu(10)/CeO_2$	IM, DT 110°C /12h, CT: 420°C /1h		T (°C) = 420	TOS (h) 20-100	100-70 100-100	%S 85-51	%S 2-5	%S 25-11	(Hou, Liu et al. 2014)
12.	$Cu_{0.5}Co_{0.5}(22.5)/CeO_2$ $Cu_{0.5}Co_{0.5}(22.5)/CeO_2$ $Cu(22.5)/CeO_2$ $Cu(22.5)/CeO_2$	IM, DT: 110°C, CT: 500°C RM, DT: 120°C /ON, CT: 500°C IM, DT: 110°C, CT: 500°C RM, DT: 120 o°C /ON, CT: 500°C	S_{BET}= 72, D_{Cu}=7.5 S_{BET}= 132, D_{Cu} =3.9 S_{BET}= 132, D_{Cu} =8.0 S_{BET}= 132, D_{Cu} =3.7	T (°C) = 500	TOS (h) 4-20 4-20 4-20 4-20	88-45 70-20 100-45 99-99	%Y 58-30 25-5 46-30 58-58			(Schuyten, Dinka et al. 2008; Mondal, Pant et al. 2015)
13.	$Co(35)/Al_{0.78}Si_{0.22}O_{1.61}$ $Co(40)/\ Al_{0.78}Si_{0.22}O_{1.61}$ $Co(45)/\ Al_{0.78}Si_{0.22}O_{1.61}$	CP, DT: 120°C /ON, CT:650°C /6 h		T=400°C, LHSV=8.0 T=400°C, LHSV=8.0 H_2O/EtOH=	H_2O/EtOH 3-12 3-12 T (°C)	100 100 100	%S 70-80 68-100 68-94	%S 10-6 7-47.5 5-37	%S 40-30 47-1 47.5-7.5	(Zhang, Li et al. 2009)

				4.0, LHSV= 8.0	400-600					
14.	$Co(27.51)/Al_2O_3$ $Co_{0.92}Ce_{0.08}(36.88)/Al_2O_3$ $Co_{0.92}Pr_{0.08}(36.32)/Al_2O_3$	CP, CT: 500°C /16h, DT:80°C /24 h.	S_{BET}= 239 (±10), V_p = 0.451, D_p = 4 S_{BET}= 201 (±10), V_p = 0.449, D_p=5 S_{BET}= 196 (±10), V_p = 0.46, D_p = 5	Time = 100 h	T (°C) = 600		Y 3.20 3.24 3.4	Y 0.51 0.43 0.51	Y 0.45 0.29 0.31	(Muñoz, Moreno et al. 2016)
15.	$Co/Al_{0.86}Mg_{0.14}O_{1.43}$	CP, DT:80°C /24h, CT:500°C /16h	S_{BET} =239, D_p = 7	GHSV = 22000, O_2/EtOH/H_2O = 0.5/1/3.	T (°C) 550	100	Y 3.09	Y 0.47	Y 0.29	(Muñoz, Moreno et al. 2014)
16.	$Co_{0.84}Rh_{0.16}/Al_{0.92}Ce_{0.8}O_{1.53}$	IM, DT: 120°C /3h, CT:600°C /3h		H_2O/EtOH = 6	T (°C) 450-600		%S 70-81	%S 36-24	%S 18-22	(Peela, Mubayi et al. 2011)
17.	$Co(17.3)/CeO_2$ $Co(17.3)/CeO_2$ $Co(17.3)/CeO_2$	IM, DT: 200°C /24h, CT: 650°C /2h IM, PYT: 500°C /1h IM, PYT: 700°C /1h	S_{BET} = 5, V_{pore} = 0.004 S_{BET} = 51, V_{pore} = 0.037 S_{BET} = 36, V_{pore} = 0.028	H_2O/ EtOH = 3, T (°C) = 325 H_2O/ EtOH = 3, T (°C) = 400 H_2O/ EtOH = 3, T (°C) = 500	TOS (h) 0.83-4.7 0.83-4.7 0.83-4.7	30-12 100 100-90	%S 80-87 62.5-75 79-82		%S 7.5-0 32.5-22.5 20-16	(Trane-Restrup, Dahl et al. 2014)
18.	$Co(18)/Al_{0.9}Gd_{0.1}O_2$	HT		H_2O/EtOH = 3, T (°C) = 500, t = 6h	T_{calc} (°C) 300-1200	50-16	%Mol 59-55	%Mol 0	%Mol 1-0	(Maia, Assaf et al. 2012; Dan, Mihet et al. 2015)

IM: Impregnation; CP: Co-precipitation method; HT: Hydro-thermal method; SG: Sol-Gel method; CI: Co-impregnation method; IWI: Incipient wetness impregnation method; RM: Reverse micro-emulsion; ON: ON; S_{BET}: BET surface area; H_2O/EtOH: Water/Steam to Ethanol molar ratio; O_2/EtOH: Oxygen to ethanol molar ratio; GHSV: Gas hourly space velocity (h^{-1}); LHSV: Liquid hourly space velocity (h^{-1}); D_{Ni} : Diameter of Ni (Å); D_{Cu}: Diameter of Cu (Å); D_p: Particle diameter (nm); V_p = Particle volume ($cm^3\ g^{-1}$);%S: Precentage selectivity;%Y: Precentage yield; Y: Yield; DP: Dispersion; D_{pore}: Pore diameter (nm); V_{pore}: Pore volume ($cm^3\ g^{-1}$); TOS: Time-on-Stream; DT: Drying Temperature; CT, T_{calc}: Calcination Temperature; S/C: Steam to carbon ratio; PYT: Pyrolyzation temperature

0.682 mL/g, respectively. Catalytic activity is performed at reaction temperature is in the range of 200-500°C, atmospheric pressure and 2.2 cm^3/min of ethanol flow rate. Activity results show that ethanol conversion increases with temperature and 100% conversion is achieved at 500°C. The main goal of this work is to show that the solution combustion synthesis method allows one not only to prepare the effective supported catalysts, but also permits to control the distribution of the active phase through the support body.

Kumar et al, (2015) have synthesized copper–nickel (molar ratio 1:1) catalysts by SCS for hydrogen production from ethanol reforming (Kumar, Cross et al. 2015). The catalyst precursors include nickel nitrate and copper nitrate as oxidizers and glycine as fuel. The BET surface area is found to be 38 m^2/g. Catalysts performance are evaluated at 100-400°C, atmospheric pressure and 1.8 cm^3/min of ethanol flow rate. At lower temperatures (T<180°C), <15% ethanol conversion with <5% H_2 selectivity is reported. 100% ethanol conversion is obtained at T≥ 300°C with H_2 selectivity ranges from 32-36%. SCS is an established method used by many researchers for catalysts preparation purpose.

BICOVOX, or any of the related BIMEVOX compounds is 1st time fabricated using SCS by Roy et al, (2009) (Roy and Fuierer 2009). Keeping equivalence ratio of the oxidizer to fuel ratio (O:F) 1:1 and 1:2, bismuth nitrate, vanadium oxide and cobalt nitrate as oxidizers and three different fuels (carbohydrazide, glycine and urea) are used as catalyst precursors. Surface area for O:F=1:1 is found to be 1.9, 1.73 and 1.5 m^2/g for carbohydrazide, glycine and urea respectively. However in case of O:F=1:2, reported surface area is 5.7, 3.2 and 2.5 m^2/g for carbohydrazide, glycine and urea respectively. $BiVO_4$ and Bi_2O_3, secondary phases are obtained along with the desired BICOVOX phase in all the prepared catalysts and glycine (O:F=1:1) as the fuel is yielded a powder with the greatest content of desired BICOVOX phase.

BIMEVOX compounds have been used in different industrial applications such as fuel cells (Krok, Bogusz et al. 1993; Abrahams, Krok et al. 1996; Kežionis, Bogusz et al. 1999; Guillodo, Fouletier et al. 2002), water electrolyzers (Kežionis, Bogusz et al. 1999), oxygen sensors (Krok, Bogusz et al. 1993; Abrahams, Krok et al. 1996; Kežionis, Bogusz et al. 1999), cathodes in rechargeable batteries (Castro, Millan et al. 2000), high transition temperature ferroelectrics (Castro, Millan et al. 2000), catalysts for vapor phase oxidation of alkane and alkene compounds (Mairesse 1999; Chetouani, Taouk et al. 2003), gas separation membranes (Abrahams, Krok et al. 1996; Kežionis, Bogusz et al. 1999) and high temperature heating elements (Kežionis, Bogusz et al. 1999). Different properties and applications of BIMEVOX catalysts are discussed in the following section.

2.4 Properties and applications of BIMEVOX catalysts

BIMEVOX is derived from the parent compound $Bi_4V_2O_{11}$ (BIVOX) by partially substituting V^{5+} with iso and/or aliovalent metallic ions (Me = Li^+, Cu^{2+}, Co^{2+}, Ni^{2+}, Zn^{2+}, Fe^{3+}, Al^{3+}, Ti^{4+}, Zr^{4+}, Ge^{4+}, Sn^{4+}, Pb^{4+}, Nb^{5+} etc.). Bismuth Vanadium Oxide (BIVOX) shows three main polymorphs, α (face centered orthorhombic, a ≅ 5.533, b ≅ 5.611, and c ≅ 15.288Å), β (orthorhombic, a ≅ 11.06, b ≅ 5.61, c ≅ 15.28Å), and γ (tetragonal, space group I4/mmm, a ≅ 3.92 and c ≅ 15.5 Å). Out of these, the higher temperature γ phase shows the highest oxygen ion conductivity due to a higher oxygen vacancy disorder in the O-V polyhedral. Figure 2.1 shows the structure of γ - $Bi_4V_2O_{11}$. Abraham et al, (1988) have reported about the high oxide conductivity of the γ phase (Mairesse, Roussel et al. 2003; Mairesse, Roussel et al. 2003; Zhao, Xia et al. 2013). To stabilize the highly conductive γ phase of BIMEVOX under 500°C, the amount of metal substitution should be approximately 10 to 15 at.% (Muller, Chateigner et al. 1996; Mairesse, Roussel et al. 2003). The general reaction Equation is given as:

$$Bi_2O_3 + \frac{1-x}{2}V_2O_5 + xMeO_n \leftrightarrow Bi_2Me_xV_{1-x}O_{5.5-\left[\frac{(5-n)x}{2}\right]-\delta} \quad (2.1)$$

Where x is the atomic% of metal doped, n is the oxidation state of metal dopant, and δ is the loss in stoichiometric oxygen (Steil, Fouletier et al. 1999; Beg, Al-Alas et al. 2010; Khaerudini, Guan et al. 2014).

The substitution results in the high O_2 conductivity at lower temperatures as a consequence of the stabilisation of the γ phase (due to disordering of the vacancies through the substitution of the vanadium sites with cation dopant) by subduing $\gamma \Leftrightarrow \alpha$ and $\gamma \Leftrightarrow \beta$ transitions and creating additional oxygen vacancies. The creation of oxygen vacancies in the vanadium pentoxide doped with a tetra valent metal ion (M) can be represented by using Kroger-Vink notation as:

$$2MO_2 \xrightarrow{V_2O_5} 2M'_V + V_O^{\cdot\cdot} + 4O_O^X \quad (2.2)$$

Where $2M'_V$ represents the occupancy of a V site by an M with a negative charge, $V_O^{\cdot\cdot}$ represents positively charged oxygen vacancies, and O_O^X represents neutral lattice oxygen.

BIMEVOX system offers ionic conductivity higher than many other conventional electrolytes at the same temperature (e.g. conductivity of BICOVOX is 0.1 Scm^{-1} at 600°C which is two magnitudes higher than that of YSZ at the same temperature). Sometimes it is also represented as BIMEVOX.x, where x represents the amount of atomic% doping.

Due to the fact that the γ -BIMEVOX phase has an aurivillius-type crystal structure—alternate stacking of $(Bi_2O_2)^{2+}$ layers and $[(V/ME)O_{3.5-\delta})]^{2-}$ perovskite sheets with intrinsic oxygen ion vacancies to conduct oxygen ions, the conductivity of the materials is anisotropic in nature. For both single crystal and highly textured pellet samples (uniaxially pressed from the powder, textured by applying magnetic field), conductivity parallel to the $(Bi_2O_2)^{2+}$ layer (ab plane) has been observed to be a few orders of magnitude higher than that perpendicular to the ab plane (Lazure, Vannier et al. 1995; Hervoches, Steil et al. 2004). Consequently, micro structural texturing may be considered for optimal performance of these materials.

In V_2O_5, V can assume a variable co-ordination number; 4, 5 or 6. For coordination numbers 4 and 5, presence of various possible oxygen vacancy positions helps in explaining the conduction mechanism of BIMEVOX. The models which have been proposed are Equatorial Vacancy Model (EVM) in which the vacancies in the vanadate layer are bound in the bridging equatorial position, and the Apical Vacancy Model (AVM) in which the vacancies could be either bound in the non-bridging apical position, or mixed i.e. the vacancies are both in the apical and equatorial positions (Abrahams and Krok 2002). Figure 2.2 shows the concept of variable coordination numbers with equatorial, apical, and mixed vacancies in vanadium. In AVM, vanadium ion occupies 75% octahedral and 25% tetrahedral sites in an oxygen cage with an average coordination number 5.5, whereas in EVM octahedral: tetrahedral occupancy ratio is 50:50 indicating the average coordination number of V to be ~5. Exchange of oxide ions and vacancies lead to ion conduction in vanadate layer (Khaerudini, Guan et al. 2014).

Figure 2.3 shows the ion conduction mechanism of vanadium polyhedral starting with 3:1 tetrahedral to octahedral ratio in the initial stage (Figure. 2.3(a)) (Abrahams and Krok 2003). Oxide ion leaves the original position in vanadium octahedral (coordination number 6) to occupy equatorial vacancy. The coordination number of vanadium octahedra changes from 6 to 5 thereby creating an intermediate state of two tetrahedral (coordination number 4) and two 5 coordination vanadium polyhedral (Figure 2.3(b)). Finally, second oxide ion from 5 coordination vanadium polyhedra leaves to occupy another vacancy resulting to the starting situation of 3:1 tetrahedra to octahedral (Figure 2.3(c)). The vanadium octahedral and tetrahedral is in the changing state leading to the mobility of oxide ion in the vanadate layer.

The intrinsically present oxygen ion vacancies result in the fast oxygen ion diffusion, thus, lowering the activation energy, and increasing the ionic conductivity. It also depends on the concentration and the nature of dopant. In general, activation energy (within the temperature range of 300-350°C) decreases (due to the increasing number of oxide ion

vacancy) with an increasing dopant concentration till the optimum value reached. The optimum value is around 10-20 atomic percent based on the type and charge of dopants. No clear trend is reported for the variation of activation energy with dopant concentration in the higher temperature range (500-600°C) (Kant, Singh et al. 2008; Al-Areqi and Beg 2012; Al-Areqi, Beg et al. 2012), but the maximum conductivity is observed with x close to the limit of stabilization of γ phase (x = 0.05 for Na, x = 0.1 for Ca, x = 0.13 for Ag for conductivity at 600°C, etc.). Detail and systematic experimental studies combined with theoretical explanation would be helpful to understand the correlation between activation energy and the nature/concentration of the dopants. Addition of extra dopant above the optimum value generally leads to the decrease in the conductivity which can be explained in terms of two ways.

In case of dopant cations of higher valence, conductivity at ~600°C is observed to decrease and activation energy of the oxygen ion conduction increases as a result of increased interaction between the dopant ions and the oxide ion vacancies. Effect of double substitution has been studied and the substitution on either the bismuth site or the vanadium site has shown relatively better mechanical properties and thermodynamic activity as compared to single cation doped BIMEVOX systems for practical applications (Alga, Ammar et al. 2005; Beg, Hafeez et al. 2014).

It has also been reported that different preparation techniques for BIMEVOX result in different microstructures which lead to differences in their conductivities. The conductivity (at 300 and 600°C) and activation energy (300-600°C range) of various metal doped polycrystalline BIMEVOX systems has been shown in Table 2.3. Samples with small crystallite/grain size (dc) exhibit higher conductivity due to lower activation energy. Small grain size helps to stabilize the disordered γ -phase over the ordered and less conductive γ'-phase at lower temperature, and reduction of the particle sizes may be helpful to acquire high density ($\geq$ 95%) in the sintered body. In general, conventional solid-state reaction between oxides, followed by ball or attrition milling to reduce the particle size, has been used to prepare BIMEVOX powders. Overall, it is a time-consuming method and requires high temperature (>800°C). Sol gel co-precipitation, monomode microwave, solution combustion synthesis and mechanically activated techniques have all been reported to achieve small particle-size material (Bhattacharya, Mallick et al. 1994; Pell, Ying et al. 1995; Gasgnier, Petit et al. 2000; Roy and Fuierer 2009).

Besides, as LT-SOFC electrolytes, several other applications of the BIMEVOX systems have been described in literature. Due to its electro-catalytic activity for the dissociation of

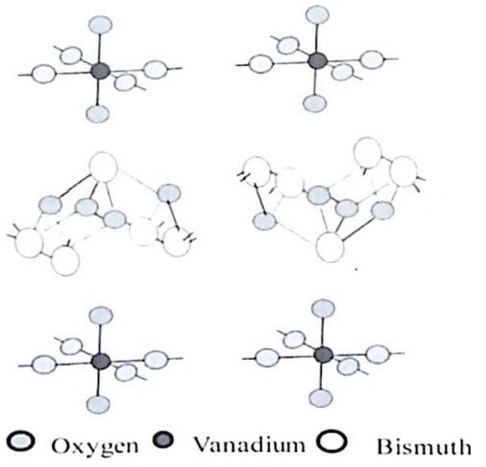

Figure 2-1 : Schematic structure of γ- $Bi_4V_2O_{11}$ (Abrahams and Krok 2003)

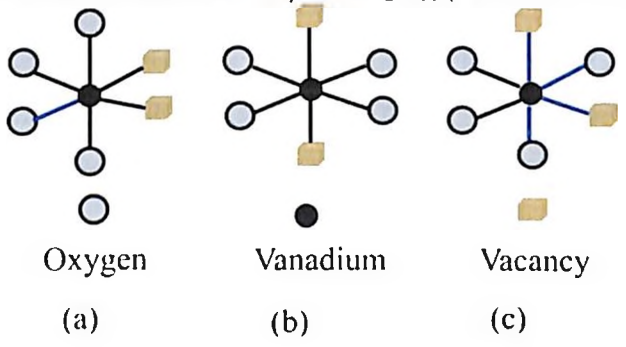

Figure 2-2 : Schematic presentation of variable coordination of vanadium in BIMEVOX with (a) equatorial vacancies, (b) Apical vacancies, and (c) mixed vacancies (Abrahams and Krok 2003)

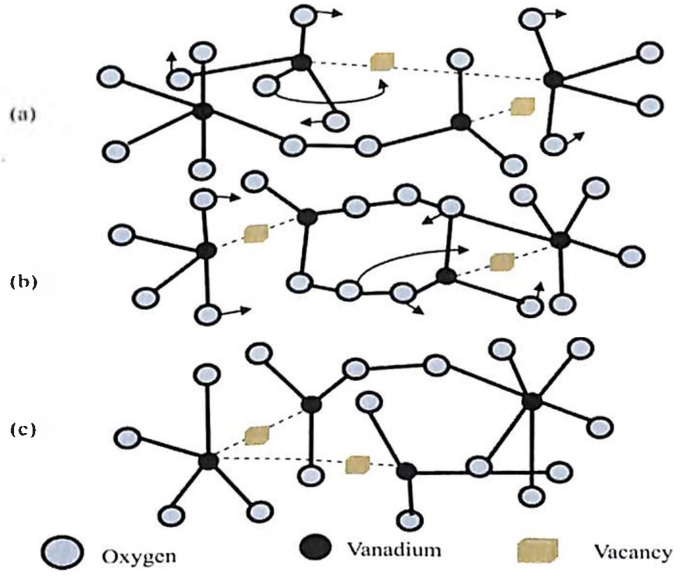

Figure 2-3 : Conduction mechanism in BIMEVOX. (a) initial state with 3:1 tetrahedra to octahedra ratio, (b) intermediate state with two five co-ordinate polyhedra and two tetrahedra, and (c) final stage with 3:1 tetrahedra to octahedra. The short arrows show the direction of movement of O, longer arrows show the transfer of O to vacancies. The dotted lines show the attachment of V to vacancies (Abrahams and Krok 2003)

oxygen along with the reversible self-transformation nature (i.e. electrolyte to electrode under polarization) BIMEVOX systems can be considered as a promising material for oxygen separation membrane (Mairesse 1999; Pirovano, Vannier et al. 2003; Pirovano, Vannier et al. 2003; Capoen, Steil et al. 2004; Paydar, Hadian et al. 2006). The high oxide ion conductivity of the BIMEVOX is employed in various oxidative processes such as dehydration of propane, coupling of methane, dehydromerization of propene and other mild oxidation processes in the catalytic dense membrane reactors (CDMR). Some of the BIMEVOX systems are tentatively used as powder catalysts in fixed bed reactor and as dense membranes in catalytic dense membrane reactor for oxidation of hydrocarbons as mention in Table 2.4. The catalytic performance of $Bi_2Cu_{0.1}V_{0.9}O_{5.35}$ (BICUVOX) and $Bi_2Co_{0.1}V_{0.9}O_{5.35}$ (BICOVOX) powders in fixed bed reactor for the oxidative dehydrodimerisation of propene have been studied by Chetouani et al, (2003-4). The powders are prepared by a standard solid oxide route by heating a mixture of Bi_2O_3, V_2O_5, CuO or CoO at 600°C in air. After regrinding, the powder is finally calcined at 850°C in air for 20 h in a gold crucible. The vapor phase oxidation is carried out in a stainless steel fixed bed reactor in the temperature range 300–550°C. For the both catalysts, at low temperature (up to 450°C), propene (C_3H_6) is mostly converted to CO_2, while from 450 -550°C zone oxidative dimerisation of C_3H_6 to 1,5-hexadiene (C_6H_{10}) increase at the expense of CO_2. Detail study show that BICOVOX is more active and more selective to formation of 1,5-hexadiene than BICUVOX (Chetouani, Taouk et al. 2003; Chetouani, Taouk et al. 2004).

Löfberg et al, (2004, 2006) demonstrate the use of polycrystalline BICOVOX and BICUVOX dense membranes in catalytic dense membrane reactor for oxidation of propene and propane. Conversion rate is observed to depend on the number of available active sites on the surface of the membranes. Mirror-polished BICUVOX and BICOVOX membranes studied are poorly active for propene oxidation because of a small number of active sites but show an excellent stability and reproducibility (lasting more than 1 month) during which products of mild oxidation (acrolein, hexadiene) and CO are formed. Membranes with depolished surfaces exhibit high conversions of propene (up to 60 mol%), and also of propane (up to 20 mol%) (Löfberg, Boujmiai et al. 2004; Löfberg, Bodet et al. 2006; Löfberg, Pirovano et al. 2006).

Löfberg et al, (2006) have studied C_1–C_3 alkanes oxidation capability of depolished $Bi_2V_{0.8}Ta_{0.2}O_{5.5}$ and $Bi_2Ni_{0.1}V_{0.9}O_{5.35}$ membranes in a catalytic dense membrane reactor. Alkenes are first produces at low conversion and CO and H_2 follow at higher conversion. Initially, with temperature, the H_2/CO ratio continues to increase and reaches to a maximum

value of ~3.5. After this, H_2 continues to increase and CO is converted to coke, which gets deposited on the catalyst, and eventually deactivates it. The fact that the membrane could be in situ regenerated means that the structure and integrity of the membranes have not been modified, as indeed are shown by physicochemical analyses such as XRD, SEM and XPS (Löfberg, Bodet et al. 2006; Löfberg, Bodet et al. 2006). Apart from these, BIMEVOX has also found applications as water electrolysers and high temperature heating elements (Kežionis, Bogusz et al. 1999; Roy and Fuierer 2009).

2.5 Existing Gaps of Research

The national and international working status on energy related catalysts is truly rich, however, according to our knowledge no national level works have been reported on the development of nanoscale 'metal doped bismuth vanadate (BIMEVOX) systems and study these as catalytic for H_2 production from biomass is so far not reported in any context; Indian or Worldwide (Chetouani, Taouk et al. 2004; Löfberg, Bodet et al. 2006; Löfberg, Pirovano et al. 2006).

In India, most of the methods use for hydrogen production need high reaction temperature (gasification, combustion, partial oxidation etc), and gasification is prerequisite (Balat and Kırtay 2010). High temperature accelerates many unwanted reactions, including those involve in catalyst sintering and favor the formation of coke, a major deactivating foulant produce by the reaction (Holladay, Hu et al. 2009). Additionally, it affects the life of the reactor system, therefore materials and operational costs increases.

Waste water from sugar, agricultural, alcohol and pharmaceutical industries contains certain sugar based biomass. These waters are neither easy to clean nor is it environment friendly to let these be free in rivers or stream. Therefore, technologies and advancements are required to control these situations (Bej, Pradhan et al. 2014).

2.6 Novelty:

The novelty of this work can be described in four points;

❖ Although, BIMEVOX compounds demonstrated potential to be used in different industrial applications such as fuel cells (Krok, Bogusz et al. 1993; Abrahams, Krok et al. 1996; Kežionis, Bogusz et al. 1999; Guillodo, Fouletier et al. 2002), water electrolyzers (Kežionis, Bogusz et al. 1999), oxygen sensors (Krok, Bogusz et al. 1993; Abrahams, Krok et al. 1996; Kežionis, Bogusz et al. 1999), cathodes in rechargeable batteries

Table 2-3: Summary of conductivity results for polycrystalline BIMEVOX systems. The Activation energies (eV) are within 300-600°C Range (Singh, Ghosh et al. 2017)

Electrolyte	Synthesis method	Conductivity (Scm^{-1}) /activation energy (eV)		Ref
		300°C	600°C	
$Bi_4V_{1.94}Nb_{0.06}O_{11}$	SSR,CT:600°C/6 h,ST:800°C /1 h	3.09e-6/1.61	-	(Roy, Sahu et al. 2014)
$Bi_4V_{1.94}Zr_{0.06}O_{11}$		5.43e-6/2.05		
$Bi_4V_{1.94}Y_{0.06}O_{11}$		2.61e-6/1.97		
$Bi_4V_{1.94}Cu_{0.06}O_{11}$		5.78e-6/1.10		
$Bi_4Co_{0.07}Ni_{0.13}V_{1.80}O_{11-\delta}$	SSR, CT:700°C/20 h,ST:800°C /12 h	2.56e-4/0.39	4.89e-2/0.31	(Beg, Hafeez et al. 2014)
$Bi_4Ag_{0.15}V_{1.85}O_{10.7-\delta}$	SSR, CT:700°C/20 h,ST:800°C /12 h	1.36e-4/0.48	1.74e-2/0.33	(Al-Areqi and Beg 2012)
$Bi_4Ag_{0.30}V_{1.70}O_{10.4-\delta}$		4.56e-4/0.44	5.36e-3/0.32	
$Bi_4Ag_{0.30}V_{1.70}O_{10.4-\delta}$	SSR, CT:700°C/20 h,ST:800°C /12 h	4.56e-4/0.27	5.20e-3/0.45	(Al-Areqi, Beg et al. 2012)
$Bi_4Ag_{0.13}V_{1.87}O_{10.74-\delta}$		1.38e-4/0.33	1.75e-2/0.46	
$Bi_4Cu_{0.08}Mg_{0.12}V_{1.8}O_{10.7}$	Citrate sol-gel,CT:650°C /3 h,ST:800°C /5 h	1.50e-3/0.82	4.90e-2/0.64	(Beg, Hafeez et al. 2014)
$Bi_4V_{1.8}Cu_{0.15}Nb_{0.05}O_{10.7}$	SSR, CT:800°C/24 h,ST:800°C /10 h	-	1.00e-1/0.21	(Alga, Ammar et al. 2005)
$Bi_4Ni_{0.20}V_{1.8}O_{10.7}$	Sol-gel, CT:600°C/24 h,ST:850°C /2 h	6.90e-3/0.41	1.10e-1/0.31	(Rusli, Abrahams et al. 2014)
$Bi_4(Cu_{0.05}Ti_{0.05}V_{0.9})_2O_{10.8}$	SSR, CT:630°C/12 h	1.40e-4/0.69[a]	2.36e-2@500°C /0.2[a]	(Exner, Fuierer et al. 2014)
$Bi_4Mg_{0.26}V_{1.74}O_{10.61}$	SSR, CT:620°C/12 h,ST:850°C /5 h	1.51e-3/0.68	8.60e-2/0.63	(Krok, Abrahams et al. 2000)
$Bi_4V_{1.9}Li_{0.1}O_{10.8}$	SSR, CT:800°C/12 h,ST:700°C /24 h	3.98e-5/0.38	2.75e-1/0.76	(Tanino uchi, Uda et al. 2010)
$Bi_4V_{1.9}Ag_{0.1}O_{10.8}$	SSR, CT:800°C/12 h,ST:700°C /24 h	6.82e-5/0.49	1.61e-1/0.37	
$Bi_4V_{1.8}Li_{0.2}O_{10.6}$	SSR, CT:700°C/12 h,ST:700°C /12 h	2.57e-4/0.52	1.14e-1/0.37	
$Bi_4V_{1.8}Ag_{0.2}O_{10.6}$	SSR, CT:800°C/12 h,ST:750°C /12 h	2.57e-4/0.85	4.05e-3/	

$Bi_4V_{1.75}Ti_{0.25}O_{10.875}$	SSR, CT:650°C/15 h + 750°C /5 h,ST:730°C /5 h	2.60e-3/0.78	1.36e-1/0.46	(Paydar, Hadian et al. 2004)
$Bi_4Zr_{0.38}V_{1.62}O_{10.81}$	SSR, CT:650°C/12 h,ST:840°C /10 h	3.58e-5/0.43	2.37e-2	(Wróbel, Abrahams et al. 2005)
$Bi_4Ca_{0.17}V_{1.83}O_{10.745}$	SSR, CT:840°C/24 h,ST:800°C /12 h	3.27e-4/0.61	7.49e-2/0.75	(Beg, Hafeez et al. 2010)
$Bi_4Ca_{0.10}V_{1.9}O_{10.8}$		1.30e-4	1.40e-1/0.28	
$Bi_4Al_{0.26}V_{1.74}O_{10.74}$	Citrate sol-gel,CT:650°C /3 h,ST:800°C /5 h	7.73e-5/0.42	1.42e-1/0.36	(Al-Areqi, Al-Alas et al. 2010)
$Bi_4Hf_{0.25}V_{1.75}O_{10.875}$	SSR, CT:700°C/20 h,ST:800°C /12 h	7.31e-5/0.63 @ 340°C	5.83e-3/0.53 @560°C	(Beg, Al-Areqi et al. 2009)
$Bi_4Ce_{0.25}V_{1.75}O_{10.875}$	SSR, CT:700°C/20 h,ST:800°C /12 h	4.81e-6/0.56	4.91e-3/0.35	(Al-Areqi and Beg 2009)
$Bi_4V_{1.5}Fe_{0.5}O_{10.5}$	Polymeric salt composition method, ST:(800-850°C)/(2-4 h)	1.08e-5/0.78	2.51e-3/0.7	(Morozova, Buyanova et al. 2011)
$Bi_4V_{1.5}Fe_{0.25}Cr_{0.25}O_{10.5}$		1.60e-5/0.66	1.89e-2/0.84	
$Bi_4Mg_{0.6}V_{1.4}O_{10.79-\delta}$	SSR, CT:650°C/12 h,ST:840°C /10 h	2.25e-6/1.01	3.60e-3/0.89	(Malys, Abrahams et al. 2008)
$Bi_4Ba_{0.17}V_{1.83}O_{10.745}$	SSR, CT:740°C/24 h	4.46e-5/0.80	4.29e-2/0.87	(Beg, Hafeez et al. 2010)
$Bi_4Cd_{0.2}V_{1.8}O_{10.7}$	SSR, CT:700°C/20 h,ST:800°C /12 h	2.05e-4/0.24	2.86e-2/0.21	(Al-Alas, Beg et al. 2012)
$Bi_4Sr_{0.26}V_{1.74}O_{10.61-\delta}$	Microwave solid synthesis method, CT:900°C /20 h, ST: 800°C /5 h	1.50e-4/0.48	3.20e-2/0.36	(Beg, Al-Alas et al. 2010)
$Bi_4Sr_{0.2}V_{1.8}O_{10.7-\delta}$		7.70e-4/0.48	3.90e-2/0.31	
$Bi_4Ce_{0.13}Cd_{0.17}V_{1.7}O_{11-\delta}$	SSR, CT:700°C/20 h,ST:800°C /12 h	3.19e-4/0.54 @ 320°C	1.75e-3/0.32 @ 550°C	(Beg and Haneef 2015)
$Bi_4Ce_{0.17}Cd_{0.13}V_{1.7}O_{11-\delta}$		2.81e-5/0.71 @ 320°C	1.18e-2/0.25 @ 550°C	

[a] Aerosol Deposition at 500°C; SSR- Solid state reaction CT- Calcination temperature of powder, ST- Sintering temperature of electrolyte for conductivity measurement.

Table 2-4: Applications of BIMEVOX as catalyst reported by France's group

S. No	Catalyst	Preparation Method	Catalyst Properties	Application	Operating Parameters	Reaction Condition	Reactant Con.	Product Distribution			Ref
1.	$Bi_2Cu_{0.1}V_{0.9}O_{5.35}$	HT: 600°C/air, CT: 850°C/20 h	S_{BET} =0.25	Oxidative dimerisation of propene	C_3H_6:O_2:N_2 = 20:10:70 (P = 1 atm).	T (°C) 300-550	5-20	C_6H_{10} Mol%	CO_2 Mol%	CO Mol%	(Chetouani, Taouk et al. 2003)
								0-40	100-56	0-5	
	$Bi_2Co_{0.1}V_{0.9}O_{5.35}$		S_{BET} =0.25			300-550	5-30	0-10	100-55	0-5	
2.	$Bi_2Cu_{0.1}V_{0.9}O_{5.35}$	SSS: 600°C, CT: 850°C/20 h	S_{BET} =0.2	Oxidative dehydrodimerisation of propene	$O_2/C_3H_6/N_2$ = 7.5/22.5/70-15/15/70	T (°C) 300-550	14-56	C_6H_{10} (% S) 0-45			(Chetouani, Taouk et al. 2004)
	$Bi_2Co_{0.1}V_{0.9}O_{5.35}$		S_{BET} =0.2			300-550	21-59	0-40			
3.	$Bi_2Co_{0.1}V_{0.9}O_{5.35}$	HT: 600°C/air, CT: 850°C/20 h	S_{BET} =0.2	Catalytic oxidation of propene	HC/He = 1% HOP = $0.21*10^5$ Pa T (°C) = 675	T (°C) 600-675	23-79	HXD+DZ Mol%	CO_2 Mol%	CO Mol%	(Lofberg, Bodet et al. 2006)
								37-24.7	2.5-1.9	50.7-53.9	
						$2*10^2$-10^5Pa	34-37	16.1-22.4	2.6-1.4	67.7-59.8	
	$Bi_2Cu_{0.1}V_{0.9}O_{5.35}$		S_{BET} =0.2		HOP = $0.21*10^5$ Pa T (°C) = 675	600-675	28-80	30.4-22.3	2.3-5	56.8-48.7	
						$2*10^2$-10^5Pa	68-66	19.5-6.2	5.3-1.1	53.9-89.5	
4.	$Bi_2Ta_{0.2}V_{0.8}O_{5.5}$	SSS: 600°C, CT: 875°C/20 h		Selective oxidation of C_1–C_3 alkanes	FF = 50 cm^3min^{-1}	T (°C) 550-700	18-58				(Lofberg, Bodet et al. 2006)
	$Bi_2Ni_{0.1}V_{0.9}O_{5.35}$	SSS: 600°C, CT: 750°C/20 h					20-44				
5.	$Bi_2Co_{0.1}V_{0.9}O_{5.35}$	SSS: 600°C, CT: 750°C/20 h	S_{BET} =0.6	Propene oxidation		T (°C) 550-675	1-2	HXD (Mol%) 10-20			(Lofberg, Boujmiai et al. 2004)
6.	$Bi_4Cu_{0.2}V_{1.8}O_{10.7}$	SSS: 600°C, CT: 750°C/20 h	S_{BET} =0.4	Oxidation of propene and propane	P = 10^5 Pa.	T (°C) 550-700	Propane 8-23 Propene				(Lofberg, Pirovano et

	$Bi_4Co_{0.2}V_{1.8}O_{10.7}$					550-700	20-68 Propane 10-40 Propene 25-70		al. 2006)
7.	$Bi_2Co_{0.1}V_{0.9}O_{5.35}$	SSS: 600°C, CT: 750°C/20 h	S_{BET} =0.3	Oxidation of propene and propane	T (°C) 700 P= 1atm	Propane Propene	16-38 17-61		(Pirovano, Lofberg et al. 2006)
	$Bi_2Cu_{0.1}V_{0.9}O_{5.35}$	SSS: 600°C, CT: 750°C/20 h	S_{BET} =0.3			Propane Propene	14-20 13-57		
	$Bi_2Ta_{0.2}V_{0.8}O_{5.5}$	SSS: 600°C, CT: 875°C/20 h	S_{BET} =0.2			Propane Propene	16-48 25-65		

HT: Heating; CT- Calcination temperature; S_{BET}: BET surface area (m^2/g); SSS: Solid-state synthesis;%S: Precentage selectivity, HC/He: Hydrocarbon to helium ratio; HOP: High oxygen partial pressure; HXD: 1,5-Hexadiene; BZ: Benzene; FF: Feed flowrate; P: Pressure

(Castro, Millan et al. 2000), high transition temperature ferroelectrics (Castro, Millan et al. 2000), catalysts for vapor phase oxidation of alkane and alkene compounds (Mairesse 1999; Chetouani, Taouk et al. 2003), gas separation membranes (Abrahams, Krok et al. 1996; Kežionis, Bogusz et al. 1999) and high temperature heating elements (Kežionis, Bogusz et al. 1999); however, the BIMEVOX systems could be potential catalysts or supports for catalysts for H_2 production due to high O^{2-} ion conductivity.

❖ The SCS route is beneficial for saving energy and obtaining submicron particle materials. The smaller grain size of BIMEVOX may be desirable not only for obtaining higher surface area, but also for the sake of increased O^{2-} conductive at lower temperature (Mairesse, Roussel et al. 2003). For this project all the catalysts are prepared by SCS.

❖ In this project ethanol present in the water is used at a relatively low temperature (250-400°C). Low-temperature steam reforming is an energy efficient process, which produces hydrogen from water-diluted oxygenated hydrocarbons obtained directly from fermentation, eliminating the energy-intensive distillation of biomass-water mixtures which makes it more economical process (Satyapal, Petrovic et al. 2007). Therefore, low-temperature steam reforming of ethanol over BIMEVOX catalysts for H_2 production is a novel idea.

❖ Ethanol can be produced from waste product after the extraction and refining of sugar from sugar cane and agro-industrial wastes. Therefore, in future, this process will help to clean the wastes at the same time producing hydrogen from it, which is one of the future goals of energy ministry.

Chapter 3: Materials and Methods

The present chapter provides the details of experimental methodology adopted for the catalyst preparation, catalyst characterization (both fresh and used), and the catalytic activity study using low temperature steam reforming for hydrogen production from ethanol. Theories regarding different catalyst preparation, characterization, and the analysis of catalytic activity are also discussed.

3.1 Catalyst preparation methods

The success of catalyst manufacturing industries depends on the understanding and improvement of the fields of basic materials science (chemistry of solids, colloid chemistry, etc.) and catalyst preparation methods (Schwarz, Contescu et al. 1995; Aupretre, Descorme et al. 2005; Li, Hu et al. 2006; Seo, Youn et al. 2008). The method (sol-gel, precipitation, co-precipitation, solution combustion synthesis, etc.) parameters in each step (for sol-gel preparation: temperature, pH, precursor concentration, peptization process, used catalyst, etc. For solution combustion synthesis: stoichiometric ratio, combustion temperature, environment, etc.), along with the nature of the precursors dictate the properties of catalysts (Perego and Villa 1997; Regalbuto 2016). Important properties of catalysts used in the industries can be classified into two categories:

(1) Physical properties: Particle size distribution, dispersion, high surface area (provides maximum number of active sites), desirable porosity and particle orientation (which may increase the selectivity and yield of certain product(s)), thermal and mechanical strength, catalyst stability, etc., are under this category and proper combination of these properties ensure successful implementation of catalyst in the process.

(2) Chemical properties: Basic materials chemistry, element oxidation state, bulk and surface chemical and phase compositions, etc., affect the fundamental mechanism of the catalyst activity, influence the selectivity and yields of the products, and dictate catalysts stability (Schwarz, Contescu et al. 1995).

For catalysts preparation the first step is the choice of chemistry: what catalysts we want to make and then the preparation method. It is already known that the physical properties would be controlled by the preparation method. There are various methods and routes for catalyst preparation and it usually involves several successive steps. On the basis of preparation procedure, catalyst can be classified into two broad categories (Patil, Aruna et al. 2002; Regalbuto 2016):

(1) One or single pot methods: These are mainly composed of catalytically active components and supports. It is applied for solution combustion synthesis, precipitation process, sol gel technique, etc.

(2) Two pot methods: Generally, these types of catalysts include supports and catalytically active metals. Supports are prepared separately and then deposition of active metals/materials on supports can happen by impregnation or ion exchange method. Different catalyst preparation methods are explained in details, in the following sub-sections.

3.1.1 Sol-Gel technique

Sol-gel is a facile, reproducible, low-cost, and low temperature chemical process known for the synthesis of high purity inorganic materials. Additionally, it is easy to achieve homogeneous distribution of dopant in the matrix by this method.

In the late 1800's, a one-step sol-gel method is used to synthesize metals containing inorganic gels (Teichner and Gardes 1976). Later, in early 1970, this method is rediscovered for glass production without high temperature melting process (Pereira, Clark et al. 1994). It is a wet chemical technique which is more often used for the preparation of nano/submicron particle size, porous, and high surface area ceramics, glass, metal catalysts supported on inorganic oxides, etc.

A sol is a colloidal or molecular suspension (dispersed phase is so small (~1 nm-1 μm) that gravitational force does not exist, only van der Waals and electrostatic forces are present) of solid particles in a solvent (water, alcohol, etc.). A gel is a semi rigid mass, wherein the solvent gets entrapped in three dimensional network of solid, that forms when the solvent from the sol begins to evaporate, and particles left behind aggregates/polymerized (Caruso and Antonietti 2001). Metal alkoxides, metal chlorides, and metal nitrates, which are soluble in alcohols or water, are the popular precursors because they can rapidly be hydrolyzed to the corresponding hydroxides (Li and Wang 2004; Carrera Cerritos, Fuentes Ramírez et al. 2011). Precursors undergo the hydrolysis step in which the hydroxyl ion gets attached to the metal atom and replaces OR ion. This OR group secures bond with the hydrogen ion as shown in the following reaction:

$$M(OR)_x + H_2O \leftrightarrow (OR)_{x-1}M - OH + HOR \tag{3.1}$$

M: metal; R: alkyl group; x: valence state of the metal; OH: hydroxyl ion

Later, two partially or completely hydrolyzed molecules link together in the condensation/poly-condensation reaction step to form M-O-M or M-OH-M network as follows (Regalbuto 2016):

Condensation:

$$(\mathrm{OR})_{x-1}M-OH+HO-M(\mathrm{OR})_{x-1} \leftrightarrow (OR)_{x-1}M-O-M(OR)_{x-1}+\mathrm{H_2}O \qquad (3.2)$$

Depending on whether the liquid in the wet gel is removed by evaporative drying or by supercritical drying, the resulting dry material is named xerogel (higher density, less porosity) or aerogel (lower density, high porosity) respectively, as explained in Figure 3.1 (Ward and Ko 1995; Caruso and Antonietti 2001).

In this method, catalytic material can be prepared as bulk or powder solids (one step method: metal can be introduced during (instead of after) the formation of the support) or nano-sized metal particles dispersed on a matrix or support (multi step method: includes preparation of the support first and then the distribution of the active component precursor over the support surface occurs by impregnation, ion exchange, anchoring, etc.). Drying, calcination or pyrolysis, and possibly reduction of the powder are the other sequential steps used to obtain the active phase/species dispersed on the support (Caruso and Antonietti 2001; Irurzun, Tan et al. 2009).

Catalysts prepared by sol gel techniques result in highly homogeneous materials with high purity. For example, Pd/SiO_2 catalyst prepared by a sol gel method shows higher surface area, narrower pore size distribution and higher thermal stability along with lower deactivation during methane combustion and higher resistance to metal particle sintering as compared to the catalyst prepared by the impregnation (Irurzun, Tan et al. 2009). However, a large scale production of xerogel or aerogel catalysts in an adequate shape with, among others, sufficient mechanical strength and resistance towards abrasion is a challenging task (Perego and Villa 1997). Consequences of the method: Catalysts prepared by this method may suffer a shortfall in homogeneous particle size distribution and shape uniformity due to agglomeration in condensation step.

3.1.2 Precipitation and Co-precipitation technique

As the name implies, in this type of method mainly the catalyst is prepared by precipitation of solids from the precursor(s) solution. For single oxide support, precipitation technique is used for the preparation of support and then the active phase is loaded separately (Example- Preparation of Zinc oxide powder: equal volumes of organic ligand (examples: triethanolamine and ethylenediamine) and Zn^{II} stock solutions are mixed and the pH adjusted to 12.0 by the addition of sodium hydroxide (Trindade, de Jesus et al. 1994)). In case of mixed oxide supports or active phase/oxide support catalysts are generally prepared by co-

precipitation technique (Example- Preparation of nanoparticulate Au catalysts: An aqueous solution of $HAuCl_4 \cdot 4H_2O$ and water soluble metal salts, most preferably nitrates, such as $Fe(NO_3)2 \cdot 9H_2O$ is poured into an aqueous alkaline solution under agitation for a few minutes to form Fe_2O_3 supported Au catalyst (Haruta 2004)).

In this process the metal hydroxides, carbonates, oxalates or citrates are precipitated from their precursor salt solution (Li and Chen 1995; Banach and Machocki 2015) and then heat treated to oxide form. The most used precipitation is in the form of metal hydroxides as they have low solubility and it can be performed in two ways. One is by starting with an alkaline solution of precursors which is acidified by adding acidic precipitating agents: perchloric acid, nitric acid, etc (Massart 1981) (Ex- Synthesis of tungsten oxide nanoparticles by precipitation technique from aqueous solutions of ammonium tungstate para pentahydrate ($(NH_4)_{10}W_{12}O_{41} \cdot 5H_2O$) and nitric acid ($HNO_3$) (Supothina, Seeharaj et al. 2007)). The other, more often used process, is using acidic solution of precursors and by raising its pH by the addition of an alkaline precipitating agents (NaOH, KOH) or ammonium hydroxide (NH_4OH), carbonates and bicarbonates (Li, Hu et al. 2006). Metal chlorides, carbonates or metal nitrates are popular metal precursors. For example, alumina could be prepared by precipitating aluminium hydroxide from aluminium nitrate solution by addition of ammonium hydroxide.

$$Al(NO_3)_3 + NH_4OH \rightarrow Al(OH)_3 + NH_4NO_3 \tag{3.3}$$

The two major steps occurring during precipitation are (de Jong 2009):

1st step: liquid mixing/super-saturation followed first by nucleation and then crystal growth to form primary particles. 2nd step: aggregation of the primary particles to form precipitation, as shown in Figure 3.2. Homogeneous particle size distribution is difficult to obtain in precipitation method. However, good mixing affects the nucleation and aggregation and provides more homogeneous product. For the second step to occur, first the solution must be made supersaturated with respect to the solid component which is desired to be precipitated. Achieving super saturation stage is a little difficult as it can only be achieved for a short time and that too in limited solution volume. In 1st step the nucleation rises through the formation of $M(OH)_n$ entities. In the 2nd step, during growth, clusters of $M(OH)_n$ start to form and continue to grow in size approaching towards equilibrium state. This precipitated phase is then separated and dried to get catalyst. In this method it is relatively easier to control particle size and composition. However, this process is not favorable for the preparation of high purity phase material or for the cases where reactants have very different

solubility and precipitation rate (Regalbuto 2016). The precipitation method is affected by many factors, such as precipitation agent, pH, solution concentration, temperature, etc. Hence in terms of reproducibility it is difficult to prepare highly efficient catalysts by this method (Philip, Iyengar et al. 1998; Li, Wang et al. 2007; Wang, Wei et al. 2013).

3.1.3 Impregnation method

This is the simplest, least expensive, most prevalent and well known process to deposit active phase of the catalyst on the support. This process involves dissolving of active part in a solvent of adequate solubility and volatility, and adding the solution drop-wise onto support under vigorous stirring. The resultant mixture is dried for removal of residual solvent and then reduced in a reducing atmosphere (example- mixture of carbon monoxide and hydrogen gases at an elevated temperature). The quality of product depends on the nature of both characteristics of surface (surface area, porosity, wettability, etc.) and the reaction conditions (such as pH, concentration and nature of dissolved substances, etc.). It can be classified into two categories on the basis of volume of impregnated liquid used (Biswas and Kunzru 2007; El Doukkali, Iriondo et al. 2012):

(1) Incipient wetness impregnation (IWI)/Dry impregnation: In this technique, volume of used impregnated liquid (aqueous or organic solution) is equal to the pore volume of support (metal oxide or metal oxide precursor). When support and impregnated liquid come in contact, it is drawn into pores by capillary suction. Obviously, the maximum active phase loading becomes limited by the solubility factor of the precursor in the solvent. The concentration profile of the impregnated compound is controlled by the mass transfer within the pores throughout impregnation and drying. Dry or incipient wetness impregnation method is generally preferred in case of weak interaction between the active catalytic phase and the support (platinum over carbon support (Zhu, Cho et al. 2013), Cu over Al_2O_3 (Delmon, Jacobs et al. 1976)) and for high metal content dispersion (Ni over /Y_2O_3–ZrO_2 (Jiang 2006)).

(2) Wet impregnation: This technique is preferred when the interaction between active catalytic phase and the support is strong (Fe over SiO_2 (Alcalá and Real 2006), H_2PtCl_6 over Al_2O_3 (Zhang, Oliaee et al. 2015)) and when we do not know the pore volume. In this method volume of impregnated liquid is in excess and more than the pore volume of support. The driving force here is the concentration gradient of active catalytic phase between the bulk solution and the solution within the pores. In this method the impregnation time is much longer than that for dry impregnation.

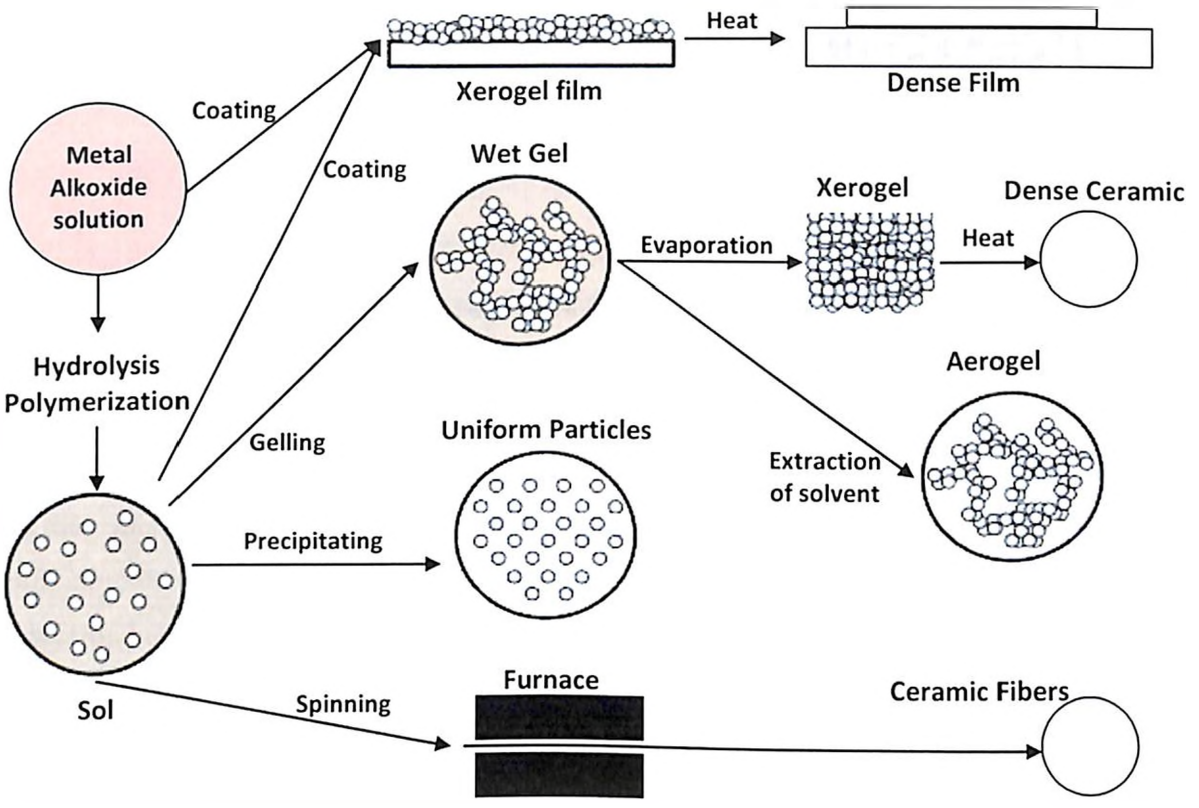

Figure 3-1 : Schematic presentation of the different stages and routes of the sol-gel technology (https://en.wikipedia.org/wiki/Sol-gel#/media/File:SolGelTechnologyStages.svg_25/09/2017)

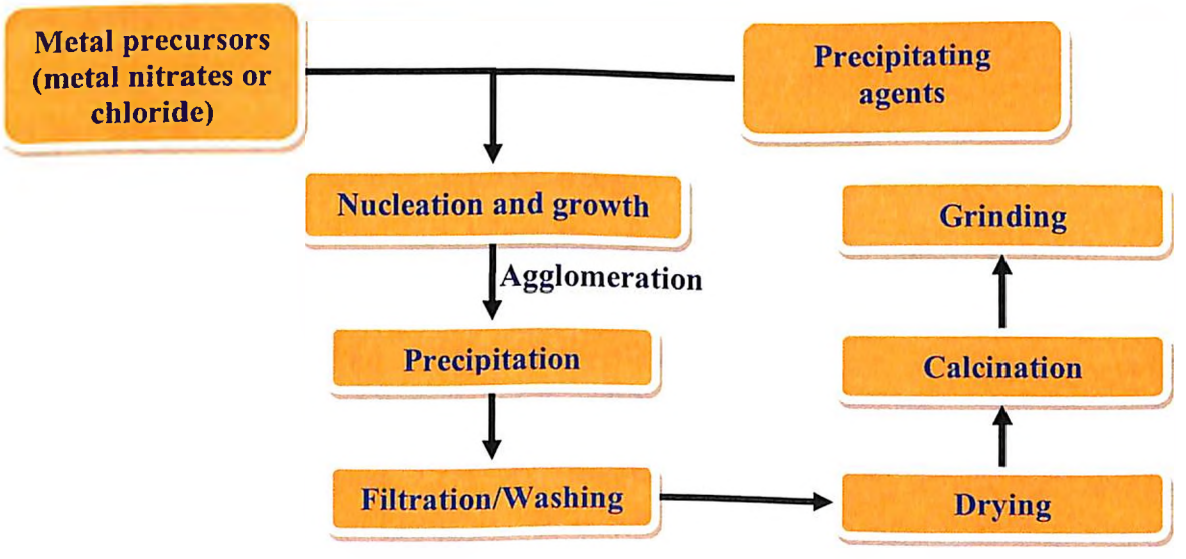

Figure 3-2 : Schematic representation of the steps involved in Co-precipitation method

Impregnation method is quite simple and because of its simplicity it is the most cited synthesis technique for the preparation of supported metal catalysts. However, this method is inadequate in providing the uniform surface coverage and may lead to undesirable product distribution (Regalbuto 2016).

3.1.4 Solution combustion synthesis technique

From mid 1980s, solution combustion synthesis (SCS) has been used for the synthesis of nano- or sub micron-scale ceramic oxides, metals, alloys, sulfides, manganite, zirconate materials, etc. for a variety of applications (Kingsley and Patil 1988; Chick, Pederson et al. 1990; Roy and Fuierer 2009; Roy, Loganathan et al. 2010; Manfro, da Costa et al. 2011; Kormányos, Thomas et al. 2016). SCS acquires distinct features that distinguish it from other combustion synthesis techniques (Aruna and Mukasyan 2008). In conventional solid state combustion synthesis (SSCS), reactants are in solid state and self-propagating high temperature (>1600 °C) reaction condition leads to much coarser particles than that observed in SCS, where initial reactants are in liquid form by mixing precursors with water or other solvents (Aruna and Mukasyan 2008).

Like SSCS, SCS is a self-sustained exothermic reaction process. A low temperature (≤ 400 °C) heating initiates the redox (reduction-oxidation or electron transfer) reactions between mixtures of oxidizers (metal nitrates) and fuel (carbohydrazide, glycine, urea, etc.) (Varma, Mukasyan et al. 2016). The exothermic characteristics of the reaction produce the self-sustaining spontaneous combustion. SCS starts with dehydration and thermal decomposition of fuel-oxidizer mixture. The term 'combustion' covers flaming (gas-phase), smoldering (heterogeneous) as well as explosive reactions (Patil, Aruna et al. 1997). Depending upon the fuel used and the metal ions involved, the nature of combustion differs from flaming to non-flaming (smoldering). The exothermicity ($T_{adiabatic}$) of redox reaction varies from ~600 °C (for smoldering) to ~1600 °C (for flaming combustion) (Patil, Aruna et al. 2002). The main difference between the smoldering and flame combustion is that the smoldering process mainly occurs in the solid surface rather than in the gas phase. It is relatively slower and mainly occurs when the low temperature as well as low fuel to oxidizer ratio is used. Higher surface area is obtained with the smoldering while agglomerated particles are obtained with flaming combustion. This marked difference in surface area and particle size can be explained by the amount of gaseous products evolved during combustion (Patil 1993).

On the basis of required properties (chemical and physical) in the final product, different oxidizers (availability also important, for example- metal nitrates, metal oxides, etc.), fuels, and solvents can be used for SCS as listed in Table 3.1 (Patil, Aruna et al. 2002; Aruna and Mukasyan 2008; Yu, Smith et al. 2015). Sometimes NH_4NO_3 or HNO_3 could be added with oxidizer and fuel (without changing the proportion) to complete the combustion because they act as extra oxidizer. Mimani in 2001 has used NH_4NO_3 for the preparation of CeO_2-ZrO_2 from their metal nitrate as oxidizer, and glycine as fuel (Mimani and Patil 2001).

Solution combustion synthesis can be accomplished in two ways (Vojisavljević, Wicker et al. 2017). Either by heating fuel-oxidizer mixture at a constant lower temperature for longer time in order to remove the extra solvents and then increasing temperature to a higher value at which the combustion of the whole mixture happens simultaneously, or by heating fuel-oxidizer mixture at a constant low temperature, and the exothermic reaction initiates locally, which further self-propagates in the form of combustion wave.

There are various factors which can affect the solution-combustion synthesis process like flame temperature, fuel-oxidizer ratio, chemistry of fuel and oxidizers, environment, etc. The equivalence ratio of an oxidizer and fuel mixture is expressed in terms of the elemental stoichiometric coefficient (O/F ratio) (Jain, Adiga et al. 1981; Chen, Huh et al. 2007).

O/F = [Σ(Coefficient of the elements in nitrates)*(Oxidation state)] / (-1) [Σ(Coefficient of the elements in fuel) * (Oxidation state)] (3.4)

A mixture is said to be stoichiometric when O/F = 1, fuel lean when O/F > 1, and fuel rich when O/F < 1. Stoichiometric mixtures generate maximum heat of reaction (Tsuji, Gupta et al. 2002). The catalyst properties such as surface area, crystallite size, morphology etc. can be controlled by adjusting a proper fuel to oxidizer ratio. Nagabhushana et al, (2010) study the effect of fuel to oxidizer ratio on the structure of $LaMnO_{3+\delta}$ powder prepared with low temperature solution combustion synthesis at 300°C. They have reported increase in the crystallite size from 32 nm to 44nm as well as decrease in surface area from 33 m^2/g to 10 m^2/g on increasing the fuel-oxidant ratio from 0.5 to 1.5. According to them increasing the fuel to oxidant ratio significantly increases the reaction temperature during the combustion process which facilitates the crystal growth and also leads to decrease in the surface area and enhance particle size of the material (Nagabhushana, Chakradhar et al. 2010).

Generally, heating of initial fuel-oxidizer mixture is done by placing the crystallization disk on a heating plate/furnace and temperature kept in the range of 300-500°C (Kormányos, Thomas et al. 2016; Piumetti, Bensaid et al. 2017). In this method, metals, carbon, and

hydrogen are considered reducing elements with the corresponding valence for metal (v), carbon (+4), and hydrogen (+1). Oxygen, as an oxidizer, possesses the valence (−2), and nitrogen is assumed to have zero valence. For example, the reducing valence of glycine (NH_2CH_2COOH) is (0 + 2 + 4 + 2 + 4 − 2 − 2 + 1) = +9, whereas the valence of a metal nitrate, $Me^{v}(NO_3)_v$, is (v + 3v(−2)) = −5v. Note that hydration water (e.g., m molecules) does not affect the overall compound valence. Reactions involved during SCS process using metal nitrate hydrate as an oxidizer and glycine as a fuel can be explained as follows (by considering H_2O, CO_2, and N_2 as gaseous products)(Varma, Mukasyan et al. 2016):

$$Me^{v}(NO_3)_v \cdot mH_2O + \frac{5}{9}vC_2H_5NO_2 \rightarrow MeO_{v/2} + \left(\frac{25}{18}v + m\right)H_2O + \left(\frac{5}{18}v + \frac{v}{2}\right)N_2 + \left(\frac{10}{9}v\right)CO_2 \quad (3.5)$$

Some of the catalysts prepared by SCS with their application, particle size and fuel used are summarized in Table 3.2. It is an effective method for preparation of highly homogeneous and nanoscale materials which provides an easy way for the formation of good quality multicomponent compounds having complex crystal structures like phosphates, spinels, perovskites etc. (Varma, Mukasyan et al. 2016). So, due to these advantages of solution combustion synthesis mainly in producing the nanoparticles along with an ease of operation, we have selected solution combustion synthesis for the preparation of the BIMEVOX catalysts.

3.1.5 BIMEVOX Preparation by solution combustion synthesis

BIMEVOX catalyst systems are synthesized by a solution combustion synthesis (SCS) method because high porosity and small particle size can lead to the desirable high surface area. Reportedly, numerous metals (ME) have been successfully substituted for vanadium and have been found to stabilize, the γ-type $Bi_4V_2O_{11}$ phase, the most conductive and symmetric crystallographic polymorph of $Bi_4V_2O_{11}$, at ambient temperature (Vannier, Pernot et al. 2003). Here, we have prepared three BIMEVOX catalyst systems – bismuth cobalt vanadate (BICOVOX), bismuth nickel vanadate (BINIVOX), and bismuth copper vanadate (BICUVOX) as these materials shows relatively high conductivities and lower activation energies at lower temperatures (Krok, Abrahams et al. 1997). To date, the best ionic conductivities have been obtained for copper, nickel, cobalt, titanium and antimony members of the BIMEVOX family in comparison with the others (Krok, Abrahams et al. 1996; Malys, Abrahams et al. 2008). Abrahams et al, (1996) mention that substitution of vanadium by

divalent cations, such as Cu, Co, or Ni leads to stabilization of the γ-phase at room temperature (Abrahams, Krok et al. 1996).

In each case 10 atomic% vanadium in parent BIVOX is replaced by the dopant metal (cobalt (Co), copper (Cu), and nickel (Ni)). Abraham et al (1988), study the BICOVOX for different compositions of Co. It is found that mostly single phase is obtained for $0.15 \leq x \leq 0.2$ (x is the fraction of Co in $Bi_4V_{2-x}Me_xO_{11}$), for $x > 0.2$, pure phase is accompanied by many secondary phases and for $x < 0.15$ by an unidentified compounds (Abraham, Debreuille-Gresse et al. 1988). Lazure et al, (1995) propose the limits of the Co fraction in between 0.15 and 0.3 and their results show that the conductivity reaches a maximum for BICOVOX.20 (x=0.2) (Lazure, Vannier et al. 1995). Krok et al, (1996) suggest that for x = 0.2 the highly conductive fully disordered γ phase is obtained but it is not stable at low temperatures but by calcination of powder it can be stabilized at low temperatures (Krok, Abrahams et al. 1996). Krok et al, (1998) study the structural and electrical behavior of BINIVOX. Obtained results suggest that for x (composition of Ni) in between 0.1 to 0.3, the structure gradually changes from the orthorhombic β-phase to the tetragonal γ-phase. When composition lies between $0.10 \leq x \leq 0.20$, the slop of conductivity vs. temperature curve at temperature window 400-200°C (low temperature conductivity regions) is different from the slop obtained within the temperature window 500-700°C (high temperature conductivity regions), which indicates structural variation with temperature (Krok, Abrahams et al. 1998). Abraham et al, (1998) report that for BICOVOX.20, BICUVOX.20 and BINIVOX.20, for x = 0.2, the oxygen vacancies are found to be exclusive (Abrahams, Nelstrop et al. 1998). Therefore 10 atomic% of metals is preferred.

Here, the process being primarily combustion, the important parameter under consideration is fuel and oxidizer to fuel ratio (O/F). The equivalence ratio of the oxidizer (metallic nitrates) to fuel (glycine) are calculated according to Equation 3.4. Here, glycine is used as fuel as it is one of the cheapest and most cited fuels for SCS studies (Purohit, Sharma et al. 2001). Glycine, serves two principal purposes: first, as fuel for the combustion reaction, being oxidized by the nitrate ions. Additionally, the glycine molecule has a carboxylic acid group at one end and an amine group at the other end. This "zwitterionic" character allows effective complexation with metal cations of varying ionic size and increases metal's solubility and prevents selective precipitation as water is evaporated to maintain compositional homogeneity among constituents. Alkali and alkaline-earth cations are most effectively complexed by the carboxylic acid group, while many transition metals are most effectively complexed by the amine group (Chick, Pederson et al. 1990; Purohit 2001).

Table 3-1 : List of various oxidizers, fuels, and solvents used for SCS (Patil, Aruna et al. 2002; Aruna and Mukasyan 2008; Yu, Smith et al. 2015)

Oxidizer	Fuel	Solvent
Metal nitrates or nitrate hydrates: $Me^{v}(NO_3)_v \cdot nH_2O$ v - metal valence	Urea (CH_4N_2O)	Water (H_2O)
Ammonium nitrate (NH_4NO_3)	Glycine ($C_2H_5NO_2$)	Hydrocarbons:
Nitric acid (HNO_3)	Sucrose ($C_{12}H_{22}O_{11}$)	Kerosene
	Glucose ($C_6H_{12}O_6$)	Benzene (C_6H_6)
	Citric acid ($C_6H_8O_7$)	Alcohols:
	Hydrazine-based fuels:	Ethanol (C_2H_6O)
	Carbohydrazide (CH_6N_4O)	Methanol (CH_4O)
	Oxalyldihydrazide ($C_2H_6N_4O_2$)	Furfuryl alcohol ($C_5H_6O_2$)
	Hexamethylenetetramine ($C_6H_{12}N_4$)	2-Methoxyethanol ($C_3H_8O_2$)
	Acetylacetone ($C_5H_8O_2$)	Formaldehyde (CH_2O)

Table 3-2 : Various catalysts, fuel used, application, achieved particle size

Catalyst	Fuel Used	Size (nm)	Application	Ref.
MgO	Glycine	12–23	Fluoride removal from drinking water	(Nagappa and Chandrappa 2007)
TiO_2	Glycine	8–12	Carcinogenic hexavalent chromium reduction	(Aarthi and Madras 2008)
WO_3	Glycine, urea	12–59	Removal of organic dye from water	(Morales, Cason et al. 2008)
WO_3–ZrO_2	Urea	10–25	Solvent-free synthesis of coumarins	(Naik, Mishra et al. 2008)
Cu/ZnO/ZrO_2/Pd	Glycine	7–14	Oxidative hydrogen production from methanol	(Schuyten, Dinka et al. 2008)
$Ce_{0.98}Pd_{0.02}O_{2-\delta}$	Oxalyl dihydrazide	30–40	Selective CO oxidation	(Ribeiro, Souza et al. 2008)
Ni/CeO_2(Al_2O_3)	Glycine	18-25	H_2 production via aqueous phase reforming	(Roy, Sullivan et al. 2011; Roy and Leclerc 2015)
$LaBO_3$ B = Cr, Mn, Fe and Co	Urea	55–75	Decomposition of N_2O to N_2 and O_2	(Russo, Mescia et al. 2007)
Co_3O_4	Glycine	10-15	Acetone detection (Chemical sensor)	(Vojisavljević, Wicker et al. 2017)
$CuNb_2O_6$, $ZnNb_2O_6$	Urea	8-20 4-32	Solar energy conversion and environmental remediation	(Kormányos, Thomas et al. 2016)
Ce-Cu-O	Urea	7-14	CO oxidation, Soot combustion	(Piumetti, Bensaid et al. 2017)

From literature, stoichiometric (O: F = 1) compositions is chosen for the preparation of BIMEVOX catalyst systems as stated below from Equation (3.6), to Equation (3.8):

$$4Bi(NO_3)_3 + 0.9V_2O_5 + 0.2Co(NO_3)_2 \cdot 6H_2O \xrightarrow{300°C/air} Bi_4[V_{0.9}Co_{0.1}]_2O_{11-\delta} \quad (3.6)$$

$$4Bi(NO_3)_3 + 0.9V_2O_5 + 0.2Ni(NO_3)_2 \cdot 6H_2O \xrightarrow{300°C/air} Bi_4[V_{0.9}Ni_{0.1}]_2O_{11-\delta} \quad (3.7)$$

$$4Bi(NO_3)_3 + 0.9V_2O_5 + 0.2Cu(NO_3)_2 \cdot 6H_2O \xrightarrow{300°C/air} Bi_4[V_{0.9}Cu_{0.1}]_2O_{11-\delta} \quad (3.8)$$

Where, δ shows the intrinsic oxygen ion vacancies.

Flow chart of SCS method for BIMEVOX catalyst preparation and characterization techniques carried out is shown in Figure 3.3. Preparation of BIMEVOX from solution combustion synthesis occurs in following steps:

Step 1: In this process, deionized water is used as an initial medium. Firstly, the metal nitrates (stoichiometric amounts of bismuth nitrate ($Bi(NO_3)_3.5H_2O$; Rankem, > 99% purity), vanadium pentoxide (V_2O_5; Himedia, > 98% purity) and dopant metal nitrate [$Co(NO_3)_2.6H_2O$; (Molychem with > 99% purity), $Ni(NO_3)_2.6H_2O$; (Qualikems, > 99% purity), and $Cu(NO_3)_2.3H_2O$; (Himedia with > 98% purity)] as oxidizer as mentioned in Table 3.3) are dissolved in solvents like deionized water or ethanol (20 ml) along with fuel glycine (H_2NCH_2COOH; Rankem, > 99% purity), to obtain a viscous solution in a mortar and pestle and thoroughly mixed for about 30 minutes. The mixture is transferred to a 500 cc beaker and dried overnight at room temperature.

Step 2: The solution is then placed on a hot plate kept inside a fume hood and heated at 300°C. The tip of a sheathed type-K thermocouple is placed just on the top of the mixture in an attempt to measure the temperature with time during combustion. From here, the process proceeds in three stages. In the initial stage, the solvent begins to boil and evaporates, due to which viscosity of solution also begins to increase. In the second stage, frothing takes place followed by ignition at one spot and in the third stage the combustion front spread out over the entire dish yielding voluminous black-brown foam as shown in Figure 3.4. Stoichiometric calculations of BIMEVOX samples are given in appendix 1.

During this process, gases are formed and escape through the cluster of particles, due to which pores are formed between the particles. The generation of a lot of amount of gases during the combustion process dissipates the heat produced in the process, thereby limiting the temperature rise, which also helps in preventing the sintering of the particles.

Step 3: The obtained mass is washed four to five times with DI water for the removal of any unwanted impurities and un-reacted chemicals. The wet paste is then dried in an oven (Macro

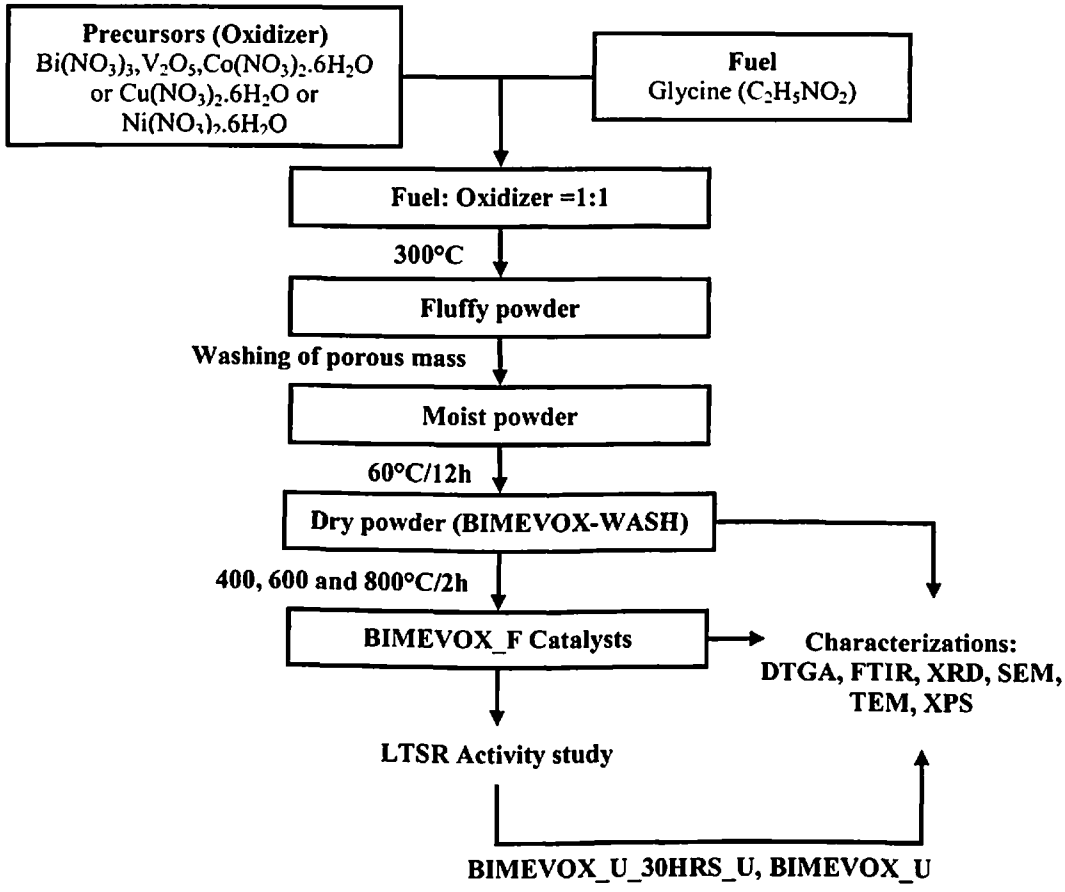

Figure 3-3: Flow chart of solution combustion synthesis procedure for BIMEVOX catalyst preparation and the relative characterization techniques carried out

Table 3-3 : Amount of precursors used for 20 gm BIMEVOX batch preparation with considering O:F=1:1

Catalyst System	$Bi(NO_3)_3$ (gm) (Rankem > 99%)	V_2O_5 (gm) (Himedia > 98%)	Metal Salt (gm)	Glycine (gm) (Rankem > 99%)	Calcing condition (C/hr) and physical appearance		
					400°C/2h	600°C/2 h	800°C/2h
BICOVOX	34.79	2.93	$Co(NO_3)_2$ (Molychem > 99%) 0.782	9.26	Brown	Dirty green	Blackish brown
BINIVOX	34.79	2.93	$Ni(NO_3)_2$ (Qualikems > 99%) 0.782	9.26	Light brown	Orange brown	Puce
BICUVOX	34.75	2.93	$Cu(NO_3)_2$ (Himedia > 98%) 0.782	9.26	Greenish yellow	Mustard yellow	Light puce

scientific works: MSW-211)) at 60°C for a period of 12 hrs. The dried sample is collected in a vile, named as catalyst 'BIMEVOX-wash'.

Step 4: Some of the after wash samples are heat treated in a muffle furnace at 400, 600 and 800°C for a period of 2 hrs each under natural ambient named as fresh catalyst. It is observed during this heat treatment that as the annealing temperature (TA) increases the appearance of the BICOVOX powder changes from brown (400°C) to dirty green (600°C) to blackish brown (800°C), for BINIVOX it changes from light brown (400°C) to orange brown (600°C) to puce (800°C), and for BICUVOX it varies from greenish yellow (400°C) to mustard yellow (600°C) to light puce (800°C) for fresh catalysts as shown in Figure 3.5. Wash and calcined at 400, 600 and 800°C in case of BICOVOX catalyst are named as BICOVOX-WASH, BICOVOX-400_F, BICOVOX-600_F and BICOVOX-800_F, respectively.

The typical temperature-time histories during the SCS process, with the help of thermocouple (K-type), for BICOVOX, BICUVOX and BINIVOX catalysts is recorded in temperature data logger and is shown in Figure 3.6. It can be seen that at ignition temperature (T_{ig} ~ 150°C), the reaction initiates and proceeds at extremely high rate reaching a maximum temperature value T_m ~ 650°C for BICOVOX, ~ 670°C for BINIVOX, and ~ 690°C for BICUVOX catalysts. After reaching to its maximum value, temperature suddenly drops to ~ 250°C within a few seconds. The total combustion process duration is in the range 10-10^2 s. In general, the process temperature profile depends on the experimental conditions (e.g., ratio between fuel and oxidizer, local mixture ignition, nature of the fuel, amount of catalyst etc.).

These fresh catalysts are used for steam reforming of ethanol and after using catalyst for 30 hrs it is named as BICOVOX-400_30HRS_U, BICOVOX-600_30HRS_U, and BICOVOX-800_30HRS_U. Catalysts used for long time run (> 300 hrs) are named as BICOVOX-400_U, BICOVOX-600_U and BICOVOX-800_U. Similar kind of nomenclature is used for BICUVOX and BINIVOX catalysts.

3.2 Catalyst characterizations

The primary objective of catalyst characterization is to understand the relationship of physical (microstructure, size, etc.) and chemical properties (chemical composition, phase composition, etc.) with catalytic activity (feed conversion, product selectivity, yield, etc.). This is essential for catalyst design and process optimization. The characterization is also carried to monitor the changes in physical and chemical properties of the catalyst during

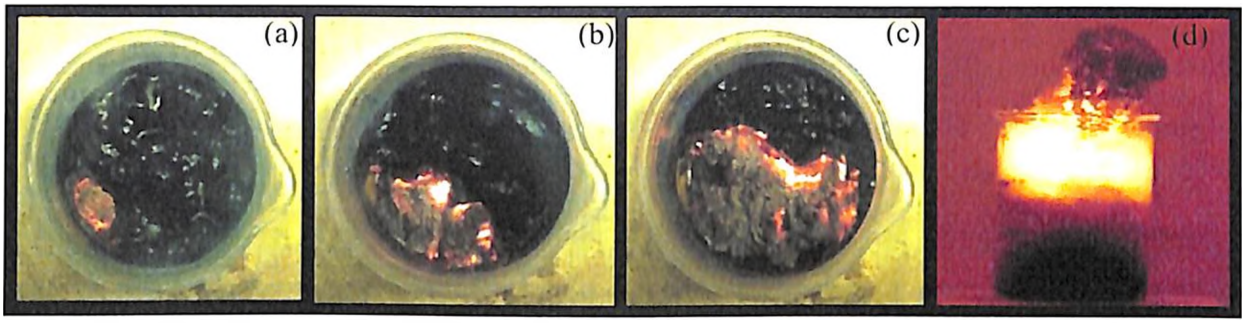

Figure 3-4: Different stages of solution combustion synthesis with time

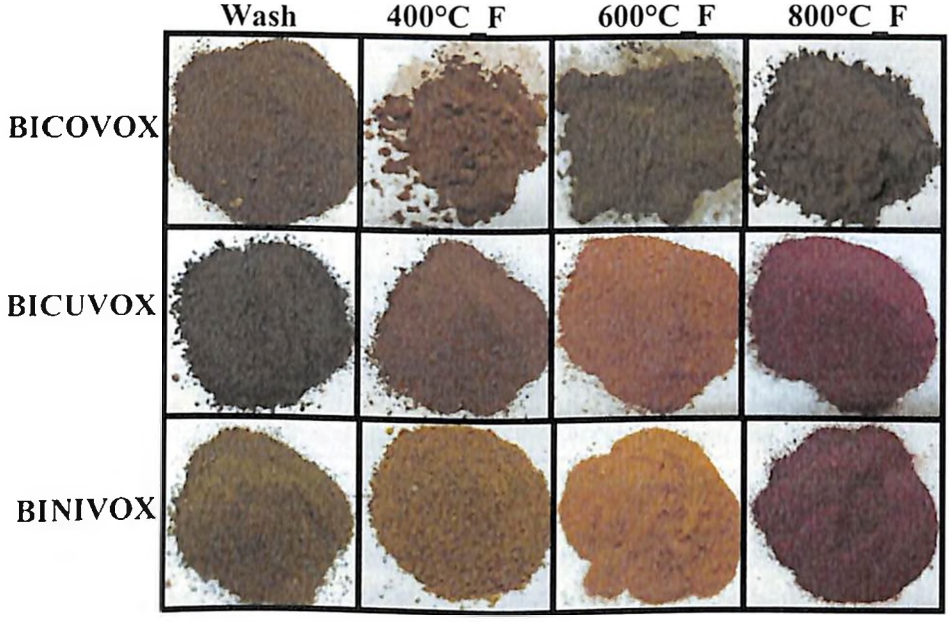

Figure 3-5: Physical appearance of the prepared BICOVOX, BICUVOX and BINIVOX catalysts after wash, calcining at 400, 600 and 800°C for 2 hrs

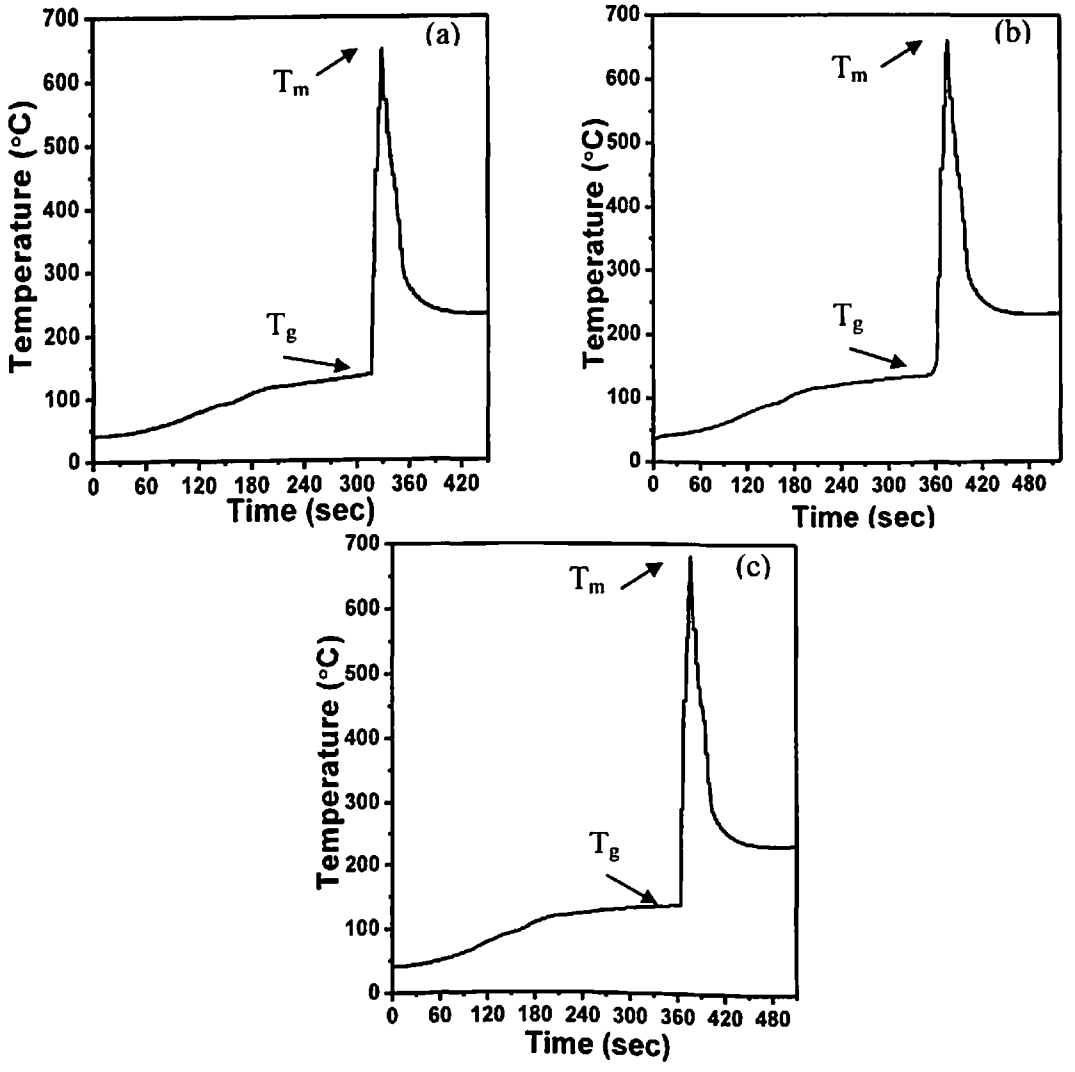

Figure 3-6: Time-temperature profile during solution combustion synthesis using thermocouple for (a) BICOVOX, (b) BINIVOX and (c) BICUVOX

preparation and reaction stages for better understanding and quality control. Determination of the extent of deactivation of catalysts during the reaction process is also important. Characterization of used catalysts can help to determine the causes of deactivation and modifying it. It also helps to design procedures for catalysts regeneration. For the present study, BIMEVOX catalysts (after wash, fresh, and used) has been examined by various characterization techniques. X-ray diffraction (XRD) analysis with rietveld refinement has been used to explain the phase composition, particle size, lattice parameters, unit cell dimension, cell volume, etc., while electron microscopy with EDX techniques is useful to understand the powder morphology, particle size distribution and elemental study. X-ray photoelectron spectroscopy (XPS) helps to characterize the chemistry of the powder surface. Thermo gravimetric analysis (TGA) and differential thermal analysis (DTA) has been used to understand thermal decomposition behavior along with Fourier transform infrared spectroscopy (FTIR) to determine the chemical bonds present in the catalysts.

3.2.1 Thermo Gravimetric Analysis (TGA) & Differential thermal analysis (DTA)

Thermo gravimetric analysis (TGA) is a thermal analytical technique which is used to identify the physical (gas adsorption, desorption) and/or chemical (decomposition due to loss of volatiles, chemisorption) changes in sample with respect to temperature or time in terms of weight loss or gain (Haines 2012; Gaisford, Kett et al. 2016). TGA instrument continuously records the change in weight of material during the heating/cooling. Results are plotted with temperature or time on the X-axis and weight loss in percentage on the Y-axis.

Differential thermal analysis (DTA) is used to determine the physical (adsorption, desorption, crystallization, melting, vaporization, sublimation etc.) and chemical (oxidation, reduction, break down reactions, chemisorption etc.) phenomena which cause the change in heat energy (exothermic or endothermic) as a function of temperature or time (Haines 2012; Gaisford, Kett et al. 2016). Results are plotted with temperature or time on the X-axis and heat flow in micro-volt on the Y-axis and by evaluating DTA curve, melting temperature and enthalpy data can be obtained.

The equipment we have used for our characterization is DTG-60H, SHIMADZU, which simultaneously provide the thermo-gravimetric and differential thermal analysis data. Instrument consists of a furnace inside which sample and reference pans (made up of platinum as we are working up to 800°C) are placed and they are supported by a precision balance. The mass and heat energy change of the samples are monitored during the experiment. The TA-60WS thermal analysis (control the temperature) workstation connects

the DTG-60 series and the computer. Intuitive data acquisition software controls the DTG-60 series and the FC-60A atmosphere control unit (to operate the gas flow). Equipment used during the analysis is shown in Figure 3.7. The experimental conditions are: Sample Weight – (25-30) mg; Temperature Range (Heating) – 40 – 800°C; Temperature Range (Cooling) –800 – 200°C; Scanning Rate – 5 and 10°C /min and Gas – Atmospheric air. During this process heating is controlled by keeping a constant heating rate however, cooling is not, it was a normal furnace cooling.

3.2.2 X-ray Diffraction (XRD)

XRD combined with Rietveld refinement technique is used for qualitative and quantitative analysis to determine the phase composition, crystallinity, lattice parameters, unit cell dimension, cell volume, particle size, internal stress, etc (Cullity and Weymouth 1957; de la Peña O'Shea, Homs et al. 2007). In this θ-2θ scan, the changes in the diffracted X-ray intensities are measured or recorded and plotted against the diffraction angle (2θ).

XRD (Θ-2Θ) of BIMEVOX catalysts are executed with the help of Rigaku miniflex II system by using with CuKα (λ = 1.54 nm) radiation (30 kV and 15 mA), 1.25° DS slit width, 150 mm goniometer radius under normal atmospheric condition. Equipment used during the XRD analysis is shown in Figure 3.8. Catalyst is ground into fine powder with the help of mortar and pestle so that it can adhere to the specimen holder, which is made of glass with a recess for powder (area: 2 cm *4 cm) and powder is pressed using a glass slide. The sample holder is mounted on the sample stage which keeps the sample aligned in the beam and controls the movement of the sample, X-rays beam focused on a sample and diffracted by it. Thus, the XRD run of the BIMEVOX samples are carried under the following conditions: Sample Weight – 0.3-0.5 gm; 2Θ Range – 10 – 100 °; Scan speed – 2 DPM (Degrees per minute); Sampling rate –0.05 °

While studying a complex material, one would like to use X-ray diffraction not only to know which chemical phases a sample contains, but also to determine the relative volume fraction of the individual phases. Rietveld refinement method uses all factors mentioned below to simulate/calculate the X-ray diffraction (θ-2θ) pattern of a sample composed of different phases (Rietveld 1969). Rietveld refinement has been carried out using Match! Software and open source Fullprof software suit. For carrying out the Rietveld refinement, the starting crystal structure models have been taken from the Crystallography Open Database (COD) and that is indexed in Appendix 1.

3.2.2.1 *Rietveld refinement of XRD data*

Rietveld refinement technique developed by Hugo Rietveld in 1967 is one of the most popular approaches used for the characterization of crystalline materials. Refinement provides structural information on atomic scale by performing least square fitting of the experimental data, because by nature it pulls off the broadening and shifting of the peaks both due to particle size and strain present in the lattice. The Rietveld method is used with the following prerequisites assumptions that: 1) An adequate structural model is opted, which makes both physical and chemical sense; 2) The model yields correct integrated intensities; and 3) SuiTable peak shape and background functions are considered.

The main motive of the Rietveld refinement is to minimize the function (M) which is essentially the difference between the calculated profile data and experimentally or observed data (Toby 2006).

$$M = \sum i\,(W_i)\left\{y(c,i) - \frac{1}{c}y_i(O,i)\right\}^2 \tag{3.9}$$

Where W_i = Statistical weight and is given by the following formula:

$$W_i = [1/(\sigma^2\, y_{(O,i)})] \tag{3.10}$$

σ^2 is the variance of the observation y_i

y_i(obs), y_i(calc) = observed data and calculated data

c= overall scale factor such that y_i(calc)= c*y_i(obs)

Generally, the intensity of the peaks from the experimental XRD data is calculated by using scattering factor (F_{hkl}). F_{hkl} basically sums all the scattering results from all atoms present in the unit cell in order to form the diffraction peak by the (hkl) planes of atoms.

While for the calculation of intensity of peaks for the calculated pattern, following formula is used (Toby 2006):

$$I_{calc} = (F^2_{hkl} L\, P\, A\, C)_{\theta,h} \tag{3.11}$$

Where F^2_{hkl} is the structure factor and vector h labels the Bragg reflections and subscript θ labels the phase vary from 1 up to the number of phases existing in the model.

L_h = Multiplicity factors and Lorentz polarization factor

P_h = Preferred orientation parameter/function

A_h = Corrected Absorption factor

C_h = Includes multiple factors like special absorption correction factor, non-linearity factor

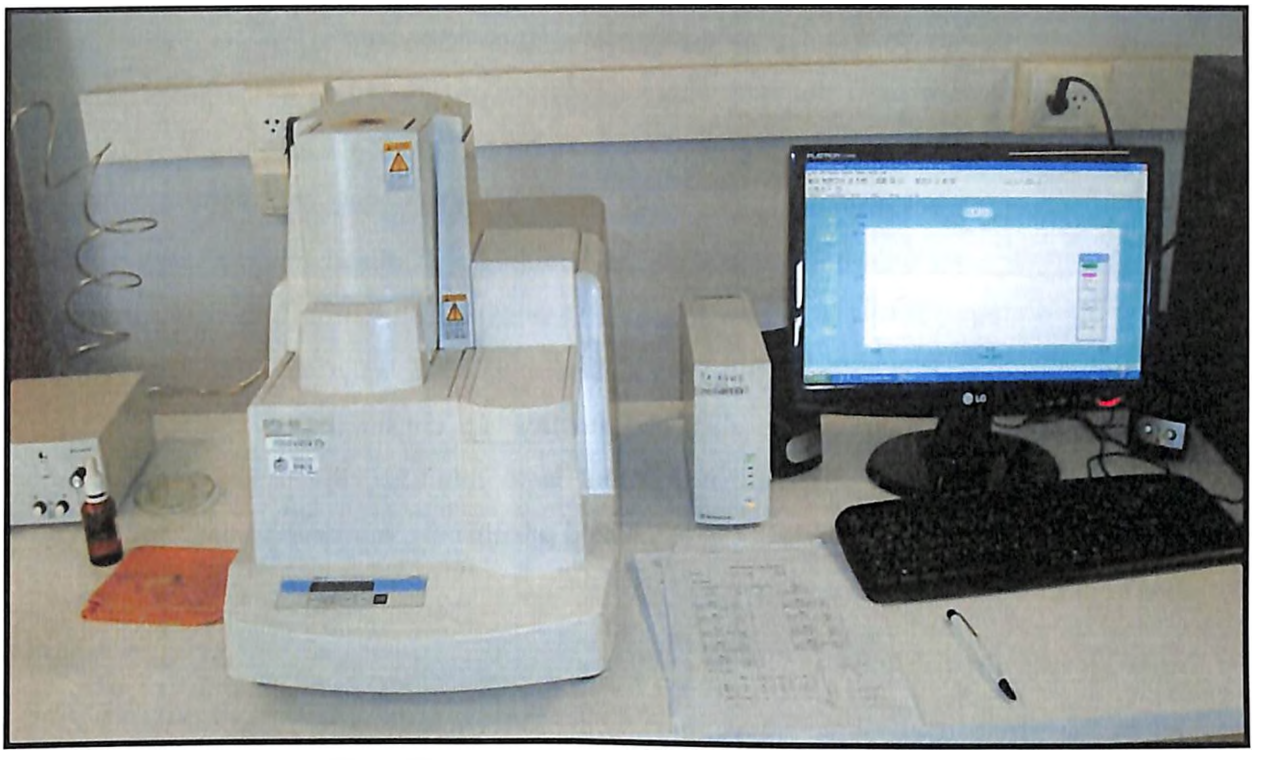

Figure 3-7:DTGA equipment used for catalyst characterization

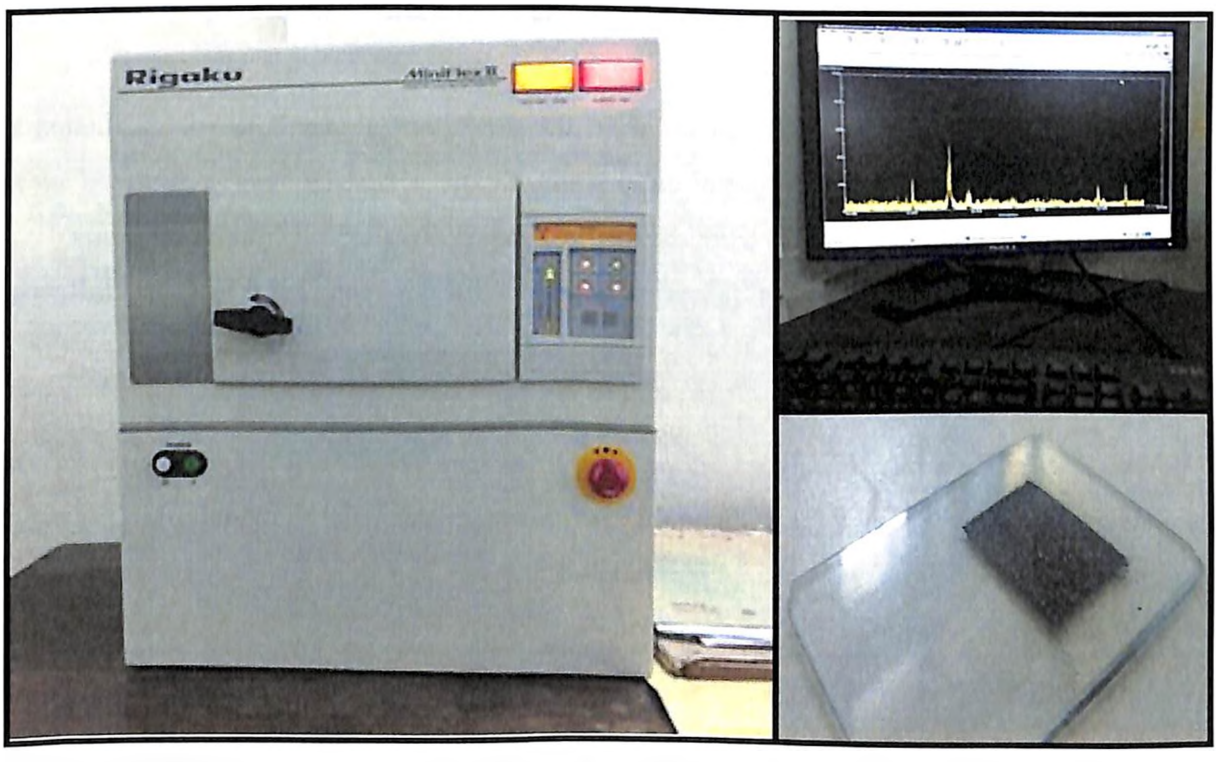

Figure 3-8:XRD equipment used in for catalyst characterization along with the catalyst placed over glass sample holder

3.2.2.2 *Parameter refined and their significance*

The following parameters are refined in Rietveld technique:

(a) Structural parameters: Isotropic temperature factors, anisotropic temperature factors, fractional positional coordinates, atomic occupancies, atomic coordinates, etc.

(b) Lattice parameters: preferred orientation parameter, (a, b, c) lattice parameters, etc.

(c) Experimental parameters: Cagliotti halfwidth parameters, peak shape parameters, asymmetry parameters, instrumental zero error, etc.

Generally, the refinement of parameter follows the following order:

1) Scale factor
2) Background
3) 2θ or zero point correction
4) Sample displacement error
5) Lattice parameters and unit cell parameter
6) Peak profile parameter
7) Asymmetry Parameters
8) Absorption and micro-absorption
9) Size-Strain Broadening
10) Strain

Few of the parameters are discussed below and rests of them are explained in Appendix 1.

• Lattice parameters and unit cell parameter

After refinement of the above mentioned parameters, the refinement of lattice parameters is followed by unit cell parameters because unit cell parameters can't be refined without refining the lattice parameters first. Although these don't make the refinement to diverge in most of the cases, they are one of the most important parameters to be refined. It is because these parameters help in estimating the expansion or contraction of the lattice structure.

• Peak profile parameter

There are two type of peak profile parameters namely peak width and peak shape parameter which are refined during the Rietveld refinement.

The first basic peak profile shape parameter is Cagliotti Half-width parameters. The Cagliotti Half-width parameters are used to characterize instrumental resolution function (IRF) of the diffractometer. The FWHM (full width at half maximum) is given by the Equation (Young and Wiles 1982):

$$FWHM = (U\,tan^2\theta + V\tan\theta + W)^{1/2} \quad (3.12)$$

Where U, V and W are instrumental resolution functions and depend upon the wavelength, geometry of the specimen and the slit width. They are related to the mosaic spread β and collimation angle α_1, α_2, α_3 of the monochromator crystal. Although the quadratic function of tan(θ) can be used to describe the variation of peak width with respect to the scattering angle, but using U, V and W parameter can result in much more better result

(Nagabhushana, Chakradhar et al. 2010). The U, V and W half-width parameter is given by the following Equation (Rodríguez-Carvajal 2000):

$$U = \frac{4(\alpha_1^2\alpha_2^2+\alpha_1^2\beta^2+\alpha_2^2\beta^2)}{\tan\theta_m^2(\alpha_1^2+\alpha_2^2+4\beta^2)}, V = \frac{-4\alpha_2^2(\alpha_1^2+2\beta^2)}{tan\,\theta_m^2(\alpha_1^2+\alpha_2^2+4\beta^2)}, W = \frac{\left(\alpha_1^2\alpha_2^2+\alpha_1^2\alpha_3^2+\alpha_2^2\alpha_3^2+4\beta^2(\alpha_1^2+\alpha_3^2)\right)}{(\alpha_1^2+\alpha_2^2+4\beta^2)} \quad (3.13)$$

The FWHM strongly depends upon the function used for the profile fitting. Generally, the refinement of profile shape parameters is carried out by using two functions namely, Gaussian functions and Lorentzian functions. The profile shape calculated using Gaussian function tends to be narrower at the bottom while wider towards peak position. Generally, the patterns obtained from the X-ray are very complicated and mainly are the mix of these two functions which is also called Pseudo-Voigt function.

The Gaussian function is given by the following formula (Rodríguez-Carvajal 2000):

$$G(x) = a_G \exp(-b_G x^2);\ a_G = \frac{2}{H}\sqrt{\frac{\ln 2}{\pi}};\ b_G = \frac{4\ln 2}{H^2} \quad (3.14)$$

While the Lorentzian function is given by the following formula (Rodríguez-Carvajal 2000):

$$L(x) = \frac{a_L}{1+b_L x^2};\ a_L = \frac{2}{\pi H};\ b_L = \frac{4}{H^2} \quad (3.15)$$

In our case, Pseudo-Voigt function which is a combination of Gaussian and Lorentzian functions has been used for the refinement of profile shape parameters.

$$\text{Pseudo Voigt Function} = (1-\eta)\left(\frac{1}{\pi^{\frac{1}{2}}}\gamma_G\right)\exp\left(\frac{-x^2}{\gamma_G^2}\right) + \eta\left(\frac{1}{\pi}\gamma_L\right)\left(1+\frac{x^2}{\gamma_L^2}\right)^{-1};0\leq\eta\leq1 \quad (3.16)$$

Where Υ_G and Υ_L is the ratio of $C_G^{1/2}/H$ and $C_L^{1/2}/H$ and are the normalization factor for Gauss and Lorentz function and η is one of the profile shape parameter (Rodríguez-Carvajal 2000).

• Strain

Strain is one of the main parameters, which also indicates the presence of defects in the crystal. More the defect concentration more will be the strain developed in the crystal. Formation of vacancies and the substitution of an ion in the lattice by another ion as well as presence of ion in the interstitial site may lead to the formation of strain in the crystal. It is also one of the main reasons behind the broadening of peaks. There are two types of strain produced in the crystal and both affect the location of peaks differently. If the strain produced in the crystal is due to the compressive stress, then the peaks of the phases moves towards lower diffraction angles, but if it is tensile in nature, then the peak moves towards the larger diffraction angle. So, it is very important to refine this parameter in order to analyze it.

For the calculation of strain in the crystal after refinement, we have used William-Hall method in order to calculate the strain developed in the crystal which is given by the following formula:

$$\beta_{total} = Size\ Broadening\ (\beta_L) + Strain\ Broadening(\beta_\epsilon) \quad (3.17)$$

$$\beta_L = \frac{K\lambda}{L\cos\theta};\ \beta_\epsilon = \varepsilon \tan\theta \quad (3.18)$$

This gives the final formula as (Rodríguez-Carvajal 2000):

$$\beta_{total}\cos\theta = \frac{K\lambda}{L} + \varepsilon \sin\theta \quad (3.19)$$

By plotting the graph and measuring the slope between β_{total}, cosθ and sinθ, one can calculate the strain (ε) present in the crystal.

All these parameters are refined in the Rietveld refinement process.

3.2.2.2.1 *Quality of Refinement*

The quality of refinement tells us about the degree of agreement between the calculated patterns and observed pattern (unknown pattern). There are some R-factors (residual factors) which can be used as an indicator to check the quality of refinement. Following are the reliability factors which are used to judge the quality of the refinement:

• **Profile Factor:** It is the ratio between the sums of difference observed and calculated intensity to that of sum of observed intensities. It is given by the following formula (Young and Wiles 1982):

$$R_p = 100\frac{\sum_{i=1,n}|y_i - y_{c,i}|^2}{\sum_{i=1,n} y_i} \quad (3.20)$$

Where y_i and $y_{c,i}$ are observed intensity and calculated intensity respectively.

• **Weighted Profile Factor:** It is given by the following formula (Toby 2006):

$$R_{wp} = 100\left[\frac{\sum_{i=1,n} w_i|y_i - y_{c,i}|^2}{\sum_{i=1,n} w_i y_i}\right]^{\frac{1}{2}} \quad (3.21)$$

Where w_i is the weight of observations, which is given by: $w_i = \frac{1}{\sigma^2[y_i]}$, in which $\sigma^2[y_i]$ is the variance of observation. The Equation in the numerator of the formula is the Equation that is minimized during the Rietveld refinement.

It is one of the most important R-factors because in this case the intensity of peaks is adjusted according to square root approach.

• **Expected Profile Factor:** $R_{exp} = 100\left[\frac{n-p}{\sum_{i=1,n} w_i y_i^2}\right]^{\frac{1}{2}}$ (3.22)

where, n refers to the no. of observations while p refers to the no. of parameters. One can't

have larger R_{wp} value than the R_{exp} (Rodríguez-Carvajal 2000). The maximum R_{wp} can have is R_{exp}.

• **GOF (Goodness of fit indicator):** $S = \frac{R_{wp}}{R_{exp}}$ (3.23)

The GOF value of 1 indicates towards the best quality of refinement.

• **Chi-Square:** It comes out to be large at the starting of the refinement and then keeps on decreasing as the degree of agreement between observed data and calculated data increases. It is given by the formula (Toby 2006):

$$\chi^2 = \left[\frac{R_{wp}}{R_{exp}}\right]^2 \quad (3.24)$$

Where R_{wp} and R_{exp} are weighted and expected profile factors.

When the value of $\chi 2$ is too less than 1, then it shows the overestimation of the model, if it much greater than 1, then it shows that the model is underestimated which also includes due to the wrong assumption of the model. The expected value of $\chi 2$ is either 1 or close to 1, and then it shows that the model is correct and degree of agreement between calculated and observed pattern is very high, which is the desired case (Varma, Mukasyan et al. 2016).

• **Bragg Factor (R_B):** It is given by (Rodríguez-Carvajal 2000):

$$R_B = 100\left[\frac{\Sigma_h|I_{obs,h} - I_{calc,h}|}{\Sigma_h|I_{obs,h}|}\right] \quad (3.25)$$

Where $I_{obs,h}$ and $I_{calc,h}$ are observed and calculated intensity

• **Crytallographic R_F-Factor:** It is given by (Young and Wiles 1982):

$$R_F = 100\left[\frac{\Sigma_h|F_{obs,h} - F_{calc,h}|}{\Sigma_h|F_{obs,h}|}\right] \quad (3.26)$$

Where $F_{obs,h}$ and $F_{calc,h}$ are observed and calculated structure factor. The value of R_F decreases rapidly as the refinement improves.

For the experiment, the crystallite size of the detected phases has been calculated using Debye-Scherer formula which is given by: $\beta_L = \frac{K\lambda}{L\cos\theta}$; where the value of λ is 1.54 Å for Cu Kα radiation, the value of K is 0.9 and θ is the position of the peak of the respective phases. For the calculation of crystallite strain, Williamson-hall plot method is used which gives the value of slope Ɛ (strain) by plotting the graph between $\beta_{tot}\cos\theta$ and $\sin\theta$.

3.2.2.2.2 *Methodology*

The whole process is carried out in the following steps:

Step 1: The powder diffraction pattern (θ-2θ) of catalyst is obtained with the help of X-ray diffracto meter.

Step 2: This XRD data file of fresh catalyst is imported into the MATCH software by converting it into suiTable file format which MATCH can read (CSV, MS DOS, DAT, etc.).
Step 3: The smoothing of the diffraction pattern is carried out if the XRD diffraction pattern is too rough i.e. contains too much noise.
Step 3: Using Crystallography Open Database (COD), the phase identification is carried out in order to find out the suiTable candidate list. The degree of agreement between unknown pattern and calculated pattern can be checked by 'Figure-of-Merit (FoM)' column. The candidate phase with high FoM is most likely to be a correct phase present in the material, although not always.

In this step, background and peak position of calculated pattern can be added, removed or changed manually in order to increase accuracy of phase identification. Constraints regarding known phase can also be defined at the start.
Step 4: Appropriate candidate phase is added to the matching phase.
Step 5: Refinement of parameters like scale factor, displacement factor, unit cell parameter etc. is carried out using Fullprof software suit as an add-on in MATCH! Software.
Step 6: Analysis of the obtained Rietveld refinement result is carried out and conclusion is made based on various factors and parameters obtained.

3.2.3 Fourier Transform Infrared Spectroscopy (FTIR)

Fourier-transform infrared spectroscopy is a vibrational spectroscopic technique, which takes advantage of asymmetric stretching, vibration and rotation of chemical bonds as they are exposed to designated wavelengths of electromagnetic spectra (Madejová 2003). Generally, molecule or material absorbs energy in the infrared (IR) region for the molecular vibration. In the intensity vs. wave-number graph the absorption/transmittance peaks corresponds to the vibration of bonds between atoms of the particular groups.

Each different material is a unique combination of groups; no two compounds produce the exact same infrared spectrum. Therefore, infrared spectroscopy can result in a qualitative analysis of every different kind of material. In addition, the area of the peaks in the spectrum is a direct indication of the amount of material present (Doyle 1992). FT-IR can take wavelength readings across the whole IR region simultaneously and smoothly, making this a very rapid technique. It is broken down into three groups: near infrared (frequency range 8000–3000 cm^{-1}), mid infrared (frequency range 4000–400 cm^{-1}) and far (frequency range 500–100 cm^{-1}) infrared (Yu, Kirkpatrick et al. 1999).

The IR data from solid sample can be acquired in transmission and reflection mode. In transmission mode sample typically need to be diluted with the IR-inactive KBr and pressed to the well known "KBr-pellet" for mechanical support. In transmission mode data signal is more clear and strong, but there are some disadvantages related to it. KBr is hygroscopic and therefore not easy to handle and store. A good KBr pellet is rather hard to make as well as it is time consuming and requires a special tool kit including a hydraulic press (Hurtubise and Krassig 1960). To overcome these disadvantages IR measurements could be performed using Attenuated Total Reflection (ATR) mode as this technique is simpler to use. The ATR crystal comprises an IR transparent material with a high refractive index and polished surfaces (Kazarian and Chan 2010). The infrared beam enters the ATR crystal at an angle of typically 45° (relative to the crystal surface) and is totally reflected at the crystal to sample interface. Because of its wave-like properties, the light is not reflected directly by the boundary surface but by a virtual layer within the optically less dense sample. The fraction of light reaching into the sample is known as evanescent wave (Hirschfeld 1977). Its penetration depth (typically of the order of a few microns, ca. 0.5 - 3 μm) depends on the wavelength, the refractive indices of the ATR crystal and the sample and the angle of the entering light beam. In the spectral regions where the sample absorbs energy, the evanescent wave is attenuated. After one or several internal reflections, the IR beam exits the ATR crystal and is directed to the IR detector (Müller, Brendler et al. 2008). The refractive index of the crystal must be significantly higher than that of the sample. Since the typical refractive indices for different ATR crystals are lie between 2 and 4 and mostly all the IR-active samples can be measured in that range. Germanium has a high refractive index and is used to study highly absorbing samples like carbon black colored rubbers. However, diamond is very robust and chemically inert making it an ideal crystal material for routine measurements on a wide range of samples (van Soest, Tournois et al. 1995).

The BIMEVOX catalysts are investigated using IR probe in the mid infrared region (Frontier, Perkin Elmer, India) equipped with ATR (GladiATR, PIKE Technologies, Inc.) to identify the presence of different chemical bonds and groups. The diamond crystal is used as an internal reflection element in ATR. Data averaged from 20 scans is plotted as% transmittance vs. wavenumber (cm^{-1}) and the peak positions on the graph are observed and corresponding functional groups are recognized and indexed comparing with the standard data base as mentioned in Appendix 1. FLUKA library is used for the primary analysis of spectrum. Equipment used for the analysis is shown in Figure 3.9.

3.2.4 Raman Spectroscopy

Raman spectroscopy is a vibrational spectroscopic technique based on inelastic scattering of monochromatic light (generally from a laser source) (Hardcastle, Wachs et al. 1991). Photons of laser light interacts with the sample and generates an infinitesimal amount of Raman scattered light (shifted frequency of the reemitted photons in comparison with. the original monochromatic frequency), which is detected as a Raman spectrum using a CCD (charge coupled device) camera (McCreery 2005; Frost, Henry et al. 2006). This shift or characteristic fingerprinting pattern (as compared with a standard data library from literature) in a Raman spectrum provides the information about vibrational, rotational and other low frequency transitions in molecules and makes it possible to identify substances including polymorphs and evaluate local crystallinity, orientation and stress (Porto and Scott 1967; Bacewicz and Kurek 2000). Raman spectroscopy can be used to study solid, liquid and gaseous samples. It has also proven useful in the explaining of structures of simple diatomic molecules, complex transition-metal oxides present as either bulk phases or surface-supported phase etc (Halford 1946; Hardcastle and Wachs 1991).

In this study, Raman of BIMEVOX catalysts are executed with the help of Horiba LabRam HR spectrometer equipped with a confocal DM 2500 Leica optical microscope (equipped with 10x and 50x objectives) and multichannel detection (liquid nitrogen cooled CCD) over the range of 150-1400 cm^{-1}. The 532 nm line of an argon laser (Model 171) is used as excitation source, with beam intensity not exceeding 10 mW on a sample. The incident beam is focused on the sample using a 50x objective lens. The diameter of the laser spot is kept ~2 μm. About 300-400 mg (about 1-mm thickness) of each catalyst is spread over a glass microscope slide. A Raman spectrum is recorded at various spots on the surface of the sample as mapping. The spectra of all samples are recorded at room temperature and normal ambience. Continuous spectral deconvolution for baseline adjustment, smoothing, determination of positions and intensities of individual bands is carried out by using XPSPEAK 4.1 software. A Voigt profile is considered for the fitting purpose. The Equipment set up used for the Raman data acquisition is shown in Figure 3.10.

3.2.5 X-ray photoelectron spectroscopy (XPS)

X-ray Photoelectron Spectroscopy (XPS), a well implemented surface chemical analysis technique, is used to analyze the surface chemistry of the materials in terms of elemental composition (qualitative and quantitative), chemical state, empirical formula, electronic state of the elements that exist within a material. XPS is used to analyze catalysts, metal alloys,

semiconductors, glasses, bio-materials, ceramics, ion modified materials, paints, inks, inorganic compounds, viscous oils, woods, plant parts, make-up, papers, polymers, teeth, bones, medical implants, glues, and many others (Roh, Potdar et al. 2004; Wu, Pantaleo et al. 2014)(XPS-NIST Standard Reference Database 20). The average depth of analysis for an XPS measurement is approximately 3-5 nm and it requires ultra-high vacuum (UHV) conditions (Jalowiecki-Duhamel, Pirez et al. 2010).

The analysis equipment we have used for BIMEVOX is Kratos Axis Ultra DLD X-ray photoelectron spectrometer with monochromatic Al Kα source operating at 13kV AC voltage and 9mA emission current. The operating pressure is ~10-9 torr. Charge compensation is achieved by the technique of charge neutralization using low energy electrons. After a wide range survey of each, high-resolution C, Bi, V, O, Ni, Co, Cu spectra of the samples are acquired in order to quantify the C/coke deposited, and find the variation of phases present. Resolution of all spectra is performed with the XPSPEAK 4.1 program using Voigt function.

3.2.6 Field Emission Scanning Electron Microscope (FESEM)

A scanning electron microscope (SEM) is used to determine particle size distribution, microstructure, and topography of the samples by scanning the surface with a focused beam of electrons. Beam of electron (primary electrons) focused and deflected by electronic lenses to produce a narrow scan beam which interacts with the surface atoms and produces signals which include secondary electrons (SE), reflected or back-scattered electrons (BSE), characteristic X-rays and transmitted electrons (Reichelt 2007). Secondary electron detector is standard equipment as they are emitted from very close to the surface and they provide high resolution image. FESEM-EDX (Energy Dispersive X-Ray) investigations allow us to reveal the quantitative analysis of elements to understand correlation between morphological changes and elemental composition.

The particle size distribution and microstructure of BIMEVOX catalyst are studied with Nova Nano FE-SEM 450 (FEI) with the specifications as: Beam landing energy can go down from 30 keV to 50 eV and resolution of 1.4 nm at 1 kV & 1nm at 10 kV and equipped with EDX spectroscopy system with 30° take-off angle for quantitative analysis, digital imaging, and X-ray mapping. The EDX (SAPPHIRE SEM) detector has 128 eV resolutions, and 20,000:1 peak-to-background ratio maintained at high throughputs. In order to prepare the FE-SEM specimen, a pinch of powder is sprinkled over carbon tape which is mounted over aluminum stub and images are taken at different magnifications (500x-100000x), along with the EDX data. Data is collected from two place; IIT Kharagpur and BITS Pilani.

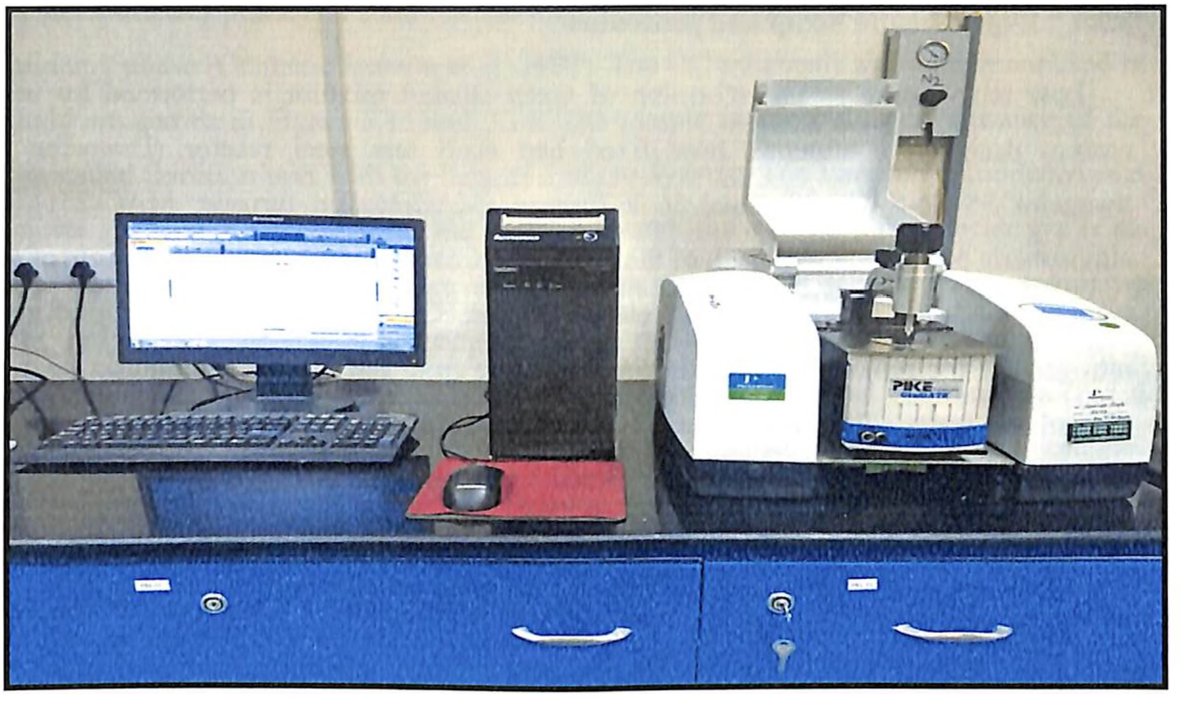

Figure 3-9: FTIR equipment used for catalyst analysis

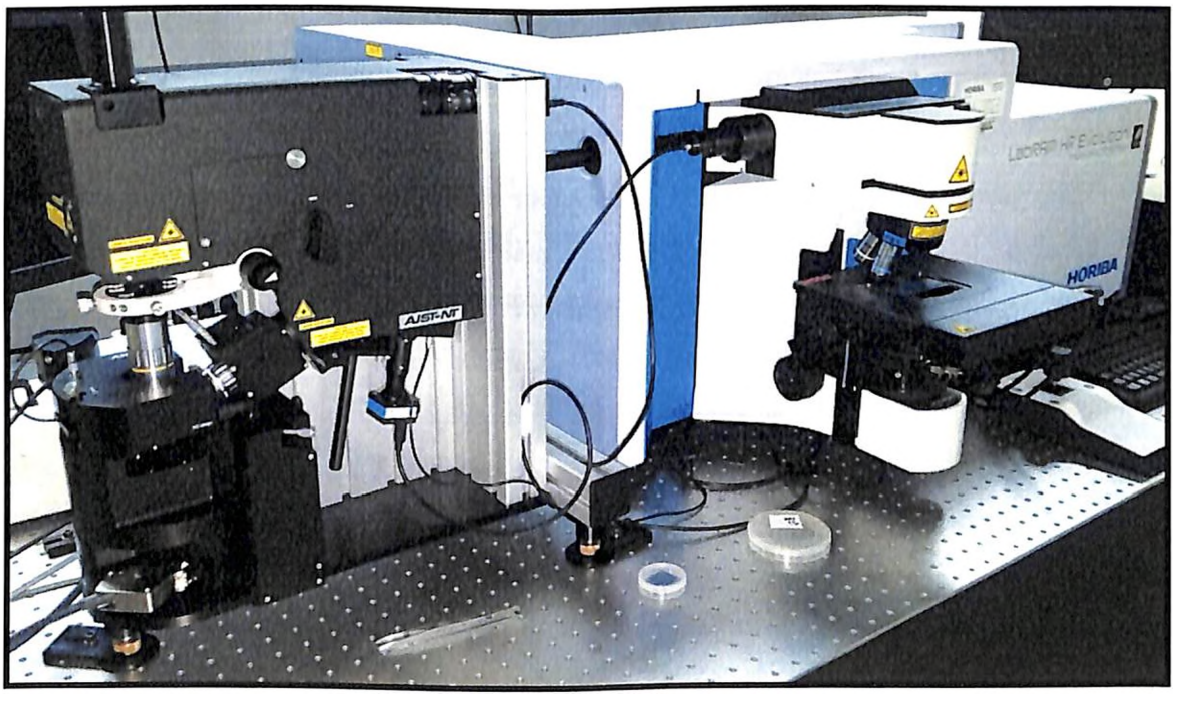

Figure 3-10: Raman equipment used for catalyst characterization

3.3 Catalytic activity measurements

3.3.1 Experimental Setup and procedure

Low temperature steam reforming of water-ethanol mixture is performed by using a custom designed continuous flow fixed bed stain less steel reactor (Diameter: 3/8"; Swagelok-SS-T6-S-049-20) sited in a furnace (MAC-Muffle furnace; MAC-251) under atmospheric pressure. 2 gm batch of the BIMEVOX catalysts in between two layers of quartz wool are loaded in the reactor and preheated at 150 °C for 30 min with flowing 10 $mlmin^{-1}$ nitrogen for the removal of the adsorbed moisture from the surface. The liquid mixture of ethanol and water with a weight ratio 10:90 (1:23 mole ratio) and 50:50 (1:2.5 mole ratio) is preheated at 105 and 115 °C in order to make two different liquid flow rate and N_2 gas (> 99.99%) is swept through the pre-heater to carry the vapor mixture to the reactor. The gas line (Diameter: 1/8"; Swagelok-SS-T2-S-028-20) connecting the pre-heater to the reactor is heated at 105-110 °C (flow rate 0.1 and 0.35 cc min^{-1}) to prevent condensation. GHSV (Gas hourly space velocity corresponding to each flow rate and feed concentration is mentioned in Table 3.4. Reaction temperature is maintained in between 200-400°C. The product mixture from the reactor is passed through an ice cooled phase separator in order to condense the liquid in the product. The gaseous and liquid products from the phase separator are analyzed by using a gas chromatography. Schematic of low temperature steam reforming experimental set-up with picture of setup used in lab is shown in Figure 3.11 and Figure 3.12.

3.3.2 Producer Gas Analysis

The gaseous mixture is analyzed by using an offline gas chromatography instrument (GC; Shimadzu-2014) equipped with TCD (Thermal conductivity detector), where porapak (6 ft*1/8" SS column with 2 mm internal diameter and 80/100mesh with Adapter Shimadzu GC-2014ATF) is the reference column and carbosphere is the sample column (6 ft*1/8" SS column with 2 mm internal diameter packed with carbo-sieve, 80/100mesh with Adapter Shimadzu GC- 2014ATF). Basic working principle for GC, selection of carrier gas, operating parameters (oven temperature, carrier gas flow rate, etc), and detail of the calibration technique are described in subsequent sections.

3.3.2.1 *Working principle for GC*

GC is a separation technique in which the components of a gas mixture are partitioned between two phases: the stationary and the mobile phase. According to the state of the

stationary phase, gas chromatography can be classified in gas-solid chromatography (GSC), where the stationary phase is a solid and gas-liquid chromatography (GLC) that uses a liquid as stationary phase (Cramers, Janssen et al. 1999). The GC schematic and equipment used in the study are shown in Figure 3.13 and 3.14. The sample is injected at the entrance of the column called injection port with the help of a micro-syringe. The sample is introduced into the carrier gas stream which carries the sample through the column. The carrier gas is an inert gas such as helium or an un-reactive gas such as nitrogen and does not interact with the sample, and thus GC separation's selectivity can be attributed to the stationary phase alone. Columns are classified as either packed or capillary columns. Packed columns are coated with a microscopic layer of polymer (silica, alumina, carbon molecular sieve, calcium carbonate, calcium phosphate, magnesia, starch, etc. depending on applications) on an inert solid support inside glass or metal tubing (Grob and Barry 2004). Temperature in GC is controlled via a heated oven and column is fixed inside the oven. The injector and detector connections are also contained in the GC oven. The immobilized coated layer is acted as the stationary phase which obstructed the motion of sample components by adsorbing them at different regions depending on their ability for adsorption. Moving rate of molecules through the column depends on the strength of adsorption, which in turn depends on the nature (intermolecular and intra-molecular hydrogen bonding forces) of packing material and sample molecules. As the mixture moves down through the column, the component with greater adsorption power is adsorbed in the starting of the column and the other is adsorbed at the end of the column. The weakly adsorbed component will be eluted more rapidly than the others which make each component to elute at different times, called retention time or residence time of that component. Generally, substances are identified (qualitatively) by the order in which they emerge from the column i.e., the retention time (Jennings 2012). The detector senses a physicochemical property of the analyte and provides a response which is amplified and converted into an electronic signal to produce a chromatogram.

The thermal conductivity detector (TCD) is a non destructive universal detector. It is widely used in gas chromatography for its high reliability, simplicity and ease of operation. The TCD measures the difference in thermal conductivity between the carrier gas flowing through a reference column and a sample component mixture flowing through a sample column (Rhodes 1996).

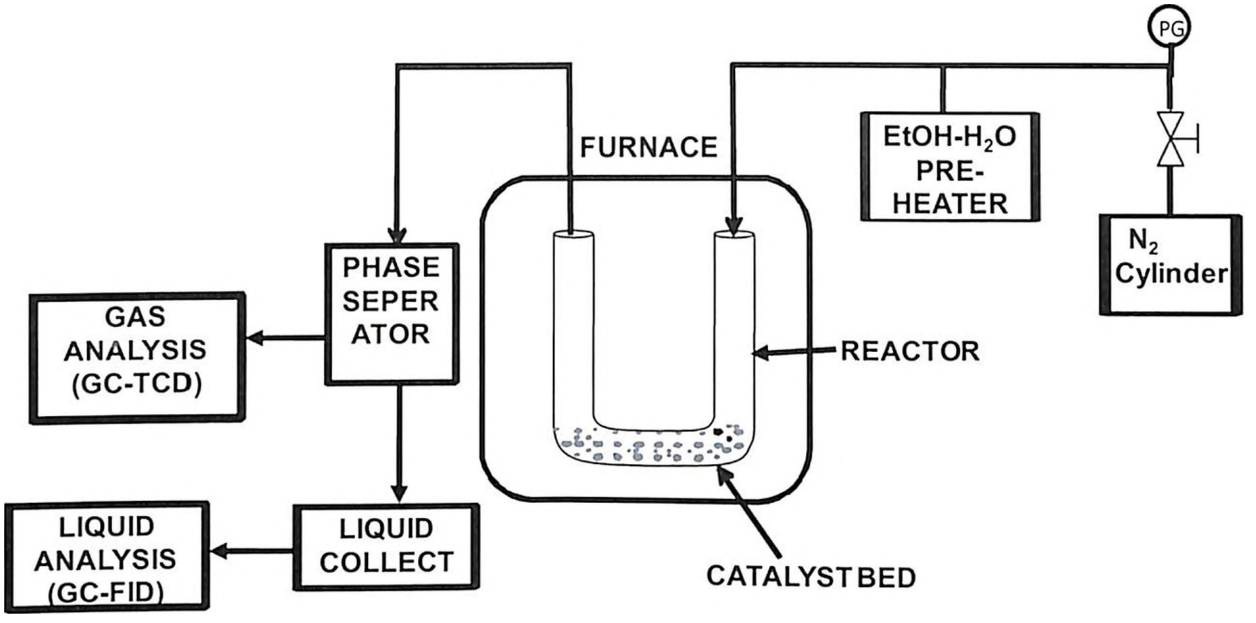

Figure 3-11 : Schematic of low temperature steam reforming experimental set-up

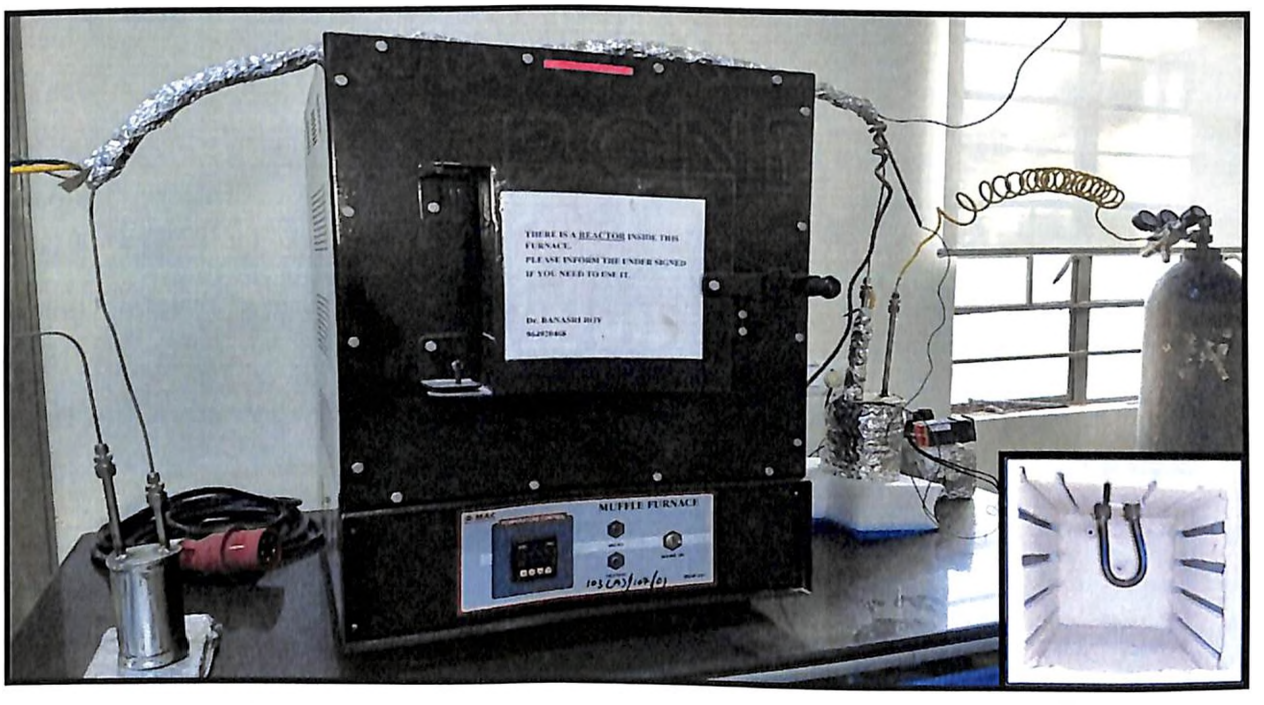

Figure 3-12: Experimental setup used for low temperature steam reforming

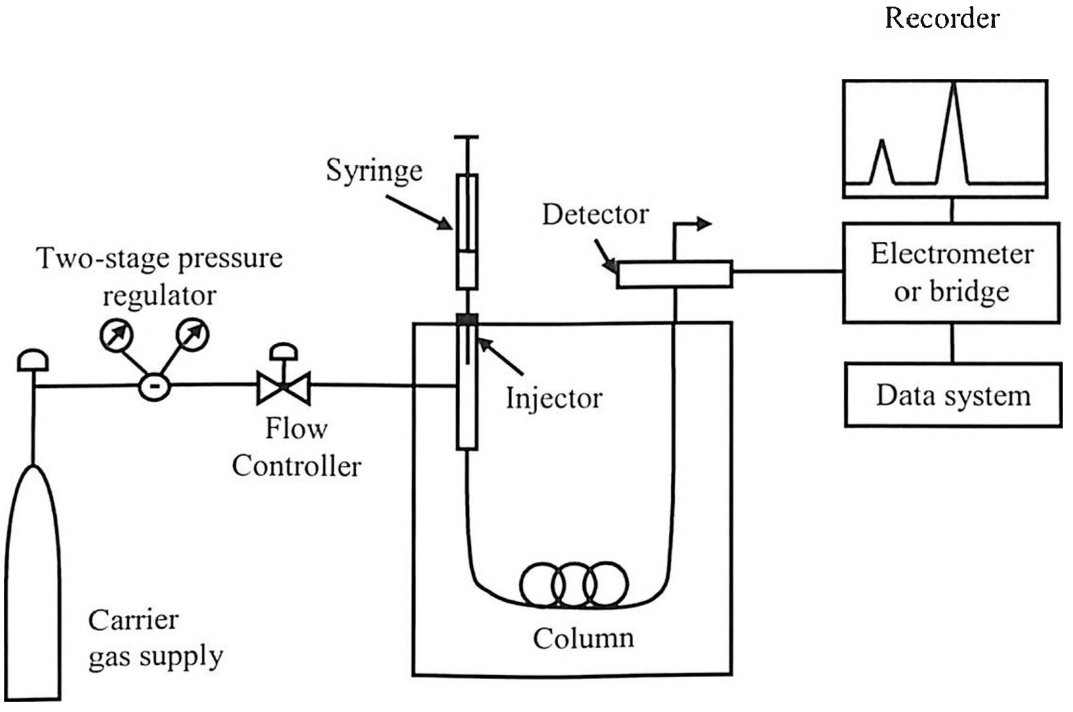

Figure 3-13: Schematic diagram of a general gas chromatography

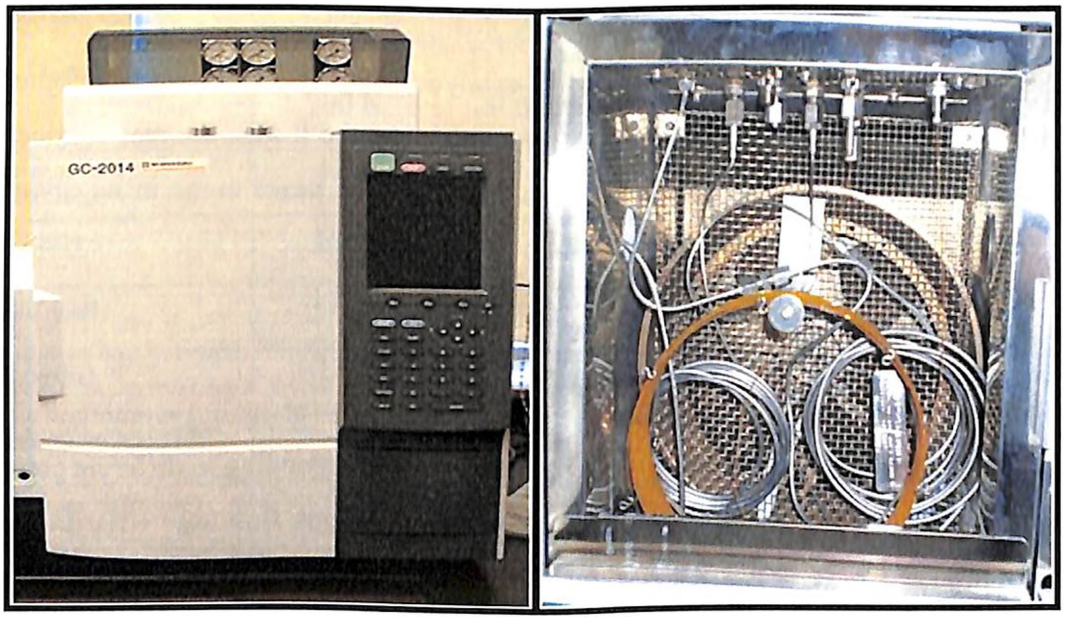

Figure 3-14: GC equipment used in the lab with insight of oven for gas product analysis

3.3.2.1.1 *Carrier gas selection*

The selection of a carrier gas is an essential factor and it depends on the products present in the sample and also on the detector. Typical carrier gases include helium, nitrogen, argon, hydrogen and air. Our product gas sample contains mainly CO, CO_2, CH_4, H_2 and N_2. Flame ionization detector (FID) cannot be used as H_2 is used to generate the flame in FID yet; H_2 is present in our product. Therefore, quantitative analysis of the producer gas is done with TCD. TCD senses the changes in the thermal conductivity of the product components and compares it to a reference flow of carrier gas and difference between these two should be large (Ueda 2003).

Most compounds have a thermal conductivity much less than that of the common carrier gas helium as shown in Table 3.5. However, thermal conductivity of hydrogen (230.9 mW m^{-1} K^{-1} at 127°C) is higher than helium (189.6 mW m^{-1} K^{-1} at 127°C) and other components present in product such as N_2 (32.8 mW m^{-1} K^{-1} at 127°C), CO_2 (25.2 mW m^{-1} K^{-1} at 127°C), CO (32.3 mW m^{-1} K^{-1} at 127°C) and CH_4 (50 mW m^{-1} K^{-1} at 127°C) have lower thermal conductivity than helium (Tsederberg and Cess 1965). Therefore, detection of hydrogen with helium results in a negative peak in comparison to other products consequently; we need another gas to quantify hydrogen. Nitrogen as a carrier gas cannot be used as it is already used as a carrier gas in catalytic activity. Hence, we have opted argon (22.4 mW m^{-1} K^{-1} at 27°C) as the carrier gas which has the lowest thermal conductivity in comparison to all product components. With argon, all the peaks come in negative and by changing the polarity we get all the peaks in positive direction.

3.3.2.1.1 *Operating parameter selection*

The carrier gas flow rate and the oven temperature are the main parameters which are required to be controlled to achieve the separate peaks corresponding to different components of the gaseous product mixture. On keeping high carrier gas flow rate (≥10 ml/min), the analytes take less time in passing through the column which results in lower retention time for the components to be analyzed. Then, for a multi-component system peaks could be overlapped and difficult to analyze quantitatively at higher flow rate. However, low carrier gas flow rate (≤ 5ml/min) increases the analysis time. The flow rate selection could be a compromise between the level of separation and analysis time. The optimum flow rate of carrier gas for the process is obtained to be 8 ml/min.

Table 3-4: Calculated GHSV values for various flow rates and feed concentrations.

Pre Heater Temp (°C)	N_2 flow rate (ml min^{-1})	H_2O:EtOH molar ratio	Feed flow rate (cc min^{-1})	GHSV (h^{-1})
105	10	23:1	0.1	5097.9
105	10	2.5:1	0.1	3550.77
125	10	23:1	0.35	17318.2
125	10	2.5:1	0.35	11976.2

Table 3-5: The thermal conductivity of some gases as a function of temperature (Tsederberg and Cess 1965)

Gases	Thermal conductivity in mW m^{-1} K^{-1} at various temperatures				
	200 K	300 K	400 K	500 K	600 K
Ar (Argon)	12.4	17.7	22.4	26.5	30.3
He (Helium)	118.3	155.7	189.6	221.4	251.6
H_2 (Hydrogen)	132.8	186.6	230.9	270.9	309.1
N_2 (Nitrogen)	18.3	26.0	32.8	39.0	44.8
CO (Carbon monoxide)	-	25.0	32.3	39.2	45.7
CO_2 (Carbon dioxide)	9.6	16.8	25.2	33.5	41.6
CH_4 (Methane)	21.8	34.4	50.0	68.4	88.6

The temperature of the oven is another important controlling parameter. A higher oven temperature (≥ 55°C) results in a lower adsorption of the analyte molecules onto the column packing materials. The increment in temperature therefore, leads to the same effect as that of increment of flow rate. However, low temperature is responsible for the irregular peak shapes or sizes. The optimum oven temperature is 45°C, after performing the analysis at different temperatures and flow rates.

3.3.2.1.2 *Calibration*

Calibration is carried out in order to quantify the components present in the gaseous product. GC provides the response for every component present in the mixture in terms of peak intensity and retention time. Pure sample for each component is injected in the GC in order to determine the retention time for each component. Based on the retention time analysis of the pure components, each peak of the chromatograph corresponds to a particular component of gaseous mixture that can be identified. The number of peaks of chromatograph depends upon the number of components present in the gaseous mixture.

The calibration (amount vs area) for the gaseous products is carried out by injecting a standard gaseous mixture (sigma gases & services, cylinder no: 74277) of different volume in the GC. The calibration curve is obtained by plotting the peak area of the standard component on the abscissa and the amounts of the standard component on the ordinate. Figure 3.15 shows the calibration curves for different components of the producer gas. The calibration Equations and R-square values are obtained by doing linear fitting of the data.

3.3.2.2 *Selectivity of gaseous components*

Gaseous products are collected in the phase separator. To know the steady state time, gaseous products are analyzed after every 1 hr. Amount of each component (H_2, CH_4, N_2, CO_2, CO) present in the gaseous phase is calculated by using calibration curves from GC-TCD. This is further divided by the sum of amount of all components present in the mixture, to get the mole fraction of each component. From this, selectivity of C-components is calculated using the following Equations (where x is the mole fraction):

$$CO_2 \text{ selectivity } (\%) = \frac{x_{CO_2}}{x_{CO_2}+x_{CH_4}+x_{CO}} \times 100 \quad (3.27)$$

$$CO \text{ selectivity } (\%) = \frac{x_{CO}}{x_{CO_2}+x_{CH_4}+x_{CO}} \times 100 \quad (3.28)$$

$$CH_4 \text{ selectivity } (\%) = \frac{x_{CH_4}}{x_{CO_2} + x_{CH_4} + x_{CO}} \times 100 \quad (3.29)$$

H_2 selectivity is calculated as the number of moles of H_2 present in the outflow gas, normalized by the number of moles of H_2 that would be formed if each mole of C in ethanol is considered to participate in the reforming reaction ideally to give 3 mole of CO_2 according to the Equation (Roy, Sullivan et al. 2014):

$$C_2H_5OH + 3H_2O \rightarrow 2CO_2 + 6H_2; \qquad \Delta H^0_{298K} = 347.4 \text{ kJmol}^{-1}$$

$$H_2 \text{ selectivity } (\%) = \frac{x_{H_2}}{3x_{CO_2}} \times 100 \quad (3.30)$$

3.3.3 Liquid sample analysis

The liquid mixture is analyzed by using a head space gas chromatograph (HSGC, Shimadzu-HS10), equipped with FID (Flame ionization detector) and fused silica capillary column (with the industry standard polyimide outer coating, 0.10 mm in diameter, -60°C-330/350°C temperature, 10 m in length). The HSGC equipment used in the study is shown in Figure 3.16. Working principle of HSGC, selection of carrier gas and operating parameters (temperature, pressure, carrier gas flow rate, etc) and detail of the calibration technique are described in subsequent sections.

3.3.3.1 *Working principle of Headspace Gas Chromatography*

Headspace with gas chromatography is a modified technique for separating the volatile components from the high molecular weight or unwanted compounds, which can contaminate the column if the mixture is directly injected into the gas chromatograph (Shijiao, Dasen et al. 1997). In general, a sample is prepared in a vial, containing the sample along with the dilutuent with headspace (certain empty space within the vial). The vapor in the headspace is syringe out through transfer line to the GC system. The Equations describing headspace theory are derived from three physical laws: 1) Dalton's law of partial pressures, 2) Henry's law for dilute solutions and 3) Raoult's law. The concentration of sample analyte in the headspace volume is given by mass balance: $C_O V_L = C_G V_G + C_L V_L$; (3.31)

Where C_G is the concentration of analyte in the headspace; C_O is the concentration of analyte in the original sample; V_G is the volume of gas in the sample vial; V_L is the volume of ingected sample; K is the partition coefficient (or distribution coefficient) = C_L/C_G at equilibrium and β (phase ratio) = V_G/V_L. Rearranging provides (Bicchi, Binello et al. 1993):

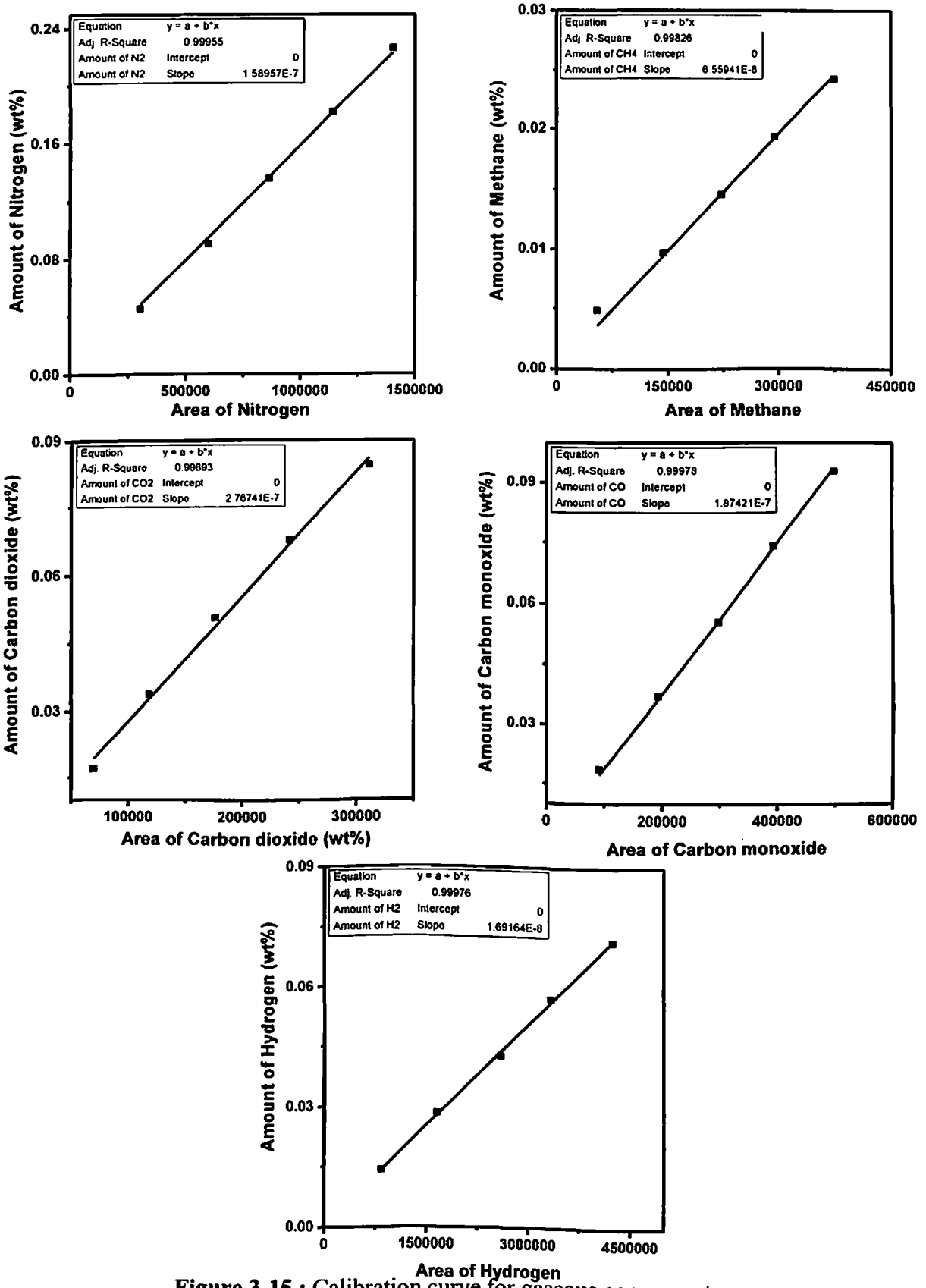

Figure 3-15 : Calibration curve for gaseous components

$$C_G = \frac{C_O}{\left(K+\frac{V_G}{V_L}\right)} = \frac{C_O}{(K+\beta)} \quad (3.32)$$

Our liquid product contains ethanol, methanol, acetone and acetaldehyde with water. High amount of water can contaminate the columns if the mixture is injected directly into the GC.

3.3.3.1.1 *Operating Parameters selection*

N_2 is used as a carrier gas and H_2 and zero air is used for generating the flame. H_2 and zero air flow rate is set at 40 and 400 ml/min respectively, as the ratio of H_2: zero air should be 1:10 due to the safety concerns associated with hydrogen, while the N_2 flow rate is kept at 30 ml/min.

Partition coefficient (K) and phase ratio (β) are the two important factors for the separation of volatiles from the mixture. For consistent results, the ratio V_G/V_L must remain constant. This means that the sample amount and vial size need to be kept the same (Russo 1994).

Minimizing the partition coefficient provides higher concentration of sample vapor in the headspace volume as shown in Equation 3.44. However, K is temperature dependent for each component in air-water mixture. For ethanol, K at 40°C is 1350, which can be reduced by increasing temperature as K= 330 at 75°C (CHEN, XIAO et al. 2005). Therefore, the oven temperature is fixed at 70°C and sample is heated for 20 min.

To avoid the loss of sample, because of the pressure differences between the vial and atmospheric conditions during transferring the sample from the vial to the injection port, vial is pressurized to 10 psi (Comberbach and Bu'Lock 1982). Subsequently, it is transferred to the sample line to keep the fixed amount of sample (as it passes only 10 µL of sample) and then it travels through transfer line. Sample line and transfer line temperature should be higher than oven temperature to avoid the condensation, so it is fixed at 90 and 120°C respectively.

Now, sample is injected into the column. However, there are two types of injection modes, split and split-less. Split mode is used if the mixture is concentrated, otherwise split-less mode is preferred. Our liquid sample is not that concentrated so split-less option is considered. Injection temperature and detector temperature is set at 200 and 250°C respectively. The boiling temperature of methanol, ethanol, acetone and acetaldehyde is 64.7, 78.37, 56 and 20.2°C, respectively. Therefore, initially the column temperature is maintained at 35°C for 3 min and then increased at a rate of 10°C/min up to 100°C to a final temperature

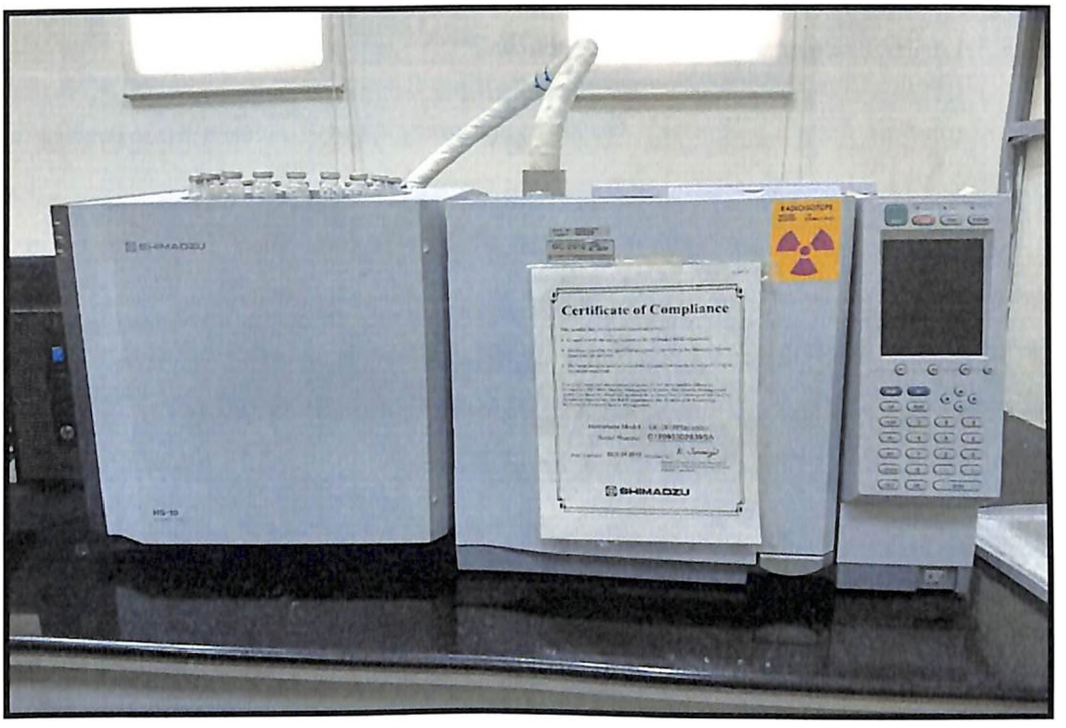

Figure 3-16 : HSGC equipment used in the liquid analysis

of 240°C with a rate of 20°C/min and maintained for 2 min by considering the boiling temperature of each component present in the mixture.

3.3.3.1.2 *Calibration*

Calibration is carried out in order to quantify the liquid products. For calibration, five different concentration solutions, varied from 0.01 to 0.5 vol% are prepared for each component separately, using water as a dilution solvent. Later, concentration is calculated by using density and molecular weight of each component, and expressed in terms of mol/10 μL as the sample line passes 10 μL of the mixture. The calibration curve is obtained by plotting peak area of the standard component on abscissa and concentration of the standard component on ordinate. Figure 3.17 shows the calibration curves for different components of the liquid mixture. The calibration Equations and R-squared values have been obtained through linear regression of data. Moles of each component present in the liquid product are calculated by using calibration Equation from HSGC-FID in terms of mol/10 μL. Further, total concentration of each component in the liquid mixture is expressed in terms of $mol.gm^{-1}$ cat hr^{-1} by measuring the total volume of the liquid obtained after a single run (6-8 hrs) for 2 gm of catalyst.

One of the gaseous and liquid sample scan from GC-TCD and HSGC are shown in Figure 3.18.

3.3.3.2 *Flow rate*

Flow rate (mole/min and ml/min) of the feed and product is calculated without or with the catalyst respectively by performing the same experiment (keeping the temperature of pre-heater and reactor, mole ratio, gas flow rate same) and collecting the liquid over six hrs. Flow rate (mol/min) for product stream we are calculating with the help of calibration curves. However, for feed stream this is calculated by measuring the collected liquid of ethanol-water in and we already know the ratio of ethanol and water so considering that and molecular weight of ethanol, flow rate of feed is calculated in mol/min.

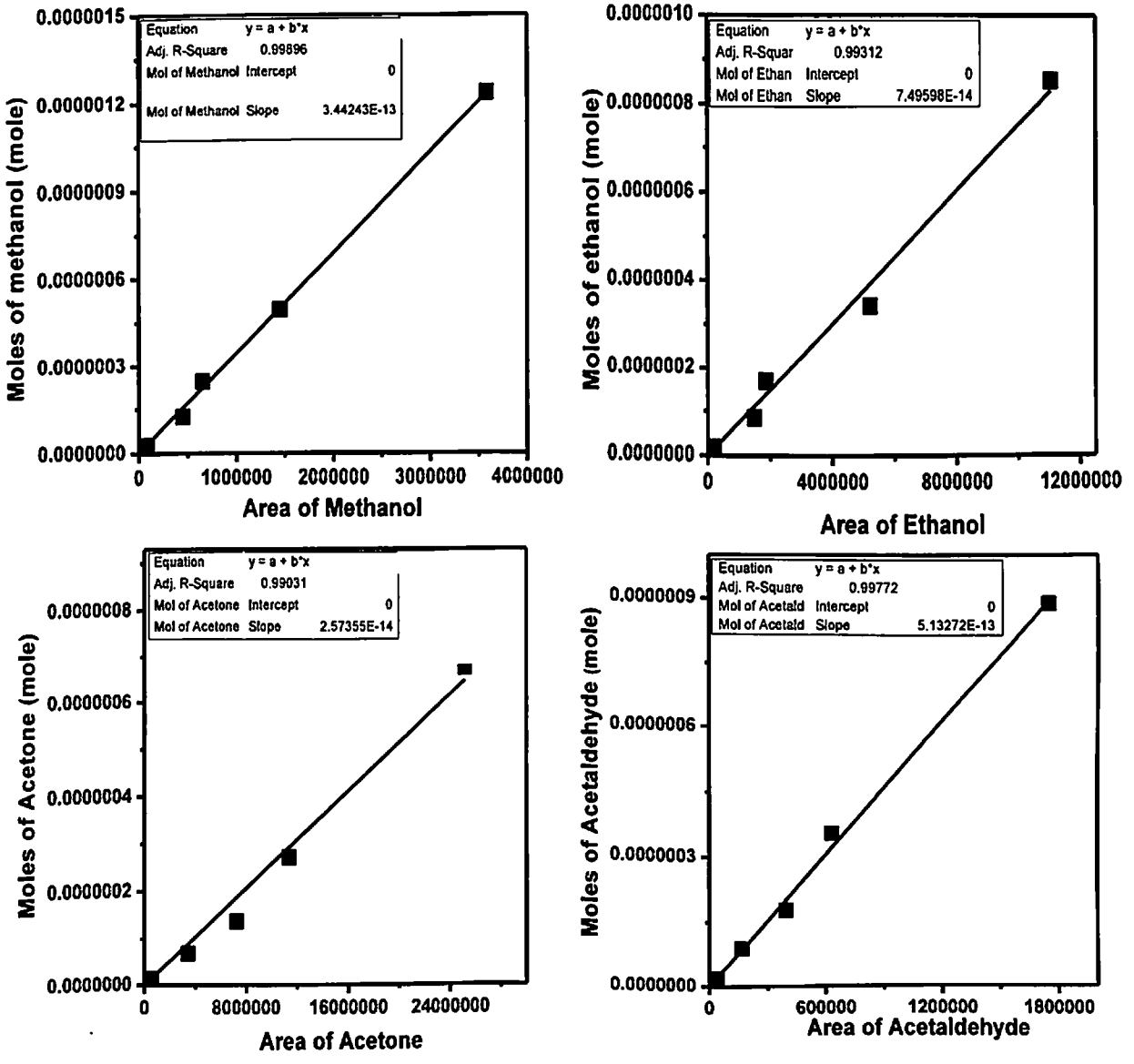

Figure 3-17 : Calibration curve for liquid components

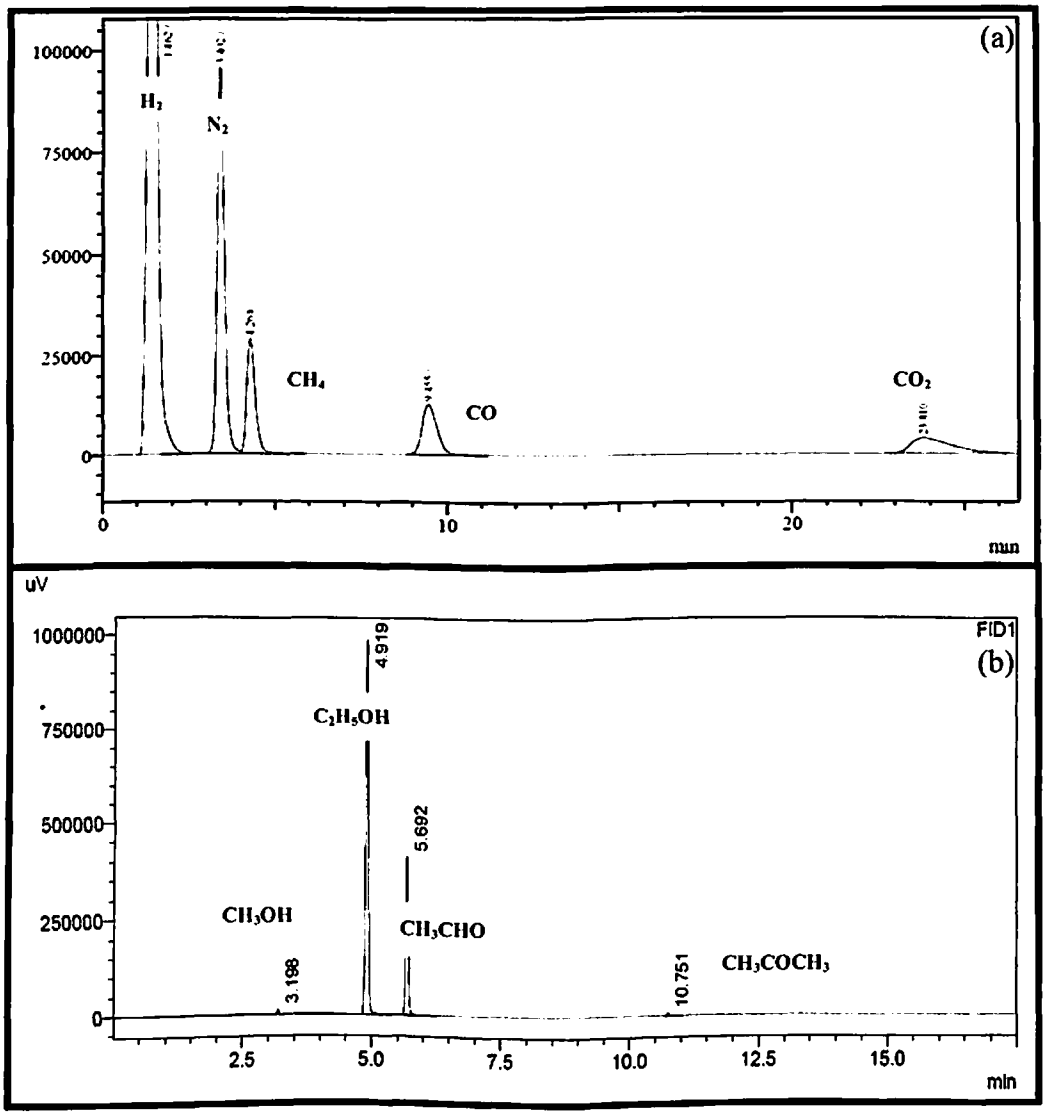

Figure 3-18: Gaseous and liquid product sample scan from (a) GC-TCD and (b) HSGC

3.3.3.3 *Ethanol conversion and Carbon in gas and liquid phase*

Consider, Ethanol (C_2H_5OH) feed flow rate (input) = x mol/min

Carbon in feed = 2 * x mol/min

Liquid products are methanol (CH_3OH), acetone (CH_3COCH_3), acetaldehyde (CH_3CHO) and unconverted ethanol (C_2H_5OH). With the help of calibration curves obtained from HSGC and flow rate, concentration of each in product stream is determined in mol/min.

Consider that, the unconverted Ethanol (output)= y mol/min

Then, Ethanol conversion = Initial conc. of ethanol in the feed - Unconverted ethanol conc.

= (x-y) mol/min

Ethanol conversion (%) = [(Initial conc. of ethanol in the feed - Unconverted ethanol conc)/ Initial conc. of ethanol in the feed]*100

$$X_{EtOH}\,(\%) = [(x-y)/x]*100 \text{ or } [(\text{mol } EtOH_{in} - \text{mol } EtOH_{out})/\text{mol } EtOH_{in}] * 100$$

Methanol (CH_3OH) concentration = A mol/min;

Acetone (CH_3COCH_3) concentration = B mol/min

Acetaldehyde (CH_3CHO) concentration = C mol/min

Carbon in liquid = Carbon in Unconverted Ethanol + Carbon in Methanol + Carbon in Acetone + Carbon in Acetaldehyde

= (2*y + A + 3*B + 2*C) mol/min

Carbon in gas = Carbon in feed - Carbon in liquid

= (2*x - 2*y - A - 3*B - 2*C) mol/min

Carbon (%) in gas = [(2*x - 2*y - A - 3*B - 2*C)/(2*x)]*100

The results of the present steam reforming studies with characterization results are analyzed and discussed in the chapter 4.

Chapter 4: Results and Discussion

4.1 Results

4.1.1 Catalytic Activity measurement

The performance of BIMEVOX catalysts in low temperature steam reforming is evaluated at atmospheric pressure, 23:1 and 2.5:1 H_2O: EtOH molar ratio, temperature range of 200–400°C, and 0.1 and 0.35 cc min^{-1} feed flow rates. The catalytic activity is presented in terms of ethanol conversion (%), C in gas product (%), selectivity (%) of gaseous (H_2, CO_2, CO and CH_4) and liquid (CH_3CHO, CH_3OH and CH_3COCH_3) products for various temperatures, feed concentrations and flow rates. All the catalysts are observed to attain the steady state within 5-6 hrs and remain stable till 30 hrs as depicted in Figures 4.1, 4.2 and 4.3, where activity is carried out at 400°C reaction temperature, 23:1 H_2O: EtOH molar ratio and 0.35 cc min^{-1} flow rates. For BICOVOX-400 catalyst, EtOH conversion, C in gas phase and selectivities of H_2 and CO_2 increases from 33 to 78%, 22 to 85%, 15 to 56% and 11 to 55%, respectively and CO and CH_4 selectivity reduces from 30 to 10% and 59 to 35%, respectively with increase in time from 1st hr to 6th hr, and remain stable till 30th hr as represented in Figure 4.1 (a). In comparison with BICOVOX-400, BICOVOX-600 shows 100% EtOH conversion after 6 hrs with 80% H_2, 71% CO_2, 0% CO and 29% CH_4. Initially after 1 hr of experiment EtOH conversion, H_2, CO_2, CO and CH_4 selectivity's are 50, 34, 23, 20 and 57%, respectively as found in Figure 4.1 (b). EtOH conversion, H_2, CO_2 selectivity increases and CO and CH_4 selectivity's reduces with time till 6 hrs and remain stable till 35 hrs. Similar to BICOVOX-400, BICOVOX-800 catalyst (Figure 4.1 (c)) is also found to be stable till 30 hrs of experiment and obtained values for EtOH conversion, H_2, CO_2, CO and CH_4 selectivity are 83, 61, 63, 8 and 29%, respectively with 96% of C in gas after 30 hrs. Analogous to BICOVOX catalyst, it can be seen in Figure 4.2 (a) that maximum EtOH conversion (80%), H_2 (55%), CO_2 (50%) selectivity and C in gas product (86%) with minimum amount of CO (23%) and CH_4 (27%) selectivity are found after 6 hrs and it remains stable till 30 hrs of reforming reactions. BINIVOX-600 (Figure 4.2 (b)) and BINIVOX-800 (Figure 4.2 (c)) catalysts also show the similar trends for all activity results as find for BINIVOX-400 catalyst. Maximum EtOH conversion (100%-BINIVOX-600 and 80%-BINIVOX-800), H_2 (76%-BINIVOX-600 and 57%-BINIVOX-800), CO_2 (64%-BINIVOX-600 and 59%-BINIVOX-800) selectivity and C in gas product (92%-BINIVOX-600 and 90%-BINIVOX-800) with minimum amount of CO (13%-BINIVOX-600 and 16%-BINIVOX-800), and CH_4 (23%-BINIVOX-600 and 25%-BINIVOX-800), selectivity are found after 6 hrs and that also

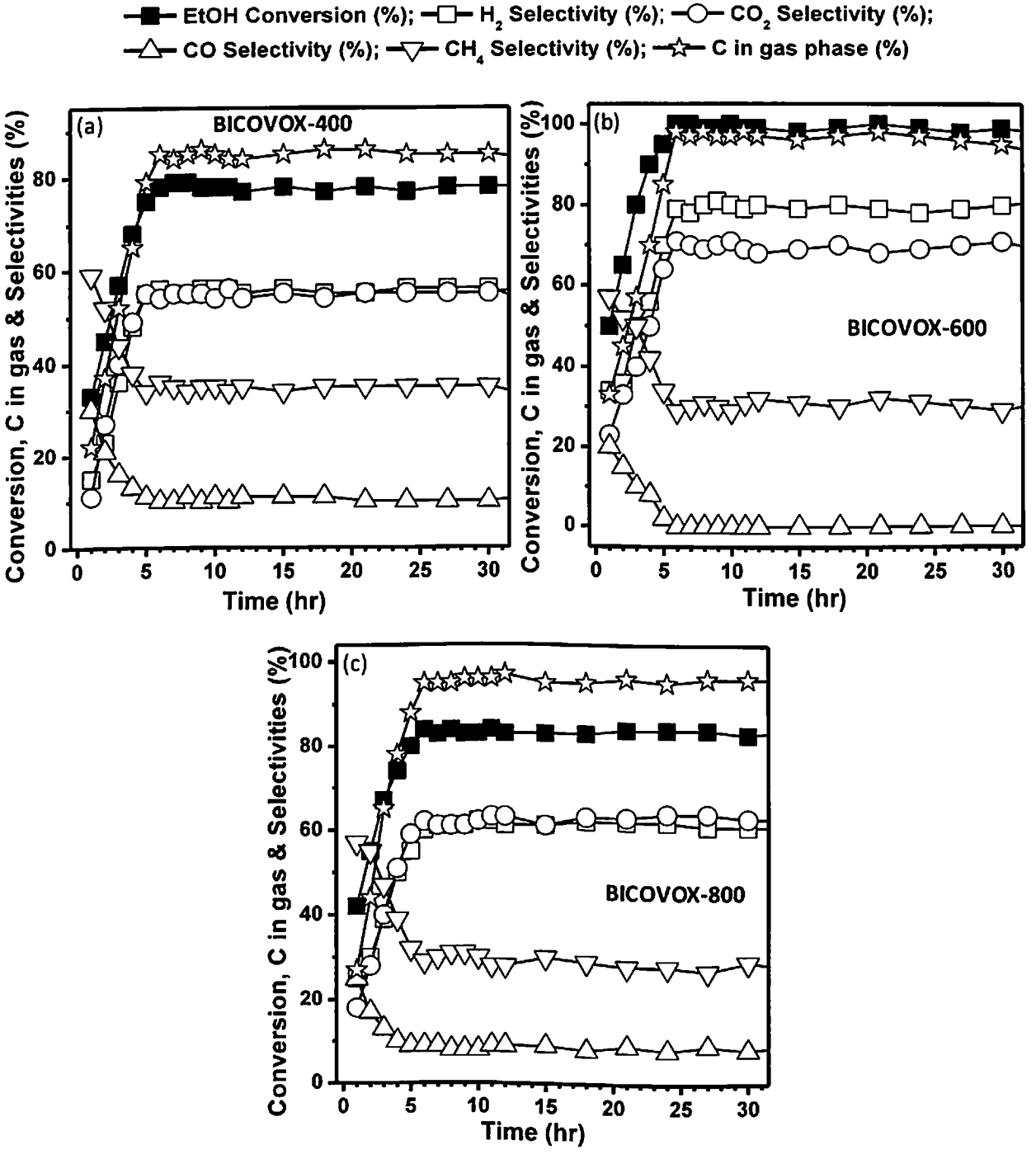

Figure 4-1: Change of EtOH conversion, and gaseous products selectivity as a function of time (30 hrs) at 400°C, atmospheric pressure, 23:1 H_2O:EtOH molar ratio and 0.35 cc min^{-1} feed flow rate for steam reforming of (a) BICOVOX-400, (b) BICOVOX-600, and (c) BICOVOX-800 catalysts

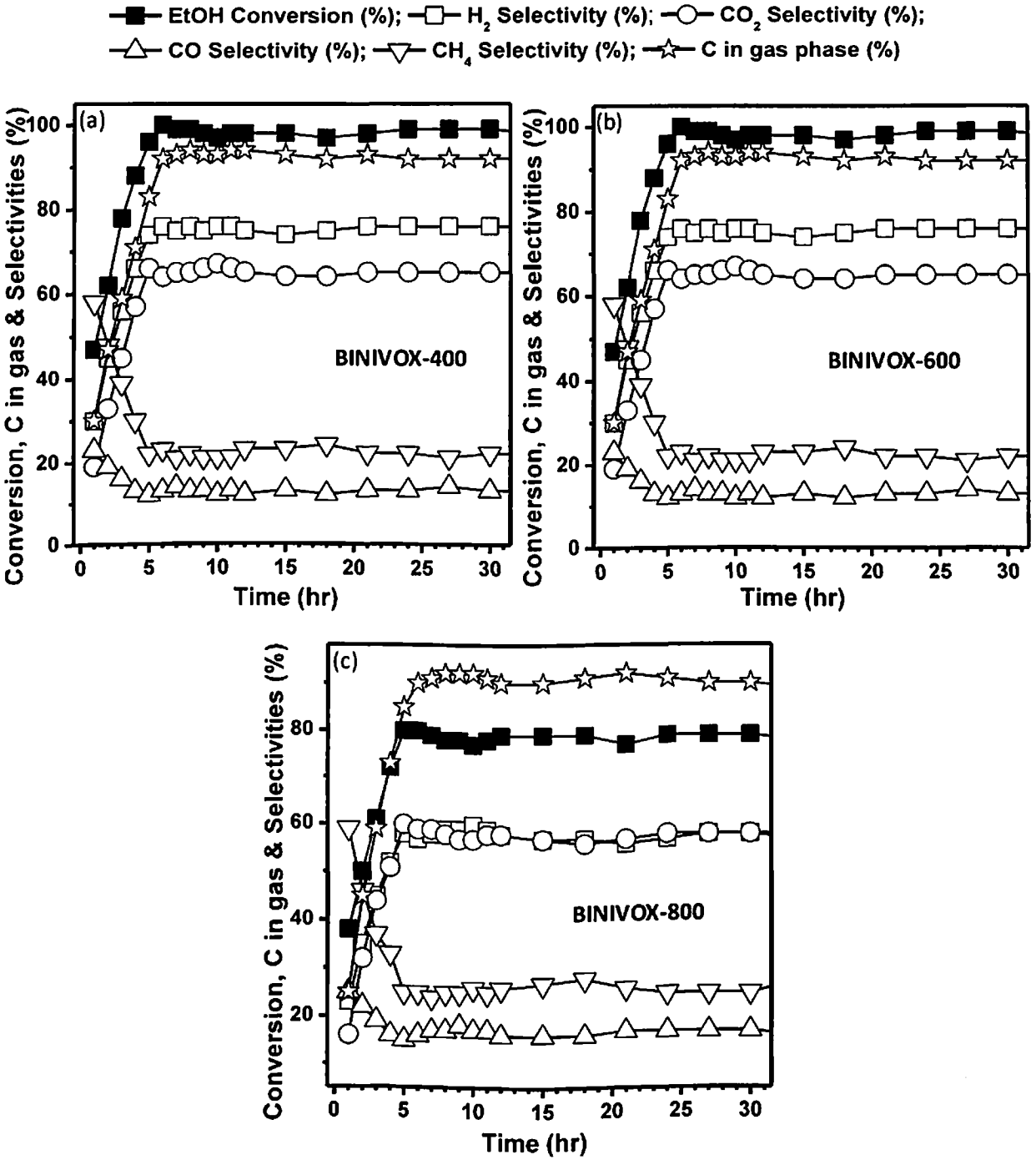

Figure 4-2: Change of EtOH conversion, and gaseous products selectivity as a function of time (30 hrs) at 400°C, atmospheric pressure, 23:1 H_2O:EtOH molar ratio and 0.35 cc min^{-1} feed flow rate for steam reforming of (a) BINIVOX-400, (b) BINIVOX-600, and (c) BINIVOX-800 catalysts

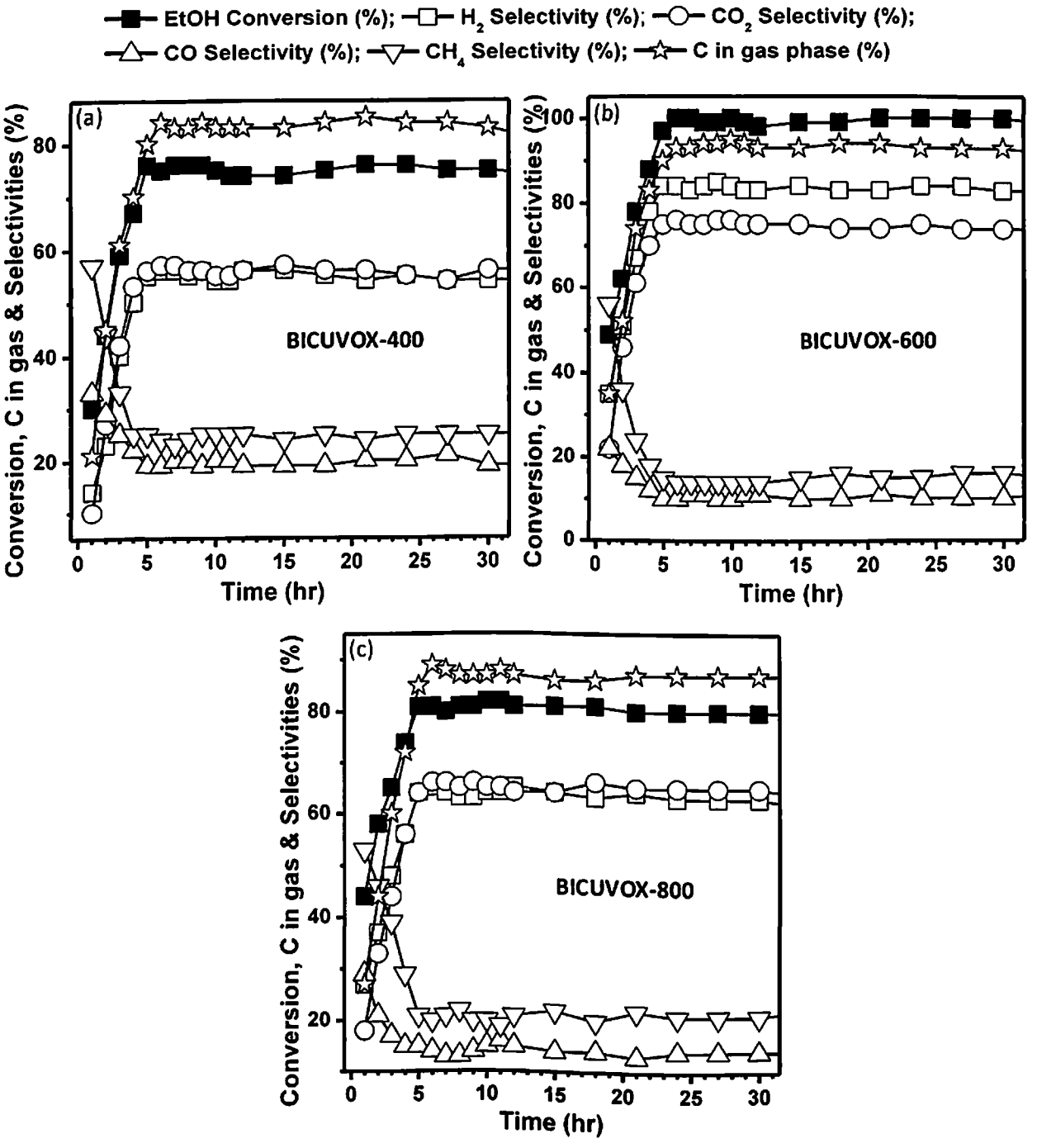

Figure 4-3: Change of EtOH conversion, and gaseous products selectivity as a function of time (30 hrs) at 400°C, atmospheric pressure, 23:1 H_2O:EtOH molar ratio and 0.35 cc min^{-1} feed flow rate for steam reforming of (a) BICUVOX-400, (b) BICUVOX-600, and (c) BICUVOX-800 catalysts

remains stable till 30 hrs. Similar to BICOVOX and BINIVOX, EtOH conversion, H_2, CO_2 selectivity are increases from 30 to 76%- BICUVOX-400 (Figure 4.3 (a)), 49 to 100%-BICUVOX-600 (Figure 4.3 (b)), and 44 to 81%-BICUVOX-800 (Figure 4.2 (c)), 14 to 56%-BICUVOX-400, 35 to 84%-BICUVOX-600, and 27 to 65%-BICUVOX-800 and 10 to 57%-BICUVOX-400, 22 to 76%-BICUVOX-600, and 18 to 66%-BICUVOX-800, respectively with time from 1st hr to 6th hr, on contrary to this CO and CH_4 selectivity's reduces from 33 to 19%-BICUVOX-400, 22 to 10%-BICUVOX-600, and 29 to 13%-BICUVOX-800 and 57 to 23%-BICUVOX-400, 56 to 14%-BICUVOX-600, and 53 to 20%-BICUVOX-800, respectively. Activity results show the stability of catalysts till 35 hrs. Taking into account these results together we have performed the catalytic activity for 6 hrs to examine the effect of temperature, flow rate and feed concentrations on steady state EtOH conversion, C-in gaseous state, selectivity of gaseous and liquid products in the following sections.

4.1.1.1 *Effect of temperature*

Effect of temperature (200-400°C) on steady state EtOH conversion (%) and C in gas products (%) for BICOVOX-400, BICOVOX-600 and BICOVOX-800 catalysts are presented in Figure 4.4 (a) and (b) at both the flow rates and feed concentrations and both EtOH conversion (%) and C in gas products (%) are found to increase with increasing temperature. For BICOVOX-400 catalyst, 54% of EtOH conversion is achieved at 200°C, 23:1 H_2O: EtOH molar ratio, and 0.1 cc min^{-1}. EtOH conversion increases with temperature and reaches to its maximum value of 83% at 400°C. Similarly, for BICOVOX-600 and BICOVOX-800 catalysts, 70% and 56% ethanol conversion, respectively are seen at 200°C which at 400°C reaches to their maximum value of almost 100% EtOH conversion for BICOVOX-600 and 88% for BICOVOX-800 catalyst. The amount of C in gas phase for BICOVOX-400, BICOVOX-600 and BICOVOX-800 catalysts are observed to be 42%, 60% and 59% at 200°C and this amount increases with temperature and reaches to their maximum value of 85%, 97% and 96%, respectively at 400°C.

Figure 4.5 (a), (b), (c) and (d) depict the trends for the selectivity of H_2, CO_2, CO and CH_4, respectively as a function of reaction temperature at both the flow rates, and feed concentrations. The H_2 and CO_2 selectivities are found to increase with increase in temperature and CO and CH_4 show an opposite trends and observed to decrease with increasing reactor temperature, in general for all catalyst systems. At 200°C, 23:1 H_2O: EtOH molar ratio, and 0.35 cc min^{-1}, BICOVOX-400 catalyst has H_2 (Figure 4.5(a)), CO_2 (Figure

4.5(b)), CO (Figure 4.5(c)) and CH_4 (Figure 4.5(d)) selectivities of 24, 4, 38 and 58%, which are 45 and 87.5% lower and 26.6 and 52.6% higher than that of the values the BICOVOX-600 catalyst obtain, respectively and 20 and 69.2% lower and 5.5 and 13.7% higher than that of the values the BICOVOX-800 catalyst show, respectively. BICOVOX-600 catalyst shows the highest H_2 (80%) and CO_2 (72%) selectivity and lowest CO (0%) and CH_4 (28%) selectivity at 400°C, where H_2 and CO_2 selectivity is 30 and 23.6% higher with respect to BICOVOX-400 and 23.7 and 12.5% higher with respect to BICOVOX-800 catalysts. CO and CH_4 selectivity are 10 and 35% in case of BICOVOX-400 and 8 and 29% in case of BICOVOX-800 catalyst, respectively at the same reaction parameters. Temperature at which 1st CO_2 is formed, called crossover point. For BICOVOX-800 catalyst the crossover point is at ~225 °C, and in case of BICOVOX-600 and BICOVOX-400 catalysts it is perceived to be < 200 °C.

Effect of temperature on liquid products is shown in Figure 4.6. Figure 4.6 (a) and 4.6 (c) shows that selectivity of CH_3CHO and CH_3COCH_3 increases with increase in reaction temperature and for BICOVOX-400, BICOVOX-600 and BICOVOX-800 catalysts the CH_3CHO and CH_3COCH_3 selectivities are found to be 29 and 9%, 38 and 2% and 37 and 8%, respectively at 200°C, 23:1 H_2O: EtOH molar ratio, and 0.35 cc min^{-1} and it reaches to 57 and 15%, 75 and 10% and 65 and 15% at 400°C. However, CH_3OH selectivity decreases with increase in temperature as observed in Figure 4.6 (b). It is found that at 200°C, the CH_3OH selectivity is 62, 60 and 55% for BICOVOX-400, BICOVOX-600 and BICOVOX-800 catalysts, respectively and that reaches to 28, 15 and 20% at 400°C, respectively.

Similar to BICOVOX catalysts, EtOH conversion and amount of C in gas for BINIVOX catalysts also increases with increase in reaction temperature as shown in Figure 4.7 (a) and (b), respectively. 40, 69 and 43% EtOH conversion is found at 200°C, 23:1 H_2O: EtOH molar ratio, and 0.1 cc min^{-1} for BINIVOX-400, BINIVOX-600 and BINIVOX-800 catalysts, respectively. At 400°C, EtOH conversion reaches to 79, 99 and 81% for BINIVOX-400, BINIVOX-600 and BINIVOX-800 catalysts, respectively. Amount of C in gas for BINIVOX-600 catalyst is observed to be 55% at 200°C and it increases upto 92% at 400°C. Similarly amount of C in gas for BINIVOX-400 and BINIVOX-800 are 46 and 52% at 200°C and reaches to 85 and 90% at 400°C, respectively.

Figure 4.8 reveals the effect of temperature on the selectivity of gaseous products at various flow rates and feed concentrations for BINIVOX catalysts. Similar to BICOVOX catalysts, selectivity of H_2 and CO_2 increases and CO and CH_4 decreases with increase in temperature for BINIVOX catalysts. The highest H_2 selectivity of 76% is found at 400°C,

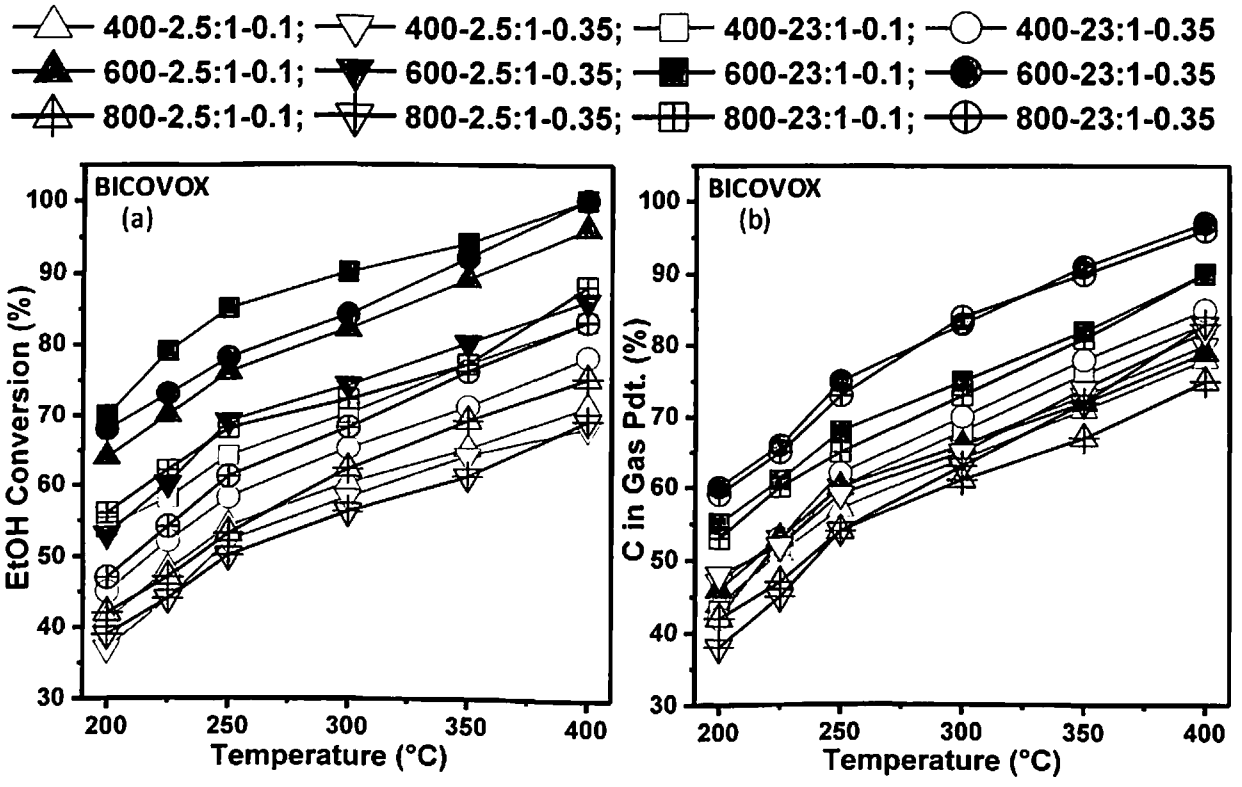

Figure 4-4: Steady state (a) EtOH conversion, and (b) C in gaseous phase as a function of temperature for steam reforming of 23:1 and 2.5:1 H_2O:EtOH molar ratio using BICOVOX-400 (□), BICOVOX-600 (■) and BICOVOX-800 (⊞) catalysts at 0.1 and 0.35 cc min^{-1} feed flow rates. Legend is represented as: Catalyst temperature-H_2O:EtOH molar ratio-Feed flow rate

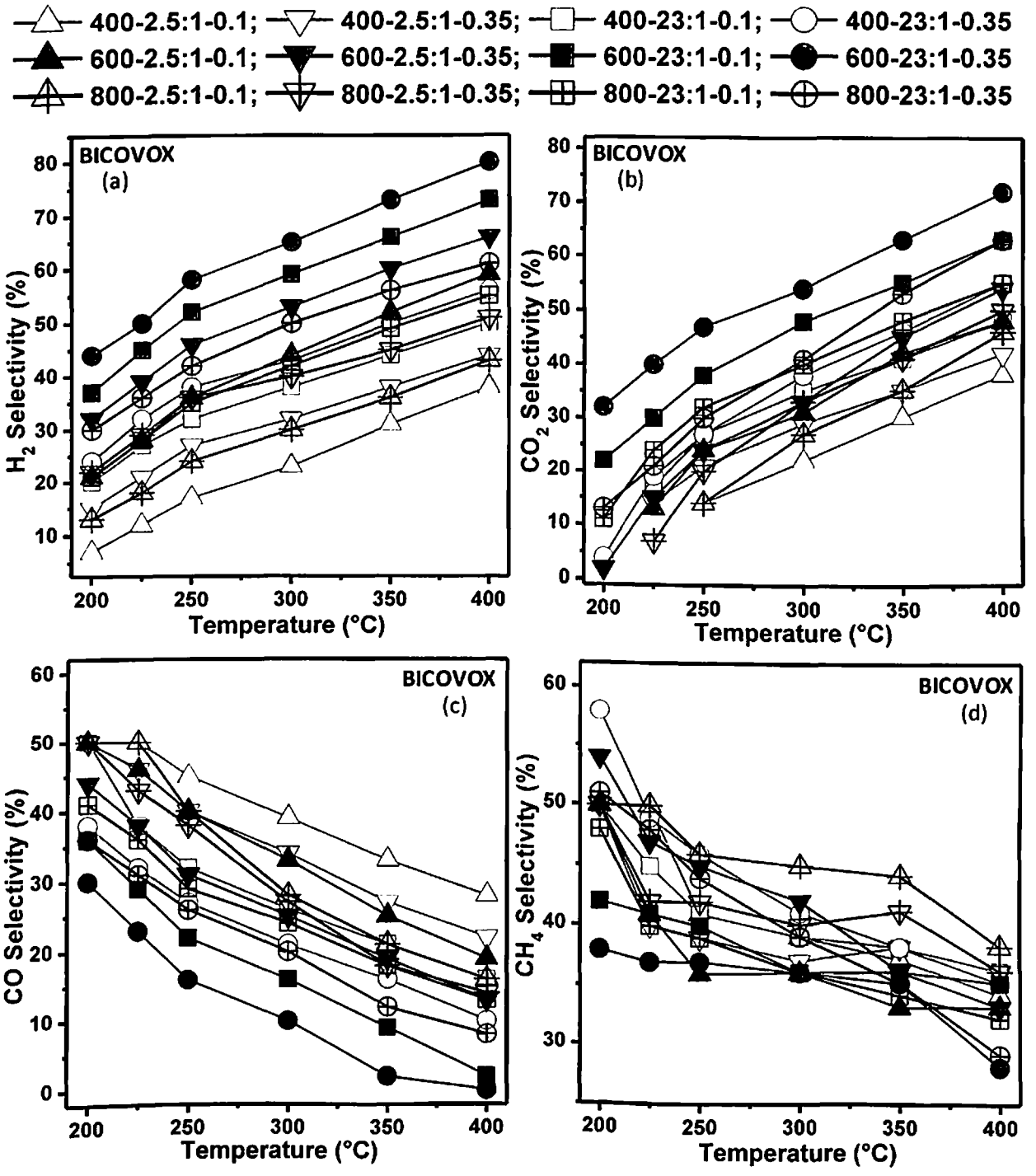

Figure 4-5: Selectivity of the gases; (a) H_2, (b) CO_2, (c) CO, and (d) CH_4 as a function of temperature for steam reforming of 23:1 and 2.5:1 H_2O:EtOH molar ratio using BICOVOX-400 (□), BICOVOX-600 (■) and BICOVOX-800 (⋕) catalysts at 0.1 and 0.35 cc min^{-1} feed flow rates. Legend is represented as: Catalyst temperature-H_2O:EtOH molar ratio-Feed flow rate

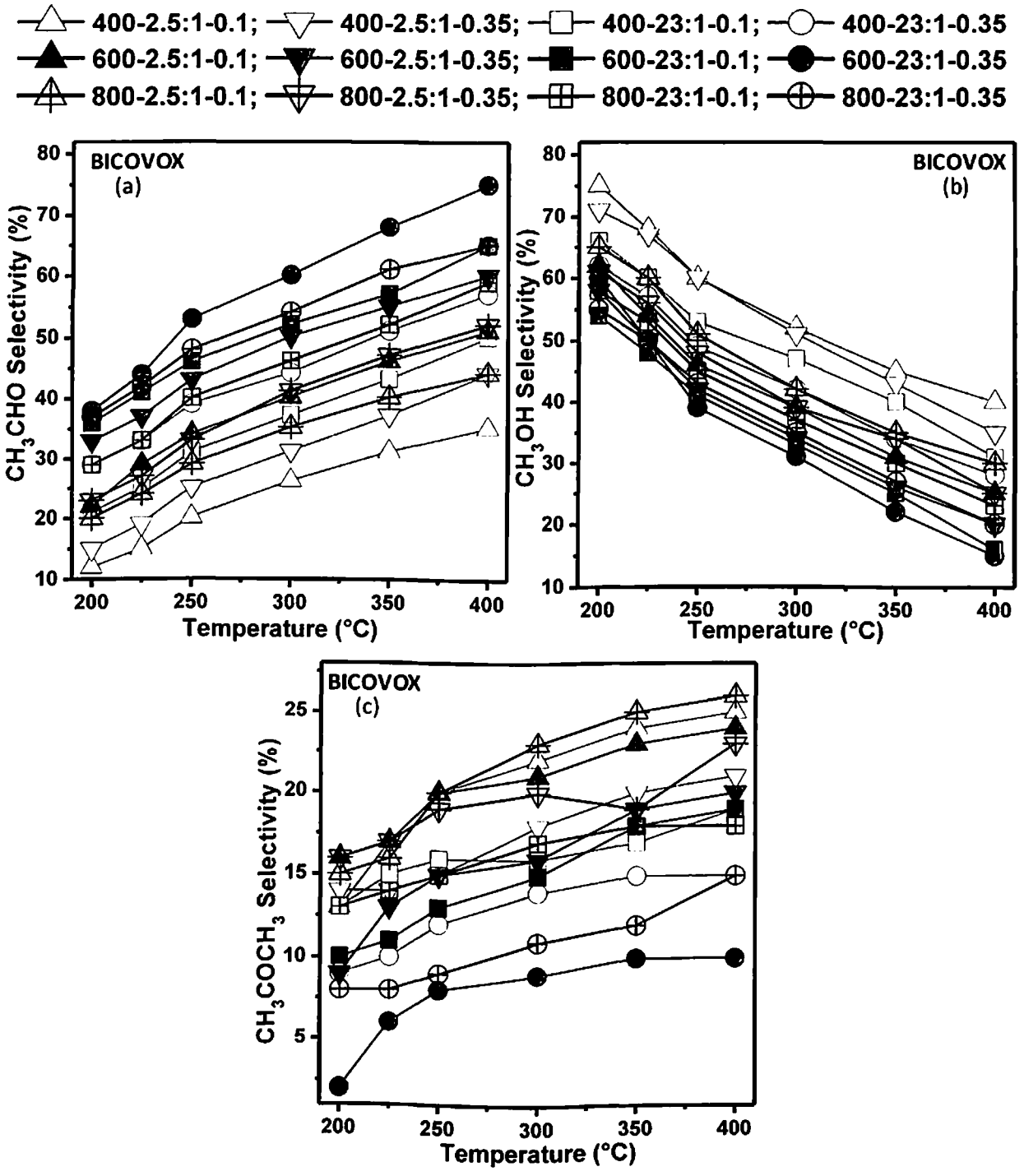

Figure 4-6: Selectivity of ; (a) CH_3CHO, (b) CH_3OH, and (c) $CH_3CO\ CH_3$ as a function of temperature for steam reforming of 23:1 and 2.5:1 H_2O:EtOH molar ratio using BICOVOX-400 (□), BICOVOX-600 (■) and BICOVOX-800 (⊕) catalysts at 0.1 and 0.35 cc min^{-1} feed flow rates. Legend is represented as: Catalyst temperature-H_2O:EtOH molar ratio-Feed flow rate

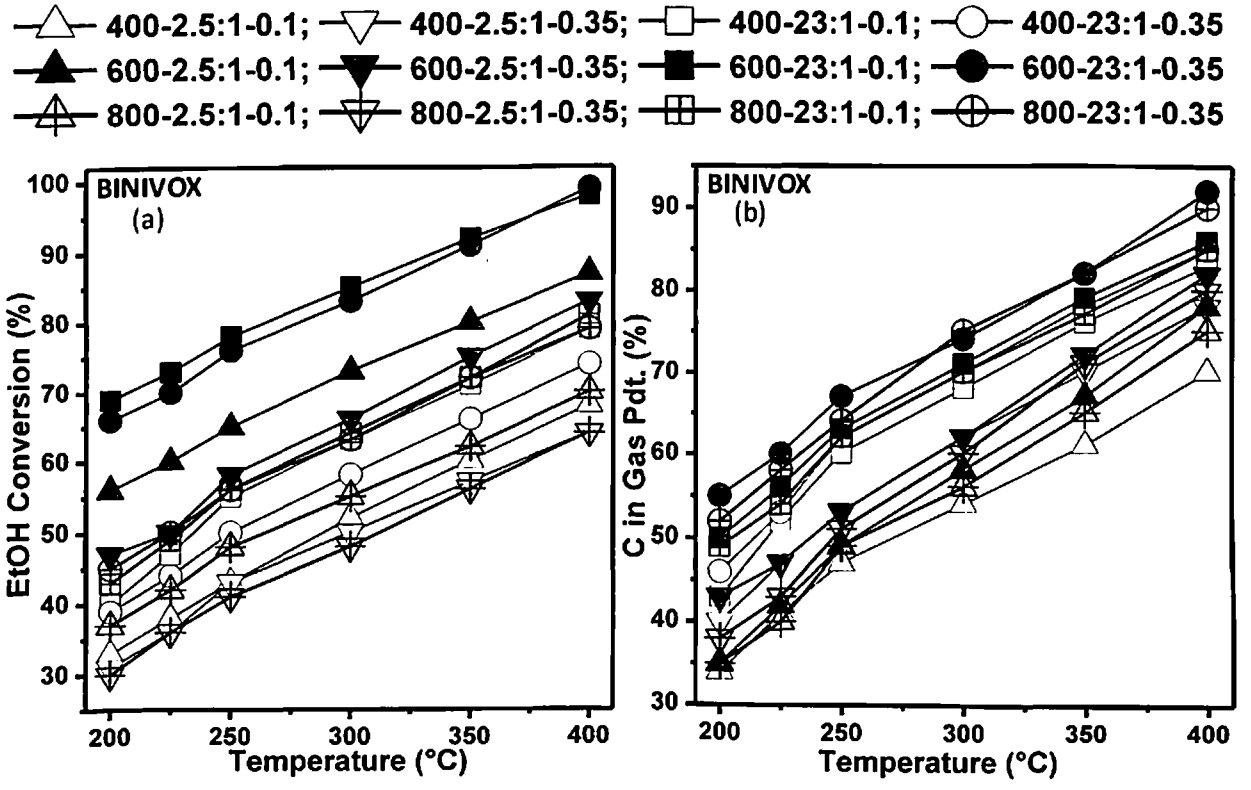

Figure 4-7: (a) EtOH conversion, and (b) C in gaseous phase as a function of temperature for steam reforming of 23:1 and 2.5:1 H_2O:EtOH molar ratio using BINIVOX-400 (□), BINIVOX-600 (■) and BINIVOX-800 (⊕) catalysts at 0.1 and 0.35 cc min^{-1} feed flow rates. Legend is represented as: Catalyst temperature-H_2O:EtOH molar ratio-Feed flow rate

23:1 H_2O: EtOH molar ratio, and 0.35 cc min^{-1} for BINIVOX-600 catalyst, and is 28.9 and 23.7% higher than that of the values obtain for BINIVOX-400 and BINIVOX-800 catalysts, respectively as appeared in Figure 4.8 (a). At 200°C, the H_2 selectivity is 19, 43, and 23% for BINIVOX-400, BINIVOX-600 and BINIVOX-800 catalysts, respectively. Figure 4.8 (b) shows that at 23:1 H_2O: EtOH molar ratio, and 0.35 cc min^{-1} the selectivity of CO_2 increases from 2 to 50%, 35 to 65% and 11 to 58% with increase in temperature from 200 to 400°C for BINIVOX-400, BINIVOX-600 and BINIVOX-800 catalysts, respectively. At 200°C, BINIVOX-400 catalyst has CO (Figure 4.8(c)) and CH_4 (Figure 4.8(d)) selectivity of 50 and 48%, which are 66.6 and 37.1% and 11.1 and 9% higher than that of the values the BINIVOX-600 and BINIVOX-800 catalysts obtain, respectively. Selectivity of CO and CH_4 reduces from 50 to 23% and 48 to 27% for BINIVOX-400, 30 to 13% and 35 to 22% for BINIVOX-600 and 45 to 17% and 44 to 25% for BINIVOX-800 catalysts with increase in temperature from 200 to 400°C.

Figure 4.9 represents the effect of temperature on the selectivity of liquid products. Similar to BICOVOX catalysts, in BINIVOX catalysts also the selectivity of CH_3CHO (Figure 4.9 (a)) and CH_3COCH_3 (Figure 4.9 (c)) increases and CH_3OH (Figure 4.9 (b)) decreases with increase in temperature. Selectivity of CH_3CHO and CH_3OH increases from 21 to 53% and 29 to 44% for BINIVOX-400, 35 to 70% and 17 to 30% for BINIVOX-600 and 20 to 60% and 30 to 40% for BINIVOX-800 catalysts with increase in temperature from 200 to 400°C at 23:1 H_2O: EtOH molar ratio, and 0.35 cc min^{-1}. On the other hand, selectivity of CH_3OH reduces from 50 to 3%, 48 to almost 0% and 50 to almost 0% for BINIVOX-400, BINIVOX-600 and BINIVOX-800 catalysts, respectively with increase in temperature from 200 to 400°C.

Similar to BICOVOX and BINIVOX catalysts, BICUVOX catalyst also shows the similar trends for EtOH conversion and C in gaseous products as depicted in Figure 4.10. EtOH conversion increases from 51 to 81%, 66 to almost 100% and 54 to 85% for BICUVOX-400, BICUVOX-600 and BICUVOX-800 catalysts, respectively with increase in temperature from 200 to 400°C at 23:1 H_2O: EtOH molar ratio, and 0.1 cc min^{-1} as observed in Figure 4.10 (a). At 200°C, the amount of C in gaseous product is 50, 58 and 52% for BICUVOX-400, BICUVOX-600, and BICUVOX-800 catalysts, respectively. Highest amount of C in gaseous product, 93%, is found for BICUVOX-600 catalyst at 400°C , which is 83 and 87% for BICUVOX-400 and BICUVOX-800 catalysts, respectively as shown in Figure 4.10 (b).

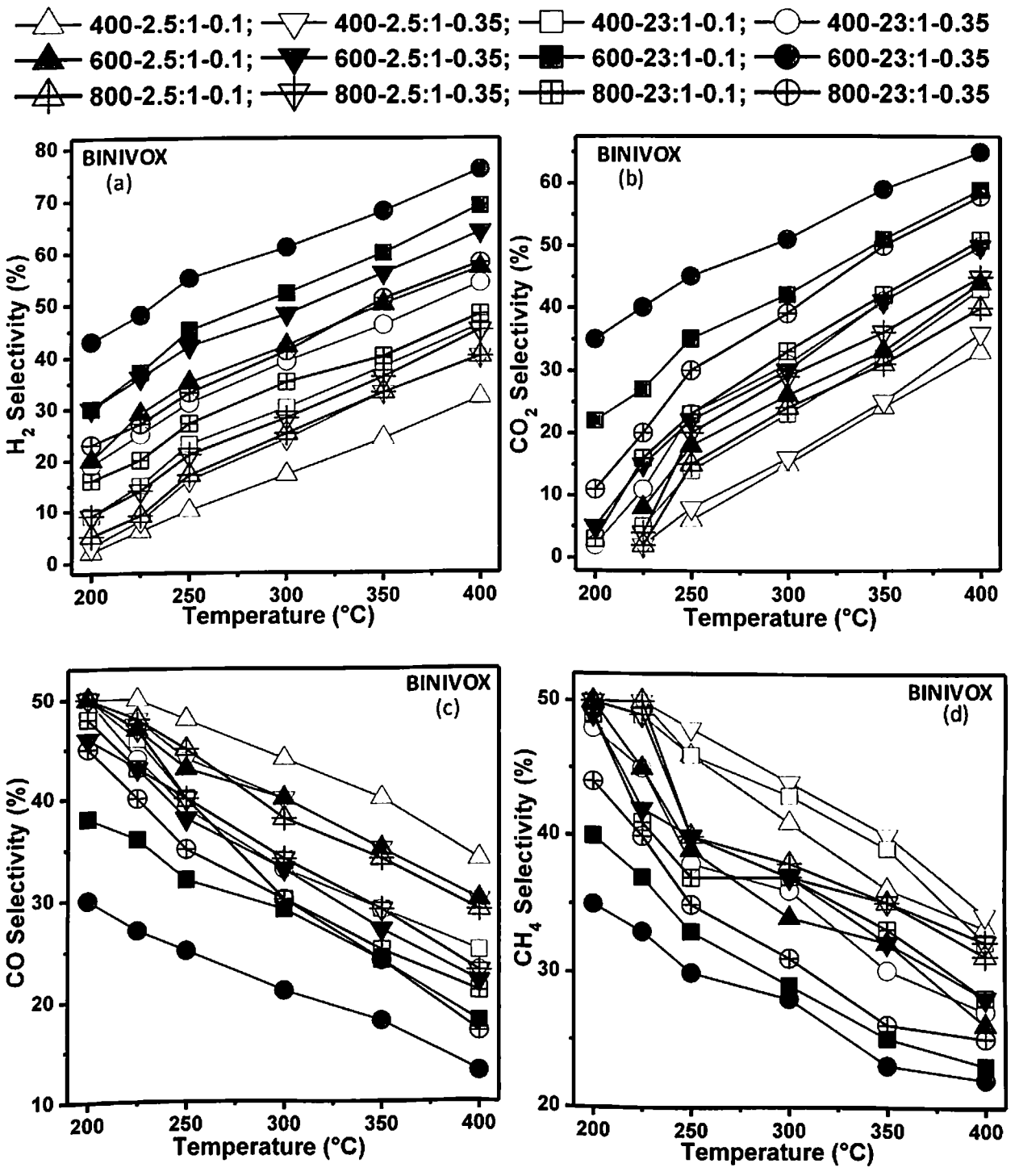

Figure 4-8: Selectivity of the gases; (a) H_2, (b) CO_2, (c) CO, and (d) CH_4 as a function of temperature for steam reforming of 23:1 and 2.5:1 H_2O:EtOH molar ratio using BINIVOX-400 (▫), BINIVOX-600 (■) and BINIVOX-800 (⊞) catalysts at 0.1 and 0.35 cc min^{-1} feed flow rates. Legend is represented as: Catalyst temperature-H_2O:EtOH molar ratio-Feed flow rate

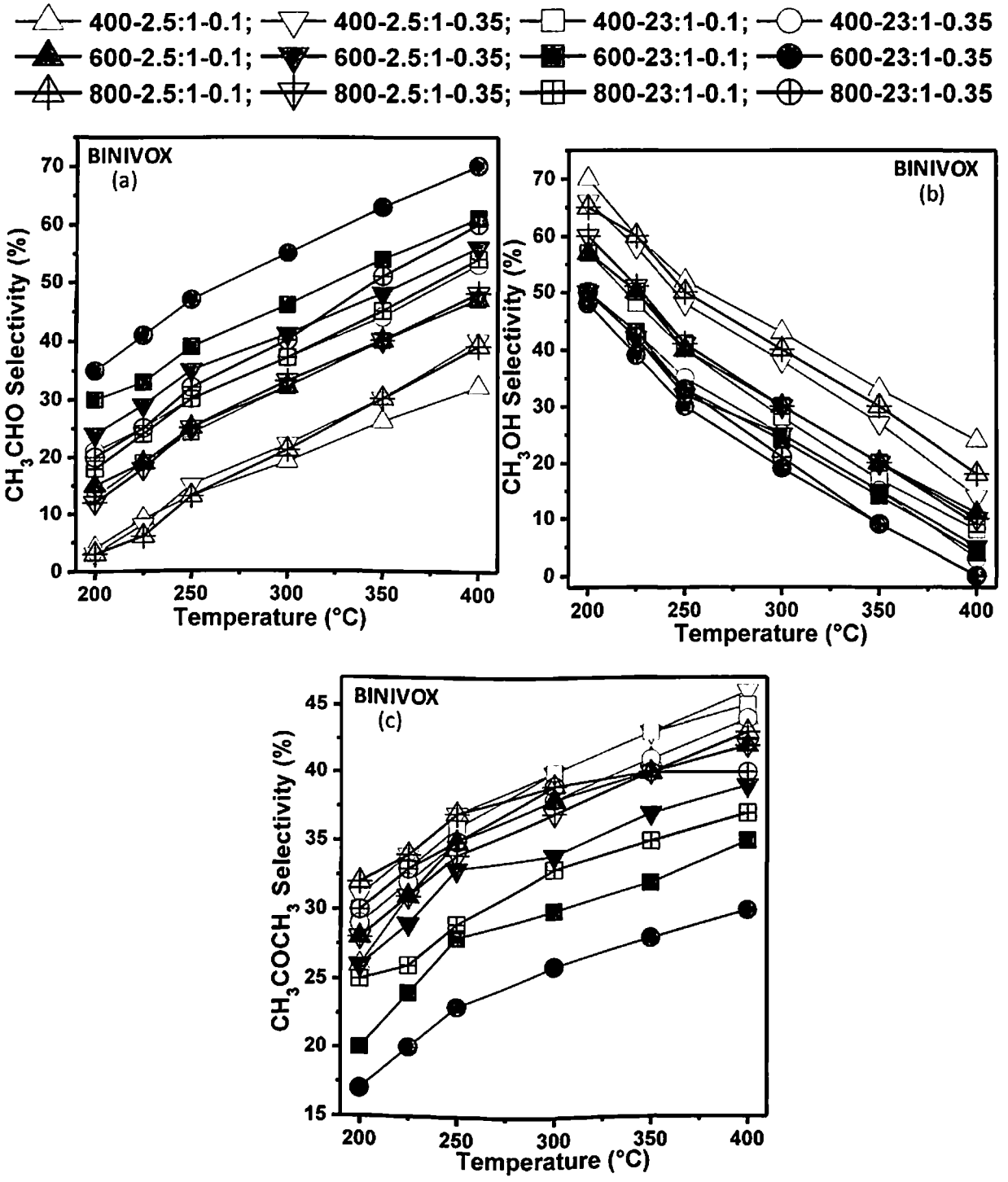

Figure 4-9: Selectivity of ; (a) CH_3CHO, (b) CH_3OH, and (c) $CH_3CO\ CH_3$ as a function of temperature for steam reforming of 23:1 and 2.5:1 H_2O:EtOH molar ratio BINIVOX-400 (□), BINIVOX-600 (■) and BINIVOX-800 (⊕) catalysts at 0.1 and 0.35 cc min^{-1} feed flow rates. Legend is represented as: Catalyst temperature-H_2O:EtOH molar ratio-Feed flow rate

Figure 4.11 shows the effect of temperature on gaseous product's selectivity for BICUVOX catalysts. Similar to BICOVOX and BINIVOX catalysts, H_2 (Figure 4.11 (a)), CO_2 (Figure 4.11 (b)) selectivity increases and CH_4 (Figure 4.11 (d)) and CO (Figure 4.11 (c)) selectivity decreases with increase in temperature for BICUVOX catalysts. Selectivity of H_2 and CO_2 increases from 20 to 54% and 2 to 56% for BICUVOX-400, 46 to 83% and 29 to 74% for BICUVOX-600 and 26 to 63% and 16 to 65% for BICUVOX-800 catalysts with increase in temperature from 200 to 400°C at 23:1 H_2O: EtOH molar ratio, and 0.35 cc min^{-1}. On the other hand, selectivity of CO and CH_4 reduces from 50 to 19% and 48 to 25% for BICUVOX-400, 35 to 10% and 36 to 16% for BICUVOX-600 and 40 to 14% and 44 to 21% for BICUVOX-800 catalysts with increase in temperature from 200 to 400°C at 23:1 H_2O: EtOH molar ratio, and 0.35 cc min^{-1}.

Effect of temperature on the selectivity of liquid products is mentioned in Figure 4.12 for BICUVOX catalysts. Selectivity of CH_3CHO (Figure 4.12 (a)) and CH_3COCH_3 (Figure 4.12 (c)) increases from 28 to 58% and 17 to 28% for BICUVOX-400, 40 to 74% and 10 to 26% for BICUVOX-600 and 35 to 64% and 11 to 25% for BICUVOX-800 catalysts with increase in temperature from 200 to 400°C at 23:1 H_2O: EtOH molar ratio, and 0.35 cc min^{-1}. CH_3OH (Figure 4.12 (b)) selectivity decreases from 55 to 14%, 50 to almost 0% and 54 to 11% for BICUVOX-400 and BICUVOX-800 catalysts, respectively with increase in temperature from 200 to 400°C at 23:1 H_2O: EtOH molar ratio, and 0.35 cc min^{-1}.

Steams reforming of ethanol over BIMEVOX catalysts have not been reported by anyone till date. Therefore, literature reports for various other catalysts for low temperature steam reforming have been considered for analyzing our results. Dai et al, (2018) perform the low temperature steam reforming over Pt nano-particles encapsulated in a hollow zeolite micro-reactor at atmospheric pressure, WHSV= 8.5 h^{-1}, H_2O:EtOH= 4:1 molar ratio and temperature ranges from 200 to 400°C (Dai, Zheng et al. 2018). Catalytic activity results show that EtOH conversion from 68 to almost 100%, and increase in H_2 and CO_2 selectivity from ~42.0 to 72.0% and ~15.0 to 23.0%, respectively on increasing temperature from 200 to 400 °C. CO and CH_4 selectivity shows an opposite trend and decreases from 9 to 3% and 18 to 4%, respectively with increase in temperature from 200 to 400°C. Lee et al, (2012) perform the ethanol steam reforming over mesoporous Sn-incorporated SBA-15 catalyst at atmospheric pressure, GHSV 6600 h^{-1}, EtOH: H_2O molar ratio of 1:1, and temperature varying from 200 to 500°C (Lee, Han et al. 2012). The maximum EtOH conversion and H_2 selectivity of 92.0 and 70.0%, respectively, are achieved at 400 °C. Mulewa et al, (2017) study the ethanol steam reforming over montmorillonite clay-supported Ni/TiO_2 catalyst at a

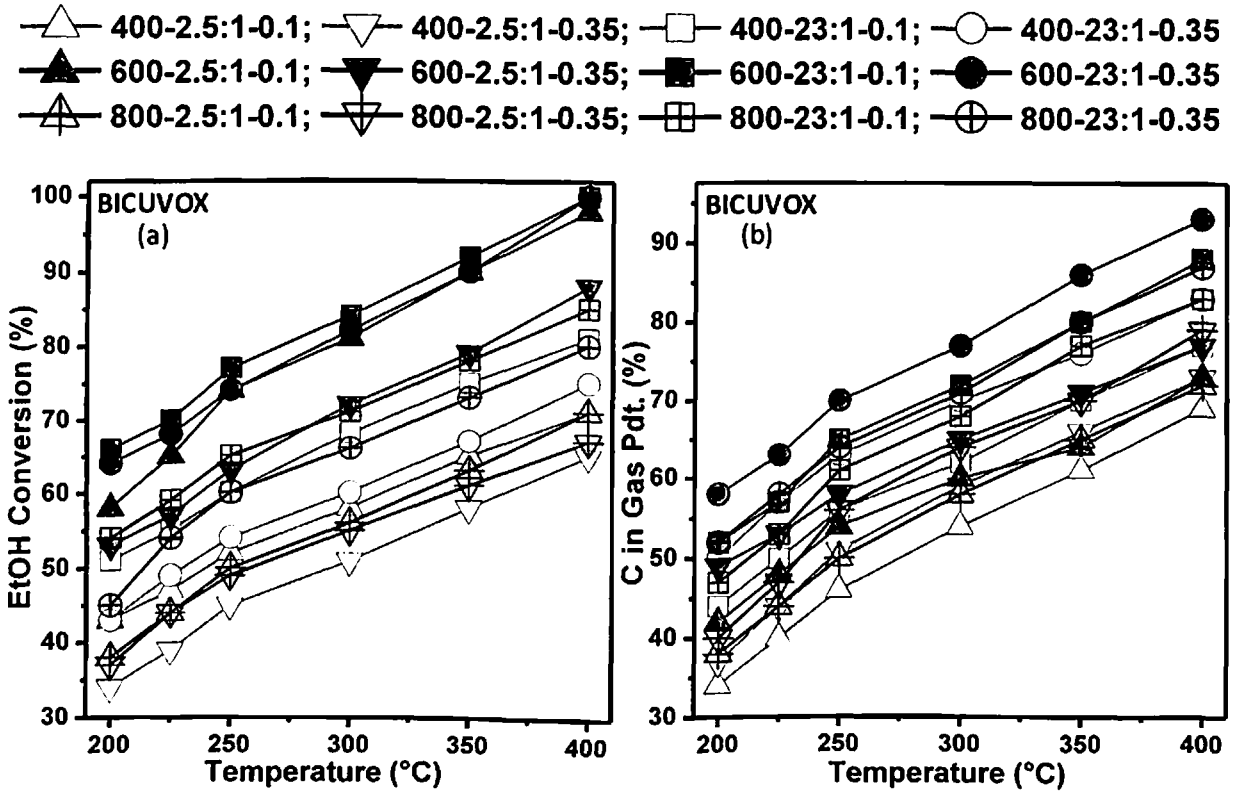

Figure 4-10: (a) EtOH conversion, and (b) C in gaseous phase as a function of temperature for steam reforming of 23:1 and 2.5:1 H_2O:EtOH molar ratio using BICUVOX-400 (□), BICUVOX-600 (■) and BICUVOX-800 (#) catalysts at 0.1 and 0.35 cc min^{-1} feed flow rates. Legend is represented as: Catalyst temperature-H_2O:EtOH molar ratio-Feed flow rate

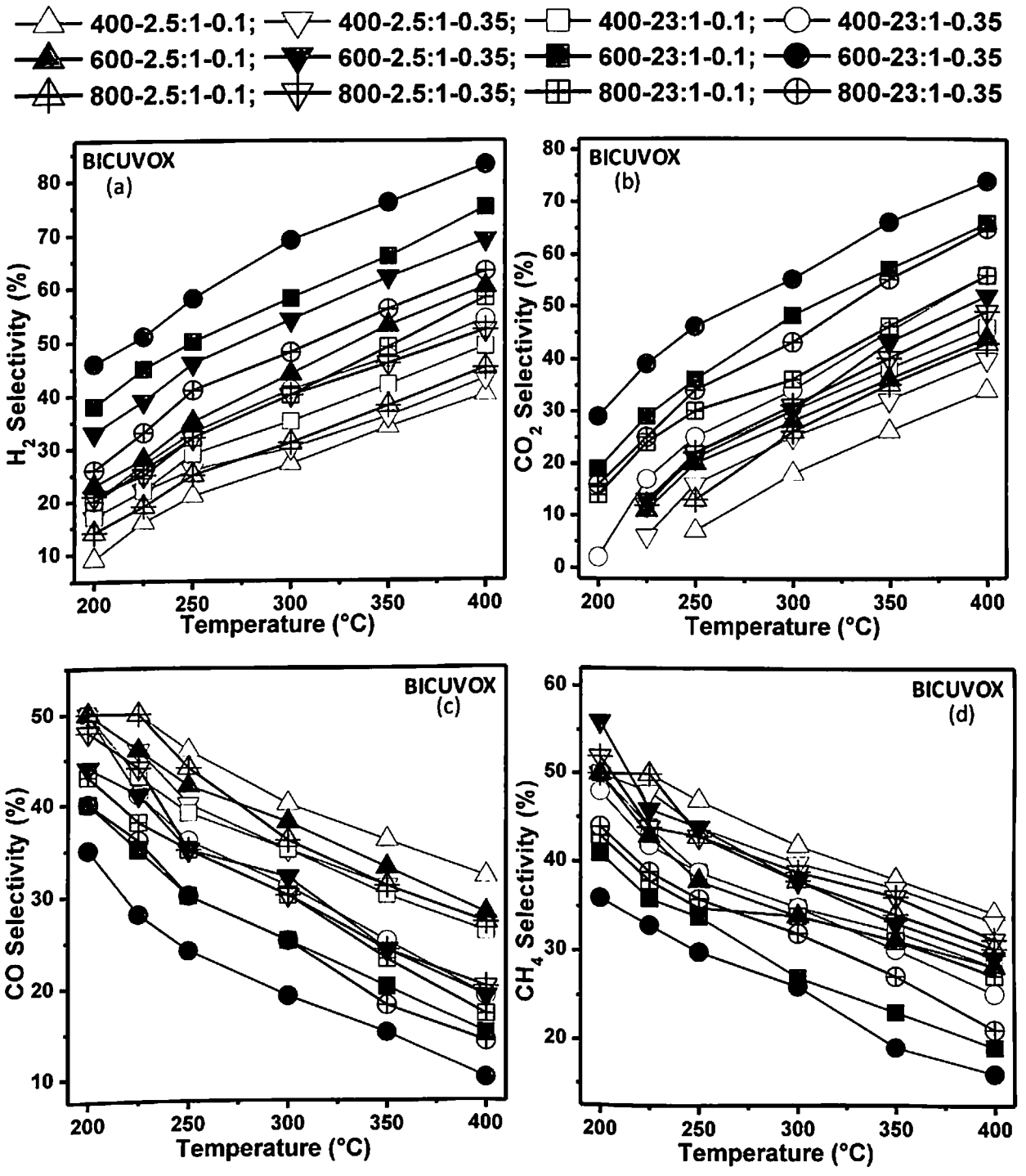

Figure 4-11: Selectivity of the gases; (a) H_2, (b) CO_2, (c) CO, and (d) CH_4 as a function of temperature for steam reforming of 23:1 and 2.5:1 H_2O:EtOH molar ratio BICUVOX-400 (□), BICUVOX-600 (■) and BICUVOX-800 (⊞) catalysts at 0.1 and 0.35 cc min^{-1} feed flow rates. Legend is represented as: Catalyst temperature-H_2O:EtOH molar ratio-Feed flow rate

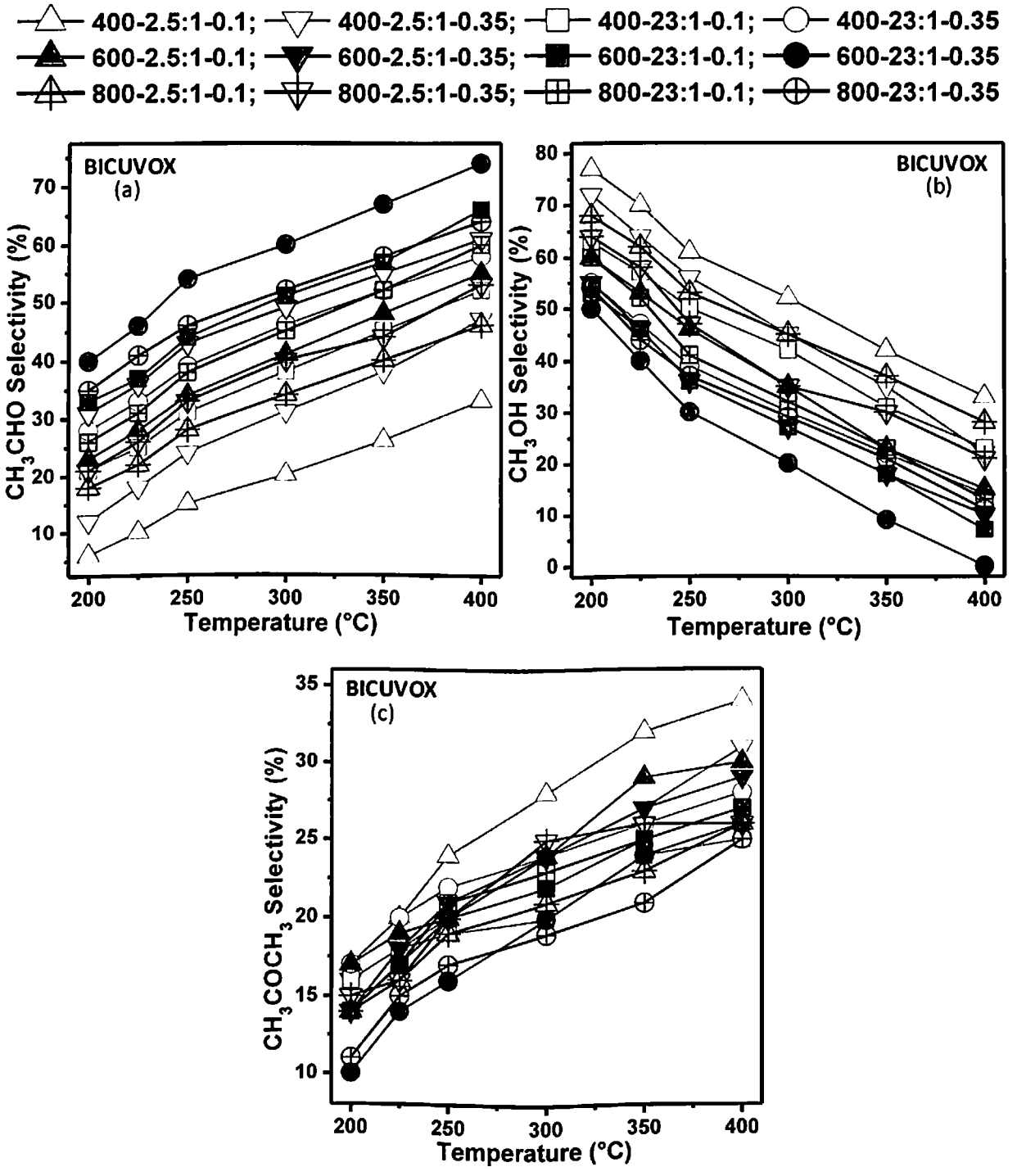

Figure 4-12: Selectivity of ; (a) CH_3CHO, (b) CH_3OH, and (c) $CH_3CO\ CH_3$ as a function of temperature for steam reforming of 23:1 and 2.5:1 H_2O:EtOH molar ratio using BICUVOX-400 (□), BICUVOX-600 (■) and BICUVOX-800 (⊕) catalysts at 0.1 and 0.35 cc min^{-1} feed flow rates. Legend is represented as: Catalyst temperature-H_2O:EtOH molar ratio-Feed flow rate

feed molar ratio (H_2O: EtOH =10:1), atmospheric pressure, GHSV = 13200 ml/gcat·h, and temperature ranges from 300 to 500°C (Mulewa, Tahir et al. 2017). EtOH conversion increases from 0.63 to 88.85% with increase in temperature from 300 to 500°C. Their results show that with increase in temperature, yield (%) of H_2, CO_2, CO and CH_4 increases from 0.534 to 54.54%, 0 to 21.39%, 0 to 2.45 and 0.025 to 12.64%, respectively with the presence of some other gaseous products. Compagnoni et al. (2017) exhibit the ethanol steam reforming over Ni (10 wt%)/CaO (4 wt%)-ZrO_2 catalyst (Compagnoni, Tripodi et al. 2017). The activity tests have been carried out at atmospheric pressure, with a GHSV of 2700 h^{-1}, H_2O: EtOH molar ratio of 3:1 and temperature varies from 300-500°C. Activity results show that EtOH conversion, H_2 yield (mol $min^{-1}kg_{cat}^{-1}$) increases from 53 to 100% and 0.75 to 1.07%, respectively and CH_4 selectivity reduces from 37 to 19% with increase in temperature from 300-500°C. Results reported in literature with respect to the effect of temperature on product distribution and EtOH conversion, are in the same line of our experimental outcomes.

4.1.1.2 *Effect of ethanol concentration in the feed*

Effect of feed concentration on the BICOVOX catalysts activity is observed in Figures (4.4-4.) and Table 4.1. As a general trend ethanol conversion, C in gaseous products and H_2 & CO_2 selectivity reduces and on contrary CO and CH_4 selectivity increases with increasing EtOH concentration from 23:1 to 2.5:1 H_2O: EtOH molar ratio for all the catalysts. Ethanol conversion and C in gaseous state reduces from 78 to 68% and 85 to 80% for BICOVOX-400, 100 to 86% and 97 to 82% for BICOVOX-600 and 83 to 69% and 96 to 83% for BICOVOX-800 catalysts, respectively with increasing EtOH concentration in feed from 23:1 to 2.5:1 H_2O: EtOH molar ratio, at 400°C, and 0.35 cc min^{-1} as shown in Figure 4.4. Similarly, H_2, CO_2 selectivities reduces from 56 to 44%, and 55 to 42% for BICOVOX-400, 80 to 66%, and 72 to 54 for BICOVOX-600, and 61 to 51% and 63 to 50% for BICOVOX-800 catalysts, respectively with increasing EtOH concentration in feed from 23:1 to 2.5:1 H_2O: EtOH molar ratio, at 400°C, and 0.35 cc min^{-1} as shown in Figure 4.5. On the other hand, very small amount of CO is observed at 23:1 H_2O: EtOH molar ratio, at 400°C, and 0.35 cc min^{-1} and for BICOVOX-600 catalyst, it is almost negligible. Increment find in CH_4 is only ~1-5% with increasing EtOH concentration in feed. CO and CH_4 selectivity are found to increase from 10 to 22%, and 35 to 36% for BICOVOX-400, 0 to 13%, and 28 to 33% for BICOVOX-600, and 8 to 14% and 29 to 36% for BICOVOX-800 catalysts, respectively with increasing EtOH concentration in feed from 23:1 to 2.5:1 H_2O: EtOH molar ratio, at 400°C,

and 0.35 cc min^{-1}. Effect of feed concentration on liquid products can be seen in Figure 4.6 for BICOVOX catalysts and obtain trend shows that selectivity of CH_3COCH_3 (15-21%-BICOVOX-400, 10-20%-BICOVOX-600, and 15-23%-BICOVOX-800) and CH_3OH (28-35%-BICOVOX-400, 15-20%-BICOVOX-600, and 20-25%-BICOVOX-800) increases and CH_3CHO (57-44%-BICOVOX-400, 75-60%-BICOVOX-600, and 65-52%-BICOVOX-800) decreases with increasing EtOH concentration in feed from 23:1 to 2.5:1 H_2O: EtOH molar ratio, at 400°C, and 0.35 cc min^{-1}.

BINIVOX and BICUVOX catalysts also show the similar trends as found for BICOVOX catalysts for product distribution with respect to feed concentration. EtOH conversion (74-64%-BINIVOX-400, 99-83%-BINIVOX-600, 79-64%-BINIVOX-800, 75-65% BICUVOX-400, 100-88%-BICUVOX-600, and 80-67%-BICUVOX-800), C in gaseous product (85-78%-BINIVOX-400, 92-82%-BINIVOX-600, 90-80%-BINIVOX-800, 83-73% BICUVOX-400, 93-77%-BICUVOX-600, and 87-79%-BICUVOX-800), selectivities of H_2 (54-40%-BINIVOX-400, 76-64%-BINIVOX-600, 58-45%-BINIVOX-800, 54-43% BICUVOX-400, 83-69%-BICUVOX-600, and 63-52%-BICUVOX-800), CO_2 (50-36%-BINIVOX-400, 65-50%-BINIVOX-600, 58-45%-BINIVOX-800, 56-40% BICUVOX-400, 74-52%-BICUVOX-600, and 65-49%-BICUVOX-800) reduces with increasing EtOH concentration in feed from 23:1 to 2.5:1 H_2O: EtOH molar ratio, at 400°C, and 0.35 cc min^{-1} as shown in Figures (4.7,4.8, 4.10 and 4.11) and Table 4.2 and 4.3. On the contrary selectivities of CO (23-30%-BINIVOX-400, 13-22%-BINIVOX-600, 17-23%-BINIVOX-800, 19-27% BICUVOX-400, 10-19%-BICUVOX-600, and 14-20%-BICUVOX-800) and CH_4 (27-34%-BINIVOX-400, 22-28%-BINIVOX-600, 25-32%-BINIVOX-800, 25-33% BICUVOX-400, 16-29%-BICUVOX-600, and 21-31%-BICUVOX-800) is found to increase with increasing EtOH concentration in feed from 23:1 to 2.5:1 H_2O: EtOH molar ratio, at 400°C, and 0.35 cc min^{-1}.

Effect of feed concentration on liquid products can be seen in Figures 4.9 and 4.12 for BINIVOX and BICUVOX catalysts and obtained trends show the similar trends as observed for BICOVOX catalysts, that selectivity of CH_3COCH_3 (44-46%-BINIVOX-400, 30-39%-BINIVOX-600, 40-42%-BINIVOX-800, 28-31% BICUVOX-400, 26-29%-BICUVOX-600, and 25-26%-BICUVOX-800) and CH_3OH (3-14%-BINIVOX-400, 0-5%-BINIVOX-600, 0-10%-BINIVOX-800, 14-22% BICUVOX-400, 0-10%-BICUVOX-600, and 11-21%-BICUVOX-800) increases and CH_3CHO (53-40%-BINIVOX-400, 70-56%-BINIVOX-600, 60-48%-BINIVOX-800, 58-47% BICUVOX-400, 74-61%-BICUVOX-600, and 64-53%-BICUVOX-800) decreases with increasing EtOH concentration in feed from 23:1 to 2.5:1 H_2O: EtOH molar ratio, at 400°C, and 0.35 cc min^{-1}.

Table 4-1: Catalytic activity data for BICOVOX catalyst from steady state steam reforming of EtOH at 400°C under different conditions

Catalysts	**BICOVOX-400**				**BICOVOX-600**				**BICOVOX-800**			
Feed flow rate (cc min^{-1})	**0.1**		**0.35**		**0.1**		**0.35**		**0.1**		**0.35**	
H_2O:EtOH (molar ratio)	**23:1**	**2.5:1**	**23:1**	**2.5:1**	**23:1**	**2.5:1**	**23:1**	**2.5:1**	**23:1**	**2.5:1**	**23:1**	**2.5:1**
EtOH conv. (%)	83	71	78	68	100	96	100	86	88	75	83	69
C in gas (%)	83	78	85	80	90	79	97	82	90	75	96	83
H_2 selectivity (%)	50	38	56	44	73	59	80	66	55	43	61	51
CO_2 selectivity (%)	48	38	55	42	63	48	72	54	55	46	63	50
CO selectivity (%)	16	28	10	22	2	19	0	13	13	16	8	14
CH_4 selectivity (%)	36	34	35	36	35	33	28	33	32	38	29	36
CH_3CHO selectivity (%)	50	35	57	44	65	51	75	60	59	44	65	52
CH_3OH selectivity (%)	31	40	28	35	16	25	15	20	23	30	20	25
CH_3COCH_3 selectivity (%)	19	25	15	21	19	24	10	20	18	26	15	23

Table 4-2: Catalytic activity data for BINIVOX catalyst from steady state steam reforming of EtOH at 400°C under different conditions

Catalysts	**BINIVOX-400**				**BINIVOX-600**				**BINIVOX-800**			
Feed flow rate (cc min^{-1})	**0.1**		**0.35**		**0.1**		**0.35**		**0.1**		**0.35**	
H_2O:EtOH (molar ratio)	**23:1**	**2.5:1**	**23:1**	**2.5:1**	**23:1**	**2.5:1**	**23:1**	**2.5:1**	**23:1**	**2.5:1**	**23:1**	**2.5:1**
EtOH conv. (%)	79	68	74	64	98	87	99	83	81	70	79	64
C in gas (%)	83	70	85	78	86	78	92	82	85	75	90	80
H_2 selectivity (%)	46	32	54	40	69	57	76	64	48	40	58	45
CO_2 selectivity (%)	43	33	50	36	59	44	65	50	51	40	58	45
CO selectivity (%)	25	34	23	30	18	30	13	22	21	29	17	23
CH_4 selectivity (%)	32	33	27	34	23	26	22	28	28	31	25	32
CH_3CHO selectivity (%)	47	32	53	40	61	47	70	56	54	39	60	48
CH_3OH selectivity (%)	8	24	3	14	4	11	0	5	9	18	0	10
CH_3COCH_3 selectivity (%)	45	44	44	46	35	42	30	39	37	43	40	42

Table 4-3: Catalytic activity data for BICUVOX catalyst from steady state steam reforming of EtOH at 400°C under different conditions

Catalysts	**BICUVOX-400**				**BICUVOX-600**				**BICUVOX-800**			
Feed flow rate (cc min^{-1})	**0.1**		**0.35**		**0.1**		**0.35**		**0.1**		**0.35**	
H_2O:EtOH (molar ratio)	**23:1**	**2.5:1**	**23:1**	**2.5:1**	**23:1**	**2.5:1**	**23:1**	**2.5:1**	**23:1**	**2.5:1**	**23:1**	**2.5:1**
EtOH conv. (%)	81	71	75	65	100	98	100	88	85	71	80	67
C in gas (%)	77	69	83	73	88	73	93	77	83	72	87	79
H_2 selectivity (%)	49	40	54	43	75	60	83	69	58	45	63	52
CO_2 selectivity (%)	46	34	56	40	66	44	74	52	56	43	65	49
CO selectivity (%)	26	32	19	27	15	28	10	19	17	27	14	20
CH_4 selectivity (%)	28	34	25	33	19	28	16	29	27	30	21	31
CH_3CHO selectivity (%)	52	33	58	47	66	55	74	61	60	46	64	53
CH_3OH selectivity (%)	23	33	14	22	7	15	0	10	13	28	11	21
CH_3COCH_3 selectivity (%)	25	34	28	31	27	30	26	29	27	26	25	26

Mulewa et al, (2017) show the effect of different feed concentration varying from 10:1 to 1:10 H_2O:EtOH molar ratio on EtOH conversion, and products yield at 1 atm, 400°C, GHSV = 13200 ml/gcat·h (Mulewa, Tahir et al. 2017). It is found that EtOH conversion, H_2 and CO_2 yield reduces from 98.89 to 88.85%, 54.55 to 28.76% and 21.4 to 13.3%, respectively with increase in feed concentration. On contrary to this, CO (2.45 to 14.28%) and CH_4 (12.64 to 13.3%) yield increases with increase in feed concentration. Comas et al, (2004) perform the ethanol steam reforming over Ni/Al_2O_3 catalyst at 1 atmosphere, 500°C, and EtOH: H_2O molar ratio varies from 1:6 to 1:1 (Comas, Marino et al. 2004). Results show that with increasing EtOH: H_2O molar ratio from 1:6 to 1:1, the H_2 and CO_2 selectivity reduces from 90 to 55% and 42 to 30%, respectively. Contrary to this, CO and CH_4 selectivity increases from 15 to 38% and 21 to 23%, respectively. Wu et al, (2012) study the effect of process conditions on steam reforming of ethanol over Ni/SiO_2 catalyst at atmospheric pressure, temperature varies from 400-650°C and H_2O: EtOH ranges from 3:1 to 6:1 (Wu and Williams 2012). On increasing ratio of H_2O: EtOH from 2:1 to 4:1, H_2 production increases from 39.4 to 50.4 wt% at 650°C. Our results are consistent the results obtained from the literature with respect to feed concentration variation.

4.1.1.3 *Effect of feed flow rate*

In general, EtOH conversion, CO and CH_4 selectivity reduces with increase in flow rate from 0.1 to 0.35 cc min^{-1}, but H_2, CO_2 selectivity and amount of C in the gas show an opposite trend. EtOH conversion reduces from 83 to 78% and 88 to 83% for BICOVOX-400 and BICOVOX-800 catalysts, respectively with increase in flow rate from 0.1 (GHSV-5097.9 h^{-1}) to 0.35 cc min^{-1} (GHSV-17318.2 h^{-1}) at 23:1 H_2O: EtOH molar ratio and 400°C as mentioned in Table 4.1. However, EtOH conversion reaches to 100% at 400°C for BICOVOX-600 catalyst. C in gaseous state increases from 83 to 85%, 90 to 97% and 90 to 96% for BICOVOX-400, BICOVOX-600 and BICOVOX-800 catalysts, respectively with increase in flow rate from 0.1 to 0.35 cc min^{-1} at 23:1 H_2O: EtOH molar ratio and 400°C. Similarly, H_2, CO_2 selectivity increases from 50 to 56%, and 48 to 55% for BICOVOX-400, 73 to 80%, and 63 to 72% for BICOVOX-600, and 55 to 61% and 55 to 63% for BICOVOX-800 catalysts, respectively with increase in flow rate from 0.1 to 0.35 cc min^{-1} at 23:1 H_2O: EtOH molar ratio and 400°C. On the other hand, CO and CH_4 selectivity are found to decrease from 16 to 10%, and 36 to 35% for BICOVOX-400, 2 to 0%, and 35 to 28% for BICOVOX-600, and 13 to 8% and 32 to 29% for BICOVOX-800 catalysts, respectively with

increase in flow rate from 0.1 to 0.35 cc min^{-1}. Effect of flow rate for BICOVOX catalysts shows that selectivity of CH_3COCH_3 (19-15%-BICOVOX-400, 19-10%-BICOVOX-600, and 18-15%-BICOVOX-800) and CH_3OH (31-28%-BICOVOX-400, 16-15%-BICOVOX-600, and 23-20%-BICOVOX-800) reduces and CH_3CHO (50-57%-BICOVOX-400, 65-75%-BICOVOX-600, and 59-65%-BICOVOX-800) increases with increase in flow rate from 0.1 to 0.35 cc min^{-1} at 23:1 H_2O: EtOH molar ratio and 400°C.

Similar trends for gaseous and liquid products are seen for BINIVOX and BICUVOX catalysts as found for BICOVOX catalysts with respect to flow rate. EtOH conversion (79-74%-BINIVOX-400, 99-98%-BINIVOX-600, 81-79%-BINIVOX-800, 81-75% BICUVOX-400, 100%-BICUVOX-600, and 85-80%-BICUVOX-800) reduces, and C in gaseous product (83-85%-BINIVOX-400, 86-92%-BINIVOX-600, 85-90%-BINIVOX-800, 77-83% BICUVOX-400, 88-93%-BICUVOX-600, and 83-87%-BICUVOX-800), selectivity of H_2 (46-54%-BINIVOX-400, 69-76%-BINIVOX-600, 48-58%-BINIVOX-800, 49-54% BICUVOX-400, 75-83%-BICUVOX-600, and 58-63%-BICUVOX-800), CO_2 (43-50%-BINIVOX-400, 59-65%-BINIVOX-600, 51-58%-BINIVOX-800, 46-56% BICUVOX-400, 66-74%-BICUVOX-600, and 56-65%-BICUVOX-800) increases with increase in flow rate from 0.1 to 0.35 cc min^{-1} at 23:1 H_2O: EtOH molar ratio and 400°C. On the contrary selectivity's of CO (25-23%-BINIVOX-400, 18-13%-BINIVOX-600, 21-17%-BINIVOX-800, 26-19% BICUVOX-400, 15-10%-BICUVOX-600, and 17-14%-BICUVOX-800) and CH_4 (32-27%-BINIVOX-400, 23-22%-BINIVOX-600, 28-25%-BINIVOX-800, 28-25% BICUVOX-400, 19-16%-BICUVOX-600, and 27-21%-BICUVOX-800) is found to be decrease with increase in flow rate from 0.1 to 0.35 cc min^{-1} at 23:1 H_2O: EtOH molar ratio and 400°C as mentioned in Tables 4.2 and 4.3.

Effect of flow rate on liquid products for BINIVOX and BICUVOX catalysts shows the similar trends as observed for BICOVOX catalysts, that selectivity of CH_3COCH_3 (45-44%-BINIVOX-400, 35-30%-BINIVOX-600, 37-40%-BINIVOX-800, 25-26% BICUVOX-400, 27-26%-BICUVOX-600, and 27-25%-BICUVOX-800) and CH_3OH (8-3%-BINIVOX-400, 4-0%-BINIVOX-600, 9-0%-BINIVOX-800, 23-14% BICUVOX-400, 7-0%-BICUVOX-600, and 13-11%-BICUVOX-800) decreases and CH_3CHO (47-53%-BINIVOX-400, 61-70%-BINIVOX-600, 54-60%-BINIVOX-800, 52-58% BICUVOX-400, 66-74%-BICUVOX-600, and 60-64%-BICUVOX-800) increases with increasing flow rate from 0.1 to 0.35 cc min^{-1} at 23:1 H_2O: EtOH molar ratio and 400°C.

Hongbo et al, (2012) perform the ethanol steam reforming over Ni/ Y_2O_3-Al_2O_3 catalyst at H_2O:EtOH=13:1 molar ratio, temperature (300-500°C), and feed flow rate varies from 0.01 to 0.3 ml min^{-1} (Hongbo, ZHANG et al. 2012). At temperature 400°C, EtOH conversion is 100% and remains unaffected as feed flow rate changes from 0.01 to 0.3 ml min^{-1}, and there is no alteration for the selectivity of CO. Hydrogen yield increases from 32.1% to 38.5% with increasing feed flow rate. Zeng et al, (2013) prepare the Ni/Mg-Al catalyst for ethanol steam reforming at 3:1 molar ratio of H_2O: EtOH, 400°C and feed flow rate varies from 2 to 10 ml h^{-1} (Zeng, Gu et al. 2013). On examining the effect of flow rate, the ethanol conversion is always 100% and increasing flow rate monotonically increases the H_2 and CO_2 yields from 4.65 to 5 mol/mol ethanol and 0.62 to 0.68 mol/mol ethanol. Effect of flow rate on product distribution, report in literature, is found in similar line with our experimental results obtained for different catalyst systems.

4.1.1.4 *Time-on-stream activity*

Deactivation or stability of catalysts is determined by conducting the catalytic activity for 150 hrs. The maximum H_2 and CO_2 selectivity are found for 400°C, 23:1 H_2O:EtOH molar ratio and 0.35 cc min^{-1} feed flow rate, therefore, these parameters are chosen for examining the stability of the catalyst. Figure 4.13 compares the selectivity's of H_2, CO, CO_2, and CH_4, C in gaseous state and EtOH conversion in the outlet streams as a function of time over the (a) BICOVOX-400, (b) BICOVOX-600, and (c) BICOVOX-800 catalysts. It can be seen that all the BICOVOX catalysts are highly active and stable in EtOH reforming reaction during the time period of 30 hrs. However, the catalysts begin to deactivate after ~35 hrs on stream. EtOH conversion, C in gas along with H_2 and CO_2 selectivity are found to reduce continuously with time and reaches to 24, 19, 12 and 15%, respectively after 100 hrs on stream whereas, CO and CH_4 selectivity increases up to 52 and 36% after 100 hrs on stream for BICOVOX-400 catalyst. Further, after using catalyst for 150 hrs, results show that BICOVOX-400 catalyst is completely deactivated in terms of H_2 selectivity as no H_2 is seen at 150^{th} hr. CO_2 selectivity is also found to 0% along with only 5% EtOH conversion. On contrary, CO and CH_4 increase upto 55 and 45%, respectively after 150 hrs of experiment. After ~38 hrs of experiment BICOVOX-600 catalyst starts to deactivate and EtOH conversion, H_2 and CO_2 selectivity reduces to 47, 43, and 24%, respectively which is 49, 72 and 37.5%, respectively higher than the values obtain for BICOVOX-400 catalyst. Further on using catalyst for 150 hrs, the EtOH conversion, H_2 and CO_2 selectivity are 15, 10 and 7%

respectively, which is also higher than the values obtained for BICOVOX-400 catalyst and BICOVOX-600 catalyst still shows the presence of H_2. This reflects that BICOVOX-600 catalyst is still active after 150 hrs of experiment. CO and CH_4 selectivity are found to be 44 and 49%, respectively after 150 hrs. BICOVOX-800 also starts to deactivate after ~ 35 hrs on stream. After 100 hrs, EtOH conversion, H_2, CO_2, CO and CH_4 selectivity's are 41, 19, 23, 48 and 29%, respectively with 16% of C in gas products. On comparing this with BICOVOX-600 catalysts, obtained values for EtOH conversion, selectivity of H_2, and CO_2 are 12.7, 55.8, and 4.1% lower than the values obtained for the BICOVOX-600 catalyst after 100 hrs. Later, EtOH conversion, H_2, CO_2, CO and CH_4 selectivity further reduces to 10, 0, 3, 53 and 44%, respectively after 150 hrs.

Similar to BICOVOX, effect of time on catalytic activity for BINIVOX catalysts is shown in Figure 4.14. Effect of time on BINIVOX-400 catalyst is shown in Figure 4.14 (a) and it can be seen that BINIVOX-400 catalyst start to deactivate after ~35 hrs, as the EtOH conversion, H_2, CO_2 selectivity decreases continuously along with constant increase in CO and CH_4 selectivity's. After 100 hrs, EtOH conversion, H_2, CO_2, CO and CH_4 selectivities are 35, 15, 16, 47 and 37%, respectively with 30% of C in gas products which further reduces to 3, 0, 0, 53 and 47%, respectively. 0% H_2 selectivity shows the complete deactivation of BINIVOX-400 catalyst. BINIVOX-600 (Figure 4.14 (b)) and BINIVOX-800 (Figure 4.14 (c)) catalysts also show the similar trends for all activity results as find for BINIVOX-400 catalyst. For BINIVOX-600 and BINIVOX-800 catalysts also reduction in activity is seen after ~35 hrs of experiment and it continues till 150 hrs. After 100 hrs, obtained EtOH conversion, H_2, CO_2, CO and CH_4 selectivity's are 36, 28, 22, 43 and 35% for BINIVOX-600 and 34, 21, 17, 46 and 37% for BINIVOX-800, respectively. Obtained data shows that BINIVOX-600 has 46.4 and 25% higher H_2 selectivity in comparison with the BINIVOX-400 and BINIVOX-800 catalysts, respectively. 11% EtOH conversion, 8% H_2, 9% CO_2, 47% CO and 44% CH_4 is found for BINIVOX-600 after 150 hrs, which is 9% EtOH conversion, 0% H_2, 4% CO_2, 51% CO and 45% CH_4 for BINIVOX-800 catalyst.

Analogous to BICOVOX and BINIVOX catalysts, BICUVOX catalyst also shows the similar trends for product distribution as a function of time as reported in Figure 4.15. After ~35 hrs catalysts start to deactivate as the activity reduces and after 100 hrs, obtained EtOH conversion, H_2, CO_2, CO and CH_4 selectivities are 25%-BICUVOX-400, 44%-BICUVOX-600 and 36%-BICUVOX-800, 20%-BICUVOX-400, 22%-BICUVOX-600 and 20%-BICUVOX-800, 18%-BICUVOX-400, 16%-BICUVOX-600 and 17%-BICUVOX-800, 46%-BICUVOX-400, 40%-BICUVOX-600 and 46%-BICUVOX-800, and 36%-BICUVOX-

400, 44%-BICUVOX-600 and 37%-BICUVOX-800, respectively. Activity of catalysts continue to reduce and after 150 hrs BICUVOX-400 and BICUVOX-800 catalysts shows maximum deactivation as no H_2 is seen for both the catalysts and EtOH conversion also reduces upto 3%-BICUVOX-400 and 8%-BICUVOX-800 with 0% CO_2, 50% CO and 50% CH_4 for BICUVOX-400, and 4% CO_2, 50% CO and 46% CH_4 for BICUVOX-800 catalyst. However, 11% H_2 selectivity is appeared for BICUVOX-600 catalyst after 150 hrs with 13% EtOH conversion, 6% CO_2, 45% CO and 49% CH_4 selectivity.

Deactivation study of any BIMEVOX catalysts for LTSR of EtOH has not reported so far. However, some articles on deactivation study of other catalysts are available in the literature. Abello et al, (2013) perform the ethanol steam reforming over Ni-Fe catalyst 500°C, H_2O:EtOH molar ratio of 6:1, atmospheric pressure and 0.2 cc min^{-1} flow rate (Abelló, Bolshak et al. 2013). The ethanol conversion remains 100.0% (with 80.0% H_2 selectivity) for the first 3 hrs and after that it starts to decline and reaches to 38.0% (with 40.0% H_2 selectivity) after 20 hrs of reaction, and remains stable till 24 hrs. Here, carbon deposition is considered to be the possible cause for the deactivation of catalyst, as evident from the SEM images of the used catalysts. Aupretre et al, (2005) investigate the ethanol steam reforming over Mg-Ni-Al_2O_3 catalyst at 700°C, GHSV of 13,400 h^{-1}, H_2O:EtOH molar ratio of 4:1, and atmospheric pressure (Aupretre, Descorme et al. 2005). Catalyst stability has been determined over 75 hrs on stream and it is found that catalyst shows a very good stability. The 100% ethanol conversion is achieved from the starting and it remains 100% for the 25 hrs after that only 5% reduction in EtOH conversion is seen till 75 hrs. 70% H_2 and 18% CO_2 selectivity is reached till 25 hrs which reduces to 55% and 15%, respectively after 75 hrs. CO and CH_4 selectivity is 14 and 5% after 25 hrs which tends to increase upto 20 and 12%, respectively after 75 hrs. They suggest that rate of ethanol dehydrogenation to acetaldehyde is more than the rate of ethanol dehydration to ethylene and that is why less carbon is formed. Chen et al, (2010) carry out the ethanol steam reforming over Rh (1 wt%)/Ca-Al_2O_3 and Rh(1 wt%)–Fe(10 wt%)/Ca–Al_2O_3 catalysts at atmospheric pressure, GHSV of 34,000 h^{-1}, 350°C, and H_2O:EtOH molar ratio of 3:1 (Chen, Choong et al. 2010). For Fe promoted catalyst only 1% reduction in EtOH conversion with 5.0 and 10.0% reduction in H_2 and CO_2 selectivity, respectively, occur after 300 hrs of reforming reaction. However, Rh/Ca-Al_2O_3 catalyst starts to deactivate after 8 hrs and EtOH conversion, H_2 and CO_2 selectivity reduce to 58.0, 22.0 and 8.0% from 100.0, 66.0 and 30.0%, respectively after 25 hrs of experiment. TEM analysis shows deposition of carbonaceous species over used catalysts, responsible for the blocking of active sites and the possible cause for decrease in

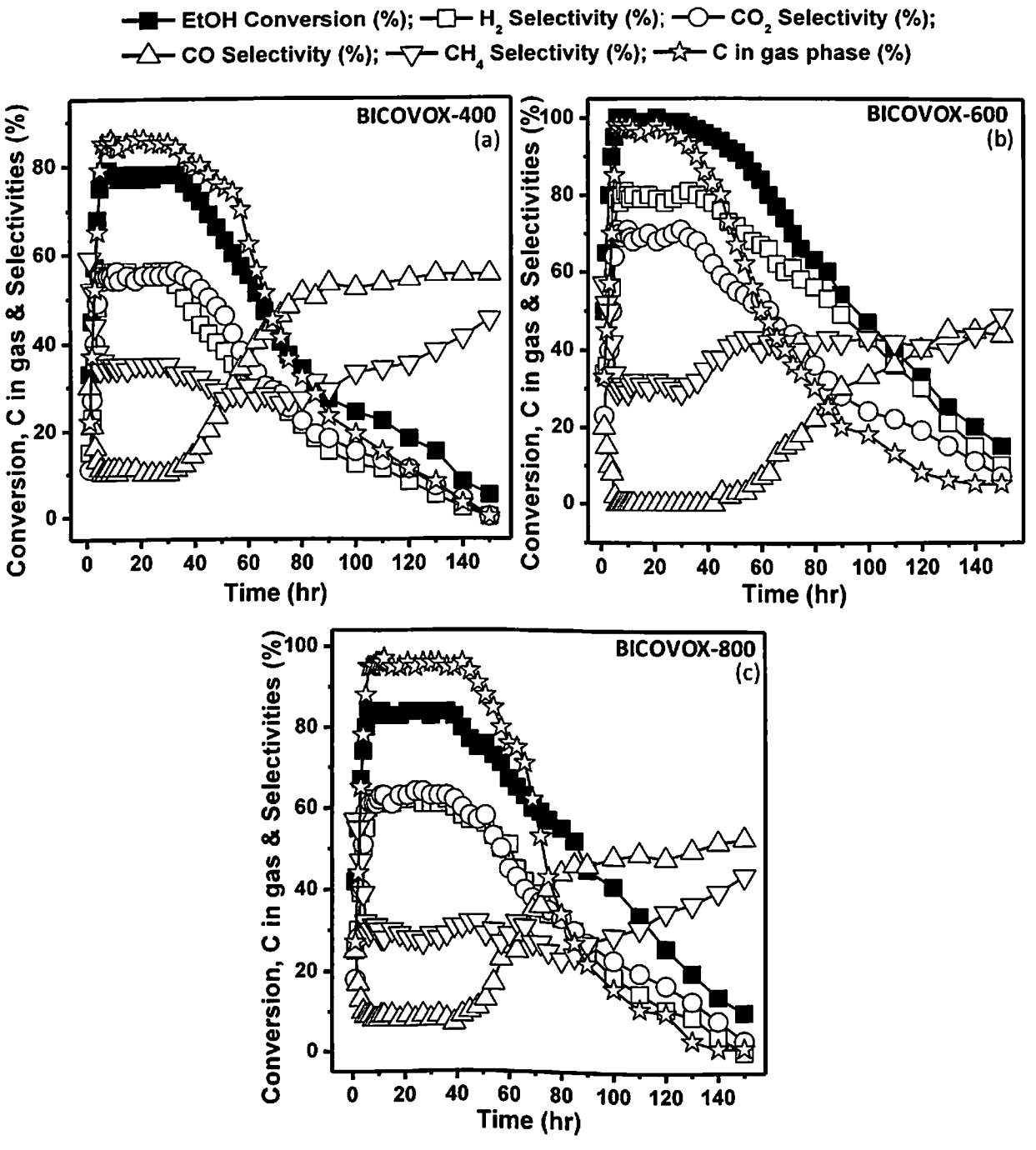

Figure 4-13: : EtOH conversion, C in gas, and selectivity of gaseous products (H_2, CO_2, CO, and CH_4) as a function of time (150 hrs) at 400°C, atmospheric pressure, 23:1 H_2O:EtOH molar ratio and 0.35 cc min^{-1} feed flow rate for steam reforming of (a) BICOVOX-400, (b) BICOVOX-600, and (c) BICOVOX-800 C catalysts

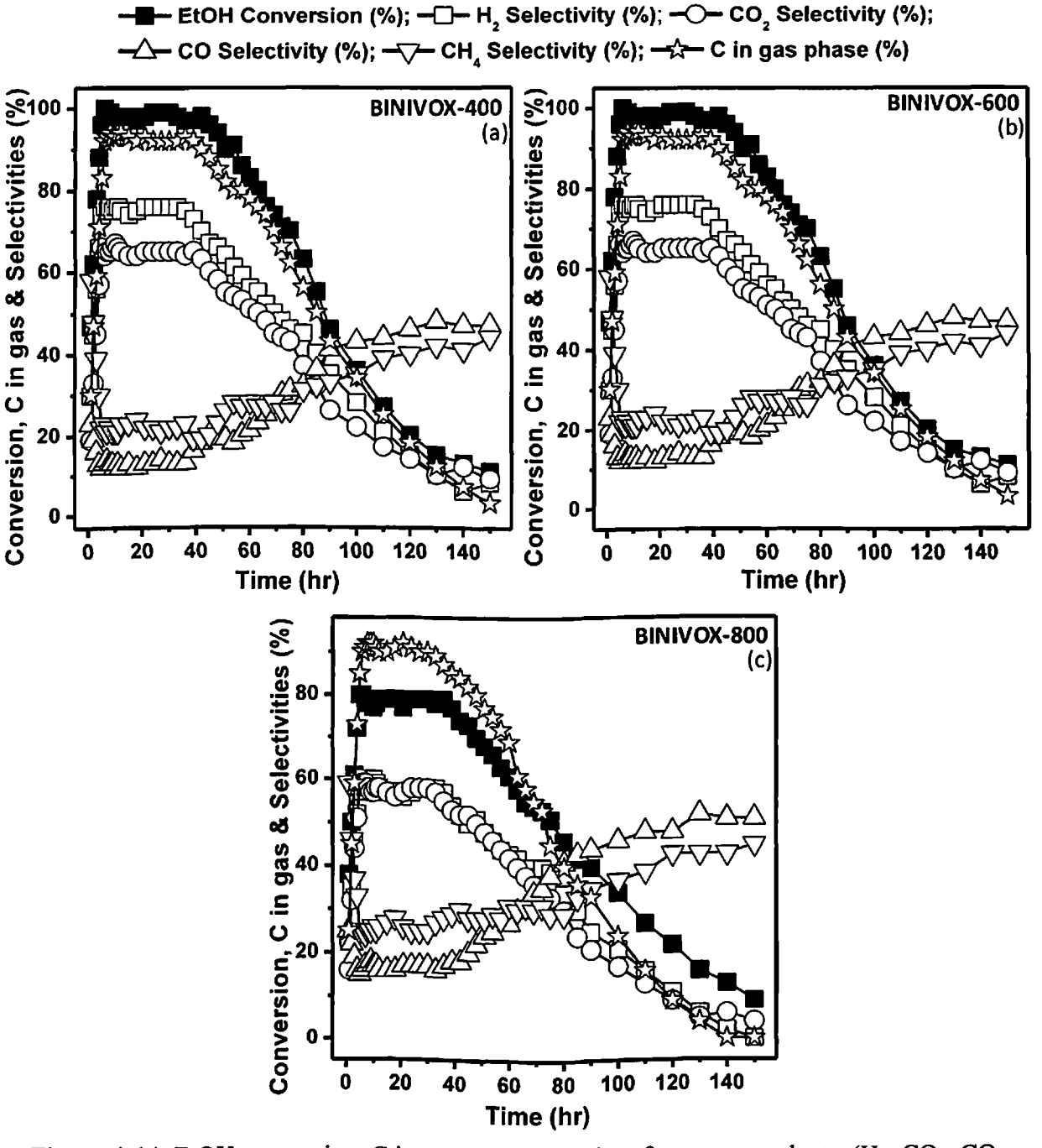

Figure 4-14: EtOH conversion, C in gas, and selectivity of gaseous products (H_2, CO_2, CO, and CH_4) as a function of time (150 hrs) at 400°C, atmospheric pressure, 23:1 H_2O:EtOH molar ratio and 0.35 cc min^{-1} feed flow rate for steam reforming of (a) BINIVOX-400, (b) BINIVOX-600, and (c) BINIVOX-800 C catalysts

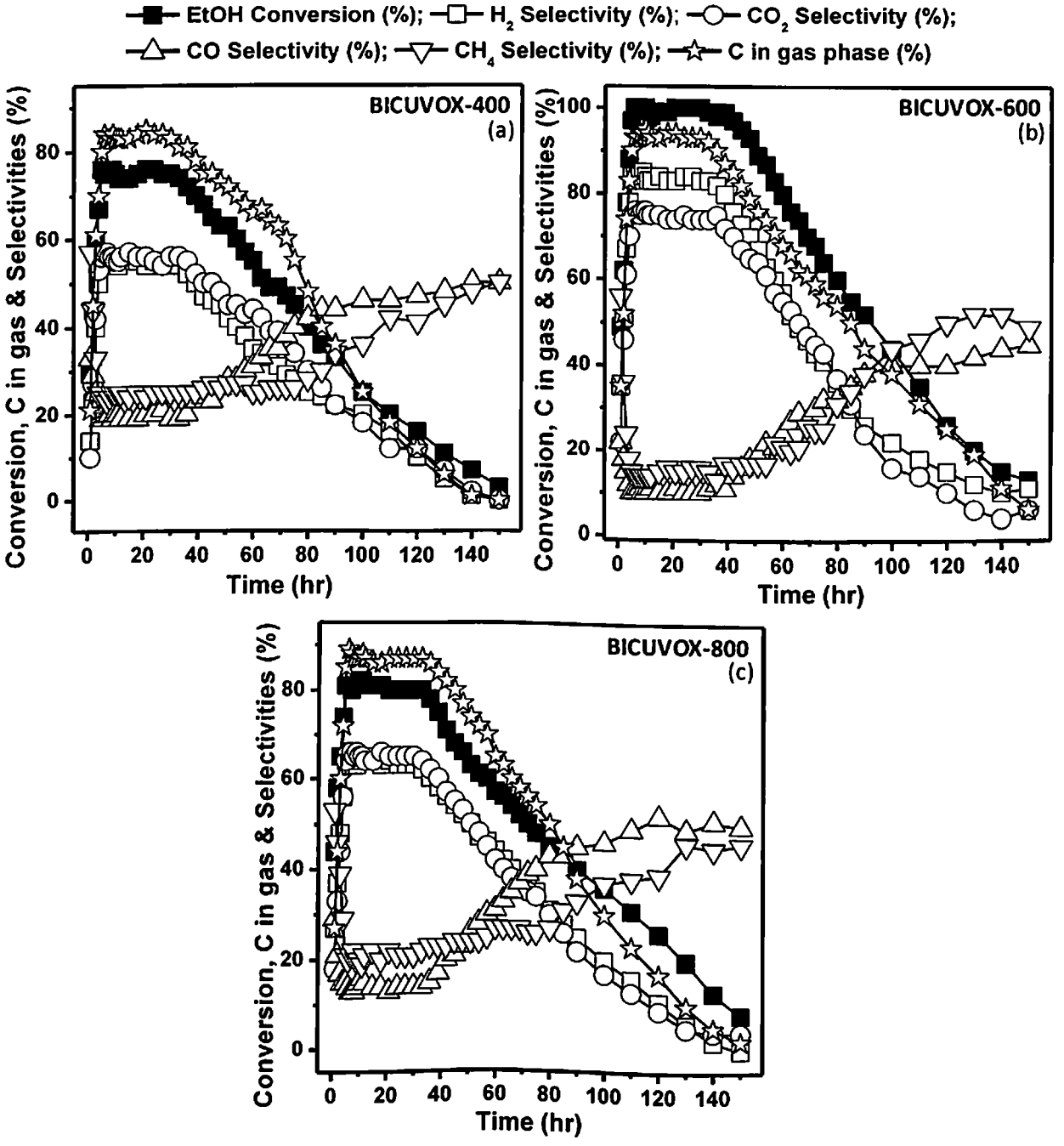

Figure 4-15: EtOH conversion, C in gas, and selectivity of gaseous products (H_2, CO_2, CO, and CH_4) as a function of time (150 hrs) at 400°C, atmospheric pressure, 23:1 H_2O:EtOH molar ratio and 0.35 cc min^{-1} feed flow rate for steam reforming of (a) BICUVOX-400, (b) BICUVOX-600, and (c) BICUVOX-800 C catalysts

catalytic activity. Vicente et al, (2014) study the ethanol steam reforming over Ni/SiO_2 catalyst at 300°C, H_2O:EtOH molar ratio of 6:1, and space time of 0.138 $g_{catalyst}$ h $g_{ethanol}^{-1}$ (Vicente, Ereña et al. 2014). Effect of time on EtOH conversion and product distribution shows that at 300°C, catalyst deactivation is very fast and EtOH conversion and H_2 production rate reaches to almost null after 2 hrs only. Sanchez et al, (2012) perform the steam reforming over Ni/Al_2O_3 calayst at 500°C, H_2O:EtOH molar ratio of 3:1, atmospheric pressure and 0.17 cc min^{-1} flow rate (Sanchez and Comelli 2012). They report that H_2 selectivity increases with time and reaches to 78.1% after 5 hrs and then start to decrease and reaches to 51.5% after 12 hrs. However, CO selectivity shows the opposite trend, initially it decrease with time till 6 hrs and then increases remarkably to 38.9% at 12 hr. Similar trend is seen for CH_4, after 6 hrs the CH_4 selectivity is 2.4% which increases to 8.5% after 12 hrs. They mention that decrease in catalytic activity can be related to soiling and blocking of active sites as result of carbonaceous deposit formation as shown in SEM images. Through literature it can be concluded that catalytic activity reduces with time as H_2 selectivity and EtOH conversion decreases. Our results also show the similar trend and are found in similar line with the literature.

Negligible amount of EtOH conversion and H_2 production is observed using BIVOX catalysts, while no EtOH conversion is detected for mixed Bi_2O_3, $BiVO_4$ and Me-O powder under similar reactor conditions.

4.1.2 Characterization of Catalysts

4.1.2.1 *XRD Analysis (X-ray powder diffraction)*

Figures 4.16 (a), (b) and (c) shows the XRD patterns of the powders resulting from combustion using the three different doping metals. The effects of post-combustion annealing are also illustrated. The graph is shown in a layer lines representing different stages of catalyst starting from BIMEVOX-Wash, BIMEVOX-400_F to BIMEVOX-800_F. All of the wash powders are multiphase, containing Bi_2O_3 and $BiVO_4$ along with the desired pure γ-BIMEVOX phase. In no case is unreacted V_2O_5, other vanadium oxide, or metal oxide detected. This affirms that reaction in terms of V_2O_5 is completed. Following the highest calcination temperature 800°C for 2 h (BIMEVOX-800_F), all powders appear to be mostly single-phase BIMEVOX. The BIMEVOX-800_F patterns in all Figures resemble that of normally prepared by solid state method and calcine BIMEVOX powders, and all major peaks can be assigned to (hkl) planes according to the "normal" tetragonal unit cell of the γ-

BIMEVOX (AMCSD-American Mineralogist Crystal Structure Database-0016748) with the presence of small amount of tetragonal-$BiVO_4$ (amcsd-0014281; peaks at ~ 18.8, 28.88 and 30.5°) (Abraham, Debreuille-Gresse et al. 1988; Joubert, Jouanneaux et al. 1994). Yu et al, (2011) synthesize the BIMNVOX powder by high temperature melting method using bismuth oxide, vanadium pentoxide and magnesium oxide as precursors in order to study the effect of Mn composition on crystal structure of catalyst. XRD patterns of BIMNVOX catalyst calcine at 800°C shows that small amount of $BiVO_4$ is present with the γ-BIMEVOX phase and no peak is observed for V_2O_5 or metal oxide (Yu, Gu et al. 2011). Figure 4.16(d) shows the XRD patterns for parent compound BIVOX, calcined at 400 and 600°C to compare the XRD of doped-BIMEVOX. It shows the presence of more secondary phases and less amount of pure phase. Same observations are reported in the literature (Abraham, Debreuille-Gresse et al. 1988).

In cases of BIMEVOX-400_F and BIMEVOX-600_F, splitting of the (hkl-103 and 200) peaks at approximately 27.97 and 46.25° are indicating the presence of tetragonal β-Bi_2O_3 (amcsd-0010069). However, in BIMEVOX-600_F besides tetragonal β-Bi_2O_3 (amcsd-0010069), monoclinic α-Bi_2O_3 (amcsd-0011925) at ~25.78 and 27.42° can be observed (Roy and Fuierer 2009). No separate vanadium related phases are observed in the XRD spectra of BIMEVOX-400_F & BIMEVOX-600_F. Roy et al, (2009) prepare the BICOVOX catalyst with glycine as fuel from solution combustion synthesis. The XRD patterns of BICOVOX-as combusted and calcined at different temperatures (600, 700 and 800°C) are reported. BICOVOX-600 results show the presence of tetragonal and monoclinic α-Bi_2O_3. However BICOVOX-700 and BICOVOX-800 contain only γ-BIMEVOX (Roy and Fuierer 2009). Trzciński et al, (2015) synthesize the BICUVOX catalyst by conventional solid-state reaction technique and calcine at 830°C. According to XRD spectra of BICUVOX catalyst only tetragonal γ-phase (I4/mmm) is observed (Trzciński, Borowska-Centkowska et al. 2015). Our XRD patterns match very well to those of the literature (Lazure, Vannier et al. 1995; Balzar, Ramakrishnan et al. 2004; Gräfe 2015).

Therefore, precursors as reactant and procure phases in BICOVOX-Wash as products can be represent through Equation 4.1. As well as effect of different calcination temperature on acquire phases in BICOVOX-Wash can be expressed through Equation 4.2.

$$Bi(NO_3)_3 \cdot 5H_2O + Co(NO_3)_2 \cdot 6H_2O + V_2O_5 + C_2H_5NO_2 \xrightarrow{\Delta} \gamma - BICOVOX + BiVO_4 + \beta - Bi_2O_3 \quad (4.1)$$

$$\gamma - BICOVOX + BiVO_4 + \beta - Bi_2O_3 \xrightarrow{400\,^{\circ}C} \gamma - BICOVOX + BiVO_4 + \beta - Bi_2O_3 \quad \text{(a)}$$
$$\gamma - BICOVOX + BiVO_4 + \beta - Bi_2O_3 \xrightarrow{600\,^{\circ}C} \gamma - BICOVOX + BiVO_4 + \beta - Bi_2O_3 + \alpha - Bi_2O_3 \quad \text{(b)} \quad (4.2)$$
$$\gamma - BICOVOX + BiVO_4 + \beta - Bi_2O_3 \xrightarrow{800\,^{\circ}C} \gamma - BICOVOX + BiVO_4 \quad \text{(c)}$$

Figure 4.17 is also shown in a layer lines representing different stages of catalyst starting from BICOVOX_F, BICOVOX_30HRS_U to BICOVOX_U, heat treated at (a) 400°C, (b) 600°C; and (c) 800°C. After use in reactor, crystallinity of all the catalysts are observed to reduce as intensity of peaks is reducing. Emergence of peaks at ~ 27.42 and 33.28° implies the formation of monoclinic α-Bi_2O_3 (amcsd-0011925) for BICOVOX-400_30Hrs _U catalyst. Which further breaks into Bi metal (amcsd-0012841; peak at ~27.19, 62.24°) and disappearance of monoclinic α-Bi_2O_3 for BICOVOX-400_U as depicted in Figure 4.17 (a). Similar trend is observed in BICOVOX-600_30HRS_U and BICOVOX-600_U catalysts as shown in Figure 4.17 (b). However, no phase change is occurred in BICOVOX-800_30HRS_U catalyst. Although, for BICOVOX-800_U catalyst, emergence of a small peak at ~ 27.97° implies the formation of tetragonal β-Bi_2O_3 (amcsd-0010069) phase as shown in Figure 4.17(c). Consequently, change in phases from BICOVOX_F to BICOVOX_30HRS_U and BICOVOX_U can be illustrated through Equation 4.3 (BICOVOX-400), Equation 4.4 (BICOVOX-600) and Equation 4.5 (BICOVOX-800).

$$\gamma - BICOVOX + BiVO_4 + \beta - Bi_2O_3 \xrightarrow{\text{30Hrs Used}} \gamma - BICOVOX + BiVO_4 + \beta - Bi_2O_3 + \alpha - Bi_2O_3 \quad \text{(a)} \quad (4.3)$$
$$\gamma - BICOVOX + BiVO_4 + \beta - Bi_2O_3 \xrightarrow{\text{Long Time Used}} \gamma - BICOVOX + BiVO_4 + \beta - Bi_2O_3 + Bi \quad \text{(b)}$$

$$\gamma - BICOVOX + BiVO_4 + \beta - Bi_2O_3 + \alpha - Bi_2O_3 \xrightarrow{\text{30Hrs Used}} \gamma - BICOVOX + BiVO_4 + \beta - Bi_2O_3 + \alpha - Bi_2O_3 \quad \text{(a)} \quad (4.4)$$
$$\gamma - BICOVOX + BiVO_4 + \beta - Bi_2O_3 + \alpha - Bi_2O_3 \xrightarrow{\text{Long Time Used}} \gamma - BICOVOX + BiVO_4 + \beta - Bi_2O_3 + Bi \quad \text{(b)}$$

$$\gamma - BICOVOX + BiVO_4 \xrightarrow{\text{30Hrs Used}} \gamma - BICOVOX + BiVO_4 \xrightarrow{\text{Long Time Used}} \gamma - BICOVOX + BiVO_4 + \beta - Bi_2O_3 \quad (4.5)$$

Similarly, precursors and procure phases in BINIVOX-wash catalysts is shown in Equation 4.6. Equation 4.7 represents different phases obtained after calcining the BINIVOX-Wash catalyst at three temperatures 400, 600 and 800°C (named as BINIVOX-400_F, BINIVOX-600_F and BINIVOX-800_F).

$$Bi(NO_3)_3 \cdot 5H_2O + Ni(NO_3)_2 \cdot 6H_2O + V_2O_5 + C_2H_5NO_2 \xrightarrow{\Delta} \gamma - BINIVOX + BiVO_4 + \beta - Bi_2O_3 + Bi \quad (4.6)$$

$$\gamma - BINIVOX + BiVO_4 + \beta - Bi_2O_3 + Bi \xrightarrow{400\,^{\circ}C} \gamma - BINIVOX + BiVO_4 + \beta - Bi_2O_3 \quad \text{(a)}$$
$$\gamma - BINIVOX + BiVO_4 + \beta - Bi_2O_3 + Bi \xrightarrow{600\,^{\circ}C} \gamma - BINIVOX + BiVO_4 + \beta - Bi_2O_3 + \alpha - Bi_2O_3 \quad \text{(b)} \quad (4.7)$$
$$\gamma - BINIVOX + BiVO_4 + \beta - Bi_2O_3 + Bi \xrightarrow{800\,^{\circ}C} \gamma - BINIVOX + BiVO_4 \quad \text{(c)}$$

BINIVOX-Wash sample contains an extra peak in comparison with BICOVOX-Wash, at ~ 27.19°, indicating the presence of Bi metal ((AMCSD-0012841)) as shown in Figure 4.18.

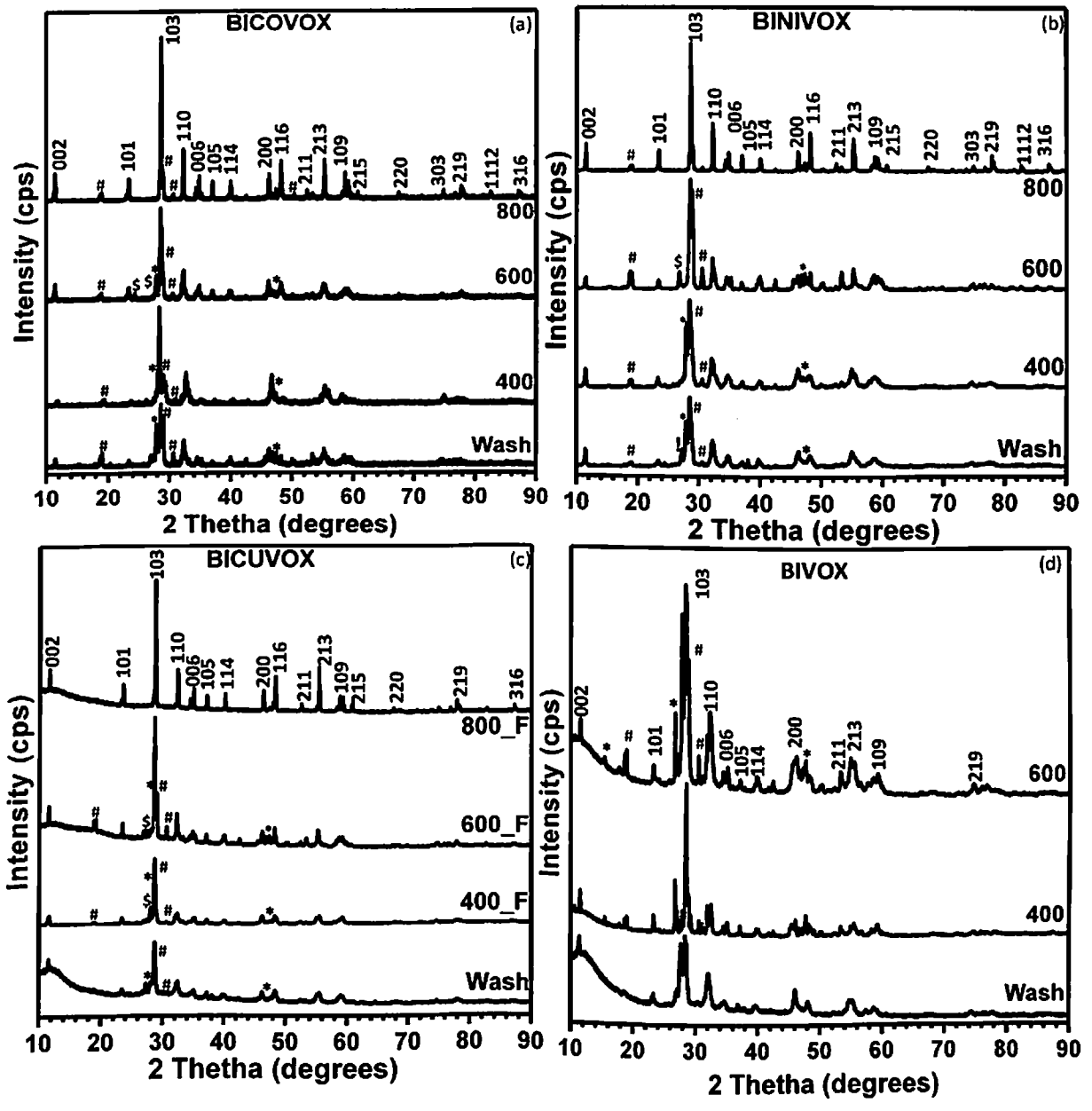

Figure 4-16: XRD spectra of the (a) BICOVOX, (b) BINIVOX, (c) BICUVOX and (d) BIVOX catalysts calcined at; 400°C, 600°C; 800°C, fresh (F) and just after wash catalyst. The symbols * and $ represent tetragonal (amcsd-0010069) and monoclinic (amcsd-0011925) Bi_2O_3, and # represents (amcsd-0014281) $BiVO_4$, and ! represents (amcsd-0012841) Bi metal-related phases, respectively

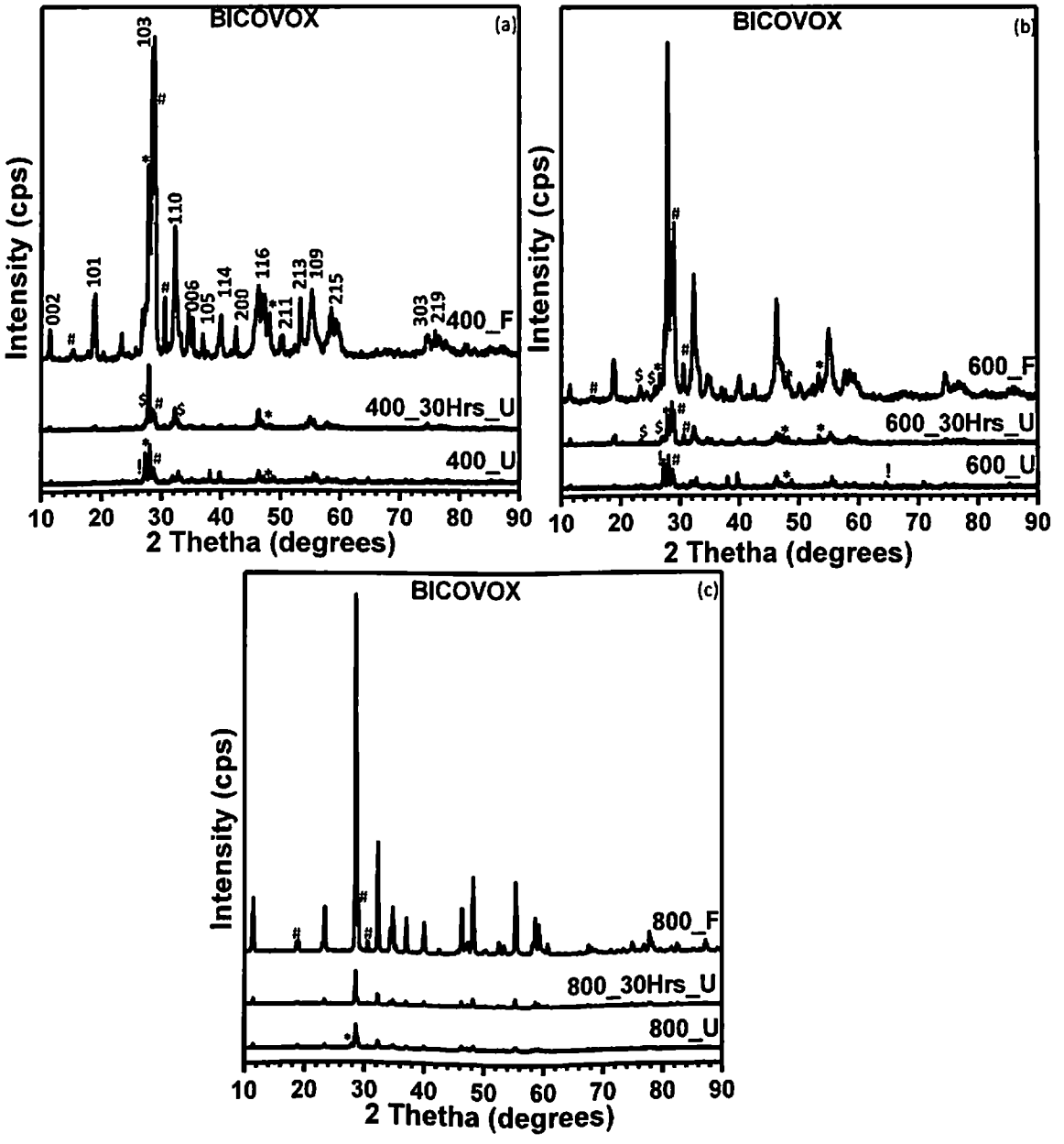

Figure 4-17: XRD spectra of the BICOVOX catalysts calcined at; (a) 400°C, (b) 600°C; and (c) 800°C, fresh (F), 30 hrs used and long time used (U). The symbols * and $ represent tetragonal (amcsd-0010069) and monoclinic (amcsd-0011925) Bi_2O_3, and # represents (amcsd-0014281) $BiVO_4$, and ! represents (amcsd-0012841) Bi metal-related phases, respectively

Possible reasons for this could be inhomogeneity in solution combustion synthesis or small amount of C is present and that is responsible for the reducing environment that can lead to formation of Bi metal.

BINIVOX_30HRS_U catalysts also show similar trend and reduction in crystallinity like BICOVOX_30HRS_U catalysts as mentioned in Equation 4.7 (a). However, BINIVOX_U catalysts show more reduction in term of number of phases. As shown in Figure 4.18 (a) and (b), BINIVOX-400_U and BINIVOX-600_U catalysts have been found to exhibit the same number of phases as BICOVOX-400_U and BICOVOX-600_U respectively, except for one extra phase of monoclinic α-Bi_2O_3 found in BINIVOX-400_U and BINIVOX-400_U at 28.65°. However, BINIVOX-800_U contains monoclinic α-Bi_2O_3 and Bi metal as an extra phase at 27.19°, 27.19° respectively, in comparison with BICOVOX-800_U, as shown in Figure 4.18 (c). Accordingly, change in phases from BINIVOX_F to BINIVOX_30HRS_U and BINIVOX_U can be illustrated through Equation 4.8 (BINIVOX-400), Equation 4.9 (BINIVOX-600) and Equation 4.10 (BINIVOX-800).

BINIVOX-400

$$\gamma - BINIVOX + BiVO_4 + \beta - Bi_2O_3 \xrightarrow{30Hrs\ Used} \gamma - BINIVOX + BiVO_4 + \beta - Bi_2O_3 + \alpha - Bi_2O_3 \quad (a)$$
$$\gamma - BINIVOX + BiVO_4 + \beta - Bi_2O_3 \xrightarrow{Long\ Time\ Used} \gamma - BINIVOX + BiVO_4 + \beta - Bi_2O_3 + \alpha - Bi_2O_3 + Bi \quad (b) \quad (4.8)$$

BINIVOX-600

$$\gamma - BINIVOX + BiVO_4 + \beta - Bi_2O_3 + \alpha - Bi_2O_3 \xrightarrow{30Hrs\ Used} \gamma - BINIVOX + BiVO_4 + \beta - Bi_2O_3 + \alpha - Bi_2O_3 \quad (a)$$
$$\gamma - BINIVOX + BiVO_4 + \beta - Bi_2O_3 + \alpha - Bi_2O_3 \xrightarrow{Long\ Time\ Used} \gamma - BINIVOX + BiVO_4 + \beta - Bi_2O_3 + Bi \quad (b) \quad (4.9)$$

BINIVOX-800

$$\gamma - BINIVOX + BiVO_4 \xrightarrow{30Hrs\ Used} \gamma - BINIVOX + BiVO_4 \xrightarrow{Long\ Time\ Used} \gamma - BINIVOX + BiVO_4 + \beta - Bi_2O_3 + \alpha - Bi_2O_3 + Bi \quad (4.10)$$

Likewise, representation of precursors and procure phases in BICUVOX-wash catalyst is mentioned in Equation 4.11. Unlike BICOVOX-400_F and BINIVOX-400_F, BICUVOX-400_F catalyst also contains monoclinic α-Bi_2O_3 at 47.38°. Equation 4.12 represents different phases obtained after calcining the BICUVOX-wash at three temperatures 400, 600 and 800°C (named as BICUVOX-400_F, BICUVOX-600_F and BICUVOX-800_F).

$$Bi(NO_3)_3 \cdot 5H_2O + Cu(NO_3)_2 \cdot 6H_2O + V_2O_5 + C_2H_5NO_2 \xrightarrow{\Delta} \gamma - BICUVOX + BiVO_4 + \beta - Bi_2O_3 \quad (4.11)$$

$$\gamma - BICUVOX + BiVO_4 + \beta - Bi_2O_3 \xrightarrow{400\,^\circ C} \gamma - BICUVOX + BiVO_4 + \beta - Bi_2O_3 + \alpha - Bi_2O_3 \quad (a)$$
$$\gamma - BICUVOX + BiVO_4 + \beta - Bi_2O_3 \xrightarrow{600\,^\circ C} \gamma - BICUVOX + BiVO_4 + \beta - Bi_2O_3 + \alpha - Bi_2O_3 \quad (b) \quad (4.12)$$
$$\gamma - BICUVOX + BiVO_4 + \beta - Bi_2O_3 \xrightarrow{800\,^\circ C} \gamma - BICUVOX \quad (c)$$

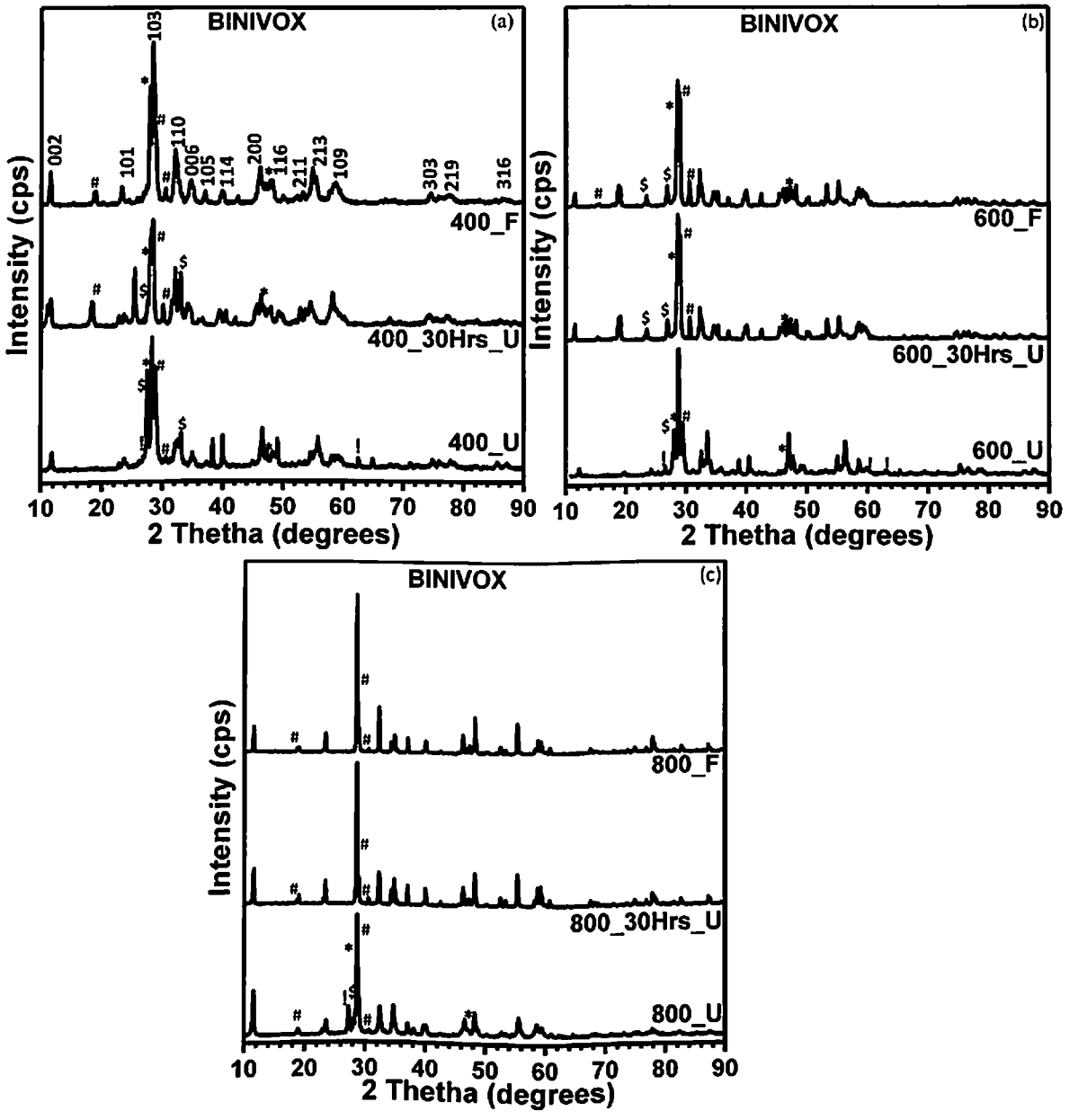

Figure 4-18: XRD spectra of the BINIVOX catalysts calcined at; (a) 400°C, (b) 600°C; and (c) 800°C, fresh (F), 30 hrs used and long time used (U). The symbols * and $ represent tetragonal (amcsd-0010069) and monoclinic (amcsd-0011925) Bi_2O_3, and # represents (amcsd-0014281) $BiVO_4$, and ! represents (amcsd-0012841) Bi metal-related phases, respectively

In contrary to BICOVOX-800_F and BINIVOX-800_F, BICUVOX-800_F appears to be essentially single-phase BICUVOX, as shown in Figure 4.15 (c).

In general, 400 & 600°C calcined BICUVOX_30HRS_U and BICUVOX_U catalysts have exhibited the same results as BICOVOX_30HRS_U and BICOVOX_U, respectively as presented in Figure 4.19 (a) and (b). Although, in case of BICUVOX-800_U, less breakage of phases has been observed, the existing phases being γ-BICUVOX and $BiVO_4$.as shown in Figure 4.19 (c) Similarly, change in phases from BICUVOX_F to BICUVOX_30HRS_U and BICUVOX_U can be illustrated through Equation 4.13, 4.14 and 4.15 for BICUVOX-400, BICUVOX-600 and BICUVOX-800.

BICUVOX-400

$$\gamma - BICUVOX + BiVO_4 + \beta - Bi_2O_3 + \alpha - Bi_2O_3 \xrightarrow{30\text{Hrs Used}} \gamma - BICUVOX + BiVO_4 + \beta - Bi_2O_3 + \alpha - Bi_2O_3 \text{ (a)} \quad (4.13)$$

$$\gamma - BICUVOX + BiVO_4 + \beta - Bi_2O_3 + \alpha - Bi_2O_3 \xrightarrow{\text{Long Time Used}} \gamma - BICUVOX + BiVO_4 + \beta - Bi_2O_3 + Bi \text{ (b)}$$

BICUVOX-600

$$\gamma - BICUVOX + BiVO_4 + \beta - Bi_2O_3 + \alpha - Bi_2O_3 \xrightarrow{30\text{Hrs Used}} \gamma - BICUVOX + BiVO_4 + \beta - Bi_2O_3 + \alpha - Bi_2O_3 \text{ (a)} \quad (4.14)$$

$$\gamma - BICUVOX + BiVO_4 + \beta - Bi_2O_3 + \alpha - Bi_2O_3 \xrightarrow{\text{Long Time Used}} \gamma - BICUVOX + BiVO_4 + \beta - Bi_2O_3 + Bi \text{ (b)}$$

BICUVOX-800

$$\gamma - BICUVOX \xrightarrow{30\text{Hrs Used}} \gamma - BICUVOX + BiVO_4 \xrightarrow{\text{Long Time Used}} \gamma - BICUVOX + BiVO_4 \quad (4.15)$$

Partial chemical substitution of vanadium by metal cations can, as per their nature and calcination temperatures, amount etc., lead to form α, β and/or γ-type phases, stable at room temperature (Huvé, Vannier et al. 1996). X-ray diffraction data shows the presence of main three polymorphs; face centred orthorhombic α-Bi_2O_3, tetragonal β-Bi_2O_3, and tetragonal pure γ-phase with tetragonal $BiVO_4$. Lattice parameter for α-Bi_2O_3 cell should be a = 5.533 Å, b = 5.611 Å, c = 15.288 Å. However, incompatibility of some weak interactions with F-cell, the cell volume must be tripled and thus the actual parameters are a = 16.599 Å, b = 5.611 Å, c = 15.288 Å (Abraham, Debreuille-Gresse et al. 1988). Similarly, for other phases, consider lattice parameters, volume, space group and crystal systems for rietveld refinement are mentioned in Table 4.4.

Figures 4.20-4.22 depict the rietveld refinement results of BICOVOX, BINIVOX and BICUVOX samples at different conditions. The sky blue lines correspond to the experimentally observed spectra, black lines are the calculated spectra, and the grey patterns display the difference between observed and calculated spectra. The colored bars at the bottom show the data base of the corresponding phases [BIVOX in blue, $BIVO_4$ in dark gray, Bi in light green, β-Bi_2O_3 in red and α-Bi_2O_3 in wine color] present in the sample.

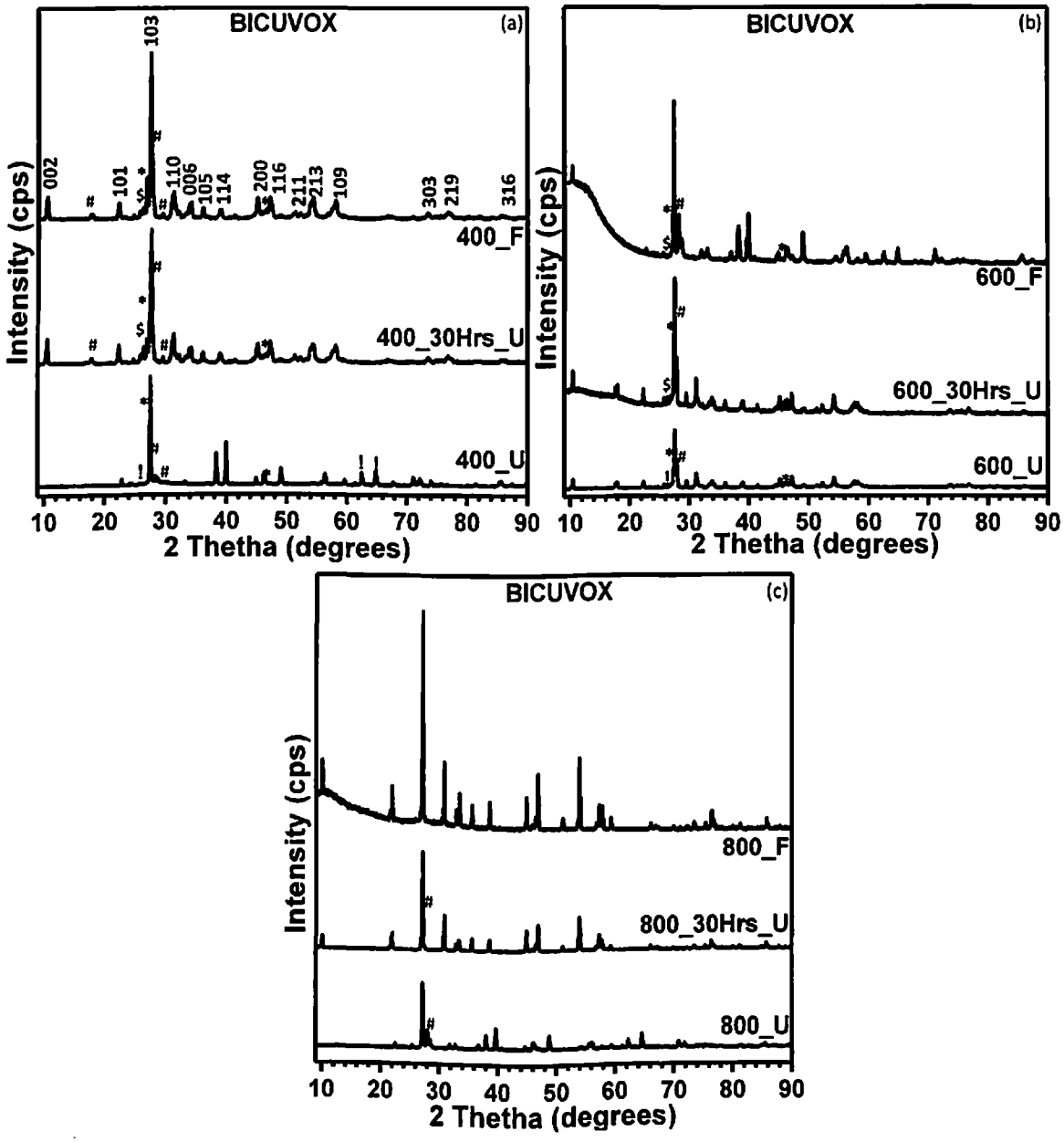

Figure 4-19: XRD spectra of the BICUVOX catalysts calcined at; (a) 400°C, (b) 600°C; and (c) 800°C, fresh (F), 30 hrs used and long time used (U). The symbols * and $ represent tetragonal (amcsd-0010069) and monoclinic (amcsd-0011925) Bi_2O_3, and # represents (amcsd-0014281) $BiVO_4$, and ! represents (amcsd-0012841) Bi metal-related phases, respectively

Calculated R factors found in literature for single phase BIMEVOX powders lie in the range of $R_f \sim 0.2$, $R_{wp} \sim 0.2$, $R_{exp} \sim 0.1$ with $\chi^2 \sim 1.5$ (Joubert, Jouanneaux et al. 1994, Joubert, Ganne et al. 1996, Abrahams, Krok et al. 1996, Abrahams, Nelstrop et al. 1998). In comparison to that, fitting errors in our analysis is somewhat higher, which could be due to the presence of multiple phases and enhanced complexity of the systems. However, in view of Rietveld refinements of other multiphase powders, our fittings could consider to be in good agreement with the experimental profiles for BICOVOX_F ($R_B \leq 0.4$, $R_f \leq 0.4$, $R_{wp} \leq 0.8$, $R_{exp} \leq 0.44$, and $1.7 \leq \chi^2 \leq 1.9$), BICOVOX_30HRS_U ($R_B \leq 0.9$, $R_f \leq 0.5$, $R_{wp} \leq 3.6$, $R_{exp} \leq 3.0$, and $1.2 \leq \chi^2 \leq 3.4$) and BICOVOX_U ($R_B \leq 0.4$, $R_f \leq 0.5$, $R_{wp} \leq 0.4$, $R_{exp} \leq 0.3$, and $1.0 \leq \chi^2 \leq 1.6$) catalysts as revealed in Figure 4.20 (a), (b), and (c), respectively (Park, Lee et al. 2001; Politaev, Nalbandyan et al. 2010; Ashima, Sanghi et al. 2012).

The $\chi 2$ values obtained in our analysis suggest good refinement of the data. Correspondingly, the acquire Rietveld refinements for BINIVOX and BICUVOX are in good agreement with the experimental profiles for BINIVOX_F ($R_B \leq 0.683$, $R_f \leq 0.772$, $R_{wp} \leq 0.278$, $R_{exp} \leq 0.125$, and $1.85 \leq \chi 2 \leq 1.89$), BINIVOX_30HRS_U catalysts ($R_B \leq 0.0.171$, $R_f \leq 0.113$, $R_{wp} \leq 0.32$, $R_{exp} \leq 0.136$, and $1.21 \leq \chi 2 \leq 1.88$), BINIVOX_U ($R_B \leq 0.079$, $R_f \leq 0.053$, $R_{wp} \leq 0.142$, $R_{exp} \leq 0.124$, and $1.11 \leq \chi 2 \leq 1.29$), BICUVOX_F ($R_B \leq 0.239$, $R_f \leq 0.265$, $R_{wp} \leq 0.733$, $R_{exp} \leq 0.434$, and $1.24 \leq \chi 2 \leq 1.91$), BICUVOX_30HRS_U catalysts ($R_B \leq 0.159$, $R_f \leq 0.144$, $R_{wp} \leq 0.238$, $R_{exp} \leq 0.420$, and $1.06 \leq \chi 2 \leq 1.92$) and BICUVOX_U catalyst ($R_B \leq 0.189$, $R_f \leq 0.203$, $R_{wp} \leq 0.723$, $R_{exp} \leq 0.331$, and $1.13 \leq \chi 2 \leq 1.91$) as depicted in Figure 14.21 (a-c) and 14.22 (a-c).

Table 4.5 summarizes the parameters refined and reliability factors obtain by Rietveld refinement for the BICOVOX-Wash, BICOVOX-_F, BICOVOX_30HRS_U and BICOVOX_U catalysts. Similarly, refine parameters and reliability factors obtain by Rietveld refinement for BINIVOX_F and BICUVOX_F, 30HRS_U and U catalysts are mentioned in Table 4.7 and Table 4.9 respectively.

The effect of powder preparation conditions (SCS environment and calcination temperature) and reactor environment (Ph, temperature, time, flow of vapor and gas mixture, etc.) on the composition and number of phases, corresponding weight %, particle size, strain in lattice, lattice parameters, and volume of unit cell of BIMEVOX catalysts are clearly revealed in Tables 4.6 (BICOVOX), 4.8 (BINIVOX) and 4.9 (BICUVOX), as obtained from the Rietveld refinement considering ±5% error (analytical and experimental).

Heat treatment eventually leads to single-phase BIMEVOX by eliminating other

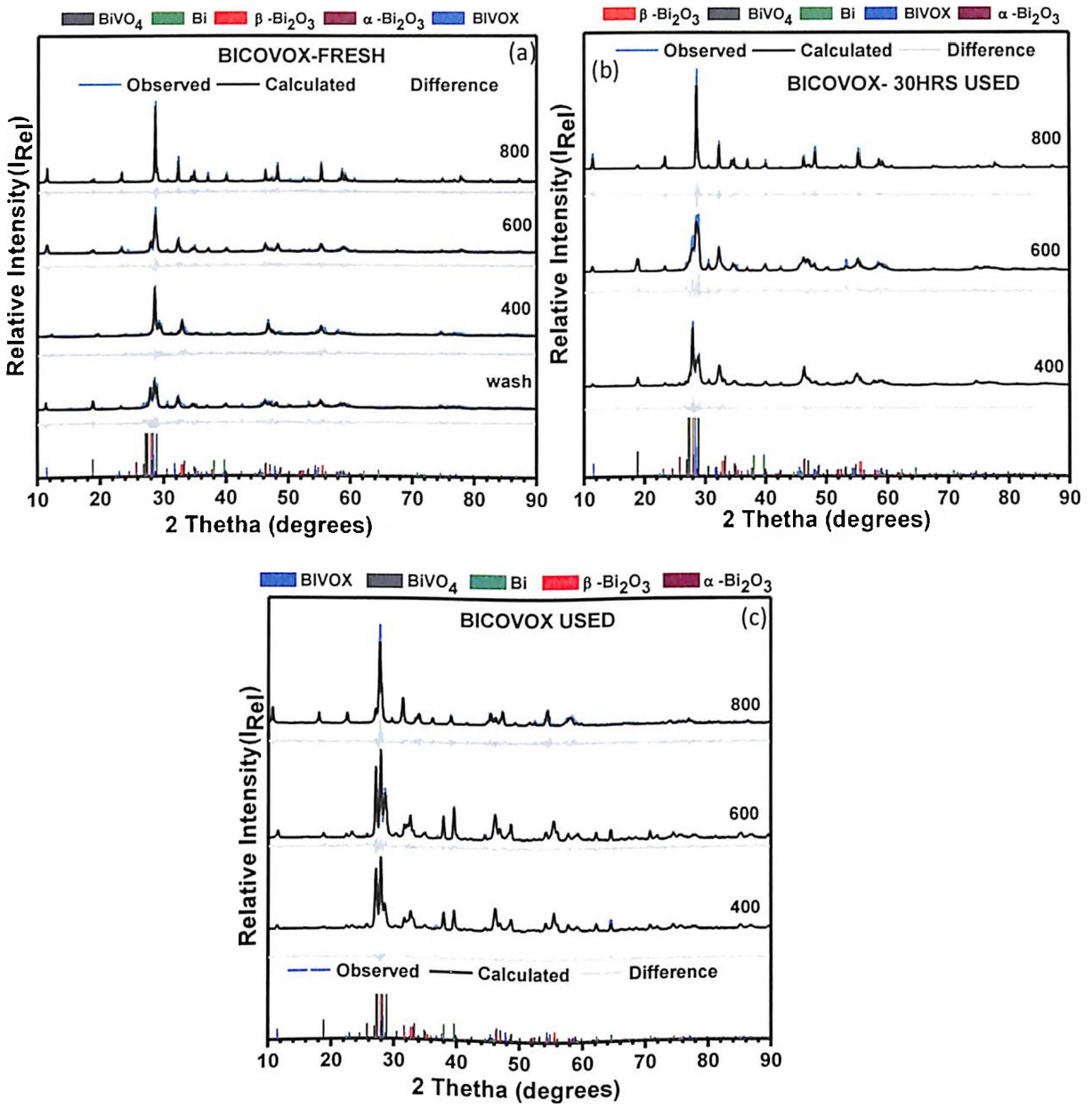

Figure 4-20: Rietveld refinement results of (a) BICOVOX_F (b) BICOVOX_30 HRS_U (c) BICOVOX_U samples at different conditions. The grey dotted lines are the calculated pattern, and the black lines are of the observed pattern. The grey curves display the difference between observed and calculated patterns. Clearly it's a mixture BIVOX(amcsd-0016748), β-Bi_2O_3(amcsd-0010069), $BiVO_4$(amcsd-0014281), Bi(amcsd-0012841) and α- Bi_2O_3(amcsd-0011925).The bars shows the corresponding Phase entries of all phases respectively

secondary phases present in BICOVOX-600, and BICOVOX-400 samples, with X-ray peaks progressively increasing in sharpness. Therefore, wt% of desirable γ-BIMEVOX phase is increasing with calcination temperature and maximum 92.8% is created for BICOVOX-800_F catalyst. For all BICOVOX_30HRS_U catalysts decrease in amount of γ-BICOVOX phase is observed. BICOVOX-400_30HRS_U catalyst shows formation of an extra α-Bi_2O_3 phase, but no phase change is occurred in BICOVOX-600_30HRS_U and BICOVOX-800_30HRS_U catalysts. After using for 150 hrs, BICOVOX-400_U and BICOVOX-600_U catalysts show 23.4 and 37.1 wt % reduction in γ-BICOVOX with an emergence of Bi metal. BICOVOX-800_U catalyst also shows reduction in wt % of γ-BICOVOX from 92.8 to 48.1 wt % with the formation of β-Bi_2O_3, however, no Bi metal could detect. No graphitic carbon peak (2θ= 26.9°) could be detected in the XRD of BICOVOX_U catalysts, which may be due to the fact that all major Bi-V-O related peaks appear in the same 2θ region.

Small increase in average particle size of γ-phase is realized with the calcination temperature and calculated to be 44.4, 46.8 and 50.5 nm for BICOVOX-400_F, BICOVOX-600_F and BICOVOX-800_F, respectively (Watson, Coats et al. 1997, Hvolbæk, Janssens et al. 2007; Han, Miranda et al. 2008; Jia, Caldwell et al. 2014; Rajh, Dimitrijevic et al. 2014, Shahid and Murugavel 2013). For all BICOVOX_30HRS_U and BICOVOX_U catalysts particle size of γ-phase is found to reduce with the usage. As the combined effect of smallest particle size (20.4 nm) and high defect density the wash catalyst shows higher lattice strain (7.2×10^{-3}) compared to BICOVOX-400_F (3.6×10^{-3}), BICOVOX-600_F (3.1×10^{-3}) and BICOVOX-800_F (2.8×10^{-3}) catalysts (Krok, Abrahams et al. 1998). In case of BICOVOX_30HRS_U and BICOVOX_U catalysts lattice strain increases probably because of emergence of more amount of secondary phases in comparison to the fresh as mentioned in Table 4.6.

The lattice parameter 'a' in BICOVOX-400_F, BICOVOX-600_F and BICOVOX-800_F is determined to be little shorter than that of the theoretical value (a= 3.99 Å for γ-BIVOX), however the 'c' values are slightly longer, compared to the theoretical value (c= 15.43 Å for γ-BIVOX). However, no particular trend is perceived after use. Capoen et al, (2004) execute the rietveld refinement on XRD data of BICOVOX catalyst. The acquire lattice parameters are a= 3.92 and c= 15.457 for BICOVOX catalyst calcined at 700°C (Capoen, Steil et al. 2004). Yu et al, (2011) synthesize the BIMNVOX catalyst by high temperature melting method and perform the refinement on BIMNVOX catalyst. Obtained values for lattice

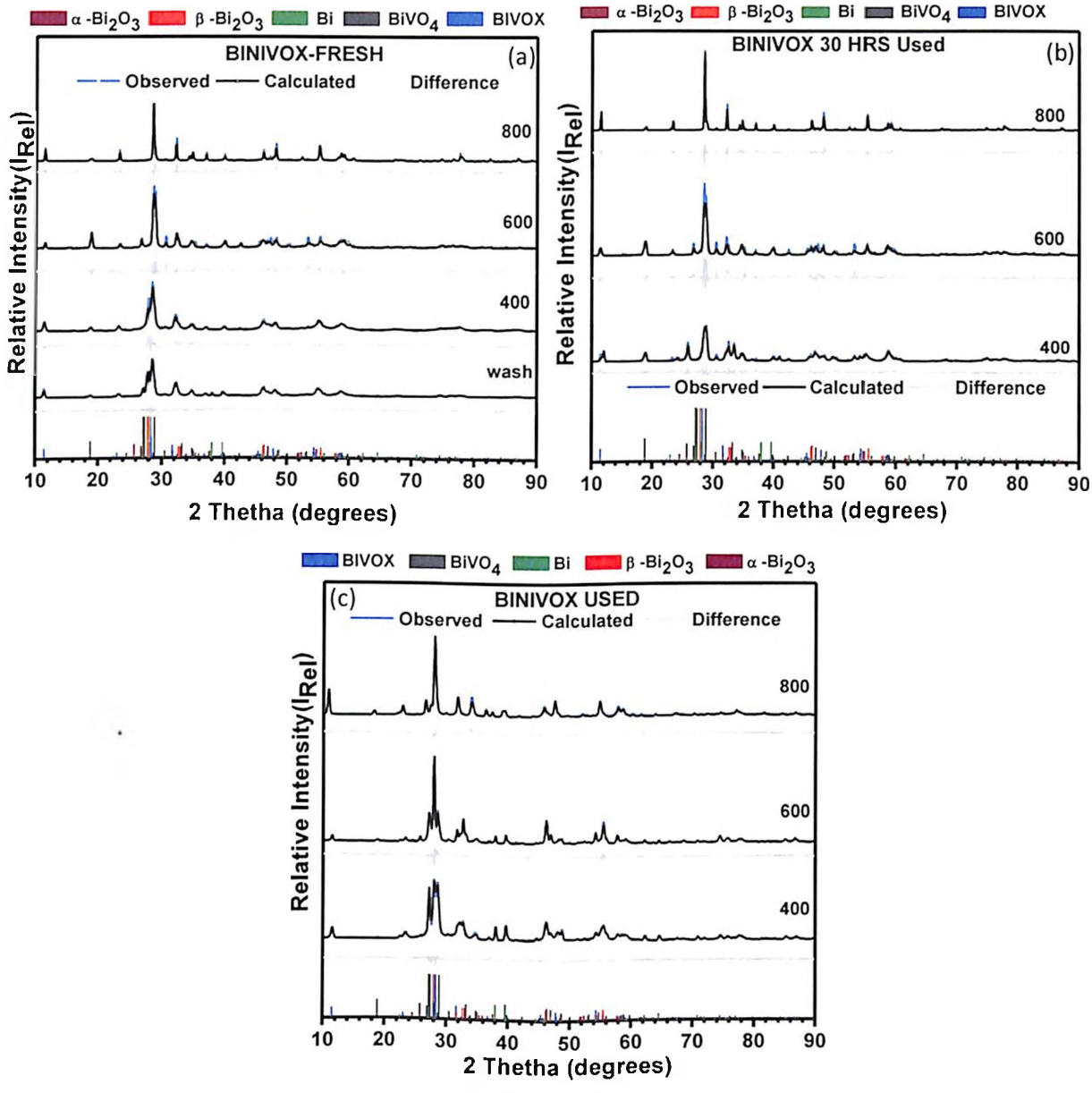

Figure 4-21: Rietveld refinement results of (a) BINIVOX_F (b) BINIVOX_30HRS_U (c) BINIVOX_U samples at different conditions. The grey dotted lines are the calculated pattern, and the black lines are of the observed pattern. The grey curves display the difference between observed and calculated patterns. Clearly it's a mixture BIVOX(COD-1533808), β-Bi_2O_3(amcsd-0010069), $BiVO_4$(amcsd-0014281), Bi(amcsd-0012841) and α- Bi_2O_3(amcsd-0011925).The bars shows the corresponding Phase entries of all phases respectively

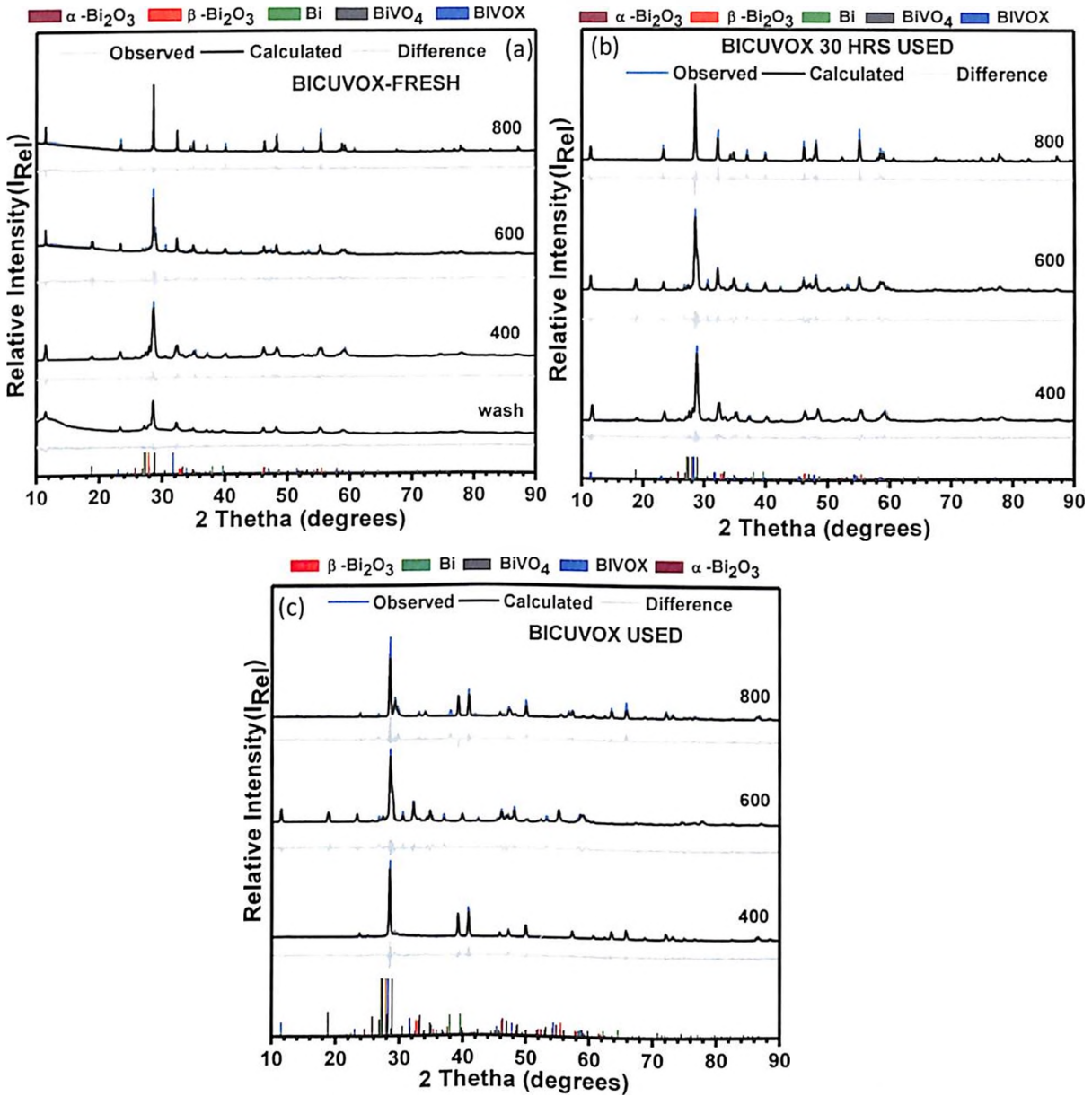

Figure 4-22: Rietveld refinement results of (a) BICUVOX_F (b) BICUVOX_30HRS_U (c) BICUVOX_U samples at different conditions. The grey dotted lines are the calculated pattern, and the black lines are of the observed pattern. The grey curves display the difference between observed and calculated patterns. Clearly it's a mixture BIVOX(COD-1533808), β-Bi_2O_3(amcsd-0010069), $BiVO_4$(amcsd-0014281), Bi(amcsd-0012841) and α- Bi_2O_3(amcsd-0011925).The bars shows the corresponding Phase entries of all phases respectively

Table 4-4: Crystallographic data used in the refinement

Formula	γ-$Bi_4V_2O_{11}$	$BiVO_4$	β-Bi_2O_3	α-Bi_2O_3	**Bi**
Unit cell	a(Å)=3.99; c(Å)=15.43	a(Å)=5.1470; c(Å)=11.7216	a(Å)=7.739; c(Å)=5.636	a≅16.59Å; b≅5.61Å, c ≅15.27 Å	a(Å)= 4.546; c(Å)=11.8620
ID	COD1533808	Amcsd0014281	Amcsd0010069	Amcsd0011925	Amcsd0012841
Crystal system	Tetragonal	Tetragonal	Tetragonal	Monoclinic	Trigonal
V($Å^3$)	245.873	310.524	337.552	1421.800	212.299
Space group	I 4/mmm	I4_1/a	P -4 21 c	A 1 1 2	R -3 m

COD-Crystallography Open Database

Amcsd- American Mineralogist Crystal Structure Database

Table 4-5: Parameters refined and reliability factors obtained by the Rietveld refinement for BICOVOX Fresh, 30hrs used and longtime Used Catalysts

		BEFORE USAGE				AFTER 30HRS USAGE				AFTER LONG TIME USAGE			
Phase	Parameter	BIVOX	$BiVO_4$	β-Bi_2O_3	α-Bi_2O_3	BIVOX	$BiVO_4$	β-Bi_2O_3	α-Bi_2O_3	BIVOX	$BiVO_4$	β-Bi_2O_3	Bi
Wash	Param. Refined	22	22	22	0	NA	NA	NA	NA	NA	NA	NA	NA
	R_B .	0.116	0.125	0.200	0	NA	NA	NA	NA	NA	NA	NA	NA
	R_f	0.096	0.140	0.138	0	NA	NA	NA	NA	NA	NA	NA	NA
	R_p	1.58	1.58	1.58	0	NA	NA	NA	NA	NA	NA	NA	NA
	R_{wp}	2.34	2.34	2.34	0	NA	NA	NA	NA	NA	NA	NA	NA
	R_{exp}	0.705	0.705	0.705	0	NA	NA	NA	NA	NA	NA	NA	NA
	$\chi 2$	1.93	1.93	1.93	0	NA	NA	NA	NA	NA	NA	NA	NA
400°C	Param. Refined	30	30	30	0	30	30	30	30	89	89	89	89
	R_B	0.362	0.251	0.151	0	0.882	0.663	0.257	0.127	0.781	0.589	0.358	0.368
	R_f	0.407	0.321	0.271	0	0.524	0.578	0.102	0.062	0.531	0.406	0.370	0.295
	R_p	0.564	0.564	0.564	0	2.59	2.59	2.59	2.59	0.091	0.091	0.091	0.091
	R_{wp}	0.818	0.818	0.818	0	3.56	3.56	3.56	3.56	0.126	0.126	0.126	0.126
	R_{exp}	0.404	0.404	0.404	0	3.02	3.02	3.02	3.02	0.040	0.040	0.040	0.040
	$\chi 2$	1.9741	1.9741	1.9741	0	3.35	3.35	3.35	3.35	1.04	1.04	1.04	1.04
600°C	Param. Refined	25	25	25	25	24	24	24	24	70	70	70	70
	R_B	0.208	0.273	0.173	0.601	0.413	0.545	1.06	0.524	0.339	0.338	0.220	0.258
	R_f	0.204	0.238	0.244	0.399	0.334	0.441	0.77	0.318	0.264	0.240	0.233	0.198
	R_p	0.326	0.326	0.326	0.326	1.43	1.43	1.43	1.43	0.105	0.105	0.105	0.105
	R_{wp}	0.505	0.505	0.505	0.505	1.82	1.82	1.82	1.82	0.137	0.137	0.137	0.137
	R_{exp}	0.289	0.289	0.289	0.289	1.79	1.79	1.79	1.79	0.102	0.102	0.102	0.102
	$\chi 2$	1.68	1.68	1.68	1.68	1.46	1.46	1.46	1.46	1.13	1.13	1.13	1.13
800°C	Param. Refined	21	21	0	0	19	19	0	0	54	54	54	0
	R_B	0.245	0.451	0	0	0.136	0.452	0	0	0.256	0.365	0.320	0
	R_f	0.263	0.621	0	0	0.143	0.567	0	0	0.203	0.287	0.277	0
	R_p	0.199	0.199	0	0	1.93	1.93	0	0	0.298	0.298	0.298	0
	R_{wp}	0.298	0.298	0	0	2.44	2.44	0	0	0.422	0.422	0.422	0
	R_{exp}	0.125	0.125	0	0	2.04	2.04	0	0	0.272	0.272	0.272	0
	$\chi 2$	1.96	1.96	0	0	1.22	1.22	0	0	1.55	1.55	1.55	0

Table 4-6: Lattice parameters, Unit cell volume(V), Crystallite size, strain and weight% of the different phases present in BICOVOX fresh, 30 hrs used and long time used catalysts

		BEFORE USAGE				AFTER 30HRS USAGE				AFTER LONG TIME USAGE			
Phase	Parameter	BIVOX	$BiVO_4$	β-Bi_2O_3	α-Bi_2O_3	BIVOX	$BiVO_4$	β-Bi_2O_3	α-Bi_2O_3	BIVOX	$BiVO_4$	β-Bi_2O_3	Bi
Wash	Lattice Para (Å)	a=3.92 c=15.40	a=5.18 c=11.69	a=7.83 c=5.55	0	NA	NA	NA	NA	NA	NA	NA	NA
	V(Å^3)	237.2	313.3	340.1	0	NA	NA	NA	NA	NA	NA	NA	NA
	Wt%	68.4	16.9	14.7	0	NA	NA	NA	NA	NA	NA	NA	NA
	size(nm)	20.4	7.8	12.4	0	NA	NA	NA	NA	NA	NA	NA	NA
	strain(β) $*10^{-3}$	7.2	10.0	1.1	0	NA	NA	NA	NA	NA	NA	NA	NA
400°C	Lattice Para (Å)	a=3.96 c=15.80	a=5.18 c=11.74	a=7.84 c=5.57	0	a=3.93 c=15.44	a=5.14 c=11.71	a=7.74 c=5.63	a=5.83 b=8.14 c=7.48	a=3.97 c=15.46	a=5.15 c=11.73	a=7.74 c=5.64	a=4.54 c=11.84
	V(Å^3)	238.7	309.9	338.9	0	244.9	308.9	339.1	330.2	245.7	310.9	338.1	211.7
	Wt%	71.5	15.5	13	0	43.3	29.9	15.6	10.2	23.4	11.3	36.8	28.5
	size(nm)	44.4	12.9	11.9	0	40.6	22.6	16.3	28.5	32.9	18.2	29.7	27.4
	strain(β) $*10^{-3}$	3.6	7.1	7.2	0	4.5	6.4	9.2	5.2	4.9	2.4	4.9	5.6
600°C	Lattice Para (Å)	a=3.93 c=15.51	a=5.14 c=11.69	a=7.76 c=5.65	a=5.90 b=8.13 c=7.30	a=3.91 c=15.43	a=5.12 c=11.72	a=7.74 c=5.63	a=5.83 b=8.14 c=7.48	a=3.95 c=15.57	a=5.13 c=11.73	a=7.75 c=5.64	a=4.55 c=11.88
	V(Å^3)	239.7	309.2	339.8	362.2	240.2	310.4	339.1	330.2	243.3	308.9	339.1	212.7
	Wt%	87.0	6.9	4.9	1.2	68.9	19.8	8.7	2.6	37.1	14.5	31.1	17.3
	size(nm)	46.8	13.8	10.09	9.2	43.3	27.9	14.2	21.9	38.1	42.9	28.4	31.1
	strain(β) $*10^{-3}$	3.1	3.4	7.4	7.7	3.7	5.4	10.2	7.0	3.8	3.4	5.3	3.4
800°C	Lattice Para (Å)	a=3.92 c=15.45	a=5.15 c=11.70	0	0	a=3.92 c=15.45	a=5.15 c=11.33	0	0	a=3.93 c=15.49	a=5.15 c=11.72	a=7.83 c=5.51	0
	V(Å^3)	238.6	311.1	0	0	239.0	310.9	0	0	247.3	310.4	339.1	0
	Wt%	92.8	7.2	0	0	79.4	20.6	0	0	48.1	28.6	23.3	0
	size(nm)	50.5	14.3	0	0	45.0	18.7	0	0	40.8	13.9	16.4	0
	strain(β) $*10^{-3}$	2.8	2.7	0	0	3.3	11.8	0	0	3.9	3.1	2.0	0

Table 4-7: Parameters refined and reliability factors obtained by the Rietveld refinement for BINIVOX fresh, 30 hrs used and long time used catalysts

	BEFORE USAGE						AFTER 30HRS USAGE					AFTER LONG TIME USAGE				
Phase	Parameter	BIVOX	$BiVO_4$	β-Bi_2O_3	α-Bi_2O_3	Bi	BIVOX	$BiVO_4$	β-Bi_2O_3	α-Bi_2O_3	BIVOX	$BiVO_4$	β-Bi_2O_3	α-Bi_2O_3	Bi
Wash	Param. Refined	44	44	44	0	44	NA	NA	NA	NA	NA	NA	NA	NA	NA
	R_B	0.683	0.780	0.561	0	0.674	NA	NA	NA	NA	NA	NA	NA	NA	NA
	R_f	0.772	0.782	0.673	0	0.423	NA	NA	NA	NA	NA	NA	NA	NA	NA
	R_p	0.102	0.102	0.102	0	0.102	NA	NA	NA	NA	NA	NA	NA	NA	NA
	R_{wp}	0.138	0.138	0.138	0	0.138	NA	NA	NA	NA	NA	NA	NA	NA	NA
	R_{exp}	0.100	0.100	0.100	0	0.100	NA	NA	NA	NA	NA	NA	NA	NA	NA
	χ^2	1.89	1.89	1.89	0	1.89	NA	NA	NA	NA	NA	NA	NA	NA	NA
400°C	Param. Refined	46	46	46	0	0	15	15	15	15	82	82	82	82	82
	R_B	0.118	0.123	0.267	0	0	0.124	0.134	0.217	0.641	0.075	0.048	0.043	0.071	0.070
	R_f	0.065	0.064	0.315	0	0	0.093	0.079	0.093	0.283	0.050	0.039	0.047	0.056	0.058
	R_p	0.222	0.222	0.222	0	0	0.242	0.242	0.242	0.242	0.089	0.089	0.089	0.089	0.089
	R_{wp}	0.278	0.278	0.278	0	0	0.32	0.32	0.32	0.32	0.119	0.119	0.119	0.119	0.119
	R_{exp}	0.098	0.098	0.098	0	0	0.12	0.12	0.12	0.12	0.118	0.118	0.118	0.118	0.118
	χ^2	1.87	1.87	1.87	0	0	1.85	1.85	1.85	1.85	1.13	1.13	1.13	1.13	1.13
600°C	Param. Refined	21	21	21	21	0	23	23	23	23	39	0	39	0	39
	R_B	0.124	0.159	0.080	0.142	0	0.171	0.177	0.166	0.416	0.079	00.048	0.035	0	0.082
	R_f	0.098	0.144	0.097	0.097	0	0.113	0.120	0.100	0.392	0.042	00.039	0.046	0	0.058
	R_p	0.174	0.174	0.174	0.174	0	0.240	0.240	0.240	0.240	0.0782	0.0782	0.0782	0	0.078
	R_{wp}	0.217	0.217	0.217	0.217	0	0.306	0.306	0.306	0.306	0.102	0.102	0.102	0	0.102
	R_{exp}	0.094	0.094	0.094	0.094	0	0.136	0.136	0.136	0.136	0.096	0.096	0.096	0	0.096
	χ^2	1.85	1.85	1.85	1.85	0	1.88	1.88	1.88	1.88	1.11	1.11	1.11	0	1.11
800°C	Param. Refined	29	29	0	0	0	31	31	0	0	89	89	89	89	89
	R_B	0.219	0.380	0	0	0	0.021	0.094	0	0	0.070	0.011	0.010	0.015	0.086
	R_f	0.192	0.455	0	0	0	0.017	0.092	0	0	0.045	0.057	0.077	0.011	0.070
	R_p	0.197	0.197	0	0	0	0.195	0.195	0	0	0.108	0.108	0.108	0.108	0.108
	R_{wp}	0.256	0.256	0	0	0	0.254	0.254	0	0	0.142	0.142	0.142	0.142	0.142
	R_{exp}	0.125	0.125	0	0	0	0.109	0.109	0	0	0.124	0.124	0.124	0.124	0.124
	χ^2	1.85	1.85	0	0	0	1.21	1.21	0	0	1.29	1.29	1.29	1.29	1.29

Table 4-8: Lattice parameters, Unit cell volume(V), Crystallite size, strain and weight% of the different phases present in BINIVOX fresh, 30 hrs used and long time used catalysts

		BEFORE USAGE					AFTER 30HRS USAGE				AFTER LONG TIME USAGE				
Phase	Parameter	BIVOX	$BiVO_4$	β-Bi_2O_3	α-Bi_2O_3	Bi	BIVOX	$BiVO_4$	β-Bi_2O_3	α-Bi_2O_3	BIVOX	$BiVO_4$	β-Bi_2O_3	α-Bi_2O_3	Bi
Wash	Lattice Para (Å)	a=3.92 c=15.40	a=5.15 c=11.69	a=7.80 c=5.57	0	a=4.55 c=11.84	NA	NA	NA	NA	NA	NA	NA	NA	NA
	V(Å^3)	237.5	310.1	339.3	0	212.2	NA	NA	NA	NA	NA	NA	NA	NA	NA
	Wt%	70.4	14	13.6	0	2	NA	NA	NA	NA	NA	NA	NA	NA	NA
	size(nm)	25.2	12.6	12.3	0	10.3	NA	NA	NA	NA	NA	NA	NA	NA	NA
	strain(β) *10^{-3}	5.8	6.8	4.3	0	7.4	NA	NA	NA	NA	NA	NA	NA	NA	NA
400°C	Lattice Para (Å)	a=3.93 c=15.45	a=5.14 c=11.69	a=7.80 c=5.56	0	0	a=3.94 c=15.52	a=5.17 c=11.73	a=7.93 c=5.52	a=5.84 b=8.15 c=7.50	a=3.933 c=15.48	a=5.19 c=11.71	a=7.76 c=5.65	a=5.86 b=8.18 c=7.53	a=4.56 c=11.88
	V(Å^3)	237.5	309.6	339.3	0	0	237.8	313.7	335.6	329.4	239.6	315.4	339.9	332.2	213.6
	Wt%	72.8	14.6	12.6	0	0	44.2	30.4	15.1	10.3	20.8	21.1	32.6	17.1	8.3
	size(nm)	28.3	27.1	12.3	0	0	25.3	17.5	12.2	20.1	14.1	16.4	20.4	16.6	26.5
	strain(β) *10^{-3}	5.2	3.4	4.3	0	0	5.8	13.6	12.3	6.3	10.3	8.3	4.7	7.7	2.8
600°C	Lattice Para (Å)	a=3.92c =15.53	a=5.14 c=11.71	a=7.77 c=5.61	a=5.96 b=8.1 c=7.30	0	a=3.92 c=15.47	a=5.16 c=11.69	a=7.78 c=5.61	a=5.83 b=8.14 c=7.48	a=3.926 c=15.48	a=5.19 c=11.71	a=7.74 c=5.63	0	a=4.54 c=11.84
	V(Å^3)	238.3	309.9	338.9	326.1	0	238.2	311.4	340.7	329.2	238.6	315.4	337.4	0	211.5
	Wt%	87.9	5.4	5.1	1.6	0	67.2	20.8	6.5	4.5	35.2	31.1	20.7	0	13
	size(nm)	29.8	12.9	11.9	21.4	0	27.5	28.9	8.8	29.1	26.2	16.4	27.7	0	19.1
	strain(β) *10^{-3}	4.9	7.1	1.1	3.7	0	5.4	5.1	17.0	5.4	5.6	8.3	2.1	0	1.1
800°C	Lattice Para (Å)	a=3.92 c=15.45	a=5.19 c=11.62	0	0	0	a=3.92 c=15.45	a=5.13 c=11.71	0	0	a=3.90 c=15.52	a=5.14 c=11.71	a=7.75 c=5.62	a=5.78 b=8.0 c=6.06	a=4.55 c=11.85
	V(Å^3)	239.7	312.6	0	0	0	239.8	309.3	0	0	237.9	310.5	338.4	264.4	212.3
	Wt%	92.9	7.1	0	0	0	78.8	21.2	0	0	47.5	28.7	9.1	1.4	6.3
	size(nm)	31.4	12.3	0	0	0	31.2	28.1	0	0	28.6	24.4	31.7	26.5	25.9
	strain(β) *10^{-3}	4.7	8.7	0	0	0	4.8	7.8	0	0	5.1	6.0	4.7	5.8	5.4

Table 4-9: Parameters refined and reliability factors obtained by the Rietveld refinement for BICUVOX fresh, 30 hrs used and long time used catalysts

	BEFORE USAGE					AFTER 30HRS USAGE				AFTER LONG TIME USAGE			
Phase	Parameter	BIVOX	$BiVO_4$	β-Bi_2O_3	α-Bi_2O_3	BIVOX	$BiVO_4$	β-Bi_2O_3	α-Bi_2O_3	BIVOX	$BiVO_4$	β-Bi_2O_3	Bi
Wash	Param. Refined	22	22	22	0	NA	NA	NA	NA	NA	NA	NA	NA
	R_B	0.239	0.170	0.208	0	NA	NA	NA	NA	NA	NA	NA	NA
	R_f	0.116	0.128	0.192	0	NA	NA	NA	NA	NA	NA	NA	NA
	R_p	0.554	0.554	0.554	0	NA	NA	NA	NA	NA	NA	NA	NA
	R_{wp}	0.733	0.733	0.733	0	NA	NA	NA	NA	NA	NA	NA	NA
	R_{exp}	0.417	0.417	0.417	0	NA	NA	NA	NA	NA	NA	NA	NA
	$\chi 2$	1.91	1.91	1.91	0	NA	NA	NA	NA	NA	NA	NA	NA
400°C	Param. Refined	15	15	15	30	30	30	30	0	26	26	26	26
	R_B	0.106	0.787	0.180	0.731	0.097	0.075	0.057	0.105	0.073	0.143	0.015	0.113
	R_f	0.068	0.557	0.083	0.573	0.054	0.040	0.037	0.071	0.062	0.085	0.012	0.094
	R_p	0.164	0.164	0.164	0.164	0.129	0.129	0.129	0.129	0.150	0.150	0.150	0.150
	R_{wp}	0.216	0.216	0.216	0.216	0.170	0.170	0.170	0.170	0.191	0.191	0.191	0.191
	R_{exp}	0.103	0.103	0.103	0.103	0.101	0.101	0.101	0.101	0.125	0.125	0.125	0.125
	$\chi 2$	1.71	1.71	1.71	1.71	1.88	1.88	1.88	1.88	1.13	1.13	1.13	1.13
600°C	Param. Refined	12	12	12	12	25	25	25	25	24	24	24	24
	R_B	0.228	0.181	0.084	0.178	0.152	0.341	0.152	0.649	0.170	0.591	0.543	0.248
	R_f	0.164	0.132	0.081	0.247	0.141	0.285	0.148	0.336	0.203	0.828	0.472	0.222
	R_p	0.142	0.142	0.142	0.142	0.730	0.730	0.730	0.730	0.484	0.484	0.484	0.484
	R_{wp}	0.183	0.183	0.183	0.183	0.101	0.101	0.101	0.101	0.723	0.723	0.723	0.723
	R_{exp}	0.101	0.101	0.101	0.101	0.420	0.420	0.420	0.420	0.331	0.331	0.331	0.331
	$\chi 2$	1.24	1.24	1.24	1.24	1.92	1.92	1.92	1.92	1.91	1.91	1.91	1.91
800°C	Param. Refined	21	0	0	0	16	16	0	0	21	21	21	0
	R_B	0.229	0	0	0	0.159	0.184	0	0	0.189	0.197	0.198	0
	R_f	0.265	0	0	0	0.137	0.123	0	0	0.128	0.338	0.477	0
	R_p	0.776	0	0	0	0.184	0.184	0	0	0.196	0.196	0.196	0
	R_{wp}	0.102	0	0	0	0.238	0.238	0	0	0.255	0.255	0.255	0
	R_{exp}	0.434	0	0	0	0.123	0.123	0	0	0.137	0.137	0.137	0
	$\chi 2$	1.91	0	0	0	1.06	1.06	0	0	1.86	1.86	1.86	0

Table 4-10: Lattice parameters, Unit cell volume(V), Crystallite size, strain and weight% of the different phases present in BICUVOX fresh, 30 hrs used and long time used catalysts

		BEFORE USAGE				AFTER 30HRS USAGE				AFTER LONG TIME USAGE			
Phase	Parameter	BIVOX	$BiVO_4$	β-Bi_2O_3	α-Bi_2O_3	BIVOX	$BiVO_4$	β-Bi_2O_3	α-Bi_2O_3	BIVOX	$BiVO_4$	β-Bi_2O_3	Bi
Wash	Lattice Para (Å)	a=3.93 c=15.41	a=5.18 c=11.69	a=7.74 c=5.64	0	NA	NA	NA	NA	NA	NA	NA	NA
	V(Å^3)	238.3	312.8	338.34	0	NA	NA	NA	NA	NA	NA	NA	NA
	Wt%	69.5	17.95	12.55	0	NA	NA	NA	NA	NA	NA	NA	NA
	size(nm)	31.0	30.8	22.9	0	NA	NA	NA	NA	NA	NA	NA	NA
	strain(β) $*10^{-3}$	4.7	4.9	7.8	0	NA	NA	NA	NA	NA	NA	NA	NA
400°C	Lattice Para (Å)	a=3.93 c=15.44	a=5.14 c=11.7	a=7.72 c=5.31	a=5.85 b=8.15 c=7.52	a=3.93 c=15.44	a=5.16 c=11.85	a=7.72 c=5.58	a=5.85 b=8.16 c=7.51	a=3.97 c=15.37	a=5.14 c=11.72	a=7.74 c=5.63	a=4.54 c=11.86
	V(Å^3)	238.3	309.2	321.1	330.8	238.5	309.4	333.4	330.5	242.9	311.6	336.8	212.1
	Wt%	72.7	16.5	9.6	1.2	45.6	29.4	14.5	10.5	22.6	34.7	18.4	24.3
	size(nm)	53.1	35.4	44.3	32.7	51.2	28.3	22.3	18.3	32.3	42.7	44.1	32.1
	strain(β) $*10^{-3}$	2.9	4.2	3.4	4.5	3.0	6.4	6.7	8.4	4.9	3.6	2.4	4.7
600°C	Lattice Para (Å)	a=3.93 c=15.36	a=5.16 c=11.69	a=7.79 c=5.52	a=5.84 b=8.16c=7.5	a=3.93 c=15.43	a=5.14 c=11.7	a=7.76 c=5.65	a=5.56 b=8.15 c=7.86	a=3.97 c=15.35	a=5.15 c=11.72	a=7.73 c=5.64	a=4.55 c=11.87
	V(Å^3)	237.2	310.9	335.6	329.8	239.7	309.2	337.4	362.2	241.8	311.8	336.8	211.3
	Wt%	88.9	5.8	3.7	1.6	66.2	19.1	8.7	6.0	36.9	11.5	31.6	20.0
	size(nm)	53.3	27.9	14.2	21.9	53.1	35.4	42.8	15.2	43.3	14.7	44.3	31.4
	strain(β) $*10^{-3}$	2.9	5.4	10.2	7.0	2.9	4.2	3.4	9.1	5.2	10.2	3.4	4.4
800°C	Lattice Para (Å)	a=3.92 c=15.44	0	0	0	a=3.92 c=15.44	a=5.14 c=11.31	0	0	a=3.96 c=15.46	a=5.15 c=11.72	a=7.72 7c=5.64	0
	V(Å^3)	237.8	0	0	0	237.6	309.2	0	0	237.57	312.1	336.8	0
	Wt%	100	0	0	0	79.9	20.1	0	0	48.2	28.6	23.2	0
	size(nm)	73.4	0	0	0	39.2	26.2	0	0	38.4	33.8	44.3	0
	strain(β) $*10^{-3}$	2.0	0	0	0	3.7	3.5	0	0	4.0	4.4	4.4	0

Table 4-11: Lattice parameters and volume of different BIMEVOX catalysts after rietveld refinement

Formula /Temperature	Lattice parameters (Å)	Volume ($Å^3$)	Reference
$Bi_2V_{0.9}Co_{0.1}O_{5.35}$ (850°C)	a= 3.926 c= 15.445	238.2	(Krok, Abrahams et al. 1996)
$Bi_2V_{0.9}Co_{0.1}O_{5.35}$ (800°C)	a= 3.913 c= 15.447		(Joshi, Nimat et al. 2009)
$Bi_4V_{1.8}Co_{0.2}O_{10.7}$ (810°C)	a= 3.926 c= 15.475 c/a=3.9416		(Essalim, Tanouti et al. 1992)
$Bi_2V_{0.9}Co_{0.1}O_{5.35}$ (850°C)	a= 3.9225 c= 15.447	237.67	(Abrahams, Krok et al. 1996)
$Bi_2V_{0.9}Co_{0.1}O_{5.35}$ (850°C)	a= 7.858 c= 15.447		(Krok, Bogusz et al. 1994)
$Bi_2V_{0.9}Co_{0.1}O_{5.35}$ (700°C)	a= 3.92 c= 15.457		(Capoen, Steil et al. 2004)
$Bi_2V_{0.9}Cu_{0.1}O_{5.35}$ (850°C)		237.18	(Krok, Abrahams et al. 1997)
$Bi_2V_{0.9}Cu_{0.1}O_{5.35}$ (850°C)	a= 3.9238 c= 15.40	237.10	(Abrahams, Nelstrop et al. 2000)
$Bi_2V_{0.9}Cu_{0.1}O_{5.35}$ (700°C)	a= 5.5534 c= 15.3537	478.98	(Beg, Hafeez et al. 2014)
$Bi_4V_{1.8}Ni_{0.2}O_{10.7}$ (700°C)	a= 5.559 c= 15.372	478.16	(Beg, Al–Areqi et al. 2015)
$Bi_2V_{0.9}Ni_{0.1}O_{5.35}$ (850°C)	a= 3.92646 c= 15.4494	238.18	(Abrahams, Nelstrop et al. 1998)
$Bi_2V_{0.9}Ni_{0.1}O_{5.35}$ (850°C)	a= 3.9225 c= 15.43	239.3	(Krok, Abrahams et al. 1998)
$Bi_4V_{1.8}Fe_{0.2}O_{10.7}$ (700°C)	a= 5.543 c= 15.41		(García-González, Arribas et al. 2001)
$Bi_4V_{1.8}Sb_{0.2}O_{11}$ (850°C)	a= 5.542 c= 15.51	477.9	(Joubert, Jouanneaux et al. 1993)
$Bi_4V_{1.8}Fe_{0.2}O_{11}$ (850°C)	a= 5.545 c= 15.44	476.5	(Joubert, Ganne et al. 1996)
$Bi_4V_{1.8}Cr_{0.2}O_{11}$ (850°C)	a= 5.54 c= 15.356	476.2	
$Bi_2V_{0.9}Mn_{0.1}O_{5.35}$ (800°C)	a= 3.914 c= 15.45		(Yu, Gu et al. 2011)

parameters are a = 3.914 and c = 15.45 (Yu, Gu et al. 2011). Our lattices parameters obtained by refinement are consistent with refinement results of different BIMEVOX report by other scientists.

The volume of unit cell (V) is observed to increases with annealing temperature for BICOVOX_F catalysts. Some of the dopant cation (Co^{2+}) may enter the lattice interstitials instead of the usual V sites and thus expanding unit cell moderately. No particular trend in unit cell volume change is observed for the catalysts after use, which could be due to the presence of multi-phases. Krok et al, (1996, 1997) execute the refinement on BICOVOX and BICUVOX catalysts calcined at 850°C. Obtained volumes from refinement are 238.2 and 237.18 $Å^3$ for BICOVOX and BICUVOX catalyst, respectively (Krok, Abrahams et al. 1996; Krok, Abrahams et al. 1997). Beg et al, (2014, 2015) also carry out the rietveld refinement on BICUVOX and BINIVOX catalysts. Reported volume for BICUVOX and BINIVOX is 478.98 and 478.16 respectively (Beg, Hafeez et al. 2014; Beg, Al–Areqi et al. 2015). Similarly, Abrahams et al, (2000) and Joubert et al, (1993, 1996) also perform the refinement on BICUVOX and BIMEVOX-(ME: Sb, Fe, Cr) respectively and the reported volume are found to be 237. 10 for BICUVOX, 477.9 for BISBVOX, 476.5 for BIFEVOX and 476.2 $Å^3$ for BICRVOX catalysts (Joubert, Jouanneaux et al. 1993; Joubert, Ganne et al. 1996; Abrahams, Nelstrop et al. 2000). Volume and lattice parameters for different BIMEVOX catalysts after executing rietveld refinement are listed in Table 4.11.

Correspondingly, for BINIVOX_F powders wt% of desirable γ-BINIVOX phase is also found to increase with calcination temperature and maximum 92.9% is created for BINIVOX-800_F catalyst. For BINIVOX-Wash, the wt% is 72.4 and that increases to 76.8% for BINIVOX-400_F and 83.9% for BINIVOX-600_F. Analogues to BICOVOX catalyst, decrease in amount of γ-BICOVOX phase for all BINIVOX_30HRS_U catalysts is seen. BINIVOX-400_30HRS_U catalyst shows formation of an extra α-Bi_2O_3 phase, but no phase change is occurred in BINIVOX-600_30HRS_U and BINIVOX-800_30HRS_U catalysts. After using for 150 hrs, BINIVOX-400_U, BINIVOX-600_U and BINIVOX-800_U catalysts show 30.8, 50.2 and 62.5 wt % reduction in γ-BICOVOX with an emergence of Bi metal.

Similar to BICOVOX_F catalysts, increase in particle size of γ-BIMEVOX phase is also seen for BINIVOX_F catalysts with the calcination temperature and it increases from 25.2 nm to 31.4 nm for BINIVOX-800 which shows that the higher temperature treatment leads to both higher nucleations making the nanoparticles bigger as reported in Table 4.8. For all

BINIVOX_30HRS_U and BINIVOX_U catalysts particle size of γ-phase is observed to reduce with the usage.

For BINIVOX catalysts the lattice strain is found to decrease with annealing temperature which is in parallel with the observations of cobalt doped compounds. For long-time used catalysts, the lattice strain is found to increase with unused catalysts. 5.8 x 10^{-3}, 5.4 x 10^{-3}, and 4.8 x 10^{-3} strain is obtained for BINIVOX-400_U, BINIVOX-600_U and BINIVOX-800_U catalysts, respectively, as the phases are increasing with the use so as strain.

The lattice parameter 'a' in BINIVOX-400_F, BINIVOX-600_F and BINIVOX-800_F is determined to be little shorter than that of the theoretical value (a = 3.99 Å for γ-BIVOX), however the 'c' values are slightly longer, compared to the theoretical value (c = 15.43 Å for γ-BIVOX), which is similar to that of BICOVOX_F catalyst. Looking at the effect of temperature on the lattice parameters, for BINIVOX-400_F, BINIVOX-600_F and BINIVOX-800_F, 'a' and 'c' values are observed to increase with respect to BINIVOX-wash catalyst. For BINIVOX-400_F, the increment is 0.3%, which is 0.8% and 0.3% in BINIVOX-600_F and BINIVOX-800_F, respectively. Contraction in lattice parameters shows the similar trend as we observed in BICOVOX_30HRS_U catalysts, as mentioned in Table 4.8 for BINIVOX-400_30HRS_U and BINIVOX-600_30HRS_U catalysts. Although, there is no noticeable change is observed in lattice parameters for BINIVOX-800_30HRS_U catalysts as reported in Table 4.8.

The volume of unit cell V ($Å^3$) is increasing with annealing temperature for BINIVOX catalysts. The same trend of increasing volume is seen in the both BINIVOX_30HRS_U and BINIVOX_U catalysts compared to the fresh ones. Obtained volume for BINIVOX-400_30HRS_U and BINIVOX-400_U is 237.79 $Å^3$ and 239.56 $Å^3$. Similarly, volumes for BINIVOX-600_30HRS_U & BINIVOX-600_U are 238.2 $Å^3$ & 238.58 $Å_3$ and for BINIVOX-800_30HRS_U & BINIVOX-800_U are 237.79 $Å^3$ & 237.88 $Å^3$ respectively.

Like BICOVOX and BINIVOX, in BICUVOX catalysts amount of pure γ-BIVOX phase increases with the calcination temperature and it ranges from 71.5% to 100% for BICUVOX-Wash to BICUVOX-800_F. For BICUVOX-400_F and BICUVOX-600_F catalysts, it is 77.4 and 88.9 wt% respectively, as reported in Table 4.11. Increase in particle size is also seen with the calcination temperature and particle size is calculated to be 71.1, 39.6 and 174% higher, for BICUVOX-400_F, BICUVOX-600_F and BICUVOX-800_F, respectively with respect to wash catalyst. This is similar to the BICOVOX_F and BINIVOX_F catalysts due to the similar effects as discussed above.

Analogues to BICOVOX and BINIVOX catalysts decrease in amount of γ-BICUVOX phase for all BICUVOX_30HRS_U catalysts is observes. After using for 150 hrs, BICUVOX-400_U and BICUVOX-600_U catalysts show 22.6 and 48.9 wt % reduction in γ-BICOVOX with an emergence of Bi metal. BICUVOX-800_U catalyst also shows the reduction in wt% of γ-BICUVOX phase from 100 to 55.2% with the formation of β-Bi_2O_3, however, no Bi metal could detect. For all BICUVOX_30HRS_U and BICUVOX_U catalysts particle size of γ-phase is found to reduce with the usage.

Alike, BICOVOX catalyst, in BICUVOX catalysts the lattice strain is found to decrease with annealing temperature ranges from 4.7 x 10^{-3} to 2.0 x 10^{-3} for BICUVOX-wash to BICUVOX-800 fresh catalyst as reported in Table 4.10. In case of BICUVOX_30HRS_U and BICUVOX_U catalysts lattice strain increases probably because of emergence of more amount of secondary phases in comparison to the fresh. The lattice parameter 'a' is observed to decrease from the parent BIVOX(amcsd-0016748) because of V^{5+} ions (0.68Å) doped with Cu which is the main reason for the contraction, however the 'c' values are slightly higher. Looking at the effect of temperature on the lattice parameters, 'a' and 'c' values are observed to decrease with calcination temperature as the strain reduces (with calcination temperature) from their elongated state in pure γ-BIVOX. Contraction in lattice parameters is observed from a(Å) = 3.991, c(Å) = 15.430 to a(Å) = 3.924-3.931; c(Å) = 15.36-15.44, which is in parallel with the observations of cobalt doped compounds. However, for long time used catalysts, particle size shrinks and strain grows as the pure phase amount drops.

The volume of unit cell V($Å^3$) in BICUVOX_F catalysts is decreasing with annealing temperature as seen in Table 4.10. However, volume of unit cell increasing for BICUVOX_30HRS_U and BICUVOX_U catalysts compared to BICUVOX_F because of the oxygen stoichiometry, as it can affect the oxidation state of vanadium because of which the volume change is observed from 238.27 $Å^3$ to 238.505 $Å^3$ and 242.908 $Å^3$ for BICUVOX-400_30HRS_U and BICUVOX-400_U, 237.2 $Å^3$ to 239.72 $Å^3$ and 241.806 $Å^3$ for BICUVOX-600_30HRS_U and BICUVOX-600_U and 237.801 $Å^3$ to 237.61 $Å^3$ and 237.57 $Å^3$ for BICUVOX-800_30HRS_U and BICUVOX-800_U catalysts, respectively.

Only γ-BIVOX phase is obtained, no α and β-BIVOX phases are seen in XRD of BIMEVOX catalysts since, the maximum temperature during SCS is > 570°C (Figure 3.6). For BIMEVOX-wash samples, only β-Bi_2O_3 with $BiVO_4$ is found in XRD. Sammes et al., reported that α-Bi_2O_3 is transformed into δ-Bi_2O_3 at temperature > 650°C and on cooling from the high temperature to room temperature δ-Bi_2O_3 transforms into intermediate

metastable tetragonal β-phase at approximately 640°C. The β-phase, however, on further heating can transform into α-phase. We are also getting α-phase for the catalysts calcined at 600°C (Sammes, Tompsett et al. 1999; Monnereau, Tortet et al. 2003). And during solution combustion, bismuth vanadate $BiVO_4$ is the main impurity in many-phase samples (Nimat, Joshi et al. 2007). Instantaneous change in temperature is accountable for the formation of γ-BIVOX, $BiVO_4$ and β-Bi_2O_3 phases as detected by XRD of wash samples. In general, the phase transition occurring in BIVOX is shown in Equation 1.23. Therefore, our results are consistent with the literature.

4.1.2.2 *S-DTGA (Simultaneous Differential thermal & Thermal gravity analysis)*

X-ray powder diffraction and S-DTGA are used for the comparative analysis of the features of BIMEVOX catalysts. The relevant DTA features are accompanied by weight loss or gain observed in TGA curves. The combustion behaviour of the dried mixtures of precursors of (a) BIVOX, (b) BICOVOX, (c) BINIVOX and (d) BICUVOX catalysts are collected prior to decomposition and recorded by S-DTGA as presented in Figure 4.23. Two consecutive endothermic peaks at 100°C and 120°C for BIVOX, 80°C and 130°C for BICOVOX, BINIVOX and BICUVOX with corresponding weight loss of ~10% (for each catalyst) are observed and these could be due to dehydration of absorbed moisture and loss of ethanol (Dinka and Mukasyan 2005). The first weight loss is followed by an abrupt and large weight loss of about 65.68% for BIVOX, 82.15% for BICOVOX, 82.85% for BINIVOX and 77.64% for BICUVOX in a very narrow temperature range 150-160°C with a sharp exothermic peak around 160°C clearly indicates the vigorous combustion and decomposition of fuel and oxidizers into their corresponding oxides (Chick, Pederson et al. 1990). Pederson et al, (1991) study the solution combustion synthesis of $YBa_2Cu_3O_{7-x}$ ceramics with glycine as fuel. A sharp exothermic peak is detected in DTGA results in the range of 160-180°C for combustion (Pederson, Maupin et al. 1991). Tian et al, (2007) investigate the S-DTGA of dried gel of glycine with lanthanum and aluminium nitrates. Their S-DTGA results also exhibit the presence of a sharp exothermic peak around 182°C, accompanied by 77.7% weight loss (Tian, Yu et al. 2007). Furthermore, one broad and small exothermic region corresponding to a slight weight loss at temperature 250 and 420°C can be ascribed to the burning of the residual nitrates and combustion of glycine entrapped in the powder respectively (Tian, Yu et al. 2007; Beg, Al-Alas et al. 2010). The reaction can be represented as follows (Tian, Yu et al. 2007):

$$4NH_2CH_2COOH + 9O_2 \rightarrow 2N_2 + 8CO_2 + 10H_2O \quad (4.16)$$

Al-Areqib et al, (2010) synthesize the BIALVOX catalyst by the sol-gel citrate route and characterize it. The DTA curve of BIALVOX catalyst exhibits small endothermic peak at temperatures above 450°C, corresponding to no mass loss, assign to β- BIVOX → γ- BIVOX phase transition (Al-Areqi, Al-Alas et al. 2010). However, our DTGA spectrum does not show any endothermic peak above 450°C. Obtained S-DTGA spectrum for BIMEVOX catalysts are consistent with the reported literature. No peak is seen in DTGA during cooling.

S-DTGA of BIMEVOX-wash samples is unveiled in Figure 4.24. The TGA profile of BIVOX shows the weight loss in two consecutive steps. At 270°C, ~0.61% change corresponding to an endothermic peak could be due to the evolution of chemisorbed moisture and ethanol and/or some Bi-V-O related phase change, as shown in Figure 4.24 (a). The second loss of ~0.31% at 645°C, accompany by an exothermic peak could be due to the Bi-V-O related phase transformation, as all the secondary phases (α-Bi_2O_3 and β-Bi_2O_3) are transformed into pure γ-BIVOX (Sammes, Tompsett et al. 1999). γ-BIVOX phase is stable at high temperature (T > 560°C) and the amount of Bi_2O_3 decreases significantly above 600°C (Szaller, Pöppl et al. 1996; Sammes, Tompsett et al. 1999). The DTA cooling spectrum shows an endothermic peak at 623°C and reflects the reverse transition of γ-BIVOX which indicates the instability of undoped parent phase (Nimat, Joshi et al. 2007). Figure 4.24 (b) describes the S-DTGA profile of the BICOVOX-wash catalyst. Analogous to BIVOX, BICOVOX-wash also contains two peaks- one endothermic at 270°C, corresponding weight loss of 1.7% and another exothermic peak at 645°C during heating. No further weight loss is observed till 800°C. The featureless DTA profile during cooling shows the phase stability of the catalyst, unlike BIVOX-wash catalyst. These results are in accordance with the XRD analysis.

Similar to BIVOX and BICOVOX-wash, in Figure 4.24 (c) and (d) S-DTGA of BINIVOX and BICUVOX-wash are presented respectively. An endothermic DTA peak at ~ 276°C corresponding weight loss of 0.9% for BINIVOX, at 274°C corresponding weight loss of 0.65% for BICUVOX are observed. This endothermic peak is followed by an exothermic DTA peak at ~ 650°C without any weight loss for BINIVOX and at 645°C for BICUVOX, corresponding to some Bi-V-O related phase transformation. Like BICOVOX-wash, DTA cooling spectrum devoid of any phase reversal peak indicates the stability of the BINIVOX and BICUVOX-wash catalysts.

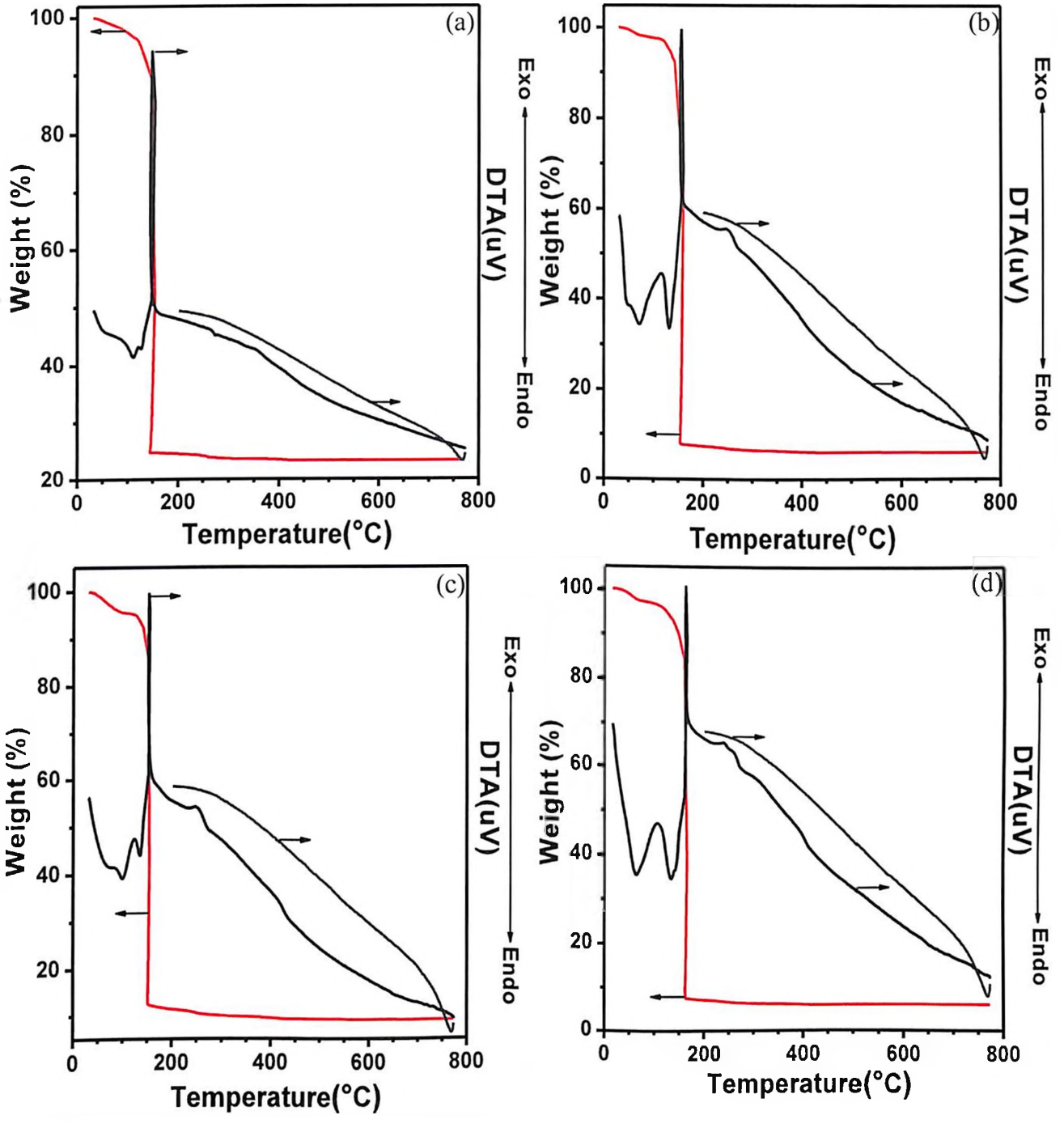

Figure 4-23: DTA/TGA spectra for mixtures of precursor's of (a) BIVOX, (b) BICOVOX, (c) BINIVOX and (d) BICUVOX

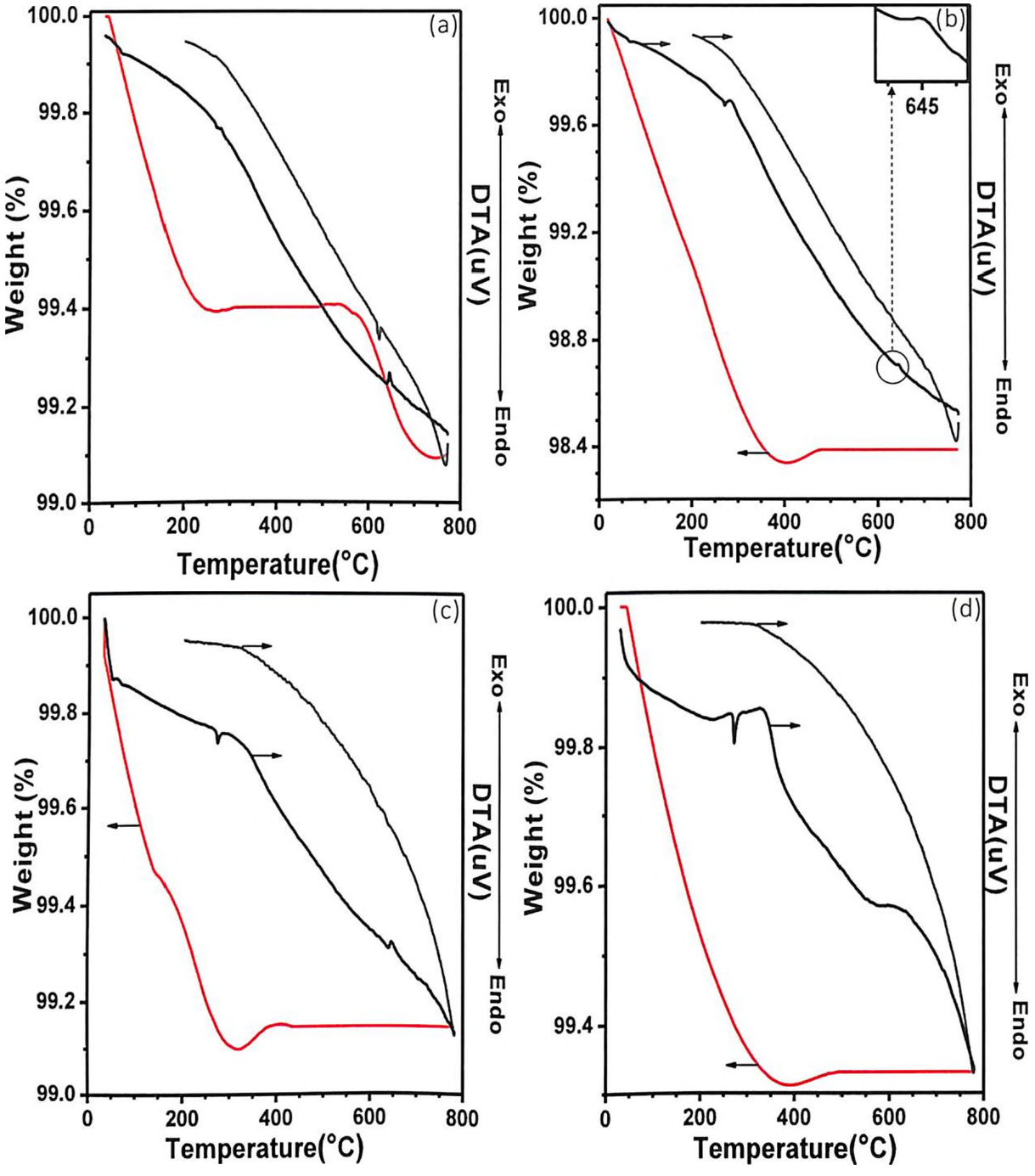

Figure 4-24: DTA/TGA spectra for (a) BIVOX, (b) BICOVOX, (c) BINIVOX and (d) BICUVOX - Wash powders

Figure 4.25 depict the DTA and TGA profile for (a) BICOVOX-400_30HRS_U and (b) BICOVOX-400_U catalysts. The exothermic peak at around 650°C has appeared due to phase transition of α-Bi_2O_3 and β- Bi_2O_3 into γ-BIVOX and $BiVO_4$ as shown in Figure 4.25 (a). Total weight loss of ~0.32% is calculated from temperature 200 to 750°C as the running tail of TGA curve is going till 750°C and then getting stabilized at 800°C. The change in weight could be attributed to C deposition. This indicates the stability (in terms of phase content and activation) of the catalyst. Maity et al, (2012) study the hydro-demetallization and hydro-desulfurization of Co-Mo catalysts supported by alumina, alumina–titania and alumina–silica by using heavy crude oil as feed. DTGA is used to identify and measure carbon deposition on spent catalysts. All DTGA curves show two principle weight losses at 100 and 400°C. Weight loss (10-20%) at 400°C is accompanied by a very sharp and prominent exothermic peak due to burning of coke. The second peak position is varied from 400 to 480°C for the different catalysts (Maity, Blanco et al. 2012). Kim et al, (2006) investigate the CO_2 reforming of methane over Ni/Al_2O_3 catalyst. DTGA of used catalyst shows an exothermic peak starting from 410°C and ending at 720°C with a weight loss of 2.28% and assign to oxidation of deposited carbon (Kim and Maier 2006). Singha et al, (2017) report the effect of metal-support interaction on activity and stability of Ni (5 wt%)-CeO_2 catalyst for partial oxidation of methane. DTGA of used catalysts is carried out to find out the nature and percentage of carbon deposited. Reported spectrum depict that 3.9% weight loss, correspond to an exothermic peak staring from 600°C and ending at 800°C, is due to loss of deposited graphitic carbon and they mention that below 600°C, CH_x species is removed and above that graphitic carbon is removed (Singha, Shukla et al. 2017). Duan et al, (2017) work on the partial oxidation of methane over Ni based catalyst prepared by modified nanocasting method. TGA of spent catalysts after reaction of 96 h at 700°C is carried out and it is noted that a sharp decline of mass (~ 40%) occurred at 300–800°C due to the oxidation of amorphous carbon and graphitic-like carbon (Duan, Wang et al. 2017). Ding et al, (2016) study the partial oxidation of methane over silica supported Ni nanoparticles. The amount and species of carbon deposition on used catalysts is investigated by DTGA technique. Results show there are two exothermic peaks in used catalyst at 600 and 680°C corresponding to a total weight loss of 20%, indicating the presence of two species of carbon: graphitic carbon and carbon nanotubes, respectively (Ding, Wang et al. 2016). Dry reforming of methane over Ni/La_2O_3 catalyst is investigated by Li et al, (2017). The amount of coke deposition is measured from the DTGA profiles and results depict that mass loss of ~10.3% in the

temperature range of 380 to 600°C corresponding to an exothermic peak at 480°C is assigned to coke combustion (Li, Li et al. 2017). Elbaba et al, (2013) study the pyrolysis–catalytic gasification of waste tyres with a nickel/dolomite catalyst. The results of DTA of spent catalysts show that oxidation peak at a temperature ~ 420°C assign to monoatomic carbon and oxidation peak at about 610°C assign to filamentous carbon. They conclude that the monoatomic carbon is deposited on the surface of the catalyst and blocks the access of pyrolysis products to the catalyst and lower the catalytic activity (Elbaba and Williams 2013). Elbaba et al, (2011) also work with nickel/cerium catalyst for hydrogen production from the pyrolysis-gasification of waste tyres. Nickel/cerium catalysts also show the high amount of carbon deposition. The weight loss is 17.0% in the temperature range of 350 to 700°C with oxidation peak at 500°C assigned to burning of the layered carbon deposited on the catalyst surface (Elbaba, Wu et al. 2011). Tishchenko et al, (2015) reveal the TGA analysis of carbon formation in silica nanocomposite. Their results show the weight loss of ~ 5% corresponding to carbon oxidation is in the range of 325–360°C (Tishchenko, Ilchenko et al. 2015). Pantaleo et al, (2016) work on Ni/CeO_2 catalysts for methane partial oxidation. The carbon build-up over the samples after the methane decomposition is checked by TGA analyses. The obtained profiles showed a weight loss of 15% in the region of 300 to 600°C due to deposited carbon (Pantaleo, Parola et al. 2016). Li et al, (2018) test the Multi-Ni-Ni phyllosilicate hollow sphere for CO_2 reforming of CH_4. In order to determine the stability, and carbon formation, catalyst is characterized through DTGA. Results show that carbon deposition is less than 5% of weight loss with a negligible exothermal peak being detected at 592°C during DTA analysis (Li 2018). Zou et al, (2016) investigate the hydrogen production from pyrolysis of cellulose in the presence of K alkali metal. DTGA of reacted catalysts reveal the two stages of carbon oxidation including a lower temperature region (~400°C) with 2 weight% loss for the oxidation of amorphous carbon and a higher temperature region (~700°C), corresponding to weight loss of ~0.7% for the oxidation of graphite carbons (e.g. filamentous carbons) (Zou, Yang et al. 2016). Waheed et al, (2016) perform the pyrolysis-reforming of rice husks over Ni-dolomite catalyst. DTGA of the used catalysts is carried out and results show that two weight loss peaks are observed at ~430°C and ~640°C. It has been concluded that the first peak of 4.5% weight loss is attributed to the oxidation of amorphous carbons while the second peak with 1.5% weight loss is due to the presence of filamentous carbon (Waheed, Wu et al. 2016). Oemar et al, (2015) perform the DTGA analysis of spent La-Ni/SBA-15 catalyst to determine the carbon formation. Carbon formation is shown by an exothermic

peak corresponding to 15% weight loss; obtain at ~450°C (Pirovano, Vannier et al. 2003; Oemar, Kathiraser et al. 2015).

Reported literature is in the same line with our results. Thermal evolution of BICOVOX-400_U catalyst in presence of atmospheric air occurs in four consecutive stages including both endothermic and exothermic peaks corresponding weight loss in TGA, as depicted in Figure 4.25 (b). During first step endothermic peak appears corresponding to weight loss of 0.5% up to 274°C and it is attributed to evolution of physisorbed and chemisorbed water and ethanol. An endothermic peak arises at 352°C could be due to some Bi-V-O related phase transformation, followed by an exothermic peak at 392°C occurs during the third step with weight loss of 0.6% in the region of 300 to 750°C and it indicates the carbon formation. The successive exothermic peak at 550°C in the fourth step infers the transition of α-Bi_2O_3 and β-Bi_2O_3 into γ-BIVOX. These endothermic and exothermic peaks are appearing due to the prolong use of the catalyst, which causes it to break into a number of phases and deposition of coke. This is in agreement with the XRD results. The featureless DTA profile is observed during cooling.

For BICOVOX-600_30HRS_U catalyst, one exothermic peak is observed at 560°C corresponding to 0.37% weight loss in the region of 250 to 800°C and it is very well matching with the weight loss due to carbon oxidation, as shown in Figure 4.26 (a). The obtained DTA curve for BICOVOX-600_U (Figure 4.26 (b)) is similar to that of the BICOVOX-400_U, but the intensity of second endothermic and first exothermic peaks appear at 354°C and 395°C, respectively are high. Weight losses corresponding to first endothermic and exothermic peaks are 2.21% and 0.47% respectively. However, no weight loss is observed for second exothermic peak at 500°C and it could be because of the presence of very small amount of carbon which is not in the sensitive limit of the instrument. The position of second exothermic peak is shifted towards the lower temperature in comparison with the BICOVOX-400_U as more amount of carbon is forming in BICOVOX-600_U and that may cause the shifting. The DTA cooling spectrum for each catalyst devoid of any phase reversal peak indicates the stability of the catalysts.

There is no DTA peak observed for BICOVOX-800_30HRS_U catalyst, as it contains mostly pure γ BIVOX, as shown in Figure 4.27 (a). However, a weight loss of 0.3% is calculated that could be due to carbon formation. BICOVOX-800_U catalyst has shown similar behavior and three peaks have been observed in Figure 4.27 (b). Two of these peaks are endothermic, appearing at 275°C and 354°C. The one extra exothermic peak that appears

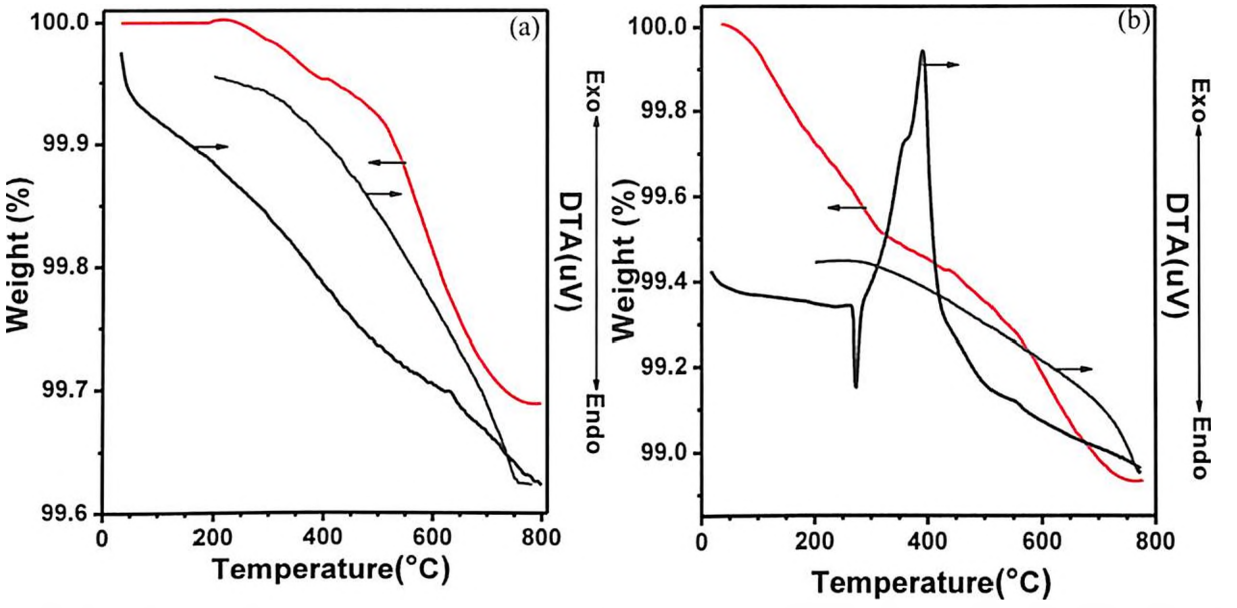

Figure 4-25: DTA/TGA spectra for BICOVOX-400 (a) 30 hrs used & (b) long time used catalyst

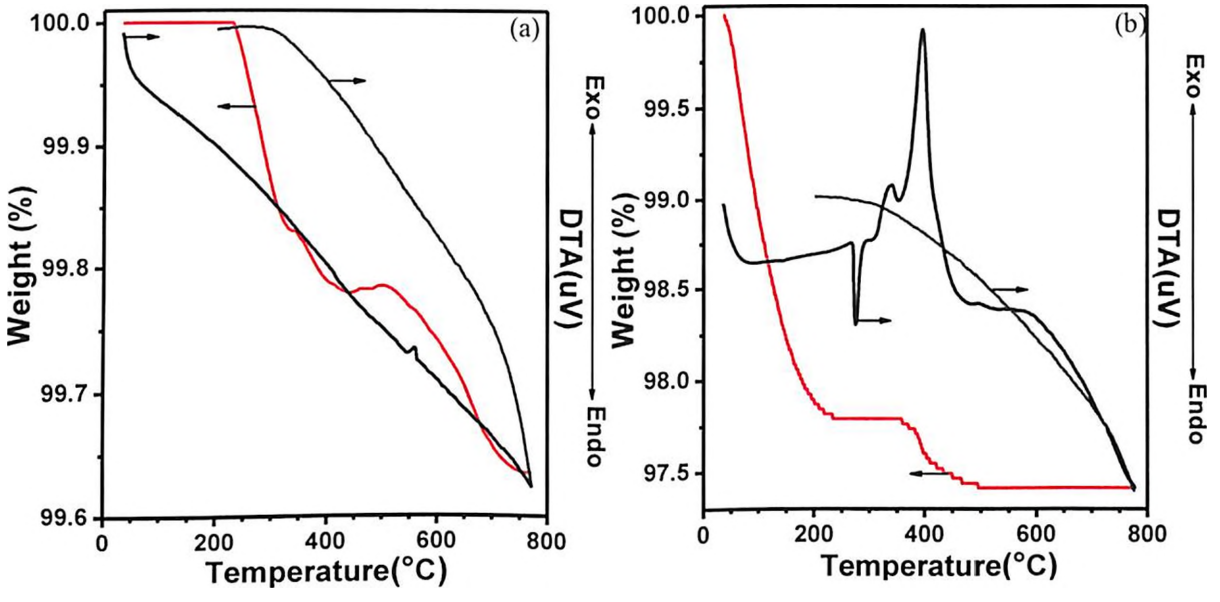

Figure 4-26: DTA/TGA spectra for BICOVOX-600 30 hrs used & (b) long time used catalyst

in BICOVOX-400_U and BICOVOX-600_U catalysts at 550°C could have been due to the transition of secondary phases into γ-BIVOX, which is absent here as it mainly contains γ-BIVOX. However, a weight loss of 8.62% is calculated and depicts that for BICOVOX-800_U catalyst, more amount of carbon is depositing on the surface.

Figure 4.28 show the DTA and TGA spectra for (a) BINIVOX-400_30HRS_U and (b) BINIVOX-400_U catalyst. Similar profile is obtained for BINIVOX-400_30HRS_U as find for BICOVOX-400_30HRS_U catalyst. One exothermic peak at 640°C and corresponding weight loss of 0.4% is found and that confirms the existence of amorphous carbon. For BINIVOX-400_U catalyst, four DTA peaks are observed, as depicted in Figure 4.28 (b). Two of these peaks are endothermic, first appearing at 274°C and the second peak is observed at 320°C. The weight loss of 1.85% is calculated, corresponding to the first endothermic peak could be due to the evolution of chemisorbed moisture and ethanol. The remaining two peaks are exothermic; first one appearing at 390°C with weight loss of 0.53% due to oxidation of amorphous carbon follows by the second peak at 646°C.

Figure 4.29 (a) shows that, for BINIVOX-600_30HRS_U catalyst no DTA peaks are observed but 0.3% weight loss is observed. This reflects the existence of very small amount of amorphous carbon. Analogous to BINIVOX-400_U catalyst, four peaks are also observed for BINIVOX-600_U catalyst, as shown in Figure 4.29 (b). Two endothermic peaks are obtained at 274°C and 320°C. The first peak corresponds to a weight loss of 1.38% could be due to the evolution of chemisorbed moisture and ethanol. The other two exothermic peaks appear at 390°C with weight loss of 0.45% confirms the oxidation of amorphous C and at 550°C without any loss infers the transition of α-Bi_2O_3 and β- Bi_2O_3 into γ-BIVOX.

Figure 4.30 (a) depicts that there is no change in phase during both heating and cooling for BINIVOX-800_30HRS_U. However, TGA analysis shows ~ 0.26% losses in weight in the temperature range of 150-550°C. The change in weight could be attributed to amorphous C deposition. BINIVOX-800_U catalyst has shown similar behavior to the BINIVOX-600_U catalyst and three peaks have been observed as shown in Figure 4.30 (b). One of these peaks is endothermic, appearing at 274°C. One exothermic peak is seen at 389°C, followed by another exothermic at 550°C. However, weight loss of 3.3% is calculated corresponding to exothermic peak at 389°C and shows that more amount of carbon is depositing on the surface.

Figure 4.31 depicts the S-DTGA spectra for (a) BICUVOX-400_30HRS_U and (b) BICUVOX-400_U catalyst. In comparison with BICOVOX-400_30HRS_U and BINIVOX-

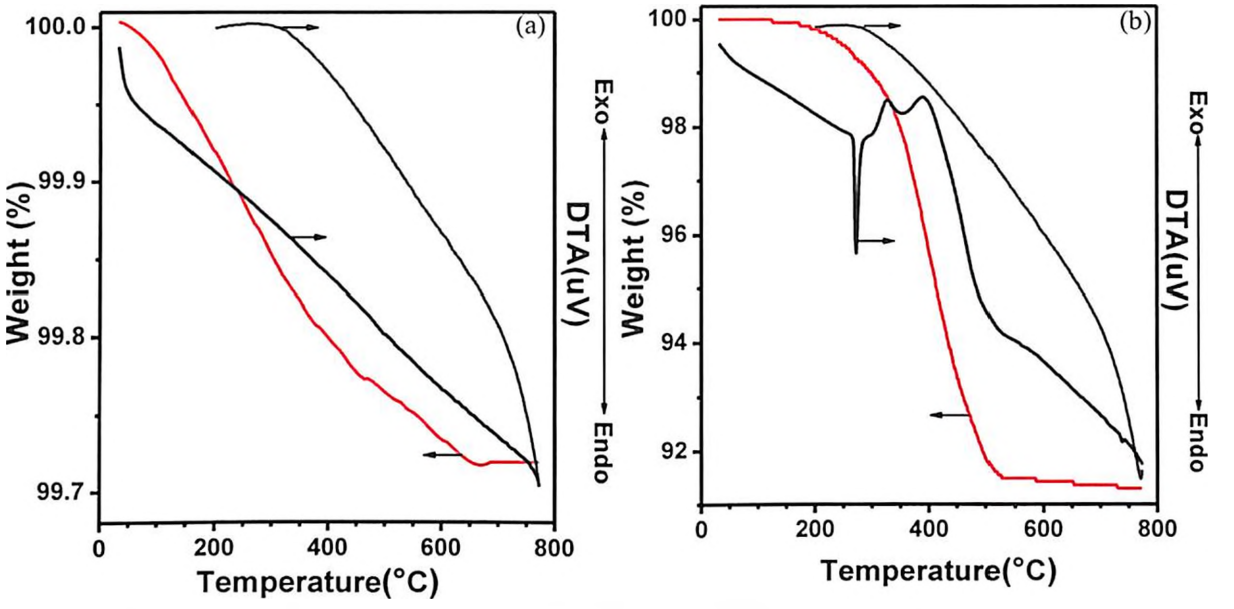

Figure 4-27: DTA/TGA spectra for BICOVOX-800 (a) 30 hrs used & (b) long time used catalyst

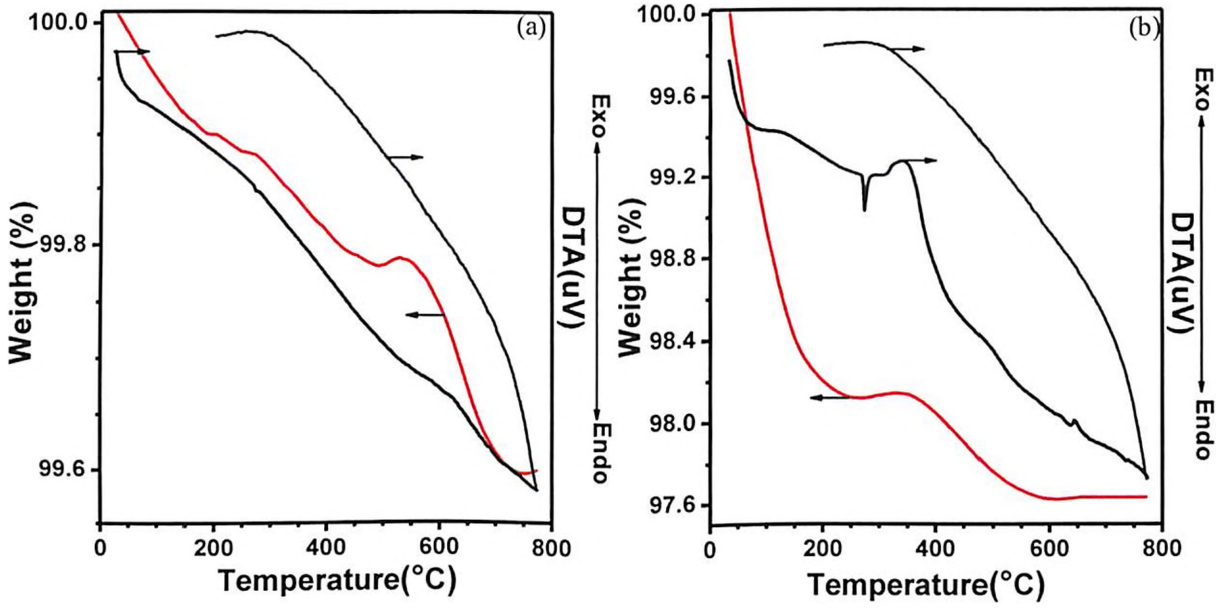

Figure 4-28: DTA/TGA spectra for BINIVOX-400 (a) 30 hrs used & (b) long time used catalyst

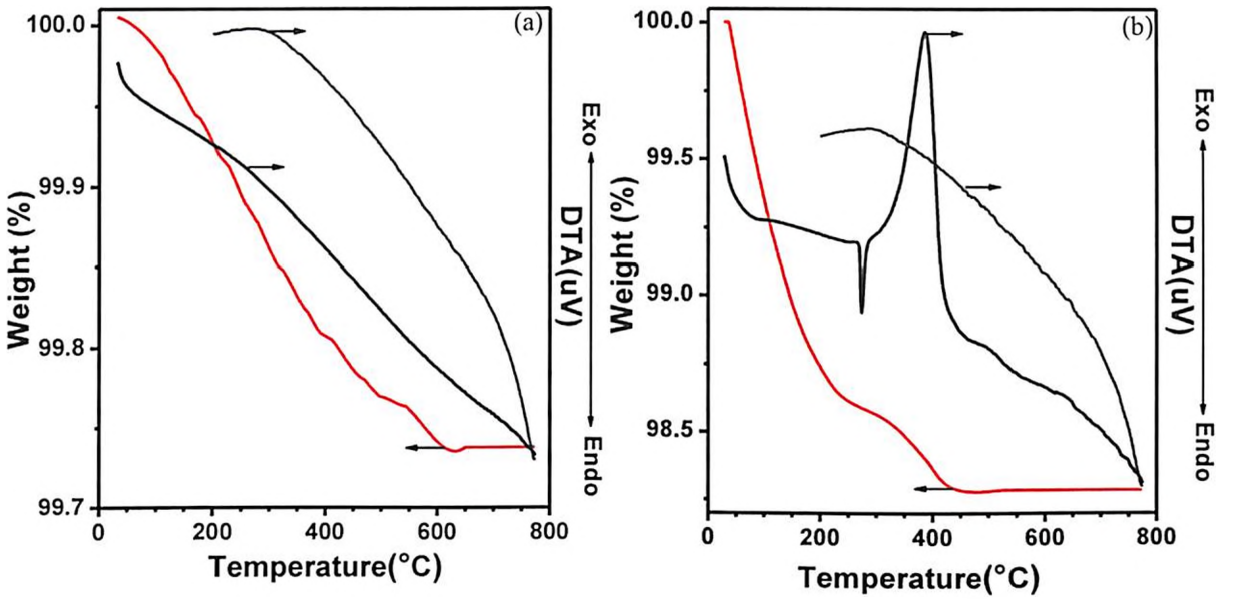

Figure 4-29: DTA/TGA spectra for BINIVOX-600 (a) 30 hrs used & (b) long time used catalyst

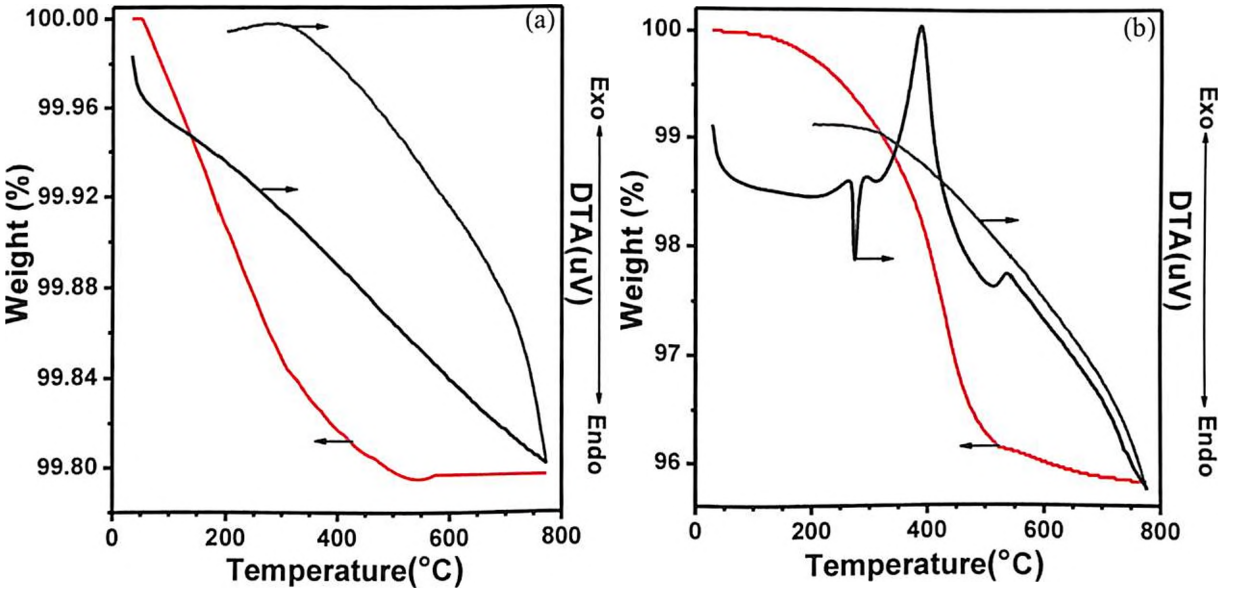

Figure 4-30: DTA/TGA spectra for BINIVOX-800 (a) 30 hrs used & (b) long time used catalyst

400_30HRS_U catalysts, one additional endothermic peak at 274°C is observed for BICUVOX-400_30HRS_U catalyst. Weight loss of ~0.42% is calculated and that could be attributed to C deposition. However, BICUVOX-400_U catalyst shows similar results as find for BINIVOX-400_U catalyst. It shows four DTA peaks, as depicted in Figure 4.31 (b). Two of these peaks are endothermic, first appearing at 275°C and the second peak is observed at 350°C. The weight loss of 1.85% is calculated, corresponding to the first endothermic peak. The remaining two peaks are exothermic; first one appearing at 400°C with weight loss of 4.2% due to oxidation of amorphous carbon follow by the second peak at 550°C with no weight loss in TGA.

For BICUVOX-600_30HRS_U catalyst no DTA peaks are observed, as observed in Figure 4.32 (a), but 0.12% weight loss is observed and that infer the oxidation of C. Similar to BICOVOX-600_U catalyst, four peaks are observed for BICUVOX-600_U catalyst, as depicted in Figure 4.32 (b). Single endothermic peak is obtained at 275°C. The other three exothermic peaks appear at 380°C, corresponding to a weight loss of 0.42% attributed to the oxidation of carbons, 410°C and 550°C without any weight loss. The DTA cooling spectrum for each catalyst devoid of any phase reversal peak indicates the stability of the catalysts.

There is no DTA peak observed for BICUVOX-800_30HRS_U catalyst, as it contains mostly pure γ BICUVOX, as shown in Figure 4.33 (a). However, a weight loss of 0.14% is calculated due to deposited carbon. Like BICOVOX and BINIVOX-800_U, BICUVOX-800_U catalyst consists of one endothermic peak at 274°C and two exothermic peaks at 389°C and 550°C, as shown in Figure 4.33 (b). Weight loss of 8.03% is calculated for BICUVOX-800_U catalyst. Table 4.12 lists the values of temperatures at which endothermic or exothermic peaks are appeared with possible reasons and the corresponding weight losses.

4.1.2.3 *FTIR (Fourier-transform infrared spectroscopy)*

The knowledge of functional groups (like C=C, C-H, N=H etc.) present in any compound help in identification and characterization. FT-IR and Raman spectroscopy provide a broader range of unknown substances identification. Here, FT-IR is used to classify the different functional groups present in the samples.

FT-IR spectra observed for different fresh and spent-(30HRS_U and U) BIMEVOX-(ME= Co, Ni, Cu) catalysts calcined at 400, 600 and 800°C have shown distinct peaks in the region of 4000 - 400 cm^{-1} (Figures.4.34 - 4.43). However, the major peaks for all species are found in the region of 1735 -1745 cm^{-1}, 1347 -1375 cm^{-1}, 1204 -702 cm^{-1} and 614 - 410 cm^{-1}.

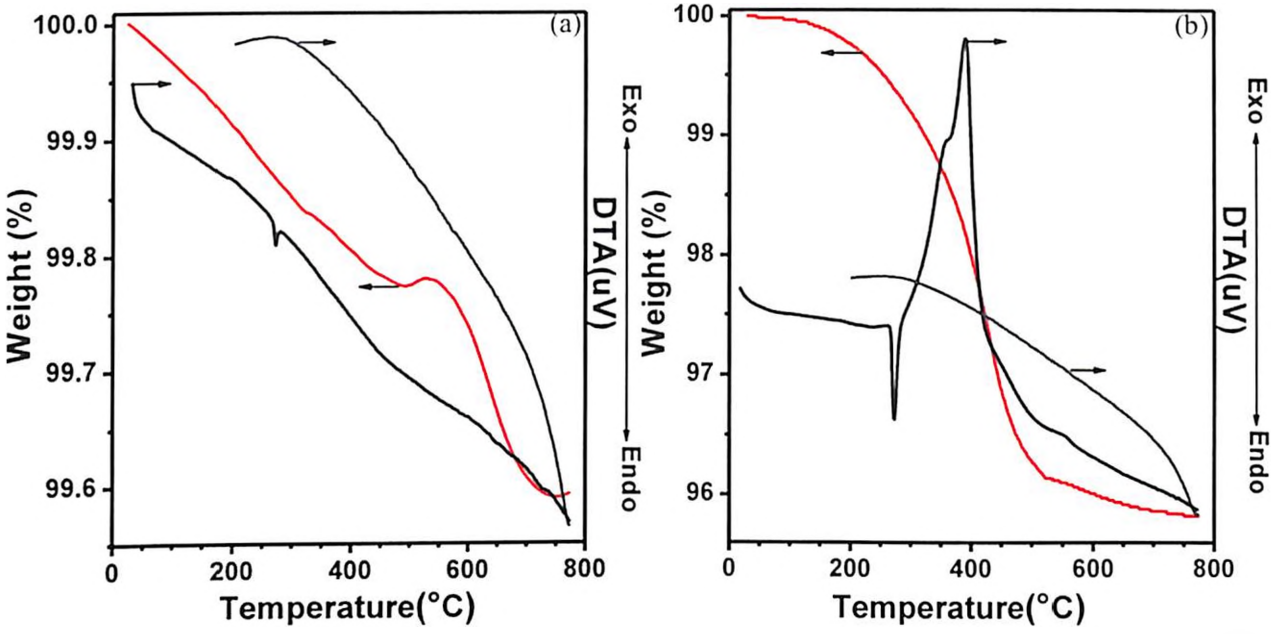

Figure 4-31: DTA/TGA spectra for BICUVOX-400 (a) 30 hrs used & (b) long time used catalyst

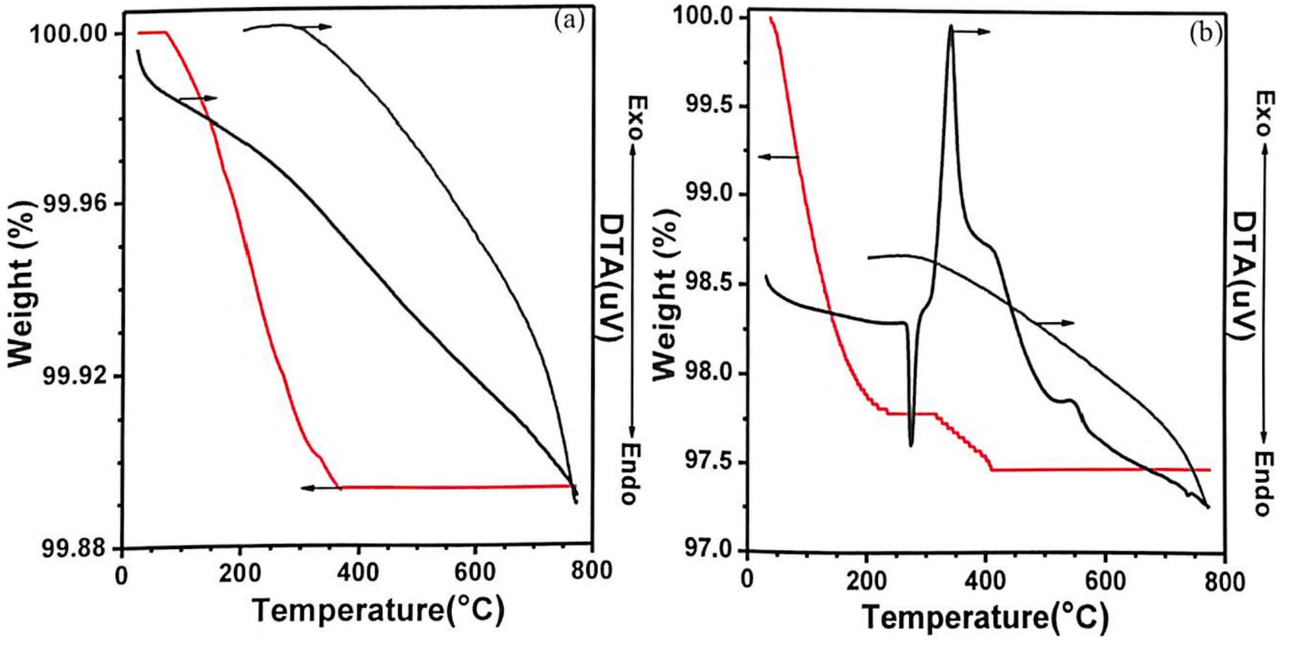

Figure 4-32: DTA/TGA spectra for BICUVOX-600 (a) 30 hrs used & (b) long time used catalyst

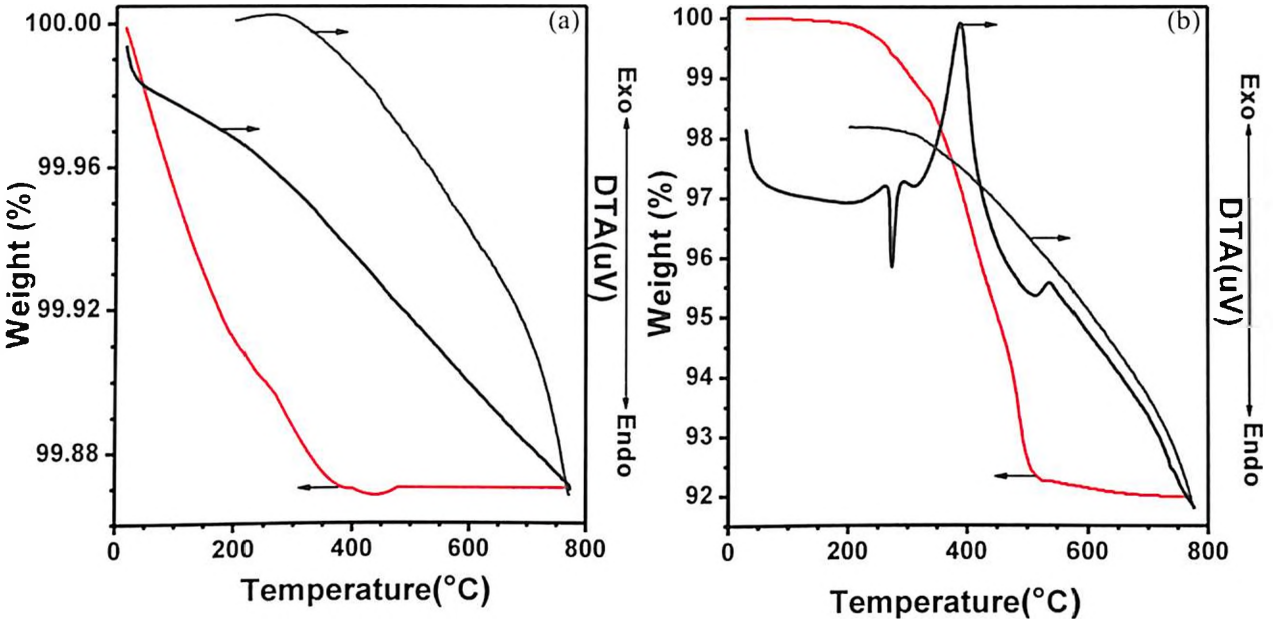

Figure 4-33: DTA/TGA spectra for BICUVOX-800 (a) 30 hrs used & (b) long time used catalyst

Table 4-12 : The values of temperatures at which endothermic or exothermic peaks are appeared with possible reasons and the corresponding weight losses for BIMEVOX catalysts

Catalysts	DTA PEAK position (with possible explanation)	TGA (wt.% loss)
BIVOX-Before SCS	100(Endo)→ EtOH loss 120(Endo)→ H_2O loss 160(Exo)→ Combustion Rxn 270(Endo)→ Decomposition of residual NO^{3-} 360(Exo)→ Combustion of residual glycine	3% 7% 65.68% - -
BIVOX-WASH	270(Endo)→ EtOH and H_2O loss 645(Exo)→ α- and β- Bi_2O_3 → γ-BIVOX Cooling: 623(Endo)→ γ-BIVOX → α- and β- Bi_2O_3	0.61% 0.31% -
BICOVOX-Before SCS	80(Endo)→ EtOH loss 130(Endo)→ H_2O loss 160(Exo)→ Combustion Rxn 260(Exo)→ Decomposition of residual NO^{3-} 360(Exo)→ Combustion of residual glycine 440(Endo)→ Bi-V-O related phase transformation	3% 7% 82.15% - - -
BICOVOX-WASH	270(Endo)→ EtOH and H_2O loss 645(Exo)→ α- and β- Bi_2O_3 → γ-BIVOX	1.7% -
BICOVOX-400_30HRS_U	640(Exo)→ α- and β- Bi_2O_3 → γ-BIVOX	0.32% (C-formation)
BICOVOX-400_U	274(Endo)→ EtOH and H_2O loss 352(Endo)→ Bi-V-O related phase transformation 392(Exo)→ Carbon formation 550(Exo)→ α- and β- Bi_2O_3 → γ-BIVOX	0.5% - 0.6% -
BICOVOX-600_30HRS_U	560(Exo)→ α- and β- Bi_2O_3 → γ-BIVOX	0.37% (C- formation)
BICOVOX-600_U	275(Endo)→ EtOH and H_2O loss 354(Endo)→ Bi-V-O related phase transformation 395(Exo)→ Carbon formation 500(Exo)→ α- and β- Bi_2O_3 → γ-BIVOX	2.2% - 0.47% -
BICOVOX-800_30HRS_U	-	0.3% (C- formation)
BICOVOX-800_U	275(Endo)→ EtOH and H_2O loss 354(Endo)→ Bi-V-O related phase transformation 390(Exo)→ Carbon formation	1.5% - 8.62%
BINIVOX-Before SCS	80(Endo)→ EtOH loss 130(Endo)→ H_2O loss 160(Exo)→ Combustion Rxn 260(Exo)→ Decomposition of residual NO^{3-} 360(Exo)→ Combustion of residual glycine 440(Endo)→ Bi-V-O related phase transformation	3% 7% 82.85% - - -
BINIVOX-WASH	276(Endo)→ EtOH and H_2O loss 650(Exo)→ α- and β- Bi_2O_3 → γ-BIVOX	0.9% -
BINIVOX-400_30HRS_U	640(Exo)→ α- and β- Bi_2O_3 → γ-BIVOX	0.4% (C- formation)
BINIVOX-400_U	274(Endo)→ EtOH and H_2O loss 320(Endo)→ Bi-V-O related phase transformation 390(Exo)→ Carbon formation 646(Exo)→ α- and β- Bi_2O_3 → γ-BIVOX	1.85% - 0.53% -
BINIVOX-600_30HRS_U	-	0.3% (C- formation)

BINIVOX-600_U	274(Endo)→ EtOH and H_2O loss 320(Endo)→ Bi-V-O related phase transformation 390(Exo) → Carbon formation 550(Exo)→ α- and β- Bi_2O_3 → γ-BIVOX	1.38% - 0.45% -
BINIVOX-800_30HRS_U	-	0.26% (C- formation)
BINIVOX-800_U	274(Endo)→ EtOH and H_2O loss 389(Exo)→ Carbon formation 550(Exo)→ α- and β- Bi_2O_3 → γ-BIVOX	0.74% 3.3% -
BICUVOX-Before SCS	80(Endo)→ EtOH loss 130(Endo)→ H_2O loss 160(Exo)→ Combustion Rxn 260(Exo)→ Decomposition of residual NO^{3-} 360(Exo)→ Combustion of residual glycine 440(Endo)→ Bi-V-O related phase transformation	3% 7% 77.64% - - -
BICUVOX-WASH	274(Endo)→ EtOH and H_2O loss 645(Exo)→ α- and β- Bi_2O_3 → γ-BIVOX	0.7% -
BICUVOX-400_30HRS_U	274(Endo)→ EtOH and H_2O loss 640(Exo)→ α- and β- Bi_2O_3 → γ-BIVOX	0.42% (C- formation) -
BICUVOX-400_U	275(Endo)→ EtOH and H_2O loss 350(Endo)→ Bi-V-O related phase transformation 400(Exo)→ Carbon formation 550(Exo)→ α- and β- Bi_2O_3 → γ-BIVOX	- - 4.2% -
BICUVOX-600_30HRS_U	-	0.12% (C- formation)
BICUVOX-600_U	275(Endo)→ EtOH and H_2O loss 380(Exo)→ Carbon formation 410(Exo)→ Bi-V-O related phase transformation 550(Exo)→ α- and β- Bi_2O_3 → γ-BIVOX	2.22% 0.42% - -
BICUVOX-800_30HRS_U	-	0.14% (C- formation)
BICUVOX-800_U	274(Endo)→ EtOH and H_2O loss 389(Exo)→ Carbon formation 550(Exo)→ α- and β- Bi_2O_3 → γ-BIVOX	- 8.03% -

FT-IR spectra of different BIMEVOX-wash samples along with that of the parent compound BIVOX-wash are together exhibited in Figure 4.34. In case of all wash samples there seems to be no notable transmittance in the spectra from 4000 to 1000 cm^{-1}, beyond which we see a broad and strong IR band near 710 cm^{-1} with shoulders at ~838 cm^{-1} and ~646 cm^{-1} which is assigned to vibration of V-O stretching (Beg, Al-Alas et al. 2010). The fine structure seen in these bands can be attributed to the symmetric stretching and bending modes of VO_4 tetrahedra and VO_6 octahedra, which arises due to the variation in the (V–O) bond length in the range of 1084-1079 Å (Joubert, Jouanneaux et al. 1994; Beg and Al-Areqi 2009). In addition, the Bi–O symmetric vibrations are observed at 609 cm^{-1}, 510 cm^{-1} and 418 cm^{-1} (Zhang and Zhang 2009; Beg, Hafeez et al. 2010; Beg, Hafeez et al. 2010). It can be observed that the parent compound shows same characteristic features as obtained for BIMEVOX- wash samples. However, peaks capture in the region of 477 to 440 cm^{-1} are only noticed in BIMEVOX samples and ascribed to doping metal-oxygen bond (ME-O) (Rameshbabu, Periasamy et al. 2001; Qiao, Wei et al. 2009; Radhakrishnan and Beena 2014; Li, Qiu et al. 2016). Rameshbabu et al, (2001) reports the IR spectrum for Co-oxide and Ni-oxide. For both the metals, bands are observed in the range of 510–520, 580–610 cm^{-1} (Rameshbabu, Periasamy et al. 2001). Li et al, (2016) perform the FT-IR and Raman analysis for cobalt oxide. FT-IR shows the peaks for Co-O at 592, 554 and 450 cm^{-1} (Li, Qiu et al. 2016). Qiao ei al, (2009) characterize the NiO nanoparticles and find the Ni-O peaks at 600–700, 457 cm^{-1} in the FT-IR spectra (Qiao, Wei et al. 2009). Radhakrishnan et al, (2014) study the IR spectra of CuO nanoparticles and notice Cu-O bonds at 601, 508, 450-490 cm^{-1} (Radhakrishnan and Beena 2014). Reported literature shows that the ME-O bonds are mainly found in the region of 450 to 700 cm^{-1}. Although, in our case, the ME-O bonds are found in the region of 477-440 cm^{-1} (with low intensity) only, not in between the 500-700 cm^{-1}, could be because only 10 at% of metal is used in catalyst or could be due to superimposition of the peaks. Balachandera et al, (2013) mention the FT-IR of Bi_2O_3 in the range of 400-600 cm^{-1} (Balachander, Ramadevudu et al. 2013). Therefore, ME-O peaks can be superimposed with peaks of Bi_2O_3 and hence they are difficult to differentiate.

Figures 4.35-4.37 illustrate the FT-IR spectra of BICOVOX-400, BICOVOX-600 and BICVOX-800 catalysts. The graph is shown in a layer lines representing different stages of catalyst starting from BICOVOX_F, BICOVOX-30HRS_U to BICOVOX_U. No remarkable peaks or bands are observed in between 4000 to 1800 cm^{-1} as seen in Figures (part (a)), therefore 1800-400 cm^{-1} and 800-400 cm^{-1} wave number ranges are considered (part (b) and (c)) to get the insight of peaks coming in the lower wave number range. Bi-O (614, 516 and

466 cm^{-1}) and V-O (710 cm^{-1}) stretching obtain in BICOVOX-400_F catalyst is at similar position to that of BICOVOX-wash (Tolstoy and Tolstobrov 2002; Nakamoto 2006; Beg, Al-Alas et al. 2010).

In BICOVOX-400_30HRS_U and BICOVOX-400_U catalysts extra band at ~ 1745 cm^{-1} is observed, and is ascribed to C=O stretching, which can be assumed to be of atmospheric carbon dioxide (CO_2). DTGA reveals the formation of carbon for BIMEVOX_30HRS_U and BIMEVOX_U catalysts. FT-IR of BICOVOX-400_30HRS_U and BICOVOX-400_U, also confirm the carbon formation as new peak emerges at 1369 cm^{-1} with respect to BICOVOX-400_F catalyst, signifies the presence of C=C stretching. It is also observed that the intensity of this peak is increasing for BIMEVOX_U catalysts from BIMEVOX_30HRS_U catalysts. In addition, band observed at 1204 cm^{-1} in both BICOVOX-400_30HRS_U and BICOVOX-400_U catalysts, corresponds to an asymmetric V-O stretching (Tolstoy and Tolstobrov 2002; Fortal'nova, Murasheva et al. 2008; Beg, Al-Alas et al. 2010). Tolstoy et al, (2002) synthesize the Bi–V–O-containing nanolayers on silica surfaces by the successive ionic layer deposition technique to study the influence of synthesis conditions (concentration and pH of the reactant solutions, time of treatment, and the number of ion-deposition cycles) on the kinetics of layer growth on a surface. FT-IR analysis shows peaks in-between 995-1205 cm^{-1} set for the asymmetric V-O stretching of vanadate ions (Tolstoy and Tolstobrov 2002). XRD affirms the formation of more secondary phases for BIMEVOX_30HRS_U and BIMEVOX_U catalysts. Like, only β-Bi_2O_3 is seen for BICOVOX-400_F catalysts. However, both β and α- Bi_2O_3 phases are found for BICOVOX-400_30HRS_U and BICOVOX-400_U catalysts. FT-IR also supported this phase transition and extra peaks appeared at 423 and 442 cm^{-1} in BICOVOX-400_30HRS_U and BICOVOX-400_U catalysts confirms the presence of α- Bi_2O_3 (Watanabe 1990; Bandoli, Barreca et al. 1996). But, along with these, an extra band at 1004 cm^{-1} is also noticed for BICOVOX-400_U catalyst which may correspond to V-O stretching possibly due to structural defects or might be due to the presence of V_2O_5 as shown in Figure 4.35 (Beg, Al-Alas et al. 2010; Beg, Hafeez et al. 2010). It is reported that the defects like oxygen vacancies and variable coordination mainly affect the vanadium layers and are dependent on the valence and coordination of metal dopants, although the extent is still difficult to determine (Löfberg, Bodet et al. 2006). Dimitriev et al, (1994) prepare V_2O_5-GeO_2-Bi_2O_3 glasses by direct combustion. FT-IR spectrum shows the pure vitreous V_2O_5 is characterized by a well-shaped band at 1020-1000 cm^{-1}. They also report that peaks appear at 1020-1000 cm^{-1}, for a mixture of Bi_2O_3 and V_2O_5, enhances as the amount of V_2O_5 increases in the mixture (Dimitrov, Dimitriev et al. 1994).

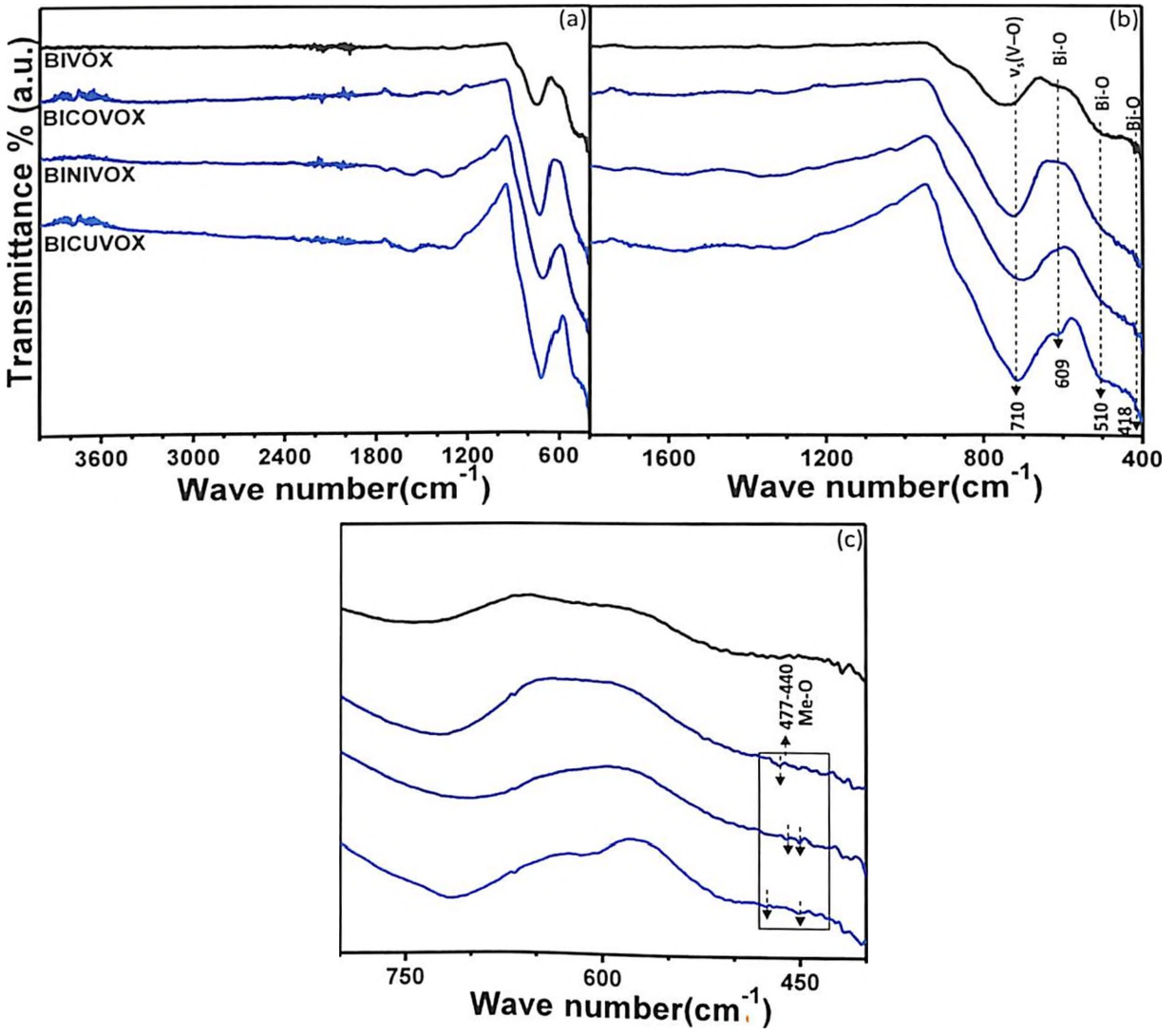

Figure 4-34: FTIR spectra for BIVOX, BICOVOX, BINIVOX, and BICUVOX -wash powders over the range of (a) 400-4000, (b) 400-1800, and (c) 400-800 cm^{-1} in order to identify the small Me-O peaks

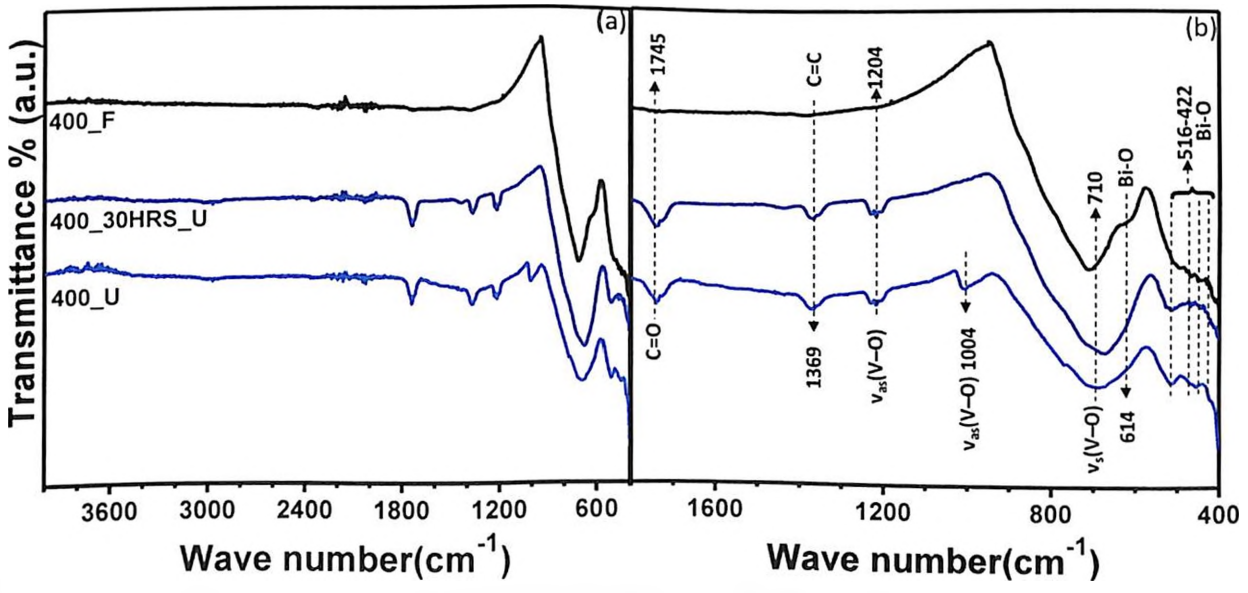

Figure 4-35: FTIR spectra of the BICOVOX -400- fresh, 30 hrs used and long time used over the range of (a) 400-4000, (b) 400-1800 cm^{-1}

Liu et al, (2003) synthesize $BiVO_4$ powders by hydrothermal method and characterize in order to study the effect of hydrothermal method on structure. The FT-IR spectra for $BiVO_4$ powders shows the peaks for asymmetric V–O stretching at 825-830 cm^{-1} and for symmetric V–O stretching at 710 cm^{-1} (Liu, Huang et al. 2009). Zhang et al, (2009) prepare $BiVO_4$ photo-catalysts via a surfactant-assisted hydrothermal method and characterize it. FT-IR show the peaks at 836, 820 cm^{-1} for asymmetric V–O stretching, at 730, 747, 700 cm^{-1} for symmetric V–O stretching and at 640, 666, 554, 518 cm^{-1} for Bi-O bonds (Zhang and Zhang 2009) [12]. Beg et al, (2010) study the structural and electrical properties of BIMEVOX catalysts synthesize by a microwave-assisted route. FTIR spectra for BICRVOX shows that Bi–O bond at 435 cm^{-1}, symmetric V–O stretching at 730 cm^{-1} and asymmetric V–O stretching at 996-860 cm^{-1} are appeared (Beg, Al-Alas et al. 2010). Beg et al, (2010) study the influence of calcium substitution on the phase transition and ionic conductivity of BICAVOX oxide, prepared by solid state reaction. FTIR of BICAVOX depict the presence of symmetric V–O stretching at 707-716 cm^{-1}, asymmetric V–O stretching at 1003, 971, 866 cm^{-1}, Bi–O bonds at 427, 540 cm^{-1} and Ca–O at 560 cm^{-1}(Beg, Hafeez et al. 2010). Fruth et al, (2006) examine the properties of Bi_2O_3. FT-IR spectra shows that Bi–O stretching modes appear at 614, 545, 506, 422 cm^{-1} (Fruth, Ianculescu et al. 2006). Reported literature reveals that V-O symmetric or asymmetric stretching vibration occurs in $BiVO_4$ and BIMEVOX cannot be characterized separately as wave-number for both lies in the same range. Similarly, vibrations of Bi–O bonds obtain in $BiVO_4$, Bi_2O_3 and BIMEVOX cannot be distinguished. However, peaks of α- and β-Bi_2O_3 can be identified separately. Bandoli et al, (1996) synthesize the pure and mixed phase Bi_2O_3 thin films by metal organic chemical vapour deposition. FTIR spectrum of the β and α- Bi_2O_3 phase shows four bands at 631 (medium (m)), 597 (m), 530 (strong (s)), and 508 cm^{-1} (s) with no strong transmittance in the 450-400 cm^{-1} region for β-phase. In contrast, the IR spectrum of the α phase shows a strong transmittance centred at 442 cm^{-1} with shoulders at 512 and 550 cm^{-1} (Bandoli, Barreca et al. 1996). Ardelean et al, (2008) also states the FT-IR spectra of crystalline α- and β-Bi_2O_3. α- Bi_2O_3 contains six absorption bands at: 380, 425, 465, 510, 540, and 595 cm^{-1}, specific to the vibrations of Bi–O bonds in BiO_6 octahedral units. For β-Bi_2O_3, the IR spectrum presents five absorption bands at: 350, 470, 520, 620, and 840 cm^{-1}, which are characteristic of the vibrations of Bi–O bonds in BiO_3 pyramidal units (Ardelean, Cora et al. 2008).

Figure 4.36 illustrates the FT-IR of BICOVOX-600 catalyst. Like BICOVOX-400_F catalyst, BICOVOX-600_F also shows bands at 614, 516 and 466 cm^{-1} however, it also shows more bands in the region of 516- 422 cm^{-1} as it contains both β and α-Bi_2O_3 phases as

mentioned in XRD. In addition, an extra peak appears at 823 cm^{-1}, assign to asymmetric V–O stretching. It is reported that asymmetric stretching with the vanadate anion of the perovskite like sheet are usually noticed in frequency regions 854–656 cm^{-1} (Murasheva, Poletaeva et al. 2010). Zhang et al, (2009) also mention that bands observed in the range of 820-836 cm^{-1} with weak shoulder are assigned to asymmetric V–O stretching vibrations and bands in the region of 700-747 cm^{-1} are specific to the vibrations of symmetric V–O stretching (Zhang and Zhang 2009). Analogous to BICOVOX-400_30HRS_U and BICOVOX-400_U catalysts, BICOVOX-600_30HRS_U and BICOVOX-600_U catalysts also show the presence of C=O (1745 cm^{-1}) stretching, C=C (1368 cm^{-1}) stretching, symmetric and asymmetric V–O stretching vibrations and β and α- Bi_2O_3 phases.

BICOVOX-800_F catalyst shows the similar nature as we observe for BICOVOX-400_F catalyst with respect to Bi_2O_3 phase. But it contains an additional band near 825 cm^{-1} as seen in BICOVOX-600_F catalyst. However, BICOVOX-800_30HRS_U and BICOVOX-800_U catalysts show very less transmittance in the range of 550-400 cm^{-1} as depicted in Figure 4.37. This reflects that transition from pure to secondary phases is very small for BICOVOX-800_30HRS_U and BICOVOX-800_U catalysts. The FTIR spectra are consistent with the XRD observations as it is found in XRD that it contains more amount of pure phase and no α-Bi_2O_3 phase is obtained. Analogous to BICOVOX-400_30HRS_U and BICOVOX-400_U catalysts, BICOVOX-800_30HRS_U and BICOVOX-800_U catalysts also show the presence of C=O (1745 cm^{-1}) stretching and C=C (1368 cm^{-1}) stretching. It can be seen that intensity of these two bands is more in BICOVOX_U catalysts compared to BICOVOX_30HRS_U. It is also noted that the intensity of these two bands is higher in BICOVOX-800_U compared to BICOVOX-400 and BICOVOX-600. Amount of C is difficult to quantify from FT-IR analysis.

In Figures 4.38-4.43, FT-IR spectra of BINIVOX and BICUVOX samples are shown. Similar to the spectra of BICOVOX, band at 1738 cm^{-1} in BINIVOX, 1735 cm^{-1} in BICUVOX for C=O carboxyl correspond to surrounding CO_2, 1368 cm^{-1} in BINIVOX, 1375 cm^{-1} in BICUVOX for C=C correspond to carbon, 1215 cm^{-1} in BINIVOX, 1213 cm^{-1} in BICUVOX for an asymmetric V-O stretching, 702 cm^{-1} with shoulders at ~790 and ~625 cm^{-1} in BINIVOX, 712 cm^{-1} shoulders at ~770 and ~585 cm^{-1} in BICUVOX for V-O symmetric stretching vibration, and 628, 521, 460, 423 cm^{-1} in BINIVOX, 624, 516, 466, 423 cm^{-1} in BICUVOX bands for B–O bond vibrations are observed at each of BINIVOX-30HRS_U, BICUVOX-30HRS_U and BINIVOX_U, BICUVOX_U catalysts calcined at 400, 600 and 800°C. Additional peak at 1005 cm^{-1} in BINIVOX, 1004 cm^{-1} in BICUVOX for V-O

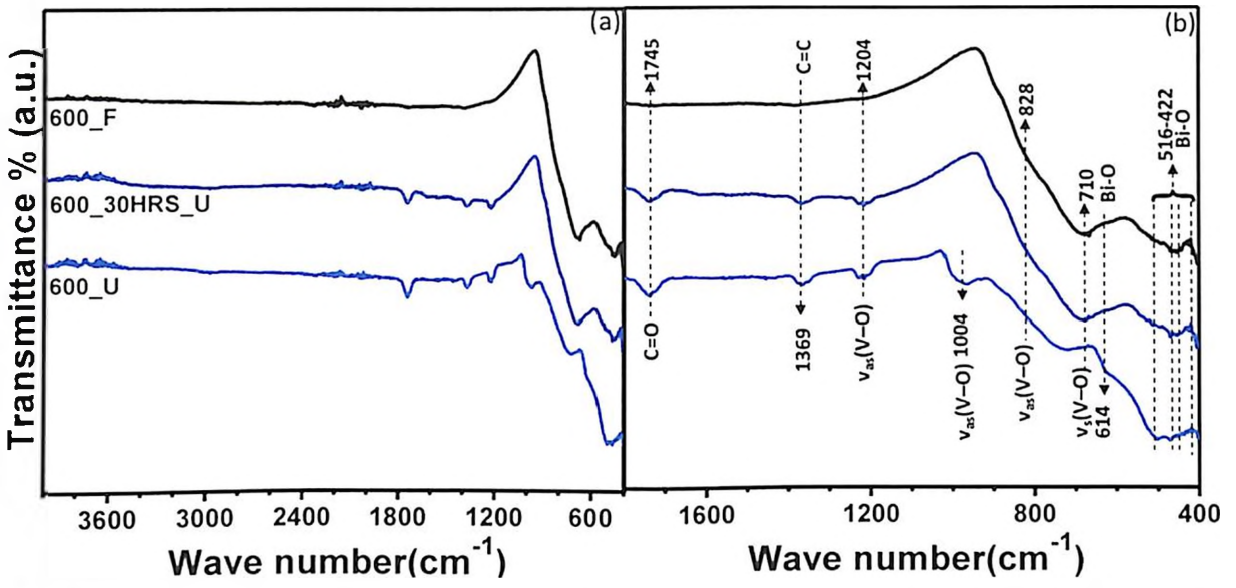

Figure 4-36: FTIR spectra of the BICOVOX-600 catalysts- fresh, 30 hrs used and long time used over the range of (a) 400-4000, (b) 400-1800 cm^{-1}

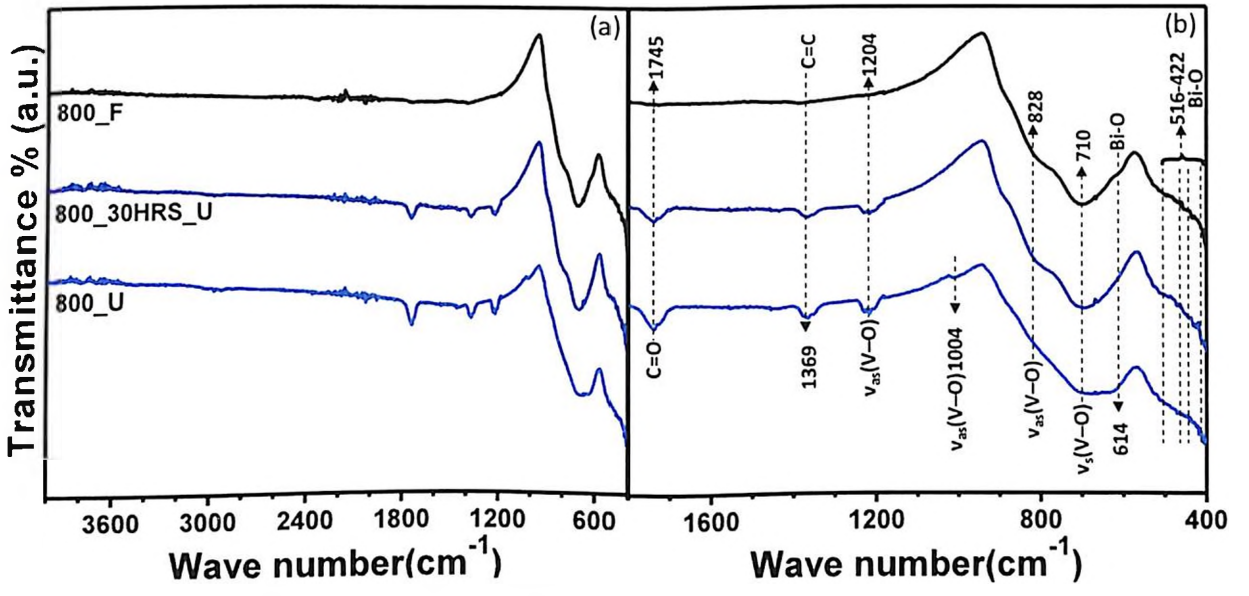

Figure 4-37: FTIR spectra of the BICOVOX-800 catalysts fresh, 30 hrs used and long time used over the range of (a) 400-4000, (b) 400-1800 cm^{-1}

stretching is also observed in BINIVOX_U, BICUVOX_U catalysts. However, for BINIVOX_U, and BICUVOX_F catalysts, no notable transmittance in the spectra up to 1000 cm^{-1} is observed which is in line with BICOVOX catalyst results.

The specific values of the wave number related to different peaks for our different BIMEVOX catalysts along with reported peak data in literature for Bi_2O_3, $BiVO_4$, BIMEVOX and for respective metals (ME-O) are given in Table 4.13 and Table 4.14, respectively.

4.1.2.4 *FESEM (Field Emission Scanning Electron Microscopy)*

Field emission scanning electron microscopy (FESEM) and X-ray energy dispersive spectroscopy (EDX) measurements have been performed to observe the micro-structural surface morphology, particle size distribution and elemental composition of the sample. The porous and flaky network of interconnected particles is a common morphology for the solution combustion synthesized BIMEVOX powder materials and it is well evident in the FESEM images (Figure 4.44 (a), (b), and (c)) of the wash catalysts (Roy and Fuierer 2009). The images reveal the sponge-like porous network of interconnected particles in the wash samples. Using these SEM surface images, the particle size distribution of the different BIMEVOX catalysts is estimated by measuring as many particles as possible and considering the following Equation:

Actual Length of a particle = (relative length in cm *unit value in μm)/ unit length in cm

The average particle sizes of (a) BICOVOX-wash, (b) BINIVOX-wash and (c) BICUVOX-wash catalysts are calculated to be 0.09-1.047 μm, 0.048-1.44 μm and 0.145-1.59 μm respectively as mentioned within Figure 4.44 (a), (c) and (d).

Figure 4.45 depicts the FESEM images for BICOVOX-400 (a) Fresh, (b) 30 hrs used and (c) long-time used catalysts. Similar to BICOVOX-wash catalyst, BICOVOX-400_F catalyst is also observed to yield a macroscopic morphology with porous network of interconnected particles with agglomeration occurring sparingly, that can also be seen in the particle size distribution. Figure 4.45 (a) shows the particle size distribution of BICOVOX-400_F catalyst and the calculated range is 0.26- 1.38 μm. After using catalyst for 30 hrs in the reactor, scale of agglomeration is increased and calculated particle size for BICOVOX-400_30HRS_U catalyst is 0.27-1.688 μm as mentioned in Figure 4.45 (c). However, in case of BICOVOX-400_U catalyst, particle size reduces and determined particle size is found in the range of 0.168-1.655 μm as shown in Figure 4.45 (e). FESEM image of BICOVOX-400_U also

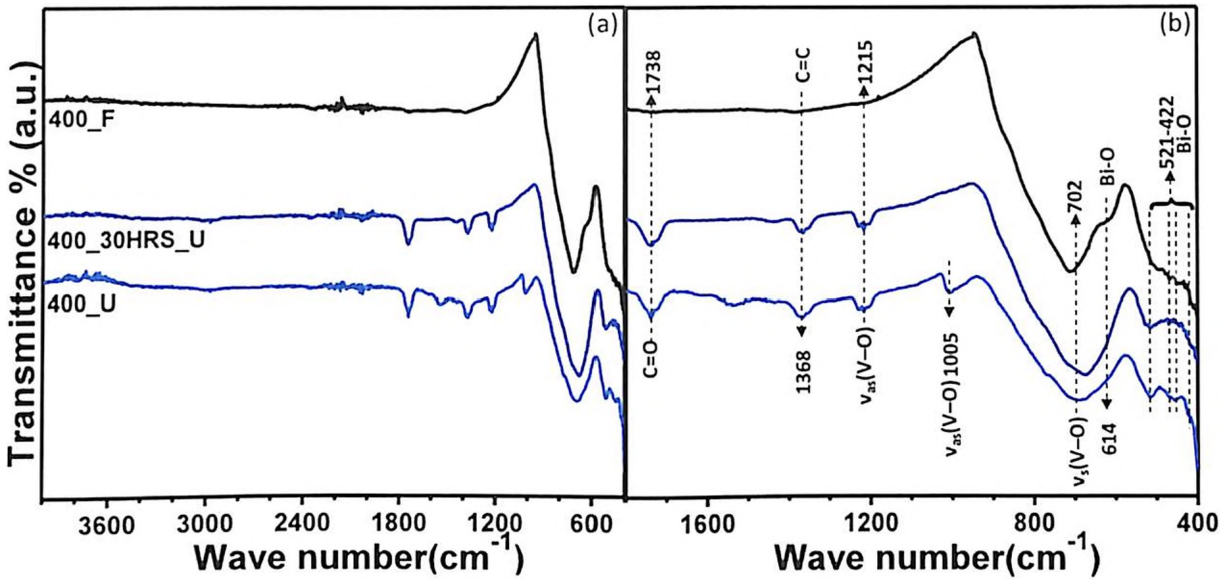

Figure 4-38: FTIR spectra of the BINIVOX-400 catalysts fresh, 30 hrs used and long time used over the range of (a) 400-4000, (b) 400-1800 cm^{-1}

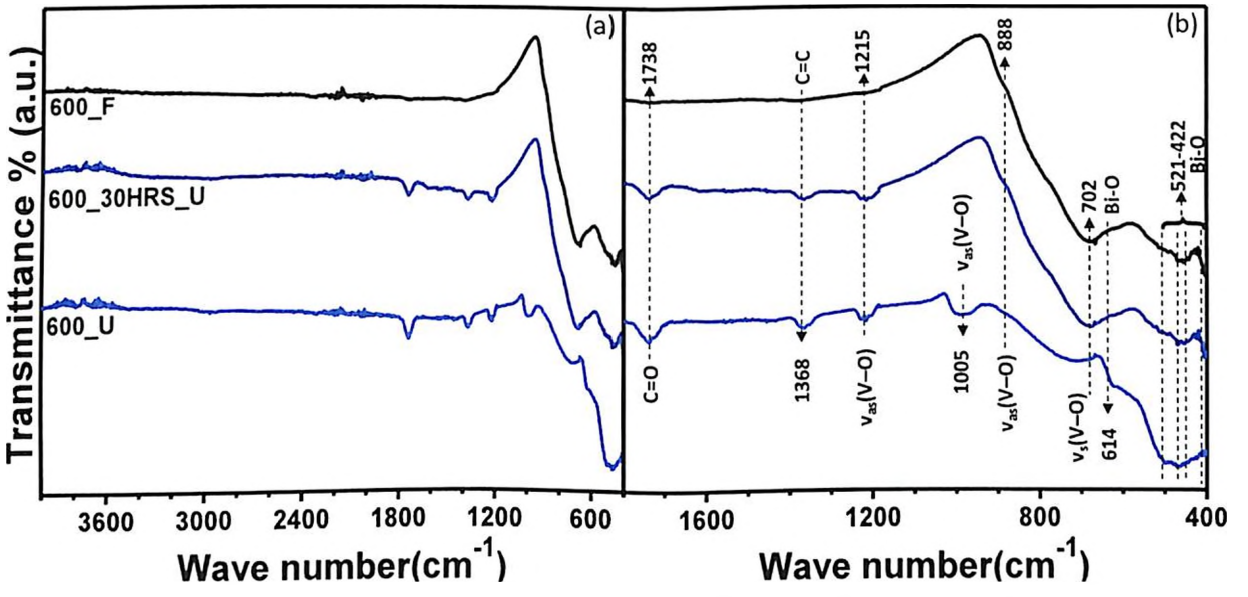

Figure 4-39: FTIR spectra of the BINIVOX-600 catalysts fresh, 30 hrs used and long time used over the range of (a) 400-4000, (b) 400-1800 cm^{-1}

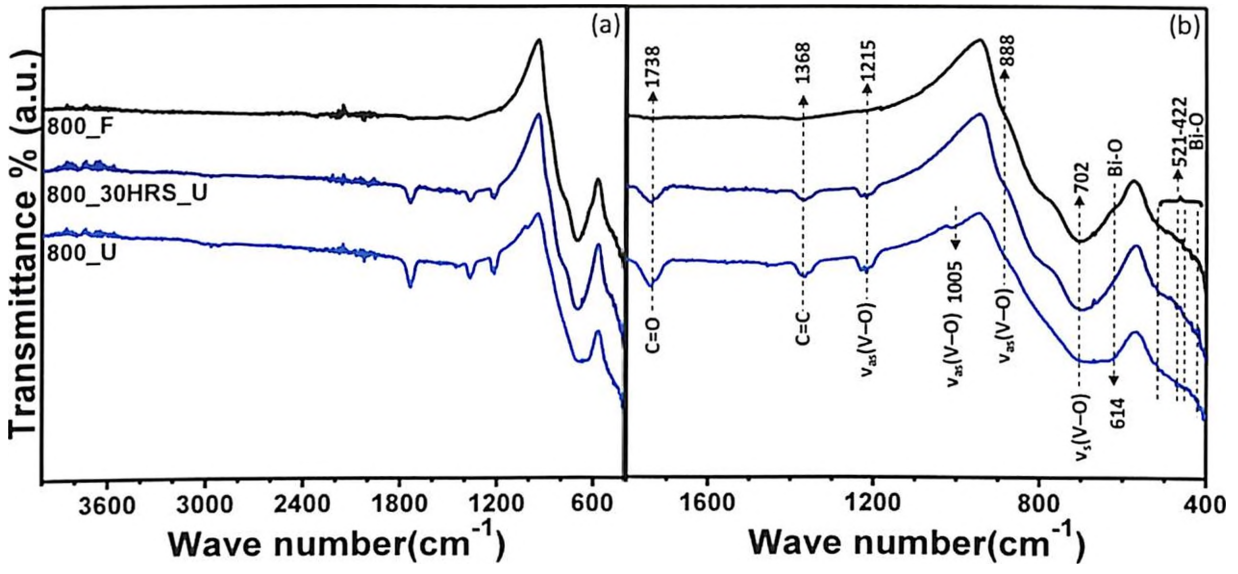

Figure 4-40: FTIR spectra of the BINIVOX-800 catalysts fresh, 30 hrs used and long time used over the range of (a) 400-4000, (b) 400-1800 cm^{-1}

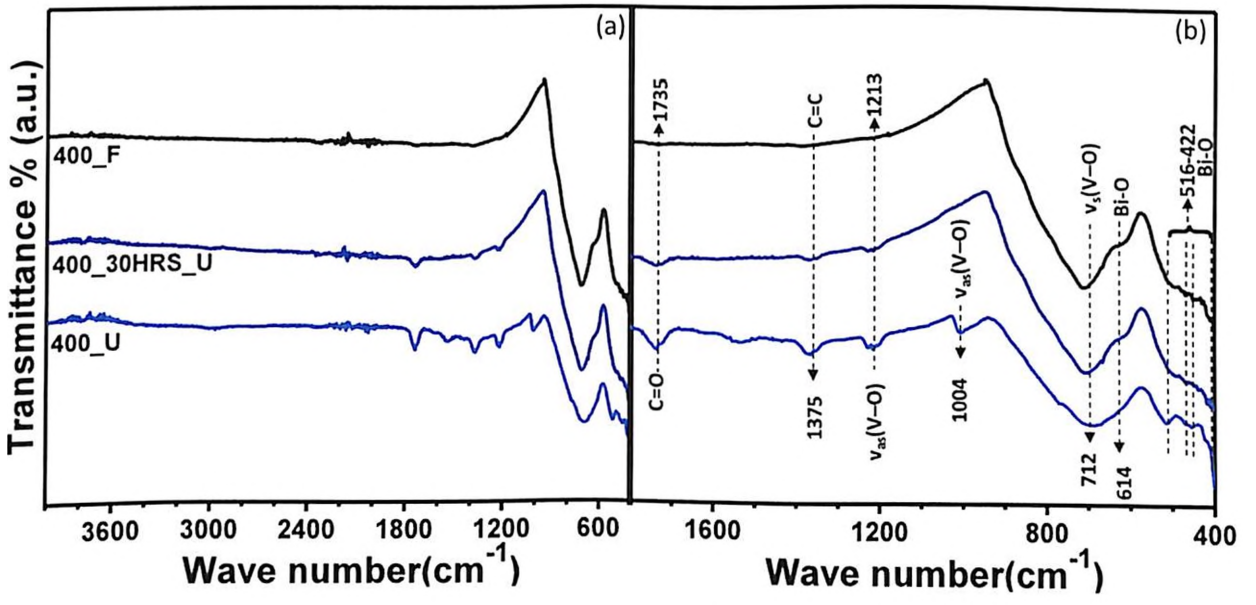

Figure 4-41: FTIR spectra of the BICUVOX-400 catalysts- fresh, 30 hrs used and long time used over the range of (a) 400-4000, (b) 400-1800 cm^{-1}

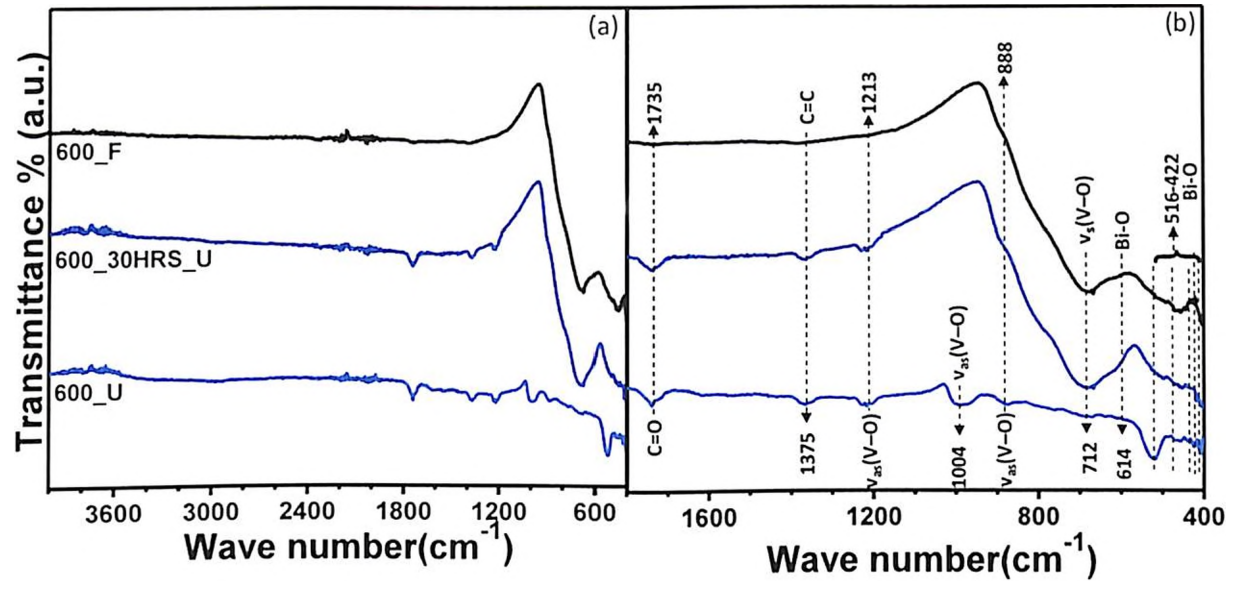

Figure 4-42: FTIR spectra of the BICUVOX-600 catalysts- fresh, 30 hrs used and long time used over the range of (a) 400-4000, (b) 400-1800 cm^{-1}

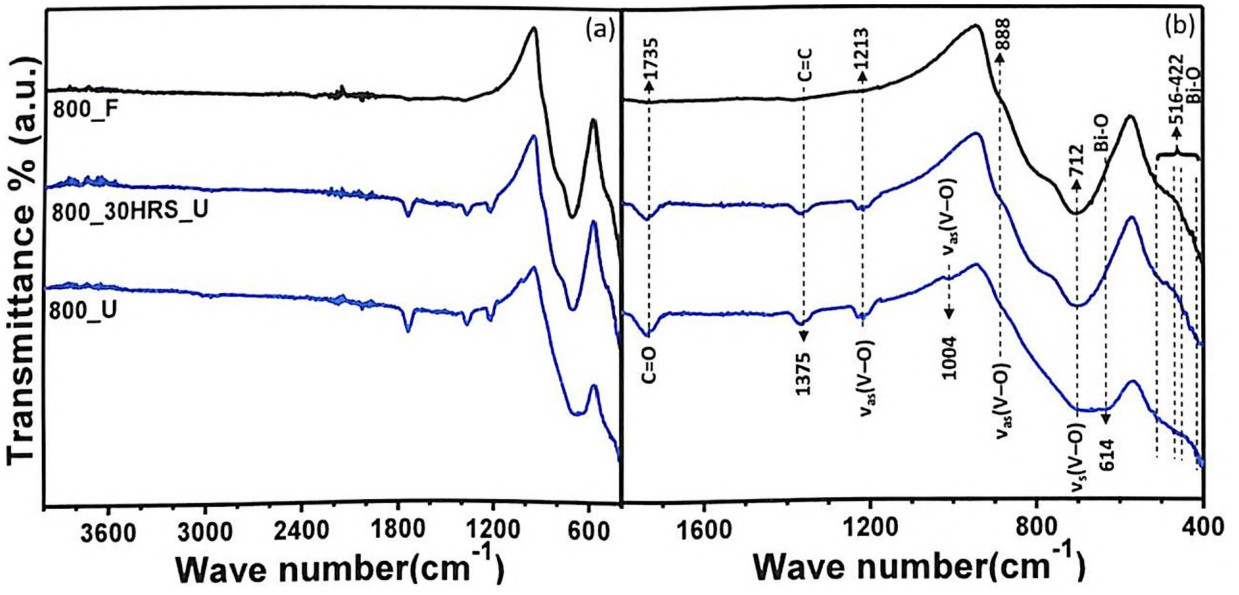

Figure 4-43: FTIR spectra of the BICUVOX-800 catalysts- fresh, 30 hrs used and long time used over the range of (a) 400-4000, (b) 400-1800 cm^{-1}

Table 4-13: Specific values of the wave number related to different peaks for various compound present in our different BIMEVOX catalysts

BIMEVOX (ME-Co, Ni, Cu)	C=O	C=C	v_s(V–O)	v_{as}(V–O)	α-Bi_2O_3	β-Bi_2O_3
BIMEVOX-Wash	1741	-	710	-	-	609, 510,418
BIMEVOX-400_F	-	-	702-712	-	-	614,516, 466
BIMEVOX-600_F	-	-	702-712	828-888	422	614,516, 472
BIMEVOX-800_F			702-712	828-888	-	614,516, 472
BIMEVOX-400_30HRS_U	1735-1745	1368-1375	702-712	1204-1215	423,442	614, 516, 472
BIMEVOX-600_30HRS_U	1735-1745	1368-1375	702-712	1204-1215,828-888	423, 442	614,516, 472
BIMEVOX-800_30HRS_U	1735-1745	1368-1375	702-712	1204-1215,828-888	-	614,516, 472
BIMEVOX-400_U	1735-1745	1368-1375	702-712	1204-1215,1004	423, 442	614,516, 472
BIMEVOX-600_U	1735-1745	1368-1375	702-712	1204-1215,1004, 828-888	423, 442	614,516, 472
BIMEVOX-600_U	1735-1745	1368-1375	702-712	1204-1215,1004, 828-888	-	614,516, 472

Table 4-14: Reported peak data in literature for Bi_2O_3, $BiVO_4$, BIMEVOX and for respective metals (ME-O)

Bi_2O_3	$BiVO_4$	BIMEVOX	Me-O
α-Bi_2O_3- 380, 425 and 445 β-Bi_2O_3- 350, 470, 540, 620, and 840 cm^{-1} **Cu-O**- 410, 500, and 610 cm^{-1} (Ardelean, Cora et al. 2008)	ν_{as}**(V–O)**- 827, 825 ν_s**(V–O)**- 710 (Liu, Wang et al. 2003)	**BIMEVOX (ME-Ga, Zr, Fe)** **V–O stretching** vibrations in VO_4 polyhedra- 870 **Bi–O bond** vibrations in BiO_6 octahedra- 470–540 cm^{-1} (Fortal'nova, Murasheva et al. 2008)	**Co-O-** 592, 554, 510–520, 580–610, 450 (Rameshbabu, Periasamy et al. 2001; Li, Qiu et al. 2016)
α-Bi_2O_3- 442(s) cm^{-1} β-Bi_2O_3- 631(m), 597(m), 530(s), and 508(s) cm^{-1} (Bandoli, Barreca et al. 1996)	**V–O**- 730, 1245 **Bi–O**- 445 cm^{-1} (Liu, Huang et al. 2009)	**BICRVOX:** **ν(Bi–O)**- 435 cm^{-1} ν_s**(V–O)**- 730 cm^{-1} ν_{as}**(V–O)**-996-860 cm^{-1} (Beg, Al-Alas et al. 2010)	
Bi-O-Bi and **Bi-O**- 400-600 **Symmetric bending vibrations of** BiO_3-470 (Balachander, Ramadevudu et al. 2013)	ν_s**(V–O)**- 836, 820 cm^{-1} ν_{as}**(V–O)**- 730, 747, 700 cm^{-1} **ν(Bi–O)**- 640, 666, 554, 518 cm^{-1} $\delta_S(VO_4^{3-})$- 506, 461 cm^{-1} (Zhang and Zhang 2009)	**BINAVOX:** ν_s**(V–O)**- 723 cm^{-1} ν_{as}**(V–O)**- 1060-820 cm^{-1} **ν(Bi–O)**- 431, 520 cm^{-1}(Beg, Al-Alas et al. 2010)	**Ni-O-** 600–700, 457, 510–520, 580–610 (Rameshbabu, Periasamy et al. 2001; Qiao, Wei et al. 2009)
Bi-O bonds in BiO_6 **groups**- 620 cm^{-1} (Chahine, Et-tabirou et al. 2004)		**BICAVOX:** ν_s**(V–O)**- 707-716 ν_{as}**(V–O)**- 1003, 971, 866 cm^{-1} **ν(Bi–O)**- 427, 540 **ν(Ca–O)**- 560 cm^{-1}(Beg, Hafeez et al. 2010)	
Bi–O stretching modes- 614, 545, 506, 422 cm^{-1} (Fruth, Ianculescu et al. 2006)		**BIBAVOX:** ν_s**(V–O)**- 716-743 ν_{as}**(V–O)**- 986, 813, 881 cm^{-1} **ν(Bi–O)**- 451-424, 520 cm^{-1} **ν(Ba–O)**- 560 cm^{-1}(Beg, Hafeez et al. 2010)	**Cu-O-** 601,508, 450-490 (Radhakrishnan and Beena 2014)
Bi–O–Bi- 825 cm^{-1} **Bi–O**- 430 cm^{-1} (Li 2006)		**BIMEVOX (ME-Ba, Sr)** **Ba – O – V**- 864 Symmetric modes of **V – O – V bonds**- 727, 823 cm^{-1} **Bi-O**- 533 cm^{-1} (Gupta and Singh 2015)	
Bi–O bonds in BiO_6 **octahedra**- 850 cm^{-1} (Zhang, Wang et al. 2006)			
Bi_2O_3-V_2O_5: V_2O_5- 1020, 930 **Bi-O**- 480 cm^{-1} (Dimitrov, Dimitriev et al. 1994)			

confirms the decrease in particle size as depicted in Figure 4.45 (e) and (f). XRD reveals the breaking of pure phase into secondary phases which is not reflected in the particle site of XRD data. However, it is well evident in FESEM. No carbon is seen in the FESEM image of BICOVOX-400_30HRS_U catalyst in Figure 4.45 (c) and (d). However, very negligible weight loss due to carbon is seen in DTGA spectrum of BICOVOX-400_30HRS_U catalyst, which reflects the presence of small amount of amorphous carbon. FESEM analysis for the deposited carbon reveals filamentous coke over BICOVOX-400_U catalyst in Figures 4.45 (e) and (f). This is also supported by DTGA spectrum of BICOVOX-400_U catalyst.

FESEM images of BICOVOX-600 (a-b) Fresh, (c-d) 30 hrs used and (e-f) long-time used catalysts are illustrated in Figure 4.46. Increase in particle size is seen for BICOVOX-600_F catalyst in comparison with the BICOVOX-400_F catalyst, as particle size increases with increase in calcination temperature. Several particles with different sizes are seen; the presence of a predominantly porous region is evident in Figure 4.46 (a-b). Calculated particle size distribution is found in the range of 0.2-1.92 μm as shown in Figure 4.46 (a) and Table 4.15. After 30 hrs of reaction, particles start agglomerating and calculated particle size for BICOVOX-600_30HRS_U catalyst is 0.28-2.39 μm as mentioned in Figure 4.46 (c). BICOVOX-600_U catalyst shows a similar trend of decreasing particle size (0.21-2 μm) as observe for BICOVOX-400_U catalysts in Figure 4.46 (e). FESEM images of BICOVOX-600_U catalyst also show the deposition of filamentous carbon over catalyst, as shown in Figure 4.46 (e-f). The filamentous carbon is highly irregular in structure. This demonstrates that they are not generated by the direct involvement of surface metal but rather they grow with mechanisms involving a surface containing both acid and base functionality (Dieuzeide, Laborde et al. 2016).

The FESEM micrographs in Figure 4.47 (a-b) reveal the microstructure of the BICOVOX-800_F catalyst which is the final stage of the sintering process. Along with particle coarsening, a decrease in the number of pores and coalescence into bigger ones takes place, with increase in calcination temperature. The sequence of SEM images shown in Figures 4.44–4.47 bears this reaction out. Calculated particle size of BICOVOX-800_F catalyst lies in the range of 0.52-5.5 μm as mentioned in Figure 4.47 (a). Compared to fresh catalysts, (Figure 4.47 (c-d) and (e-f)), it can be revealed that all the catalysts surfaces appear to be covered by coke deposition to some degree. Agglomeration of particles is clearly observed for BICOVOX-800_30HRS_U catalyst and calculated particle size is 0.55-8.79 μm as shown in Figure 4.47 (c). No carbon is seen in FESEM images of BICOVOX-800_30HRS_U catalyst as the amount of carbon calculated from DTGA is very less, similar

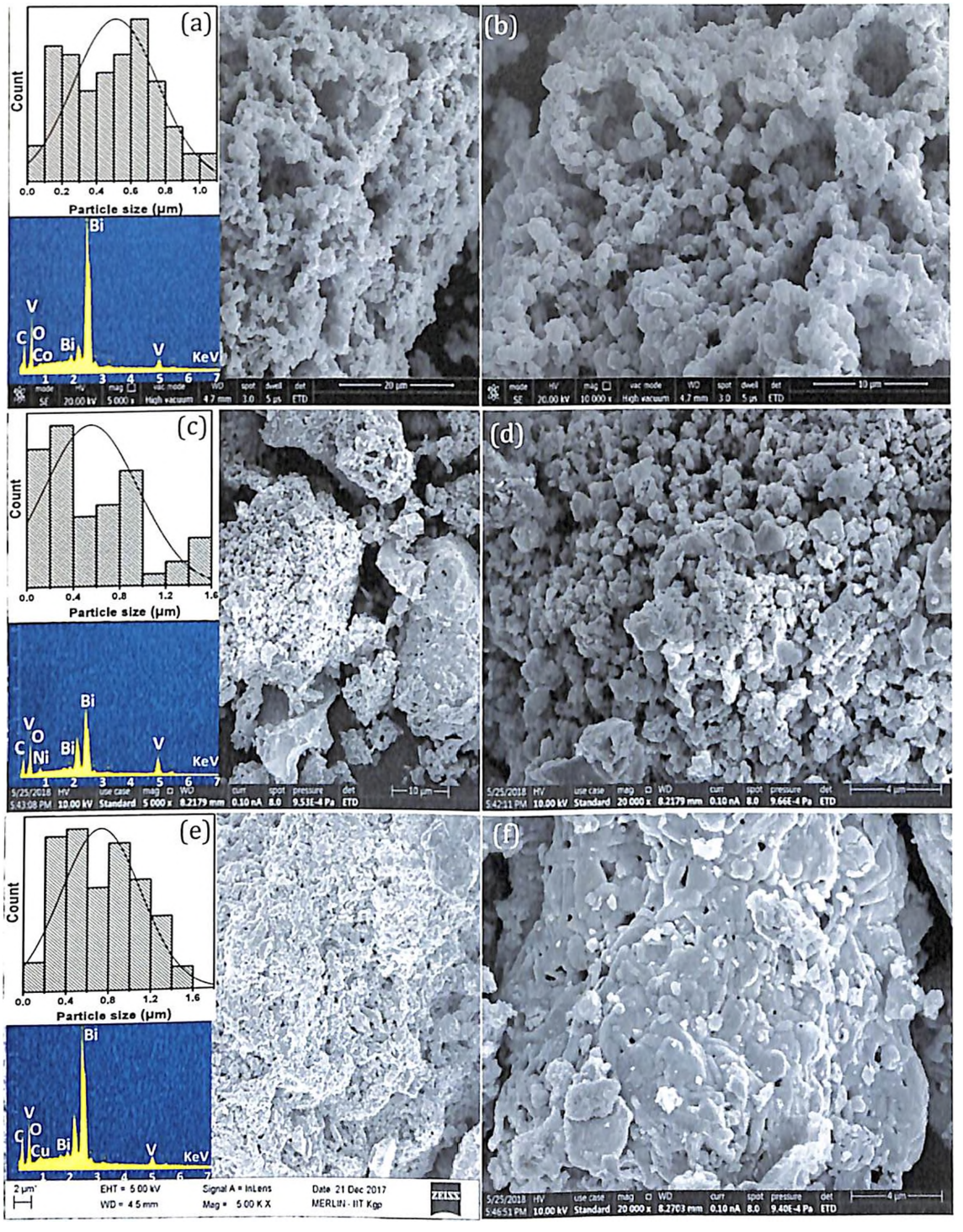

Figure 4-44: FESEM images of the (a-b) BICOVOX (c-d) BINIVOX and (e-f) BICUVOX- Wash catalysts along with their partisize distribution and EDX spectrum

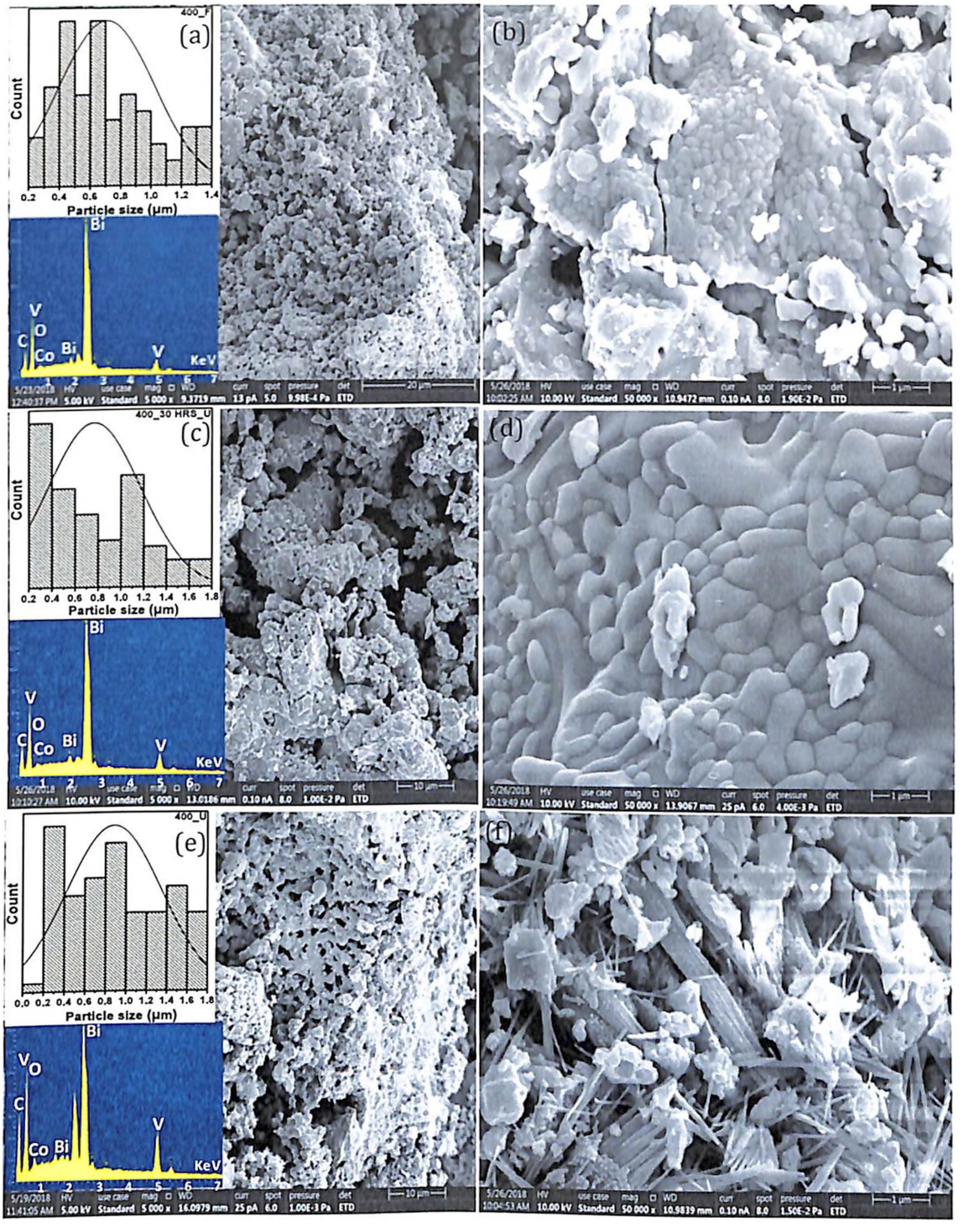

Figure 4-45: FESEM images of the BICOVOX catalysts calcined at 400°C (a-b) Fresh (c-d) 30 hrs used (e-f) Long time used catalysts along with their partisize distribution and EDX spectrum

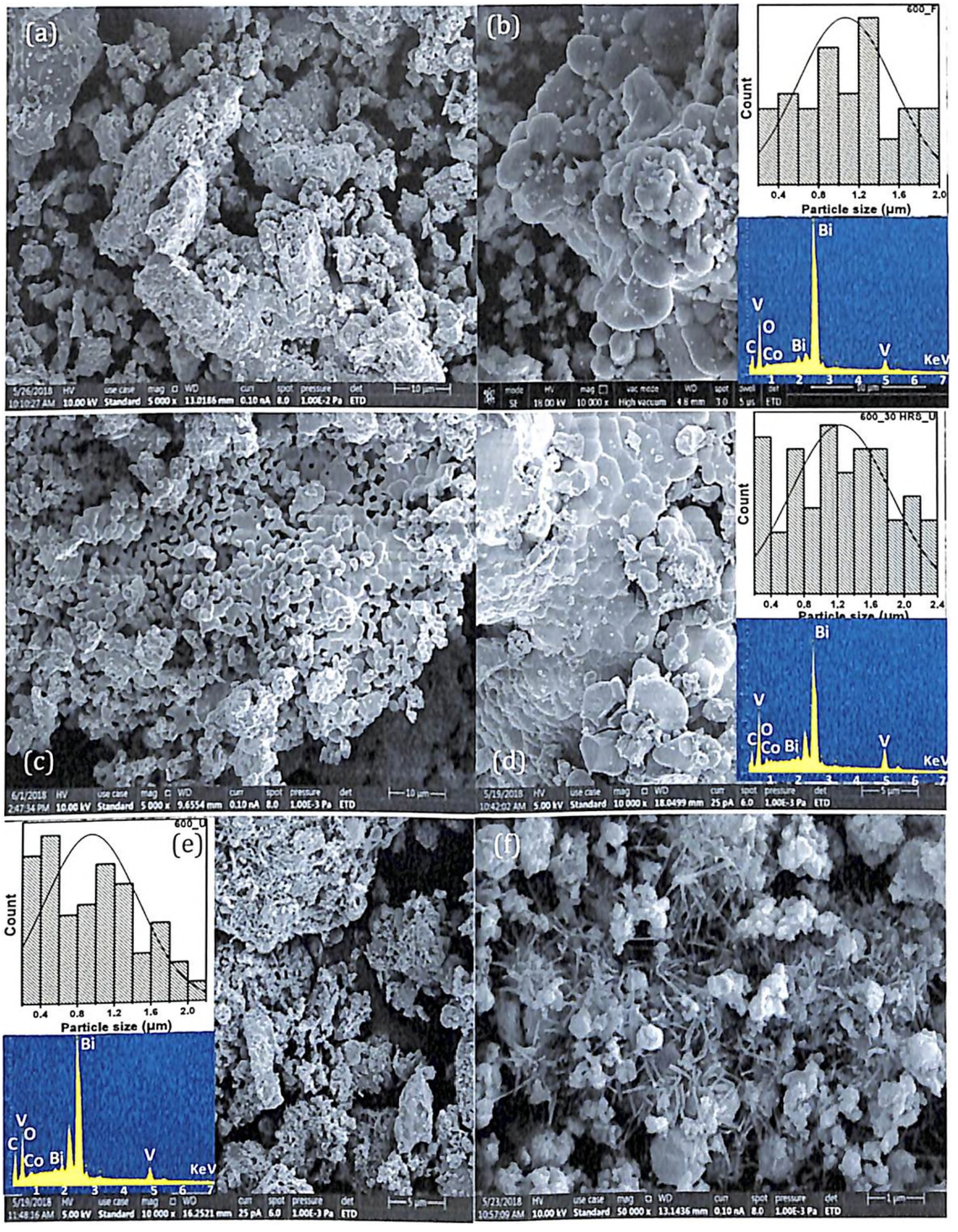

Figure 4-46: FESEM images of the BICOVOX catalysts calcined at 600°C (a-b) Fresh (c-d) 30 hrs used (e-f) Long time used catalysts along with their partisize distribution and EDX spectrum

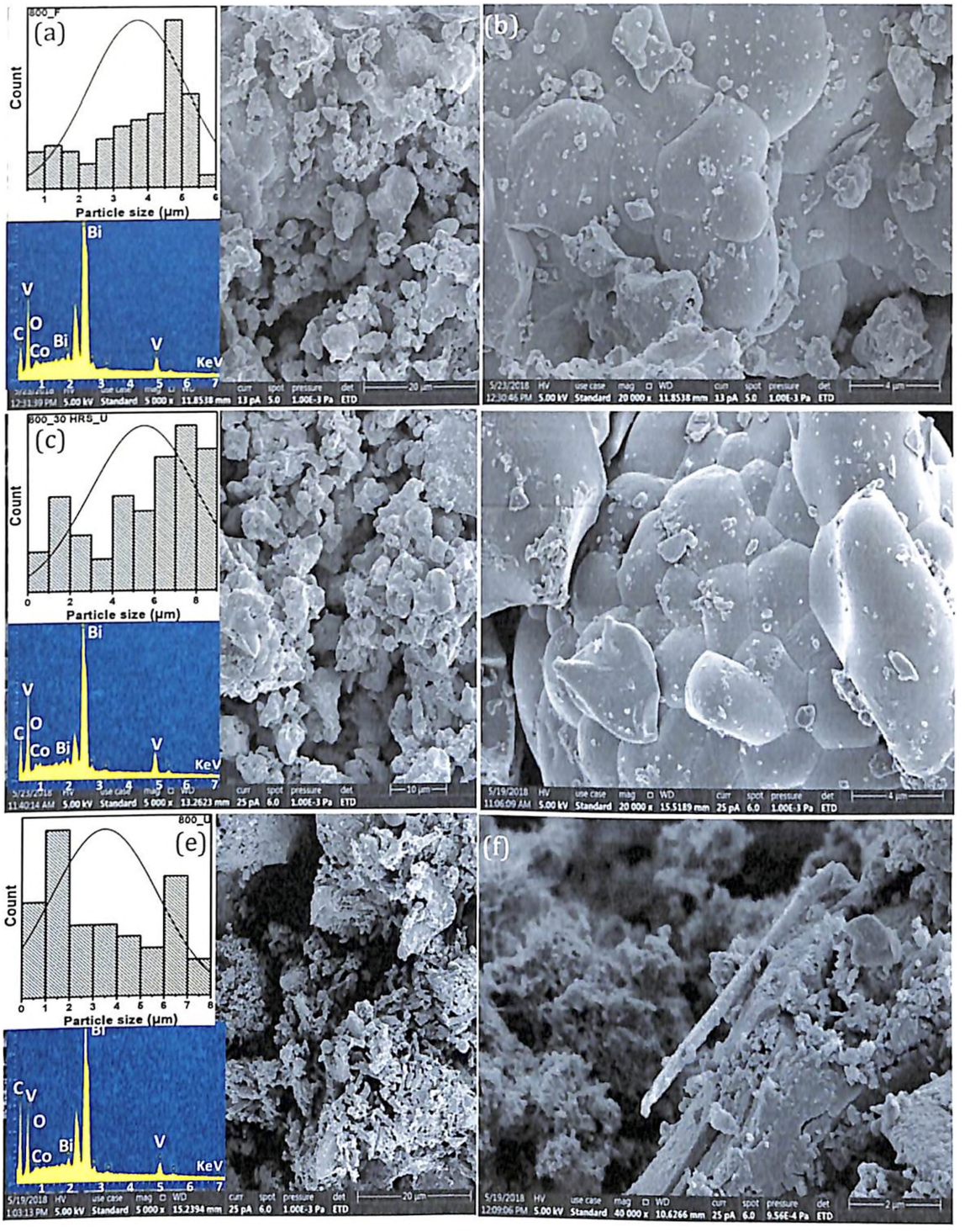

Figure 4-47: FESEM images of the BICOVOX catalysts calcined at 800°C (a-b) Fresh (c-d) 30 hrs used (e-f) Long time used catalysts along with their partisize distribution and EDX spectrum

to that of BICOVOX-400_30HRS_U and BICOVOX-600_30HRS_U catalysts. However, FESEM images of BICOVOX-800_U catalyst indicate the presence of two species; graphitic carbon and filamentous carbon as depicted in Figure 4.47 (e-f). Obtain results are in the similar line of DTGA results. DTGA spectrum of BICOVOX-800_U catalyst also shows the presence of two types of carbon as we observe an exothermic peak corresponding to weight loss in TGA in the range of 350-750°C. The graphitic carbon is the main form of coke for catalysts, which may be the reason for catalyst deactivation (Ding, Wang et al. 2016). BICOVOX-800_U catalyst shows a similar trend of decreasing particle size (0.49-7.86 μm) as observed for BICOVOX-400_U and BICOVOX-600_U catalysts in Figure 4.47 (e-f).

Particle size of BINIVOX-400_F catalysts is higher than that of the BINIVOX-wash catalyst. Figure 4.48 depicts the FESEM images of BINIVOX (a-b) fresh, (c-d) 30 hrs used and (e-f) long-time used catalysts. Macroscopic morphology is seen with porous network of interconnected particles in BINIVOX-400_F catalyst. Calculated particle size distribution is 0.089-1.64 μm as observed in Figure 4.48 (a). Like BICOVOX-400_30HRS_U catalyst, agglomeration of particles is observed in BINIVOX-400_30HRS_U as represented in Figure 4.48 (c-d) and evaluated particle size is 0.202-2.1 μm as indicated in Figure 4.48 (c). Morphology of BINIVOX-400_U catalyst is illustrated in Figure 4.48 (e-f). This image reflects the breaking of particles and presence of whisker carbon which appears usually below ~700°C. Obtained results are consistent with the DTGA analysis. The average particle size of BINIVOX-400_U catalysts is 0.069-1.848 μm, as mentioned in Figure 4.48 (e).

Correspondingly, growth in particle size of BINIVOX-600_F with respect to BINIVOX-400_F catalysts is recognized in Figure 4.49 (a-b). Heat treatment eventually leads to increase in the content of pure phase as analyzed by XRD and that is accountable for the growth in particle size with temperature. The ceramic microstructure is characterized by pores, is small, interconnected and with particle sizes between 0.186-1.77 μm as shown in Figure 4.49 (a). The particle size increases with the use of catalyst for 30 hrs in the reactor and it lies between 0.24-2.163 μm as mentioned in Figure 4.49 (c). FESEM images of BINIVOX-600_30HRS_U also confirm the agglomeration of particles and no carbon is identified in picture as depicted in Figure 4.49 (c-d). DTGA spectrum shows presence of very less amount of amorphous carbon and small quantity of amorphous carbon cannot be visualized in the FESEM images. Similar to BICOVOX-600_U, FESEM images of BINIVOX-600_U catalyst also confirm the breaking of phases and deposition of filamentous carbon, as shown in Figure 4.49 (e-f). Particle size of BINIVOX-600_U catalyst is between 0.215-1.95 μm, as represented in Figure 4.49 (e).

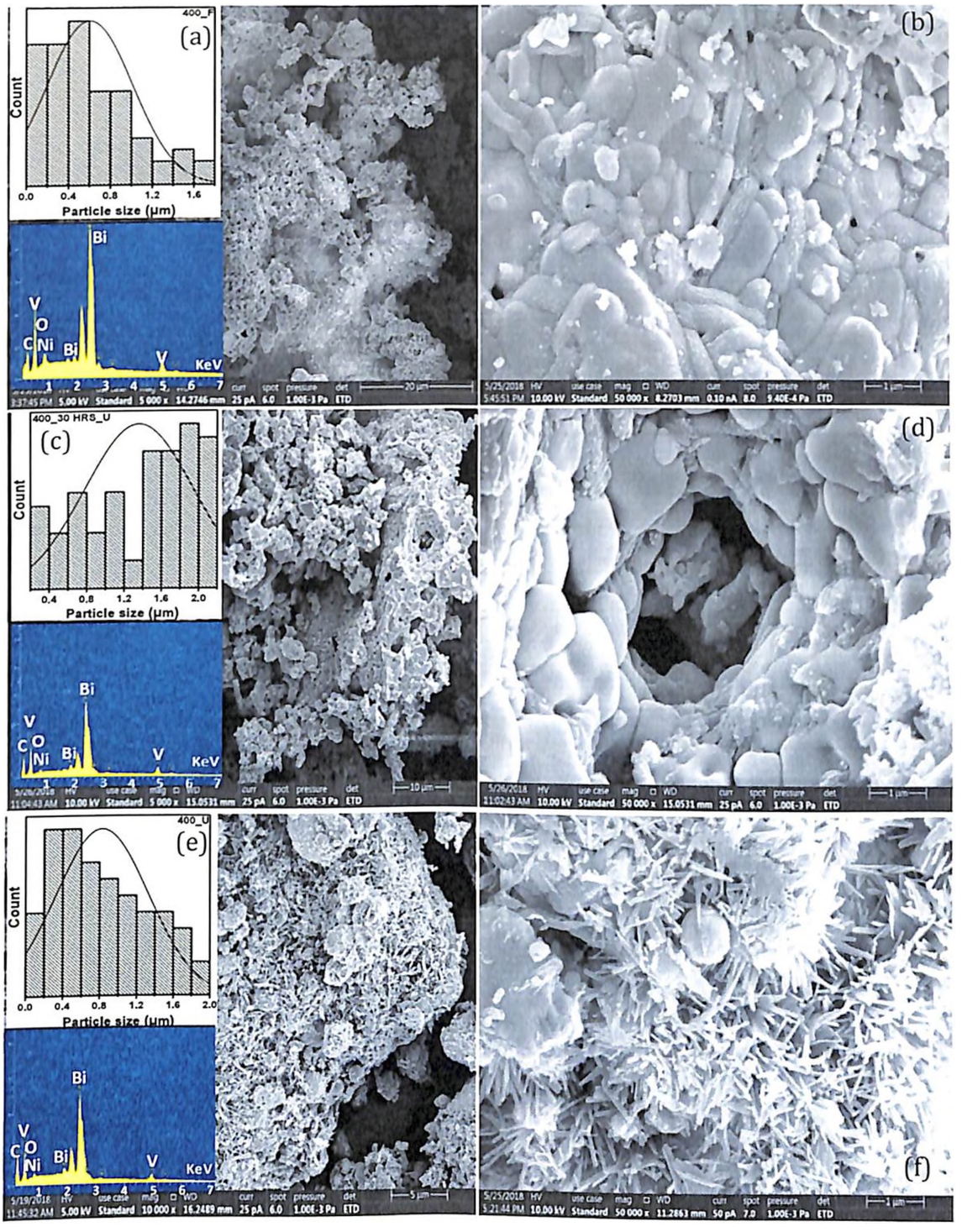

Figure 4-48: FESEM images of the BINIVOX catalysts calcined at 400°C (a-b) Fresh (c-d) 30 hrs used (e-f) Long time used catalysts along with their partisize distribution and EDX spectrum

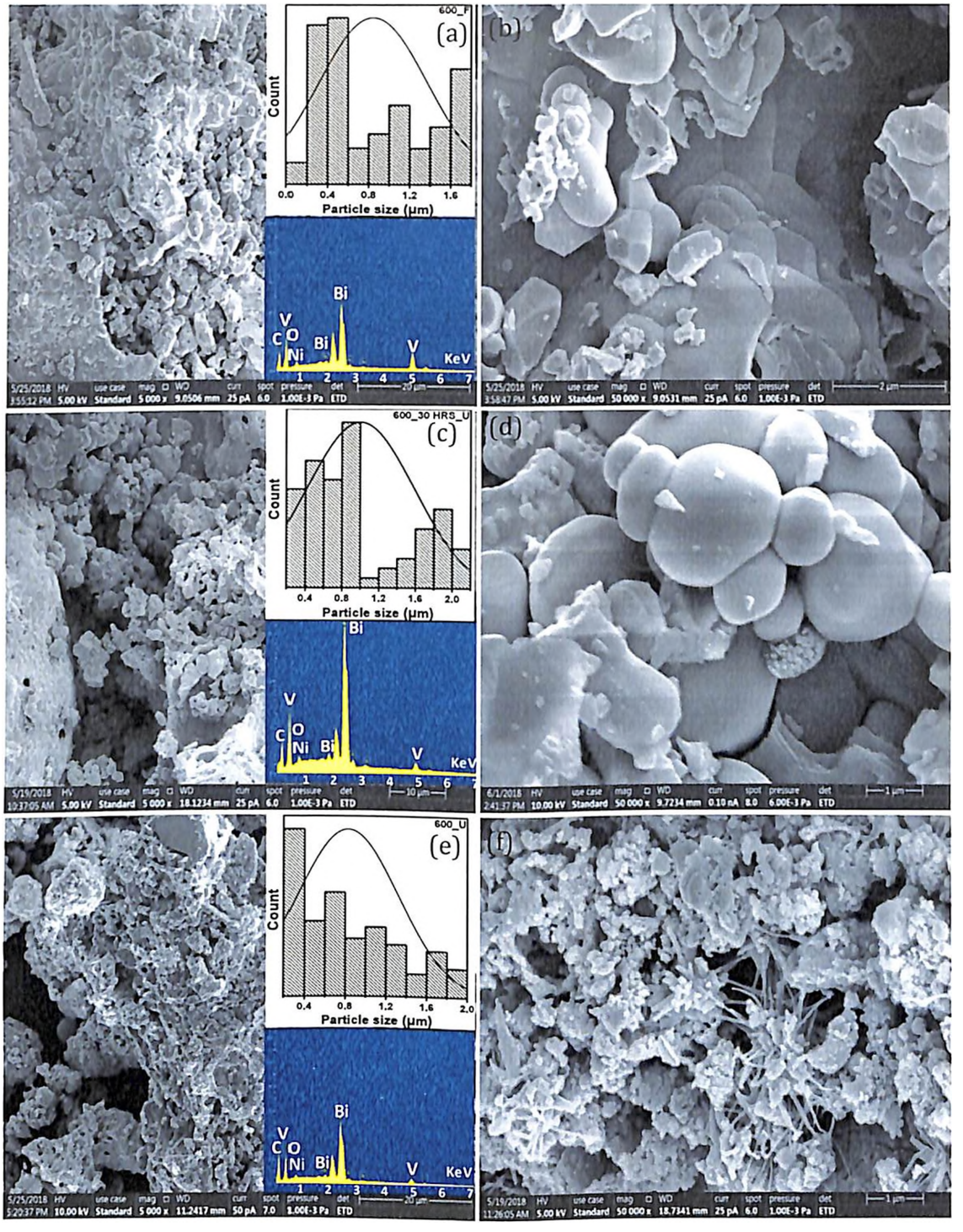

Figure 4-49: FESEM images of the BINIVOX catalysts calcined at 600°C (a-b) Fresh (c-d) 30 hrs used (e-f) Long time used catalysts along with their partisize distribution and EDX spectrum

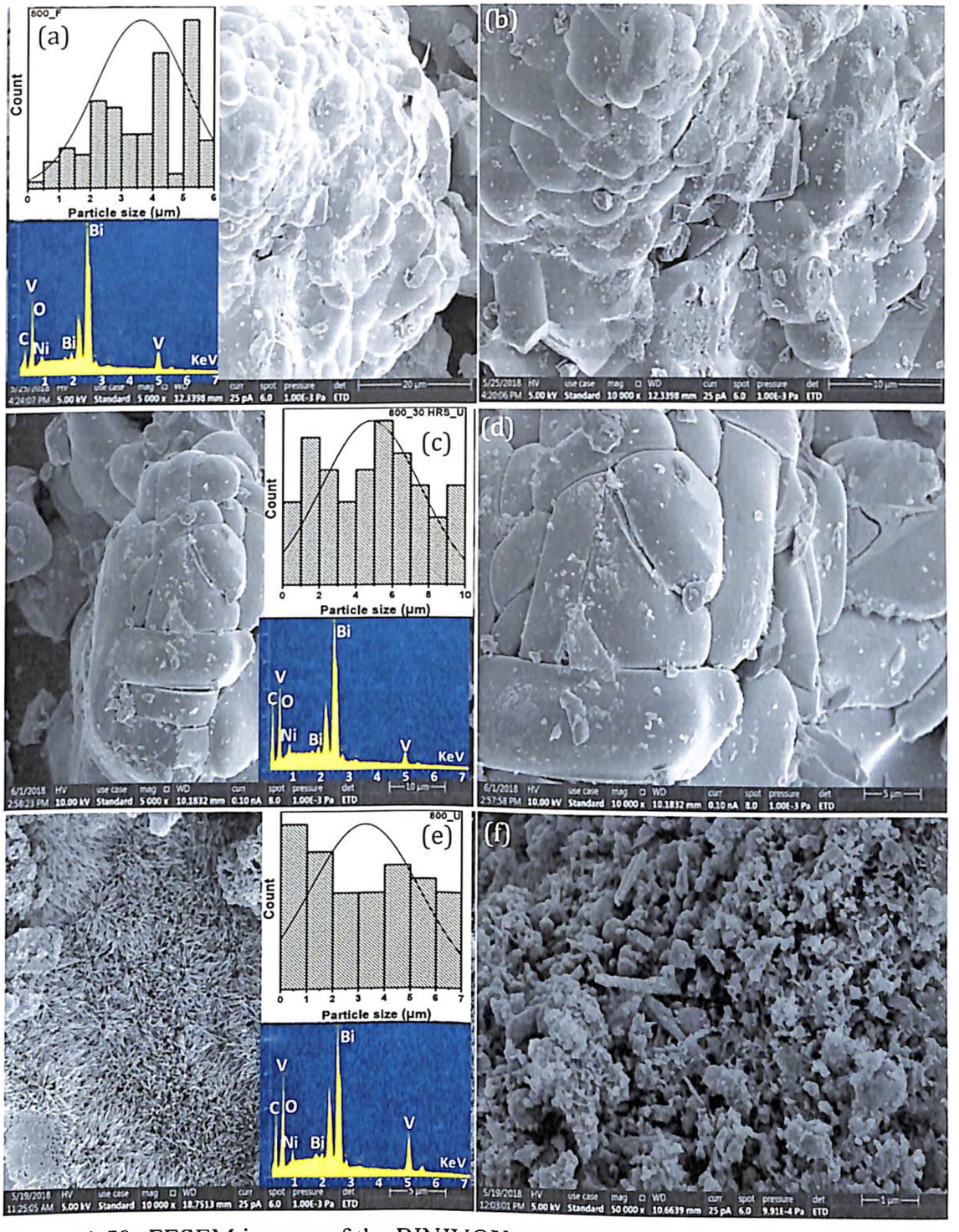

Figure 4-50: FESEM images of the BINIVOX catalysts calcined at 800°C (a-b) Fresh (c-d) 30 hrs used (e-f) Long time used catalysts along with their partisize distribution and EDX spectrum

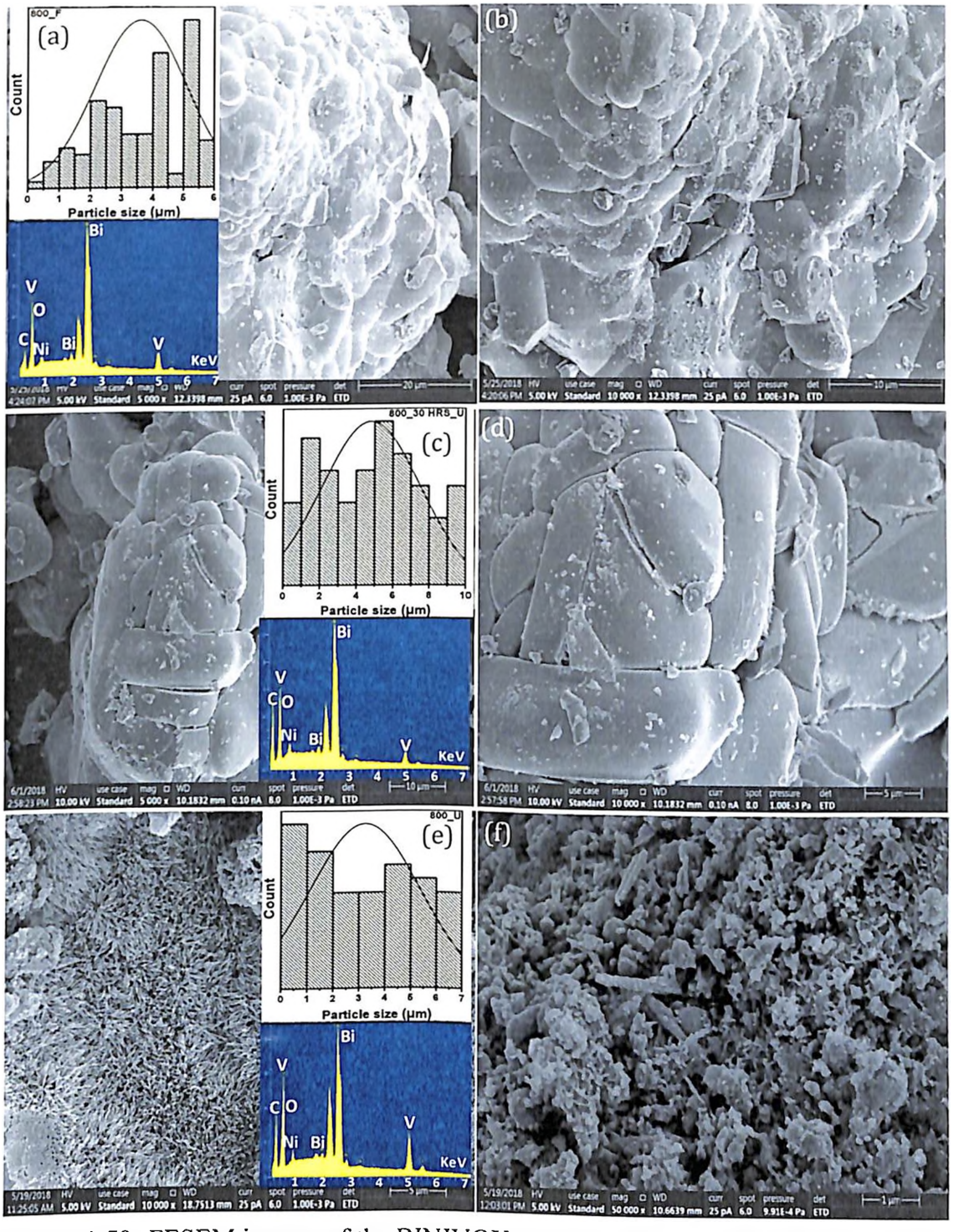

Figure 4-50: FESEM images of the BINIVOX catalysts calcined at 800°C (a-b) Fresh (c-d) 30 hrs used (e-f) Long time used catalysts along with their partisize distribution and EDX spectrum

An increase in grain size is clearly evident when the sintering temperature increased to 800 as shown in Figure 4.50 (a-b) and calculated particle size is 0.48-5.65 μm as mentioned in Figure 4.50 (a) for BINIVOX-800_F catalyst. The same trend of increasing particle size is seen in BINIVOX-800_30HRS_U catalyst due to agglomeration as depicted in Figure 4.50 (c-d) with average particle size of 0.67-9.45 μm as notified in Figure 4.50 (c). After using the catalysts for a long time, filamentous coke can transform into non-filamentous coke or graphite carbon which is clearly visible in the FESEM images (Figure 4.50 (e-f)) of BINIVOX-800_U catalyst. Reduction in particle size is also evident in the images and calculated particle size is 0.28-6.95 μm (Figure 4.50 (e)).

Like BICOVOX-400_F and BINIVOX-400_F, BICUVOX-400_F catalyst also shows the same morphology and increase in particle size with respect to wash catalyst which is clearly evident in the FESEM images (Figure 4.51 (a-b)). Determined particle size for BICUVOX-400_F catalyst is in the range of 0.145-1.59 μm as notified in Figure 4.51 (a) which is higher than that of the BICOVOX-400_F and BINIVOX-400_F catalysts. After 30 hrs of reaction, BICUVOX-400_30HRS_U catalyst shows higher rate of agglomeration in comparison to the BICOVOX-400_30HRS_U and BINIVOX-400_30HRS_U catalyst. FESEM images (Figure 4.51 (c-d)) of BICUVOX-400_30HRS_U also show the presence of carbon, which is not visible in case of BICOVOX-400_30HRS_U and BINIVOX-400_30HRS_U catalysts and that could be due to bigger particle size of BICUVOX-400_30HRS_U. Observed particle size for BICUVOX-400_30HRS_U is 0.435-3.91 μm as illustrated in Figure 4.51 (c). Similar trend of decreasing particle size is observed in BICUVOX-400_U catalyst as compared to BICUVOX-400_30HRS_U catalyst and calculated particle size is 0.27-2.72 μm as shown in Figure 4.51 (e). FESEM images (Figure 4.51 (e-f)) of BICUVOX-400_U catalyst show the presence of amorphous carbon and graphitic-like carbon which is in line with the DTGA results. Generally, oxidation of amorphous carbon and graphitic-like carbon occurs in the range of 300–800°C, which is evident in the DTGA spectrum of BICUVOX-400_U catalyst.

Analogous to BICOVOX-600_F and BINIVOX-600_F catalysts, particles grow in BICUVOX-600_F catalyst with respect to BICUVOX-400_F with the presence of a predominantly porous region as observed in Figure 4.52 (a-b) and computed particle size (Figure 4.52 (a)) is found to be in the range of 0.307-3.08 μm. Similar to BICOVOX and BINIVOX, FESEM pictures (Figure 4.52 (c-d)) of BICUVOX-600_30HRS_U catalyst also shows the agglomeration of particles and determined particles size range is 0.18-5.27 μm, as mentioned in Figure 4.52 (c). BICUVOX-600_U catalyst shows a similar trend of decreasing particle size (0.1875-4.75 μm) as observe for BICUVOX-400_U catalysts in Figure 4.52 (e).

FESEM images of BICUVOX-600_U catalyst also show the deposition of filamentous carbon over the catalyst, as represented in Figure 4.52 (e-f). The filamentous carbon is highly irregular in structure. It is known that filamentous carbon does not pose a severe threat to catalytic activity by encapsulating the active sites in conditions of high H_2/CO or steam/hydrocarbon ratio, as compared to graphite carbon (Song, Han et al. 2016; Duan, Wang et al. 2017).

The FESEM micrographs in Figure 4.53 (a-b) reveal the microstructure of the BICUVOX-800_F catalyst which is the final stage of the sintering process. Analogous to BICOVOX-800_F and BINIVOX-800_F catalysts, particle coarsening, a decrease in the number of pores and coalescence into bigger ones take place in BICUVOX-800_F catalyst with increase in annealing temperature. Calculated particle size of BICUVOX-800_F catalyst lies in the range of 0.8-10 μm as mentioned in Figure 4.53 (a). FESEM and DTGA analysis reveal that compared to fresh catalysts, all the catalysts surfaces appear to be covered by coke to some extent. Similar to BICOVOX-800_30HRS_U and BINIVOX-800_30HRS_U catalysts, agglomeration of particles is clearly observed in the FESEM images (Figure 4.53 (c-d)) for BICUVOX-800_30HRS_U catalyst and calculated particle size is 0.96-12.8 μm as represented in Figure 4.53 (c). FESEM images of BICUVOX-800_U catalyst indicate the presence of graphitic carbon and carbon nanotubes i.e. whiskers and that destroys the catalyst irreversibly as depicted in Figure 4.53 (e-f) (Rostrup-Nielsen and Trimm 1977). Obtained results are in line with DTGA results. DTGA spectrum of BICUVOX-800_U catalyst also shows the presence of two types of carbon as we get exothermic peak corresponding to weight loss in TGA in the range of 350-750°C. It also shows similar trend of decreasing particle size (0.79-9.27 μm) as observe for BICUVOX-400_U and BICUVOX-600_U catalysts in Figure 4.53 (e). XRD and DTGA analysis are consistent with the results obtain from FESEM of different catalysts.

In most of the reported works, BIMEVOX catalysts are prepared by solid state technique. Steil et al, (2005) synthesize the BICUVOX.10 and BICOVOX.10 catalysts by classical solid-state technique for oxygen separators or catalytic dense membrane reactors. SEM micrographs corresponding to BICOVOX.10 and BICUVOX.10 powders show the porous network of particles and report the particle size for both the catalysts is in the range of 15 μm (Steil, Ratajczak et al. 2005). Ceramic solid solutions on the base of bismuth vanadate with Ga, Fe, Cu metal are prepared by Politova et al, (2011) using conventional solid-state reaction method to investigate their structure, phase transitions, dielectric and transport properties. Obtained particle size for BICUVOX was 10 μm (Politova, Fortalnova et al.

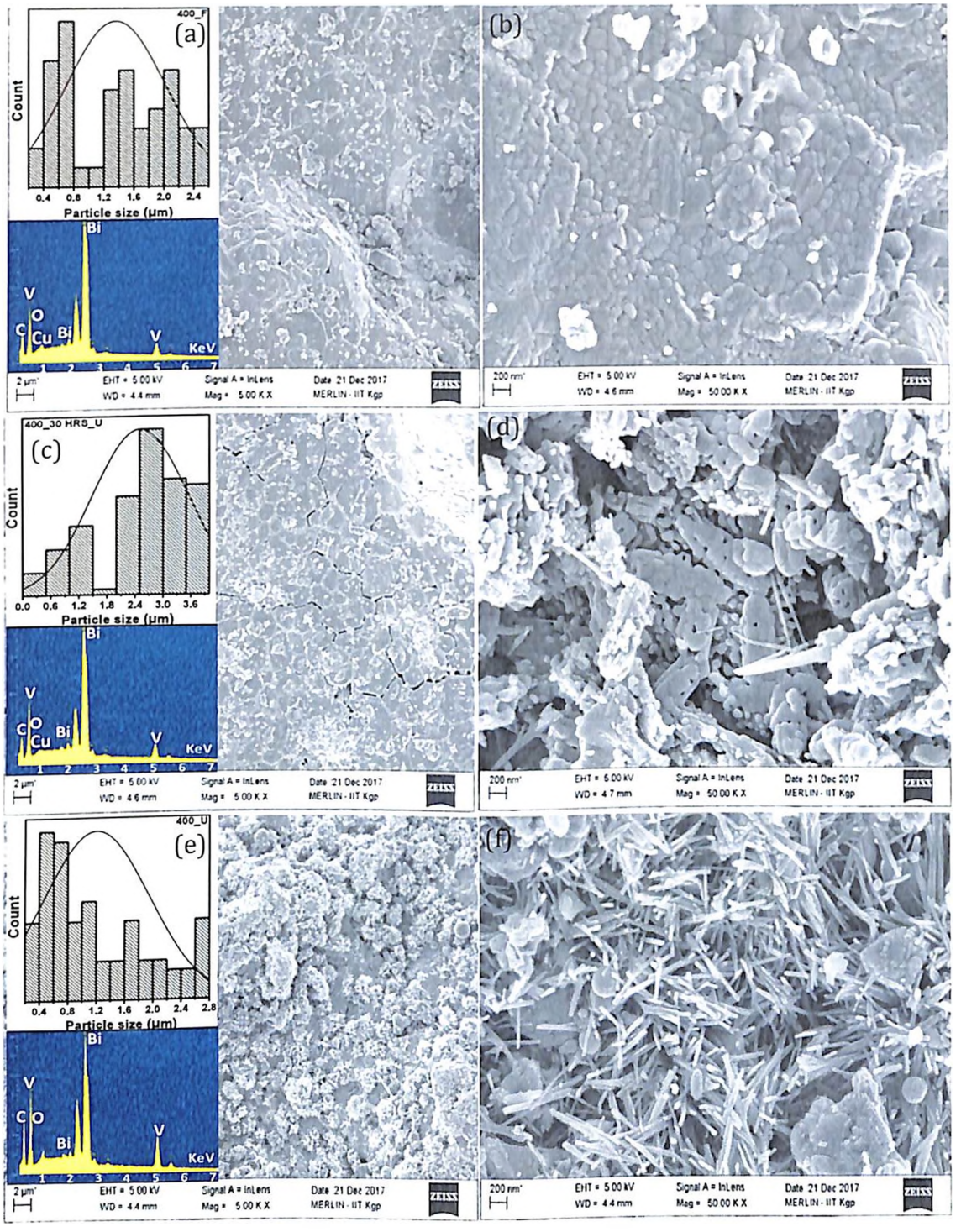

Figure 4-51: FESEM images of the BICUVOX catalysts calcined at 400°C (a-b) Fresh (c-d) 30 hrs used (e-f) Long time used catalysts along with their partisize distribution and EDX spectrum

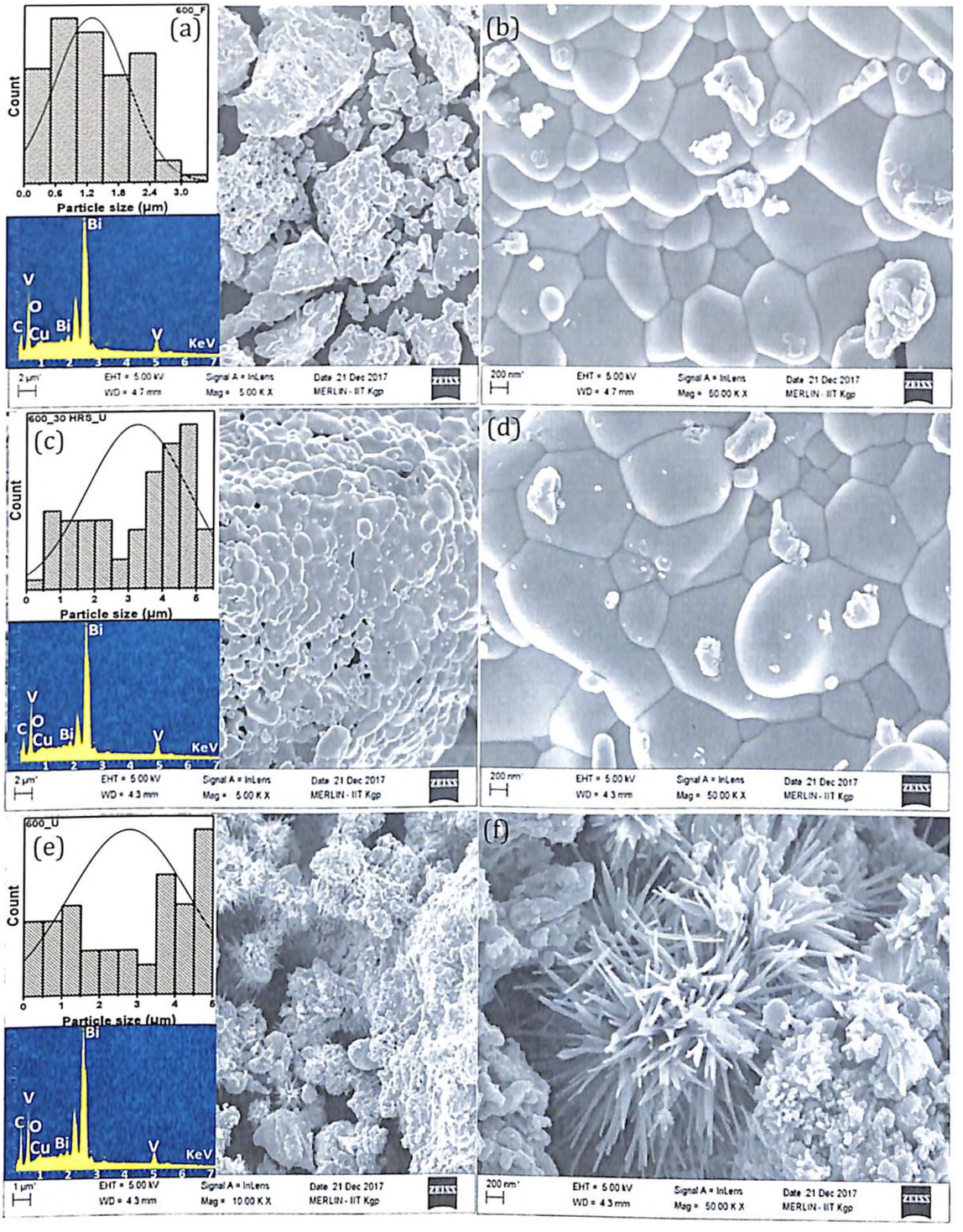

Figure 4-52: FESEM images of the BICUVOX catalysts calcined at 600°C (a-b) Fresh (c-d) 30 hrs used (e-f) Long time used catalysts along with their partisize distribution and EDX spectrum

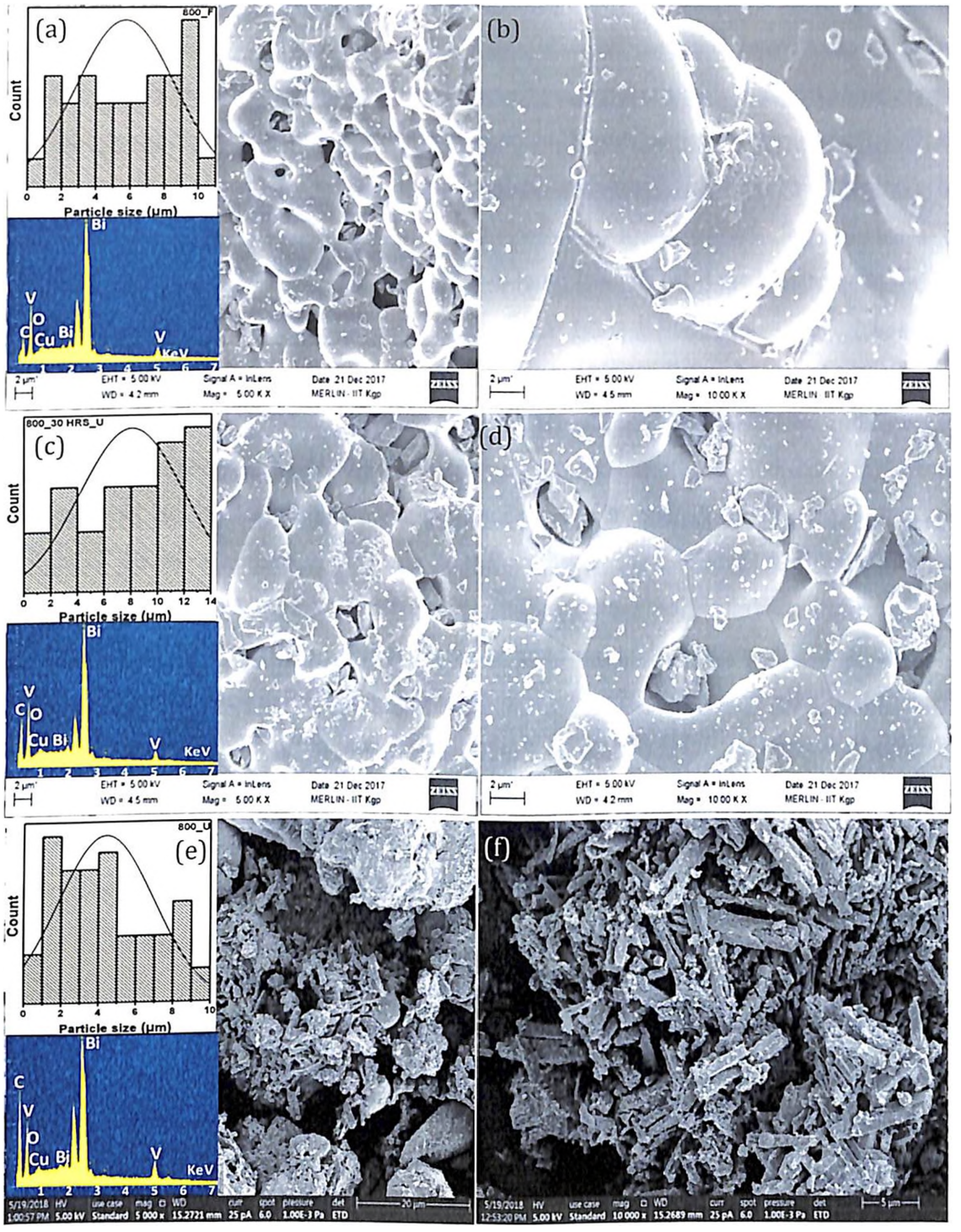

Figure 4-53: FESEM images of the BICUVOX catalysts calcined at 800°C (a-b) Fresh (c-d) 30 hrs used (e-f) Long time used catalysts along with their partisize distribution and EDX spectrum

2011). Jibo et al, (2009) study the effects of synthesis methods of BICUVOX.10 powder on oxygen permeation. Catalyst is synthesized by solid-state reaction (SSR) and EDTA-citric acid (EC) methods and sinter at 700, 750, and 800°C. An increase in grain size is clearly evident in SEM images when the sintering temperature is increased. Particle size distributions of BICUVOX.10 powder prepare by EC method are 2-7 μm at 700°C, 5-19 μm at 750°C and 17-35 μm at 800°C, while the particle size distribution in case of SSR is 5-25 μm at 800°C (Jibo, Baofeng et al. 2009). Effect of sintering and grain size of BICOVOX powder on the electrical properties has been investigated by Steil at el, (1999) BICOVOX powder is synthesized by the conventional solid-state reaction method. Particle size distribution has been estimated by SEM and finds particle size is 5-10 μm at 750°C and 30-60 μm at 800°C (Steil, Fouletier et al. 1999). Literature shows that particle sizes for BIMEVOX catalysts prepared by solid state reaction lies in the range of ~10-25 μm. However, particle size distribution of our catalysts, prepare by solution combustion synthesis, recline between ~ 0.5-8 μm, indicating formation of finer particles. Roy et al, (2009) synthesize the BICOVOX0.15 catalyst by solution combustion synthesis using glycine as fuel in a stoichiometric ratio (Roy and Fuierer 2009). Prepare catalyst has been calcined at 600, 700 and 800°C and characterize by FESEM to obtain the particle size. Reported particle sizes for as-combusted, 600, 700 and 800 calcined catalysts are 0.1-1 μm, 0.2-1.8 μm, 0.5-3.5 μm and 1-10 μm, respectively which is in the same line of our results.

Acquire FESEM analysis shows that the calculated particle size distribution of BICUVOX catalysts is higher than that of the BICOVOX and BINIVOX catalysts and decreasing order of particle size distribution is found to be

BICUVOX> BICOVOX≥ BINIVOX.

XRD also shows a similar trend for particle size of BICOVOX, BINIVOX and BICUVOX catalysts. There are several features of the solute and solvent atoms that determine the degree to which the former dissolves in the latter or the level of stress (Callister and Rethwisch 2007). If the prepared solution is substitution solid solution, then the level of stress will be less and will result in bigger particle size (Callister and Rethwisch 2011). Atomic size factor, crystal structure, electro-negativity and valences are the factors that decide the degree of solubility. In case of BIMEVOX catalysts, V is replaced by different metals. Atomic radii of V, Co, Ni, and Cu are 0.132 nm, 0.125 nm, 0.125 nm and 0.128 nm respectively (Speight 2005). If the difference between atomic radii of solute and solvent atoms is small, then the stress will be less. Here, the difference in radii w.r.t. V is 0.07 nm for Co and Ni and 0.04 for Cu. Valence of V, Co, Ni, and Cu are +5, +2, +2 and +1 respectively

(Bonds 1971). A metal will have more of a tendency to dissolve another metal of higher valence than one of a lower valence. Here, Cu has the lowest valence in comparison to Co and Ni and V has the higher valence. Electronegativity of V is 1.63 and for Co, Ni, and Cu it is 1.9 (Allred 1961). So, there is no difference in the electronegativity of doping metals. Therefore, it can be concluded from the above discussion that BICUVOX solid solution will have less amount of stress in comparison to BICOVOX and BINIVOX catalysts, which results in bigger particle size.

The homogeneity and ratio of the constituent elements in BIMEVOX-wash catalysts are examined by SEM-EDX analysis (Figures 4.44 (a), (c) and (e)). The elemental composition (in atomic%) of the BIMEVOX's catalysts is measured by EDX as present in Table 4.15. The EDX analysis indicates the presence of Bi, V, Co, C and O in BICOVOX catalysts. The 2.22: 1 (considering ± 5% error) ratio of Bi: V in the product is confirmed from the EDX spectrum of BICOVOX catalysts (Figures 4.45 (a, c, and e), 3 (a, c, and e), and 4 (a, c, and e)), where the atomic percentages of bismuth and vanadium are found in the range of 30.99-39.98 at% and 13.12-17.44 at%, respectively. The V: Co ratio of 9:1 (considering ± 5% error) is also confirmed by the EDX spectrum of BICOVOX catalysts and atomic percentages of cobalt lie in the range of 1.52-2.05 at%. BICOVOX_30HRS_U and BICOVOX_U catalysts show decrease in the atomic% of V as the ratio of Bi: V increases and V: Me decrease. Similar trend is observed in XRD analysis also, where the total V content is less than the required one. For BICOVOX-400, BICOVOX-600 and BICOVOX-800 (for fresh to long time used catalysts) catalysts, Bi: V ratio increases from 2.09-2.46, 2.15-2.3 and 2.12-2.44 respectively. Similarly, V: Co ratio decrease from 8.95-8.2, 9.07-8.34 and 8.94-8.08 for BICOVOX-400, BICOVOX-600 and BICOVOX-800 (for fresh to long time used catalysts) respectively. Obtained carbon content also follows the same trend as we observe from FESEM images.

Subsequently, the EDX analysis indicates the presence of Bi, V, Ni, O and C in BINIVOX catalysts (Figures 4.48 (a, c, and e), 4.49 (a, c, and e), and 4.50 (a, c, and e)). The results further confirm the trend of Bi: V and V: Ni as observe in BICOVOX, the amount of bismuth with respect to vanadium varies from 2.07-2.25, 1.99-2.29 and 2.1-2.34 for BINIVOX-400, BINIVOX-600 and BINIVOX-800 (for fresh to long time used catalysts) respectively. The amount of vanadium with respect to nickel decreases from 9.14-8.67, 9.15-8.65 and 9.05-8.42 for BINIVOX-400, BINIVOX-600 and BINIVOX-800 (for fresh to long time used catalysts) respectively.

The EDX spectra of x-ray counts vs. energy (in keV) for BICUVOX catalysts are shown

Table 4-15: EDX analysis of different elements and particle size distribution of wash, fresh, 30 hrs used and long time used BIMEVOX catalysts

Catalyst	Elements Present (at%)					Bi: V ratio	V: Me ratio	Particle size Distribution
	Bi	V	Metal	C	O			
BICOVOX-WASH	30.99	14.93	1.65	14.35	38.08	2.07	9.05	0.095-1.05
BICOVOX-400_F	34.67	16.55	1.52	12.03	35.23	2.09	8.95	0.26-1.39
BICOVOX-400_30HRS_U	35.98	16.39	1.85	16.54	29.24	2.19	8.85	0.27-1.68
BICOVOX-400_U	32.33	13.12	1.60	25.24	27.71	2.46	8.2	0.17-1.66
BICOVOX-600_F	35.99	16.7	1.84	10.52	34.94	2.15	9.07	0.2-1.92
BICOVOX-600_30HRS_U	38.54	16.8	1.9	15.69	27.07	2.29	8.84	0.29-2.4
BICOVOX-600_U	39.98	17.1	2.05	24.91	15.96	2.3	8.34	0.21-2
BICOVOX-800_F	36.88	17.44	1.95	8.52	35.21	2.12	8.94	0.52-5.5
BICOVOX-800_30HRS_U	36.22	15.81	1.85	17.68	28.44	2.29	8.54	0.56-8.79
BICOVOX-800_U	38.53	15.77	1.95	31.33	12.42	2.44	8.08	0.49-7.86
BINIVOX-WASH	24.94	12.3	1.35	15.31	46.1	2.02	9.1	0.048-1.44
BINIVOX-400_F	31.98	15.45	1.69	12.03	38.85	2.07	9.14	0.08-1.64
BINIVOX-400_30HRS_U	33.76	15.14	1.70	17.1	32.3	2.22	8.9	0.2-2.1
BINIVOX-400_U	38.05	16.91	1.95	22.69	20.4	2.25	8.67	0.06-1.8
BINIVOX-600_F	35.56	17.86	1.95	9.52	35.11	1.99	9.15	0.19-1.77
BINIVOX-600_30HRS_U	34.59	15.28	1.72	16.95	31.46	2.26	8.88	0.24-2.16
BINIVOX-600_U	39.57	17.22	1.99	20.98	20.24	2.29	8.65	0.22-1.95
BINIVOX-800_F	36.52	17.39	1.92	7.52	36.65	2.1	9.05	0.48-5.66
BINIVOX-800_30HRS_U	37.69	16.51	1.87	19.86	24.07	2.28	8.82	0.67-9.45
BINIVOX-800_U	40.58	17.27	2.05	26.58	13.52	2.34	8.42	0.28-6.96
BICUVOX-WASH	28.15	13.95	1.52	15.95	40.43	2.02	9.17	0.145-1.59
BICUVOX-400_F	28.76	14.15	1.58	14.65	40.86	2.03	8.96	0.37-2.41
BICUVOX-400_30HRS_U	30.52	13.54	1.55	17.23	37.16	2.25	8.73	0.43-3.91
BICUVOX-400_U	35.68	15.59	1.80	26.54	20.39	2.28	8.66	0.37-2.42
BICUVOX-600_F	32.96	14.5	1.6	11.52	39.42	2.27	9.06	0.32-3.07
BICUVOX-600_30HRS_U	39.54	17.15	1.95	16.89	24.47	2.31	8.79	0.18-5.27
BICUVOX-600_U	42.09	17.85	2.06	25.98	12.02	2.35	8.67	0.18-4.75
BICUVOX-800_F	34.65	15.8	1.74	8.95	38.86	2.19	9.08	0.8-10
BICUVOX-800_30HRS_U	39.07	16.98	1.94	18.55	23.46	2.3	8.75	0.96-12.8
BICUVOX-800_U	45.98	19.33	2.35	30.34	2.0	2.38	8.22	0.79-9.27

in Figures 4.51 (a, c, and e), 9 (a, c, and e), and 10 (a, c, and e). EDX analysis indicates the presence of Bi, V, Cu, O and C in BICUVOX catalysts. The experimental values of the elemental content (Bi: V and V: Cu atomic percent ratio) of different compositions have been tabulated in Table 4.15 and obtain values are consistent with the theoretical ratio of elemental contents with ± 5% error which suggests that proper stoichiometry is maintained in the compositions. It has been observed that the experimental values of the atomic percentage ratio of Bi: V and V: Co and carbon content follows the same trend as we observe for BICOVOX and BINIVOX catalysts. Bi: V ratio varies from 2.03-2.28, 2.27-2.35 and 2.19-2.38 for BICUVOX-400, BICUVOX-600 and BICUVOX-800 (for fresh to long time used catalysts) respectively. V: Cu ratio decreases from 8.96-8.66, 9.06-8.67 and 9.08-8.22 for BICUVOX-400, BICUVOX-600 and BICUVOX-800 (for fresh to long time used catalysts) respectively.

4.1.2.4.1 *Possible causes for C-deposition*

The nature of the support and metal directly influences the product distribution and catalyst stability during ethanol reforming reactions (Vaidya and Rodrigues 2006; de Lima, da Silva et al. 2009). Metal oxide catalysts can be used to produce hydrogen with little carbon deposition on the catalyst surface. However, many undesirable by-products (e.g., ethylene, acetaldehyde, and acetone) are formed with oxide catalyst during SR of ethanol (Nishiguchi, Matsumoto et al. 2005; Laosiripojana and Assabumrungrat 2006). Acidic and basic nature of catalyst affects the deactivation. Acid supports favour dehydration reactions toward ethylene, which goes into polymerization reaction to form coke (Vizcaíno, Arena et al. 2008; Montero, Ochoa et al. 2015). On contrary to this, basic supports mainly favour the ethanol dehydrogenation along with condensation reactions to form acetaldehyde and acetone, followed by C-C cleavage and WGSR along with methane reforming at high temperatures to avoid coke formation (Wang, Liu et al. 2008). Al_2O_3 is generally used as a support but its acid sites promote the dehydration of ethanol to ethylene (Fatsikostas and Verykios 2004). MgO contains strongly basic sites, which are proposed to be highly active for ethanol dehydrogenation to acetaldehyde (Llorca, Piscina et al. 2001). Ceria and ceria-containing mixed oxides have also been proposed to be catalytically active components of supported metal catalysts for ethanol conversion reactions due to their high oxygen storage and mobility that minimizes coke formation on the metal (Kugai, Subramani et al. 2006; Roh, Platon et al. 2006; Cai, Wanga et al. 2008; de Lima, da Silva et al. 2009). Pereira et al, (2008) propose that the loss of activity of Co-based catalysts is directly related to the oxidation of metallic Co

particles during reaction (Pereira, Homs et al. 2008). They mention that the surfaces of Co particles are oxidized by surface oxygen, which favours the dehydrogenation of ethanol to acetaldehyde. The mechanism of coke formation over supported Ni catalysts during steam reforming of methane is well described in the literature (Trimm 1997; Trimm 1999; Navarro, Pena et al. 2007; de la Piscina and Homs 2008). Methane dissociates on nickel surface, producing highly reactive carbon species (Trimm 1997). This carbon may undergo a number of processes, including (1) reaction with water; (2) encapsulation of the Ni particle surface; or (3) dissolution in the Ni crystallite follows by the nucleation and growth of carbon filaments (e.g., whiskers).

Wang et al, (2008) study the deposition of carbon during SR over Co/CeO_2 as a function of reaction temperature; between 350 and 450°C, where severe deactivation is observed and cobalt particles are found to be completely encapsulated by coke (Wang, Liu et al. 2008). They propose that coke covers the active sites responsible for ethanol dehydrogenation as a result; ethanol is preferentially dehydrated to ethylene. However, at 500 or 550°C, carbon filaments are detected but the catalyst remains quite stable till 8 hrs. Above 600°C, no carbon is detected by TEM analysis. Galeti et al, (2008) also investigate the effect of reaction temperature on the performance of CuCoZnAl catalyst during steam reforming (Galetti, Gomez et al. 2008). Activity results show that CuCoZnAl rapidly deactivates at 400 and 500°C due to formation of carbon filaments, whereas the activity remain unchanged at 600°C due to amorphous carbon and that can be removed from the surface of the catalyst by the reverse Boudouard reaction.

Moreover, it is also well established in the literature that coke formation in steam reforming processes can be minimized by controlling metal particle size (Da Silva, Den Breejen et al. 2014; Liu, Xu et al. 2015; Montero, Ochoa et al. 2015). Vicente et al, (2014) study the effect of operating conditions on the nature of the coke deposited on Ni and Co catalysts in the SRE (Vicente, Montero et al. 2014). Thus, the main cause of deactivation has proven to be the fraction corresponding to encapsulating coke (monoatomic and polymeric), which blocks metal active sites, whereas the filamentous coke fraction (filamentous particles) covers the catalyst but does not hinder ethanol adsorption due to its considerable porosity, thus having little effect on deactivation, particularly on catalysts with high surface area. Nevertheless, for higher values of time on stream, Ni particles (with a smaller size) favour the growth of nonfilamentous coke. This result is consistent with the opinion of several authors that the reduction in Ni particle size leads to a change in the mechanism of coke formation, so that large particles favour the growth of filamentous coke and smaller ones the growth of

nonfilamentous coke (Alberton, Souza et al. 2007; Gohier, Ewels et al. 2008). It is also known that small Ni particles are less active for coke formation (Chen, Christensen et al. 2005; Da Silva, Den Breejen et al. 2014; Rossetti, Lasso et al. 2014; Liu, Xu et al. 2015) and that the formation and growth of filamentous coke causes the rearrangement of the monoatomic layer of Ni on the support surface [56]. Many researchers have reported the carbon deposition in ethanol steam reforming. Nickel/dolomite catalysts have been prepared and investigated by Elbaba et al, (2013) for their suitability for the production of hydrogen. The catalyst is prepared by precipitating metallic nickel onto calcined dolomite. Catalytic experiments are performed at 500°C and atmospheric pressure. The oxidation peaks in DTA curve for the used catalyst occurs at a temperature of about 520°C and refers to monoatomic carbon corresponding to 10 wt% loss in TGA curve. This observation is confirmed by the SEM images of the used catalyst. It is suggested that monoatomic carbon is deposited on the surface of the used catalyst and block the access of products to the catalyst which explains the lower catalytic activity (Elbaba and Williams 2013). Dieuzeide et al, (2016) investigate Mg doping effects on the catalytic behaviour of Ni/Al_2O_3 catalysts during H_2 production by glycerol steam reforming. The catalyst is prepared by the incipient wetness impregnation method. Catalytic tests are carried out at atmospheric pressure, reaction temperatures ranging from 500 to 600°C; water to glycerol molar ratio (H_2O/Gly) of 3.5:1. TGA shows 12% loss in weight due to carbon deposited. From a comparative evaluation of all images, the nature of the coke that forms is mainly filamentous nature (Dieuzeide, Laborde et al. 2016). Ekaterini et al, (2010) has investigated the properties of ceria–zirconia-supported Ni and Rh catalysts and their performance in acetic acid steam reforming. The wet impregnation method is applied for the catalysts preparation and catalytic experiments are performed at atmospheric pressure and temperature ranging from 550 to 750°C. TGA analysis of used catalyst show 4.5 wt% coke after acetic acid steam reforming at 750°C for 15 h. SEM image of the used catalyst clearly reveal that the coke deposited on the catalyst is in the form of filamentous coke (Vagia and Lemonidou 2010). Kambolis et al, (2010) develop Ni/CeO_2-ZrO_2 catalyst for the dry reforming of methane (Kambolis, Matralis et al. 2010). The ceria–zirconia binary oxides are prepared by the co-precipitation technique and calcined at 550°C. The catalytic performance of the catalyst is evaluated in a fixed bed plug flow reactor operating at atmospheric pressure and 700°C for 24 h. DTGA profile of used catalyst shows the peak around 300°C that attributed to amorphous carbon (C_a type) and peak at temperatures higher than 530°C show the presence of whisker type carbon (C_b type). The SEM images of the used catalysts also show the presence of different types and extent of carbonaceous deposits.

Hydrogen production from the pyrolysis-gasification of waste tyres is investigated with a $Ni/CeO_2/Al_2O_3$ catalyst by Elbaba et al, (2011). The catalyst is prepared by co-impregnation method and pyrolysis-gasification is carried out in a two-stage fixed bed reactor with maximum temperature of 800°C. Reported TGA results of used catalyst shows 17 wt% losses corresponding to an oxidation peak in DTA at around 500°C assign to the layered carbon deposition, along with few filamentous carbons. SEM images also confirm the presence of both types of carbon and it is suggested that the layered carbon deposited on the surface is responsible for the low catalytic activity (Elbaba, Wu et al. 2011). Kawi et al, (2018) study Multi-Ni-Ni phyllosilicate hollow sphere catalysts for CO_2 reforming of CH_4 (Li 2018). SiO_2 spheres are synthesized via the Stober method and Ni phyllosilicate hollow spheres are prepared by a hydrothermal method. Two different nickel precursors (nickel acetate tetrahydrate- denoted as NiPhy-OAc and Ni acetylacetonate- denoted as $NiPhy(Ac)_2$) are used to prepare two different catalysts. Catalytic experiments are performed at 700°C. TGA-DTA results for the spent catalysts after 20 h reaction at 700°C display the weight loss of 5.6 corresponding to an exothermic peak below 600°C for $NiPhy(Ac)_2$), and 69.2 wt% corresponding to an exothermic peak at 700°C for NiPhy-OAc indicate the presence of carbon deposition. SEM images also affirmed the formation of carbon for both the catalysts. Large amounts of carbon nanotubes are observed which result in the high weight loss for NiPhy-OAc catalyst and only a tiny amount of carbon nanotubes with amorphous carbon are observed for $NiPhy(Ac)_2$. Kim et al, (2012) has been demonstrated the catalytic properties of Co_3O_4 nanoparticles for rechargeable Li/air batteries. They prepare three types of Co_3O_4 nanoparticles by a hydrothermal reaction method. The electrochemical performance of Co_3O_4 nanoparticles is examined using a modified Swagelok cell. After 10 cycles, the electrode is discharged and the surface is observed by SEM to investigate the morphology change during cycling and from the images, carbon fibers (Ketjen black) could be clearly identified (Kim and Park 2012). Wei et al, (2015) study the fracture behavior of carbon-fibers. In their study, microscopic morphology is examined by using FESEM and images show the carbon fiber fracture topography (Wei, An et al. 2015). Reported microscopic morphology of fractured carbon-fibers and Ketjen black carbon is similar to the morphology obtained for BICOVOX-800_U catalyst. This shows that our results are consistent with the FESEM results of different catalysts for carbon deposition, as reported by other scientists.

4.1.2.5 *Raman Spectroscopy*

Raman spectroscopy is a prominent technique for analysing the nature of the local structure or coordination around the vanadium atoms and discriminating the different molecular structures present in a chemical species. Only vanadium is considered for detail Raman analysis as its valency affects the oxygen mobility. Mainly, two approaches are reported in the literature for differentiating molecular structures present in the system (Baran, Botto et al. 1978). First is the group frequency approach, where the characteristic vibrational frequencies are ascribed to certain structural units. In pursuant to this approach, distinct features for ortho-, para- and meta- position of oxygen in tetrahedral and octahedral vanadates are manifested in the Raman spectra (Hardcastle, Wachs et al. 1991). Hardcastle et al, 1991 study different characteristics of vanadium oxide using group frequency approach and they report that discrimination between tetrahedral and octahedral coordination of vanadium in vanadium oxides is difficult (Hardcastle and Wachs 1991). According to the reported detail structure study of BIMEVOX systems, it is observed that vanadium present in BIMEVOX systems is found in both, yet distorted coordination. Therefore, another approach is developed by Hardcastle and Wachs to analyse the Raman spectra of distorted systems and it is based on the concept of bond length and bond order and their correlation with bond valence and the stretching force constant (Hardcastle and Wachs 1991). They establish an empirical Equation to correlate Raman frequencies and V–O bond lengths from large number of experimental data of compounds containing V-O bond and is given as:

$$R = \frac{ln\left(\frac{21,349}{\nu}\right)}{1.9176} \tag{4.17}$$

Where R is the V–O bond length in Å and ν is the Raman shift in cm^{-1}. The method uses diatomic approximation which assumes that each (ortho-, para- and meta-) distinct metal–oxygen bond is vibrationally independent of the crystalline lattice. Each V-O bond corresponds to separate signal or stretching frequency and is uniquely related to bond length (Hardcastle and Wachs 1991; De Waal and Hutter 1994).

The Pauling bond strengths (in valence units) or bond valences, of the V-O bonds and the calculated valence state of the vanadium cation are useful in describing the possible molecular structures (Brown 1978; Hardcastle and Wachs 1991). Brown and Wu have developed the empirical expression to correlate bond length with bond valence or bond order and is given as (Brown 1978):

$$s(V-O) \approx \left(\frac{R}{1.791}\right)^{-5.1} \quad (4.18)$$

Where, s is the bond valence and 1.791 Å is the estimated bond length for a V-O bond of unit valence. The empirical parameters in Equation 4.20, 1.791 and 5.1, are determined based on data from 43 different compounds having V^{5+} oxidation state (Brown and Wu 1976; Hardcastle and Wachs 1991). Further the valence sum rule is applied in order to estimate valence states of vanadium cations by adding the contributions from each V-O bond in vanadate structures as determined by Equation 4.20 (Brown 1978; Hardcastle and Wachs 1991). Bond valence provides a quantitative estimation of the relative strength of the various bonds and hence it can be used to describe the structures.

In the present study different BIMEVOX (ME: Co, Ni, Cu) catalysts at different stages (fresh, 30HRS_U, and used) are analyzed by using Raman spectroscopy in order to study the change in their molecular structures after each stage. The V-O Raman spectra of BICOVOX, BINIVOX, and BICUVOX-wash catalysts are shown in Figures 4.54 (a), (b) and (c) respectively. Generally, BIMEVOX catalysts are characterized by four Raman active internal vibrations that includes symmetric stretching mode (ν_1), symmetric bending mode (ν_2), asymmetric stretching mode (ν_3), and asymmetric bending mode (ν_4) (Halford 1946; McCreery 2005). Higher frequency range (640-910 cm^{-1}) is attributed to the stretching modes (ν_1 and ν_3) as compared to bending modes (ν_2 and ν_4) that falls in the range of 290-425 cm^{-1} (Halford 1946; Porto and Scott 1967; Galembeck and Alves 2000; McCreery 2005; Xing, Li et al. 2011). Stretching mode is the most intense among all the Raman bands (Frost, Henry et al. 2006). All the BIMEVOX-wash spectra show some similarity, with a number of overlapping bands in the frequency range of 600 to 1000 cm^{-1}. To obtain the position and intensity of individual signal, deconvolution of Raman spectra (600-1000 cm^{-1}) have been carried out. Insets images in Figure 4.54 represent the deconvolution of each catalyst. Four bands are obtained; the most intense one is found at similar position ~826 cm^{-1} for BICOVOX, BICUVOX and ~836 cm^{-1} for BINIVOX wash catalysts and attributed to symmetric V-O stretching mode and three of almost similar intensity bands are found for BICOVOX (~665, 755, 884 cm^{-1}), BINIVOX (~721, 787, 870 cm^{-1}) and BICUVOX (~721, 805, 901 cm^{-1}) wash catalysts, out of that bands emerge at 721, 787, 805, 665 and 755 cm^{-1} assign to asymmetric V-O stretching (V_{as}(V-O)) and the rest of them are assign to symmetric V-O stretching (V_s(V-O)) (Galembeck and Alves 2000; McCreery 2005; Frost, Henry et al. 2006). In a low frequency region, all spectra reveal a distinct band at ~216-235 cm^{-1} and

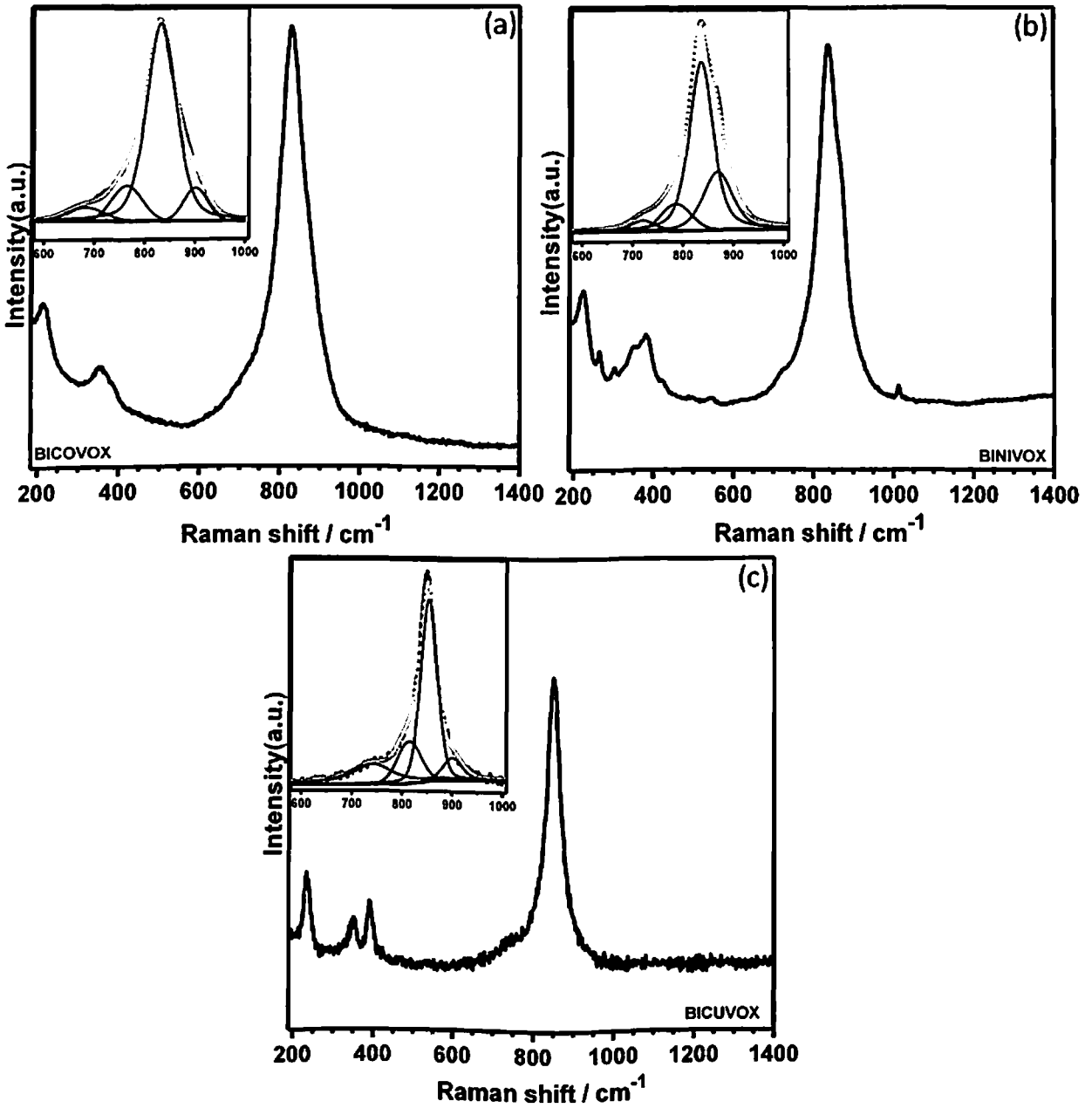

Figure 4-54: Raman spectra of a) BICOVOX, b) BINIVOX, and c) BICUVOX wash powders (Insets: deconvolution of Raman spectra obtained in the range of 600-1000 cm^{-1})

ascribed to lattice mode or vibration chain bending (McCreery 2005). Along with this, two bends of almost similar intensity at ~350-354 and 380-390 cm^{-1} are evident in the Figures and attributed to symmetric V-O bending or symmetric deformation mode (Frost, Henry et al. 2006).

Figure 4.55 (a) shows the Raman spectra of BICOVOX-400 catalyst over wide range of frequency from 150-1400 cm^{-1}. The graph is shown in a layer lines representing different stages of catalyst starting from BICOVOX-400_F to BICOVOX-400_U. Deconvoluted Raman spectra (600-1000 cm^{-1}) of each stage are presented in Figure 4.55 (b), (c) and (d). Fitting of spectrum gives 3 distinct peaks for BICOVOX-400_F and BICOVOX-400_30HRS_U and 4 peaks for BICOVOX-400_U. Most intense peak for BICOVOX-400 F, 30HRS_U and U catalysts is found at ~826-845 cm^{-1} and assigned to symmetric V-O stretching. Rest of the two bands of almost similar intensity are found at 772 (V_{as}(V-O)), 887 cm^{-1} (V_s(V-O)) for BICOVO-400_F, 796 (V_{as}(V-O)), 907 cm^{-1} (V_s(V-O)) for BICOVOX-400_30HRS_U catalysts and for BICOVOX-400_U catalyst, along with these two bands at 792 (V_{as}(V-O)) and 884 cm^{-1} (V_s(V-O)), an extra peak at 715 cm^{-1} (V_{as}(V-O)) emerges out. In lower frequency region, bands at 209-230 and 358-370 cm^{-1} are found and assigned to vibration chain bending and symmetric deformation mode, respectively. Figure 4.56 (a) reveals the Raman spectra of BICOVOX-600 catalyst for all the stages varying from fresh (F) to used (U). The deconvolutions of spectra for each stage are presented in Figure 4.56 (b-d). Same numbers of peaks are obtained after deconvolution of BICOVOX-600_F, 30HRS_U and U catalysts. Peak with maximum intensity is found at 826-845 cm^{-1} (V_s(V-O)), along with two other peaks of similar intensity at ~775-797 (V_{as}(V-O)) and 887-918 cm^{-1} (V_s(V-O)). Two low frequency bands are also observed at ~221-231 and 360-366 cm^{-1}. Similar to BICOVOX-600 catalyst, BICOVOX-800 catalyst also shows the same number of peaks for all stages varying from fresh (F) to used (U) after deconvolution as depicted in Figure 4.57 (b-d). Figure 4.57 (a) shows the wide range of Raman spectra for BICOVOX-800 catalyst. Similar to other BICOVOX catalysts, the most intense peak is found at ~ 836-842 cm^{-1} frequency range in BICOVOX-800 catalyst. Two low frequency region peaks are also evident at ~225-231 and 353-380 cm^{-1} for all BICOVOX-800 catalysts. However, one extra peak emerges at 464 cm^{-1} in case of BICOVOX-800_U catalyst and assigned to V-O vibration mode (Kumar and Sahare 2013).

Raman spectra of BINIVOX-400 (F, 30HRS_U and U) catalysts over wide range of frequency (150-1400 cm^{-1}) is depicted in Figure 4.58 (a) along with the deconvoluted Raman

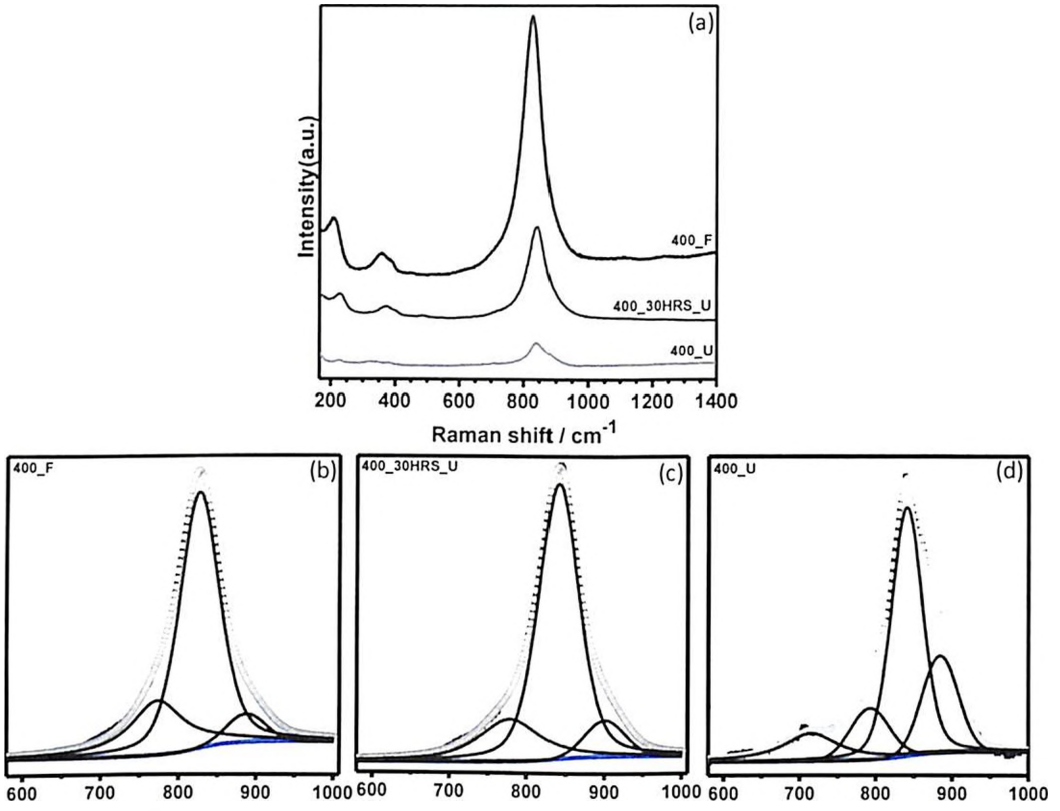

Figure 4-55: Raman spectra of a) BICOVOX-400 fresh (F), 30 hrs used and long time used (U) catalysts in the 150–1400 cm^{-1} region, and deconvoluted raman spectrum of BICOVOX-400 b) F, c) 30HRS_U, and d) U catalysts in the 600–1000 cm^{-1} region

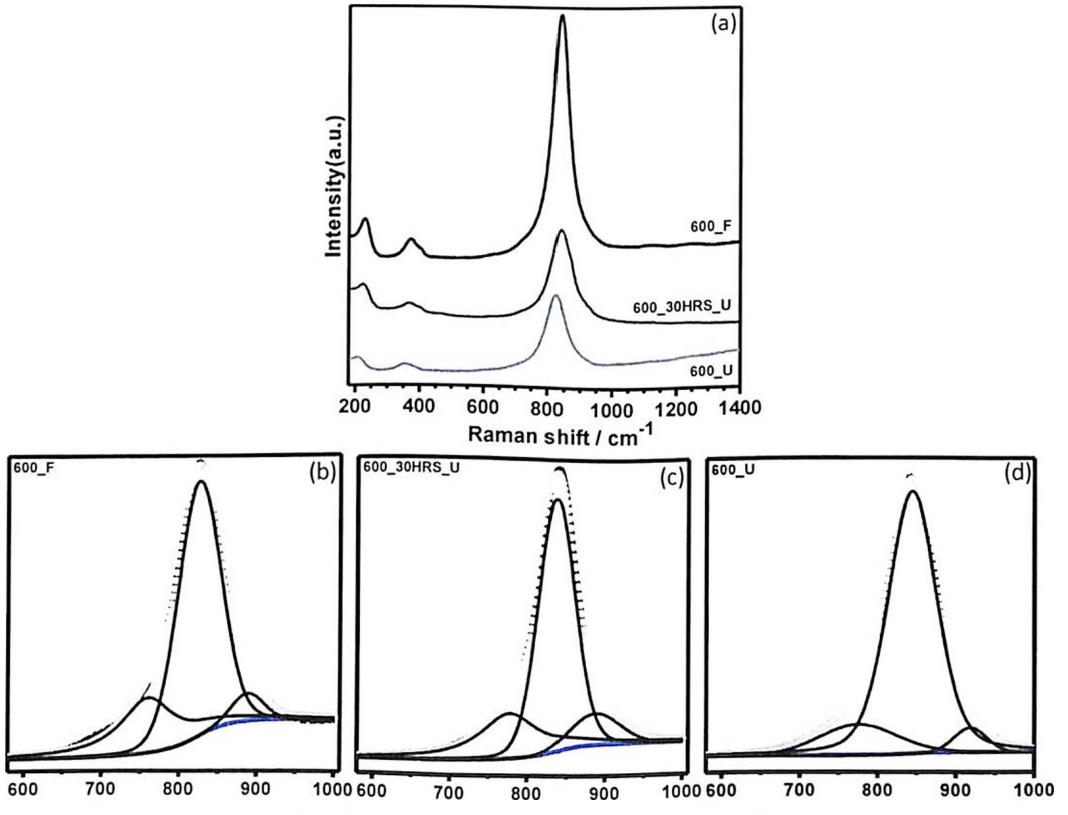

Figure 4-56: Raman spectra of a) BICOVOX-600 fresh (F), 30 hrs used and long time used (U) catalysts in the 150–1400 cm^{-1} region, and deconvoluted raman spectrum of BICOVOX-400 b) F, c) 30HRS_U, and d) U catalysts in the 600–1000 cm^{-1} region

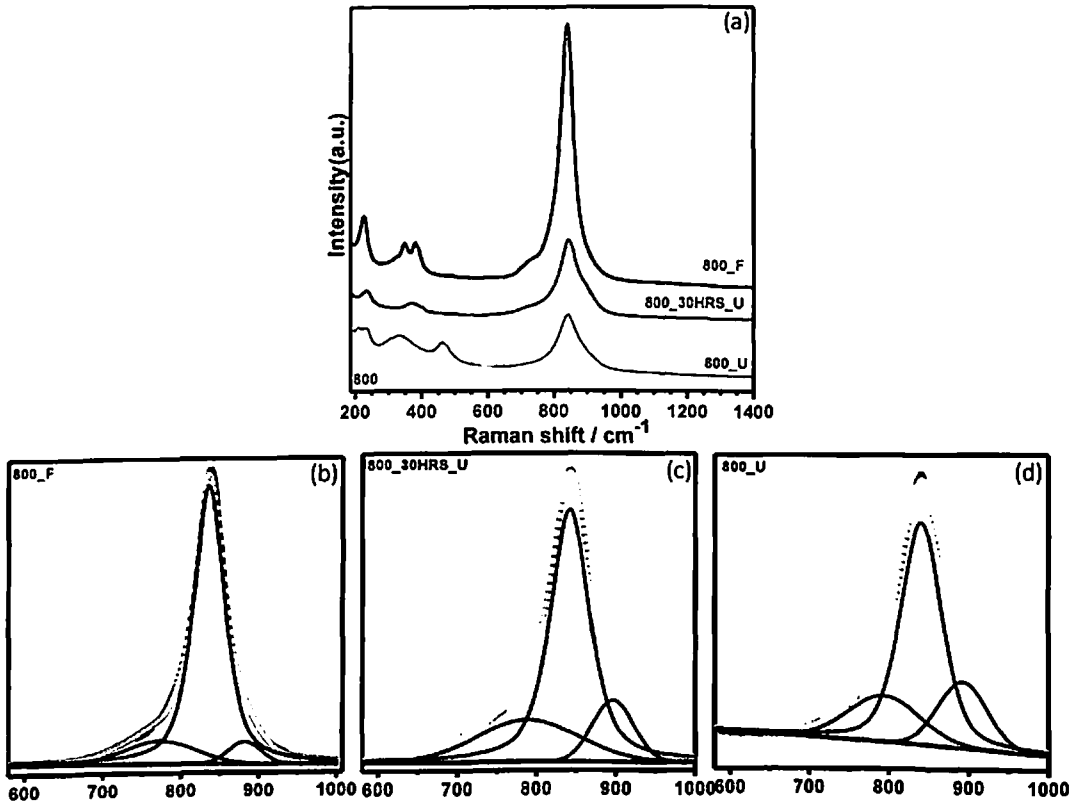

Figure 4-57: Raman spectra of a) BICOVOX-800 fresh (F), 30 hrs used and long time used (U) catalysts in the 150–1400 cm^{-1} region, and deconvoluted raman spectrum of BICOVOX-400 b) F, c) 30HRS_U, and d) U catalysts in the 600–1000 cm^{-1} region

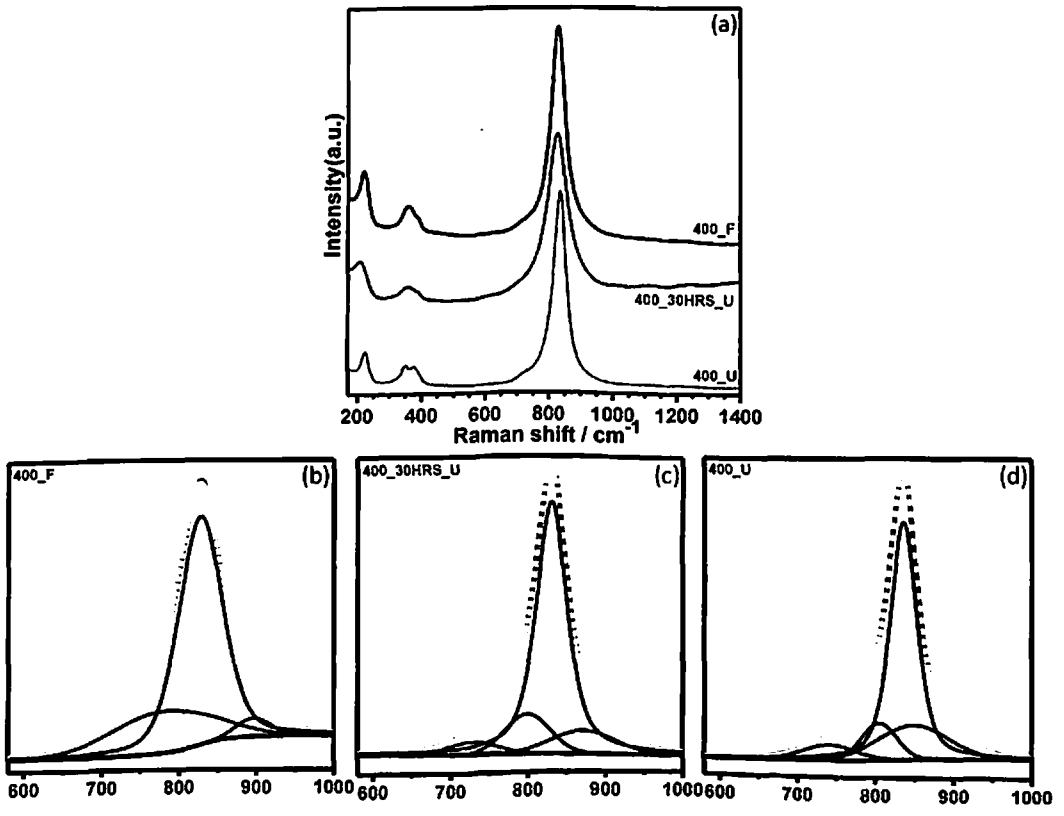

Figure 4-58: Raman spectra of a) BINIVOX-400 fresh (F), 30 hrs used and long time used (U) catalysts in the 150–1400 cm^{-1} region, and deconvoluted raman spectrum of BICOVOX-400 b) F, c) 30HRS_U, and d) U catalysts in the 600–1000 cm^{-1} region

spectra of each in Figure 4.58 (b-d). There are three vibrations for $(VO_4)^{3-}$ for BINIVOX-400_F, namely, symmetric V-O stretching (V_s(V-O)) at around 827.64, 896.5 cm^{-1} and asymmetric V-O stretching (V_{as}(V-O)) at 779.3 cm^{-1} and in spite of all the peaks present, peak at 827.64 cm^{-1} (V_s(V-O)) shows the maximum intensity. However, four vibrations are seen in case of BINIVOX-400_30HRS_U and BINIVOX-400_U. The most intense peak for BINIVOX-400_30HRS_U and BINIVOX-400_U catalysts are found at ~830-836 cm^{-1} and assigned to symmetric V-O stretching. Rest of the three bends are found at 729, 799 (V_{as}(V-O)), 871 cm^{-1} (V_s(V-O)) for BINIVOX-400_30HRS_U and bends at 740, 804 (V_{as}(V-O)), 848 cm^{-1} (V_s(V-O)) for BINIVOX-400_30HRS_U catalysts. In lower frequency region bends at 212-219, 345-357 and 380-386 cm^{-1} are found and assign to vibration chain bending, symmetric deformation mode, and V-O vibration mode, respectively. Figure 4.59 (a) reveals the Raman spectra of BINIVOX-600 catalyst for all the stages. Deconvolution of Raman spectra for each of BINIVOX-600 catalysts are presented in Figure 4.59 (b-d). Fitting of spectrum gives 3 distinct peaks for BINIVOX-600_F and BINIVOX-600_30HRS_U and 4 peaks for BINIVOX-600_U. Peak with maximum intensity is found at 831-839 cm^{-1} (V_s(V-O)), along with two other peaks at ~735-788.7 (V_{as}(V-O)) and 874-910 cm^{-1} (V_s(V-O)) with an extra peak at 816.9 cm^{-1} (V_{as}(V-O)) for BINIVOX-600_U catalyst. Raman bands at 213-227, 344-354 and 377-389 cm^{-1} are also observed and attribute to the bending modes and V-O vibration mode, respectively. Raman spectra of BINIVOX-800 catalyst are shown in Figure 4.60. Deconvoluted Raman spectrum of BINIVOX-800_F catalyst exhibits 3 bands at 726 (V_{as}(V-O)), 827 (V_s(V-O)), and 856 cm^{-1} (V_s(V-O)). Although deconvoluted Raman spectrum of BINIVOX-800_30HRS_U and BINIVOX-800_U manifest 4 bands at 689 (V_{as}(V-O)), 745 (V_{as}(V-O)), 800-815 (V_{as}(V-O)) and 855-900 cm^{-1} (V_s(V-O)). Vibration chain bending, symmetric deformation mode, and V-O vibration mode are also seen at 217-228, 324-344 and 377-384 cm^{-1} in BINIVOX-800 catalysts, respectively.

Raman spectrum of BICUVOX-400 catalyst over the range of 150 and 1400 along deconvoluted peaks for BICUVOX-400_F, BICUVOX-400_30HRS_U and BICUVOX-400_U over frequency range of 600-1000 cm^{-1} are depicted in Figure 4.61. The BICUVOX-400_F spectrum could be best deconvoluted with 3 Raman bands at 800, 832, and 867. However, BICUVOX-400_30HRS_U and BICUVOX-400_U catalysts spectra could be best deconvoluted with 4 Raman bands at 706-746 (V_{as}(V-O)), 778-804 (V_{as}(V-O)), 826-836 (V_s(V-O)), and 861-876 (V_s(V-O)). It is to be noted that the strongest Raman band is found at ~826-836. Three low frequency bands are also observed at ~221-226, 322-352 and 372-382. Similar to BICOVOX-600 catalyst, BICUVOX-600 catalyst also shows the same number of

peaks for all stages varying from fresh (F) to used (U) after deconvolution as depicted in Figure 4.62 (b-d). Figure 4.62 (a) shows the wide range of Raman spectra for BICUVOX-600 catalyst. Peak with maximum intensity is found at 840-843 (V_s(V-O)), along with two other peaks at ~729-793.7 (V_{as}(V-O)) and 803-807 (V_s(V-O)). Bands appearing at 227-229, 345-348 and 382-387 are assigned to vibration chain bending, symmetric deformation mode, and V-O vibration mode, respectively. Figure 4.63 (a) reveals the Raman spectra of BICUVOX-800 catalyst. Deconvolution of spectra for BICUVOX-800_F, BICUVOX-800_30HRS_U and BICUVOX-800_U are presented in Figure 4.63 (b-d). Each Figure contains three peaks including the most intense peak at 828-877 (V_s(V-O)). Three low frequency region peaks are also seen at ~210-223, 346-352 and 385-390 for all BICUVOX-800 catalysts.

Raman spectrum of BIVOX-600 catalyst over the range of 150 and 1400 along deconvoluted peaks for BIVOX-600_F, and BIVOX-600_U over frequency range of 600-1000 cm^{-1} are depicted in Figure 4.64. BIVOX-600_F spectrum could be best deconvoluted with 3 Raman bands at 782 (V_{as}(V-O)), 829 (V_s(V-O)), and 856 cm^{-1} (V_s(V-O)). However, BIVOX-600_U shows only two deconvoluted peaks at 813 (V_s(V-O)), and 714 cm^{-1} (V_{as}(V-O)).

Raman spectra of present data along with the data report in literature for different BIMEVOX systems or parent compound, discussed in later section, unveil the shifting of peaks. There are many possible reasons to explain this phenomenon. Firstly, it may be attributed to the quantum size confinement effect or the change in the local coordination environment of samples (Yu and Kudo 2005). Quantum size confinement effect comes in picture when the size of particles is too small to be comparable to the wavelength of the electron. Secondly, Raman band positions are very sensitive to the short range order, whereas the Raman width are more sensitive to the degree of crystallinity, particle size or the aggregation of particles, disorder, and defect (Kumar and Sahare 2013). Another reason could be the shape of particles as Raman features might also be affected by the particles shape (Yu and Kudo 2006).

Table 4.16 includes bond lengths (R), and bond orders (s) of deconvoluted peaks calculated from Equations 4.19 and 4.20, respectively for BICOVOX catalysts. It also includes valence state of vanadium cation calculated by adding the contributions from each V-O bond in terms of bond order. The deconvoluted frequency range (600–1000 cm^{-1}) corresponds to bond lengths between 1.64 and 1.8 and orders in the range 0.95 to 1.56 for BICOVOX catalysts.

The presence of significant disorder in the structures is confirmed by the obtained range of bond order. Considering the V^{5+} valence of vanadium in these materials, the Pauling sum rule should give 5 as a sum of bond order contributions. However, V^{4+} valence state is also found in these materials, as reported in the literature (Abrahams, Bush et al. 1998). As we see from Table 4.16, sum value for BICOVOX-wash catalyst is close to 5. According to the structural data of BICOVOX catalyst by Abraham et al, (2000) the V/Co-O bond lengths are 2.02 and 1.67 Å for vanadium (cobalt) in distorted tetrahedral coordination, and for an apical oxygen in the octahedral coordination, the V/Co–O bond length is 1.62 Å (Abrahams, Krok et al. 1996; Bacewicz and Kurek 2000). Sum value for BICOVOX-400_F, BICOVOX-600_F and BICOVOX-800_F catalysts is found to be 4. This shows the presence of V^{4+} valence or more oxygen deficiency in the fresh catalysts and it is observed to reduce after using catalysts as sum value is found to be increase from 4 to 5.12 for BICOVOX-400_U, 4 to 4.2 for BICOVOX-600_U and 4 to 4.24 for BICOVOX-800_U catalysts.

Similarly, Table 4.17 and Table 4.18 include the bond lengths, bond order and sum value of deconvoluted peaks for BINIVOX and BICUVOX catalysts, respectively. The calculated bond lengths are 1.64-1.82, and 1.65-1.78 with corresponding bond order of 1.57-0.92 and 1.03-1.53 for BINIVOX and BICUVOX catalysts, respectively. Similar to BICOVOX structural data, in BINIVOX structural data the V/Ni-O bond lengths are 2.01 and 1.60 Å for vanadium (nickel) in distorted tetrahedral coordination, and for apical oxygen in the octahedral coordination, the V/Ni–O bond length is 1.63 Å (Abrahams, Nelstrop et al. 1998; Bacewicz and Kurek 2000). Sum value for BINIVOX and BICUVOX wash catalysts is close to 5 and it is found to be 4 for all BINIVOX_F and BICUVOX_F catalysts, respectively. Similar to BICOVOX, the sum value is found to increase from 4 to 5.12, 4.9, 5.08, 5.08, 4.25 and 4.45 for BINIVOX-400_U, BINIVOX-600_U, BINIVOX-800_U, BICUVOX-400_U, BICUVOX-600_U, and BICUVOX-800_U catalysts, respectively. This reflects the presence of more oxygen deficiency in the fresh catalysts, observed to reduce after using them. Calculated sum value for BIVOX-600_F and BIVOX-600_U catalysts are 4.8 and 5.12, respectively. This shows the presence of mainly V^{5+} valence in BIVOX-600_F and BIVOX-600_U catalysts.

The obtained spectra for different BIMEVOX catalysts show similarity to the Raman spectrum of parent compound ($Bi_4V_2O_{11}$) of the BIMEVOX family. Kumar et al, (2013) prepare $Bi_4V_2O_{11}$ nanoparticles by combustion method and investigate about the phases present by using various characterization methods (Kumar and Sahare 2013). Raman spectrum of $Bi_4V_2O_{11}$ reflects the structure of one type of VO_4 tetrahedron. The most intense

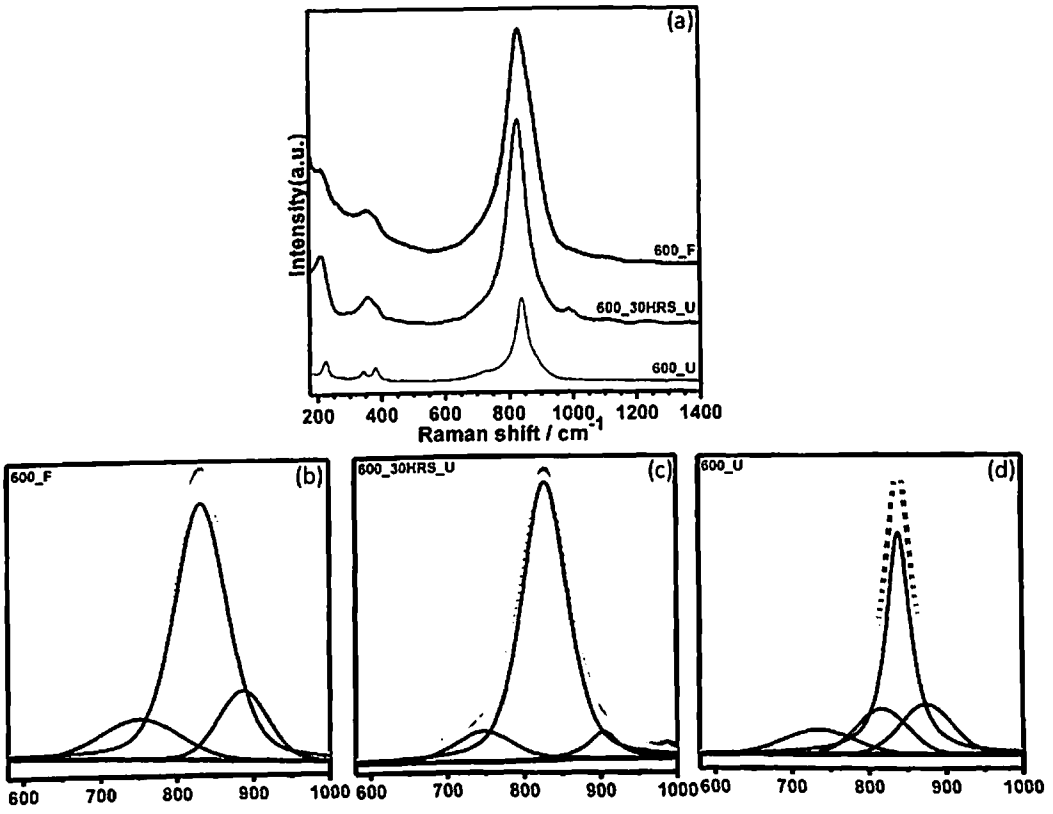

Figure 4-59: Raman spectra of a) BINIVOX-600 fresh (F), 30 hrs used and long time used (U) catalysts in the 150–1400 cm^{-1} region, and deconvoluted raman spectrum of BICOVOX-400 b) F, c) 30HRS_U, and d) U catalysts in the 600–1000 cm^{-1} region

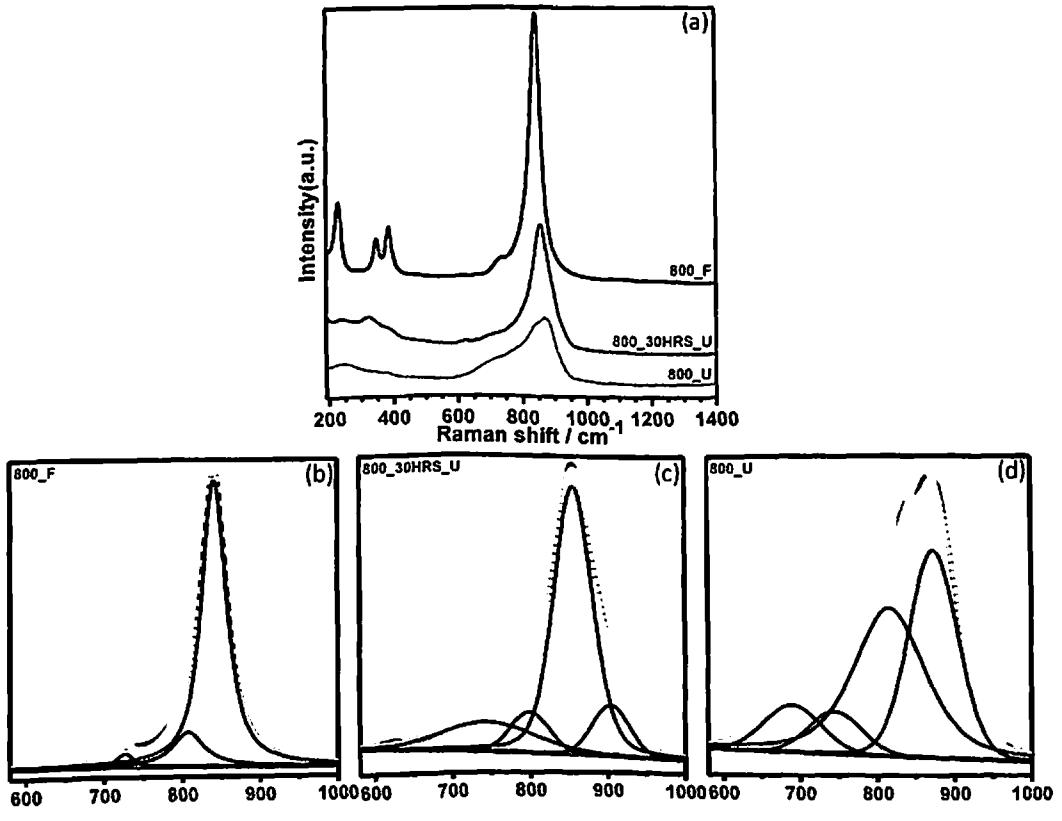

Figure 4-60: Raman spectra of a) BINIVOX-800 fresh (F), 30 hrs used and long time used (U) catalysts in the 150–1400 cm^{-1} region, and deconvoluted raman spectrum of BICOVOX-400 b) F, c) 30HRS_U, and d) U catalysts in the 600–1000 cm^{-1} region

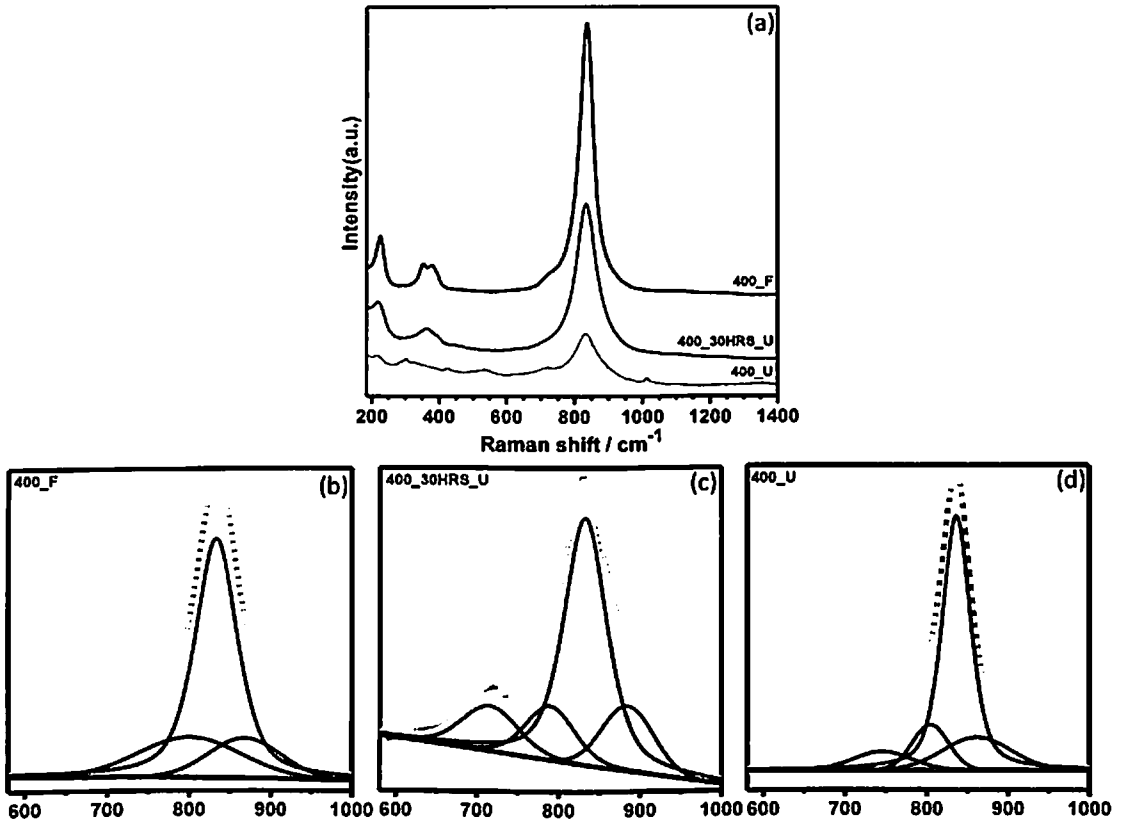

Figure 4-61: Raman spectra of a) BICUVOX-400 fresh (F), 30 hrs used and long time used (U) catalysts in the 150–1400 cm^{-1} region, and deconvoluted raman spectrum of BICOVOX-400 b) F, c) 30HRS_U, and d) U catalysts in the 600–1000 cm^{-1} region

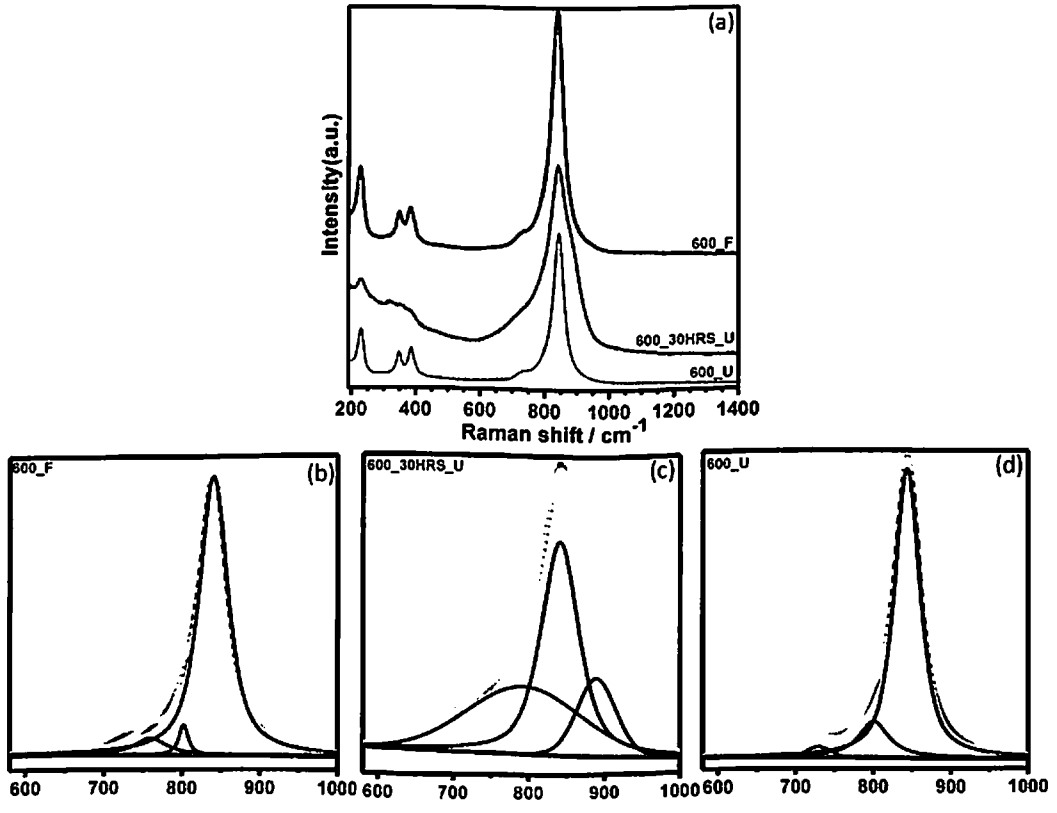

Figure 4-62: Raman spectra of a) BICUVOX-600 fresh (F), 30 hrs used and long time used (U) catalysts in the 150–1400 cm^{-1} region, and deconvoluted raman spectrum of BICOVOX-400 b) F, c) 30HRS_U, and d) U catalysts in the 600–1000 cm^{-1} region

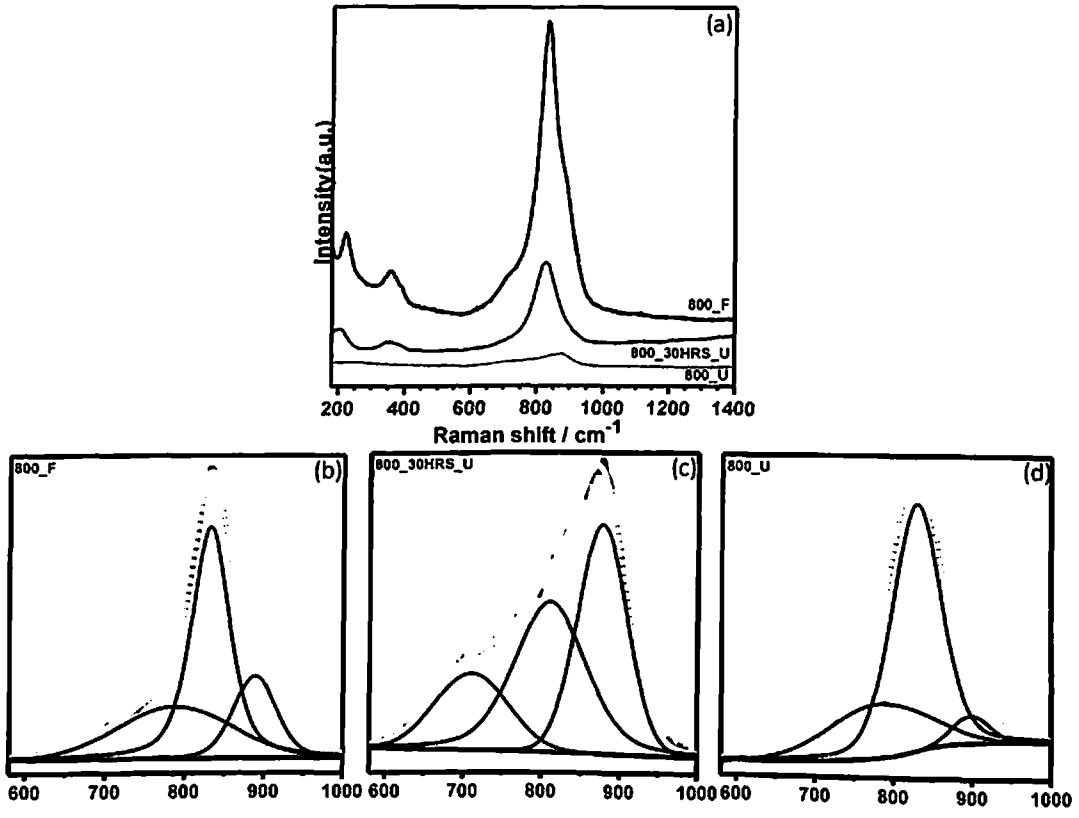

Figure 4-63: Raman spectra of a) BICUVOX-800 fresh (F), 30 hrs used and long time used (U)catalysts in the 150–1400 cm^{-1} region, and deconvoluted raman spectrum of BICOVOX-400 b) F, c) 30HRS_U, and d) U catalysts in the 600–1000 cm^{-1} region

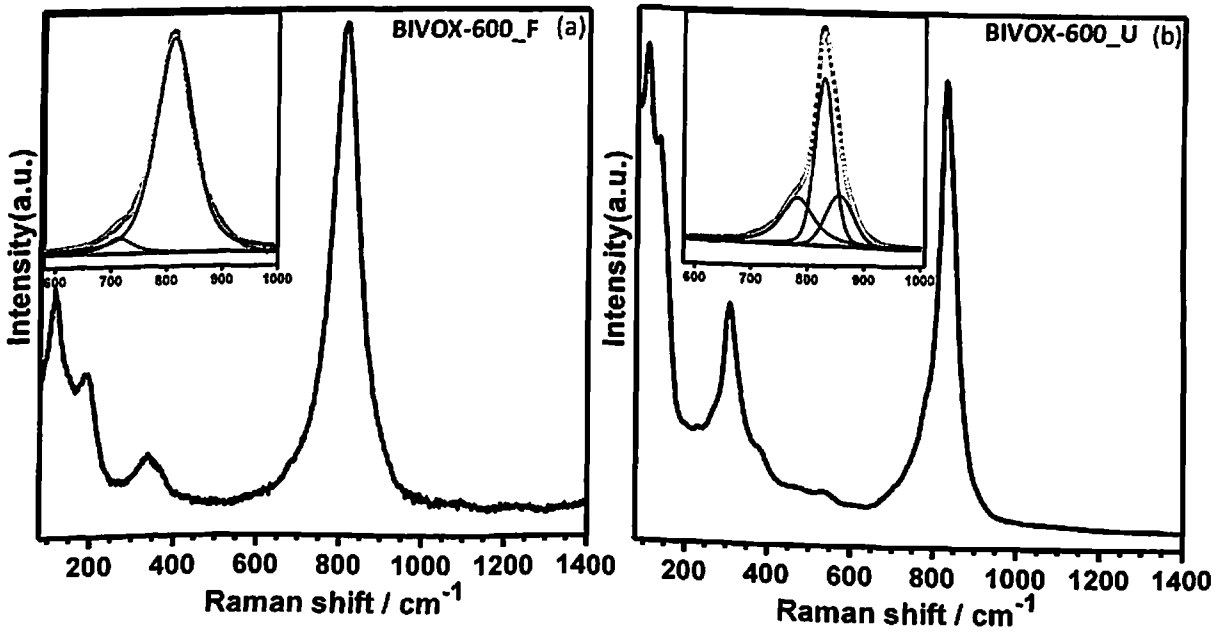

Figure 4-64: Raman spectra of a) BIVOX-600_F and b) BIVOX-600_U catalysts (Insets: deconvolution of Raman spectra obtained in the range of 600-1000 cm^{-1})

Table 4-16: Vibration modes and corresponding V-O bond lengths, bond order and valence state of vanadium estimated from the deconvoluted Raman spectra for wash, fresh (F), 30 hrs used and longtime used (U) BICOVOX catalysts

Catalysts	υ/cm^{-1}	R/Å	*s*	*Sum*
BICOVOX-WASH	665.6	1.8	0.95	4.94
	755.72	1.74	1.14	
	826.5	1.69	1.32	
	884.25	1.65	1.52	
BICOVOX-400_F	772.94	1.73	1.19	4.00
	826.57	1.69	1.32	
	887.05	1.66	1.49	
BICOVOX-600_F	777	1.73	1.19	4.00
	826.57	1.69	1.32	
	887.05	1.66	1.49	
BICOVOX-800_F	882.82	1.67	1.47	4.01
	836	1.69	1.35	
	773.49	1.73	1.19	
BICOVOX-400_30HRS_U	796.94	1.72	1.25	4.20
	845.12	1.68	1.42	
	907.3	1.65	1.53	
BICOVOX-600_30HRS_U	896.34	1.65	1.50	4.12
	845.34	1.68	1.37	
	797.49	1.72	1.25	
BICOVOX-800_30HRS_U	842	1.68	1.36	4.16
	788.9	1.71	1.25	
	896	1.65	1.55	
BICOVOX-400_U	840.69	1.68	1.36	5.12
	792.51	1.71	1.24	
	884.33	1.66	1.47	
	715.08	1.77	1.06	
BICOVOX-600_U	844	1.68	1.45	4.20
	918	1.64	1.56	
	775	1.72	1.19	
BICOVOX-800_U	840	1.68	1.48	4.24
	794	1.72	1.24	
	892	1.65	1.52	

R:bond lengths; s:bond orders; υ: Raman frequency; Sum: Calculated total valence

Raman band is obtained at about 827 cm^{-1} (V_s(V-O)) with the weak shoulder at about 709 cm^{-1} (V_{as}(V-O)). The symmetric and asymmetric bending modes are also present at 366 and 324 cm^{-1} with the external modes (rotation/translation) occur at 209 cm^{-1} and 126 cm^{-1}. Patwe et al, (2013) prepare polycrystalline sample of $Bi_4V_2O_{11}$ by conventional solid-state reaction method (Patwe, Patra et al. 2013). They report the Raman spectrum of $Bi_4V_2O_{11}$ over the range between 550 and 1200 cm^{-1} and mention that the spectrum could be best deconvoluted with five Raman bands at 830, 862, 653, 756, and 920 cm^{-1}. Hardcastle et al, (1991) also report the Raman spectrum of $Bi_4V_2O_{11}$. The most intense peak report by them is observed at 826 cm^{-1} (Hardcastle, Wachs et al. 1991). In comparison with the $Bi_4V_2O_{11}$, an important difference is the position of the main band: it is at 826 cm^{-1} for $Bi_4V_2O_{11}$, versus 827–868 cm^{-1} in BIMEVOX catalysts. Also the band widths in the $Bi_4V_2O_{11}$ spectrum are lower than for BICOVOX, BINIVOX and BICUVOX catalysts.

Raman scattering in different BIMEVOX (ME: Mg, Ni, Cu, and Zn) systems is studied by Bacewicz and Kurek. Raman spectra for all the BIMEVOX systems show some level of similarity, with a number of overlapping bands in the range 600 to 900 cm^{-1}as a dominant feature. Three bands are found at similar positions for the BINIVOX, BIZNVOX and BICUVOX; the most intense one at 855 cm^{-1} and two of similar intensity at 707–715 and 770–819 cm^{-1} and an extra band is seen for BIZNVOX at 912. However, BIMGVOX shows more number of peaks at around 860, 847, 520, 616, 633 and 673 cm^{-1}. Low frequency region also contain peaks at 155, 220-240 and 370 cm^{-1} (Bacewicz and Kurek 2000). Trzciński et al. (2017) also report the Raman spectra for different BIMEVOX (ME: Cu, Zn, Mn) systems (Trzciński, Borowska-Centkowska et al. 2015; Trzciński, Gasiorowski et al. 2017). They present the deconvoluted Raman spectrum for each system over the range of 580-1000 cm^{-1} and 5 peaks are found for BICUVOX and BIZNVOX, and 4 peaks for BIMNVOX. Table 4.19 includes the vibration modes and corresponding V-O bond lengths and bond order for parent and different BIMEVOX compounds reported in the literature. Shifting of peaks is observed for the same catalysts reported by two different authors and hence, shifting is seen in our results also in comparison with different F, 30_HRS_U and U catalysts.

4.1.2.6 *XPS (X-ray photoelectron spectroscopy)*

XPS spectra of BIMEVOX catalysts at different stages (wash, fresh, short and long term use) are carried out in order to understand, qualitatively and quantitatively, the surface elemental composition, carbon deposition and oxidation state of the components present

Table 4-17: Vibration modes and corresponding V-O bond lengths, bond order and valence state of vanadium estimated from the deconvoluted Raman spectra for wash, fresh (F), 30 hrs used and longtime used (U) BINIVOX catalysts

Catalysts	υ/cm^{-1}	R/Å	*s*	*Sum*
BINIVOX-WASH	870.55	1.67	1.43	5
	836.55	1.76	1.34	
	787	1.72	1.22	
	721	1.76	1.11	
BINIVOX-400_F	827.64	1.69	1.32	4.04
	779.3	1.73	1.21	
	896.5	1.65	1.50	
BINIVOX-600_F	831.8	1.69	1.36	4.00
	886.8	1.66	1.48	
	751.95	1.74	1.17	
BINIVOX-800_F	856.6	1.68	1.39	4.03
	827.53	1.68	1.4	
	726.7	1.71	1.25	
BINIVOX-400_30HRS_U	830.77	1.69	1.33	5.07
	729.8	1.76	1.09	
	799.7	1.71	1.26	
	871.6	1.68	1.39	
BINIVOX-600_30HRS_U	910	1.64	1.57	4.20
	837.5	1.69	1.38	
	788	1.72	1.25	
BINIVOX-800_30HRS_U	872.75	1.68	1.39	4.69
	815.46	1.71	1.27	
	689.12	1.82	0.92	
	744	1.75	1.12	
BINIVOX-400_U	836.1	1.69	1.35	5.12
	740.93	1.75	1.12	
	848.49	1.68	1.38	
	804.85	1.71	1.27	
BINIVOX-600_U	839.48	1.71	1.28	4.90
	735	1.77	1.06	
	874.4	1.69	1.32	
	816.91	1.71	1.25	
BINIVOX-800_U	855.89	1.69	1.35	5.08
	745	1.76	1.08	
	903.6	1.65	1.49	
	799.13	1.74	1.16	

Table 4-18: Vibration modes and corresponding V-O bond lengths, bond order and valence state of vanadium estimated from the deconvoluted Raman spectra for wash, fresh (F), 30 hrs used and longtime used (U) BICUVOX catalysts

Catalysts	υ/cm^{-1}	R/Å	*s*	*Sum*
BICUVOX-WASH	901	1.66	1.31	5.12
	826	1.69	1.3	
	805	1.7	1.26	
	721	1.76	1.1	
BICUVOX-400_F	832.68	1.69	1.34	4.03
	800.4	1.71	1.25	
	867.8	1.67	1.44	
BICUVOX-600_F	840.23	1.68	1.38	3.91
	807.98	1.69	1.30	
	777.89	1.72	1.23	
BICUVOX-800_F	831.89	1.69	1.34	4.03
	883.43	1.66	1.47	
	788.65	1.72	1.23	
BICUVOX-400_30HRS_U	706	1.78	1.03	4.99
	778	1.73	1.2	
	826	1.69	1.32	
	875.8	1.67	1.44	
BICUVOX-600_30HRS_U	889.46	1.67	1.47	4.15
	841.1	1.73	1.19	
	793.06	1.66	1.49	
BICUVOX-800_30HRS_U	877.3	1.65	1.51	4.28
	810.8	1.68	1.41	
	710.6	1.74	1.36	
BICUVOX-400_U	836.45	1.7	1.29	5.08
	746.06	1.76	1.11	
	804.4	1.71	1.27	
	861.8	1.67	1.41	
BICUVOX-600_U	843.55	1.65	1.51	4.25
	729.76	1.73	1.35	
	803.55	1.68	1.39	
BICUVOX-800_U	828.8	1.69	1.53	4.45
	781.1	1.73	1.41	
	897.89	1.65	1.51	

Table 4-19: Vibration modes and corresponding V-O bond lengths and bond order for parent and different BIMEVOX compounds reported in the literature

Catalysts	Preparation method	υ/cm^{-1}	R/Å	*s*	*Ref*
$Bi_4V_2O_{11}$	SSM, CT: 750°C /24h	644.4 716 812.6 826.7 855.1 925.6	1.83 1.77 1.7 1.7 1.68 1.64	0.89 1.06 1.30 1.30 1.39 1.57	(Trzciński, Borowska-Centkowska et al. 2015; Trzciński, Gasiorowski et al. 2017)
BICUVOX	SSM, CT: 830°C /24h	701.9 783 825.9 866.4 914.8	1.78 1.72 1.7 1.67 1.64	1.03 1.23 1.30 1.41 1.57	
BIZNVOX	SSM, CT: 840°C /24h	645.8 775.1 836.5 857.9 905.1	1.82 1.73 1.69 1.68 1.65	0.92 1.193 1.34 1.39 1.52	
BIMNVOX	SSM, CT: 750°C /24h	707.7 825.1 857.8 904.8	1.78 1.7 1.68 1.65	1.03 1.30 1.39 1.52	
$Bi_4V_2O_{11}$	SSM, CT: 820°C /15h	926 858 826 770 660	1.64 1.68 1.69 1.73 1.81	1.58 1.40 1.32 1.18 0.94	(Patwe, Patra et al. 2013)
BICUVOX	SSM, CT: 820°C /15h	978 868 826 709	1.61 1.67 1.69 1.78	1.73 1.43 1.32 1.05	
BIMGVOX	Combustion method:630°C and annealed at 900°C	762 847 860 912 930	1.74 1.68 1.67 1.64 1.63	1.16 1.38 1.41 1.55 1.6	(Bacewicz and Kurek 2000)
BINIVOX		707 770 856	1.78 1.77 1.68	0.96 1.18 1.4	
BICUVOX		707 777 855	1.78 1.73 1.68	0.96 1.19 1.4	
BIZNVOX		715 819 857 912	1.77 1.7 1.68 1.64	1.06 1.31 1.4 1.55	
$Bi_4V_2O_{11}$	Combustion	636	1.83	0.89	(Kumar and

	method:300°C and annealed at 800°C/5h	726	1.76	1.08	Sahare 2013)
		773	1.73	1.19	
		856	1.68	1.39	
		926	1.64	1.58	

SSM: Solid state method; CT: Combustion temperature

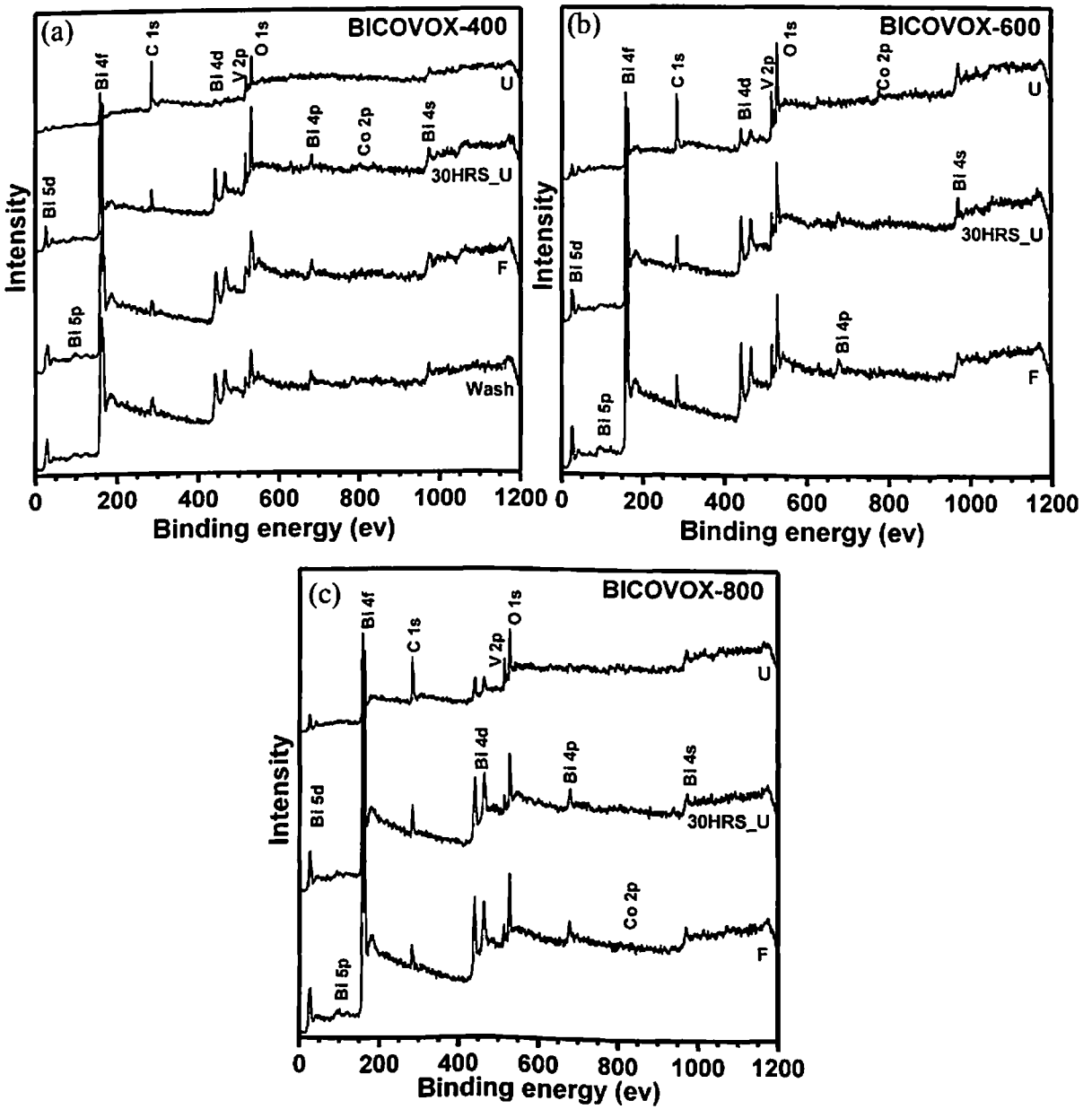

Figure 4-65: Wide range XPS spectra for the wash, fresh (F), 30 hrs used and long time used (U) BICOVOX catalysts; calcined at (a) 400, (b) 600, and (c) 800°C. All essential elements, Bi, V, O, and Co along with adventitious C are present for all samples

(Varga, Ferencz et al. 2015). Wide range XPS spectra of the BICOVOX catalysts (Figure 4.65), (a) washed and heat treated at 400°C, (b) heat treated at 600°C, and (c) heat treated at 800°C. in layer lines representing different stages of catalyst BICOVOX_F, BICOVOX-30Hrs_U and BICOVOX_U, show the presence of all essential elements, Bi, V, O, and Co, along with adventitious C in the samples. The peaks at ~ 27, 93, 163, 440, 460, 680, and 940 eV can be assigned to Bi5d, Bi5p, Bi4f, $Bi4d_{5/2}$, $Bi4d_{3/2}$, Bi4p, Bi4s, respectively (Nyholm R. 1980; Ling, Sun et al. 2010). Peaks at ~ 284, ~ 530, ~ 515, and ~ 779 eV correspond to C1s, O1s, V2p, and Co2p, respectively. Binding energies of all the elements are calibrated by carbon V2p, and Co2p, respectively. Binding energies of all the elements are calibrated by carbon i.e. 284.4 eV as it is found to be the maximum intensity peak for C1s.

Figure 4.66 shows the high resolution XPS spectra of all the elements, (a) Bi, (b) C, (c) V, (d) Co, and (e) O, present in the BICOVOX-wash catalyst. High resolution XPS spectra of the core level Bi4f, heat treated at (a) 400, (b) 600, (c) 800, and V2p, heat treated at (d) 400, (e) 600, (f) 800, in layer lines for different stages of BICOVOX catalysts is depicted in Figure 4.67. The Bi4f XPS spectrum of BICOVOX-400_F catalyst exhibits two peaks with two shoulders which suggest that the Bi is in doublet oxidation states. The two main peaks appear with their centers at 163.71 and 158.43 eV, correspond to the $Bi4f_{5/2}$ and $Bi4f_{7/2}$ binding energies of Bi metal (Vila, Díaz-Guerra et al. 2013). The shoulders, center at 164.2 and 159.04 eV, might ascribe to the $Bi4f_{5/2}$ and $Bi4f_{7/2}$ binding energies of Bi^{3+} (Vila, Díaz-Guerra et al. 2013). Similar trend is seen for BICOVOX-wash and BICOVOX-600_F catalysts. However, for BICOVOX-800_F catalyst, $Bi4f_{5/2}$ and $Bi4f_{7/2}$ peaks are found at binding energies of 164.71 and 159.36 eV, respectively, which is characteristic of Bi^{3+} in Bi_2O_3. After using the catalysts in the reactor, intensity and area of the lower binding energy peaks are observed to increase, suggesting the reduction of Bi^{3+} to lower oxidation states Bi^0 (Gan, Lu et al. 2015). Three peaks are obtained for BICOVOX-400_30HRS_U catalyst after deconvolution with their centers at 161.71, 158.1 and 159.24 eV, correspond to the $Bi4f_{5/2}$ and $Bi4f_{7/2}$ binding energies of Bi metal and $Bi4f_{7/2}$ binding energy of Bi^{3+}, respectively, as shown in Figure 4.67 (a). For Bi spectrum of BICOVOX-600_30HRS_U catalyst, the peaks with binding energies 158.62 and 163.9 eV are assigned to the $Bi4f_{7/2}$ and $Bi4f_{5/2}$ of Bi metal, respectively, and the deconvoluted peaks at 160.11 and 165.33 eV are attributed to $Bi4f_{7/2}$ and $Bi4f_{5/2}$ of Bi^{3+}, respectively, as depicted in Figure 4.67 (b). In comparison to BICOVOX-800_F, Bi4f spectrum of the BICOVOX-800_30HRS_U catalyst shows the presence of $Bi4f_{7/2}$ binding energy of Bi metal and both $Bi4f_{7/2}$ and $Bi4f_{5/2}$ of Bi^{3+} as mention in Figure 4.67 (c). For all BICOVOX_U catalysts, Bi4f spectra show both the

oxidation states. Peaks at 158.21($Bi4f_{7/2}$), 163.54 eV($Bi4f_{5/2}$) in BICOVOX-400_U, 158.15($Bi4f_{7/2}$), 162($Bi4f_{5/2}$) and 163.48 eV($Bi4f_{5/2}$) in BICOVOX-600_U, and 158.8 eV($Bi4f_{7/2}$) in BICOVOX-800_U are attributed to Bi metal. However, peaks corresponding to Bi^{3+} are seen at 159($Bi4f_{7/2}$), 164.42 eV($Bi4f_{5/2}$) in BICOVOX-400_U, 159.1 eV($Bi4f_{7/2}$) in BICOVOX-600_U and 159.52($Bi4f_{7/2}$), 164.08($Bi4f_{5/2}$) and 164.6 eV($Bi4f_{5/2}$) in BICOVOX-800_U catalysts. Table 4.20 shows the peak position, peak area (calculated after deconvolution) and peak area ratio of two different Bismuth oxidation states present in BICOVOX Fresh, 30HRS_Used and long time used catalysts. Ratio of Bi metal (Bi°) to Bi^{3+} is calculated in order to identify the phase distribution before and after use. Maximum Bi°: Bi^{3+} (4.54:1) ratio is acquired for BICOVOX-wash catalyst, which is happening due to the presence of reducing environment (glycine as fuel) during catalyst preparation (Varma, Mukasyan et al. 2016). Oxidation of metal during calcination is responsible for the reduction in the Bi°: Bi^{3+} ratio. However with use in the reactor, this ratio is found to increase (2.1 to 2.4 for BICOVOX-400_30HRS_U and further to 4.14 for BICOVOX-400_U catalysts, 0.66 to 1.53 and 3.69 for BICOVOX-600_30HRS_U and BICOVOX-600_U, respectively and 0 to 0.74 and 0.96 in case of BICOVOX-800_30HRS_U and BICOVOX-800_U, respectively), as the reforming reaction provides the reducing environment (presence of C, CO) inside the reactor (Lima da Silva, Malfatti et al. 2009; Garbarino, Finocchio et al. 2014). Increasing order of Bi°:Bi^{3+} for all BICOVOX catalysts is: BICOVOX-800_F<BICOVOX-600_F<BICOVOX-800_30HRS_U<BICOVOX-800_U<BICOVOX-600_30HRS_U<BICOVOX-400_F<BICOVOX-400_30HRS_U< BICOVOX-600_U< BICOVOX-400_U.

Turning to the high resolution $V2p_{3/2}$ core level XPS data as shown in Figure 4.67 (d-f), curve fitting with voigt function of $V2p_{3/2}$ XPS signal helps to detect the different oxidation states (V^{5+} and V^{4+}) of V element. For all BICOVOX_F catalysts, the $V2p_{3/2}$ is found at ~517 eV, which attributes to the V^{5+} oxidation state and $V2p_{3/2}$ is found at ~516.15 eV that features to V^{4+} oxidation state (Khaerudini, Guan et al. 2016). BICOVOX-wash also shows the same behavior. After catalytic activities, the intensity of peaks toward low binding energies (for V^{4+} oxidation state) is found to reduce, however, intensity of high binding energy peaks, indicating the presence of V^{5+} state, are found to increase (Wu, Thissen et al. 2004). All peak positions and the respective valence states are well explained in Table 4.21. The quantitative measures of V^{5+} and V^{4+} in BICOVOX catalysts are also mentioned in the Table. The calculated ratio of V^{5+}:V^{4+} for BICOVOX-wash catalyst is 0.96, which after calcining is found to reduce and ratio of V^{5+}:V^{4+} for BICOVOX-400_F, BICOVOX-600_F

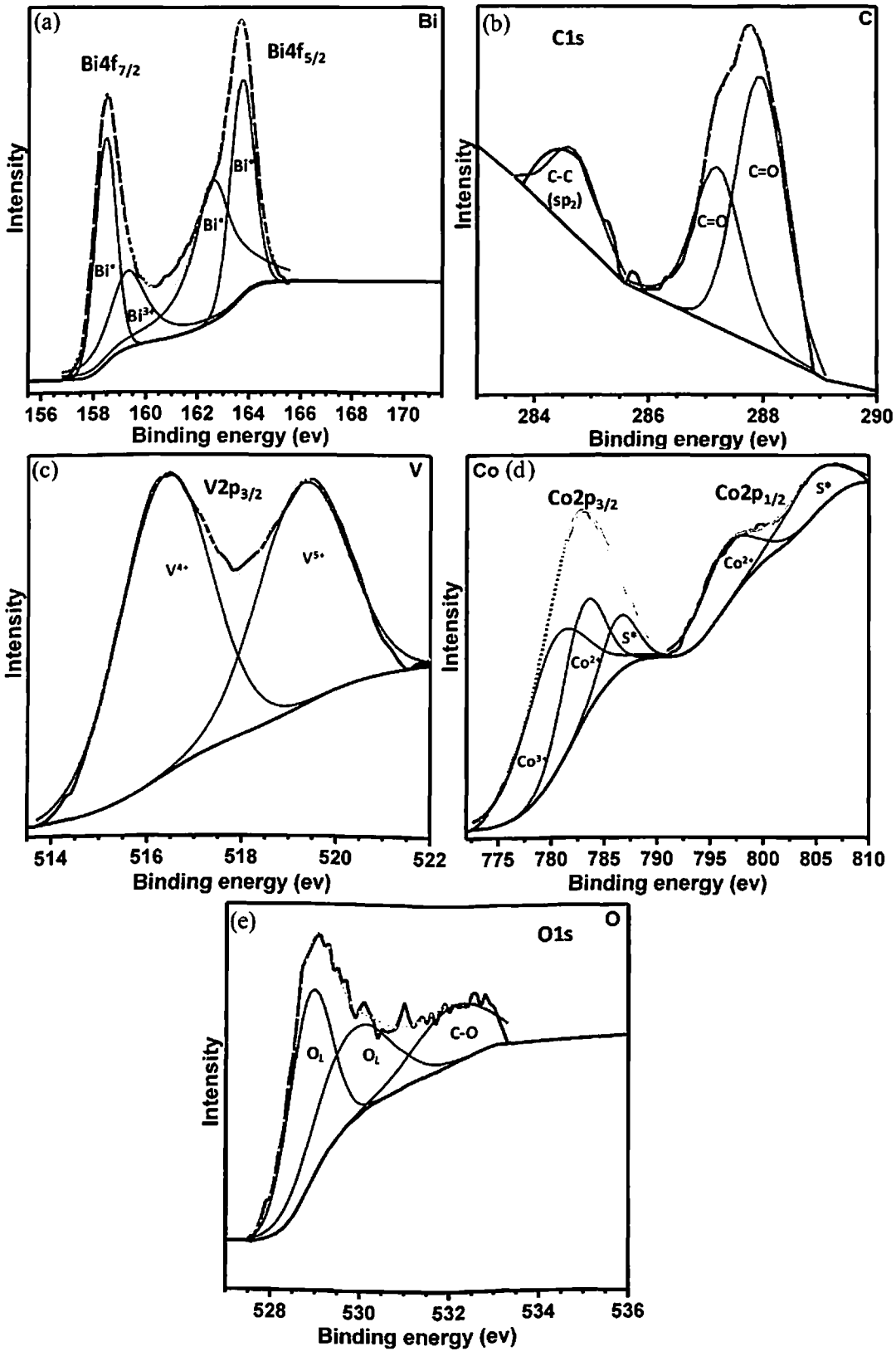

Figure 4-66: High resolution XPS spectra of (a) Bi, (b) C, (c) V, (d) Co and (e) O present in BICOVOX-wash catalyst. (O_L: Lattice oxygen; O_V: Oxygen valence; S*: Satellite peak)

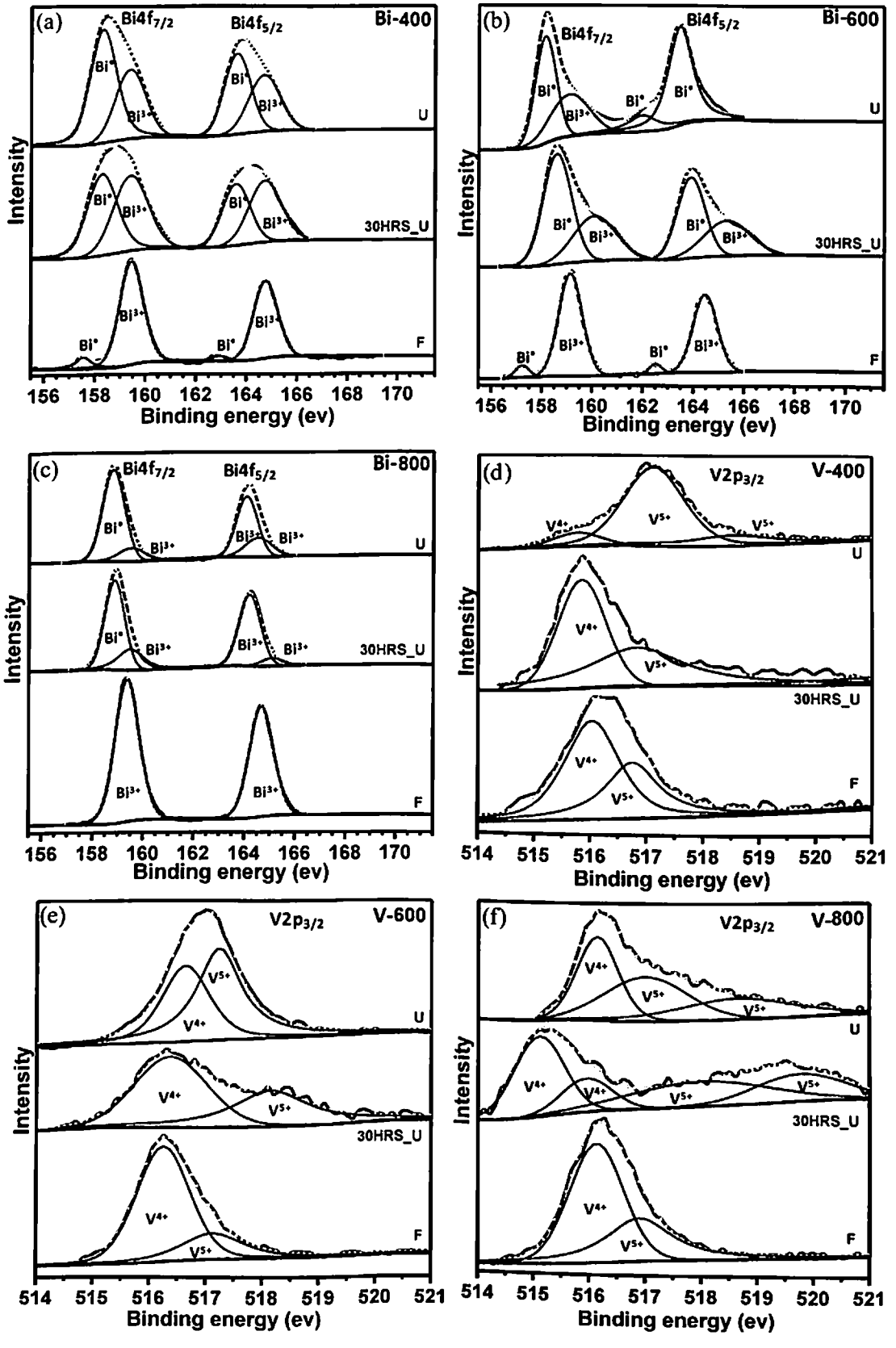

Figure 4-67: High resolution XPS spectra of Bi (a) 400, (b) 600, (c) 800, and V (d) 400, (e) 600, (f) 800 showing the variation of oxidation states for fresh, 30 hrs used and long time used BICOVOX catalysts

Table 4-20: Peak position, peak area (calculated after deconvolution) and peak area ratio of two different Bismuth oxidation states present in BICOVOX Fresh, 30 hrs used and long time used catalysts

Catalysts	Bismuth Peak position (eV)	Oxidation States	Peak area	Bi^0:Bi^{+3}	Error in fitting χ^2
Wash	158.45	$Bi^0(4f_{7/2})$	3814.12	4.54	1.83
	159.3	$Bi^{3+}(4f_{7/2})$	3236.24		
	162.6	$Bi^0(4f_{5/2})$	6636.46		
	163.74	$Bi^0(4f_{5/2})$	4233.85		
BICOVOX_400_F	158.43	$Bi^0(4f_{7/2})$	10019.1	2.1	1.235
	159.04	$Bi^{3+}(4f_{7/2})$	4345.93		
	163.71	$Bi^0(4f_{5/2})$	6650.9		
	164.2	$Bi^{3+}{}_3(4f_{5/2})$	3567.28		
BICOVOX_400_30_HRS_U	158.1	$Bi^0(4f_{7/2})$	1649.06	2.4	1.46
	159.24	$Bi^{3+}(4f_{7/2})$	3057.38		
	161.71	$Bi^0(4f_{5/2})$	5731.02		
BICOVOX_400_U	158.21	$Bi^0(4f_{7/2})$	7688.9	4.14	1.83
	159	$Bi^{3+}(4f_{7/2})$	2361.35		
	163.54	$Bi^0(4f_{5/2})$	5615.47		
	164.42	$Bi^{3+}(4f_{5/2})$	848.65		
BICOVOX_600_F	156.98	$Bi^0(4f_{7/2})$	498.31	0.66	1.589
	159	$Bi^{3+}(4f_{7/2})$	823.03		
	162.27	$Bi^0(4f_{5/2})$	497.39		
	164.22	$Bi^{3+}(4f_{5/2})$	676.78		
BICOVOX_600_30_HRS_U	158.62	$Bi^0(4f_{7/2})$	10707.77	1.53	1.758
	160.11	$Bi^{3+}(4f_{7/2})$	6481.98		
	163.92	$Bi^0(4f_{5/2})$	7367.83		
	165.33	$Bi^{3+}(4f_{5/2})$	5352.8		
BICOVOX_600_U	158.15	$Bi^0(4f_{7/2})$	7491.91	3.69	1.86
	159.1	$Bi^{3+}(4f_{7/2})$	5474.49		
	162.0	$Bi^0(4f_{5/2})$	2396.46		
	163.48	$Bi^0(4f_{5/2})$	10317.6		
BICOVOX_800_F	159.36	$Bi^{3+}(4f_{7/2})$	7937.05	No metal	1.797
	164.71	$Bi^{3+}(4f_{5/2})$	6053.61		
BICOVOX_800_30_HRS_U	158.9	$Bi^0(4f_{7/2})$	3179.31	0.74	1.75
	159.5	$Bi^{3+}(4f_{7/2})$	1196.04		
	164.22	$Bi^{3+}(4f_{5/2})$	2792.49		
	165.1	$Bi^{3+}(4f_{5/2})$	316.6		
BICOVOX_800_U	158.8	$Bi^0(4f_{7/2})$	4376.97	0.96	1.508
	159.52	$Bi^{3+}(4f_{7/2})$	735.4		
	164.08	$Bi^{3+}(4f_{5/2})$	2741.23		
	164.6	$Bi^{3+}(4f_{5/2})$	1073		

and BICOVOX-800_F are 0.65, 0.33 and 0.63, respectively and this reflects that BICOVOX-600_F catalyst illustrates the maximum amount of V^{4+} oxidation state. This ratio increases to 1.04, 0.74 and 1.02 for BICOVOX-400_30HRS_U, BICOVOX-600_30HRS_U and BICOVOX-800_30HRS_U, respectively. Later, after using catalysts for long time, this ratio further increases to 3.6, 1.4 and 1.78 for BICOVOX-400_U, BICOVOX-600_U and BICOVOX-800_U, respectively. The decreasing order of V^{4+} oxidation state for all catalysts is found to be:

BICOVOX-600_F> BICOVOX-800_F> BICOVOX-400_F> BICOVOX-600_30HRS_U> BICOVOX-WASH> BICOVOX-800_30HRS_U> BICOVOX-400_30HRS_U> BICOVOX-600_U> BICOVOX-800_U> BICOVOX-400_U.

Apparently the anomalous oxidation/reduction behavior is observed in reactor conditions, that V gets oxidized but bismuth reduces could be due to reducing environment inside reactor causes Bi^{3+} reduction to Bi^0 and V oxidation state influence by doping metal.

Kim et al, (1997) study and report the Bi4f and V2p XPS spectra for $Bi_4V_2O_{11}$ and $Bi_4V_{1.8}Co_{0.2}O_{11-\delta}$ catalyst, prepared by solid state method (Kim and Miyayama 1997). Bi4f spectrum shows the presence of Bi^{3+} at 159($Bi4f_{7/2}$), 164.42 eV($Bi4f_{5/2}$) with a very weak shoulder line on the low binding energy side due to $Bi4f_{7/2}$ and $Bi4f_{5/2}$ of Bi metal for both the compounds. V2p spectrum shows the presence of only V^{5+} oxidation state in case of $Bi_4V_2O_{11}$, however, in case of $Bi_4V_{1.8}Co_{0.2}O_{11-\delta}$, shifting of peak toward lower binding energy is inspected which refers the presence of V^{4+} oxidation state.

Khaerudini et al, (2016) report the XPS spectrum of V2p for $Bi_4V_2O_{11}$ and BINBVOX catalyst, prepared by solid state reaction (Khaerudini, Guan et al. 2016). For $Bi_4V_2O_{11}$ catalyst, the $V2p_{3/2}$ is seen at 516.7 eV, attributes to V^{5+} state. However, for BINBVOX, the shift transformation in V species towards a smaller oxidation state is detected and peak at 516.3 is featured to V^{4+} state. They report that formation of V^{4+} oxidation state, caused by the stabilization of good ionic conductivity of the γ phase, reflects the creation of more vacancies. Lu et al, (2015) examine the XPS of $Bi_4V_2O_{11}$ nanoparticles, prepared by Pechini method on the base of citrate-complexation route (Lu, Pu et al. 2015). The XPS curve of V2p shows the presence of $V2P_{3/2}$ and $V2P_{1/2}$ peaks appear at 516 and 525 eV, respectively and both are ascribed to V^{5+} in the $Bi_4V_2O_{11}$. The Bi4f XPS curve is also reported and it exhibits the characteristic of Bi $4f_{5/2}$ and Bi $4f_{7/2}$ signals for Bi^{3+} and Bi^0. Lv et al, (2017) execute the XPS study over $Bi_4V_2O_{11}$ catalyst, prepared by direct combustion (Lv, Chen et al. 2017). Peaks located at 159.2 and 164.5 eV in Bi4f XPS curve are corresponding to Bi^{3+}

with small shoulder towards low binding energies indicates the presence of Bi metal. As for V2p XPS spectra, V peaks are located at 516.7 and 524.3 eV belong to V^{5+}, whereas no V^{4+} is emerges. Our results are also consistent with the literature and it is concluded that binding energy of Bi4f electrons is independent of metal substitution and no inter-metallic peak is detected.

High resolution XPS spectra of C1s (Figure 4.68 (a-c)) show the variation of coke deposition on the surface of the BICOVOX catalysts at fresh and used conditions. For all BICOVOX_F along with BICOVOX-wash catalysts, core level XPS spectra of C-1s comprises mainly of the adventitious carbon (C-C) at ~284 eV and ascribe to sp^2 hybridized C-C bonding (Zhang, Liu et al. 2016). Right extended peaks of C-1s at 287(C = O), and 287.95 eV(C = O) in BICOVOX-wash, 285.6(sp^3 hybridized carbon) and 288.01 eV(C = O) in BICOVOX-400_F, 285.2(sp^3 hybridized carbon), 288.1 eV(C = O) in BICOVOX-600_F and 285(sp^3 hybridized carbon) and 287.6(C = O) eV in BICOVOX-800_F denote the presence of C = O, sp^3 hybridized carbon (Blume, Rosenthal et al. 2015; Ma, Ran et al. 2015; Tatarova, Dias et al. 2017). After using catalysts in the reactor, the amount of carbon is found to increase. C1s spectrum of BICOVOX-400_30HRS_U and BICOVOX-600_30HRS_U catalysts show increase in the intensity and area of peak at ~284 eV(C-C(sp^2)) with small shoulder peak at ~285.4(C-C(sp^3)) and ~287.88 eV(C=O). However, BICOVOX-800_30HRS_U catalyst shows the presence of C-O at 286.68 eV. For long time used catalysts, BICOVOX-600_U shows the existence of C-C(sp^2 and sp^3) bonds only. While, BICOVOX-400_U and BICOVOX-800_U show the presence of C-C(sp^2 and sp^3) bonds with C=O bond at ~288.9 eV. Peak position and peak area of different forms of carbon present in BICOVOX_F, 30HRS_U and long time used catalysts are given in Table 4.22. It shows that, among the fresh catalysts BICOVOX-400_F has the highest amount, which is expected because of the organic precursor (glycine) used for the powder synthesis. As the heat treatment temperature increases, more and more carbon burns off the surface as evident from the spectra of the BICOVOX-600_F and BICOVOX-800_F catalysts. The decreasing order of carbon amount for all fresh and wash catalysts is: BICOVOX-WASH> BICOVOX-400_F> BICOVOX-600_F> BICOVOX-800_F.

Ratio of BICOVOX_F: BICOVOX _30HRS_U: BICOVOX_U is also evaluated to compare the catalysts. BICOVOX_F: BICOVOX _30HRS_U: BICOVOX_U ratio is 1:2.19:3.21, 1:1.93:2.98 and 1:2.79:4.05 for BICOVOX-400, BICOVOX-600 and BICOVOX-800 catalysts, respectively. The decreasing order for BICOVOX_F: BICOVOX _30HRS_U: BICOVOX_U ratio is: BICOVOX-800> BICOVOX-400> BICOVOX-600.

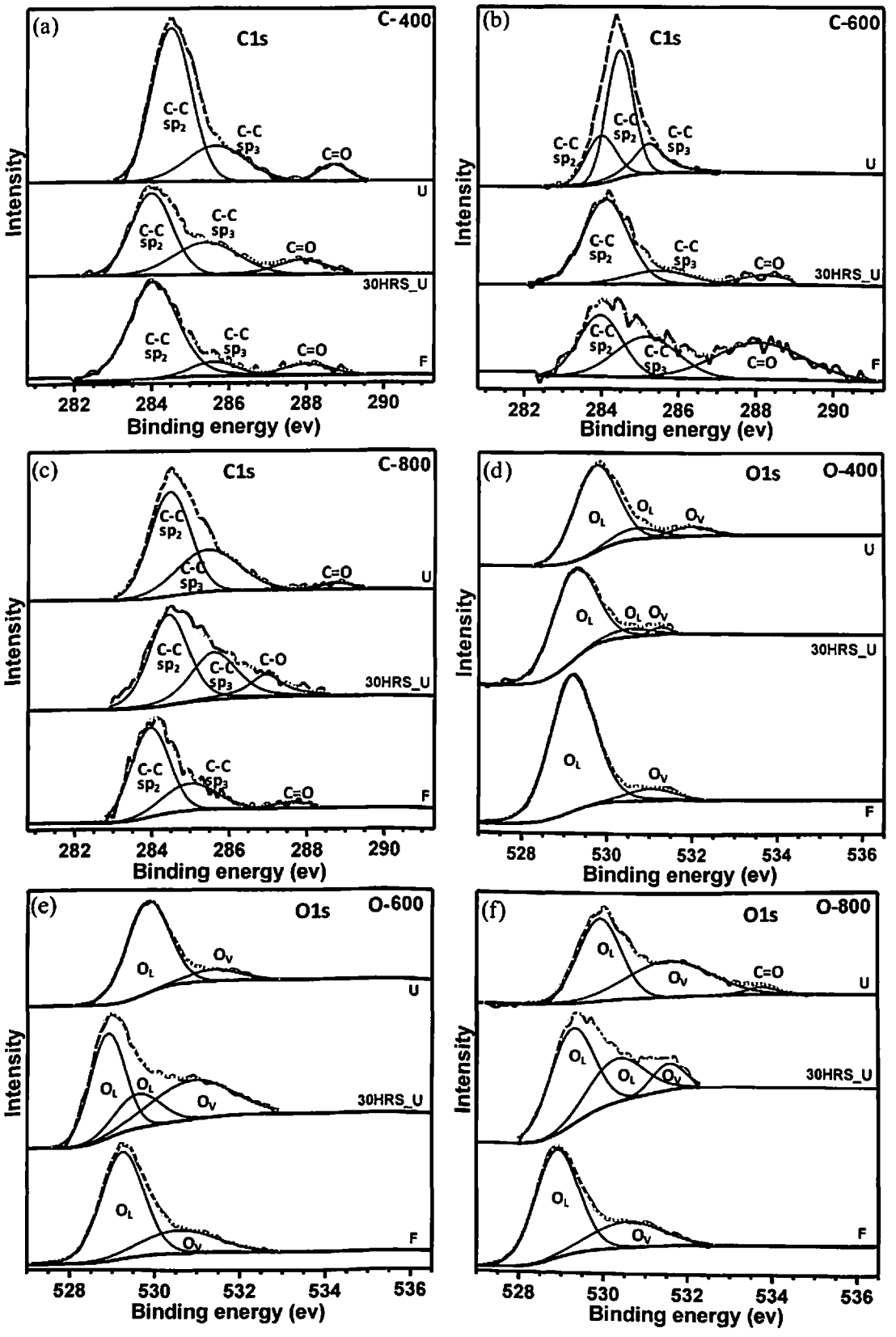

Figure 4-68: High resolution XPS spectra of C [(a) 400, (b) 600, (c) 800°C] and O [(d) 400, (e) 600, (f) 800°C] showing the variation of coke deposition and oxygen phase variation for fresh (F) 30 hrs used and long time used BICOVOX catalysts

Figure 4.68 (d-f) represents the XPS spectra for O1s for all the BICOVOX catalysts. These peaks indicate the presence of oxygen in various forms. In Figure 4.68 (d) deconvoluted peaks at 529.2 and 531.04 eV in BICOVOX-400_F, in Figure 4.68 (e) peaks at 529.23 and 531.2 eV in BICOVOX-600_F and in Figure 4.68 (f) peaks at 528.89 and 531.2 eV confirm the presence of lattice oxygen peak (O_L) and oxygen vacancies (O_V), respectively (Kundu, Satpati et al. 2017). In BICOVOX-wash catalyst along with these two peaks, an extra peak at 532.08 eV is emerges and attribute to chemisorbed oxygen (O-C) (Kundu, Satpati et al. 2017). Similar to BICOVOX_F catalysts, BICOVOX_30HRS_U catalysts also confirms the presence of lattice oxygen peak (O_L) and oxygen vacancies (O_V). Peaks at 529.23(O_L), 530.52(O_L), and 531.27 eV(O_V) in BICOVOX-400_30HRS_U, at 528.87(O_L), 529.59(O_L), and 531.2 eV(O_V) in BICOVOX-600_30HRS_U, and at 529.24(O_L), 530.31(O_L), and 531.54 eV(O_V) in BICOVOX-800_30HRS_U are observed. O 1s spectra of BICOVOX-400_U and BICOVOX-600_U catalysts show the similar nature. However, BICOVOX-800_U catalyst shows an extra peak at 533.75 eV and affirms the presence of C=O bond. The peak position, peak area and corresponding assignments are well explained in Table 4.23.

XPS spectra of Co2p for all BICOVOX catalysts are depicted in Figure 4.69 (a-c). The five deconvoluted peaks at ~780(Co^{3+}), ~782.56(Co^{2+}), 786.5(satellite), 797.2(Co^{2+}) and 804.8(satellite) eV denote the presence of Co in the lattice in Co^{3+} and Co^{2+} oxidation state along with satellite peaks (Petitto, Marsh et al. 2008). Peak position, peak area and corresponding ratio of two oxidation states of cobalt present in BICOVOX_F, 30HRS_Used and long time used catalysts are summarized in Table 4.24.

Table 4.25 includes the atomic% of each element present in the catalyst with Bi to V and V to metal (Co) ratio for all cases of BICOVOX catalyst. Atomic% of each element of a catalyst is determined using wide spectrum and considering the core shell peaks for each element. Bi to V and V: Co ratios are ~2 and ~9 (taking ±0.5 error) for all BICOVOX catalysts suggest that proper stoichiometry is maintained in the compositions.

Figure 4.70 also shown in a layer lines representing different stages of catalyst starting from BINIVOX_F to BINIVOX_U, heat treated at (a) 400, (b) 600; and (c) 800°C to depict the wide range XPS spectra of the BINIVOX catalysts. The elements present in the BINIVOX catalysts are Bi, V, C, Ni, and O. Bi peaks are observed at ~ 27.4, 93.4, 163.8, 440, 460, 680, and 940.1 eV, and can ascribe to Bi5d, Bi5p, Bi4f, $Bi4d_{5/2}$, $Bi4d_{3/2}$, Bi4p, Bi4s, respectively (Nyholm R. 1980; Ling, Sun et al. 2010). V2p, C1s, Ni2p and O1s peaks are emerged at ~516, ~284.3, ~854 and ~530 eV, respectively.

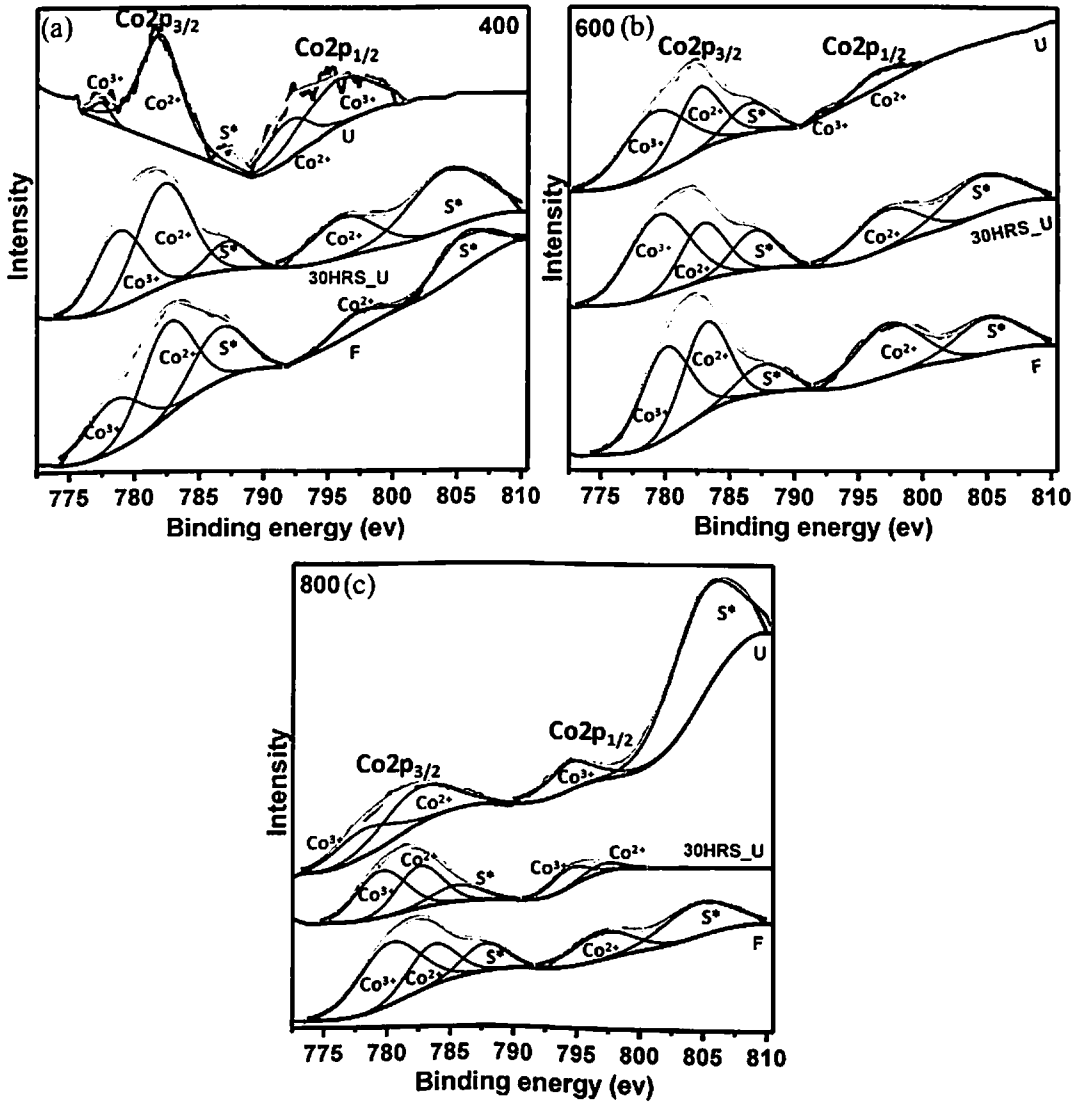

Figure 4-69: High resolution XPS spectra of Co for the fresh (F), 30 hrs used and long time used BICOVOX catalysts; calcined at (a) 400, (b) 600, and (c) 800°C

Table 4-21: Peak position, peak area (after deconvolution) and corresponding ratio of two oxidation states of V present in BICOVOX Fresh, 30 hrs used and long time used catalysts

Catalysts	Vanadium Peak position (eV)	Oxidation States	Peak area	Ratio (V^{5+}/V^{4+})	Error in fitting χ^2
Wash	516.38 519.29	V^{4+} V^{5+}	904.94 863.21	0.96	1.021
BICOVOX_400_F	516.05 516.99	V^{4+} V^{5+}	1687.88 1092.8	0.37	1.95
BICOVOX_400_30_HRS_U	515.89 516.96	V^{4+} V^{5+}	1312.62 1360.69	1.04	1.62
BICOVOX_400_U	515.77 517.13 518.25	V^{4+} V^{5+} V^{5+}	460 1327.38 336.897	3.6	1.342
BICOVOX_600_F	516.26 517.16	V^{4+} V^{5+}	2665.21 860.7	0.23	1.456
BICOVOX_600_30_HRS_U	516.38 518.15	V^{4+} V^{5+}	1385.73 1027.56	0.74	1.46
BICOVOX_600_U	516.64 517.23	V^{4+} V^{5+}	1796.76 2515.57	1.4	1.39
BICOVOX_800_F	516.15 516.95	V^{4+} V^{5+}	2118.6 1332.12	0.32	1.376
BICOVOX_800_30_HRS_U	515.2 516 517.65 519.5	V^{4+} V^{4+} V^{5+} V^{5+}	985.56 408.82 838.0203 593.16	1.02	1.366
BICOVOX_800_U	516.17 517 518.6	V^{4+} V^{5+} V^{5+}	1196.34 1204.67 924.85	1.78	1.422

Table 4-22: Peak position and peak area (calculated after deconvolution) of different forms of carbon present in BICOVOX Fresh, 30 hrs used and long time used catalysts

Catalysts	Carbon Peak position (eV)	Carbon forms	Peak area	Amount of total C Ratio (F:30HRS_U:U)	Error in fitting χ^2
Wash	284.57 287.19 287.95	C-C(sp_2) C=O C=O	1325.86 1547.16 2129.89		0.913
BICOVOX_400_F	284.1 285.61 288.01	C-C(sp_2) C-C(sp_3) C=O	843.66 293.40 244.99	1:2.19:3.21	0.853
BICOVOX_400_30_HRS_U	284 285.41 287.88	C-C(sp_2) C-C(sp_3) C=O	1546.85 944.9 382.46		0.948
BICOVOX_400_U	284.5 285.66 288.7	C-C(sp_2) C-C(sp_3) C=O	2699.6 946.63 227.61		1.142
BICOVOX_600_F	283.96 285.18 288.09	C-C(sp_2) C-C(sp_3) C=O	448.27 424.92 598.87	1:1.93:2.98	0.966
BICOVOX_600_30_HRS_U	284.12 285.51 288.24	C-C(sp_2) C-C(sp_3) C=O	1387.7 297.99 169.42		0.949
BICOVOX_600_U	283.99 284.48 285.24	C-C(sp_2) C-C(sp_2) C-C(sp_3)	634.53 1407.28 556.09		0.855
BICOVOX_800_F	283.98 284.98 287.63	C-C(sp_2) C-C(sp_3) C=O	601.76 217.17 27.09	1:2.79:4.05	0.975
BICOVOX_800_30_HRS_U	284.42 285.42 286.68	C-C(sp_2) C-C(sp_3) C-O	1583.72 708.38 512.83		1.179
BICOVOX_800_U	284.44 285.43 288.78	C-C(sp_2) C-C(sp_3) C=O	2060.95 1258.42 158.73		0.853

Table 4-23: Peak position and peak area (calculated after deconvolution) of different forms of oxygen present in BICOVOX Fresh, 30 hrs used and long time used catalysts

Catalysts	Oxygen Peak position (eV)	Oxygen forms	Peak area	Ratio (O_L: O_V)	Error in fitting χ^2
Wash	528.88 529.84 532.08	O_L(ME-O) O_L(ME-O) C-O	993.52 844.35 550.37	5.2	0.978
BICOVOX_400_F	529.2 531.04	O_L(ME-O) O_V	5526.42 468.14	2.8	0.808
BICOVOX_400_30_HRS_U	529.23 530.52 531.27	O_L(ME-O) O_L(ME-O) O_V	2639.59 225.19 92.18	3.2	1.337

BICOVOX_400_U	529.74 530.69 531.97	O_L(ME-O) O_L(ME-O) O_V	2806.1 369.09 274.28	4.5	1.249
BICOVOX_600_F	529.23 531.2	O_L(ME-O) O_V	5465.26 1988.09	1.7	0.921
BICOVOX_600_30_HRS_U	528.87 529.59 531.2	O_L(ME-O) O_L(ME-O) O_V	2210.89 949.78 1868.02	2.1	0.905
BICOVOX_600_U	529.81 531.39	O_L(ME-O) O_V	4483.35 669.29	3.1	0.915
BICOVOX_800_F	528.89 531.2	O_L(ME-O) O_V	4554.88 1718.63	2.4	1.178
BICOVOX_800_30_HRS_U	529.24 530.31 531.54	O_L(ME-O) O_L(ME-O) O_V	2156.45 1221.57 431.56	2.9	1.459
BICOVOX_800_U	529.9 531.55 533.75	O_L(ME-O) O_V C=O	1681.71 1434.83 103.22	3.6	1.117

Table 4-24: Peak position, peak area (calculated after deconvolution) and corresponding ratio of two oxidation states of Cobalt present in BICOVOX Fresh, 30 hrs used and long time used catalysts

Catalysts	Cobalt Peak position (eV)	Oxidation States	Peak area	Ratio (Co^{3+}:Co^{2+})	Error in fitting $\chi 2$
Wash	780.20 782.96 786.34 796.37 804.52	$Co^{3+}(2p_{3/2})$ $Co^{2+}(2p_{3/2})$ Satellite $Co^{2+}(2p_{1/2})$ Satellite	514.77 464.98 180.14 496.43 183.69	0.53	0.92
BICOVOX_400_F	778.27 782.56 786.74 797.21 805.46	$Co^{3+}(2p_{3/2})$ $Co^{2+}(2p_{3/2})$ Satellite $Co^{2+}(2p_{1/2})$ Satellite	326.33 653.98 308.3 106.23 252.79	0.43	0.93
BICOVOX_400_30_HRS_U	778.75 782.19 787.16 796.19 804.27	$Co^{3+}(2p_{3/2})$ $Co^{2+}(2p_{3/2})$ Satellite $Co^{2+}(2p_{1/2})$ Satellite	452.67 683.27 140.25 325.85 574.92	0.45	0.94
BICOVOX_400_U	777.43 781.96 787.5 791.77 795.62	$Co^{3+}(2p_{3/2})$ $Co^{2+}(2p_{3/2})$ Satellite $Co^{3+}(2p_{1/2})$ $Co^{2+}(2p_{1/2})$	23.49 63.16 3.34 21.78 31.49	0.47	0.92
BICOVOX_600_F	779.95 783.12 787.68 797.28 805.14	$Co^{3+}(2p_{3/2})$ $Co^{2+}(2p_{3/2})$ Satellite $Co^{2+}(2p_{1/2})$ Satellite	644.55 595.32 194.06 477.56 318.07	0.6	0.95

BICOVOX_600_30_HRS_U	779.43	$Co^{3+}(2p_{3/2})$	668.26	0.88	0.92
	782.94	$Co^{2+}(2p_{3/2})$	392.61		
	787.02	Satellite	246.33		
	797.06	$Co^{2+}(2p_{1/2})$	359.81		
	804.42	Satellite	385.48		
BICOVOX_600_U	779.12	$Co^{3+}(2p_{3/2})$	306.8	1.1	0.92
	782.61	$Co^{2+}(2p_{3/2})$	241.44		
	789.12	Satellite	306.8		
	792.14	$Co^{3+}(2p_{1/2})$	6.977		
	796.53	$Co^{2+}(2p_{1/2})$	56.11		
BICOVOX_800_F	780.17	$Co^{3+}(2p_{3/2})$	542.97	1.1	0.93
	783.56	$Co^{2+}(2p_{3/2})$	272.82		
	787.72	Satellite	171.84		
	797.03	$Co^{2+}(2p_{1/2})$	229.34		
	804.62	Satellite	323.38		
BICOVOX_800_30_HRS_U	779.33	$Co^{3+}(2p_{3/2})$	290.09	1.2	0.92
	782.37	$Co^{2+}(2p_{3/2})$	295.86		
	785.41	Satellite	125.09		
	794.28	$Co^{3+}(2p_{1/2})$	102.03		
	796.98	$Co^{2+}(2p_{1/2})$	40.29		
BICOVOX_800_U	778.02	$Co^{3+}(2p_{3/2})$	115.18	1.32	0.92
	782.3	$Co^{2+}(2p_{3/2})$	180.92		
	794.38	$Co^{3+}(2p_{1/2})$	125.38		
	804.79	Satellite	507.27		

Table 4-25: Atomic% of each element and corresponding Bi: V and V: Co surface ratio data from XPS Analysis for wash, fresh, 30 hrs used and long time used BICOVOX catalysts

Catalyst	Elements Present (at%)					Bi: V ratio	V: Co ratio
	Bi	C	Co	O	V		
BICOVOX-WASH	13.25	47.15	0.72	32.29	6.59	2.01	9.15
BICOVOX-400_F	20.02	43.18	1.1	25.9	9.8	2.04	8.9
BICOVOX-400_30HRS_U	12.9	49.97	0.7	30.15	6.28	2.05	8.97
BICOVOX-400_U	14.3	65.59	0.75	12.82	6.54	2.18	8.72
BICOVOX-600_F	15.31	39.62	0.83	36.71	7.53	2.03	9.07
BICOVOX-600_30HRS_U	11.65	48.8	0.61	33.46	5.48	2.12	8.98
BICOVOX-600_U	10.18	61.19	0.56	23.01	5.06	2.01	9.0
BICOVOX-800_F	16.15	33.97	0.89	40.94	8.05	2.00	9.04
BICOVOX-800_30HRS_U	12.02	52.26	0.63	29.33	5.76	2.08	9.1
BICOVOX-800_U	8.92	74.63	0.49	11.51	4.45	2.0	9.05

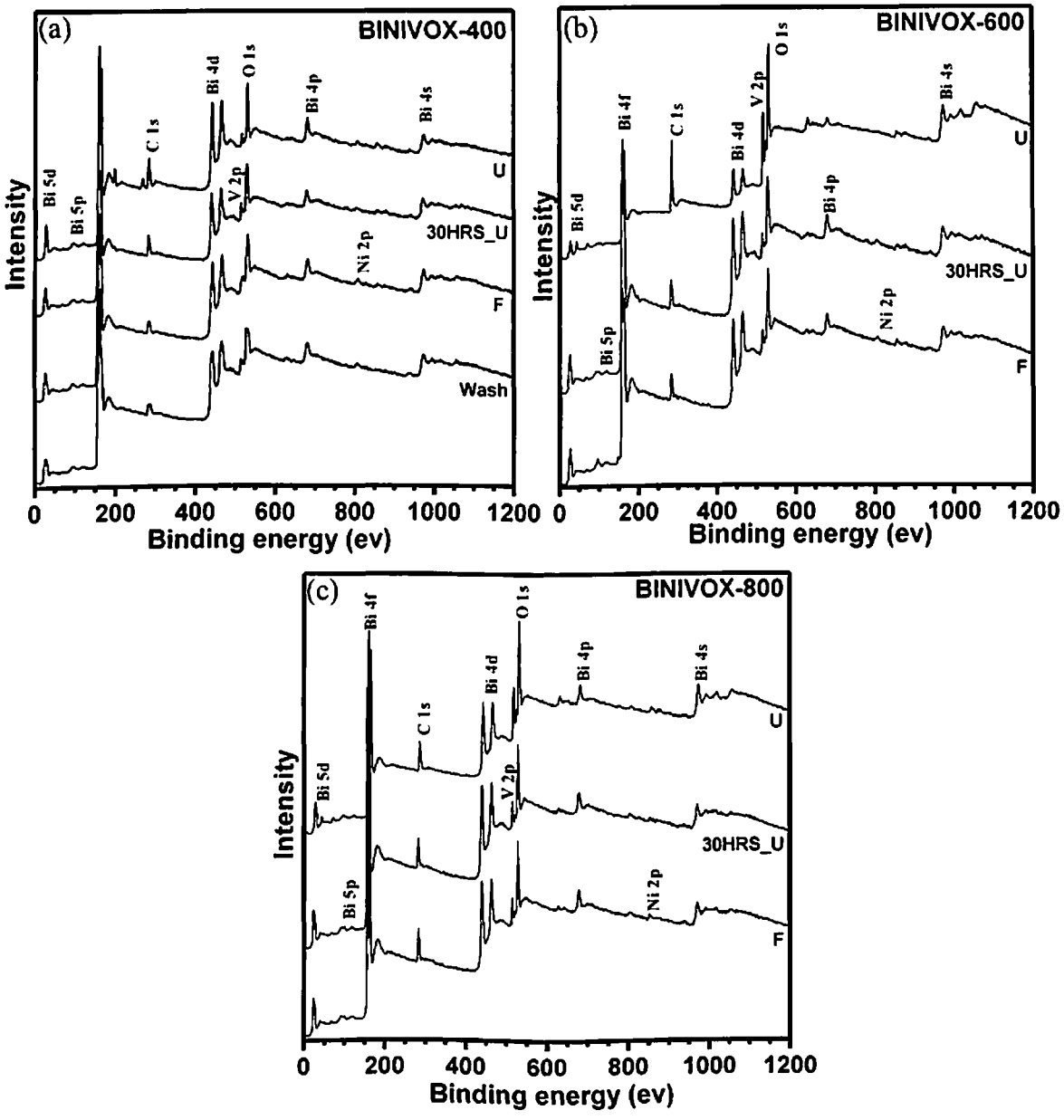

Figure 4-70: Wide range XPS spectra for the wash, fresh (F), 30 hrs used and long time used (U) BINIVOX catalysts; calcined at (a) 400, (b) 600, and (c) 800°C. All essential elements, Bi, V, O, and Ni along with adventitious C are present for all the samples

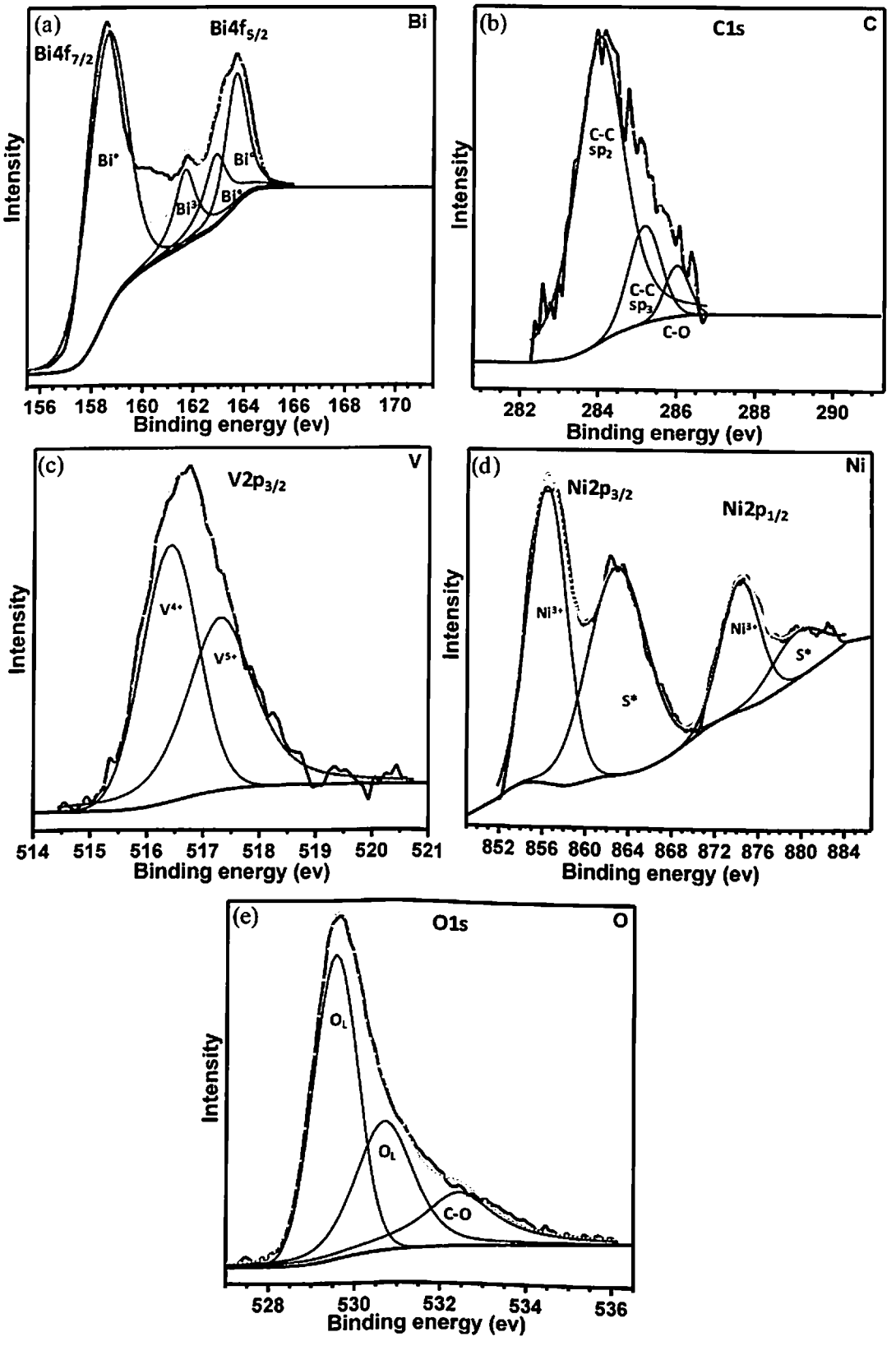

Figure 4-71: High resolution XPS spectra of (a) Bi, (b) C, (c) V, (d) Ni and (e) O present in BINIVOX-wash catalyst

High resolution XPS spectra of all the elements ((a) Bi, (b) C, (c) V, (d) Co, and (e) O) present in BINIVOX-wash catalyst are shown in Figure 4.71. Figure 4.72 (a-c) shows the XPS spectra of high resolution Bi4f orbital for BINIVOX catalysts. The Bi4f spectrum of BINIVOX-400_F catalyst is displayed in Figure 4.72 (a) and two symmetric, high intensity peaks are noted at 160.5 and 165.8 eV, indicating the Bi ions are in Bi^{3+} oxidation state (Liu, Yin et al. 2012; Liu, Niu et al. 2014). Both high intensity peaks are followed by small shoulder peaks toward low binding energies at 158.7 and 164.4 eV and assign to Bi° oxidation state. Similar curve character is observed for BINIVOX-wash catalyst and it show two high intensity Bi^{3+} oxidation state peaks follow by another two low binding energy peaks for Bi° oxidation state. Analogous to BICOVOX-800_F, BINIVOX-600_F and BINIVOX-800_F catalysts also show only Bi^{3+} oxidation state and two high intensity peaks at ~160 and ~165 eV are found. After 30 hrs of reforming reactions, BINIVOX-400_30HRS_U catalyst shows the peak shift towards low binding energies relative to BINIVOX-400_F and the intensity of peaks, indicating the presence of Bi^{3+} oxidation state at 159.7 eV, reduces. BINIVOX-600_30HRS_U and BINIVOX-800_30HRS_U catalysts show the presence in Bi° oxidation state at ~158 and ~163 eV, which is not seen in BINIVOX-600_F and BINIVOX-800_F catalysts. After using catalysts for long time, in all three BINIVOX_U catalysts, intensity of low binding energy peaks are found to increase and indicates the formation of more Bi in Bi° oxidation state at ~158 and ~163 eV. On the other hand intensity of Bi^{3+} oxidation state peaks at ~159 and ~164.3 eV is reduces. All peak positions, peak areas and the respective valence states are well explained in Table 4.26 along with the ratio of Bi metal (Bi°) to Bi^{3+}. Similar to BICOVOX-wash, BINIVOX-wash catalyst shows the maximum value for the Bi°: Bi^{3+} (7.47) ratio and with calcination this ratio reduces and for BINIVOX-600_F and BINIVOX-800_F, no Bi° oxidation state is present. This ratio further increase with use and maximum value (2.99), in all used catalysts, is detected for BINIVOX-400_U catalyst. Increasing order of Bi°:Bi^{3+} for all BINIVOX catalysts is:

BINIVOX-800_F=BINIVOX-600_F<BINIVOX-400_F<BINIVOX-800_30HRS_U<BINIVOX-600_30HRS_U<BINIVOX-400_30HRS_U<BINIVOX-800_U<BINIVOX-600_U<BINIVOX-400_U.

It is evident in Figures 4.72 (d-f) that vanadium in all the BINIVOX exists in the V^{5+} and V^{4+} oxidation states. The binding energies of $V2p_{3/2}$ peaks are ~516.4 and ~517.4 eV for all BINIVOX_F catalysts along with wash, which can be characteristic of V^{4+} in VO_2 and V^{5+}

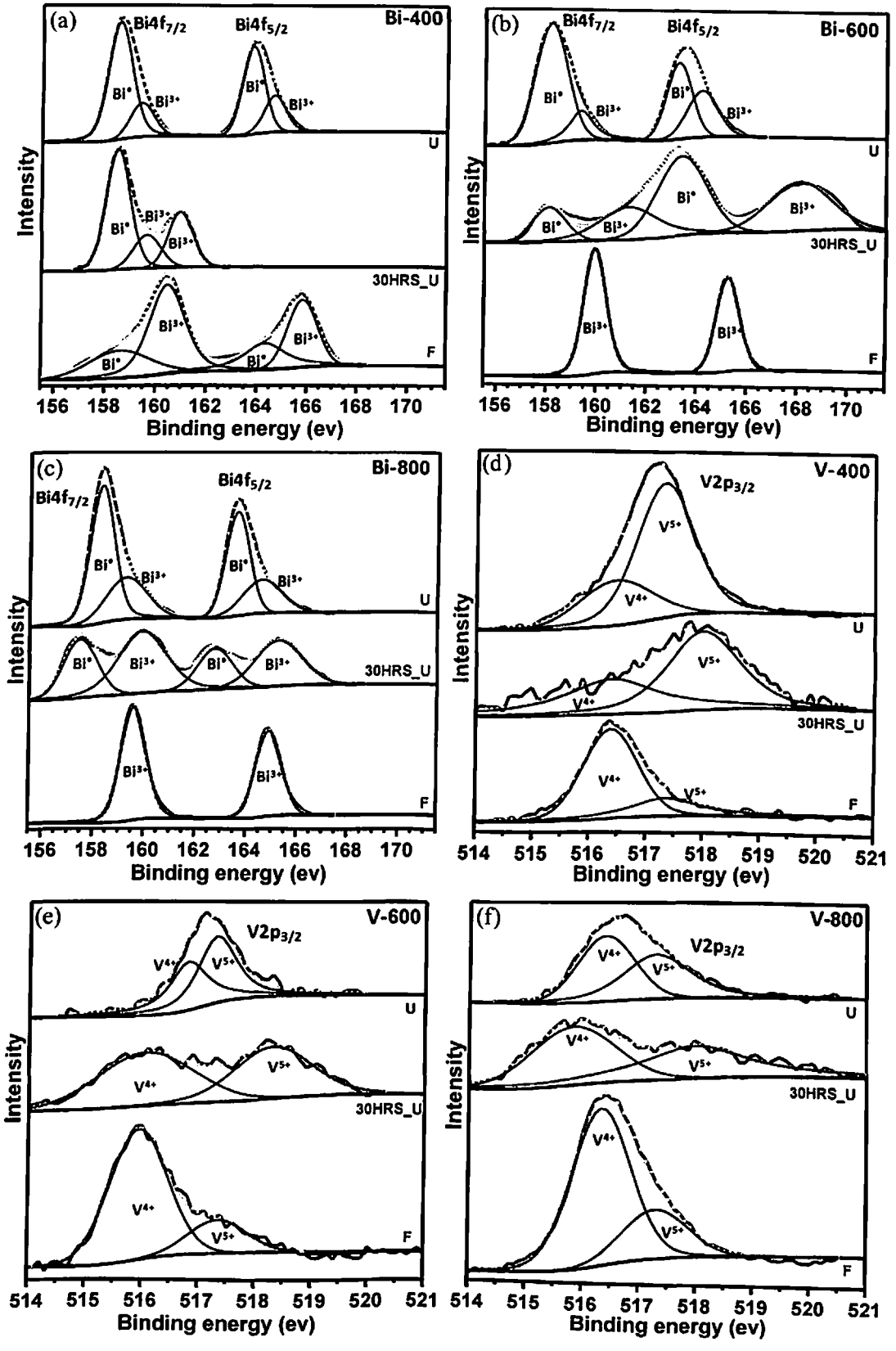

Figure 4-72: High resolution XPS spectra of Bi (a) 400, (b) 600, (c) 800, and V (d) 400, (e) 600, (f) 800 showing the oxidation states for fresh, 30 hrs used and long time used BINIVOX catalysts

Table 4-26: Peak position, peak area (calculated after deconvolution) and corresponding ratio of two different Bismuth oxidation states present in BINIVOX Fresh, 30 hrs used and long time used catalysts

Catalysts	Bismuth Peak position (eV)	Oxidation States	Peak area	Bi^0:Bi^{+3}	Error in fitting χ^2
Wash	158.6	$Bi^0(4f_{7/2})$	8844.07	7.47	1.64
	161.7	$Bi^{3+}(4f_{7/2})$	1786.01		
	162.8	$Bi^0(4f_{5/2})$	1850.57		
	163.7	$Bi^0(4f_{5/2})$	2654.63		
BINIVOX_400_F	158.7	$Bi^0(4f_{7/2})$	6140.18	0.57	1.56
	160.5	$Bi^{3+}(4f_{7/2})$	13538.55		
	164.4	$Bi^0(4f_{5/2})$	5712.51		
	165.8	$Bi^{3+}(4f_{5/2})$	7354.22		
BINIVOX_400_30_HRS_U	158.6	$Bi^0(4f_{7/2})$	4652.94	1.33	1.32
	159.7	$Bi^{3+}(4f_{7/2})$	1404.38		
	160.95	$Bi^{3+}(4f_{5/2})$	2097.62		
BINIVOX_400_U	158.5	$Bi^0(4f_{7/2})$	11122.92	2.99	1.3
	159.4	$Bi^{3+}(4f_{7/2})$	2897.98		
	163.8	$Bi^0(4f_{5/2})$	6945.81		
	164.7	$Bi^{3+}(4f_{5/2})$	3144.32		
BINIVOX_600_F	160	$Bi^{3+}(4f_{7/2})$	6308.25	No metal	1.48
	165.2	$Bi^{3+}(4f_{5/2})$	4493.53		
BINIVOX_600_30_HRS_U	158.1	$Bi^0(4f_{7/2})$	4049.78	0.98	1.56
	161.2	$Bi^{3+}(4f_{7/2})$	7659.76		
	163.5	$Bi^0(4f_{5/2})$	13875.67		
	168.2	$Bi^{3+}(4f_{5/2})$	10560.71		
BINIVOX_600_U	158.2	$Bi^0(4f_{7/2})$	13512.63	2.44	1.46
	159.4	$Bi^{3+}(4f_{7/2})$	3301.03		
	163.2	$Bi^0(4f_{5/2})$	6686.47		
	164.3	$Bi^{3+}(4f_{5/2})$	4990.89		
BINIVOX_800_F	159.6	$Bi^{3+}(4f_{7/2})$	10508.86	No metal	1.56
	164.9	$Bi^{3+}(4f_{5/2})$	7642.17		
BINIVOX_800_30_HRS_U	157.5	$Bi^0(4f_{7/2})$	5226.63	0.62	1.5
	159.9	$Bi^{3+}(4f_{7/2})$	8824.02		
	162.7	$Bi^0(4f_{5/2})$	3717.82		
	165.2	$Bi^{3+}(4f_{5/2})$	5615.39		
BINIVOX_800_U	158.3	$Bi^0(4f_{7/2})$	12130.74	2.02	1.91
	159.2	$Bi^{3+}(4f_{7/2})$	5728.04		
	163.5	$Bi^0(4f_{5/2})$	8252.48		
	164.7	$Bi^{3+}(4f_{5/2})$	4369.84		

species in $Bi_4V_2O_{11}$, respectively (Liu, Niu et al. 2014). After 30 hrs of catalytic activity, peak shift towards higher binding energy is spotted and the major part of the spectra consists of V^{5+} oxidation state. Similar to BINIVOX_30HRS_U and BICOVOX_U, BINIVOX_U catalysts also show the similar characteristics of peak shift in the direction of higher binding energy to confirm the reduction in V^{4+} oxidation state i.e. loss of vacancy (Wu, Thissen et al. 2004). All peak positions, corresponding area and oxidation state with V^{5+}: V^{4+} ratio for each BINIVOX catalysts are tabulated in Table 4.27. Similar trend for V^{5+}: V^{4+} ratio is observed for BINIVOX catalysts as seen in case of BICOVOX catalysts. BINIVOX-600_F catalyst shows maximum V^{4+} oxidation state i.e. more oxygen vacancies as calculated V^{5+}: V^{4+} ratio is 0.25 (minimum). V^{5+}: V^{4+} ratio for BINIVOX-wash, BINIVOX-400_F and BINIVOX-800_F are 1.01, 0.35 and 0.33, respectively. After 30 hrs of catalytic activity, this ratio is found to increase from 0.35 to 1.39, 0.25 to 0.84 and 0.33 to 1 for BINIVOX-400_30HRS_U, BINIVOX-600_30HRS_U and BINIVOX-800_30HRS_U catalysts, respectively. After long period of catalytic activity, further increment is measured as more V^{5+} oxidation state is detected and maximum V^{5+}: V^{4+} ratio of 2.68 is determined for BINIVOX-400_U catalyst. The decreasing order of V^{4+} oxidation state for all catalysts is found to be:

BINIVOX-600_F> BINIVOX-800_F> BINIVOX-400_F> BINIVOX-600_30HRS_U> BINIVOX-800_30HRS_U> BINIVOX-WASH> BINIVOX-600_U> BINIVOX-400_30HRS_U> BINIVOX-800_U> BINIVOX-400_U.

High resolution XPS spectra of C1s show the variation of coke deposition on the surface of the BINIVOX catalysts as depicted in Figure 4.73 (a-c). BINIVOX-400_F catalyst shows adventitious carbon (C-C) at ~284 eV, indicating the presence of sp^2 hybridized C-C bonding (Zhang, Liu et al. 2016), follow by two high bonding energy peaks at 287.1 and 288.7 eV to confirm the existence of C=O bond. BINIVOX-600_F and BINIVOX-800_F catalysts exhibit sp^2, sp^3 hybridized carbon and C=O bond at ~284, ~285.5 and ~287.4 eV, respectively. After using catalysts in the reactor, the amount of carbon is found to increase and sp^3 hybridized carbon is also seen for BINIVOX-400_30HRS_U catalyst at 285.9 eV along with other forms of carbon. Analogous to BINIVOX-600_F, BINIVOX-600_30HRS_U and BINIVOX-800_30HRS_U catalysts show sp^2, sp^3 hybridized carbon and C=O bond, but with higher intensity. For long time used catalysts, BINIVOX-800_U shows the existence of C-C (sp^2 and sp^3) bonds with highest intensity and area. While, BINIVOX-400_U and BINIVOX-600_U show the presence of C-C (sp^2 and sp^3) bonds with C=O bond

at ~288.4 eV. Peak position and peak area of different forms of carbon present in BINIVOX fresh and used catalysts are mentioned in Table 4.28. Similar to BICOVOX-400_F, BINIVOX-400_F shows the highest amount among all the fresh catalysts. Amount of carbon reduces with calcination temperature and BINIVOX-800_F exhibits the minimum amount of carbon. The decreasing order of carbon amount for all fresh and wash catalysts is: BINIVOX-WASH> BINIVOX-400_F> BINIVOX-600_F> BINIVOX-800_F.

To compare all the used catalysts, ratio of BINIVOX_F: BINIVOX _30HRS_U: BINIVOX_U is calculated. Highest and lowest ratio of 1:4.43:5.96 and 1:1.8:2.43 are obtained for BINIVOX-800_U and BINIVOX-600_U catalysts, respectively and for BINIVOX-400_U, the calculated value of the ratio is 1:2.94:4.26. The decreasing order for BINIVOX_F: BINIVOX _30HRS_U: BINIVOX_U ratio is: BINIVOX-800> BINIVOX-400> BINIVOX-600.

XPS analysis of the BINIVOX catalysts shows asymmetric O 1s spectra that can be deconvoluted into three peaks, as shown in Figure 4.73 (d-f). The binding energy values at ~529, ~531.1, and ~532.4 eV, associate with O^{2-} species in the lattice (O_L), oxygen vacancies or defects (O_V) and chemisorbed or dissociated (O_C) oxygen species, respectively, are observed in BINIVOX-wash, BINIVOX-400_F and BINIVOX-600_F catalysts. BINIVOX-800_F catalysts shows only lattice (O_L) and oxygen vacancies or defects (O_V) at 529.6 and 531.1 eV, respectively and that reflects the reduce amount of carbon and it is consistent with the XPS of C1s spectra. Similar to BICOVOX_30HRS_U catalysts, BINIVOX_30HRS_U catalyst also confirms the presence of lattice oxygen peak (O_L) and oxygen vacancies (O_V). Peaks at 529.8(O_L), and 531.67 eV(O_V) in BINIVOX-400_30HRS_U, at 528.9(O_L), and 531.1 eV(O_V) in BINIVOX-600_30HRS_U, and at 529.5(O_L), and 531.1 eV(O_V) in BINIVOX-800_30HRS_U are observed. O1s spectrum of all BINIVOX-_U catalysts shows the similar characteristics as find for BICOVOX_U catalysts. The peak position, peak area and corresponding assignments are well explained in Table 4.29.

XPS spectra of Ni2p for all BINIVOX catalysts are depicted in Figure 4.74 (a-c). The four deconvoluted peaks at ~856.7(Ni^{3+}($Ni2p_{3/2}$)), ~862.9(satellite), ~874.4(Ni^{3+}($Ni2p_{1/2}$)) and ~879.8(satellite) eV denote the presence of Ni in the lattice in Ni^{3+} ionic form along with satellite peaks (Wang, Wu et al. 2015). Peak position, peak area of nickel present in BINIVOX_F, 30HRS_Used and long time used catalysts are summarized in Table 4.30.

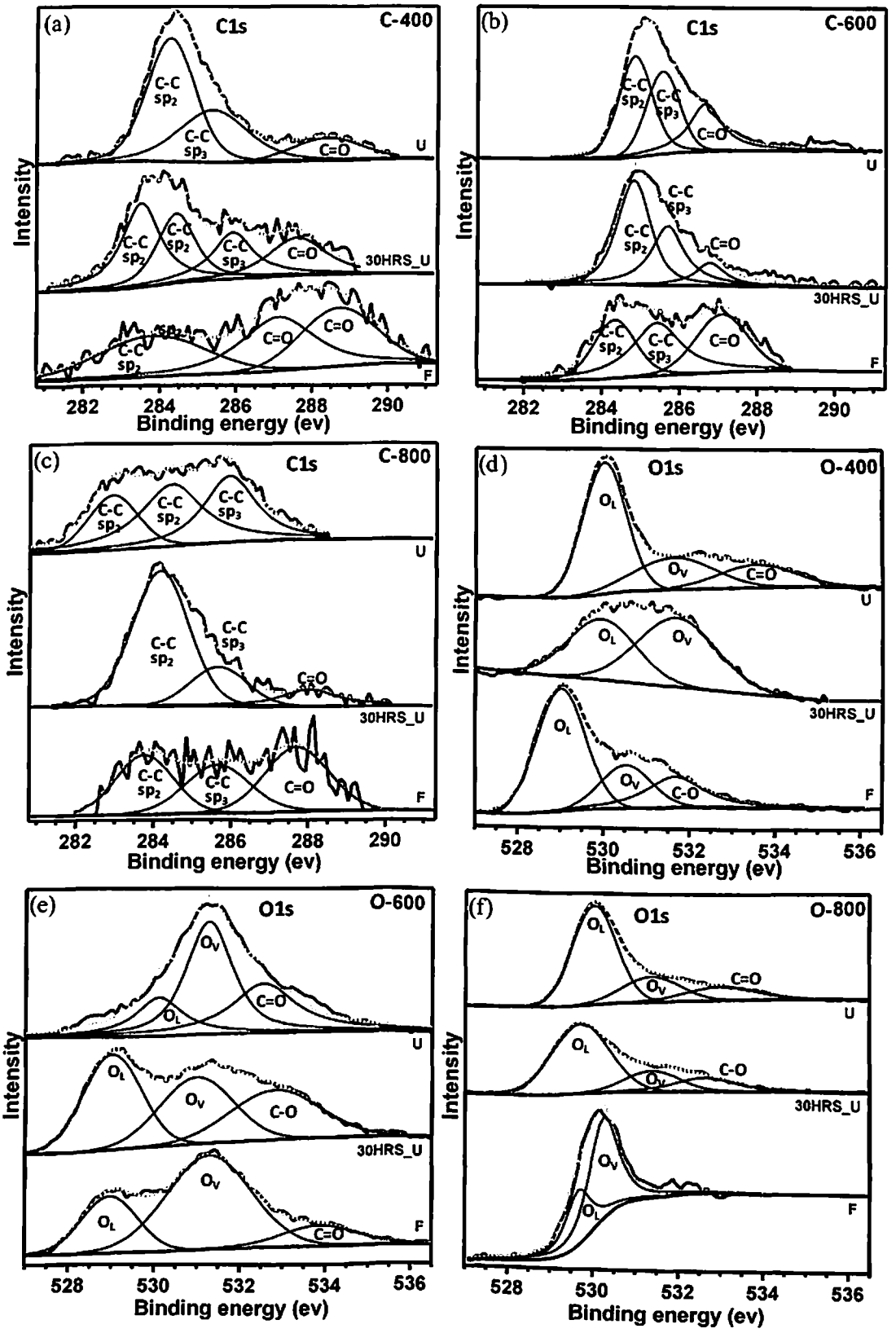

Figure 4-73: High resolution XPS spectra of C [(a) 400, (b) 600, (c) 800°C] and O [(d) 400, (e) 600, (f) 800°C] showing the variation of coke deposition and oxygen phase variation for (F) 30 hrs used and long time used BINIVOX catalysts

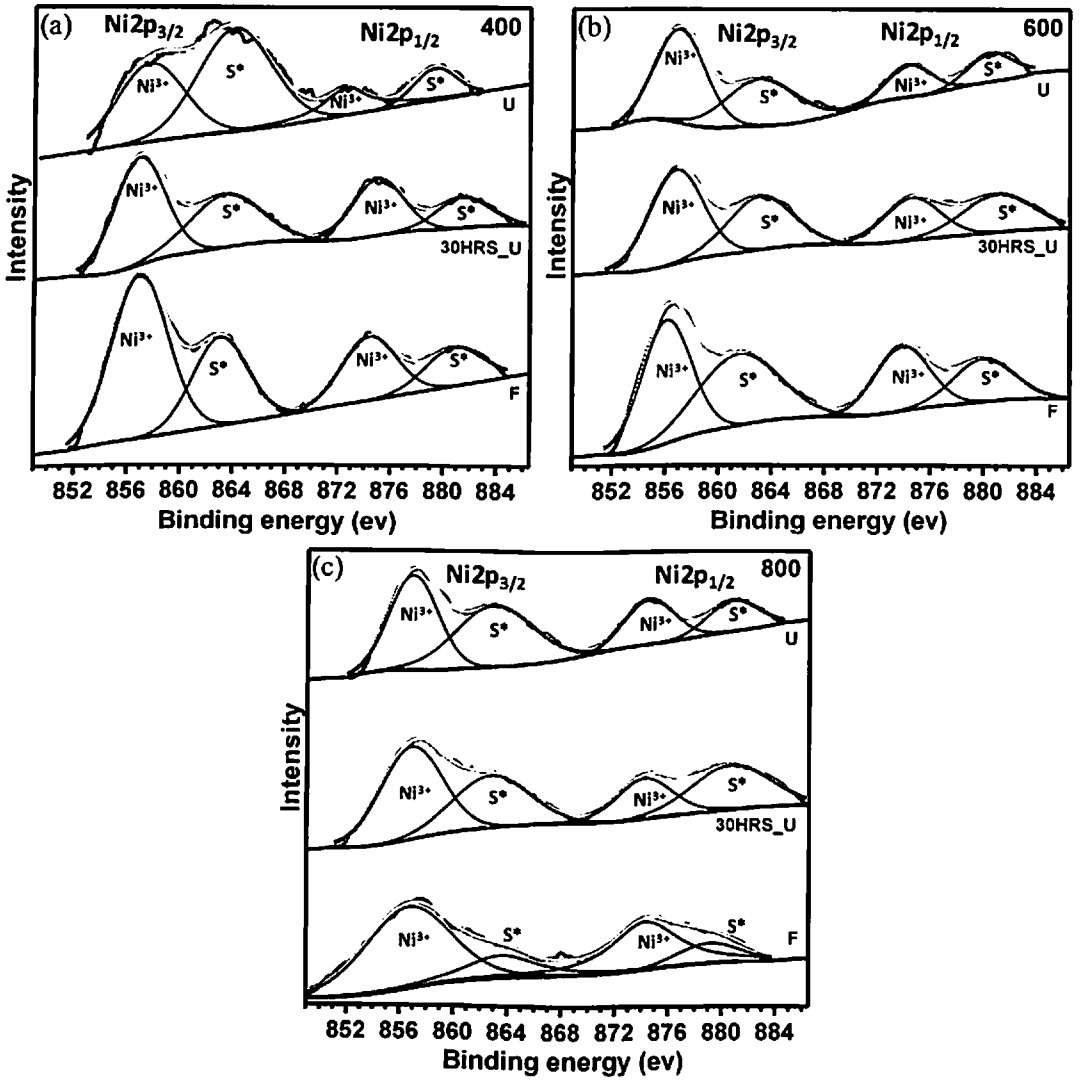

Figure 4-74: High resolution XPS spectra of Ni for the fresh (F), 30 hrs used and long time used BINIVOX catalysts; calcined at (a) 400, (b) 600, and (c) 800°C

Table 4-27: Peak position, peak area (after deconvolution) and corresponding ratio of two oxidation states of V present in BINIVOX Fresh, 30 hrs used and long time used catalysts

Catalysts	Vanadium Peak position (eV)	Oxidation States	Peak area	Ratio (V^{5+}/V^{4+})	Error in fitting $\chi 2$
Wash	516.4 517.3	V^{4+} V^{5+}	1010.47 1016.65	1.01	1.32
BINIVOX_400_F	516.4 517.3	V^{4+} V^{5+}	1699.21 597.57	0.35	1.55
BINIVOX_400_30_HRS_U	516.4 517.9	V^{4+} V^{5+}	645.55 901.22	1.39	1.44
BINIVOX_400_U	516.5 517.3	V^{4+} V^{5+}	1077.01 2882.54	2.68	1.10
BINIVOX_600_F	515.9 517.4	V^{4+} V^{5+}	1404.40 357.72	0.25	1.38
BINIVOX_600_30_HRS_U	516.2 518.2	V^{4+} V^{5+}	938.54 792.72	0.84	1.38
BINIVOX_600_U	516.8 517.3	V^{4+} V^{5+}	511.86 618.79	1.21	1.32
BINIVOX_800_F	516.4 517.3	V^{4+} V^{5+}	2625.34 878.07	0.33	1.55
BINIVOX_800_30_HRS_U	515.9 518	V^{4+} V^{5+}	1133.27 1136.90	1.00	1.41
BINIVOX_800_U	516.4 517.3	V^{4+} V^{5+}	711.38 1247.71	1.75	1.36

Table 4-28: Peak position and peak area (calculated after deconvolution) of different forms of carbon present in BINIVOX Fresh, 30 hrs used and long time used catalysts

Catalysts	Carbon Peak position (eV)	Carbon forms	Peak area	Amount of total C Ratio (F:30HRS_U:U)	Error in fitting χ^2
Wash	284	C-C(sp_2)	1401.2		1.06
	285.2	C-C(sp_3)	250.5		
	286	C-O	96.93		
BINIVOX_400_F	283.8	C-C(sp_2)	680.53	1:2.94:4.26	1.63
	287.1	C=O	802.55		
	288.7	C=O	681.22		
BINIVOX_400_30_HRS_U	283.5	C-C(sp_2)	846.46		1.58
	284.4	C-C(sp_2)	623.70		
	285.9	C-C(sp_3)	532.15		
	287.7	C=O	517.58		
BINIVOX_400_U	284.2	C-C(sp_2)	1767.84		1.39
	285.5	C-C(sp_3)	1129.97		
	288.4	C=O	430.19		
BINIVOX_600_F	284.4	C-C(sp_2)	561.82	1:1.8:2.43	1.75
	285.4	C-C(sp_3)	818.96		
	287	C=O	675.15		
BINIVOX_600_30_HRS_U	284.8	C-C(sp_2)	1491.2		1.44
	285.7	C-C(sp_3)	1003.32		
	287	C=O	350.659		
BINIVOX_600_U	284.8	C-C(sp_2)	1926.46		1.52
	285.6	C-C(sp_3)	1439.06		
	287	C=O	1186.03		
BINIVOX_800_F	283.8	C-C(sp_2)	296.09	1:4.43:5.96	1.55
	285.6	C-C(sp_3)	285.86		
	287.7	C=O	364.54		
BINIVOX_800_30_HRS_U	284.2	C-C(sp_2)	2013.45		1.76
	285.8	C-C(sp_3)	566.35		
	288.1	C=O	357.71		
BINIVOX_800_U	283	C-C(sp_2)	753.21		1.66
	284.5	C-C(sp_2)	1462.78		
	285.9	C-C(sp_3)	1252.36		

Table 4-29: Peak position and peak area (calculated after deconvolution) of different forms of oxygen present in BINIVOX Fresh, 30 hrs used and long time used catalysts

Catalysts	Oxygen Peak position (eV)	Oxygen forms	Peak area	Ratio (O_L: O_V)	Error in fitting χ^2
Wash	529.55	O_L(ME-O)	4632.14	5.4	0.94
	530.73	O_V(ME-O)	3061.89		
	532.4	C-O	1997.91		
BINIVOX_400_F	529	O_L(ME-O)	3747.54	2.9	0.83
	531.1	O_V	1483.38		
	531.9	C-O	1623.05		

BINIVOX_400_30_HRS_U	529.8 531.67	O_L(ME-O) O_V	1586.94 2085.97	3.4	0.99
BINIVOX_400_U	530 531.6 533.5	O_L(ME-O) O_V C=O	3438.84 1525.33 1061.77	4.7	0.83
BINIVOX_600_F	528.9 531.1 533.8	O_L(ME-O) O_V C=O	1472.64 3741.35 772.56	1.9	0.94
BINIVOX_600_30_HRS_U	528.9 531.1 532.7	O_L(ME-O) O_V C-O	2562.53 2261.26 2057.20	2.4	0.96
BINIVOX_600_U	530.1 531 532.8	O_L(ME-O) O_V C=O	1280.30 3250.84 2236.93	3.3	1.89
BINIVOX_800_F	529.68 531.1	O_L(ME-O) O_V	702.27 1397.76	2.5	0.86
BINIVOX_800_30_HRS_U	529.5 531.1 532.6	O_L(ME-O) O_V C-O	4511.66 1260.06 1147.26	3.2	0.98
BINIVOX_800_U	530 531.4 533.1	O_L(ME-O) O_V C=O	4821.404 1628.508 1096.669	3.9	0.95

Table 4-30: Peak position and peak area (calculated after deconvolution) of oxidation states of Nickel present in BINIVOX Fresh, 30 hrs used and long time used catalysts

Catalysts	Nickel Peak position (eV)	Oxidation States	Peak area	Error in fitting χ^2
Wash	856.4 862.9 874.4 879.9	$Ni^{3+}(2p_{3/2})$ Satellite $Ni^{3+}(2p_{1/2})$ Satellite	447.11 471.08 188.50 93.00	0.97
BINIVOX_400_F	857 863.2 874.8 880.7	$Ni^{3+}(2p_{3/2})$ Satellite $Ni^{3+}(2p_{1/2})$ Satellite	696.92 371.88 264.96 170.25	0.88
BINIVOX_400_30_HRS_U	857.2 863.7 875 881.4	$Ni^{3+}(2p_{3/2})$ Satellite $Ni^{3+}(2p_{1/2})$ Satellite	415.14 291.96 221.31 123.70	0.98
BINIVOX_400_U	857.5 863.5 872.3 879.2	$Ni^{3+}(2p_{3/2})$ Satellite $Ni^{3+}(2p_{1/2})$ Satellite	302.11 292.16 170.78 51.24	0.89
BINIVOX_600_F	856.3 861.7 874.1 880.3	$Ni^{3+}(2p_{3/2})$ Satellite $Ni^{3+}(2p_{1/2})$ Satellite	641.09 610.09 372.43 273.16	0.94
BINIVOX_600_30_HRS_U	857.2	$Ni^{3+}(2p_{3/2})$	531.12	0.93

	863.2	Satellite	365.99	
	874.9	$Ni^{3+}(2p_{1/2})$	255.23	
	881.2	Satellite	283.12	
BINIVOX_600_U	857.1	$Ni^{3+}(2p_{3/2})$	485.09	0.99
	863.2	Satellite	343.61	
	874.6	$Ni^{3+}(2p_{1/2})$	150.12	
	880.4	Satellite	138.78	
BINIVOX_800_F	856.9	$Ni^{3+}(2p_{3/2})$	761.78	0.97
	864.1	Satellite	227.52	
	874.4	$Ni^{3+}(2p_{1/2})$	462.07	
	879	Satellite	127.54	
BINIVOX_800_30_HRS_U	857.1	$Ni^{3+}(2p_{3/2})$	602.44	0.88
	862.8	Satellite	414.72	
	874.2	$Ni^{3+}(2p_{1/2})$	254.31	
	880.7	Satellite	366.62	
BINIVOX_800_U	857.1	$Ni^{3+}(2p_{3/2})$	471.58	0.96
	863.2	Satellite	490.54	
	874.6	$Ni^{3+}(2p_{1/2})$	229.74	
	881.1	Satellite	161.19	

Table 4-31: Atomic% of each element and corresponding Bi: V and V: Ni surface ratio data from XPS Analysis for wash, fresh, 30 hrs used and long time used BINIVOX catalysts

Catalyst	Elements Present (at%)					Bi: V ratio	V: Ni ratio
	Bi	C	Ni	O	V		
BINIVOX-WASH	20.54	49.49	1.05	19.39	9.53	2.15	9.08
BINIVOX-400_F	22.06	42.54	1.21	23.21	10.98	2.01	9.07
BINIVOX-400_30HRS_U	10.68	45.32	0.58	38.18	5.24	2.04	9.03
BINIVOX-400_U	12.88	51.81	0.7	28.3	6.31	2.05	9.01
BINIVOX-600_F	10.32	40.46	0.57	43.51	5.14	2.01	9.02
BINIVOX-600_30HRS_U	11.59	44.8	0.64	37.2	5.77	2.01	9.02
BINIVOX-600_U	10.81	47.41	0.57	36.06	5.15	2.1	9.04
BINIVOX-800_F	13.23	39.5	0.71	40.07	6.49	2.04	9.14
BINIVOX-800_30HRS_U	12.56	46.79	0.66	34.04	5.95	2.11	9.02
BINIVOX-800_U	14.16	59.63	0.78	18.45	6.98	2.03	8.95

Atomic% of each element present if BINIVOX catalysts are determined by analyzing the wide spectra and considering the core shell peaks for each element exists in the catalyst and tabulated in Table 4.31. To understand the stoichiometry, Bi to V and V to Ni ratio is also mentioned in the Table and Bi: V and V: Ni ratio is ~2 and ~9, respectively for all the BINIVOX catalyst. This reflects that proper stoichiometry is maintained in the compositions.

Wide spectra for BICUVOX catalysts is also represented in a layer lines to indicate the different stages of catalyst starting from BICUVOX_F to BICUVOX_U, heat treated at (a) 400, (b) 600; and (c) 800 °C in Figure 4.75. The elements present in the BICUVOX catalysts are Bi (at ~ 27.4 (Bi5d), 93.4 (Bi5p), 163.8 (Bi4f), 440 ($Bi4d_{5/2}$), 460 ($Bi4d_{3/2}$), 680 (Bi4p), and 940.1 (Bi4s) eV), V (~516 (V2p)), C (~284.3 (C1s)), Cu (~936 (Cu2p)), and O (~530 (O1s) eV) (Nyholm R. 1980; Ling, Sun et al. 2010).

High resolution XPS spectra of all the elements ((a) Bi, (b) C, (c) V, (d) Co, and (e) O) present in BICUVOX-wash catalyst are shown in Figure 4.76. High resolution XPS spectra of the core level Bi4f, heat treated at (a) 400, (b) 600, (c) 800, and V2p, heat treated at (d) 400, (e) 600, (f) 800, in layer lines for different stages of BICUVOX catalysts is depicted in Figure 4.77. The Bi4f XPS spectrum of all BICUVOX_F catalysts exhibit two peaks with two shoulders which suggest that the Bi is in doublet oxidation states. Two high intensity peaks are noted at ~159.4 and ~164.5 eV, indicating the Bi ions are in Bi^{3+} oxidation state (Liu, Yin et al. 2012; Liu, Niu et al. 2014) and both small shoulder peaks toward low binding energies at ~157.5 and ~162.7 eV are observed and assign to Bi° oxidation state. BICUVOX-wash catalyst also shows the similar trend. After using catalysts for 30 hrs, intensity of Bi° oxidation state peaks are found to increase in all BICUVOX-30HRS_U catalysts at ~158.2 and ~163.4 eV. However, for all BICUVOX_U catalysts, intensity of Bi° oxidation state peaks (~158.2, ~163.2 eV) are further found to increase and simultaneously intensity of Bi^{3+} oxidation state peaks (~159.4, ~164.6 eV) are observed to reduce. Table 4.32 summarizes all peak position, peak area and corresponding ratio of two different Bismuth phases present in BICUVOX Fresh, 30HRS_Used and long time used catalysts. Increasing order of Bi°:Bi^{3+} for all BICUVOX catalysts is: BICUVOX-800_F<BICUVOX-600_F<BICUVOX-400_F<BICUVOX-800_30HRS_U<BICUVOX-600_30HRS_U<BICUVOX-400_30HRS_U<BICUVOX-800_U<BICUVOX-600_U< BICUVOX-400_U.

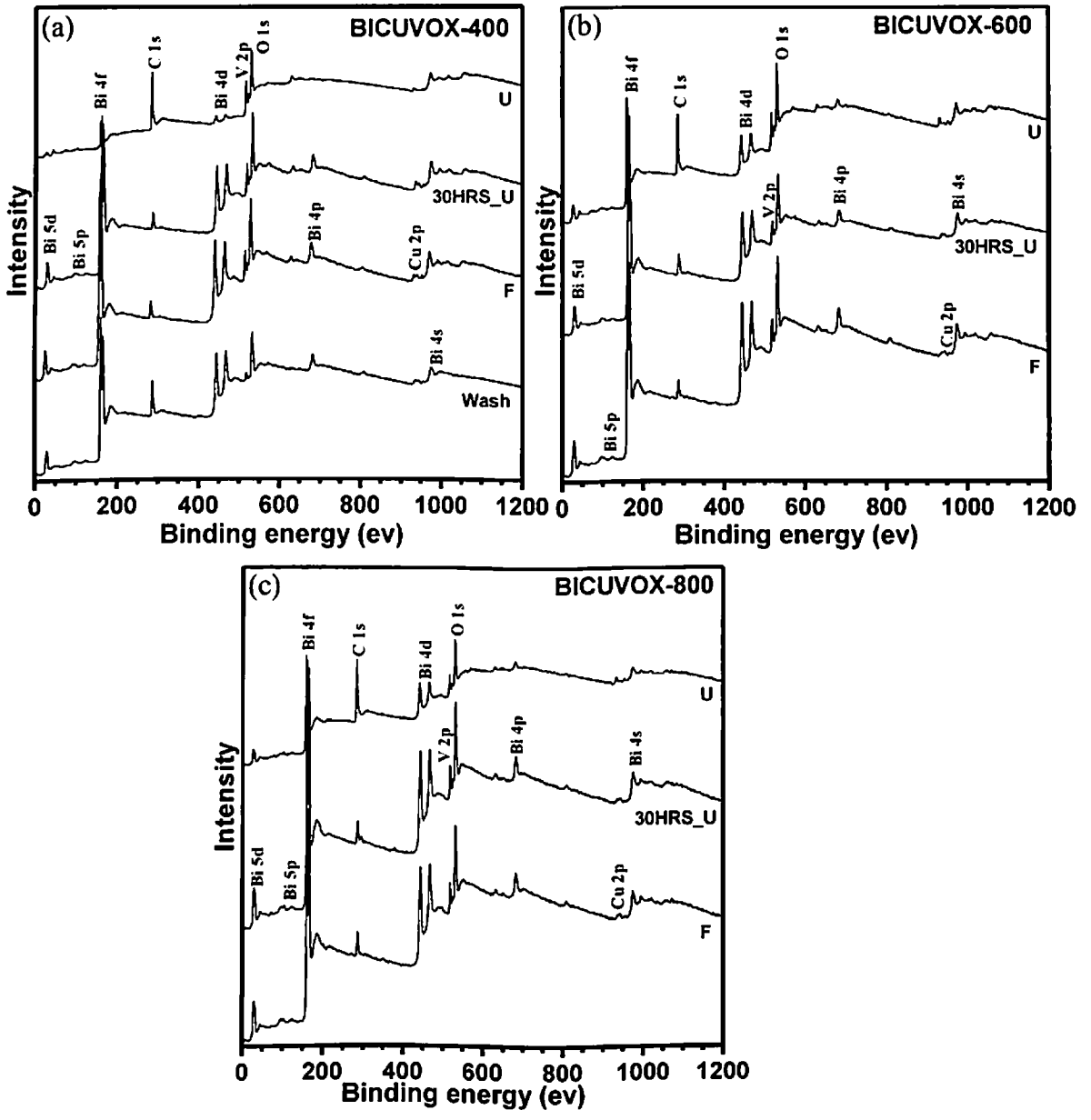

Figure 4-75: Wide range XPS spectra for the wash, fresh (F), 30 hrs used and long time used (U) BICUVOX catalysts; calcined at (a) 400, (b) 600, and (c) 800°C. All essential elements, Bi, V, O, and Cu along with adventitious C are present for all samples

Table 4-32: Peak position, peak area (calculated after deconvolution) and corresponding ratio of two different Bismuth oxidation states present in BICUVOX Fresh, 30 hrs used and long time used catalysts

Catalysts	Bismuth Peak position (eV)	Oxidation States	Peak area	Bi^0:Bi^{+3}	Error in fitting $\chi 2$
Wash	158.6	$Bi^0(4f_{7/2})$	14337.43	3.09	0.89
	160.3	Bi^{3+} $(4f_{7/2})$	3331.96		
	163.8	$Bi^0(4f_{5/2})$	8108.73		
	165.3	Bi^{3+} $(4f_{5/2})$	3937.1		
BICUVOX_400_F	157.5	$Bi^0(4f_{7/2})$	258.35	0.11	1.01
	159.4	Bi^{3+} $(4f_{7/2})$	1997.13		
	162.9	$Bi^0(4f_{5/2})$	112.72		
	164.7	Bi^{3+} $(4f_{5/2})$	1424.64		
BICUVOX_400_30_HRS_U	158.3	$Bi^0(4f_{7/2})$	7303.35	0.96	1.33
	159.4	Bi^{3+} $(4f_{7/2})$	6975.43		
	163.5	$Bi^0(4f_{5/2})$	4525.48		
	164.7	Bi^{3+} $(4f_{5/2})$	5293.48		
BICUVOX_400_U	158.35	$Bi^0(4f_{7/2})$	11975.81	1.45	1.71
	159.4	Bi^{3+} $(4f_{7/2})$	7214.35		
	163.6	$Bi^0(4f_{5/2})$	7348.21		
	164.7	Bi^{3+} $(4f_{5/2})$	6082.91		
BICUVOX_600_F	157.4	$Bi^0(4f_{7/2})$	689.60	0.09	1.17
	159.4	Bi^{3+} $(4f_{7/2})$	5939.83		
	162.7	$Bi^0(4f_{5/2})$	326.78		
	164.6	Bi^{3+} $(4f_{5/2})$	4242.43		
BICUVOX_600_30_HRS_U	157.9	$Bi^0(4f_{7/2})$	7226.49	0.93	1.31
	159.2	Bi^{3+} $(4f_{7/2})$	8964.89		
	163.4	$Bi^0(4f_{5/2})$	6069.06		
	164.7	Bi^{3+} $(4f_{5/2})$	5368.29		
BICUVOX_600_U	157.8	$Bi^0(4f_{7/2})$	8852.02	1.04	0.92
	159.5	Bi^{3+} $(4f_{7/2})$	6715.07		
	163.1	$Bi^0(4f_{5/2})$	4369.90		
	164.5	Bi^{3+} $(4f_{5/2})$	5982.11		
BICUVOX_800_F	157.8	$Bi^0(4f_{7/2})$	390.20	0.05	1.49
	159.7	Bi^{3+} $(4f_{7/2})$	5489.78		
	163.1	$Bi^0(4f_{5/2})$	83.75		
	165	Bi^{3+} $(4f_{5/2})$	3995.93		
BICUVOX_800_30_HRS_U	158.2	$Bi^0(4f_{7/2})$	4808.66	0.87	1.27
	159.5	Bi^{3+} $(4f_{7/2})$	4777.48		
	163.5	$Bi^0(4f_{5/2})$	2720.27		
	164.7	Bi^{3+} $(4f_{5/2})$	3903.59		
BICUVOX_800_U	158.5	$Bi^0(4f_{7/2})$	9885.41	1.03	0.81
	159.4	Bi^{3+} $(4f_{7/2})$	8374.61		
	163.7	$Bi^0(4f_{5/2})$	5963.97		
	164.7	Bi^{3+} $(4f_{5/2})$	6969.89		

Analogous to BINIVOX and BICOVOX, vanadium in all the BICUVOX also exists in the V^{5+} and V^{4+} oxidation states as mentioned in Figures 4.77 (d-f). The binding energies of $V2p_{3/2}$ peaks are 516.3 and 517.4 eV in BINIVOX-wash catalyst, which can be characteristic of V^{4+} and V^{5+} oxidation states, respectively (Liu, Niu et al. 2014). BICUVOX-800_F catalyst also shows the same number of peaks and peak positions. However, in BICUVOX-400_F an extra peak emerges at 518.2 eV for V^{5+} oxidation state and an extra peak at 515.8 eV in BICUVOX-600_F shows more amount of V^{4+} oxidation state. Similar to BICOVOX-30HRS_U and BINIVOX-30HRS_U, BICUVOX-30HRS_U shows peak shift towards higher binding energy and the major part of the spectra consists of V^{5+} oxidation state. Similar trend is also observed for all BICUVOX_U catalysts and more amount of V^{5+} oxidation state is spotted. All peak positions, corresponding area and oxidation state with V^{5+}: V^{4+} ratio for each BICUVOX catalysts are tabulated in Table 4.33. BICUVOX-600_F catalyst shows maximum V^{4+} oxidation state i.e. more oxygen vacancies as calculated V^{5+}: V^{4+} ratio is 0.22 (minimum). V^{5+}: V^{4+} ratio for BICUVOX-wash, BICUVOX-400_F and BICUVOX-800_F are 1.28, 1.19 and 1.14, respectively. After 30 hrs of catalytic activity, this ratio is found to increase from 1.19 to 2.66, 0.22 to 0.89 and 1.14 to 1.3 for BICUVOX-400_30HRS_U, BICUVOX-600_30HRS_U and BICUVOX-800_30HRS_U catalysts, respectively. After long period of catalytic activity, further increment is measured as more V^{5+} oxidation state is detected and maximum V^{5+}: V^{4+} ratio of 4.47 is determined for BICUVOX-400_U catalyst. The decreasing order of V^{4+} oxidation state for all catalysts is found to be: BICUVOX-600_F> BICUVOX-600_30HRS_U>BICUVOX-800_F> BICUVOX-400_F>BICUVOX-WASH>BICUVOX-800_30HRS_U>BICUVOX-600_U>BICUVOX-400_30HRS_U> BICUVOX-800_U> BICUVOX-400_U.

High resolution XPS spectra of C1s (Figure 4.78 (a-c)) show the variation of coke deposition on the surface of the BICUVOX catalysts at fresh and used conditions. All BICUVOX_F and BICUVOX-wash catalysts show adventitious carbon (C-C) at ~284.2 eV, indicating the presence of sp^2 hybridized C-C bonding (Zhang, Liu et al. 2016), followed by three high bonding energy peaks at ~285.2, ~286.4 and ~288.3 eV to confirm the existence of sp^3 hybridized carbon, C-O bond and C = O bond, respectively. After using catalysts in the reactor, the amount of carbon is found to increase. C1s spectrum of BICUVOX-400_30HRS_U catalyst shows increase in the intensity and area of peak at 284.2(C-C(sp^2)) eV with shoulder peak at 285.9(C-C(sp^3)) and 288.3(C=O) eV. Similar trend is observed for BICUVOX-600_30HRS_U catalyst. However, BICUVOX-800_30HRS_U catalyst shows the presence of C-O at 286.1 eV. For long time used catalysts, BICUVOX-800_U and

BICUVOX-400_U show the existence of C-C(sp^2 and sp^3) bonds with highest intensity. While, BICUVOX-600_U shows the presence of C-C(sp^2 and sp^3) bonds with C=O bond at ~288.2 eV. Peak position and peak area of different forms of carbon present in BICUVOX fresh and used catalysts are mentioned in Table 4.34. Similar to BICOVOX-400_F and BINIVOX-400_F, BICUVOX-400_F shows the highest amount among all the fresh catalysts. Amount of carbon reduces with calcination temperature and BICUVOX-800_F exhibits the minimum amount of carbon. The decreasing order of carbon amount for all fresh and wash catalysts is: BICUVOX-WASH> BICUVOX-400_F> BICUVOX-600_F> BICUVOX-800_F.

To compare all the used catalysts, ratio of BICUVOX_F: BICUVOX _30HRS_U: BICUVOX_U is calculated. BICUVOX-800_U shows the highest value of ratio, 1:3.42:5.44 and lowest is obtained for BICUVOX-600_U, 1:1.43:2.85 and for BICUVOX-400_U, the calculated value of the ratio is 1:1.48:3.01. The decreasing order for BICUVOX_F: BICUVOX _30HRS_U: BICUVOX_U ratio is: BICUVOX-800> BICUVOX-400> BICUVOX-600.

Analogous to BINIVOX catalysts, XPS analysis of the BICUVOX catalysts shows asymmetric O 1s spectra that can be deconvoluted into three peaks, as shown in Figure 4.78 (d-f). The binding energy values at ~529.9, ~531.4, and ~532.2 eV, associated with O^{2-} species in the lattice (O_L), oxygen vacancies or defects (O_V) and chemisorbed or dissociated (O_C) oxygen species, respectively, are observed in BICUVOX-wash, all BICUVOX_F, all BICUVOX_30HRS_U and all BICUVOX_U catalysts. The peak position, peak area and corresponding oxygen phases are well explained in Table 4.35.

XPS spectra of Cu2p for all BICUVOX catalysts are depicted in Figure 4.79 (a-c). The three deconvoluted peaks at ~934.8(Cu^{2+}($Cu2p_{3/2}$)), ~942.8(satellite), and ~954.5(Cu^{2+}($Cu2p_{1/2}$)) eV denote the presence of Cu in the lattice in Cu^{2+} oxidation state along with satellite peak (Wang, Wu et al. 2015). Peak position, peak area of cupper present in BICUVOX_F, 30HRS_Used and long time used catalysts are reported in Table 4.36.

Atomic% of each element presents if BICUVOX catalysts are also determined and tabulated in Table 4.37. To understand the stoichiometry, Bi to V and V to Cu ratio is mentioned in the Table and analogous to BICOVOX and BINIVOX, Bi: V and V: Cu ratio is ~2 and ~9, respectively for all the BICUVOX catalysts.

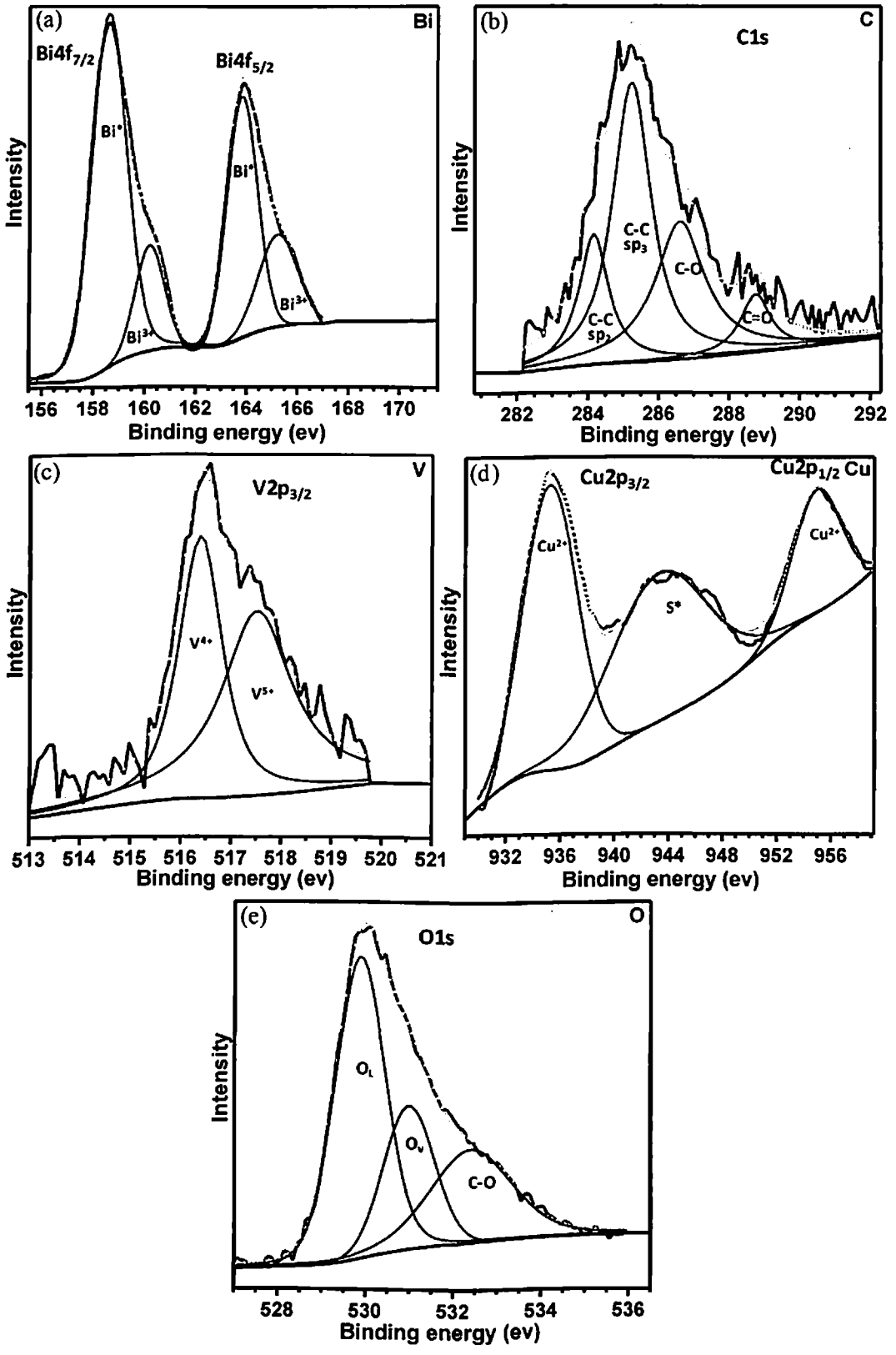

Figure 4-76: High resolution XPS spectra of (a) Bi, (b) C, (c) V, (d) Cu and (e) O present in BICUVOX-wash catalyst

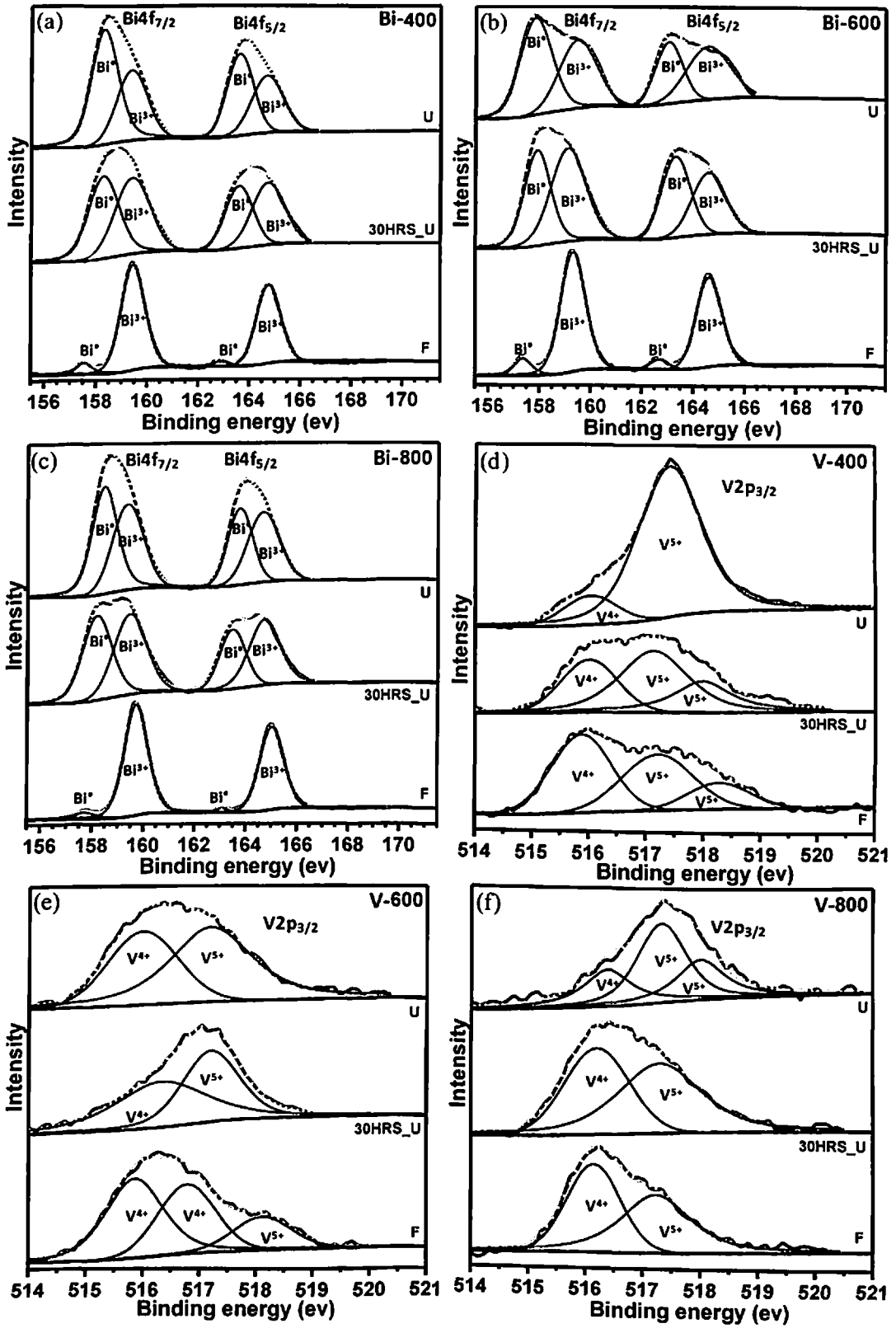

Figure 4-77: High resolution XPS spectra of Bi (a) 400, (b) 600, (c) 800, and V (d) 400, (e) 600, (f) 800 showing the oxidation states for fresh, 30 hrs used and long time used BICUVOX catalysts

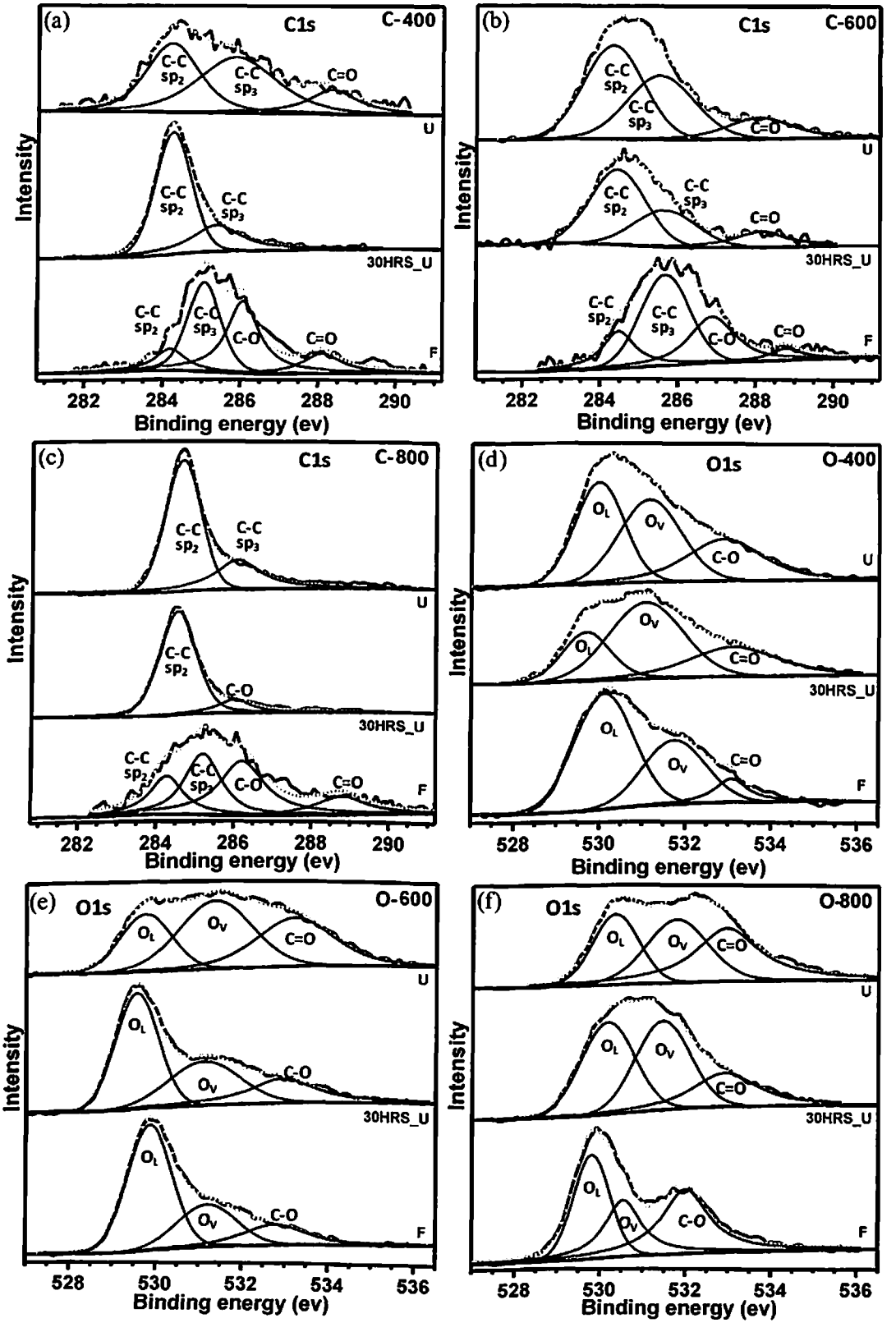

Figure 4-78: High resolution XPS spectra of C [(a) 400, (b) 600, (c) 800°C] and O [(d) 400, (e) 600, (f) 800°C] showing the variation of coke deposition and oxygen phase variation for fresh (F) 30 hrs used and long time used BICUVOX catalysts

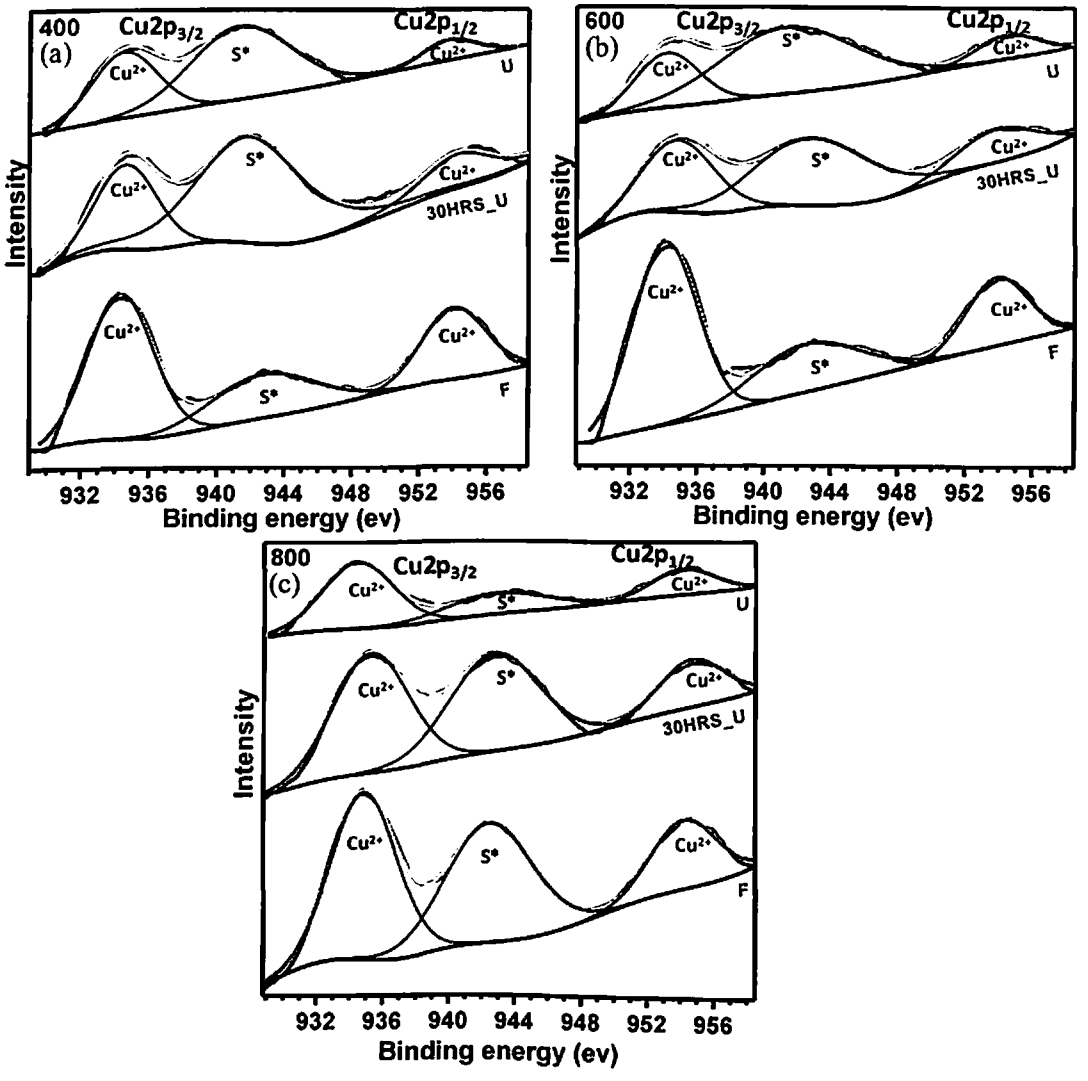

Figure 4-79: High resolution XPS spectra of Cu for the fresh (F), 30 hrs used and long time used BICUVOX catalysts; calcined at (a) 400, (b) 600, and (c) 800°C

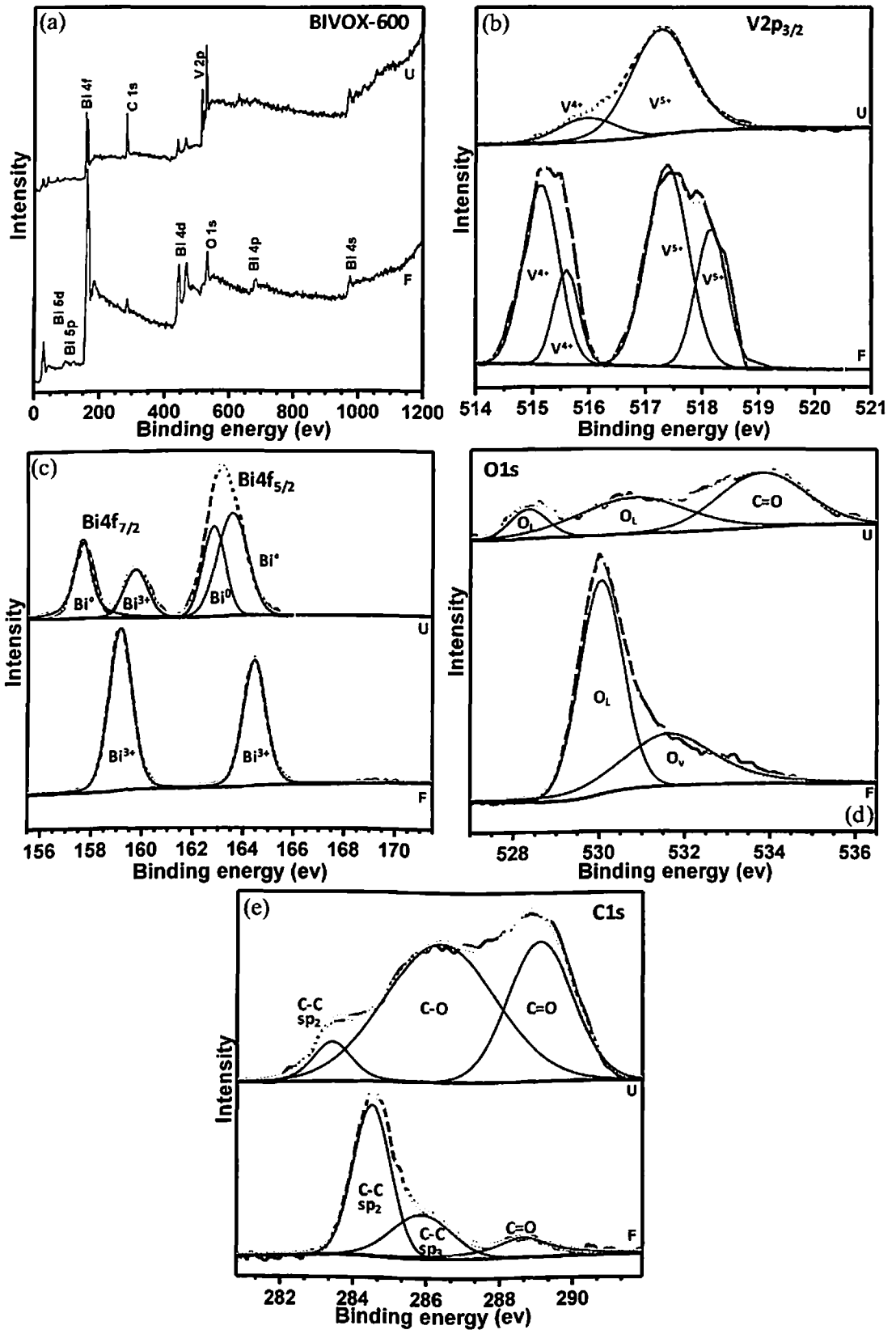

Figure 4-80: (a) Wide range XPS spectra for the fresh and long time used BIVOX-600 catalysts; High resolution XPS spectra of (b) V, (c) Bi, (d) O, and (e) C showing the oxidation states for fresh, long time used BIVOX-600 catalyst

Table 4-33: Peak position, peak area (after deconvolution) and corresponding ratio of two oxidation states of V present in BICUVOX Fresh, 30 hrs used and long time used catalysts

Catalysts	Vanadium Peak position (eV)	Oxidation States	Peak area	Ratio (V^{5+}/V^{4+})	Error in fitting χ^2
Wash	516.3 517.6	V^{4+} V^{5+}	529.54 679.89	1.28	1.282
BICUVOX_400_F	515.8 517.2 518.2	V^{4+} V^{5+} V^{5+}	1006.549 848.97 348.25	0.38	1.21
BICUVOX_400_30_HRS_U	516 517.2 518	V^{4+} V^{5+} V^{5+}	451.35 791.24 408.65	1.66	1.23
BICUVOX_400_U	516 517.45	V^{4+} V^{5+}	523.05 2340.01	2.87	1.46
BICUVOX_600_F	515.8 516.2 518.1	V^{4+} V^{4+} V^{5+}	1360.17 1003.38 524.26	0.29	1.266
BICUVOX_600_30_HRS_U	516.3 517.3	V^{4+} V^{5+}	1303.37 1167.41	0.89	1.32
BICUVOX_600_U	516 517.2	V^{4+} V^{5+}	1292.97 2009.42	1.55	1.35
BICUVOX_800_F	516.2 517.3	V^{4+} V^{5+}	1090.21 1238.21	0.35	1.39
BICUVOX_800_30_HRS_U	516.2 517.3	V^{4+} V^{5+}	1270.741 1656.54	1.3	1.19
BICUVOX_800_U	516.4 517.3 518.1	V^{4+} V^{5+} V^{5+}	355.87 643.87 378.03	1.87	1.33

Table 4-34: Peak position and peak area (calculated after deconvolution) of different forms of carbon present in BICUVOX Fresh, 30 hrs used and long time used catalysts

Catalysts	Carbon Peak position (eV)	Carbon forms	Peak area	Amount of total C Ratio (F:30HRS_U:U)	Error in fitting $\chi 2$
Wash	284.2	C-C(sp_2)	478.05		0.973
	285.2	C-C(sp_3)	1256.03		
	286.6	C-O	856.13		
	288.8	C=O	211.24		
BICUVOX_400_F	284.2	C-C(sp_2)	295.09	1:1.48:3.01	1.35
	285	C-C(sp_3)	1010.77		
	286	C-O	1077.36		
	288.1	C=O	358.73		
BICUVOX_400_30_HRS_U	284.2	C-C(sp_2)	883.73		1.535
	285.9	C-C(sp_3)	1052.02		
	288.3	C=O	358.28		
BICUVOX_400_U	284.2	C-C(sp_2)	2759.533		0.85
	285.4	C-C(sp_3)	1176.556		
BICUVOX_600_F	284.4	C-C(sp_2)	400	1:1.43:2.85	0.85
	285.7	C-C(sp_3)	982.79		
	286.8	C-O	632.65		
	288.8	C=O	128.54		
BICUVOX_600_30_HRS_U	284.4	C-C(sp_2)	1276.55		1.49
	285.7	C-C(sp_3)	705.26		
	288.2	C=O	370.13		
BICUVOX_600_U	284.3	C-C(sp_2)	2198.63		1.433
	285.5	C-C(sp_3)	1737.47		
	288.2	C=O	680.16		
BICUVOX_800_F	284.2	C-C(sp_2)	364.61	1:3.42:5.44	0.88
	285.2	C-C(sp_3)	590.303		
	286.2	C-O	724.05		
	288.8	C=O	264.38		
BICUVOX_800_30_HRS_U	284.5	C-C(sp_2)	3275.11		0.92
	286.1	C-O	527.93		
BICUVOX_800_U	284.6	C-C(sp_2)	3671.34		1.54
	285.9	C-C(sp_3)	1524.03		

Table 4-35: Peak position and peak area (calculated after deconvolution) of different forms of oxygen present in BICUVOX Fresh, 30 hrs used and long time used catalysts

Catalysts	Oxygen Peak position (eV)	Oxygen forms	Peak area	Ratio (O_L: O_V)	Error in fitting $\chi 2$
Wash	529.9	O_L(ME-O)	3595.96	5.6	1.36
	531	O_V	1633.06		
	532.5	C-O	1951.33		
BICUVOX_400_F	530	O_L(ME-O)	4209.25	2.6	1.08
	531.8	O_V	2436.51		

	533	C=O	692.35		
BICUVOX_400_30_HRS_U	529.7 531 532.9	O_L(ME-O) O_V C-O	1097.59 2410.82 1373.05	3.3	1.29
BICUVOX_400_U	530 531.2 532.9	O_L(ME-O) O_V C-O	3010.09 3067.96 2359.64	4.8	1.48
BICUVOX_600_F	529.9 531.1 532.1	O_L(ME-O) O_V C-O	2991.03 1325.82 863.41	1.8	1.38
BICUVOX_600_30_HRS_U	529.6 531.2 532.9	O_L(ME-O) O_V C-O	2666.55 1672.01 1251.88	2.5	0.99
BICUVOX_600_U	529.4 531.4 533.2	O_L(ME-O) O_V C=O	1566.08 2688.739 2329.39	3.2	1.49
BICUVOX_800_F	529.8 531.3 532.8	O_L(ME-O) O_V C-O	1351.25 1056.71 1560.84	2.3	0.89
BICUVOX_800_30_HRS_U	530.2 531.4 532.9	O_L(ME-O) O_V C-O	2888.56 2845.77 1736.57	3.4	0.89
BICUVOX_800_U	530.3 531.8 533.1	O_L(ME-O) O_V C=O	1955.29 2483.86 3029.72	4.1	0.99

Table 4-36: Peak position and peak area (calculated after deconvolution) of oxidation states of Cupper present in BICUVOX Fresh, 30 hrs used and long time used catalysts

Catalysts	Cupper Peak position (eV)	Oxidation States	Peak area	Error in fitting $\chi 2$
Wash	935.2 943.5 955	$Cu^{2+}(2p_{3/2})$ Satellite $Cu^{2+}(2p_{1/2})$	751.37 706.94 287.64	0.96
BICUVOX_400_F	934.3 941.7 954.2	$Cu^{2+}(2p_{3/2})$ Satellite $Cu^{2+}(2p_{1/2})$	831.23 399.26 406.17	1.1
BICUVOX_400_30_HRS_U	934.6 941.8 954.1	$Cu^{2+}(2p_{3/2})$ Satellite $Cu^{2+}(2p_{1/2})$	432.65 1138.72 241.57	0.88
BICUVOX_400_U	934.8 941.3 953.7	$Cu^{2+}(2p_{3/2})$ Satellite $Cu^{2+}(2p_{1/2})$	334.25 637.69 97.10	0.95
BICUVOX_600_F	934.2 942.8 953.9	$Cu^{2+}(2p_{3/2})$ Satellite $Cu^{2+}(2p_{1/2})$	1023.88 440.23 361.96	0.97
BICUVOX_600_30_HRS_U	934.9 942.3 953.7	$Cu^{2+}(2p_{3/2})$ Satellite $Cu^{2+}(2p_{1/2})$	498.06 675.92 222.14	0.96

BICUVOX_600_U	934.4	$Cu^{2+}(2p_{3/2})$	292.65	0.99
	941.6	Satellite	763.44	
	954.4	$Cu^{2+}(2p_{1/2})$	176.078	
BICUVOX_800_F	934.9	$Cu^{2+}(2p_{3/2})$	1163.47	0.98
	942.4	Satellite	1105.42	
	954.3	$Cu^{2+}(2p_{1/2})$	479.10	
BICUVOX_800_30_HRS_U	935.3	$Cu^{2+}(2p_{3/2})$	839.09	0.96
	942.7	Satellite	901.58	
	954.6	$Cu^{2+}(2p_{1/2})$	315.26	
BICUVOX_800_U	934.5	$Cu^{2+}(2p_{3/2})$	496.08	0.99
	943.2	Satellite	221.44	
	954.2	$Cu^{2+}(2p_{1/2})$	173.34	

Table 4-37: Atomic% of each element and corresponding Bi: V and V: Cu surface ratio data from XPS Analysis for wash, fresh, 30 hrs used and long time used BICUVOX catalysts

Catalyst	Elements Present (at%)					Bi: V ratio	V: Cu ratio
	Bi	C	Cu	O	V		
BICUVOX-WASH	10.06	51.48	0.55	32.9	5.01	2.01	9.11
BICUVOX-400_F	14.42	44.46	0.77	33.36	6.99	2.06	9.08
BICUVOX-400_30HRS_U	11.31	53.98	0.62	28.57	5.52	2.05	8.9
BICUVOX-400_U	12.36	57.55	0.67	23.39	6.03	2.04	9
BICUVOX-600_F	15.52	40.28	0.85	35.66	7.69	2.02	9.05
BICUVOX-600_30HRS_U	13.98	50.93	0.75	27.55	6.79	2.06	9.05
BICUVOX-600_U	12.55	55.23	0.69	25.32	6.21	2.02	9
BICUVOX-800_F	15.66	39.04	0.85	36.74	7.71	2.03	9.07
BICUVOX-800_30HRS_U	14.68	56.62	0.81	20.59	7.3	2.01	9.01
BICUVOX-800_U	10.77	78.02	0.59	5.31	5.31	2.03	9

4.1.3 Regeneration of Catalyst

The catalyst can be regenerated by calcination. We have calcined the BINIVOX-600_30HRS_U and BINIVOX-600_U catalysts at 600 °C for 2 hours. XRD analysis shows the regeneration in terms of relative intensity of most prominent secondary phases with respect to the γ-BIMEVOX phase as shown in Figure 4.81. The obtained relative intensity ratio of BINIVOX-600_F catalyst is 29.34 and 60.2% for Bi_2O_3 and $BiVO_4$ phase, respectively which increases to 45.63 and 75.38%, respectively in BINIVOX-600_300HRS_U catalyst. After calcination, this relative intensity ratio for Bi_2O_3 and $BiVO_4$ phases reduces and reaches to 31.23 and 63.86%, respectively for BINIVOX-600_300HRS_U_Regenerated_(600 °C/ 2h) catalyst. On comparing the time of calcination, BINIVOX-600_U catalyst is calcined at 2 and 6 hours and the relative intensity ratio data reflects that 6 hours calcined catalyst (BINIVOX-600_U_Regenerated_(600 °C/ 6h)) is showing better results than 2 hours calcined catalyst (BINIVOX-600_U_Regenerated_(600 °C/ 2h)). FESESM images along with the EDX spectrum (Figure 4.82) of BINIVOX-600_300HRS_U_Regenerated_(600 °C/ 2h) and BINIVOX-600_U_Regenerated_(600 °C/ 2h) catalyst show burning of carbon as no carbon is detected in FESESM images. Particle size distribution of BINIVOX-600_300HRS_U_Regenerated_(600 °C/ 2h) and BINIVOX-600_U_Regenerated_(600 °C/ 2h) catalyst is found in the range of 0.35-2.4, and 0.4-3.14 μm, respectively and reflects the small increment in the particle size compare to used catalysts.

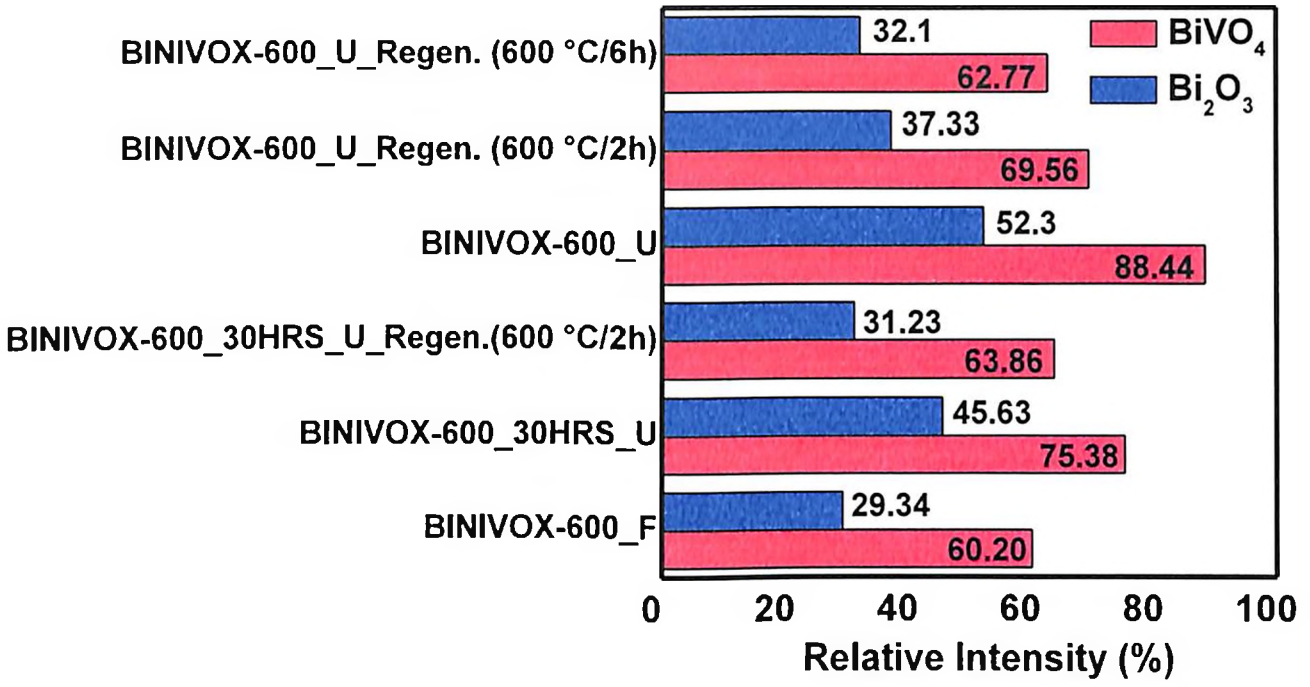

Figure 4-81: Relative intensity of most prominent secondary phases with respect to the γ-BIMEVOX phase for BINIVOX-600 catalyst at different conditions.

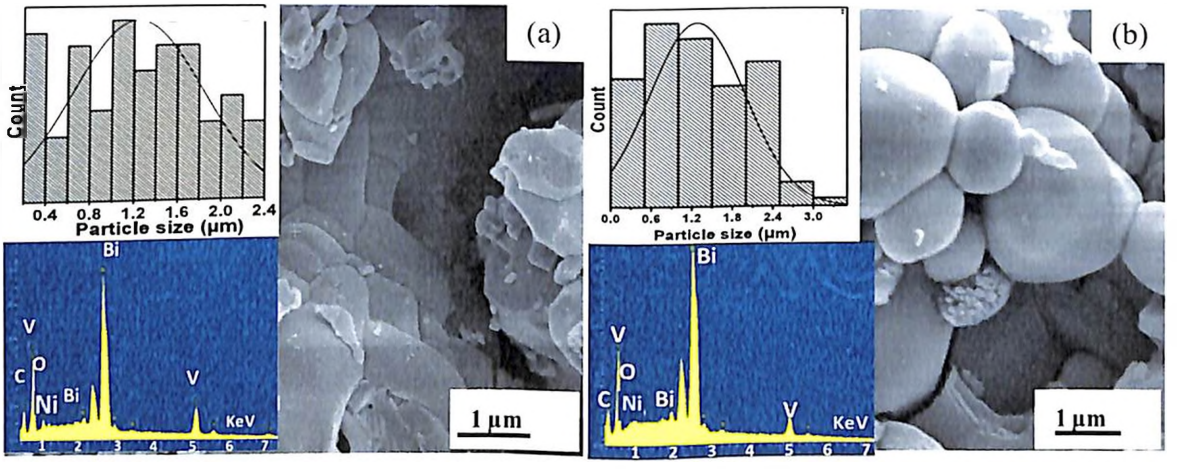

Figure 4-82: FESEM images of the (a) BINIVOX-600_30HRS_U and (b) BINIVOX-600_U catalysts after calcination at 600 °C for 2 hours along with their partisize distribution and EDX spectrum.

4.2 Discussion

4.2.1 Possible reaction pathways

A set of possible reaction pathways which can be drawn based on the products is schematically presented in Figure 4.81 and described as follows. Here, the standard heat of reactions is calculated by considering the gaseous state of the reactant and products as these are presented in gaseous form at reaction temperature. The overall steam reforming reaction is

$$C_2H_5OH(g) + 3H_2O(g) \leftrightarrows 2CO_2(g) + 6H_2(g); \qquad \Delta H^0_{298K} = 174\ kJmol^{-1} \tag{4.19}$$

Reaction Step 1: Dehydrogenation leading to formation of CH_3CHO

$$C_2H_5OH(g) \leftrightarrows CH_3CHO(g) + H_2(g); \qquad \Delta H^0_{298K} = 68.9\ kJmol^{-1} \tag{4.20}$$

CH_3CHO can undergo to various pathways:

Pathway 1: Reaction Step 2: C-C bond breakage in acetaldehyde

$$CH_3CHO(g) \leftrightarrows CH_4(g) + CO(g); \qquad \Delta H^0_{298K} = -19\ kJmol^{-1} \tag{4.21}$$

Reaction Step 3: Water gas shift reaction (WGSR)

$$CO(g) + H_2O(g) \leftrightarrows CO_2(g) + H_2(g); \qquad \Delta H^0_{298K} = -41.2\ kJmol^{-1} \tag{4.22}$$

Reaction Steps 4 and 5: Formation of methane via Fischer-Tropsch reactions (FTR)

$$CO(g) + 3H_2(g) \leftrightarrows CH_4(g) + H_2O(g); \qquad \Delta H^0_{298K} = -205.8\ kJmol^{-1} \tag{4.23}$$

$$CO_2(g) + 4H_2(g) \leftrightarrows CH_4(g) + 2H_2O(g); \qquad \Delta H^0_{298K} = -165\ kJmol^{-1} \tag{4.24}$$

Reaction Steps 6 and 7: Steam reforming of methane (either created by C-C bond breaking or via FTR)

$$CH_4(g) + H_2O(g) \leftrightarrows CO(g) + 3H_2(g); \qquad \Delta H^0_{298K} = 205.8\ kJmol^{-1} \tag{4.25}$$

$$CH_4(g) + 2H_2O(g) \leftrightarrows CO_2(g) + 4H_2(g); \qquad \Delta H^0_{298K} = 165\ kJmol^{-1} \tag{4.26}$$

Reaction Step 8: Formation of CO via reverse WGSR

$$CO_2(g) + H_2(g) \leftrightarrows CO(g) + H_2O(g); \qquad \Delta H^0_{298K} = 41.2\ kJmol^{-1} \tag{4.27}$$

Reaction Step 9: Formation of CH_3OH

$$CO_2(g) + 3H_2(g) \leftrightarrows CH_3OH(g) + H_2O(g); \qquad \Delta H^0_{298K} = -48.9\ kJmol^{-1} \tag{4.28}$$

Pathway 2: Reaction Step 10: Formation of CH_3COCH_3

$$CH_3CHO(g) + CH_3OH(g) \leftrightarrows CH_3COCH_3(g) + H_2O(g); \qquad \Delta H^0_{298K} = -93.4\ kJmol^{-1} \tag{4.29}$$

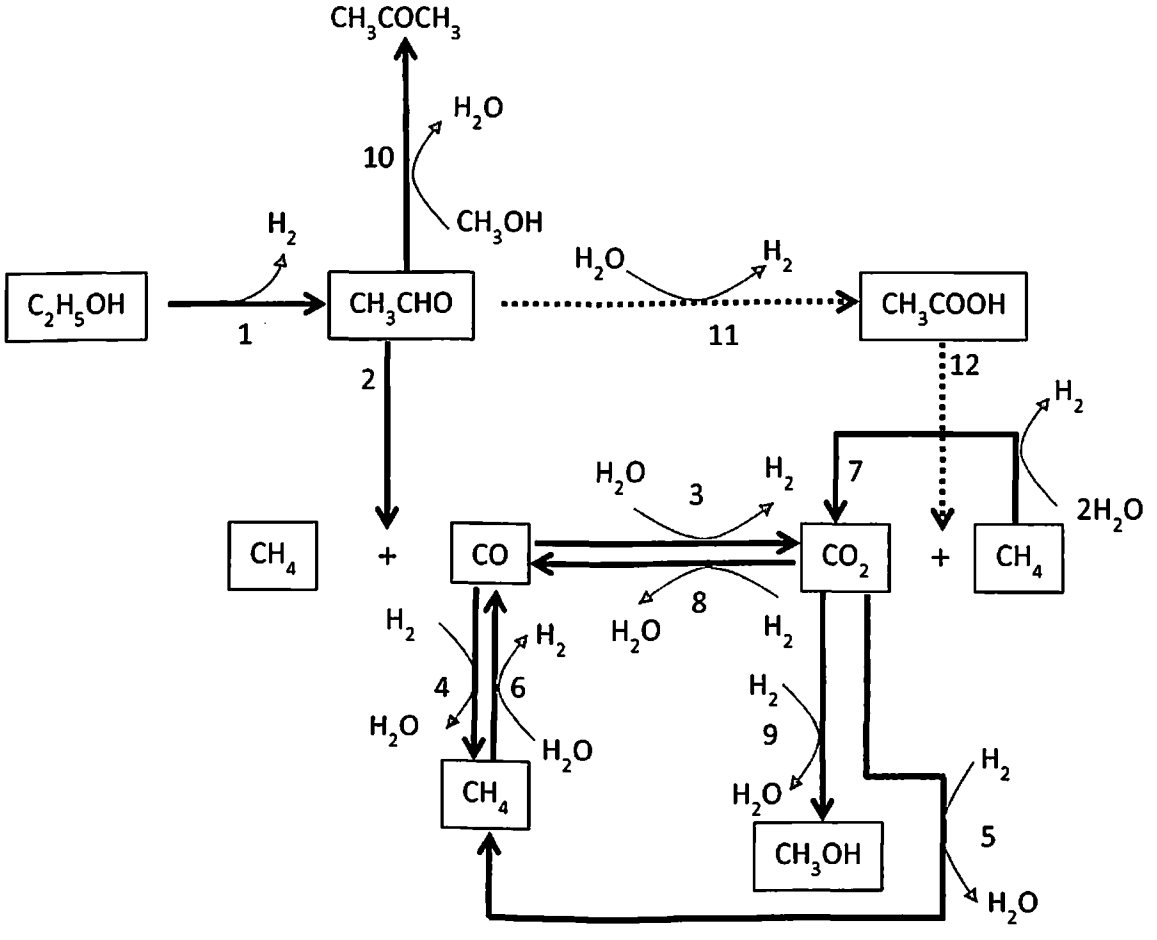

Figure 4-83: Possible reaction steps for steam reforming of EtOH on the catalysts

Pathway 3: Reaction Step 11: Hydration of CH_3CHO to CH_3COOH

$$CH_3CHO(g) + H_2O(g) \leftrightarrows CH_3COOH(g) + H_2(g); \qquad \Delta H^0_{298K} = -30.1 \text{ kJmol}^{-1} \quad (4.30)$$

Reaction Step 12: C-C bond breakage in acetic acid to form CO_2

$$CH_3COOH(g) \leftrightarrows CO_2(g) + CH_4(g); \qquad \Delta H^0_{298K} = -29.9 \text{ kJmol}^{-1} \quad (4.31)$$

However, in our case CH_3COOH is not comprehended in liquid product, presumably because the amount present could very small or the survival time of the intermediate is too short as both the reaction steps 11 and 12 are exothermic with almost same amount of heat of reaction and therefore this step-in Figure 4.81 is showed with dash line.

At low temperatures, below 250°C, along with high EtOH concentration in the feed mixture, the predominant reaction could be the decomposition of ethanol (Fishtik, Alexander et al. 2000).

$$C_2H_5OH(g) \leftrightarrows CH_4(g) + CO(g) + H_2(g); \qquad \Delta H^0_{298K} = 50 \text{ kJmol}^{-1} \quad (4.32)$$

At lower temperatures with amounts of water in the feed, the contribution of the WGSR (step 3, Equation 4.22) is small. Therefore, no CO_2 is observed at temperature 200°C and 2.5:1 H_2O: EtOH molar ratio. The presence of large amount of CO and CH_4 indicates the dehydrogenation of ethanol to CH_3CHO (step 1, Equation 4.20) as the most probable, which is followed by C-C bond breakage (step 2, Equation 4.21) along with the formation methane via FTR (step 4 and 5, Equation 4.23 and 4.24). An increase in temperature, ethanol reforming reaction (Equation 4.19) and the WGSR (step 3, Equation 4.22) become dominant and lead to an increase in the selectivity of H_2 and CO_2. Meanwhile, the low selectivity of by-products (CO and CH_4) are also exhibited in the gas products, suggesting that the acetaldehyde decomposition reaction (step 1, Equation 4.20 followed by step 2, Equation 4.21) is occurred obvious in parallel with the methane steam reforming (step 6 and 7, Equation 4.25 and 4.26) and WGSR (step 3, Equation 4.22), as methane reforming and WGSR are promoted at the higher temperature (Fatsikostas and Verykios 2004; Barattini, Ramis et al. 2009; Vicente, Ereña et al. 2014).

It is already seen that at small amounts of water (high ethanol concentration), both at low and high temperatures, the predominant reactions is the decomposition of ethanol (Equation 4.32), which favors the formation of more amount CO and CH_4 (Fishtik, Alexander et al. 2000). At low H_2O/EtOH ratios, CO is more likely to produce methane via FTR (step 4 and 5, Equation 4.23 and 4.24) which further increases the CH_4 selectivity, thus reducing overall H_2 selectivity (Mulewa, Tahir et al. 2017). As the amount of water increases, water inhibits

the ethanol decomposition reaction by channeling ethanol reactivity towards the main ESR reaction (Equation 4.21) (Byrd, Pant et al. 2007). An increase in the amount of water also has the effect of increasing the extents of the WGSR (step3, Equation 4.22) and methane steam reforming reactions (step 6 and 7, Equation 4.25 and 4.26) and consequently, a reduction in the amounts of the undesired products, CO and CH_4 which leads to increasing overall H_2 selectivity (Comas, Marino et al. 2004; Özkan, Gök et al. 2011).

Ethanol conversion is found to decrease with increasing flow rate, as flow rate increases, residence time reduces. High residence time allows subsequent promotion of all possible and feasible reactions along with enough time for complete conversion of ethanol and vice versa. On contrary to this, longer residence time (low flow rate) decreases H_2 and CO_2 selectivity due to methane formation reaction between CO_2 and H_2 (step 4 and 5, Equation 4.23 and 4.24), which further responsible for high amount of carbon formation (Roy, Artyushkova et al. 2012; Roy, Martinez et al. 2012).

The variation of product distribution with reaction time shows the decomposition of acetaldehyde (Equation 4.22) species produce H_2, CO, and CH_4 species, which may in turn result in carbon formation depending on the rate of hydrogen recombination (Equation 4.23, 4.24, and 4.27). Figure 4.13, 4.14 and 4.15 shows reduction in H_2, CO_2 selectivity and maximum amount of CO and CH_4 is forming with time (after 150 hrs). More amount of carbon formation can be seen from the characterization of long time used catalysts, and that causes the deactivation. There are three main reactions that may contribute to carbon formation (de Lima, da Silva et al. 2009):

Boudouard reaction: $2CO(g) \rightarrow C(s) + CO_2(g);\ \Delta H^0_{298K} = -172.5\ kJmol^{-1}$ (4.33)

Reverse of C-gasification: $CO(g) + H_2(g) \rightarrow H_2O(g) + C(s); \Delta H^0_{298K} = -131.2\ kJmol^{-1}$ (4.34)

Methane decomposition: $CH_4(g) \rightarrow 2H_2(g) + C(s);\ \Delta H^0_{298K} = 74.5\ kJmol^{-1}$ (4.35)

The capacity of the catalyst particles to cleave C–C bonds decreases gradually with time, and thus the accumulated acetaldehyde is converted into acetone, which acts as the precursor of coke (Alberton, Souza et al. 2007; Chen, Choong et al. 2010). Activity results shows increase in CO selectivity and decrease in CO_2 selectivity with time on stream, which proves that WGS reaction (Equation 4.22) is affected by catalyst deactivation and reverse of WGS reaction (Equation 4.27) is more dominant to produce more CO. These results suggest that the reaction rates of all the reactions involve in the reaction pathway are notably affected by catalyst deactivation. It is reported in the literature, that with increase in reaction time, the

content of C_2H_4 increases, suggesting the rate of ethanol dehydration increases, this could be due to the blockage of active sites for ethanol dehydrogenation by deposited carbon leading to more ethanol being dehydrated to C_2H_4 and then the cleavage of C-C bond or formation of coke, and so on. However, C_2H_4 is not seen in our results, presumably because of very short survival time or probably it is reacting with catalyst surface and adsorbs to the surface as a C-species and fail to escape (Roh, Potdar et al. 2004; Roh, Platon et al. 2006; Alberton, Souza et al. 2007; Cheng, Foo et al. 2011; Özkan, Gök et al. 2011; El Doukkali, Iriondo et al. 2014; Vicente, Montero et al. 2014). This is likely to lead directly to deterioration of the catalyst.

Addition to C-deposition, solid-state transformations of the catalytic phases during reaction is also the major cause for deactivation of complex multi-component catalysts (Bartholomew 2001; Argyle and Bartholomew 2015). Delmon et al, (1997) explain that the catalytic active phase is generally a high-surface area, defect structure of high surface energy and as a whole stable material. Reaction processes, like redox process, or the acidic reactor environment may themselves trigger the solid-state conversion of the active phase to an inactive phase (Delmon 1997). Rossetti et al, (2005) study deactivation of a commercial K-modified Fe oxide catalyst ($KFeO_2$) used for dehydrogenation of ethylbenzene to styrene (Rossetti, Bencini et al. 2005). Electron probe micro-analysis shows that due to presence of reducing environment inside the reactor Fe^{3+} converts to Fe^{2+}, causes a rapid segregation into inactive Fe_3O_4 and KOH phases with a considerable drop in catalytic activity. Delmono et al, (1999) study the ammonia synthesis over Fe-K/Al_2O_3 catalyst and report the deactivation of catalyst due to formation of KAl_2O_3 at catalyst surface (Delmono, Froment et al. 1999). Bielanski et al, (1980) investigate the deactivation of V_2O_5-MoO_3 catalyst in the selective oxidation of benzene and report that formation of inactive vanadium compounds and loss of volatile MoO_3 at higher temperatures lead to decrease in the activity (Bielanski, Najbar et al. 1980). Decomposition of the active phase PdO to inactive Pd metal during catalytic combustion of methane on PdO/Al_2O_3 and PdO/ZrO_2 catalysts causes reduction in catalytic activity (Farrauto, Hobson et al. 1992). Piva et al, (2015) study decomposition behavior of BICUVOX ($Bi_2V_{0.9}Cu_{0.1}O_{5.5-\delta}$) powder in reducing environment at 300 °C for 12 hrs and propose that at first the $Bi_2V_{0.9}Cu_{0.1}O_{5.5-\delta}$ phase reacts with H_2 to form an intermediate compound $Bi_2V_{0.6}^{5+}V_{0.3}^{4+}Cu_{0.1}O_{5.5-(x+\delta)}$ lacking structural oxygen atoms (Piva, Piva et al. 2015). Further exposure of H_2 leads to the decomposition of $Bi_2V_{0.6}^{5+}V_{0.3}^{4+}Cu_{0.1}O_{5.5-(x+\delta)}$ phase to Bi_2O_3 and Bi metal phases. Similar observations are found in our case and reduction of Bi^{3+} to Bi^0 has been noted for long time used catalyst by XPS. XRD also confirms the

formation of Bi metal could be due to reducing capability of H_2 and CO_2 in the reaction medium (Montero, Ochoa et al. 2015). C-deposition also responsible for the decrease in the oxygen mobility by covering the catalyst surface, and that result in more reducing environment inside the reactor. Bi metal formation along with more secondary phases (as mention in XRD) leads to reduction in the amount of pure γ-phase. Hence, decomposition of BIMEVOX catalyst results very sharp drop in catalytic activity after 150 hrs.

Order of different BIMEVOX catalysts is calculated on the basis of EtOH conversion, amount of C in gas, and the selectivity of gaseous products at the best operating parameters in terms of H_2 selectivity (400°C, 10:90 wt% EtOH: H_2O, atmospheric pressure and 0.11 cc min^{-1} feed flow rate).

The decreasing order of the EtOH conversion is:

BICOVOX-600≈BICUVOX-600>BINIVOX-600>BICOVOX-800>BICUVOX-800>BINIVOX-800>BICOVOX-400>BICUVOX-400>BINIVOX-400

The decreasing order of the Amount of C in gas:

BICOVOX-600>BICOVOX-800>BICUVOX-600>BINIVOX-600>BINIVOX-800>BICUVOX-800>BICOVOX-400>BINIVOX-400>BICUVOX-400

The decreasing order of the H_2 selectivity is:

BICUVOX-600>BICOVOX-600>BINIVOX-600>BICUVOX-800>BICOVOX-800>BINIVOX-800>BICOVOX-400>BICUVOX-400≈BINIVOX-400

The decreasing order of the CO_2 selectivity is:

BICUVOX-600>BICOVOX-600>BINIVOX-600>BICUVOX-800>BICOVOX-800>BINIVOX-800>BICUVOX-400>BICOVOX-400>BINIVOX-400

The decreasing order of the CO selectivity is:

BINIVOX-400>BICUVOX-400>BINIVOX-800>BICUVOX-800>BINIVOX-600>BICUVOX-600≈BICOVOX-400>BICOVOX-800>BICOVOX-600

The decreasing order of the CH_4 selectivity is:

BICOVOX-400>BICOVOX-800>BICOVOX-600>BINIVOX-400>BINIVOX-800≈BICUVOX-400>BINIVOX-600>BICUVOX-800>BICUVOX-600

Decreasing order of H_2, CO_2 selectivity, and EtOH conversion shows that all BIMEVOX-600 catalysts have higher H_2, CO_2 selectivity, and EtOH conversion compares to all BIMEVOX-800 catalysts, which also have higher H_2, CO_2 selectivity, and EtOH conversion

formation of Bi metal could be due to reducing capability of H_2 and CO_2 in the reaction medium (Montero, Ochoa et al. 2015). C-deposition also responsible for the decrease in the oxygen mobility by covering the catalyst surface, and that result in more reducing environment inside the reactor. Bi metal formation along with more secondary phases (as mention in XRD) leads to reduction in the amount of pure γ-phase. Hence, decomposition of BIMEVOX catalyst results very sharp drop in catalytic activity after 150 hrs.

Order of different BIMEVOX catalysts is calculated on the basis of EtOH conversion, amount of C in gas, and the selectivity of gaseous products at the best operating parameters in terms of H_2 selectivity (400°C, 10:90 wt% EtOH: H_2O, atmospheric pressure and 0.11 cc min^{-1} feed flow rate).

The decreasing order of the EtOH conversion is:

BICOVOX-600≈BICUVOX-600>BINIVOX-600>BICOVOX-800>BICUVOX-800>BINIVOX-800>BICOVOX-400>BICUVOX-400>BINIVOX-400

The decreasing order of the Amount of C in gas:

BICOVOX-600>BICOVOX-800>BICUVOX-600>BINIVOX-600>BINIVOX-800>BICUVOX-800>BICOVOX-400>BINIVOX-400>BICUVOX-400

The decreasing order of the H_2 selectivity is:

BICUVOX-600>BICOVOX-600>BINIVOX-600>BICUVOX-800>BICOVOX-800>BINIVOX-800>BICOVOX-400>BICUVOX-400≈BINIVOX-400

The decreasing order of the CO_2 selectivity is:

BICUVOX-600>BICOVOX-600>BINIVOX-600>BICUVOX-800>BICOVOX-800>BINIVOX-800>BICUVOX-400>BICOVOX-400>BINIVOX-400

The decreasing order of the CO selectivity is:

BINIVOX-400>BICUVOX-400>BINIVOX-800>BICUVOX-800>BINIVOX-600>BICUVOX-600≈BICOVOX-400>BICOVOX-800>BICOVOX-600

The decreasing order of the CH_4 selectivity is:

BICOVOX-400>BICOVOX-800>BICOVOX-600>BINIVOX-400>BINIVOX-800≈BICUVOX-400>BINIVOX-600>BICUVOX-800>BICUVOX-600

Decreasing order of H_2, CO_2 selectivity, and EtOH conversion shows that all BIMEVOX-600 catalysts have higher H_2, CO_2 selectivity, and EtOH conversion compares to all BIMEVOX-800 catalysts, which also have higher H_2, CO_2 selectivity, and EtOH conversion

than all BIMEVOX-400. On contrary to this, all BIMEVOX-400 catalysts have higher CH_4 and CO selectivity than all BIMEVOX-800 catalysts, which also have higher CH_4 and CO selectivity than all BIMEVOX-600 catalysts. This provides the order for best catalytic activity results as:

BIMEVOX-600>BIMEVOX-800>BIMEVOX-400

4.2.2 Possible Mechanisms over Oxide Catalyst

Most of the steam reforming catalysts are based on metal related active center on ceramic oxide supports. The ethanol or feed electronically attaches on the active center and high oxygen ion mobility of the support helps in WGSR. Only a few works have been reported on mechanism of ethanol steam reforming over unreduced oxide catalysts.

Lee et al, (2018) perform ethanol steam reforming over unreduced Zn-doped ($Zn_{0.3}Mg_{0.7}Al_2O_4$) and Zn-Pb doped ($Pd_{0.01}Zn_{0.29}Mg_{0.7}Al_2O_4$) $MgAl_2O_4$ catalysts. The proposed mechanism path of reaction indicates attachment of ethanol molecules on the basic active sites of Zn-O-Mg surfaces to produce intermediate CH_3CHO, followed by decarboxylation on Mg-O-Al acidic surfaces to give CO and CH_4 (Lee, Do et al. 2018). Further, CH_4 reforming reaction takes place over Mg-O-Al/Zn-O-Al-O-Mg surfaces to give H_2 and CO. At this point exact reaction mechanism for LTSR of ethanol on BIMEVOX is not clear, but a possible process could be that similar. This is proposed and represented in Figure 4.82 as 'Possible Mechanism-I'. Accordingly, ethanol might be activated sequentially on the acidic or basic sites of oxide catalyst (electronegativity difference between the metals present in the oxide could create acidic and basic active sites) to produce the intermediate products. Ethanol would be attached on the localised basic sites to form acetaldehyde by C–H bond cleavage which can undergo further decomposition through C–C bond cleavage on the acidic sites of catalyst to produce CH_4 and CO species (Bion, Epron et al. 2010; Sun and Wang 2014). Later, oxygen mobility on V(Co)-O(□) layer (□ indicates oxygen vacancy) are expected to act as a promoters in CH_4 reforming and WGSR (Ebiad, El-Hafiz et al. 2012). The creation of oxygen vacancies in the V_2O_5 layer doped with a Co metal ion could be represented through kroger-vink equation as (Singh, Ghosh et al. 2017):

$$V_2O_5 \rightarrow 2V' + V_O^{\cdot\cdot} + 4O_X^o \tag{4.36}$$

$$2CoO \xrightarrow{V_2O_5} 2Co_V''' + 3V_O^{\cdot\cdot} + 2O_X^o \tag{4.37}$$

$$2NiO \xrightarrow{V_2O_5} 2Ni_V''' + 3V_O^{\cdot\cdot} + 2O_X^0 \quad (4.38)$$

$$2CuO \xrightarrow{V_2O_5} 2Cu_V''' + 3V_O^{\cdot\cdot} + 2O_X^0 \quad (4.39)$$

Where $2Co_V'''/2Ni_V'''/2Cu_V'''$ represents the occupancy of a V^{5+} site by a Co^{2+}/ Ni^{2+} / Cu^{2+} with three negative charge, $V_O^{\cdot\cdot}$ represents positively charged oxygen vacancies, and O_X^0 represents neutral lattice oxygen.

Zhu et al, (2014) study the role of oxygen vacancy in methane reforming over unreduced CeO_2-Fe_2O_3 catalyst at 850 °C (Zhu, Li et al. 2014).Under a reductive atmosphere in the methane-conversion (CH_4 to CO/CO_2) step, Fe_2O_3 partially reduced to metal/oxide (Fe/FeO) system and $CeFeO_3$ is formed, via $3CeO_2 + Fe_2O_3 + Fe \rightarrow Ce^{4+}Fe^{2+}O_3$ and/or $CeO_2 + FeO \rightarrow Ce^{4+}Fe^{2+}O_3$ reactions. $CeFeO_3$ formation causes the generation of additional O^{2-} vacancies, which enhances the WGSR and reduces the carbon deposition. It is also seen in the literature that O^{2-} vacancies are able to accept hydried species and enhances the ability of abstracting H_2 from ethanol during dehydrogenation step ($O^{2-}M^{n+}\square + H_2 \rightarrow OH^-M^{n+}H^-$ with $\square$ anionic vacancy) (Jalowiecki-Duhamel, Pirez et al. 2010). Thus, O-vacancies present in BIMEVOX catalyst favor the CH_4 reforming and WGSR as mentioned in 'Possible Mechanism-I'.

Another probable mechanism for ethanol steam reforming over BICOVOX oxide catalyst could involve the reduced bismuth metal (generated in the reducing atmosphere (CH_4, CO, H_2, N_2) during the reforming reactions) as active metal center. XPS (XPS analysis, Figure 5 (a-c)) also shows small amount of Bi metal on the surface of fresh catalyst. Mutual interaction between ethanol and basic sites of catalyst could create acetaldehyde as an intermediate product, which undergoes the decarbonylation reaction over Bi metal to form CO and CH_4 as depicted in Figure 4.82 as 'Possible Mechanism-II'. Similar reaction has already been reported in the literature majorly in the field of oxidative C-C cleavage of epoxides over Bi-mandelate catalyst to give carboxylic acid (Zevaco, Duñach et al. 1993; Le Boisselier, Duñach et al. 1994). Later, oxygen mobility, via oxygen vacancies, plays its role in CH_4 reforming and WGSR as discussed above.

4.2.3 Correlating the catalysts' microstructure chemistry with catalytic activity

Catalytic activity can be affected by various characterization parameters, including;

1) Amount of pure γ-BIMEVOX phase present: After preparation of BIMEVOX catalysts, along with the pure γ-BIMEVOX phase, some secondary phases (Bi_2O_3, $BiVO_4$, etc) are also present as impurity, which complicate the structure of catalysts (Abrahams, Krok et al. 1996;

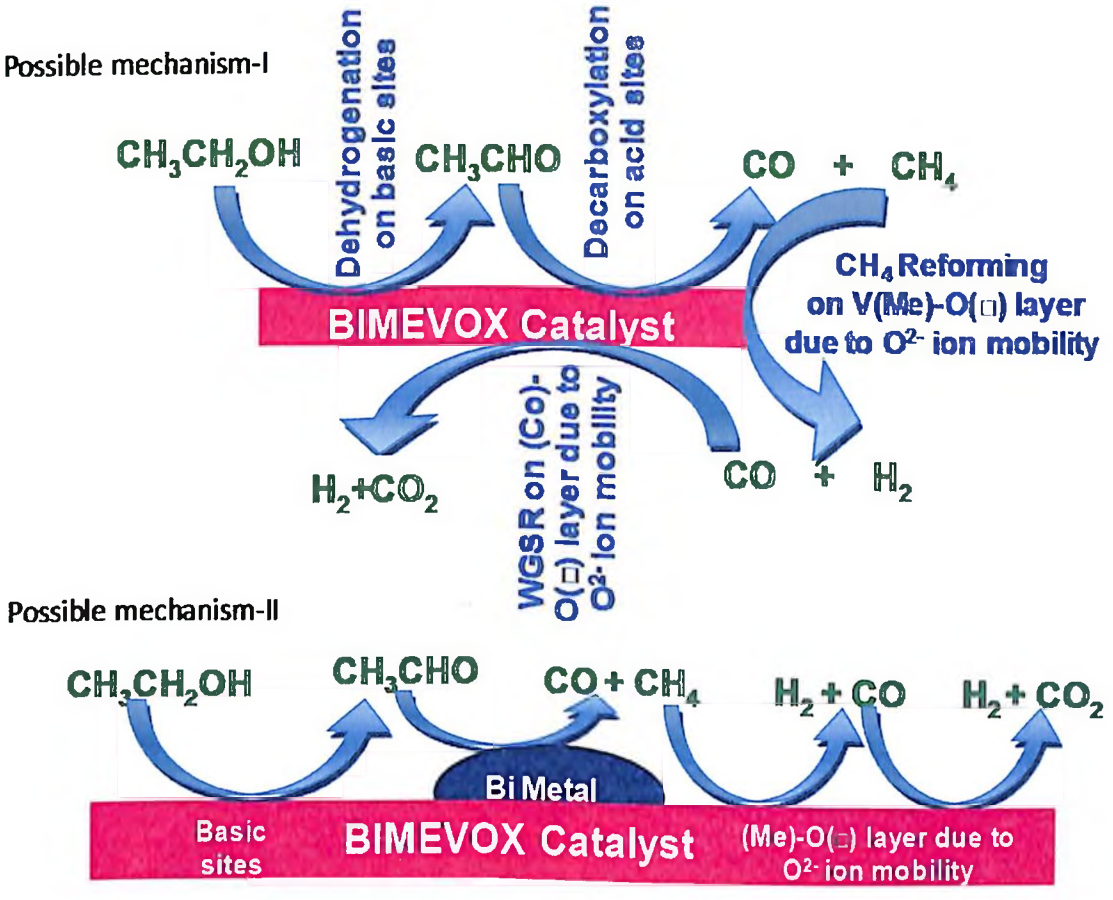

Figure 4-84: Possible mechanisms for the low temperature steam reforming reaction over the BIMEVOX catalyst. Where □ shows the oxygen vacancies

Abrahams, Nelstrop et al. 1998; Abrahams and Krok 2003). Like, presence of the tetragonal Bi_2O_3 can be attributed to oxygen deficiency in the system (Roy and Fuierer 2009). Presence of highly conductive pure γ-BIMEVOX phase in BIMEVOX catalyst results in more oxide ion conductivity at lower temperatures (~300°C), compared to parent compound BIVOX due to introduction of dopants onto the vanadium site that stabilizes the pure γ-phase at room temperature (Shao, Mederos et al. 2010). Higher the ionic conductivity, lower will be the activation energy of catalyst and high oxide ion conductivity also employs in various oxidative processes (Abrahams, Krok et al. 1996; Krok, Abrahams et al. 1996; Abrahams, Bush et al. 1998). More amount of pure γ-BIMEVOX phase leads to more ionic conductivity compare to γ-BIMEVOX phase with more impurities. The acidic environment in the reactor could be considered to be responsible for formation of Bi metal along with other secondary phases leading to reduction in the amount of pure γ-phase in BIMEVOX_U catalysts (XRD and XPS results). Consequently, oxygen ion mobility through the lattice decreases significantly.

2) Particle size: Particle size distribution of the catalysts also plays an important role in coke deposition phenomena. Zhou et al, (2001) investigate the effect of decreasing CeO_2 particle size between 4 and 60 nm and report that oxygen vacancies increase by 2 orders of magnitude when particle size is reduced from 60 to 4 nm (Zhou and Huebner 2001). Haga et al, (1997) investigate the effect of particle size on catalytic activity of Co/Al_2O_3 catalyst for ethanol steam reforming (Haga, Nakajima et al. 1997). H_2 selectivity increases with decrease in particle size (more numbers of active centres) and higher amount of C-deposition on larger particle catalyst is observed by FESEM (Haga, Nakajima et al. 1998). They also show that the adsorption strength of ethanol on catalyst depends on the crystallite size of cobalt. Ceria samples with similar polyhedral morphologies but different particle sizes are investigated by Soykal et al, (2014) (Soykal, Sohn et al. 2014). Their results show that ceria sample with the larger particle size (120 nm) has negligible reducibility below 600°C and ceria sample with particle size of 3.5 nm are found to reduce much more easily both with H_2 as well as during steady-state ethanol steam reforming, at temperatures as low as 400°C. Smaller particle size, increases reducibility and a higher surface density of the basic sites are thought to lead to higher activity for steam reforming.

It is found that smaller the particle, more the surface area and with higher surface area a greater number of active sites are available and that leads to better activity results. In BIMEVOX catalysts, along with these advancement, smaller particle size shows high

conductivity due to lower activation energy and it also helps in stabilizing the disordered γ-phase (Abrahams, Krok et al. 2001; Abrahams and Krok 2002). Therefore, it can be concluded that smaller the particle size, better the activity results.

3) Oxygen vacancy: There have been several studies showing the effect of high oxygen mobility in enhancing oxidation reactions, such as CO oxidation, and steam reforming of methane, etc (Song and Ozkan 2010). The role of oxygen mobility in improving the catalytic stability during reforming reactions through preventing metal particles from sintering and suppressing the formation of carbonaceous species by gasification (Song, Tan et al. 2009). The availability of oxygen plays a key role in determining both the H_2 yield and the stability of the catalysts. As discussed in the possible reaction pathway that high oxygen mobility through the O-vacancies present in γ-BIMEVOX lattice favors the conversion of CH_4 and CO to H_2 and CO_2 by CH_4 reforming (equations 4.23 & 4.26) and water gas shift reaction (WGSR- equation 4.22) (da Silva, da Costa et al. 2010; Oemar, Hidajat et al. 2015; Roy and Leclerc 2015). If there is sufficient oxygen available/accessible, ethanol can be fully oxidized to CO_2.

$$CH_4(g) + 1/2O_2(g) \leftrightarrows CO(g) + 2H_2(g); \qquad \Delta H^0_{298K} = -36 \text{ kJmol}^{-1} \tag{4.40}$$

$$CH_4(g) + O_2(g) \leftrightarrows CO_2(g) + 2H_2(g); \qquad \Delta H^0_{298K} = -318.9 \text{ kJmol}^{-1} \tag{4.42}$$

However, if replenishment of oxygen on the surface is slower compared to its depletion, other by-products with intermediate oxidation states will be formed, including CH_4, carbon and CO. Therefore, effective delivery of oxygen to the oxidation sites plays a key role in determining the hydrogen yield and maintaining catalyst stability. Song et al, (2009) perform the ethanol steam reforming over Co/CeO_2 and Co/ZrO_2 catalysts and finds higher oxygen mobility in ceria-supported samples compare to ZrO_2-supported ones (Song and Ozkan 2009). Co/ZrO_2 catalysts shows very rapid deactivation, not allowing data collection at steady-state and for Co/CeO_2 catalyst, 84% H_2 yield is obtained at 550°C. However, incorporation of CeO_2 with ZrO_2 shows better results than only ZrO_2 as a support and obtains H_2 yield is 66%. Huang et al, (2005) show that high oxygen mobility lessens the possible carbon deposition (coking) due to the reaction of surface carbon species with the lattice oxygen (Huang, Lin et al. 2005). Khaerudini et al, (2016) prepare BIVOX and BINBVOX catalyst by solid state reaction and report that formation of V^{4+} oxidation state, cause by the stabilization of good ionic conductivity of the γ phase, reflects the creation of more oxygen vacancies (Khaerudini, Guan et al. 2016). They determine the valance in both the catalysts and find that BIVOX shows only V^{5+} and BINBVOX shows both V^{4+} and V^{5+} oxidation

state. Therefore, it can be said that more V^{4+}/V^{5+} ratio, more amount of oxygen vacancy. This concludes that with increasing V^{4+}/V^{5+} ratio catalytic activity results should increase.

4) Carbon deposition: The coke deposition on the catalysts is one of the main causes for deactivation during ethanol steam reforming (Prasad, Dhand et al. 2010; Ma, Ran et al. 2015). The direct deactivation of catalysts occurs predominantly by covering active phases (Alberton, Souza et al. 2007). Goala et al, (1996) and. Tsipouriari et al, (1994) study carbon deposition over Ni/Al_2O_3 catalyst and suggest that carbon deposited on catalyst surface is one of the main reasons for the deactivation of catalysts (Tsipouriari, Efstathiou et al. 1994; Goula, Lemonidou et al. 1996; Wang, Liu et al. 2008). For example, catalysts for catalytic cracking lose their activity within seconds due to carbon deposition on the surface while promoted iron catalysts used in ammonia synthesis have a lifetime of years (Glüer, Förster et al. 2015; Ihli, Jacob et al. 2017). For any catalytic process, the life of catalyst is a major economic factor and carbon deposition is the major cause for that. Therefore, this can be concluded that catalysts with more amount of carbon on the surface will deactivate first.

From the points discussed above, following interpretations can be made:

- γ-BIMEVOX phase increases → Catalytic activity increases
- Particle size increases → Catalytic activity decreases
- V^{4+}/V^{5+} ratio increases →Catalytic activity increases
- C-deposition increases → Catalytic activity decreases

Order of all BIMEVOX catalyst systems determine from various characterization techniques:

For fresh catalysts:

1) XRD (Decreasing order of amount of pure γ-phase)

BICUVOX-800_F>BINIVOX-800_F>BICOVOX-800_F>BICUVOX-600_F>BINIVOX-600_F>BICOVOX-600_F> BICUVOX-400_F>BINIVOX-400_F> BICOVOX-400_F

This shows BIMEVOX-800 catalysts shows maximum amount of γ-BIMEVOX phase compare to BIMEVOX-600 catalysts, which also have higher amount of γ-BIMEVOX phase compare to BIMEVOX-400 catalysts. According to this decreasing order for activity is; *BIMEVOX-800>BIMEVOX-600>BIMEVOX-400*

2) FESEM (Increasing particle size)

BINIVOX-400_F<BICOVOX-400_F<BINIVOX-600_F<BICOVOX-600_F<BICUVOX-400_F<BICUVOX-600_F<BINIVOX-800_F<BICOVOX-800_F<BICUVOX-800_F

Here, smaller particle size is found for BIMEVOX-400 catalysts and maximum particle size is for BIMEVOX-800 catalysts. Therefore, from here the decreasing order for activity is; *BIMEVOX-400>BIMEVOX-600>BIMEVOX-800*

3) RAMAN (Decreasing order of V^{4+}/V^{5+} ratio)

BICUVOX-600_F>BICOVOX-600_F≈BINIVOX-600_F≈BICOVOX-800_F≈BICOVOX-400_F>BINIVOX-800_F≈BICUVOX-800_F≈BICUVOX-400_F> BINIVOX-400_F

Raman shows maximum V^{4+}/V^{5+} ratio for BIMEVOX-600 catalysts and smallest ratio is calculated for BIMEVOX-400 catalysts. According to this the decreasing order for activity is; *BIMEVOX-600>BIMEVOX-800>BIMEVOX-400*

4) XPS (Decreasing order of V^{4+}/V^{5+} ratio)

BICUVOX-600_F>BINIVOX-600_F>BICOVOX-600_F>BINIVOX-800_F>BINIVOX-400_F>BICOVOX-800_F>BICOVOX-400_F>BICUVOX-800_F> BICUVOX-400_F

Like Raman, XPS also shows the similar trends for V^{4+}/V^{5+} ratio and found decreasing order for activity is; *BIMEVOX-600>BIMEVOX-800>BIMEVOX-400*

After 30hrs use of catalysts:

1) XRD (Increasing order of reduction of pure γ-phase)

BICOVOX-800_30HRS_U<BINIVOX-800_30HRS_U<BICUVOX-800_30HRS_U< BICOVOX-600_30HRS_U<BICUVOX-600_30HRS_U<BINIVOX-600_30HRS_U< BICUVOX-400_30HRS_U <BICOVOX-400_30HRS_U< BINIVOX-400_30HRS_U

After using catalysts for 30HRS, BIMEVOX-800 catalysts shows minimum reduction in the amount of γ-BIMEVOX phase compare to BIMEVOX-600 catalysts, which also shows lower reduction in γ-BIMEVOX phase compare to BIMEVOX-400 catalysts. According to this decreasing order for activity is; *BIMEVOX-800>BIMEVOX-600>BIMEVOX-400*

2) RAMAN (Decreasing order of V^{4+}/V^{5+} ratio)

BICOVOX-600_30HRS_U>BICUVOX-600_30HRS_U>BICOVOX-800_30HRS_U> BINIVOX-600_30HRS_U>BICOVOX-400_30HRS_U>BICUVOX-800_30HRS_U> BINIVOX-800_30HRS_U >BICUVOX-400_30HRS_U>BINIVOX-400_30HRS_U

After using catalysts, the V^{4+}/V^{5+} ratio is still maximum for BIMEVOX-600 catalysts and calculated decreasing order for activity is; *BIMEVOX-600>BIMEVOX-800>BIMEVOX-400*

3) XPS

(i) Decreasing order of V^{4+}/V^{5+} ratio

BICOVOX-600_30HRS_U>BINIVOX-600_30HRS_U>BICUVOX-600_30HRS_U>
BINIVOX-800_30HRS_U>BICOVOX-800_30HRS_U>BICOVOX-400_30HRS_U>
BICUVOX-800_30HRS_U >BINIVOX-400_30HRS_U>BICUVOX-400_30HRS_U

Similar to Raman, XPS also shows the similar trends for V^{4+}/V^{5+} ratio and found decreasing order for activity is; *BIMEVOX-600>BIMEVOX-800>BIMEVOX-400*

(ii) Increasing order of Carbon deposition

BICUVOX-600_30HRS_U<BICUVOX-400_30HRS_U<BINIVOX-600_30HRS_U<
BICOVOX-600_30HRS_U<BICOVOX-400_30HRS_U<BINIVOX-400_30HRS_U<
BICOVOX-800_30HRS_U <BICUVOX-800_30HRS_U< BINIVOX-800_30HRS_U

XPS also shows the amount of C-deposition after using the catalysts for 30 hrs and minimum carbon deposition is seen for BIMEVOX-600 catalysts compared to BIMEVOX-400 and BIMEVOX-800. Determined order for decreasing activity is; *BIMEVOX-600>BIMEVOX-400>BIMEVOX-800*

(4) DTGA (Increasing order of Carbon deposition)

BICOVOX-600_30HRS_U<BICUVOX-600_30HRS_U<BICUVOX-800_30HRS_U<
BINIVOX-600_30HRS_U<BINIVOX-800_30HRS_U<BICOVOX-800_30HRS_U<
BICOVOX-400_30HRS_U <BINIVOX-400_30HRS_U< BICUVOX-400_30HRS_U

According to DTGA order for decreasing activity is; *BIMEVOX-600>BIMEVOX-800>BIMEVOX-400*

(5) FESEM-EDX (Increasing order of Carbon deposition)

BICOVOX-600_30HRS_U<BICOVOX-400_30HRS_U<BICUVOX-600_30HRS_U<
BINIVOX-600_30HRS_U<BINIVOX-400_30HRS_U<BICUVOX-400_30HRS_U<
BICOVOX-800_30HRS_U <BICUVOX-800_30HRS_U< BINIVOX-800_30HRS_U

Similar to XPS, FESEM-EDX also show the similar trend for decreasing activity and it is; *BIMEVOX-600>BIMEVOX-400>BIMEVOX-800*

After long time use of catalysts:

Similar to fresh and 30 hrs used BIMEVOX catalysts, order of catalysts from various characterization techniques for long time used BIMEVOX catalysts is determined to see the effect of time on catalysts.

1) XRD (Increasing order of reduction of pure γ-phase)

BINIVOX-800_U<BICOVOX-800_U<BICUVOX-800_U<BINIVOX-600_U<BICOVOX-600_U<BICUVOX-600_U<BICOVOX-400_U<BICUVOX-400_U<BINIVOX-400_U

Analogous to fresh and 30 hrs used catalysts, long time used catalysts also shows the minimum and maximum reduction in pure γ-phase for BIMEVOX-800 and BIMEVOX-400, respectively and find decreasing order for activity is; *BIMEVOX-800>BIMEVOX-600>BIMEVOX-400*

2) RAMAN (Decreasing order of V^{4+}/V^{5+} ratio)

BICOVOX-600_U>BICOVOX-800_U>BICUVOX-600_U>BICUVOX-800_U>BINIVOX-600_U>BINIVOX-800_U≈BICUVOX-400_U>BICOVOX-400_U≈BINIVOX-400_U

Even after using catalysts for very long time the V^{4+}/V^{5+} ratio is found maximum for BIMEVOX-600 catalysts and determine order for decreasing activity is; *BIMEVOX-600>BIMEVOX-800>BIMEVOX-400*

3) XPS

(i) Decreasing order of V^{4+}/V^{5+} ratio

BINIVOX-600_U>BICOVOX-600_U>BICUVOX-600_U>BINIVOX-800_U>BICOVOX-800_U>BINIVOX-400_U>BICUVOX-800_U>BICOVOX-400_U>BICUVOX-400_U

Similar to Raman, XPS shows the similar behavior and decreasing order for activity is; *BIMEVOX-600>BIMEVOX-800>BIMEVOX-400*

(ii) Increasing order of Carbon deposition

BINIVOX-600_U<BICUVOX-600_U<BICOVOX-600_U<BICUVOX-400_U<BICOVOX-400_U<BICOVOX-800_U<BINIVOX-400_U<BICUVOX-800_U<BINIVOX-800_U

After using catalysts for long time, maximum C-deposition is found in BIMEVOX-800 catalysts and minimum is for BIMEVOX-600 catalysts and order of decreasing activity is; *BIMEVOX-600>BIMEVOX-400>BIMEVOX-800*

(4) DTGA (Increasing order of Carbon deposition)

BINIVOX-600_U<BINIVOX-400_U<BICOVOX-600_U<BICUVOX-600_U<BICOVOX-400_U<BICUVOX-400_U<BINIVOX-800_U<BICOVOX-800_U<BICUVOX-800_U

(5) FESEM-EDX (Increasing order of Carbon deposition)

BINIVOX-600_U<BINIVOX-400_U<BICOVOX-600_U<BICOVOX-400_U<BICUVOX-600_U<BICUVOX-400_U<BINIVOX-800_U<BICUVOX-800_U<BICOVOX-800_U

DTGA and FESEM-EDX both shows the similar trend as observe in XPS for carbon deposition and the order for decreasing activity is; *BIMEVOX-600>BIMEVOX-400>BIMEVOX-800.*

Figure 4.83 shows the possible steps for deactivation of BICOVOX catalysts with time after using in reactor. BIMEVOX-600 shows better catalytic activity compare to BIMEVOX-800 and BIMEVOX-400, which is supported by the characterization results. BIMEVOX-400_U contains the lowest particle size, but maximum reduction in amount of γ-phase is seen for this catalysts. On the contrary, BIMEVOX-800_U accommodates the higher amount of γ-phase, but the largest particle size (at least four times than that of the others) causes maximum amount of C-deposition. In terms of amount of γ-phase and average particle size BIMEVOX-600 catalyst holds middle position, but shows the maximum amount of O^{2-} vacancies (maximum V^{4+} oxidation state) which leads to maximum performance.

4.2.4 Effect of Dopant

Overall activity and physico-chemical properties of the catalysts could be explained by the metal dopants present in the powders.

The FESEM and XRD analysis of the fresh BICUVOX, BINIVOX and BICOVOX catalysts, show that the particle size for BICUVOX systems is the largest and BICOVOX systems are the smallest, in general. The particle size differences could be explained by the degree of stress level (if stress will be less, it will result in bigger particle size) present in the lattice, which depends on the following factors:

Atomic radius difference: rV(0.132 nm)>rNi(0.125 nm)≈ rCo(0.125 nm)>rCu(0.128 nm).

According to Hume-Rothery rule % difference between rV and rNi or rCo is 5.3% and in case of Cu it is 3.03%.

Electronegativity: V≈Ni≈Cu≈ Co

Therefore, it can be concluded that BICUVOX powder, with least amount of stress results in bigger particle size. Additionally, we have to keep in mind that the presence of complex combination of secondary oxide phases in fresh catalysts and continuous change of phase composition in reactor environment is affecting the lattice stress.

Now, smaller BIMEVOX particle implies more disordered lattice, presence of more defects and result in more O^{2-} vacancies. Accordingly, BINIVOX and BICOVOX should show higher V^{4+}/V^{5+} ratio, higher O^{2-} vacancies, but this is not what we are observing.
The activation energy data (0.53, 0.41 and 0.33 eV at 300 °C and 0.47, 0.33 and 0.21 eV at 600 °C for the BICOVOX, BINIVOX and BICUVOX catalysts, respectively (Abraham, Debreuille-Gresse et al. 1988; Muller, Chateigner et al. 1996; Steil, Fouletier et al. 1999)) suggest that oxygen mobility through the lattice of BICUVOX should be higher (higher O^{2-} vacancies and V^{4+}/V^{5+} ratio) and through the BINIVOX and BICOVOX should be lower. Therefore, clearly the activation energy and particle size effects are counter balancing each other and that is why V^{4+}/V^{5+} (Table 4.21, 4.27 and 4.33) and O_V/O_L (oxygen vacancy to lattice oxygen) ratio (Table 4.23, 4.29 and 4.35) is coming almost similar for BICUVOX, BINIVOX and BICUVOX catalysts and ultimately the overall activity results and carbon deposition are coming very similar for used catalysts.

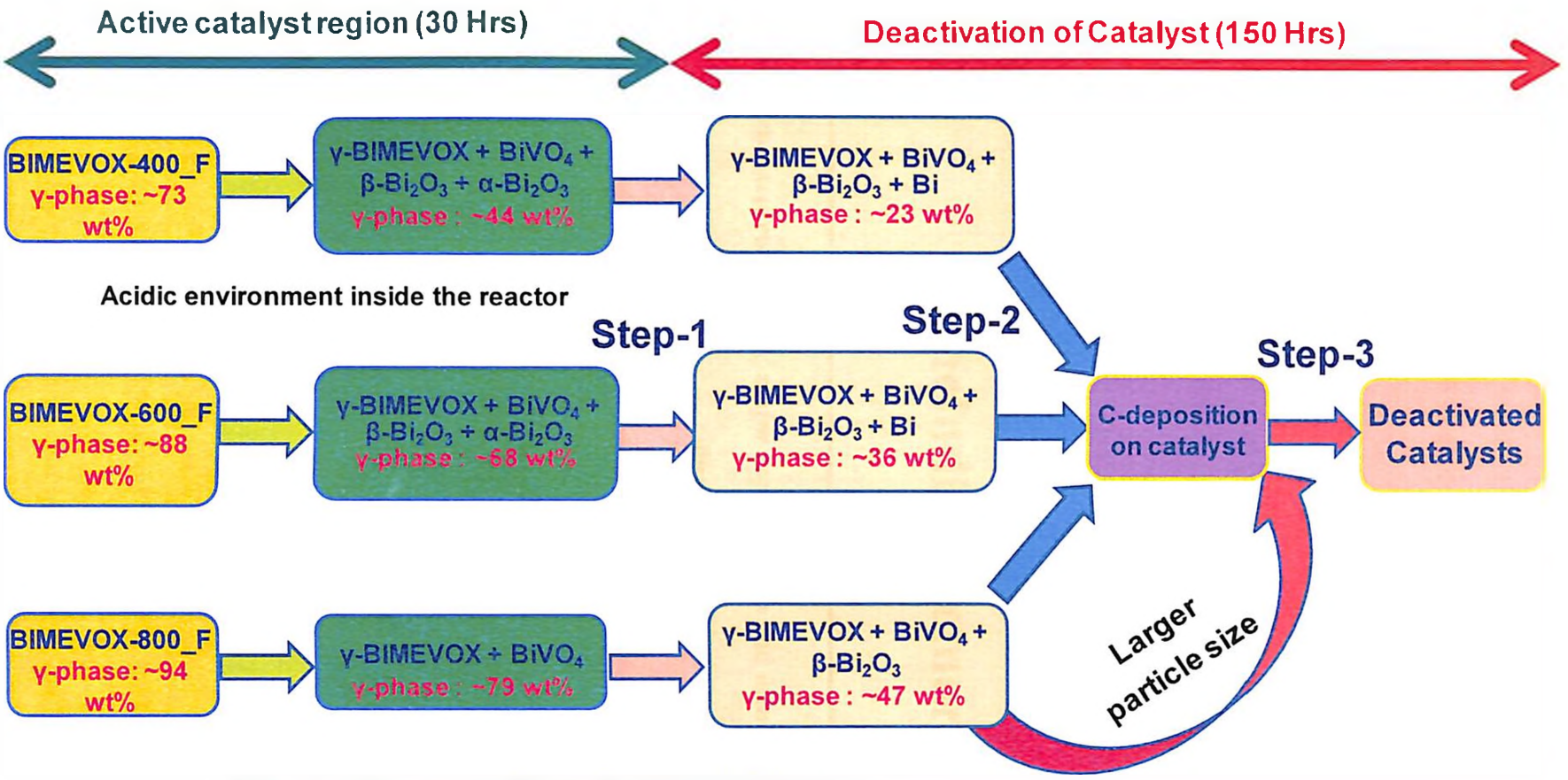

Figure 4-85: Possible steps for deactivation of BIMEVOX catalysts after using in reactor

Concluding Remarks

In present chapter, conclusions, major contributions and future scope for research are discussed.

5.1 Conclusions

The following conclusions are drawn based on the results obtain in the present study:

1. It is demonstrated that BIMEVOX (ME-Co, Ni, and Cu) catalysts can be useful for H_2 production by steam reforming of ethanol at low temperatures (200-400°C).
2. Effect of time on stream data shows that the catalysts attain steady state within 5-6 hrs and remain stable till ~ 30 hrs and afterword slowly begin to deactivate. H_2 selectivity reduces to 0% with minimal amount of EtOH conversion (10-3%) and CO_2 (4-0%) selectivity after 150 hrs of reforming reactions for BIMEVOX-400 and BIMEVOX-800 catalysts. Although, BIMEVOX-600 shows 8-11% of H_2 selectivity even after 150 hrs with 9-6% CO_2 and 11-15% EtOH conversion.
3. EtOH conversion, C in gas phase, and H_2 and CO_2 selectivity is found to increase with increasing reactor temperature and decreasing EtOH concentration in the feed for all the BIMEVOX catalysts. Selectivity for CO and CH_4 shows an opposite trend with increasing temperature and decreasing EtOH concentration. With increasing flow rate, C in gas phase, and H_2 and CO_2, CO and CH_4 selectivity values are observed to increase. However, EtOH conversion is found to decrease with increasing flow rate.
4. Maximum H_2 selectivity of 80% for BICOVOX-600, 76% for BINIVOX-600 and 83% for BICUVOX-600 catalysts with almost 100% EtOH conversion at reactor conditions of 400°C, 23:1 H_2O: EtOH molar ratio and 0.35 cc min^{-1} feed flow rate is observed. Along with higher EtOH conversion and a higher selectivity for H_2, BIMEVOX-600 catalysts show a higher amount of C in the gas phase and CO_2, and a lower selectivity for CO and CH_4 compared to BIMEVOX-400 and BIMEVOX-800 catalysts.
5. The gas and liquid phase product distribution explains that probably EtOH is dehydrogenated to the aldehyde as a primary step follow by decarbonylation of the aldehyde to CH_4 and CO, which is followed by the methane reforming and WGS reaction, as expected in the temperature range of our experiments.
6. Negligible amount of EtOH conversion and H_2 production is observed using BIVOX catalysts, while no EtOH conversion is detected for mixed Bi_2O_3, $BiVO_4$ and Me-O powder under similar reactor conditions.
7. S-DTGA analysis infers the purity and thermal stability of BIMEVOX catalysts compare to BIVOX catalyst. On cooling an endothermic peak at ~ 623°C is found,

and that reflects the reverse transition of γ-BIVOX, indicates the instability of in BIVOX, which is not seen for BIMEVOX catalysts.

8. S-DTGA also confirms the presence of small amount of amorphous carbon in all 30 hrs used BIMEVOX catalysts. Long time (150 hr) used BIMEVOX-400 and BIMEVOX-600 catalysts shows amorphous and whisker carbon. On the other hand, long time (150 hr) used BIMEVOX-800 catalysts show the existence of amorphous, and graphite carbon only.
9. XRD study reveals that the BIMEVOX-400_F and BIMEVOX-600_F samples contain little amount of secondary phases (α, β-Bi_2O_3 and α-$BiVO_4$) compare to BIMEVOX-800_F catalysts, as they shows mainly pure γ-BIMEVOX phase. XRD analysis also reveals breaking of the pure γ-phase (~41, ~22, and ~9% in BIMEVOX-400_30HRS_U, BIMEVOX-600_30HRS_U, BIMEVOX-800_30HRS_U,respectively and ~70, ~60, and ~22% in BIMEVOX-400_U, BIMEVOX-600_U, BIMEVOX-800_U, respectively) into more secondary phases (Bi metal, α, β-Bi_2O_3 and α-$BiVO_4$) after using it.
10. FTIR analysis reveals the presence of V-O and Bi-O vibration bonds. It confirms the breaking of phases as the number of bands in the region of 516-423 cm^{-1} increases due to formation of more Bi_2O_3 phase and it also reveals that carbon is increasing after using the catalyst for 150 hrs and maximum intensity peak is observe for BIMEVOX-800 catalysts.
11. FESEM analysis shows the porous and flaky network of interconnected particles in all BIMEVOX_F catalysts. Growth in particle size is noticed with calcination temperature from 400 to 800°C. After using catalyst for 30 hrs in the reactor, scale of agglomeration is increased and very less traces of carbon is seen in the FESEM images, reflects the presence of small amount of amorphous carbon. For long time (after 150 hrs) used BIMEVOX catalysts, reduction in particle size is seen and that reflects the breaking of phases. BIMEVOX-400 and BIMEVOX-600 shows the presence of whisker carbon and non-filamentous coke or graphite carbon is clearly visible in BIMEVOX-800 catalysts.
12. XPS spectra of the BIMEVOX catalysts show the presence of all essential elements, Bi, V, O, and Me, along with adventitious C in the samples. Higher V^{4+}:V^{5+} ratio, observed for BIMEVOX-600_F samples compare to BIMEVOX-800_F and BIMEVOX-400_F catalysts, indicates more oxygen mobility in BIMEVOX-600 catalysts. XPS data confirms the presence of more carbon in long time used catalysts

and it also confirms the deposition of maximum amount of C in BIMEVOX-800 catalysts.

13. XPS also shows the reduction in V^{4+}:V^{5+} ratio with use and confirms the breaking of catalysts after long time use as more Bi metal is found.
14. Raman also confirms the maximum oxygen mobility in BIMEVOX-600 catalysts as it also shows the maximum V^{4+}:V^{5+} ratio for BIMEVOX-600 catalysts.

5.2 Major contributions

1. BIMEVOX (ME- Co, Ni, and Cu) systems with high O^{2-} ion conductivity are identified as potential catalysts or supports for H_2 production.
2. BIMEVOX catalysts prepare by SCS route could be beneficial for saving energy and obtaining comparatively smaller particle size as the smaller grain size of BIMEVOX may be desirable not only for obtaining higher surface area, but also for the sake of increased O^{2-} conductive at lower temperature.
3. Successful demonstration of low-temperature (200-400°C) steam reforming over BIMEVOX catalysts, as LTSR is an energy efficient process.
4. In this project ethanol present in the water is used as feed, which might be produced from waste product after the extraction and refining of sugar from sugar cane and agro-industrial wastes. Therefore, in future, this process will help to clean the wastes at the same time producing hydrogen from it, which is one of the future goals of energy ministry.

5.3 Future scope

1. BIMEVOX catalyst development by varying the doping metal and amount of doping metal to see the effects of doping on steam reforming of ethanol.
2. Development of double substituted BIMEVOX systems needs to be investigated for increasing catalytic activity.
3. Effect of high temperature (500-700°C), flow rate, other feed and their different concentrations on steam reforming can be studied to evaluate the temperature effect on breaking of catalyst after long time as well as the application of BIMEVOX catalysts with other feed.

4. Exhaustive experimental studies on the regeneration or disposal of catalyst and to see its effect on environment.
5. Cost estimation analysis of the whole process, including catalyst development, catalytic activity and regeneration or disposal of the catalyst can be performed.

REFERENCES

Aarthi, T. and Madras G. (2008). "Photocatalytic reduction of metals in presence of combustion synthesized nano-TiO_2." Catalysis Communications **9**(5): 630-634.

Abelló, S., Bolshak E., et al. (2013). "Ni–Fe catalysts derived from hydrotalcite-like precursors for hydrogen production by ethanol steam reforming." Applied Catalysis A: General **450**: 261-274.

Abraham, F., Debreuille-Gresse M. F., et al. (1988). "Phase transitions and ionic conductivity in $Bi_4V_2O_{11}$ an oxide with a layered structure." Solid State Ionics **28–30, Part 1**: 529-532.

Abrahams, I., Bush A. J., et al. (1998). "Effects of preparation parameters on oxygen stoichiometry in $Bi_4V_2O_{11-\delta}$." Journal of Materials Chemistry **8**(5): 1213-1217.

Abrahams, I. and Krok F. (2002). "Defect chemistry of the BIMEVOXes." Journal of Materials Chemistry **12**(12): 3351-3362.

Abrahams, I. and Krok F. (2003). "A model for the mechanism of low temperature ionic conduction in divalent-substituted γ-BIMEVOXes." Solid State Ionics **157**(1-4): 139-145.

Abrahams, I., Krok F., et al. (2001). "Defect structure and ionic conductivity as a function of thermal history in BIMGVOX solid electrolytes." Journal of Materials Science **36**(5): 1099-1104.

Abrahams, I., Krok F., et al. (1996). "Defect structure of quenched γ-BICOVOX by combined X-ray and neutron powder diffraction." Solid State Ionics **90**(1-4): 57-65.

Abrahams, I., Nelstrop J., et al. (2000). "BICUVOF: a new copper fluoride doped BIMEVOX." Solid State Ionics **136**: 61-66.

Abrahams, I., Nelstrop J., et al. (1998). "Defect structure of quenched γ-BINIVOX." Solid State Ionics **110**(1-2): 95-101.

Al-Alas, A., Beg S., et al. (2012). "Investigation of phase stability and oxide ion performance in new perovskite-type bismuth vanadate." Materials Chemistry and Physics **136**(1): 15-20.

Al-Areqi, N. A., Al-Alas A., et al. (2010). "Synthesis, characterization, and electrical conductivity of new Aurivillius-type oxide-ion conductor." Russian Journal of Physical Chemistry A **84**(13): 2334-2344.

Al-Areqi, N. A. and Beg S. (2009). "Phase transition changes in $Bi_4Ce_xV_{2-x}O_{11-(x/2)-\delta}$ system." Materials Chemistry and Physics **115**(1): 5-8.

Al-Areqi, N. A. and Beg S. (2012). "Studies in composition and temperature dependence of phase stability in the $Bi_4Ag_xV_{2-x}O_{11-(2\,x)-\delta}$ system and their influence on the oxide ion performance." Phase Transitions **85**(3): 255-263.

Al-Areqi, N. A., Beg S., et al. (2012). "Study on phase stability and oxide ion conductivity in the BIAGVOX system." Journal of Physics and Chemistry of Solids **73**(6): 730-734.

Alberton, A. L., Souza M., et al. (2007). "Carbon formation and its influence on ethanol steam reforming over Ni/Al_2O_3 catalysts." Catalysis Today **123**: 123-257.

Alcalá, M. and Real C. (2006). "Synthesis based on the wet impregnation method and characterization of iron and iron oxide-silica nanocomposites." Solid State Ionics **177**(9): 955-960.

Alga, M., Ammar A., et al. (2005). "Effect of Niobium doping on structural, thermal, sintering and electrical properties of $Bi_4V_{1.8}Cu_{0.2}O_{10.7}$." Journal of Solid State Chemistry **178**(9): 2873-2879.

Allred, A. (1961). "Electronegativity values from thermochemical data." Journal of inorganic and nuclear chemistry **17**(3-4): 215-221.

Angeli, S. D., Turchetti L., et al. (2016). "Catalyst development for steam reforming of methane and model biogas at low temperature." Applied Catalysis B: Environmental **181**: 34-46.

Ardelean, I., Cora S., et al. (2008). "EPR and FT-IR spectroscopic studies of Bi_2O_3–B_2O_3–CuO glasses." Physica B: Condensed Matter **403**(19): 3682-3685.

Arslan, A. and Doğu T. (2016). "Effect of calcination/reduction temperature of Ni impregnated CeO_2–ZrO_2 catalysts on hydrogen yield and coke minimization in low temperature reforming of ethanol." International Journal of Hydrogen Energy **41**(38): 16752-16761.

Aruna, S. T. and Mukasyan A. S. (2008). "Combustion synthesis and nanomaterials." Current Opinion in Solid State and Materials Science **12**(3): 44-50.

Asadullah, M., Ito S.-i., et al. (2002). "Highly Efficient Catalyst for Biomass Gasification to Produce Hydrogen and Syngas at Low Temperature." Fuel Chemistry Division Preprints, **47**(2): p. 766-768.

Ashima, Sanghi S., et al. (2012). "Rietveld refinement, electrical properties and magnetic characteristics of Ca–Sr substituted barium hexaferrites." Journal of Alloys and Compounds **513**: 436-444.

Aupretre, F., Descorme C., et al. (2005). "Ethanol steam reforming over $Mg_xNi_{1-x}Al_2O_3$ spinel oxide-supported Rh catalysts." Journal of Catalysis **233**(2): 464-477.

Bacewicz, R. and Kurek P. (2000). "Raman scattering in BIMEVOX (ME= Mg, Ni, Cu, Zn) single crystals." Solid State Ionics **127**(1-2): 151-156.

Bailera, M., Kezibri N., et al. (2017). "Future applications of hydrogen production and CO_2 utilization for energy storage: Hybrid Power to Gas-Oxycombustion power plants." International Journal of Hydrogen Energy **42**(19): 13625-13632.

Balachander, L., Ramadevudu G., et al. (2013). "IR analysis of borate glasses containing three alkali oxides." ScienceAsia **39**(3): 278.

Balat, H. and Kırtay E. (2010). "Hydrogen from biomass – Present scenario and future prospects." International Journal of Hydrogen Energy **35**(14): 7416-7426.

Balzar, D., Ramakrishnan P., et al. (2004). "Defect-related lattice strain and the transition temperature in ferroelectric thin films." Physical Review B **70**(9): 092103.

Banach, B. and Machocki A. (2015). "Effect of potassium addition on a long term performance of Co–ZnO–Al_2O_3 catalysts in the low-temperature steam reforming of ethanol: Co-precipitation vs citrate method of catalysts synthesis." Applied Catalysis A: General **505**: 173-182.

Bandoli, G., Barreca D., et al. (1996). "Pure and mixed phase Bi_2O_3 thin films obtained by metal organic chemical vapor deposition." Chemical Vapor Deposition **2**(6): 238-242.

Baran, E. J., Botto I. L., et al. (1978). "Das Schwingungsspektrum von $Sr_2V_2O_7$ und die Schwingungseigenschaften des Divanadat-Ions." Monatshefte für Chemie/Chemical Monthly **109**(1): 41-51.

Basagiannis, A. C. and Verykios X. E. (2007). "Catalytic steam reforming of acetic acid for hydrogen production." International Journal of Hydrogen Energy **32**(15): 3343-3355.

Beg, S., Al-Alas A., et al. (2010). "Layered Aurivillius compound: Synthesis, characterization and electrical properties." Journal of Alloys and Compounds **504**(2): 413-419.

Beg, S., Al-Alas A., et al. (2010). "Microwave solid synthesis and electrical properties of Aurivillius-type oxide-ion conductor." Journal of Physics and Chemistry of Solids **71**(10): 1421-1427.

Beg, S., Al-Alas A., et al. (2010). "Structural and electrical properties of hexavalent-substituted BIMEVOX synthesized by a microwave-assisted route." Radiation Effects & Defects in Solids: Incorporating Plasma Science & Plasma Technology **165**(12): 894-906.

Beg, S., Al-Alas A., et al. (2010). "Study on structural and electrical properties of layered perovskite-type oxide-ion conductor." Materials Chemistry and Physics **124**(1): 305-311.

Beg, S. and Al-Areqi N. A. (2009). "Structural and electrical study of CeIV-substituted bismuth vanadate." Journal of Physics and Chemistry of Solids **70**(6): 1000-1007.

Beg, S., Al-Areqi N. A., et al. (2009). "Influence of dopant concentration on the phase transition and ionic conductivity in BIHFVOX system." Physica B: Condensed Matter **404**(14-15): 2072-2079.

Beg, S., Al–Areqi N. A., et al. (2015). "Improved structural and electrical properties of nickel and aluminum co-doped $Bi_4V_2O_{11}$ solid electrolyte." Ionics **21**(2): 421-428.

Beg, S., Hafeez S., et al. (2010). "Layered $Bi_4Ba_xV_{2-x}O_{11-(3x/2)-\delta}$ perovskite oxide as solid electrolyte for intermediate temperature solid oxide fuel cells." Physica B: Condensed Matter **405**(20): 4370-4376.

Beg, S., Hafeez S., et al. (2014). "Study of phase stabilization and oxide–ion conductivity in BICUMGVOX solid electrolyte." Solid State Ionics **261**: 125-130.

Beg, S., Hafeez S., et al. (2010). "Influence of calcium substitution on the phase transition and ionic conductivity in BICAVOX oxide ion conductor." Phase Transitions **83**(3): 169-181.

Beg, S. and Haneef S. (2015). "Synthesis, phase stability and oxide ion conductivity of Ce (IV)–Cd (II) double substituted bismuth vanadate." Phase Transitions **88**(11): 1074-1085.

Bej, B., Pradhan N. C., et al. (2014). "Production of hydrogen by steam reforming of ethanol over alumina supported nano-NiO/SiO_2 catalyst." Catalysis Today **237**: 80-88.

Bekhet, H. A., Matar A., et al. (2017). "CO_2 emissions, energy consumption, economic growth, and financial development in GCC countries: Dynamic simultaneous Equation models." Renewable and Sustainable Energy Reviews **70**: 117-132.

Bepari, S., Basu S., et al. (2017). "Steam reforming of ethanol over cerium-promoted Ni-Mg-Al hydrotalcite catalysts." Catalysis Today.

Berndes, G., Abt B., et al. (2016). "Forest biomass, carbon neutrality and climate change mitigation.", Report, U.S. Depaetment of Energy.

Bhattacharya, A., Mallick K., et al. (1994). "Low temperature synthesis of a bismuth vanadium oxide isomorphous with γ-$Bi_4V_2O_{11}$." Solid state communications **91**(5): 357-360.

Bicchi, C. P., Binello A. E., et al. (1993). "Characterization of roasted coffee by S-HSGC and HPLC-UV and principal component analysis." Journal of agricultural and food chemistry **41**(12): 2324-2328.

Bilal, M. and Jackson S. D. (2017). "Ethanol steam reforming over Pt/Al_2O_3 and Rh/Al_2O_3 catalysts: The effect of impurities on selectivity and catalyst deactivation." Applied Catalysis A: General **529**: 98-107.

Bimbela, F., Chen D., et al. (2012). "Ni/Al coprecipitated catalysts modified with magnesium and copper for the catalytic steam reforming of model compounds from biomass pyrolysis liquids." Applied Catalysis B: Environmental **119–120**: 1-12.

Bimbela, F., Oliva M., et al. (2013). "Hydrogen production via catalytic steam reforming of the aqueous fraction of bio-oil using nickel-based coprecipitated catalysts." International Journal of Hydrogen Energy **38**(34): 14476-14487.

Bioenergy, I. (2009). "Bioenergy–a sustainable and reliable energy source." Report, International Energy Agency Bioenergy, Paris, France.

Bion, N., Epron F., et al. (2010). "Bioethanol reforming for H_2 production. A comparison with hydrocarbon reforming." Catalysis **22**: 1-55.

Biswas, P. and Kunzru D. (2007). "Steam reforming of ethanol for production of hydrogen over Ni/CeO–ZrO catalyst: Effect of support and metal loading." International Journal of Hydrogen Energy **32**(8): 969-980.

Biswas, P. and Kunzru D. (2008). "Oxidative steam reforming of ethanol over Ni/CeO_2-ZrO_2 catalyst." Chemical Engineering Journal **136**(1): 41-49.

Blume, R., Rosenthal D., et al. (2015). "Characterizing graphitic carbon with X-ray photoelectron spectroscopy: a step-by-step approach." ChemCatChem 7(18): 2871-2881.

Bobadilla, L. F., Palma S., et al. (2013). "Steam reforming of methanol over supported Ni and Ni–Sn nanoparticles." International Journal of Hydrogen Energy **38**(16): 6646-6656.

Samsonov, Valentinovich G., (2013). "The oxide handbook." Springer Science & Business Media.

Bosze, E. J., McKittrick J., et al. (2003). "Investigation of the physical properties of a blue-emitting phosphor produced using a rapid exothermic reaction." Materials Science and Engineering: B **97**(3): 265-274.

Brown, I. D. (1978). "Bond valences—a simple structural model for inorganic chemistry." Chemical Society Reviews **7**(3): 359-376.

Brown, I. t. and Wu K. K. (1976). "Empirical parameters for calculating cation–oxygen bond valences." Acta Crystallographica Section B **32**(7): 1957-1959.

Cai, W., Wanga F., et al. (2008). "Hydrogen production from ethanol over Ir/CeO_2 catalysts: A comparative study of steam reforming, partial oxidation and oxidative steam reforming." Journal of Catalysis **257**: 96-107.

Caillé, A., Al-Moneef M., et al. (2007). "2007 Survey of Energy Resources." Report, World Energy Council London.

Callister, W. D. and Rethwisch D. G. (2007). "Materials science and engineering: an introduction. " John Wiley & Sons., New York **7**.

Callister, W. D. and Rethwisch D. G. (2011). Materials science and engineering, John Wiley & Sons New York **8**.

Capoen, E., Steil M., et al. (2004). "Time resolved in-situ neutron diffraction investigation of the electrochemical reduction of BIMEVOX." Solid State Ionics **175**(1-4): 419-424.

Carbajal-Ramos, I., Gomez M., et al. (2016). "Catalytic behavior of Ru supported on $Ce_{0.8}Zr_{0.2}O_2$ for hydrogen production." Applied Catalysis B: Environmental **181**: 58-70.

Carrera Cerritos, R., Fuentes Ramírez R., et al. (2011). "Steam Reforming of Ethanol over $Ni/Al_2O_3–La_2O_3$ Catalysts Synthesized by Sol–Gel." Industrial & Engineering Chemistry Research **50**(5): 2576-2584.

Carbon Elemental analysis [database on the Internet]. Thermo Scientific XPS, Waltham, MA USA; [updated 2015]; cited [Aug, 2018].
Available from: http://xpssimplified.com/elements/carbon.php

Caruso, R. A. and Antonietti M. (2001). "Sol–Gel Nanocoating: An Approach to the Preparation of Structured Materials." Chemistry of Materials **13**(10): 3272-3282.

Casanovas, A., Leitenburg C. de, et al. (2009). "Ethanol steam reforming and water gas shift reaction over Co–Mn/ZnO catalysts." Chemical Engineering Journal **154**(1–3): 267-273.

Casas-Led, Yannay N., et al. (2012). "Thermodynamic Analysis of the Hydrogen Production from Ethanol: First and Second Laws Approaches." ISRN Thermodynamics **2012**: 8.

Castro, A., Millan P., et al. (2000). "Room temperature stabilisation of [gamma]-$Bi_2VO_{5.5}$ and synthesis of the new fluorite phase f-Bi_2VO_5 by a mechanochemical activation method." Journal of Materials Chemistry **10**(3): 767-771.

CERA, I. (2012). "Energy for Economic Growth Energy Vision 2012." Report, World economic forum, Cologny, Switzerland.

Chahine, A., Et-tabirou M., et al. (2004). "FTIR and Raman spectra of the $Na_2O–CuO–Bi_2O_3–P_2O_5$ glasses." Materials Letters **58**(22): 2776-2780.

Cheekatamarla, P. K. and Finnerty C. M. (2008). "Synthesis gas production via catalytic partial oxidation reforming of liquid fuels." International Journal of Hydrogen Energy **33**(19): 5012-5019.

Chen, D., Christensen K. O., et al. (2005). "Synthesis of carbon nanofibers: effects of Ni crystal size during methane decomposition." Journal of Catalysis **229**(1): 82-96.

Chen, H.-T., Huh S., et al. (2007). "Fine tuning the functionalization of mesoporous silica." CRC Press, Taylor & Francis Publishing Group: New York.

Chen, L., Choong C. K. S., et al. (2010). "Carbon monoxide-free hydrogen production via low-temperature steam reforming of ethanol over iron-promoted Rh catalyst." Journal of Catalysis **276**(2): 197-200.

CHEN, X.-h., XIAO J., et al. (2005). "Research on the factors affecting HSGC in the measuring of VLE data." Chemical Engineer **12**: 006.

Chetouani, A., Taouk B., et al. (2004). "Catalytic behaviour of BIMEVOX powders in the oxidative dehydrodimerisation of propene." Catalysis Today **91–92**: 73-77.

Chetouani, A., Taouk B., et al. (2003). "Correlation between EPR and TPD characterisation and catalytic activity of BIMEVOX in oxidation of propene." Applied Catalysis A: General **252**(2): 269-281.

Chettibi, S., Wojcieszak R., et al. (2006). "Ni–Ce intermetallic phases in CeO_2-supported nickel catalysts synthesized by γ-radiolysis." Catalysis Today **113**(3–4): 157-165.

Chick, L. A., Pederson L., et al. (1990). "Glycine-nitrate combustion synthesis of oxide ceramic powders." Materials Letters **10**(1-2): 6-12.

Chiou, J. Y. Z., Siang J.-Y., et al. (2012). "Pathways of ethanol steam reforming over ceria-supported catalysts." International Journal of Hydrogen Energy **37**(18): 13667-13673.

Chitsazan, S., Sepehri S., et al. (2016). "Steam reforming of biomass-derived organics: Interactions of different mixture components on Ni/Al_2O_3 based catalysts." Applied Catalysis B: Environmental **187**: 386-398.

Ciambelli, P., Palma V., et al. (2010). "Low temperature catalytic steam reforming of ethanol. 2. Preliminary kinetic investigation of Pt/CeO_2 catalysts." Applied Catalysis B: Environmental **96**(1): 190-197.

Cifuentes, B., Hernández M., et al. (2016). "Hydrogen production by steam reforming of ethanol on a $RhPt/CeO_2/SiO_2$ catalyst: Synergistic effect of the Si:Ce ratio on the catalyst performance." Applied Catalysis A: General **523**: 283-293.

Comas, J., Marino F., et al. (2004). "Bio-ethanol steam reforming on Ni/Al_2O_3 catalyst." Chemical Engineering Journal **98**: 61-68.

Comberbach, D. and Bu'Lock J. (1982). "Automatic on-line gas chromatography (HSGC) for the quantitative determination of fermentation ethanol." Chromatog. Newslett. **10**: 19-23.

Compagnoni, M., Tripodi A., et al. (2017). "Low temperature ethanol steam reforming for process intensification: New $Ni/M_xO–ZrO_2$ active and stable catalysts prepared by flame spray pyrolysis." International Journal of Hydrogen Energy **42**(47): 28193-28213.

Conti, J., Holtberg P., et al. (2016). "International Energy Outlook 2016 With Projections to 2040." Report, USDOE Energy Information Administration (EIA), Washington, DC (United States), Office of Energy Analysis 290 p.

Cortright R.D., Davda R.R., et al. (2002). "Hydrogen from catalytic reforming of biomass-derived hydrocarbons in liquid water." Nature **418**: 964-967.

Cramers, C. A., Janssen H.-G., et al. (1999). "High-speed gas chromatography: an overview of various concepts." Journal of chromatography A **856**(1-2): 315-329.

Cross, A., Kumar A., et al. (2012). "Combustion Synthesis of a Nickel Supported Catalyst: Effect of Metal Distribution on the Activity during Ethanol Decomposition." Industrial & Engineering Chemistry Research **51**(37): 12004-12008.

Cullity, B. D. and Weymouth J. W. (1957). "Elements of X-ray Diffraction." American Journal of Physics **25**(6): 394-395.

D., S. W. and W. C. W. (1985). "Chemical reaction equilibrium analysis: Theory and algorithms by William R. Smith and Ronald W. Missen." John Wiley, AIChE Journal **31**(1): 176-176.

Da-Silva, LM A. L., et al. (2014). "Cobalt particle size effects on catalytic performance for ethanol steam reforming–Smaller is better." Journal of Catalysis **318**: 67-74.

Dai, R., Zheng Z., et al. (2018). "Pt nanoparticles encapsulated in a hollow zeolite microreactor as a highly active and stable catalyst for low-temperature ethanol steam reforming." Fuel **214**: 88-97.

Dan, M., Mihet M., et al. (2011). "Supported nickel catalysts for low temperature methane steam reforming: comparison between metal additives and support modification." Reaction Kinetics, Mechanisms and Catalysis **105**(1): 173-193.

Dan, M., Mihet M., et al. (2015). "Hydrogen production by ethanol steam reforming on nickel catalysts: Effect of support modification by CeO_2 and La_2O3." Fuel **147**: 260-268.

Dancini-Pontes, I., DeSouza M., et al. (2015). "Influence of the CeO_2 and Nb_2O_5 supports and the inert gas in ethanol steam reforming for H_2 production." Chemical Engineering Journal **273**: 66-74.

Das, D. and Veziroğlu T. N. (2001). "Hydrogen production by biological processes: a survey of literature." International Journal of Hydrogen Energy **26**(1): 13-28.

Davda, R., Shabaker J., et al. (2003). "Aqueous-phase reforming of ethylene glycol on silica-supported metal catalysts." Applied Catalysis B: Environmental **43**(1): 13-26.

Davda, R. R. and Dumesic J. A. et al. (2004)." Renewable hydrogen by aqueous-phase reforming of glucose." Chemical Communications 36-37.

Davda, R. R., J. W. Shabaker, et al. (2005). "A review of catalytic issues and process conditions for renewable hydrogen and alkanes by aqueous-phase reforming of oxygenated hydrocarbons over supported metal catalysts." Applied Catalysis B: Environmental **56**(1–2): 171-186.

De-Jong K.P., (2009). "Synthesis of solid catalysts." 1st ed. John Wiley & Sons., USA, p. 1-391.

De la Peña O'Shea, V. A., Homs N., et al. (2007). "X-ray diffraction study of Co_3O_4 activation under ethanol steam-reforming." Catalysis Today **126**(1–2): 148-152.

De la Piscina, P. R. and Homs N. (2008). "Use of biofuels to produce hydrogen (reformation processes)." Chemical Society Reviews **37**: 2459-2467.

De Lima, S. M., da Silva A. M., et al. (2012). "Hydrogen production through oxidative steam reforming of ethanol over Ni-based catalysts derived from $La_{1-x}Ce_xNiO_3$ perovskite-type oxides." Applied Catalysis B: Environmental **121–122**: 1-9.

De Lima, S. M., da Silva A. M., et al. (2009). " Study of catalyst deactivation and reaction mechanism of steam reforming, partial oxidation, and oxidative steam reforming of ethanol over Co/CeO_2 catalyst " Journal of Catalysis **268**: 268-281.

De Waal, D. and Hutter C. (1994). "Vibrational spectra of two phases of copper pyrovanadate and some solid solutions of copper and magnesium pyrovanadate." Materials research bulletin **29**(8): 843-849.

Delmon, B., Jacobs P. A., et al. (1976). "Preparation of Catalysts I: Scientific Bases for the Preparation of Heterogeneous Catalysts." Proceedings of the First International Symposium Held at the Solvay Research Centre, Brussels, October 14-17, 1975, Elsevier.

Demirbas, A. (2002). " Biodiesel from vegeTable oils via transesterification in supercritical methanol." Energy Conversion and Management **43**: 2349-2356.

Demirbas, A. (2007). " Progress and recent trends in biofuels." Progress in Energy and Combustion Science **33**: 1-18.

Demirbas, A. (2009). "Biohydrogen: for future engine fuel demands." 1st ed. Springer Science & Business Media, London p. 1-276.

Devi, L., Ptasinski K. J., et al. (2003). "A review of the primary measures for tar elimination in biomass gasification processes." Biomass and Bioenergy **24**(2): 125-140.

Dias, J. A. C. and Assaf J. M. (2008). "Autothermal reforming of methane over Ni/γ-Al_2O_3 promoted with Pd: The effect of the Pd source in activity, temperature profile of reactor and in ignition." Applied Catalysis A: General **334**(1–2): 243-250.

Díaz Alvarado, F. and Gracia F. (2010). "Steam reforming of ethanol for hydrogen production: Thermodynamic analysis including different carbon deposits representation." Chemical Engineering Journal **165**(2): 649-657.

Dieuzeide, M. L., Laborde M. et al. (2016). "Hydrogen production by glycerol steam reforming: How Mg doping affects the catalytic behaviour of Ni/Al_2O_3 catalysts." International Journal of Hydrogen Energy **41**(1): 157-166.

Dimitrov, V., Dimitriev Y., et al. (1994). "IR spectra and structure of V_2O_5 · GeO_2 · Bi_2O_3 glasses." Journal of Non-Crystalline Solids **180**(1): 51-57.

Dincer, I. (2012). "Green methods for hydrogen production." International Journal of Hydrogen Energy **37**(2): 1954-1971.

Ding, C., Wang J., et al. (2016). "Partial oxidation of methane over silica supported Ni nanoparticles with size control by alkanol solvent." Fuel **175**: 1-12.

Dinka, P. and Mukasyan A. S. (2005). "In situ preparation of oxide-based supported catalysts by solution combustion synthesis." The Journal of Physical Chemistry B **109**(46): 21627-21633.

Dou, B., Dupont V., et al. (2009). "Hydrogen production by sorption-enhanced steam reforming of glycerol." Bioresource Technology **100**(14): 3540-3547.

Doyle, W. M. (1992). "Principles and applications of Fourier transform infrared (FTIR) process analysis." Process control and quality **2**(1): 11-41.

Duan, Q., Wang J., et al. (2017). "Partial oxidation of methane over Ni based catalyst derived from order mesoporous $LaNiO_3$ perovskite prepared by modified nanocasting method." Fuel **193**: 112-118.

Dunn, S. (2002). "Hydrogen futures: toward a sustainable energy system." International Journal of Hydrogen Energy **27**(3): 235-264.

Ebiad, M. A., El-Hafiz D. R. A., et al. (2012). "Ni supported high surface area CeO_2–ZrO_2 catalysts for hydrogen production from ethanol steam reforming." RSC Advances **2(21)**: 8145-8156.

Ebshish, A., Yaakob Z., et al. (2012). "Steam Reforming of Glycerol over Ni Supported Alumina Xerogel for Hydrogen Production." Energy Procedia **18**: 552-559.

El Doukkali, M., Iriondo A., et al. (2012). "A comparison of sol–gel and impregnated Pt or/and Ni based γ-alumina catalysts for bioglycerol aqueous phase reforming." Applied Catalysis B: Environmental **125**: 516-529.

El Doukkali, M., Iriondo A., et al. (2014). "Deactivation study of the Pt and/or Ni-based γ-Al_2O_3 catalysts used in the aqueous phase reforming of glycerol for H_2 production." Applied Catalysis A: General **472**: 80-91.

Elbaba, I. F. and Williams P. T., (2013). "High yield hydrogen from the pyrolysis–catalytic gasification of waste tyres with a nickel/dolomite catalyst." Fuel **106**: 528-536.

Elbaba, I. F., Wu C., et al. (2011). "Hydrogen production from the pyrolysis–gasification of waste tyres with a nickel/cerium catalyst." International Journal of Hydrogen Energy **36**(11): 6628-6637.

Elias, K. F. M., Lucrédio A. F., et al. (2013). "Effect of CaO addition on acid properties of Ni–Ca/Al_2O_3 catalysts applied to ethanol steam reforming." International Journal of Hydrogen Energy **38**(11): 4407-4417.

Essalim, R., Tanouti B., et al. (1992). "Elaboration and electrical properties of $Bi_4V_{2-x}Co_xO_{11-3x}$ ($0.20 \leqslant x \leqslant 0.55$) ceramics with the Y-$Bi_4V_2O_{11}$ type structure." Materials Letters **13**(6): 382-386.

Eswaramoorthi, I., Sundaramurthy V., et al. (2006). "Partial oxidation of methanol for hydrogen production over carbon nanotubes supported Cu-Zn catalysts." Applied Catalysis A: General **313**(1): 22-34.

Exner, J., Fuierer P., et al. (2014). "Aerosol deposition of (Cu, Ti) substituted bismuth vanadate films." Thin Solid Films **573**: 185-190.

F. Brown, L. (2001). "A comparative study of fuels for on-board hydrogen production for fuel-cell-powered automobiles." International Journal of Hydrogen Energy **26**(4): 381-397.

Farrauto, R. J., Dorazio L., et al. (2016). "Introduction to catalysis and industrial catalytic processes." 1st ed., John Wiley & Sons., USA, p. 1-293.

Fatsikostas, A. N. and Verykios X. E. (2004). "Reaction network of steam reforming of ethanol over Ni-based catalysts." Journal of Catalysis **225**(2): 439-452.

Ferreira-Aparicio, P., Benito M., et al. (2005). "Catalysis in membrane reformers: a high-performance catalytic system for hydrogen production from methane." Journal of Catalysis **231**(2): 331-343.

Ferreira-Aparicio, P., Benito M. J., et al. (2005). "New Trends in Reforming Technologies: from Hydrogen Industrial Plants to Multifuel Microreformers." Catalysis Reviews **47**(4): 491-588.

Fishtik, I., Alexander A., et al. (2000). "A thermodynamic analysis of hydrogen production by steam reforming of ethanol via response reactions." International Journal of Hydrogen Energy **25**(1): 31-45.

Fortal'nova, E. A., Murasheva V. V., et al. (2008). "Phase transitions and electroconducting properties of BIMEVOX solid electrolytes." Russian Journal of Physical Chemistry A, Focus on Chemistry **82**(10): 1633.

Fridleifsson, I. (2003). Status of geothermal energy amongst the world's energy sources. Geothermics, **32**: 379-388

Frost, R. L., Henry D. A., et al. (2006). "Raman spectroscopy of three polymorphs of $BiVO_4$: clinobisvanite, dreyerite and pucherite, with comparisons to $(VO_4)^3$-bearing minerals: namibite, pottsite and schumacherite." Journal of Raman Spectroscopy: An International Journal for Original Work in all Aspects of Raman Spectroscopy,

Including Higher Order Processes, and also Brillouin and Rayleigh Scattering **37**(7): 722-732.

Fruth, V., Ianculescu A., et al. (2006). "Synthesis, structure and properties of doped Bi_2O_3." Journal of the European Ceramic Society **26**(14): 3011-3016.

Gaisford, S., Kett V., et al. (2016). "Principles of thermal analysis and calorimetry." 2nd ed. Royal society of chemistry.

Galembeck, A. and Alves O. (2000). "$BiVO_4$ thin film preparation by metalorganic decomposition." Thin Solid Films **365**(1): 90-93.

Galetti, A. E., Gomez M. F., et al. (2008). "Study of CuCoZnAl oxide as catalyst for the hydrogen production from ethanol reforming." Catalysis Communications **9**: 1201-1208.

Gan, J., Lu X., et al. (2015). "Efficient Photoelectrochemical Water Oxidation over Hydrogen-Reduced Nanoporous $BiVO_4$ with Ni–Bi Electrocatalyst." ChemElectroChem **2**(9): 1385-1395.

Garbarino, G., Finocchio E., et al. (2014). "Steam reforming of ethanol–phenol mixture on Ni/Al_2O_3: Effect of magnesium and boron on catalytic activity in the presence and absence of sulphur." Applied Catalysis B: Environmental **147**: 813-826.

Garbarino, G., Sanchez Escribano V., et al. (2012). "Steam reforming of phenol–ethanol mixture over 5% Ni/Al_2O_3." Applied Catalysis B: Environmental **113–114**: 281-289.

García-González, E., Arribas M., et al. (2001). "Short-Range− Long-Range Order Transformation in the $Bi_4V_{2-x}Fe_xO_{11-y}$ Series." Chemistry of Materials **13**(1): 96-102.

Garcia, E. Y. and Laborde M. A., (1991). "Hydrogen production by the steam reforming of ethanol: Thermodynamic analysis." International Journal of Hydrogen Energy **16**: 307-312.

Gasgnier, M., Petit A., et al. (2000). "Synthesis of Bi (Cu) VO_x compounds by means of a monomode microwave: Crystallographic, calorimetric, electrical and low temperature magnetic properties." Journal of Alloys and Compounds **309**(1-2): 219-224.

Ghude, S. D., Jena C., et al. (2014). "Reductions in India's crop yield due to ozone." Geophysical Research Letters **41**(15): 5685-5691.

Giaconia, A., Turchetti L., et al. (2013). Development of a solar-powered, fuel-flexible compact steam reformer: The CoMETHy project. Chemical Engineering Transactions. **35:** 433-438.

Gohier, A., Ewels C., et al. (2008). "Carbon nanotube growth mechanism switches from tip- to base-growth with decreasing catalyst particle size." Carbon **46**(10): 1331-1338.

González-Gil, R., Chamorro-Burgos I., et al. (2015). "Production of hydrogen by catalytic steam reforming of oxygenated model compounds on Ni-modified supported catalysts. Simulation and experimental study." International Journal of Hydrogen Energy **40**(34): 11217-11227.

Goyal, N., Pant K., et al. (2013). "Hydrogen production by steam reforming of model bio-oil using structured Ni/Al_2O_3 catalysts." International Journal of Hydrogen Energy **38**(2): 921-933.

Gräfe, W. (2015). Calculation of Surface Stress and Herring's Formula. Quantum Mechanical Models of Metal Surfaces and Nanoparticles, Springer: 85-89.

Grenoble, D. C., Estadt M. M., et al. (1981). "The chemistry and catalysis of the water gas shift reaction." Journal of Catalysis **67**(1): 90-102.

Grenoble, D. C., Estadt M. M., et al. (1981). "The chemistry and catalysis of the water gas shift reaction: 1. The kinetics over supported metal catalysts." Journal of Catalysis **67**(1): 90-102.

Grob, R. L. and Barry E. F. (2004). "Modern practice of gas chromatography." 4th ed., John Wiley & Sons., USA. p. 1-1064.

Guillodo, M., Fouletier J., et al. (2002). "Redox stability of BIMEVOX.10 materials (ME=Co, Cu)." Electrochimica Acta **47**(17): 2809-2815.

Gupta, S. and Singh K. (2015). "Structural and optical study of γ–BIMEVOX; ME: Ba^{2+} and Sr^{2+}." AIP Conference Proceedings, AIP Publishing.

Haines, P. J. (2012). "Thermal methods of analysis: principles, applications and problems." 1st ed. Springer Science & Business Media, UK, p. 1-269.

Halford, R. S. (1946). "Motions of Molecules in Condensed Systems: I. Selection Rules, Relative Intensities, and Orientation Effects for Raman and Infra-Red Spectra." The Journal of chemical physics **14**(1): 8-15.

Han, B., Miranda C., et al. (2008). "Effect of particle size and surface structure on adsorption of O and OH on platinum nanoparticles: A first-principles study." Physical Review B **77**(7): 075410.

Han, S. J., Bang Y., et al. (2013). "Hydrogen production by steam reforming of ethanol over mesoporous Ni–Al_2O_3–ZrO_2 xerogel catalysts: Effect of nickel content." International Journal of Hydrogen Energy **38**(20): 8285-8292.

Hardcastle, F. D. and Wachs I. E., (1991). "Determination of vanadium-oxygen bond distances and bond orders by Raman spectroscopy." The Journal of Physical Chemistry **95**(13): 5031-5041.

Hardcastle, F. D., Wachs I. E., et al. (1991). "Vanadium (V) environments in bismuth vanadates: a structural investigation using Raman spectroscopy and solid state 51V NMR." Journal of Solid State Chemistry **90**(2): 194-210.

Haruta, M. (2004). "Gold as a novel catalyst in the 21st century: Preparation, working mechanism and applications." Gold Bulletin **37**(1): 27-36.

Haryanto, A., Fernando S., et al. (2005). "Current Status of Hydrogen Production Techniques by Steam Reforming of Ethanol: A Review." Energy & Fuels **19**(5): 2098-2106.

Hernández, L. and Kafarov V., (2009). "Thermodynamic evaluation of hydrogen production for fuel cells by using bio-ethanol steam reforming: Effect of carrier gas addition." Journal of Power Sources **192**(1): 195-199.

Hervoches, C., Steil M., et al. (2004). "Synthesis by the polymeric precursor technique of $Bi_2Co_{0.1}V_{0.9}O_{5.35}$ and electrical properties dependence on the crystallite size." Solid State Sciences **6**(2): 173-177.

Herzog, A. V., Lipman T. E., et al. (2001). "Renewable energy sources." Report, Energy and Resources Group, Renewable and Appropriate Energy Laboratory (RAEL), University of California, Berkeley, USA.

Hirschfeld, T. (1977). "Subsurface layer studies by attenuated total reflection Fourier transform spectroscopy." Applied spectroscopy **31**(4): 289-292.

Holladay, J. D., Hu J., et al. (2009). "An overview of hydrogen production technologies." Catalysis Today **139**(4): 244-260.

Hollingdale, A., Breag G., et al. (1988). "Producer gas fuelling of a 20kW output engine by gasification of solid biomass (ODNRI Bulletin No. 17)." Report, University of Greenwich, London, U.K..

Homs, N., Llorca J., et al. (2006). "Low-temperature steam-reforming of ethanol over ZnO-supported Ni and Cu catalysts: The effect of nickel and copper addition to ZnO-supported cobalt-based catalysts." Catalysis Today **116**(3): 361-366.

Hongbo, M., Zhang R., et al. (2012). "Ni/Y_2O_3-Al_2O_3 catalysts for hydrogen production from steam reforming of ethanol at low temperature." Journal of Rare Earths **30**(7): 683-690.

Hou, J., Liu Z.-M., et al. (2014). "Novel Ni–ZrO_2 catalyst doped with Yb_2O_3 for ethanol steam reforming." International Journal of Hydrogen Energy **39**(3): 1315-1324.

Hua, T., Ahluwalia R., et al. (2014). "Status of hydrogen fuel cell electric buses worldwide." Journal of Power Sources **269**: 975-993.

Hubbert, M. K. (1949). "Energy from fossil fuels." Science **109**(2823): 103-109.

Huber, G. W. and Dumesic J. A. (2006). "An overview of aqueous-phase catalytic processes for production of hydrogen and alkanes in a biorefinery." Catalysis Today **111**(1-2): 119-132.

Huber, G. W., Iborra S., et al. (2006). "Synthesis of Transportation Fuels from Biomass: Chemistry, Catalysts, and Engineering." Chemical Reviews, **106** p. 4044-4098.

Hurtubise, F. G. and Krassig H. (1960). "Classification of fine structural characteristics in cellulose by infared spectroscopy. Use of potassium bromide pellet technique." Analytical Chemistry **32**(2): 177-181.

Huvé, M., Vannier R.-N., et al. (1996). "From $Bi_4V_2O_{11}$ to $Bi_4V_2O_{10.66}$: the VV–V IV transformation in the aurivillius-type framework." Journal of Materials Chemistry **6**(8): 1339-1345.

Hvolbæk, B., Janssens T. V., et al. (2007). "Catalytic activity of Au nanoparticles." Nano Today **2**(4): 14-18.

IEA O., (2015). "Energy and climate change, world energy outlook special report." Report, OECD, International Energy Agency, Paris, France.

Igarashi, A., Ohtaka T., et al. (1992). "Low-temperature steam reforming ofn-butane over Rh and Ru catalysts supported on ZrO_2." Catalysis Letters **13**(3): 189-194.

Inhaber, H. (1979). "Risk with energy from conventional and nonconventional sources." Science **203**(4382): 718-723.

Irurzun, V. M., Tan Y., et al. (2009). "Sol–Gel Synthesis and Characterization of Co–Mo/Silica Catalysts for Single-Walled Carbon Nanotube Production." Chemistry of Materials **21**(11): 2238-2246.

Jacobsohn, L., Blair M., et al. (2008). "Y_2O_3: Bi nanophosphor: Solution combustion synthesis, structure, and luminescence." Journal of Applied Physics **104**(12): 124303.

Jain, S., Adiga K., et al. (1981). "A new approach to thermochemical calculations of condensed fuel-oxidizer mixtures." Combustion and flame **40**: 71-79.

Jalowiecki-Duhamel, L., Pirez C., et al. (2010). "Hydrogen production from ethanol steam reforming over cerium and nickel based oxyhydrides." International Journal of Hydrogen Energy **35**(23): 12741-12750.

Jennings W., and Takayuki S., (2012). "Qualitative analysis of flavor and fragrance volatiles by glass capillary gas chromatography." Academic Press, New York, USA, p. 1-114.

Jia, Q., Caldwell K., et al. (2014). "Improved oxygen reduction activity and durability of dealloyed PtCo x catalysts for proton exchange membrane fuel cells: strain, ligand, and particle size effects." ACS Catalysis **5**(1): 176-186.

Jiang, S. P. (2006). "A review of wet impregnation—An alternative method for the fabrication of high performance and nano-structured electrodes of solid oxide fuel cells." Materials Science and Engineering: A **418**(1): 199-210.

Jibo, W., Baofeng J., et al. (2009). "Effects of synthesis methods of BICUVOX. 10 membranes on oxygen permeation at moderate temperatures." Chinese Journal of Catalysis **30**(9): 926-932.

Jones, H. G. and Nobel P. S. (2010). "Physicochemical and Environmental Plant Physiology." Experimental Agriculture **46**(2): 262.

Joshi, R., Nimat R., et al. (2009). "Synthesis of fuel cell grade $Bi_2Co_{0.1}V_{0.9}O_{5.35}$ solid electrolyte thin films." Journal of Alloys and Compounds **471**(1-2): 461-465.

Joubert, O., Ganne M., et al. (1996). "Solid phase synthesis and characterization of new BIMEVOX series: $Bi_4V_{2-x}M_xO_{11-x}$ (M= CrIII, FeIII)." Solid State Ionics **83**(3-4): 199-207.

Joubert, O., Jouanneaux A., et al. (1993). "X-Ray Powder Diffraction Study of Bimevox Phases $Bi_4V_{2-x}Sb_xO_{11}$ (O< x< 1)." Materials Science Forum, Trans Tech Publication.

Joubert, O., Jouanneaux A., et al. (1994). "Crystal structure of low-temperature form of bismuth vanadium oxide determined by rietveld refinement of X-ray and neutron diffraction data (α-$Bi_4V_2O_{11}$)." Materials research bulletin **29**(2): 175-184.

Kahia, M., Aïssa M. S. B., et al. (2017). "Renewable and non-renewable energy use - economic growth nexus: The case of MENA Net Oil Importing Countries." Renewable and Sustainable Energy Reviews **71**: 127-140.

Kalamaras, C. M. and Efstathiou A. M. (2013). "Hydrogen production technologies: current state and future developments." Conference Papers in Science, Hindawi Publishing Corporation.

Kambolis, A., Matralis H., et al. (2010). "Ni/CeO_2-ZrO_2 catalysts for the dry reforming of methane." Applied Catalysis A: General **377**(1–2): 16-26.

Kant, R., Singh K., et al. (2008). "Synthesis and characterization of bismuth vanadate electrolyte material with aluminium doping for SOFC application." International Journal of Hydrogen Energy **33**(1): 455-462.

Kant, R., Singh K., et al. (2009). "Microstructural and electrical behavior of $Bi_4V_{2-x}Cu_xO_{11-\delta}$ ($0 \leq x \leq 0.4$)." Ceramics International **35**(1): 221-227.

Kathe, M. V., Empfield A., et al. (2016). "Hydrogen production from natural gas using an iron-based chemical looping technology: Thermodynamic simulations and process system analysis." Applied Energy **165**: 183-201.

Kazarian, S. G. and Chan K. A. (2010). "Micro-and macro-attenuated total reflection Fourier transform infrared spectroscopic imaging." Applied spectroscopy **64**(5): 135A-152A.

Kežionis, A., Bogusz W., et al. (1999). "Relaxation dispersion of ionic conductivity of BICOVOX." Solid State Ionics **119**(1–4): 145-150.

Khaerudini, D. S., Guan G., et al. (2016). "Oxide ion conductors based on niobium-doped bismuth vanadate: conductivity and phase transition features." Ionics **22**(1): 93-97.

Khaerudini, D. S., Guan G., et al. (2014). "Prospects of oxide ionic conductivity bismuth vanadate-based solid electrolytes." Reviews in Chemical Engineering **30**(6): 539-551.

Kim, D. K. and Maier W. F. (2006). "Combinatorial discovery of new autoreduction catalysts for the CO_2 reforming of methane." Journal of Catalysis **238**(1): 142-152.

Kim, K. S. and Park Y. J. (2012). "Catalytic properties of Co_3O_4 nanoparticles for rechargeable Li/air batteries." Nanoscale Research Letters **7(1)**: 47.

Kim, P., Kim Y., et al. (2004). "Synthesis and characterization of mesoporous alumina with nickel incorporated for use in the partial oxidation of methane into synthesis gas." Applied Catalysis A: General **272**(1–2): 157-166.

Kim, S.-K. and Miyayama M. (1997). "Anisotropy in oxide ion conductivity of $Bi_4V_{2-x}Co_xO_{11-\delta}$." Solid State Ionics **104**(3): 295-302.

Kingsley, J. and Patil K. (1988). "A novel combustion process for the synthesis of fine particle α-alumina and related oxide materials." Materials Letters **6**(11-12): 427-432.

Kormányos, A., Thomas A., et al. (2016). "Solution Combustion Synthesis, Characterization, and Photoelectrochemistry of $CuNb_2O_6$ and $ZnNb_2O_6$ Nanoparticles." The Journal of Physical Chemistry C **120** (29): 16024-16034.

Kourtelesis, M., Panagiotopoulou P., et al. (2015). "Influence of structural parameters on the reaction of low temperature ethanol steam reforming over Pt/Al_2O_3 catalysts." Catalysis Today **258, Part 2**: 247-255.

Krok, F., Abrahams I., et al. (1998). "Structural and electrical characterisation of BINIVOX." Solid State Ionics **111**(1-2): 37-43.

Krok, F., Abrahams I., et al. (1996). "Electrical and structural study of BICOVOX." Solid State Ionics **86–88, Part 1**: 261-266.

Krok, F., Abrahams I., et al. (2000). "Structural and electrical consequences of high dopant levels in the BIMGVOX system." Solid State Ionics **136**: 119-125.

Krok, F., Abrahams I., et al. (1997). "Structural and electrical characterisation of BICOCUVOX." Ionics **3**(3-4): 235-238.

Krok, F., Bogusz W., et al. (1994). "Studies on preparation and electrical conductivity of BICOVOX." Solid State Ionics **70–71, Part 1**: 211-214.

Krok, F., Bogusz W., et al. (1993). "Influence of preparation procedure on some physical properties of BICUVOX." Materials Science and Engineering: B **21**(1): 70-76.

Krummenacher, J. J., West K. N., et al. (2003). "Catalytic partial oxidation of higher hydrocarbons at millisecond contact times: decane, hexadecane, and diesel fuel." Journal of Catalysis **215**(2): 332-343.

Kugai, J., Subramani V., et al. (2006). "Effects of nanocrystalline CeO_2 supports on the properties and performance of Ni–Rh bimetallic catalyst for oxidative steam reforming of ethanol." Journal of Catalysis **238**(2): 430-440.

Kumar, A., Cross A., et al. (2015). "Combustion synthesis of copper–nickel catalysts for hydrogen production from ethanol." Chemical Engineering Journal **278**: 46-54.

Kumar, A., Mukasyan A. S., et al. (2011). "Combustion synthesis of Ni, Fe and Cu multi-component catalysts for hydrogen production from ethanol reforming." Applied Catalysis A: General **401**(1): 20-28.

Kumar, S. and Sahare P. (2013). "Photocatalytic activity of bismuth vanadate for the degradation of organic compounds." Nano **8**(01): 1350007.

Kundu, S., Satpati B., et al. (2017). "Hydrothermal synthesis of polyaniline intercalated vanadium oxide xerogel hybrid nanocomposites: effective control of morphology and structural characterization." New Journal of Chemistry **41**(9): 3634-3645.

Laosiripojana, N. and Assabumrungrat S., (2006). "Catalytic steam reforming of ethanol over high surface area CeO2: The role of CeO2 as an internal pre-reforming catalyst." Applied Catalysis B: Environmental **66**(1-2): 29-39.

Lazure, S., Vannier R.-N., et al. (1995). "BICOVOX family of oxide anion conductors: chemical, electrical and structural studies." Journal of Materials Chemistry **5**(9): 1395-1403.

Le Boisselier, V., Duñach E., et al. (1994). "Bismuth(III)-catalyzed oxidative cleavage of aryl epoxides: Substituent effects on the kinetics of the oxidation reaction." Journal of Organometallic Chemistry **482(1)**: 119-123.

Lee, J. H., Do J. Y., et al. (2018). "Hydrogen production on $Pd_{0.01}Zn_{0.29}Mg_{0.7}Al_2O_4$ spinel catalyst by low temperature ethanol steam reforming reaction." Journal of the Energy Institute.

Lee, J. S., Han G. B., et al. (2012). "Low temperature steam reforming of ethanol for carbon monoxide-free hydrogen production over mesoporous Sn-incorporated SBA-15 catalysts." Energy **44**(1): 248-256.

Li, C. and Chen Y.-W. (1995). "Temperature-programmed-reduction studies of nickel oxide/alumina catalysts: effects of the preparation method." Thermochimica Acta **256**(2): 457-465.

Li, D., Li X., et al. (2016). "Catalytic reforming of oxygenates: state of the art and future prospects." Chemical Reviews **116**(19): 11529-11653.

Li, G., Hu L., et al. (2006). "Comparison of reducibility and stability of alumina-supported Ni catalysts prepared by impregnation and co-precipitation." Applied Catalysis A: General **301**(1): 16-24.

Li, H. and Wang J. (2004). "Study on CO_2 reforming of methane to syngas over Al_2O_3–ZrO_2 supported Ni catalysts prepared via a direct sol–gel process." Chemical Engineering Science **59**(22–23): 4861-4867.

Li, Q., Wang L.-S., et al. (2007). "Preparation and characterization of NiO nanoparticles through calcination of malate gel." Materials Letters **61**(8): 1615-1618.

Li, S., Lu Y., et al. (2011). "Hydrogen production by biomass gasification in supercritical water with bimetallic Ni–M/γAl_2O_3 catalysts (M= Cu, Co and Sn)." International Journal of Hydrogen Energy **36**(22): 14391-14400.

Li, W. (2006). "Facile synthesis of monodisperse Bi_2O_3 nanoparticles." Materials Chemistry and Physics **99**(1): 174-180.

Li, X., Li D., et al. (2017). "Dry reforming of methane over Ni/La_2O_3 nanorod catalysts with stabilized Ni nanoparticles." Applied Catalysis B: Environmental **202**: 683-694.

Li, Y., Qiu W., et al. (2016). "Identification of cobalt oxides with Raman scattering and Fourier transform infrared spectroscopy." The Journal of Physical Chemistry C **120**(8): 4511-4516.

Li, Z. (2018). "Multi-Ni@ Ni phyllosilicate hollow sphere for CO_2 reforming of CH_4: influence of Ni precursors on structure, sintering and carbon resistance." Catalysis Science & Technology.

Lima-da Silva, A., Malfatti C. d. F., et al. (2009). "Thermodynamic analysis of ethanol steam reforming using Gibbs energy minimization method: A detailed study of the conditions of carbon deposition." International Journal of Hydrogen Energy **34**(10): 4321-4330.

Lima da Silva, A. and Müller I. L. (2011). "Hydrogen production by sorption enhanced steam reforming of oxygenated hydrocarbons (ethanol, glycerol, n-butanol and methanol): Thermodynamic modelling." International Journal of Hydrogen Energy **36**(3): 2057-2075.

Lindsey, R. (January 14, 2009). "Climate and Earth's Energy Budget." Report, NASA Earth Laboratory, Washington, DC.

Ling, B., Sun X. W., et al. (2010). "One-Dimensional Single-Crystalline Bismuth Oxide Micro/Nanoribbons: Morphology-Controlled Synthesis and Luminescent Properties." Journal of Nanoscience and Nanotechnology **10**(12): 8322-8327.

Liu, C., Wang H., et al. (2014). "Catalytic fast pyrolysis of lignocellulosic biomass." Chemical Society Reviews **43**(22): 7594-7623.

Liu, J., Wang H., et al. (2003). "Hydrothermal preparation of $BiVO_4$ powders." Materials Science and Engineering: B **104**(1): 36-39.

Liu, P. and Rodriguez J. A. (2007). "Water-gas-shift reaction on metal nanoparticles and surfaces." The Journal of chemical physics **126**(16): 164705.

Liu, S., Yin K., et al. (2012). "Tandem photocatalytic oxidation of Rhodamine B over surface fluorinated bismuth vanadate crystals." Journal of Materials Chemistry **22**(34): 17759-17767.

Liu, Y., Huang B., et al. (2009). "Selective ethanol formation from photocatalytic reduction of carbon dioxide in water with $BiVO_4$ photocatalyst." Catalysis Communications **11**(3): 210-213.

Liu, Z., Niu J., et al. (2014). "One-pot synthesis of $Bi_{24}O_{31}Br_{10}/Bi_4V_2O_{11}$ heterostructures and their photocatalytic properties." RSC Advances **4**(82): 43399-43405.

Liu, Z., Xu W., et al. (2015). "Superior performance of Ni–W–Ce mixed-metal oxide catalysts for ethanol steam reforming: Synergistic effects of W-and Ni-dopants." Journal of Catalysis **321**: 90-99.

Llorca J., Piscina P. R. d. l., et al., (2004) "Transformation of Co_3O_4 during Ethanol Steam-Re-forming. Activation Process for Hydrogen Production." Chemistry Of Materials, **16**: 3573-78.

Llorca J., Piscina P. R. d. l., et al., (2002). "Efficient Production of Hydrogen over Supported Cobalt Catalysts from Ethanol Steam Reforming." Journal of Catalysis, **209:** 306-317.

Llorca, J., Piscina P. R. d. l., et al. (2001). "Direct production of hydrogen from ethanolic aqueous solutions over oxide catalysts." Chemical Communications(7): 641-642.

Löfberg, A., Bodet H., et al. (2006). "Catalytic dense membranes of doped $Bi_4V_2O_{11}$ (BIMEVOX) for selective partial oxidation: chemistry of defects versus catalysis." Topics in Catalysis **38**(1-3): 169-179.

Löfberg, A., Bodet H., et al. (2006). "$Bi_2V_{1-x}Me_xO_{5.5-\delta}$ (Me = Ta, Ni) membranes for selective oxidation of C_1–C_3 alkanes in a catalytic dense membrane reactor." Catalysis Today **117**(1–3): 168-173.

Löfberg, A., Boujmiai S., et al. (2004). "Oxygen permeation versus catalytic properties of bismuth-based oxide ion conductors used for propene oxidation in a catalytic dense membrane reactor." Catalysis Today **91–92**: 79-83.

Löfberg, A., Pirovano C., et al. (2006). "Transient behaviour of dense catalytic membranes based on Cu- and Co-doped $Bi_4V_2O_{11}$ (BIMEVOX) in the oxidation of propene and propane." Catalysis Today **112**(1–4): 8-11.

Lu, Y., Pu Y., et al. (2015). "On structure and methylene blue degradation activity of an Aurivillius-type photocatalyst of $Bi_4V_2O_{11}$ nanoparticles." Applied Surface Science **347**: 719-726.

Luo, N., Fu X., et al. (2008). "Glycerol aqueous phase reforming for hydrogen generation over Pt catalyst – Effect of catalyst composition and reaction conditions." Fuel **87**(17): 3483-3489.

Lutz, A. E., Bradshaw R. W., et al. (2004). "Thermodynamic analysis of hydrogen production by partial oxidation reforming." International Journal of Hydrogen Energy **29**(8): 809-816.

Lv, C., Chen G., et al. (2017). "Oxygen-Induced Bi^{5+}-Self-Doped $Bi_4V_2O_{11}$ with a p–n Homojunction Toward Promoting the Photocatalytic Performance." ACS Applied Materials & Interfaces **9**(28): 23748-23755.

Ma, H., Zhang R., et al. (2012). "Ni/Y_2O_3-Al_2O_3 catalysts for hydrogen production from steam reforming of ethanol at low temperature." Journal of Rare Earths **30**(7): 683-690.

Ma, T. Y., Ran J., et al. (2015). "Phosphorus-Doped Graphitic Carbon Nitrides Grown In Situ on Carbon-Fiber Paper: Flexible and Reversible Oxygen Electrodes." Angewandte Chemie International Edition **54**(15): 4646-4650.

Madejová, J. (2003). "FTIR techniques in clay mineral studies." Vibrational spectroscopy **31**(1): 1-10.

Maia, T. A., Assaf J. M., et al. (2012). "Steam reforming of ethanol for hydrogen production on Co/CeO_2–ZrO_2 catalysts prepared by polymerization method." Materials Chemistry and Physics **132**(2–3): 1029-1034.

Mairesse, G. (1999). "Advances in oxygen pumping concept with BIMEVOX." Comptes Rendus de l'Académie des Sciences - Series IIC - Chemistry **2**(11): 651-660.

Mairesse, G., Roussel P., et al. (2003). "Crystal structure determination of α, β and γ-$Bi_4V_2O_{11}$ polymorphs. Part I: γ and β-$Bi_4V_2O_{11}$." Solid State Sciences **5**(6): 851-859.

Mairesse, G., Roussel P., et al. (2003). "Crystal structure determination of α-, β- and γ-$Bi_4V_2O_{11}$ polymorphs. Part II: crystal structure of α-$Bi_4V_2O_{11}$." Solid State Sciences **5**(6): 861-869.

Maity, S. K., Blanco E., et al. (2012). "Early stage deactivation of heavy crude oil hydroprocessing catalysts." Fuel **100**: 17-23.

Malys, M., Abrahams I., et al. (2008). "The appearance of an orthorhombic BIMEVOX phase in the system $Bi_2Mg_xV_{1-x}O_{5.5-3x/2-\delta}$ at high values of x." Solid State Ionics **179**(1-6): 82-87.

Manfro, R. L., da Costa A. F., et al. (2011). "Hydrogen production by aqueous-phase reforming of glycerol over nickel catalysts supported on CeO_2." Fuel Processing Technology **92**(3): 330-335.

Mani, M., Markandya A., et al. (2016). "Estimating the Cost of Environmental Degradation in India." Environment and Development: Essays in Honour of Dr U. Sankar:1.

Mariño, F. J., Cerrella E. G., et al. (1998). "Hydrogen from steam reforming of ethanol. characterization and performance of copper-nickel supported catalysts." International Journal of Hydrogen Energy **23**(12): 1095-1101.

Martínez T, L. M., Araque M., et al. (2013). "Effect of Ce/Zr ratio in CeZr-CoRh catalysts on the hydrogen production by glycerol steam reforming." Applied Catalysis B: Environmental **132–133**: 499-510.

Massart, R. (1981). "Preparation of aqueous magnetic liquids in alkaline and acidic media." IEEE Transactions on Magnetics **17**(2): 1247-1248.

Matsumura, Y. and Nakamori T. (2004). "Steam reforming of methane over nickel catalysts at low reaction temperature." Applied Catalysis A: General **258**(1): 107-114.

Mattos, L. V., Jacobs G., et al. (2012). "Production of Hydrogen from Ethanol: Review of Reaction Mechanism and Catalyst Deactivation." Chemical Reviews **112**(7): 4094-4123.

McCreery, R. L. (2005). "Raman spectroscopy for chemical analysis." Vol. 225. John Wiley & Sons., USA, 1-420.

Meier, P., Vagliasindi M., et al. (2014). "The design and sustainability of renewable energy incentives: an economic analysis." 1st ed. World Bank Publications, Washington, DC 1-263.

Melchor-Hernández, C., Gómez-Cortés A., et al. (2013). "Hydrogen production by steam reforming of ethanol over nickel supported on La-modified alumina catalysts prepared by sol–gel." Fuel **107**: 828-835.

Mielenz, J. R. (2001). "Ethanol production from biomass: technology and commercialization status." Current Opinion in Microbiology **4**(3): 324-329.

Milbrandt, A., Bush B., et al. (2016). "Biogas and Hydrogen Systems Market Assessment." Report. National Renewable Energy Lab.(NREL), Golden, CO (United States).

Mimani, T. and Patil K. (2001). "Solution combustion synthesis of nanoscale oxides and their composites." Materials Physics and Mechanics(Russia) **4**(2): 134-137.

Mohan, S. V., Bhaskar Y. V., et al. (2007). "Biohydrogen production from chemical wastewater treatment in biofilm conFigured reactor operated in periodic discontinuous batch mode by selectively enriched anaerobic mixed consortia." Water research **41**(12): 2652-2664.

Momirlan, M. and Veziroglu T. N. (2005). "The properties of hydrogen as fuel tomorrow in sustainable energy system for a cleaner planet." International Journal of Hydrogen Energy **30**(7): 795-802.

Mondal, T., Pant K. K., et al. (2015). "Catalytic oxidative steam reforming of bio-ethanol for hydrogen production over Rh promoted Ni/CeO_2–ZrO_2 catalyst." International Journal of Hydrogen Energy **40**(6): 2529-2544.

Monnereau, O., Tortet L., et al. (2003). "Synthesis of Bi_2O_3 by controlled transformation rate thermal analysis: a new route for this oxide?" Solid State Ionics **157**(1-4): 163-169.

Montero, C., Ochoa A., et al. (2015). "Monitoring Ni0 and coke evolution during the deactivation of a Ni/La_2O_3–αAl_2O_3 catalyst in ethanol steam reforming in a fluidized bed." Journal of Catalysis **331**: 181-192.

Morales, W., Cason M., et al. (2008). "Combustion synthesis and characterization of nanocrystalline WO_3." Journal of the American Chemical Society **130**(20): 6318-6319.

Moretti, E., Storaro L., et al. (2015). "Ceria–zirconia based catalysts for ethanol steam reforming." Fuel **153**: 166-175.

Morozova, M., Buyanova E., et al. (2011). "Highconducting oxide ceramics bimevox: Synthesis, structure, and properties." Solid State Ionics **192**(1): 153-157.

Morris, I. (2015). "Foragers, Farmers, and Fossil Fuels: How Human Values Evolve: How Human Values Evolve." 1st ed., Princeton University Press, New Jersey, USA, 2-258.

Mulewa, W., Tahir M., et al. (2017). "MMT-supported Ni/TiO_2 nanocomposite for low temperature ethanol steam reforming toward hydrogen production." Chemical Engineering Journal **326**: 956-969.

Muller, C., Chateigner D., et al. (1996). " Pressure and magnetic field effects on the crystallographic texture and electrical conductivity of the $Bi_4(V_{0.85}Co_{0.15})_2O_{11-\delta}$ compound." Journal of Physics D: Applied Physics **29**(12): 3106.

Müller, K., Brendler V., et al. (2008). "Aqueous uranium (VI) hydrolysis species characterized by attenuated total reflection Fourier-transform infrared spectroscopy." Inorganic chemistry **47**(21): 10127-10134.

Muñoz, M., Moreno S., et al. (2014). "The effect of the absence of ni, co, and ni–co catalyst pretreatment on catalytic activity for hydrogen production via oxidative steam reforming of ethanol." International Journal of Hydrogen Energy **39**(19): 10074-10089.

Muñoz, M., Moreno S., et al. (2016). "Promoter effect of Ce and Pr on the catalytic stability of the Ni-Co system for the oxidative steam reforming of ethanol." Applied Catalysis A: General **526**: 84-94.

Muradov, N. and Veziroğlu T., (2005). "From hydrocarbon to hydrogen–carbon to hydrogen economy." International Journal of Hydrogen Energy **30**(3): 225-237.

Muradov N.Z. and Veziroğlu T.N., (2011). "Carbon-neutral fuels and energy carriers." 1st ed. CRC Press, Taylor & Francis Publishing Group: New York, USA, 1-787.

Murasheva, V. V., Poletaeva N. A., et al. (2010). "Phase formation of BICUVOX solid solutions." Russian Journal of Inorganic Chemistry **55**(12): 1867-1873.

Nagabhushana, B., Chakradhar R., et al. (2010). "Effect of fuel on the formation structure, transport and magnetic properties of $LaMnO_{3+\delta}$ nanopowders." Philosophical Magazine **90**(15): 2009-2025.

Nagappa, B. and Chandrappa G. T. (2007). "Mesoporous nanocrystalline magnesium oxide for environmental remediation." Microporous and Mesoporous Materials **106**(1): 212-218.

Naik, M. A., Mishra B. G., et al. (2008). "Combustion synthesized WO_3–ZrO_2 nanocomposites as catalyst for the solvent-free synthesis of coumarins." Colloids and Surfaces A: Physicochemical and Engineering Aspects **317**(1): 234-238.

Nakamoto, K. (2006). "Infrared and R aman Spectra of Inorganic and Coordination Compounds." Handbook of Vibrational Spectroscopy.

Nath, K. and Das D. (2003). "Hydrogen from biomass." Current science: 265-271.

Nath K. and Das D.,(2004). "Improvement of fermentative hydrogen production: various approaches." Applied Microbiology and Biotechnology. **65**: 520-529.

Navarro, R. M., Pena M. A., et al. (2007). "Hydrogen Production Reactions from Carbon Feedstocks: Fossil Fuels and Biomass." Chemical Reviews **107**: 3952.

Ni, M., Leung D. Y. C., et al. (2006). "An overview of hydrogen production from biomass." Fuel Processing Technology **87**(5): 461-472.

Ni, M., Y. C. Leung, et al. (2007). Int. J. Hydrogen Energy **32**: 3238.

Ni M., Leung Y.C., et al. (2007). "A review on reforming bio-ethanol for hydrogen production." International Journal of Hydrogen Energy. **32**: 3238-3247.

Nicoletti, G., Arcuri N., et al. (2015). "A technical and environmental comparison between hydrogen and some fossil fuels." Energy Conversion and Management **89**(Supplement C): 205-213.

Nimat, R., Joshi R., et al. (2007). "Temperature dependent conductivity and dielectric properties of $Bi_2V_{0.9}Cu_{0.1}O_{5.35}$ solid electrolyte thin films." Materials Science and Engineering: B **137**(1-3): 93-98.

Nishiguchi, T., Matsumoto T., et al. (2005). "Catalytic steam reforming of ethanol to produce hydrogen and acetone." Applied Catalysis A: General **279**: 273-277.

Nordgreen, T., Nemanova V., et al. (2012). "Iron-based materials as tar depletion catalysts in biomass gasification: Dependency on oxygen potential." Fuel **95**(Supplement C): 71-78.

Nyholm R., Berndtsson A., et al., (1980). "Core level binding energies for the elements Hf to Bi (Z=72-83)." Journal of Physics **13**: 1091-1096.

Oemar, U., Kathiraser Y., et al. (2015). "Catalytic Biomass Gasification to Syngas Over Highly Dispersed Lanthanum-Doped Nickel on SBA-15." ChemCatChem **7**(20): 3376-3385.

Owusu, P. A. and Asumadu-Sarkodie S. (2016). "A review of renewable energy sources, sustainability issues and climate change mitigation." Cogent Engineering **3**(1): 1167990.

Palma, V., Castaldo F., et al. (2014). "CeO_2-supported Pt/Ni catalyst for the renewable and clean H_2 production via ethanol steam reforming." Applied Catalysis B: Environmental **145**: 73-84.

Panagiotopoulou, P. and Verykios X. E. (2012). "Mechanistic aspects of the low temperature steam reforming of ethanol over supported Pt catalysts." International Journal of Hydrogen Energy **37**(21): 16333-16345.

Pantaleo, G., Parola V. L., et al. (2016). "Ni/CeO_2 catalysts for methane partial oxidation: Synthesis driven structural and catalytic effects." Applied Catalysis B: Environmental **189**: 233-241.

Park, H. M., Lee H. J., et al. (2001). "Crystal structure refinement of $(Ba_{1-x}La_x)[Mg_{(1+x)/3}Nb_{(2-x)/3}]O_3$ with $0.3 \leq x \leq 0.7$ by Rietveld method." Materials research bulletin **36**(12): 2163-2174.

Patel, M., Jindal T. K., et al. (2013). "Kinetic Study of Steam Reforming of Ethanol on Ni-Based Ceria–Zirconia Catalyst." Industrial & Engineering Chemistry Research **52**(45): 15763-15771.

Patil, K. (1993). "Advanced ceramics: combustion synthesis and properties." Bulletin of Materials Science **16**(6): 533-541.

Patil, K. C., Aruna S. T., et al. (1997). "Combustion synthesis." Current opinion in solid state and materials science **2**(2): 158-165.

Patil, K. C., Aruna S. T., et al. (2002). "Combustion synthesis: an update." Current Opinion in Solid State and Materials Science **6**(6): 507-512.

Patwe, S. J., Patra A., et al. (2013). "Probing the Local Structure and Phase Transitions of $Bi_4V_2O_{11}$-Based Fast Ionic Conductors by Combined Raman and XRD Studies." Journal of the American Ceramic Society **96**(11): 3448-3456.

Paydar, M., Hadian A., et al. (2004). "Ionic conductivity and crystal structure relationships in Ti/Cu substituted $Bi_4V_2O_{11}$." Journal of materials science **39**(4): 1357-1361.

Paydar, M., Hadian A., et al. (2006). "A new look at oxygen pumping characteristics of BICUVOX. 1 solid electrolyte." Journal of materials science **41**(7): 1953-1957.

Pederson, L., Maupin G., et al. (1991). "Combustion synthesis of $YBa_2Cu_3O_{7-x}$: glycine/metal nitrate method." Materials Letters **10**(9-10): 437-443.

Peela, N. R., Mubayi A., et al. (2011). "Steam reforming of ethanol over $Rh/CeO_2/Al_2O_3$ catalysts in a microchannel reactor." Chemical Engineering Journal **167**(2-3): 578-587.

Pell, J. W., Ying J. Y., et al. (1995). "Sol-gel synthesis of α-$Bi_2VO_{5.5}$ using a soluble bismuth precursor." Materials Letters **25**(3-4): 157-160.

Perego, C. and Villa P. (1997). "Catalyst preparation methods." Catalysis Today **34**(3-4): 281-305.

Pereira, E. B., Homs N., et al. (2008). "Oxidative steam-reforming of ethanol over Co/SiO_2, $Co–Rh/SiO_2$ and $Co–Ru/SiO_2$ catalysts: Catalytic behavior and deactivation/regeneration processes." Journal of Catalysis **257**: 206-214.

Pereira, M., Clark A., et al. (1994). "Calcium phosphate formation on sol-gel-derived bioactive glasses in vitro." Journal of Biomedical Materials Research Part A **28**(6): 693-698.

Petitto, S. C., Marsh E. M., et al. (2008). "Cobalt oxide surface chemistry: The interaction of CoO(100), Co_3O_4(110) and Co_3O_4(111) with oxygen and water." Journal of Molecular Catalysis A: Chemical **281**(1): 49-58.

Philip, L., Iyengar L., et al. (1998). "Cr (VI) reduction by Bacillus coagulans isolated from contaminated soils." Journal of Environmental Engineering **124**(12): 1165-1170.

Pirovano, C., Löfberg A., et al. (2006). "BIMEVOX as dense membrane in catalytic reactor (ME = Co, Cu, Ta)." Solid State Ionics **177**(26–32): 2241-2244.

Pirovano, C., Vannier R., et al. (2003). "Characterisation of the electrode–electrolyte BIMEVOX system for oxygen separation: Part I. In situ synchrotron study." Solid State Ionics **159**(1-2): 167-179.

Piumetti, M., Bensaid S., et al. (2017). "Cerium-copper oxides prepared by solution combustion synthesis for total oxidation reactions: From powder catalysts to structured reactors." Applied Catalysis B: Environmental **205**(Supplement C): 455-468.

Politaev, V. V., Nalbandyan V. B., et al. (2010). "Mixed oxides of sodium, antimony (5+) and divalent metals (Ni, Co, Zn or Mg)." Journal of Solid State Chemistry **183**(3): 684-691.

Politova, E., Fortalnova E., et al. (2011). "Solid solutions on the base of bismuth vanadate: Preparation, structure, phase transitions, dielectric and transport properties." Solid State Ionics **192**(1): 248-251.

Porto, S. and Scott J. (1967). "Raman Spectra of $CaWO_4$, $SrWO_4$, $CaMoO_4$, and $SrMoO_4$." Physical Review **157**(3): 716.

Prabhu, M. (2016). "Impact of Business Environment Advanced Manufacturing Technologies and Competitive Priorities on Business Performance of Manufacturing Industries in Union Territory of Puducherry." Pondicherry University, India.

Prasad, J. S., Dhand V., et al. (2010). "Production of hydrogen and carbon nanofibers through the decomposition of methane over activated carbon supported Pd catalysts." International Journal of Hydrogen Energy **35**(20): 10977-10983.

Purohit, R., Sharma B., et al. (2001). "Ultrafine ceria powders via glycine-nitrate combustion." Materials research bulletin **36**(15): 2711-2721.

Qiao, H., Wei Z., et al. (2009). "Preparation and characterization of NiO nanoparticles by anodic arc plasma method." Journal of Nanomaterials **2009**: 2.

Rabenstein, G. and Hacker V., (2008). "Hydrogen for fuel cells from ethanol by steam-reforming, partial-oxidation and combined auto-thermal reforming: A thermodynamic analysis." Journal of Power Sources **185**(2): 1293-1304.

Radhakrishnan, A. A. and Beena B. B., (2014). "Structural and optical absorption analysis of CuO nanoparticles." Indian Journal of Advances in Chemical Science **2**(2): 158-161.

Rajh, T., Dimitrijevic N. M., et al. (2014). "Titanium dioxide in the service of the biomedical revolution." Chemical Reviews **114**(19): 10177-10216.

Rameshbabu, B., Periasamy P., et al. (2001). "Solid-state synthesis and characterization of $LiNi_yCo_{1-y}O_2$ ($0.0 <= y <= 0.4$)." International Journal of Inorganic Materials **3**(4): 401-407.

Randolph, K., Miller E. L., et al. (2017). "An Overview of Hydrgen, a DOE Energy Materials Network Consortium Aimed at Accelerating the Development of Advanced Water Splitting Materials." Meeting Abstracts, The Electrochemical Society.

Regalbuto J., (2016). "Catalyst preparation: science and engineering." 1st ed. CRC Press, Taylor & Francis Publishing Group: New York, USA. 1-488.

Reichelt R., (2007). "Scanning Electron Microscopy, in Science of Microscopy." 1st ed. Springer-Verlag New York, USA: 133-272.

Ren, N., Li J., et al. (2006). "Biohydrogen production from molasses by anaerobic fermentation with a pilot-scale bioreactor system." International Journal of Hydrogen Energy **31**(15): 2147-2157.

Rhodes R.P., inventor (1996); Hewlett-Packard Company, A Delaware Corporation, Thermal conductivity detector. United States Patent US5587520A.

Ribeiro, N. F., Souza M. M., et al. (2008). "Combustion synthesis of copper catalysts for selective CO oxidation." Journal of Power Sources **179**(1): 329-334.

Rietveld, H. (1969). "A profile refinement method for nuclear and magnetic structures." Journal of applied Crystallography **2**(2): 65-71.

Rioche, C., Kulkarni S., et al. (2005). "Steam reforming of model compounds and fast pyrolysis bio-oil on supported noble metal catalysts." Applied Catalysis B: Environmental **61**(1–2): 130-139.

Rodríguez C. J., (2000). "An introduction to the program: Full prof, 2000." Report, Laboratoire Léon Brillouin (CEA-CNRS) Saclay, France.

Rodriguez, J. A., Liu P., et al. (2007). "Water Gas Shift Reaction on Cu and Au Nanoparticles Supported on CeO_2 (111) and ZnO: Intrinsic Activity and Importance of Support Interactions." Angewandte Chemie International Edition **46**(8): 1329-1332.

Roh, H.-S., Platon A., et al. (2006). "Catalyst deactivation and regeneration in low temperature ethanol steam reforming with Rh/CeO_2–ZrO_2 catalysts." Catalysis Letters **110**(1): 1-6.

Roh, H.-S., Potdar H. S., et al. (2004). "Carbon dioxide reforming of methane over Ni incorporated into Ce–ZrO_2 catalysts." Applied Catalysis A: General **276**(1–2): 231-239.

Rossetti, I., Lasso J., et al. (2014). "Silica and zirconia supported catalysts for the low-temperature ethanol steam reforming." Applied Catalysis B: Environmental **150**: 257-267.

Rossi, C. C. R. S., Alonso C. G., et al. (2009). "Thermodynamic analysis of steam reforming of ethanol and glycerine for hydrogen production." International Journal of Hydrogen Energy **34**(1): 323-332.

Rostrup-Nielsen, J. and Trimm D. L. (1977). "Mechanisms of carbon formation on nickel-containing catalysts." Journal of Catalysis **48**(1-3): 155-165.

Roy, B. and Fuierer P. A. (2009). "Synthesis of cobalt-doped bismuth vanadate by combustion-synthesis: Influence of fuel on phase content and morphology." Journal of Materials Research **24**(10): 3078-3086.

Roy, B. and Leclerc C. A. (2015). "Study of preparation method and oxidization/reduction effect on the performance of nickel-cerium oxide catalysts for aqueous-phase reforming of ethanol." Journal of Power Sources **299**: 114-124.

Roy, B., Loganathan K., et al. (2010). "Surface modification of solution combustion synthesized Ni/Al_2O_3 catalyst for aqueous-phase reforming of ethanol." International Journal of Hydrogen Energy **35**(21): 11700-11708.

Roy, B., Sullivan H., et al. (2011). "Aqueous-phase reforming of n-BuOH over Ni/Al_2O_3 and Ni/CeO_2 catalysts." Journal of Power Sources **196**(24): 10652-10657.

Roy, B., Sullivan H., et al. (2014). "Effect of variable conditions on steam reforming and aqueous phase reforming of n-butanol over Ni/CeO_2 and Ni/Al_2O_3 catalysts." Journal of Power Sources **267**: 280-287.

Roy, M., Sahu S., et al. (2014). "Synthesis, electrical and thermal properties of $Bi_4V_{2-x}Me_xO_{11}$ (Me= Nb, Zr, Y and Cu with x= 0.0 and 0.06) ceramics." Journal of Thermal Analysis and Calorimetry **115**(2): 1265-1271.

Rusli, R., Abrahams I., et al. (2014). Ionic conductivity of $Bi_2Ni_xV_{1-x}O_{5.5-3x/2}$ ($0.1 \leq x \leq 0.2$) oxides prepared by a low temperature sol-gel route. AIP Conference Proceedings 1589, **178**.

Russo, M. (1994). "Static headspace gas chromatography of residual solvents in pharmaceutical products." Chromatographia **39**(11): 645-648.

Russo, N., Mescia D., et al. (2007). "N_2O decomposition over perovskite catalysts." Industrial & Engineering Chemistry Research **46**(12): 4226-4231.

Sahoo, D. R., Vajpai S., et al. (2007). "Kinetic modeling of steam reforming of ethanol for the production of hydrogen over Co/Al_2O_3 catalyst." Chemical Engineering Journal **125**(3): 139-147.

Sammes, N., Tompsett G., et al. (1999). "Bismuth based oxide electrolytes—structure and ionic conductivity." Journal of the European Ceramic Society **19**(10): 1801-1826.

Sanchez, E. A. and Comelli R. A. (2012). "Hydrogen by glycerol steam reforming on a nickel–alumina catalyst: Deactivation processes and regeneration." International Journal of Hydrogen Energy **37**(19): 14740-14746.

Saraswat, S. K. and Pant K., (2013). "Synthesis of carbon nanotubes by thermo catalytic decomposition of methane over Cu and Zn promoted Ni/MCM-22 catalyst." Journal of Environmental Chemical Engineering **1**(4): 746-754.

Sarkar A., Mukhi N., et al. (2016). "India's State-Level Energy Efficiency Implementation Readiness." Report, International bank for reconstruction and development/ The World Bank, Washington, D.C., U.S.A.

Satyapal, S., Petrovic J., et al. (2007). "The US Department of Energy's National Hydrogen Storage Project: Progress towards meeting hydrogen-powered vehicle requirements." Catalysis Today **120**(3-4): 246-256.

Schuyten, S., Dinka P., et al. (2008). "A novel combustion synthesis preparation of $CuO/ZnO/ZrO_2/Pd$ for oxidative hydrogen production from methanol." Catalysis Letters **121**(3-4): 189-198.

Schwarz, J. A., Contescu C., et al. (1995). "Methods for Preparation of Catalytic Materials." Chemical Reviews **95**(3): 477-510.

Scienceclarified (2017). The Development of Energy- A Brief Historyof Power Use, Fossil Fuels, Nuclear Energy [monograph on the Internet]. Science clarified, May 2014 [cited 2018 2 March].
Available from: http://www.scienceclarified.com/scitech/Energy-Alternatives/The-Development-of-Energy.html.

Segal, S. R., Anderson K. B., et al. (2002). "Low temperature steam reforming of methanol over layered double hydroxide-derived catalysts." Applied Catalysis A: General **231**(1): 215-226.

Sekar, M. M. A. and Patil K. C., (1992). "Combustion synthesis and properties of fine-particle dielectric oxide materials." Journal of Materials Chemistry **2**(7): 739-743.

Sekine, Y., Haraguchi M., et al. (2011). "Low temperature steam reforming of methane over metal catalyst supported on $Ce_xZr_{1-x}O_2$ in an electric field." Catalysis Today **171**(1): 116-125.

Seo, J. G., Youn M. H., et al. (2009). "Hydrogen production by steam reforming of liquefied natural gas (LNG) over $Ni/Al_2O_3–ZrO_2$ xerogel catalysts: effect of calcination temperature of $Al_2O_3–ZrO_2$ xerogel supports." International Journal of Hydrogen Energy **34**(9): 3755-3763.

Seo, J. G., Youn M. H., et al. (2008). "Hydrogen production by steam reforming of LNG over Ni/Al_2O_3-ZrO_2 catalysts: Effect of ZrO_2 and preparation method of Al_2O_3-ZrO_2." Korean Journal of Chemical Engineering **25**(1): 95-98.

Shabaker J.W., Davda R. R., et al. (2003). "Aqueous-phase reforming of methanol and ethylene glycol over alumina-supported platinum catalysts. Journal of Catalysis. **215(2):** 344-352.

Shabaker, J.W., Huber G. W., et al. (2003). "Aqueous-phase reforming of ethylene glycol over supported platinum catalysts." Catalysis Letters **88**: 1-8.

Shah, A. K., Prathap K. J., et al. (2014). "$Fe(OH)_3$ nano solid material: An efficient catalyst for regioselective ring opening of aryloxy epoxide with amines under solvent free condition." Applied Catalysis A: General **469**: 442-450.

Shahid, R. and Murugavel S. (2013). "Particle size dependent confinement and lattice strain effects in $LiFePO_4$." Physical Chemistry Chemical Physics **15**(43): 18809-18814.

Sharma, R., Anand M., et al. (2012). "Jatropha-oil conversion to liquid hydrocarbon fuels using mesoporous titanosilicate supported sulfide catalysts." Catalysis Today **198**(1): 314-320.

Shen, J.-P. and Song C. (2002). "Influence of preparation method on performance of Cu/Zn-based catalysts for low-temperature steam reforming and oxidative steam reforming of methanol for H_2 production for fuel cells." Catalysis Today **77**(1–2): 89-98.

Sheth, P. N. and Babu B. V. (2009). "Experimental studies on producer gas generation from wood waste in a downdraft biomass gasifier." Bioresource Technology **100**(12): 3127-3133.

Shijiao, L., Dasen H., et al. (1997). "Application of HSGC in Food Volatile Components Analysis [J]." Journal of Zhejiang Normal University (Natoral Sciences) **3**.

Shinde, V. M. and Madras G. (2012). "Water gas shift reaction over multi-component ceria catalysts." Applied Catalysis B: Environmental **123**: 367-378.

Sieminski, A. (2014). "International energy outlook." Report, Energy Information Administration (EIA) U.S.A.

Sinfelt, J. H. and Yates D. J. (1967). "Catalytic hydrogenolysis of ethane over the noble metals of Group VIII." Journal of Catalysis **8**(1): 82-90.

Singh, B., Ghosh S., et al. (2017). "Low temperature solid oxide electrolytes (LT-SOE): A review." Journal of Power Sources **339**: 103-135.

Singh, I. and Chandra A. (2013). "Need for optimizing catalyst loading for achieving affordable microbial fuel cells." Bioresource Technology **142**: 77-81.

Singha, R. K., Shukla A., et al. (2017). "Effect of metal-support interaction on activity and stability of Ni-CeO_2 catalyst for partial oxidation of methane." Applied Catalysis B: Environmental **202**: 473-488.

Song, H., Zhang L., et al. (2007). "Investigation of bio-ethanol steam reforming over cobalt-based catalysts." Catalysis Today **129**(3): 346-354.

Song, J. H., Han S. J., et al. (2016). "Hydrogen production by steam reforming of ethanol over Ni-Sr-Al_2O_3-ZrO_2 aerogel catalyst." Journal of Molecular Catalysis A: Chemical **424**: 342-350.

Soykal, I. I., Bayram B., et al. (2012). "Ethanol steam reforming over Co/CeO_2 catalysts: Investigation of the effect of ceria morphology." Applied Catalysis A: General **449**: 47-58.

Speight, J. G. (2005). "Lange's handbook of chemistry." McGraw-Hill New York.

StatisticsTimes (2017). "GDP growth of India" [monograph on the Internet]. Statistics Times, [cited 2018 13 Feb 2017].
Available from: http://statisticstimes.com/economy/sectorwise-gdp-contribution-of-india.php.

Steil, M. C., Fouletier J., et al. (1999). "BICOVOX: Sintering and grain size dependence of the electrical properties." Journal of the European Ceramic Society **19**(6–7): 815-818.

Steil, M. C., Ratajczak F., et al. (2005). "Thermal stability and preparation of dense membrane ceramics of BIMEVOX." Solid State Ionics **176**(29): 2305-2312.

Stein, W., Edwards J., et al. (2009). "Fuels – Hydrogen Production | Natural Gas: Solar-Thermal Steam Reforming." Encyclopedia of Electrochemical Power Sources. J. Garche. Amsterdam, Elsevier: 300-312.

Stern D., (2010). "The Role of Energy in Economic Growth." Report, Centre for Climate Economics & amp; Policy, Crawford School of Public Policy, The Australian National University.

Stocker T.F., Qin D., et al. (2013). "Technical summary, in Climate change 2013: the physical science basis." Report, University of Cambridge Press, U.K.

Sudarsanam, P., Mallesham B., et al. (2014). "Nano-Au/CeO_2 catalysts for CO oxidation: Influence of dopants (Fe, La and Zr) on the physicochemical properties and catalytic activity." Applied Catalysis B: Environmental **144**: 900-908.

Sukumaran, R. K., Singhania R. R., et al. (2009). "Cellulase production using biomass feed stock and its application in lignocellulose saccharification for bio-ethanol production." Renewable energy **34**(2): 421-424.

Sun, J., Qiu X.-P., et al. (2005). "from steam reforming of ethanol at low temperature over, and catalysts for fuel-cell application." International Journal of Hydrogen Energy **30**(4): 437-445.

Sun, J. and Wang Y. (2014). "Recent Advances in Catalytic Conversion of Ethanol to Chemicals." ACS Catalysis **4(4)**: 1078-1090.

Supothina, S., Seeharaj P., et al. (2007). "Synthesis of tungsten oxide nanoparticles by acid precipitation method." Ceramics International **33**(6): 931-936.

Świerczyński, D., Libs S., et al. (2007). "Steam reforming of tar from a biomass gasification process over Ni/olivine catalyst using toluene as a model compound." Applied Catalysis B: Environmental **74**(3): 211-222.

Szaller, Z., Pöppl L., et al. (1996). "Study of the formation of $Bi_2Te_4O_{11}$." Journal of Solid State Chemistry **121**(2): 251-261.

Taninouchi, Y.-k., Uda T., et al. (2010). "High oxide-ion conductivity of monovalent-metal-doped bismuth vanadate at intermediate temperatures." Solid State Ionics **181**(15-16): 719-723.

Tatarova, E., Dias A., et al. (2017). "Towards large-scale in free-standing graphene and N-graphene sheets." Scientific reports **7**(1): 10175.

TechSciResearch (2018). "India Hydrogen Market By Technology (Steam Methane Reforming Vs. Membrane Cell Technology), By Mode (Captive Vs. Merchant), By Application (Petroleum Refinery, Ammonia Cracking, & Others), Competition Forecast & Opportunities-2012-2030." Report, TechSciResearch.

Teichner S. and Gardes G. (1976) inventor; Agence National de Valorisation de la Recherche ANVAR. "Methods for the manufacture of composite catalysts containing a composition of a transition metal on a support." United States Patent US3963646A.

Teske S., Sawyer S., et al. (2015). "Energy revolution: a sustainable world." Report, Energy outlook (5th ed.), International Renewable Energy Agency,U.A.E.

Tian, Z.-Q., Yu H.-T., et al. (2007). "Combustion synthesis and characterization of nanocrystalline $LaAlO_3$ powders." Materials Chemistry and Physics **106**(1): 126-129.

Tiba, S. and Omri A. (2017). "Literature survey on the relationships between energy, environment and economic growth." Renewable and Sustainable Energy Reviews **69**: 1129-1146.

Tijare, S., Bakardjieva S., et al. (2014). "Synthesis and visible light photocatalytic activity of nanocrystalline $PrFeO_3$ perovskite for hydrogen generation in ethanol–water system." Journal of Chemical Sciences **126**(2): 517-525.

Timmons, D. S., Buchholz T., et al. (2016). "Forest biomass energy: assessing atmospheric carbon impacts by discounting future carbon flows." GCB Bioenergy **8**(3): 631-643.

Tishchenko, I. Y., Ilchenko O., et al. (2015). "TGA-DSC-MS analysis of silicon carbide and of its carbon-silica precursor." Chemistry, Physics and Technology of Surface. **6**: 216-223.

Toby, B. H. (2006). "R factors in Rietveld analysis: how good is good enough?" Powder diffraction **21**(1): 67-70.

Tolstoy, V. and Tolstobrov E. (2002). "The synthesis of Bi–V–O-containing nanolayers on silica surfaces by the successive ionic layer deposition technique." Solid State Ionics **151**(1-4): 165-169.

Trane-Restrup, R., Dahl S., et al. (2014). "Steam reforming of ethanol over Ni-based catalysts: Effect of feed composition on catalyst stability." International Journal of Hydrogen Energy **39**(15): 7735-7746.

Trimm, D. L. (1997). "Coke formation and minimisation during steam reforming reactions." Catalysis Today. **37**: 233-238.

Trimm, D. L. (1999). "Catalysts for the control of coking during steam reforming." Catalysis Today **49**: 3-10.

Trindade, T., de Jesus J. D. P., et al. (1994). "Preparation of zinc oxide and zinc sulfide powders by controlled precipitation from aqueous solution." Journal of Materials Chemistry **4**(10): 1611-1617.

Trzciński, K., Borowska-Centkowska A., et al. (2015). "Photoelectrochemical properties of BIMEVOX (ME= Cu, Zn, Mn) electrodes in contact with aqueous electrolyte." Solid State Ionics **271**: 63-68.

Trzciński, K., Gasiorowski J., et al. (2017). "Optical and photoelectrochemical characterization of pulsed laser deposited $Bi_4V_2O_{11}$, BICUVOX, and BIZNVOX." Thin Solid Films **638**: 251-257.

Tsederberg, N. V. and Cess R. D. (1965). Thermal conductivity of gases and liquids, MIT press Cambridge, Massachusetts.

Tsuji H., Gupta A. K., et al. (2002). "High temperature air combustion: from energy conservation to pollution reduction." 1st ed. CRC press, Taylor & Francis Publishing Group: New York, USA :1-424.

Ueda, M., (2003) inventor; Shimadzu Corporation, Japan. "Thermal conductivity detector." United States Patent US6550961B1.

Vagia, E. C. and Lemonidou A. A. (2010). "Investigations on the properties of ceria–zirconia-supported Ni and Rh catalysts and their performance in acetic acid steam reforming." Journal of Catalysis **269**(2): 388-396.

Vaidya, P. D. and Rodrigues A. E. (2006). "Kinetics of Steam Reforming of Ethanol over a Ru/Al_2O_3 Catalyst." Industrial & Engineering Chemistry Research **45**(19): 6614-6618.

Van Soest, J. J., Tournois H., et al. (1995). "Short-range structure in (partially) crystalline potato starch determined with attenuated total reflectance Fourier-transform IR spectroscopy." Carbohydrate Research **279**: 201-214.

Vannice, M. (1977). "The Catalytic Synthesis of Hydrocarbons from H_2/CO Mixtures over the Group VIII Metals." Journal of Catalysis **50**: 228-236.

Vannier, R., Pernot E., et al. (2003). "$Bi_4V_2O_{11}$ polymorph crystal structures related to their electrical properties." Solid State Ionics **157**(1-4): 147-153.

Varga, E., Ferencz Z., et al. (2015). "Oxidation states of active catalytic centers in ethanol steam reforming reaction on ceria based Rh promoted Co catalysts: An XPS study." Journal of Molecular Catalysis A: Chemical **397**: 127-133.

Varma, A., Mukasyan A. S., et al. (2016). "Solution Combustion Synthesis of Nanoscale Materials." Chemical Reviews **116** (23): 14493-14586.

Vasudeva, K., Mitra N., et al. (1996). "Steam reforming of ethanol for hydrogen production: thermodynamic analysis." International Journal of Hydrogen Energy **21**(1): 13-18.

Vicente, J., Ereña J., et al. (2014). "Reaction pathway for ethanol steam reforming on a Ni/SiO_2 catalyst including coke formation." International Journal of Hydrogen Energy **39**(33): 18820-18834.

Vicente, J., Montero C., et al. (2014). "Coke deactivation of Ni and Co catalysts in ethanol steam reforming at mild temperatures in a fluidized bed reactor." International Journal of Hydrogen Energy **39**(24): 12586-12596.

Vila, M., Díaz-Guerra C., et al. (2013). "Structural and luminescence properties of Eu and Er implanted Bi_2O_3 nanowires for optoelectronic applications." Journal of Materials Chemistry C **1**(47): 7920-7929.

Viswanathan B. (2005). "Catalysis Research in India as seen from Web of Science Data Base." Bulletin of the Catalysis Society of India **4**: 5-11.

Vizcaíno, A., Arena P., et al. (2008). "Ethanol steam reforming on Ni/Al_2O_3 catalysts: effect of Mg addition." International Journal of Hydrogen Energy **33**(13): 3489-3492.

Vojisavljević, K., Wicker S., et al. (2017). "Nanocrystalline cobalt-oxide powders by solution-combustion synthesis and their application in chemical sensors." Advanced Powder Technology **28**(4): 1118-1128.

Waheed, Q. M. K., Wu C., et al. (2016). "Pyrolysis/reforming of rice husks with a Ni–dolomite catalyst: Influence of process conditions on syngas and hydrogen yield." Journal of the Energy Institute **89**(4): 657-667.

Wang, B., Wei Q., et al. (2013). "Synthesis and characterization of uniform and crystalline magnetite nanoparticles via oxidation-precipitation and modified co-precipitation methods." International Journal of Electrochemical and Science **8**: 3786-3793.

Wang, H., Liu Y., et al. (2008). "Study on the carbon deposition in steam reforming of ethanol over Co/CeO_2 catalyst." Chemical Engineering Journal **145**(1): 25-31.

Wang, X., Wu W., et al. (2015). "Bauxite-supported Transition Metal Oxides: Promising Low-temperature and SO_2-tolerant Catalysts for Selective Catalytic Reduction of NO_x." Scientific reports **5**: 9766.

Ward, D. A. and Ko E. I., (1995). "Preparing Catalytic Materials by the Sol-Gel Method." Industrial & Engineering Chemistry Research **34**(2): 421-433.

Watanabe, A. (1990). "Is it possible to stabilize δ-Bi_2O_3 by an oxide additive?" Solid State Ionics **40**: 889-892.

Watson, C. J., Coats A., et al. (1997). "Synthesis, phase stability and electrical characterisation of BINAVOX solid solutions." Journal of Materials Chemistry **7**(10): 2091-2095.

Wei, Y., An Q., et al. (2015). "Influence of Fiber Orientation on Single-Point Cutting Fracture Behavior of Carbon-Fiber/Epoxy Prepreg Sheets." Materials **8**(10): 5336.

Wenju, W. and Y. Q. W. (2008). "Thermodynamic analysis of steam reforming of ethanol for hydrogen generation." International Journal of Energy Research **32**(15): 1432-1443.

Wenju, W., Yaquan W., et al. (2011). "Production of hydrogen by ethanol steam reforming over nickel–metal oxide catalysts prepared via urea–nitrate combustion method." International Journal of Energy Research **35**(6): 501-506.

Wild, M., Folini D., et al. (2013). "The global energy balance from a surface perspective." Climate dynamics **40**(11-12): 3107-3134.

Wróbel, W., Abrahams I., et al. (2005). "Phase transitions in the BIZRVOX system." Solid State Ionics **176**(19-22): 1731-1737.

Wu, C. and Williams P. (2012). "Effect of process conditions on the steam reforming of ethanol with a nano-Ni/SiO_2 catalyst." Environmental technology **33**(6): 631-638.

Wu, H., Pantaleo G., et al. (2014). "Bi- and trimetallic Ni catalysts over Al_2O_3 and Al_2O_3-MO_x (M = Ce or Mg) oxides for methane dry reforming: Au and Pt additive effects." Applied Catalysis B: Environmental **156–157**: 350-361.

Wu, Q.-H., Thissen A., et al. (2004). "Photoelectron spectroscopy study of oxygen vacancy on vanadium oxides surface." Applied Surface Science **236**(1-4): 473-478.

Wu, Y.-W., Chung W.-C., et al. (2015). "Modification of Ni/γ-Al_2O_3 catalyst with plasma for steam reforming of ethanol to generate hydrogen." International Journal of Hydrogen Energy **40**(25): 8071-8080.

Xing, G., Li Y., et al. (2011). "Morphology-controllable synthesis of $SrMoO_4$ hierarchical crystallites via a simple precipitation method." Materials Chemistry and Physics **127**(3): 465-470.

Xu, W., Liu Z., et al. (2013). "Steam Reforming of Ethanol on Ni/CeO_2: Reaction Pathway and Interaction between Ni and the CeO_2 Support." ACS Catalysis **3**(5): 975-984.

XPS-NIST Standard Reference Database 20, Version 4.1. [database on the Internet]. Alexander V. N., Anna K.-V., Stephen W. G., and Cedric J. P, Material Measurement Laboratory (MML), U.S. Department of Commerce. c2000 [updated 2012]; cited [Aug, 2018].
Available from: http://srdata.nist.gov/xps/

Yadav, G. D. and Sharma R. V. (2014). "Biomass derived chemicals: Environmentally benign process for oxidation of 5-hydroxymethylfurfural to 2, 5-diformylfuran by using nano-fibrous Ag-OMS-2-catalyst." Applied Catalysis B: Environmental **147**: 293-301.

Yadav, G. D. and Sharma R. V. (2014). "Synthesis, characterization and applications of highly active and robust sulfated $Fe–TiO_2$ catalyst (ICT-3) with superior redox and acidic properties." Journal of Catalysis **311**: 121-128.

Young, R. and Wiles D. (1982). "Profile shape functions in Rietveld refinements." Journal of applied Crystallography **15**(4): 430-438.

Yu, J. and Kudo A. (2005). "Hydrothermal synthesis of nanofibrous bismuth vanadate." Chemistry letters **34**(6): 850-851.

Yu, J. and Kudo A. (2006). "Effects of structural variation on the photocatalytic performance of hydrothermally synthesized $BiVO_4$." Advanced Functional Materials **16**(16): 2163-2169.

Yu, P., Kirkpatrick R. J., et al. (1999). "Structure of calcium silicate hydrate (C-S-H): Near-, Mid-, and Far-infrared spectroscopy." Journal of the American Ceramic Society **82**(3): 742-748.

Yu, X., Smith J., et al. (2015). "Spray-combustion synthesis: Efficient solution route to high-performance oxide transistors." Proceedings of the National Academy of Sciences **112**(11): 3217-3222.

Yu, X. H., Gu H. X., et al. (2011). Crystal Structure and Chemical Composition of BIMEVOX (ME= Mn). Advanced Materials Research, Trans Tech Publication.

Yue, D., You F., et al. (2014). "Biomass-to-bioenergy and biofuel supply chain optimization: overview, key issues and challenges." Computers & Chemical Engineering **66**: 36-56.

Zainal, Z. A., Rifau A., et al. (2002). "Experimental investigation of a downdraft biomass gasifier." Biomass and Bioenergy **23**(4): 283-289.

Zeng, G., Gu R., et al. (2013). "The preparation and catalytic behavior of a shell–core Ni/Mg–Al catalyst for ethanol steam reforming." International Journal of Hydrogen Energy **38**(26): 11256-11267.

Zerta, M., Schmidt P. R., et al. (2008). "Alternative World Energy Outlook (AWEO) and the role of hydrogen in a changing energy landscape." International Journal of Hydrogen Energy **33**(12): 3021-3025.

Zevaco, T., Duñach E., et al. (1993). "Bi(III)-mandelate/DMSO : A new oxidizing system for the catalyzed C-C cleavage of epoxides." Tetrahedron Letters **34(16)**: 2601-2604.

Zhang, A. and Zhang J. (2009). "Characterization of visible-light-driven $BiVO_4$ photocatalysts synthesized via a surfactant-assisted hydrothermal method." Spectrochimica acta. Part A, Molecular and biomolecular spectroscopy **73**(2): 336-341.

Zhang, B., Tang X., et al. (2007). "Hydrogen production from steam reforming of ethanol and glycerol over ceria-supported metal catalysts." International Journal of Hydrogen Energy **32**(13): 2367-2373.

Zhang, C., Oliaee S. N., et al. (2015). "A Generic Wet Impregnation Method for Preparing Substrate-Supported Platinum Group Metal and Alloy Nanoparticles with Controlled Particle Morphology." Nano letters **16**(1): 164-169.

Zhang, J. (2014). "National Renewable Energy Laboratory." Private Communication. Received January **24**: 2016.

Zhang, L., Li W., et al. (2009). "Ethanol steam reforming reactions over $Al_2O_3 \cdot SiO_2$-supported Ni–La catalysts." Fuel **88**(3): 511-518.

Zhang, L., Liu J., et al. (2009). "Ethanol steam reforming over Ni-Cu/Al_2O_3-M_yO_z (M= Si, La, Mg, and Zn) catalysts." Journal of Natural Gas Chemistry **18**(1): 55-65.

Zhang, L., Wang W., et al. (2006). "Sonochemical synthesis of nanocrystallite Bi_2O_3 as a visible-light-driven photocatalyst." Applied Catalysis A: General **308**: 105-110.

Zhang, Z., Liu K., et al. (2016). "Hierarchical sheet-on-sheet $ZnIn_2S_4/gC_3N_4$ heterostructure with highly efficient photocatalytic H_2 production based on photoinduced interfacial charge transfer." Scientific reports **6**: 19221.

Zhao, Y., Xia C., et al. (2013). "Recent progress on solid oxide fuel cell: lowering temperature and utilizing non-hydrogen fuels." International Journal of Hydrogen Energy **38**(36): 16498-16517.

Zhu, T. and Flytzani-Stephanopoulos . M. (2001). "Catalytic partial oxidation of methane to synthesis gas over Ni–CeO_2." Applied Catalysis A: General **208**(1–2): 403-417.

Zhu, X., Cho H.-r. et al. (2013). "Charge-enhanced dry impregnation: A simple way to improve the preparation of supported metal catalysts." ACS Catalysis **3**(4): 625-630.

Zou, J., Yang H., et al. (2016). "Hydrogen production from pyrolysis catalytic reforming of cellulose in the presence of K alkali metal." International Journal of Hydrogen Energy **41**(25): 10598-10607.

Zhu, X., Li K., et al. (2014). "Chemical-Looping Steam Methane Reforming over a CeO_2–Fe_2O_3 Oxygen Carrier: Evolution of Its Structure and Reducibility." Energy & Fuels **28(2)**: 754-760.

List of Publications

International Journals

1. **S. Sharma,** B. Patil, A. Pathak, S. Ghosalkar, H. K. Mohanta, B. Roy, "Application of BICOVOX catalyst for hydrogen production from ethanol", **Clean Technologies and Environmental Policy**, 20(4), 695-701 (2017).
2. B. Patil, **S. Sharma**, H.K. Mohanta, B. Roy, "BINIVOX Catalyst for Hydrogen Production from Ethanol by Low Temperature Steam Reforming (LTSR)", **Journal of Chemical Sciences**, 129(11), 1741–1746 (2017).
3. **S. Sharma**, et al.,"Low Temperature Steam Reforming of Ethanol Over BICOVOX Catalyst for Hydrogen Production", **Applied Surface Science**, (2020) Communicated, Under Review.
4. **S. Sharma**, et al.,"Deactivation study of the BICOVOX catalysts used in Steam Reforming of Ethanol for H_2 production", **Journal of Alloys and Compounds**, (2020) Communicated, Under Review.
5. **S. Sharma**, et al.," Metal (Ni, Cu) doped bismuth vanadate (BIMEVOX) systems for low temperature steam reforming of ethanol", **Journal of Power Sources**, (2020) Communicated, Under Review.
6. **S. Sharma**, et al.,"Effect of reaction parameters on the performance of BIMEVOX catalysts for steam reforming of ethanol: Deactivation study", To be communicated.
7. **S. Sharma**, et al.," Vanadium (V) environments in BIMEVOX catalysts: An investigation using Raman and XPS", To be communicated.

International and National Conferences

1. **S. Sharma,** H. K. Mohanta, B. Roy, Development of BICOVOX Catalyst For Hydrogen Production From Ethanol. Proceedings of 2017 Asia Pacific Congress on Catalysis (APCAT), Hotel The Lalit, Mumbai, India, January 17 – 21, 2017.
2. **S. Sharma,** H. K. Mohanta, B. Roy, Ethanol Steam Reforming Over BICOVOX Catalyst for Hydrogen Production. Proceedings of International Symposium & 70th Annual Session of IIChE in association with International Partners (CHEMCON-2017), Department of Chemical Engineering, Haldia Institute of Technology, West Bengal, India, December 27-30, 2017.
3. **S. Sharma,** B. Roy, Steam Reforming of Ethanol Over BICUVOX Catalyst. National Conference on Solid State Ionics (NCSSI-12), BITS Pilani, Pilani campus, December 21-23, 2017.
4. **S. Sharma,** B. Roy, Hydrogen from Renewable Sources. International Conference Nano and Functional Materials, BITS Pilani, Pilani campus, July, 2014.

BIOGRAPHIES

Biography of the Candidate

Shweta Sharma is gold medalist of Chemical Engineering batch of 2012 of Banasthali Vidyapeeth University. She completed her master's degree with gold medal again in Chemical Engineering from Birla Institute of Technology Pilani, in 2014. She joined BITS Pilani campus as a research scholar in July 2014. She is currently carrying out research in th field of producing hydrogen and hydrogen rich gas production from ethanol using BIMEVOX catalyst through low temperature steam reforming. Her research interests include catalysts preparation, Green Technology, Renewable Energy Sources, and Smart Materials. She was awarded INSPIRE-DST fellowship from year 2016-2019. She was also involved in the tutorials of courses such as Material Science, Process Design Principles, Fluid Mechanics, and Heat Transfer.

Biography of Supervisor

Professor Dr. Banasri Roy is currently associated with BITS Pilani as Associate Professor in Chemical Engineering department. She joined as Assistant Professor in Department of Chemical Engineering in BITS Pilani in 2013. She has also been visiting assistant professor in Chemical Engineering in New Mexico Inst. of Tech. Socorro, NM, USA. She holds two post doctorates from New Mexico Inst. of Tech. Socorro, NM, USA, one in Department of Chemical Engineering 2009-2011 and other in Department of Material Engineering 2006-2009. She pursued her doctorate from Colorado School of Mines, Golden, CO, USA in Materials Engineering. She holds two master's degrees as well, M.Sc. from New Mexico Inst. of Tech. Socorro, NM, USA, 2001 batch and M. Tech. in Materials Engineering, IIT/Kanpur, Kanpur, India, 1999 batch. She completed her engineering degree in Chemical Technology from Calcutta University in 1996 and B.Sc.(Hons.) in 1993 from same university.

Till now she has around 30 publications in SCI journals, around 40 in peer reviewed conferences and has reviewed approx. 50 articles in referred journals. Her recent publications are 'Application of BICOVOX catalyst for hydrogen production from ethanol, 2018', 'BINIVOX Catalyst for Hydrogen Production from Ethanol by Low Temperature Steam Reforming (LTSR), 2018'; 'Study of preparation method and oxidization/reduction effect on the performance of nickel-cerium oxide catalyst's for aqueous-phase reforming of ethanol, 2015'; 'Effect of variable conditions on steam reforming and aqueous phase reforming of n-butanol over Ni/CeO_2 and Ni/Al_2O_3 catalysts, 2014'; Effect of preparation method on the performance of the Ni/Al_2O_3 Catalysts for Aqueous-Phase Reforming of Ethanol: Part II-Characterization, 2012'; 'Investigating the Effect of Dopant Type and Concentration on TiO_2 Powder Microstructure via Rietveld Analysis, 2018'; 'Low temperature solid oxide electrolytes (LT-SOE): A review, 2017'; 'Synthesis of Al-doped Nano Ti-O scaffolds using a hydrothermal route on Titanium foil for biomedical applications, 2016'; 'Effect of preparation methods on the performance of Ni/Al_2O_3 catalysts for aqueous-phase reforming of ethanol: Part I-Catalytic activity, 2012'; and 'Aqueous-phase reforming of n-BuOH over Ni/Al_2O3 and Ni/CeO_2 catalysts, 2011'.

She is currently leading three research projects; BIMEVOX Catalyst Systems for Hydrogen and Hydrogen-Rich Gas Production from Ethanol by Low Temperature Steam Reforming, Hydrogen Production from Ethanol by Low Temperature Steam Reforming Using Modified Ni-Sn/Al_2O_3 and Ni-Sn/CeO_2 Catalysts and Development of Carbon and/ or Sulfur Tolerant Catalyst for Reforming of Model Biogas. Courses in which she has imparted her knowledge are Advance Thermodynamics, Material Science, Fluid Mechanics, Bio-medical Application and Catalysis. Currently, Dr Banasri Roy is guiding/co-guiding 3 PhD students, and 2 M.E Dissertation students.

Biography of Co-Supervisor

Professor Dr. Hare Krishna Mohanta is currently heading Department of Chemical Engineering, BITS Pilani. He is doctorate in process control from BITS Pilani, batch of 2006. Further his academics include M.Tech. in Chemical Engineering from IIT Kanpur in 1998 and graduation in Chemical Engineering, 1995 batch of NIT Rourkela. He has been associated with BITS Pilani from 1998.

He has keen research interest in Advanced Process Control, Process Monitoring and Control, Sensors and Micro reactors, Catalysis and Pyrolysis, Applied Wavelet Analysis, Reactive Distillation, and Modeling and Simulation. Courses in which he has imparted his knowledge are Thermodynamics, Chemical Process Calculations, Chemical Process Technology, Petroleum Refining and Petrochemicals, Process Plant Safety, Mass Transfer Operations, Process Control, Advanced Heat Transfer and Advanced Process Control.

His major publications in referred journals are Particle Swarm Optimization based Fuzzy Logic Control of pH Neutralization Process, Online monitoring and control of particle size in the grinding process using least square support vector regression and resilient back propagation neural network, Genetic Optimization based Adaptive Fuzzy Logic Control of a pH Neutralization Process, Soft sensing of particle size in a grinding process: Application of support vector regression, fuzzy inference and adaptive neuro fuzzy inference techniques for online monitoring of cement fineness, Development and comparison of neural network based soft sensors for online estimation of cement clinker quality.

He has also contributed in writing various books and book chapters' like Advanced Process Control, Educational Development Division, BITS-Pilani, April 2010, Chemical Engineering Laboratory Manual, Educational Development Division, BITS-Pilani, 2002, Part – IX "Industrial Safety" in "Chemical Engineering", Lecture Notes compiled by B V Babu, Academic Refresher Course Programme–III, for the Employees of Hindustan Zinc Limited, Udaipur, Part - VIII "Industrial Safety" in "Chemical Engineering", Lecture Notes compiled for Academic Development Programme in Basic Process Engineering - 4,5,6,7,8,9,10 for the Employees of Hindustan Zinc Limited, Udaipur.

APPENDIX 1

Stoichiometric Calculations of BIMEVOX samples

Oxidation Number of Elements:

Electrochemical reactions involve the transfer of electrons. Mass and charge are conserved when balancing these reactions, but you need to know which atoms are oxidized and which atoms are reduced during the reaction. Oxidation numbers are used to keep track of how many electrons are lost or gained by each atom (Skoog, Holler et al. 2017).

1) Cobalt = +2

In cobalt nitrate, nitrate (NO_3.) has a charge of -1. Since there's two of them in the compound, cobalt must be +2 to balance it.

2) Nickel = +2

In nickel nitrate, nitrate (NO_3.) has a charge of -1. Since there's two of them in the compound, nickel must be +2 to balance it.

3) Copper = +2

In copper nitrate, nitrate (NO_3.) has a charge of -1. Since there's two of them in the compound, copper must be +2 to balance it.

4) Oxygen = - 2

The oxidation number of oxygen in compounds is usually -2.

5) Vanadium = +5

Oxygen is always -2, so to balance out total negative charge of five oxygen, vanadium is taken as +5.

6) Bismuth = +3 In compounds of bismuth, the most common oxidation numbers of bismuth are: +3 (Skoog, Holler et al. 2017).

7) Hydrogen = +1

The oxidation number of a Group IA element in a compound is +1.Hydrogen is the first element in Group IA.

8) Carbon = +4

Here, Carbon is oxidized to CO_2 on reaction, so its oxidation number is taken as +4.

9) Nitrogen = 0

The oxidation number of a free element is always 0. Thus, atoms in Nitrogen have 0 oxidation number.

Molecular Weight of Compounds:

1) Glycine = 75.07
2) Vanadium Pentoxide = 182
3) Bismuth Nitrate = 485
4) Cobalt Nitrate Hexahydrate = 291.03
5) Cupric Nitrate Hexahydrate = 296
6) Nickel Nitrate Hexahydrate = 290.8
7) BICOVOX = 1116.4
8) BICUVOX = 1117.82

9) BINIVOX = 1116.31

1. BICOVOX catalyst

$$4Bi(NO_3)_3 + 0.9V_2O_5 + 0.2Co(NO_3)_2 \cdot 6H_2O \xrightarrow{300°C/O_2} Bi_4[V_{0.9}Co_{0.1}]_2O_{11-\delta}$$

Glycine = $C_2H_5NO_2 = 2*(+4) + 5*(+1) + 0 + 2*(-2) = 9$

Vanadium Pentoxide = $0.85*V_2O_5 = 2*(5) + 5*(-2) = 0$

Cobaltous Nitrate = $0.2*Co(NO_3)_2 = 0.2*[+2+2(0)+6*(-2)] = 0.2*[-10] = -2$

Water = $6 * H2O = 6* [2(+1) + (-2)] = 0$

Bismuth Nitrate = $4*Bi(NO_3)_3 = 4*[+3+3(0)+9*(-2)] = -60$

$Oxidizer_{Total}$ (O) = $0.9V_2O_5 + 0.2Co(NO_3)_2 + 4*Bi(NO_3)_3 = 0 - 2 - 60 = -62$

Fuel Glycine (F) = 9

Thus, we have O:F given by Patil et al., as (Chen, Huh et al. 2007)

O/F = [Σ(Coefficient of the elements in nitrates)*(Oxidation state)] / (-1) [Σ(Coefficient of the elements in fuel) * (Oxidation state)]

O / F = 1

Basis: 20gm of BICOVOX sample.

Thus, for 20gm of BICOVOX sample to be prepared, we have

$$\text{Moles of BICOVOX} = \frac{\text{Mass of BICOVOX}}{\text{Mol. Wt. of BICOVOX}}$$

$$= \frac{20}{1116.4} = 0.0179\ moles$$

So, for bismuth nitrate, we have

$= 4 * 485 * 0.0179 = 134.79$ gm

$V_2O_5 = 0.9 * 182 * 0.0179 = 2.93$ gm

Cobalt nitrate $= 0.2 * 291.03 * 0.0179 = 0.782$ gm

Glycine $= 62/9 * 75.07 * 0.0179 = 9.26$ gm

2. BINIVOX catalyst

$$4Bi(NO_3)_3 + 0.9V_2O_5 + 0.2Ni(NO_3)_2 \cdot 6H_2O \xrightarrow{300°C/O_2} Bi_4[V_{0.9}Ni_{0.1}]_2O_{11-\delta}$$

For Oxidation State, Nickel Nitrate

$0.2 * Ni(NO_3)_2 = 0.2 * (+2+0+6*(-2)) = -2$

Other quantities are calculated,

$Oxidizer_{Total}$ (O) = $0.9V_2O_5 + 0.2*Ni(NO_3)_2 + 4*Bi(NO_3)_3 = 0 - 2 - 60 = -62$

Fuel glycine (F) = 9

Thus, we have O:F given by Patil et al., as (Chen, Huh et al. 2007)

O/F = [Σ(Coefficient of the elements in nitrates)*(Oxidation state)] / (-1) [Σ(Coefficient of the elements in fuel) * (Oxidation state)]

O / F = 1

Basis: 20gm of BINIVOX sample.

Thus, for 20gm of BINIVOX sample to be prepared, we have

$$\text{Moles of BINIVOX} = \frac{\text{Mass of BINIVOX}}{\text{Mol. Wt. of BINIVOX}}$$

$$= \frac{20}{1116.31} = 0.0179\ moles$$

So, for bismuth nitrate, we have

$= 4 * 485 * 0.0179 = 134.79$ gm

$V_2O_5 = 0.9 * 182 * 0.0179 = 2.93$ gm

Nickel nitrate $= 0.2 * 290.8 * 0.0179 = 0.782$ gm

Glycine $= 62/9 * 75.07 * 0.0179 = 9.26$ gm

3. BICUVOX catalyst

$$4Bi(NO_3)_3 + 0.9V_2O_5 + 0.2Cu(NO_3)_2 \cdot 6H_2O \xrightarrow{300°C/O_2} Bi_4[V_{0.9}Cu_{0.1}]_2O_{11-\delta}$$

For Oxidation State, Cupric Nitrate

$0.2 * Cu(NO_3)_2 = 0.2 * (+2+0+6*(-2)) = -2$

Other quantities are calculated,

$Oxidizer_{Total}$ (O) = $0.9V_2O_5 + 0.2*Cu(NO_3)_2 + 4*Bi(NO_3)_3 = 0 - 2 - 60 = -62$

Fuel glycine (F) = 9

Thus, we have O:F given by Patil et al., as (Chen, Huh et al. 2007)

O/F = [Σ(Coefficient of the elements in nitrates)*(Oxidation state)] / (-1) [Σ(Coefficient of the elements in fuel) * (Oxidation state)]

O / F = 1

Basis: 20gm of BICUVOX sample.

Thus, for 20gm of BICUVOX sample to be prepared, we have

$$\text{Moles of BICUVOX} = \frac{\text{Mass of BICUVOX}}{\text{Mol. Wt. of BICUVOX}}$$

$$= \frac{20}{1117.82} = 0.01789\ moles$$

So, for bismuth nitrate, we have

$= 4 * 485 * 0.01789 = 134.75$ gm

$V_2O_5 = 0.9 * 182 * 0.01789 = 2.93$ gm

Cupric nitrate $= 0.2 * 296 * 0.01789 = 0.782$ gm

Glycine $= 62/9 * 75.07 * 0.01789 = 9.26$ gm

Crystallography Open Database

1. The crystal structure of α-Bi_2O_3

Database_Code_Amcsd 0011925
Cell Parameters: 5.8486 8.1661 7.5097 90.000 113.000 90.000
Space Group: P2_1/c
X-Ray Wavelength: 1.541838

2-Theta	Intensity	D-Spacing	H	K	L	Multiplicity
16.8	2.48	5.2761	0	1	1	4
19.74	2.98	4.498	-1	1	1	4
19.75	1.39	4.4948	1	1	0	4
21.77	3.26	4.083	0	2	0	2
24.58	12.7	3.6223	-1	0	2	2
25.33	1.26	3.5156	0	2	1	4
25.78	33.66	3.4564	0	0	2	2
26.93	28.93	3.3112	-1	1	2	4
26.96	22.76	3.3073	1	1	1	4
27.4	58.35	3.2545	-1	2	1	4
27.42	100	3.2533	1	2	0	4
28.03	36.95	3.183	0	1	2	4
32.52	6.53	2.7531	-2	1	1	4
33.06	26.09	2.7097	-1	2	2	4
33.09	25.76	2.7075	1	2	1	4
33.25	29.49	2.6946	-2	0	2	2
33.28	35.32	2.6918	2	0	0	2
33.98	8.72	2.6381	0	2	2	4
35.07	17.18	2.5589	-2	1	2	4
35.1	3.34	2.5565	2	1	0	4
35.44	10.72	2.5327	0	3	1	4
35.95	8.96	2.4984	1	0	2	2
37	4.41	2.4297	-1	3	1	4
37.01	2.78	2.4292	1	3	0	4
37.61	6.29	2.3915	-1	1	3	4
37.65	14.28	2.3891	1	1	2	4
40.09	6.86	2.249	-2	2	2	4
40.68	1.02	2.2176	0	1	3	4
41.5	1.66	2.1761	-1	3	2	4
41.52	3.95	2.175	1	3	1	4
41.92	4.82	2.1549	-2	1	3	4
41.98	1.18	2.152	2	1	1	4
42.42	9.87	2.1311	1	2	2	4
44.37	1.47	2.0415	0	4	0	2
45.18	7.74	2.0067	0	2	3	4
46.33	5.01	1.9599	-2	2	3	4
46.38	29.75	1.9579	0	4	1	4
47.48	1.54	1.915	-2	3	2	4

47.64	3.33	1.9089	1	4	0	4
48.44	7.61	1.879	-3	1	2	4
48.46	2.51	1.8783	-3	1	1	4
48.64	16.43	1.8721	-1	0	4	2
49.49	4.5	1.8417	-1	3	3	4
49.52	4.6	1.8406	1	3	2	4
50.03	8.88	1.8232	1	1	3	4
50.46	1.2	1.8086	2	0	2	2
51.38	2	1.7785	-1	4	2	4
51.7	3.37	1.7682	-2	1	4	4
51.77	10.06	1.7658	2	1	2	4
52	11.35	1.7587	0	3	3	4
52.03	1.27	1.7578	0	4	2	4
52.42	11.88	1.7455	-3	2	2	4
52.44	10.33	1.7449	-3	2	1	4
53.03	5.45	1.7269	-2	3	3	4
53.08	11.48	1.7254	2	3	1	4
54.25	1.18	1.6907	0	1	4	4
54.84	19.96	1.674	-2	4	1	4
55.5	12.13	1.6556	-2	2	4	4
55.57	3.69	1.6536	2	2	2	4
55.92	1.11	1.6443	-3	2	3	4
55.97	9.81	1.6429	3	2	0	4
56.56	1.25	1.6272	-2	4	2	4
57.83	7.66	1.5944	-3	0	4	2
57.95	9.2	1.5915	0	2	4	4
58.03	1.6	1.5895	0	5	1	4
58.34	9.81	1.5816	-1	4	3	4
58.37	1.05	1.5809	1	4	2	4
58.63	2.72	1.5744	-3	3	1	4
59.03	2.47	1.5649	-3	1	4	4
59.11	6.76	1.5628	3	1	1	4
61.53	1.68	1.5071	-2	4	3	4
61.58	6.43	1.5061	2	4	1	4
61.88	5.7	1.4993	-3	3	3	4
61.93	1.31	1.4983	3	3	0	4
62.37	1.48	1.4889	-1	5	2	4
62.38	2.83	1.4885	1	5	1	4
62.54	5.1	1.4852	1	0	4	2
62.62	1.68	1.4834	3	2	1	4
63.64	4.31	1.4621	-4	0	2	2
66.32	2.2	1.4094	-4	1	3	4
66.36	2.22	1.4086	-4	1	1	4
66.9	5.06	1.3987	-2	2	5	4
66.98	2.48	1.3971	2	2	3	4
67	1.18	1.3967	-2	5	2	4

67.97	4.58	1.3791	1	4	3	4
68.63	2.2	1.3675	-1	5	3	4
68.66	3.32	1.367	1	5	2	4
68.66	1.09	1.3669	3	1	2	4
68.88	2.02	1.3631	0	1	5	4
69	1.1	1.361	0	6	0	2
69.73	1.96	1.3486	-3	4	3	4
69.89	3.36	1.3459	4	0	0	2
70.89	1.01	1.3293	-4	1	4	4
70.97	1.79	1.328	4	1	0	4
71.49	6.12	1.3196	-1	6	1	4
71.5	2	1.3195	1	6	0	4
71.56	2.53	1.3185	-2	5	3	4
72.13	3.17	1.3095	0	2	5	4
72.43	3.84	1.3049	2	3	3	4
72.5	1.11	1.3038	1	3	4	4
73.53	1.21	1.2881	-4	3	2	4
74.1	3.79	1.2795	-4	2	4	4
74.49	4.33	1.2738	1	6	1	4
77.22	1.96	1.2354	3	3	2	4
77.61	1.69	1.2302	1	5	3	4
77.69	2.34	1.2292	-1	0	6	2
78.73	1.75	1.2155	-1	1	6	4
78.78	1.15	1.2148	1	1	5	4
78.8	1.08	1.2146	2	6	0	4
79.28	1.42	1.2084	-3	5	3	4
79.32	1.44	1.2079	3	5	0	4
79.36	3.14	1.2074	-3	0	6	2
79.82	6.14	1.2016	-1	4	5	4
80.29	3.51	1.1958	-2	2	6	4
80.31	1.32	1.1955	-1	6	3	4
80.39	2.18	1.1945	2	2	4	4
80.53	2.62	1.1928	3	1	3	4
81.38	3.12	1.1824	-4	2	5	4
82.27	2.59	1.1719	0	6	3	4
82.28	1.43	1.1718	-4	4	3	4
82.32	4.54	1.1713	-4	4	1	4
83.1	2.4	1.1623	-2	6	3	4
84.36	6.29	1.1481	-3	4	5	4
85.09	1.49	1.1401	3	5	1	4
86.63	4.21	1.1237	4	3	1	4
87.02	2.06	1.1197	1	3	5	4
87.75	1.69	1.1123	-3	-6	1	4
87.94	1.06	1.1104	-1	7	2	4
88.45	2.39	1.1053	0	7	2	4
88.46	1.9	1.1052	4	1	2	4

89.11	1.18	1.0988	1	5	4	4

2. The crystal structure of β-Bi_2O_3

Database_Code_Amcsd 0010069
Cell Parameters: 7.7390 7.7390 5.6360 90.000 90.000 90.000
Space Group: P-42_1c
X-Ray Wavelength: 1.541838

2-Theta	Intensity	D-Spacing	H	K	L	Multiplicity
25.74	1.89	3.461	2	1	0	8
27.97	100	3.19	2	0	1	8
30.31	1.61	2.9493	2	1	1	8
31.75	15.08	2.818	0	0	2	2
32.73	26.59	2.7361	2	2	0	4
41.32	1.56	2.1852	2	1	2	8
46.25	25.62	1.963	2	2	2	4
46.96	11.98	1.9347	4	0	0	4
51.3	1.89	1.7808	4	1	1	8
54.28	14.02	1.69	2	0	3	8
55.55	24.39	1.6543	4	2	1	8
57.81	10.26	1.595	4	0	2	8
59.14	1.03	1.5622	4	1	2	8
66.34	1.82	1.409	0	0	4	2
68.6	2.96	1.3681	4	4	0	4
74.56	8.66	1.2728	4	2	3	8
75.63	3.89	1.2573	6	0	1	8
75.97	4.3	1.2527	2	2	4	4
77.57	3.61	1.2307	4	4	2	4
78.1	3.38	1.2236	6	2	0	8
85.2	2.83	1.139	4	0	4	8
86.76	4.96	1.1224	6	2	2	8

3. The crystal structure of $BiVO_4$

Database_Code_Amcsd 0014281
Cell Parameters: 5.1470 5.1470 11.7216 90.000 90.000 90.000
Space Group: I4_1/a
X-Ray Wavelength: 1.541838

2-Theta	Intensity	D-Spacing	H	K	L	Multiplicity
18.83	43	4.7127	1	0	1	8
28.69	12.56	3.1121	1	0	3	8
28.88	100	3.0918	1	1	2	8
30.51	17.29	2.9304	0	0	4	2
34.86	21.56	2.5735	2	0	0	4

39.48	1.21	2.2825	1	1	4	8
39.91	12.51	2.2587	2	1	1	8
39.91	4.37	2.2587	1	2	1	8
42.37	8.31	2.1334	1	0	5	8
45.75	4.35	1.9832	2	1	3	8
45.75	8.03	1.9832	1	2	3	8
46.99	26.55	1.9337	2	0	4	8
50.13	10.42	1.8197	2	2	0	4
53.21	15.93	1.7213	1	1	6	8
54.02	3.13	1.6976	3	0	1	8
55.99	1.65	1.6424	2	1	5	8
55.99	1.83	1.6424	1	2	5	8
57.91	2.8	1.5924	1	0	7	8
58.78	2.72	1.5709	3	0	3	8
58.89	9.74	1.5683	3	1	2	8
58.89	12.89	1.5683	1	3	2	8
59.83	10.44	1.5459	2	2	4	8
63.49	1.64	1.4652	0	0	8	2
65.92	1.83	1.4171	3	2	1	8
69.41	1.09	1.3541	1	2	7	8
70.19	1.1	1.3408	2	3	3	8
73.61	2.62	1.2867	4	0	0	4
74.52	5.69	1.2733	2	0	8	8
76.12	5.7	1.2505	3	1	6	8
76.12	3.74	1.2505	1	3	6	8
78.44	1.07	1.2193	2	3	5	8
80.92	3.84	1.188	3	3	2	8
81.74	3.7	1.1782	4	0	4	8
84.11	1.93	1.1509	2	4	0	4
84.11	1.91	1.1509	4	2	0	4
84.99	3.19	1.1412	2	2	8	8
87.41	3.06	1.1157	1	1	10	8

4. The crystal structure of γ-BIVOX

Database_Code_Amcsd 0016748
Cell Parameters: 3.9200 3.9200 15.5000 90.000 90.000 90.000
Space Group: I4/mmm
X-Ray Wavelength: 1.541838

2-Theta	Intensity	D-Spacing	H	K	L	Multiplicity
11.42	26.16	7.75	0	0	2	2
22.95	2.59	3.875	0	0	4	2
23.41	12.79	3.8003	1	0	1	8
28.58	100	3.1229	1	0	3	8
32.3	31.12	2.7719	1	1	0	4

34.36	5.56	2.6099	1	1	2	8
34.73	11.61	2.5833	0	0	6	2
36.97	9.01	2.4315	1	0	5	8
39.99	6.89	2.2545	1	1	4	8
46.32	15.64	1.96	2	0	0	4
47.14	2.03	1.928	1	0	7	8
47.87	3.28	1.9002	2	0	2	8
48.15	23.64	1.8898	1	1	6	8
52.53	3.51	1.742	2	1	1	16
55.34	28.34	1.6601	2	1	3	16
58.09	2.39	1.588	1	1	8	8
58.54	12.16	1.5768	1	0	9	8
59.17	9.77	1.5614	2	0	6	8
60.69	2.75	1.526	2	1	5	16
67.59	3.76	1.3859	2	2	0	4
68.23	1.01	1.3745	2	1	7	16
68.81	1.05	1.3643	2	2	2	8
73.29	1.42	1.2917	0	0	12	2
74.97	4.71	1.2668	3	0	3	8
76.91	3.72	1.2396	3	1	0	8
77.73	8.38	1.2286	2	1	9	16
78.28	4.01	1.2213	2	2	6	8
82.37	3.38	1.1708	1	1	12	8
87.23	6.66	1.1176	3	1	6	16
89.16	1.07	1.0983	2	1	11	16

5. The crystal structure of Bi

Database_Code_Amcsd 0012841
Cell Parameters: 4.5460 4.5460 11.8620 90.000 90.000 120.000
Space Group: R-3m
X-Ray Wavelength: 1.541838

2-Theta	Intensity	D-Spacing	H	K	L	Multiplicity
22.49	5.02	3.954	0	0	3	2
23.81	1.49	3.7365	1	0	1	6
27.19	100	3.2801	0	1	2	6
37.99	34.96	2.3687	1	0	4	6
39.65	36.44	2.273	1	1	0	6
44.59	5.97	2.032	0	1	5	6
45.9	5.21	1.977	0	0	6	2
46.06	4.1	1.9706	1	1	3	12
48.74	18.35	1.8683	2	0	2	6
56.08	10.1	1.64	0	2	4	6
59.38	4.15	1.5565	1	0	7	6

61.18	2.08	1.5149	2	0	5	6
62.24	11.22	1.4917	1	1	6	12
64.57	14.02	1.4433	1	2	2	12
67.5	2.97	1.3876	0	1	8	6
70.85	8.9	1.33	2	1	4	12
71.59	1.06	1.318	0	0	9	2
71.95	4.99	1.3123	3	0	0	6
73.78	1.94	1.2843	0	2	7	6
75.4	2	1.2606	1	2	5	12
81.22	1.58	1.1844	2	0	8	6
85.08	3.61	1.1402	1	1	9	12
87.18	2.28	1.1181	2	1	7	12
89.67	1.69	1.0934	0	3	6	6
89.67	1.69	1.0934	3	0	6	6

Rietveld Refinement

Parameter refined and their significance

• Scale factor

The scale factors are the parameters which are used for scaling up the intensities of peaks in order to match the calculated pattern with observed pattern. They are one of the most important parameters which are refined during the Rietveld refinement. It directly affects the number of phases which are refined, as wrong scaling factor causes the mismatch between the intensity of observed profile and calculated profile and it is entirely possible that outcome of the refinement would come out to be totally wrong. Moreover, it also leads to the error in the profile shape parameters. Thus, it is should be minimized first.

It is given by the following Equation:

$I_c = I_b + S_h \sum S_{ph} Y_{ph}$

Where I_b=background intensity, S_{ph}=phase scale factor, S_h=histogram scale factor

• Background

The baseline of the pattern can affect the whole refinement process. Every powder diffraction pattern contains statistical noise, which can cause the baseline of the pattern to deviate from its ideal flat line at various theta positions.

There are two approaches with the help of which one can deal with background in the XRD pattern. One approach is to use linear interpolation of selected point between peaks, while another is to use a semiempirical formula or empirical formula/function containing definable parameters.

In the simple pattern where there is no overlapping between the peaks, both approaches can be used; however, the problem comes when the pattern with overlapping of peaks comes into play. Since there are many overlapping of peaks, hence the many of the peaks doesn't belong to the same baseline, so it becomes very difficult to estimate the background points (McCusker, Von Dreele et al. 1999). If the first approach is used in this problem, then one has to subtract and re-estimate the background points many times during the refinement procedure, which if wrongly chosen may also lead to calculation during refinement to diverge.

The benefit of using second approach is that first this eliminates some of the drawbacks of the first approach of subtracting background several times during refinement and another

benefit of this approach is that other parameters can also be refined along with this background parameter.

But there is one major drawback of this approach is that if the empirical formula used for refining describes the background parameter well, then the refinement would not diverge. But, if doesn't then the refinement result would never come correct (McCusker, Von Dreele et al. 1999).

In our case, the MATCH! Software is using Chebyshev polynomial to rectify this problem.

Background $(2\theta) = b_1$ Back $[(1+ b_3)2\theta + b_4] + b_2$

Where b_1, b_2, b_3, b_4 are the background coefficients (Rodríguez-Carvajal 2000).

The background should never be subtracted directly in between the refinement as it will totally change the R-factors.

• 2Θ or zero point correction

2Θ or zero point error refers to the shift in peak position of the diffraction pattern. It may be due to the misaligned detector, misaligned sample, or misaligned goniometer. In the refinement process of zero point correction following Equation is used:

$T_{true} = T_{exp} - ZERO$

Where T_{true}=True displacement; T_{exp}=Experimental displacement; ZERO=Zero(0) displacement/Reference displacement

• Sample displacement error

Sample displacement error occurs when the sample is not in the center of goniometer or it is outside the focusing circle of diffractometer. It increases rapidly when 2Θ begins to fall below 20°. It is one of the largest systematic errors affecting line positions in the geometry. Following Equation is used in the refinement process of sample displacement error (McCusker, Von Dreele et al. 1999):

$$\Delta 2\theta = \frac{-2s}{R}\cos\theta$$

Where 'R' is the radius of goniometer focusing circle and's' is the displacement of the sample surface w.r.t the goniometer axis.

• Asymmetry Parameters

This is used to carry out the refinement of peak shape error produced due to some peak asymmetry. Rietveld refinement allows the correction of this error by the introduction of an empirical asymmetry parameter P. Following Equation is used in the refinement process (Rodríguez-Carvajal 2000):

$$As(z) = 1 + \frac{P_1 F_a(z) + P_2 F_b(z)}{\tan\theta_h} + \frac{P_3 F_a(z) + P_4 F_b(z)}{\tan 2\theta_h}$$

$$Z = \frac{2\theta_i - 2\theta_h - Sshf}{FWHM}, F_a(z) = 2z\exp(-z^2), F_b(z) = 2\,(2z^2 - 3)F_a(z)$$

Where, P_1, P_2, P_3 and P_4 are independent asymmetry parameters.

After refining the preferred orientation (which happens due to presence of the random orientation of crystallites in sample), refinement of site occupancy factor, microstructure parameters and micro-absorption parameters are carried out.

• **Absorption and micro-absorption:**

The effect of sample absorption on the intensity is adjusted by refining the absorption and micro-absorption parameter by using the transmission factor T_h and is given by the following formula (Rodríguez-Carvajal 2000):

$$T_h = exp[(0.0927 + 0.375\,sin^2\theta_h)(\mu R)^2 + (1.7133 - 0.0368\,sin^2\theta_h)(\mu R)]$$

Where R refers to the cylindrical sample radius and μ refers to the linear absorption coefficient. This is mainly used in the case of debye-geometry.

For geometry related to bragg-brentano, the refinement of an angular dependent micro-absorption has to be carried out. It uses the following Equation (Rodríguez-Carvajal 2000):

$$P(h) = P_0 + C_p\frac{\tau}{\sin\theta_h}\left(1 - \frac{\tau}{\sin\theta_h}\right)$$

$$T_h = T_h S_r(h) = T_h[1 - P(h)]$$

Where P(h) is the preferred orientation parameter and T_h is the transmission factor. The preferred orientation factor is mainly uses two functions during the refinement. One by exponential function whiles other by the modified March's function.

The exponential function for preferred orientation is given by (Rodríguez-Carvajal 2000):

$$P_h = G_2 + (1 - G_2)\exp(G_1\alpha_h^2)$$

Where α_h denotes the acute angle in between the scattering vector and the normal to the crystallites which is also known as the platy habit.

While the modified March's function is given by (Rodríguez-Carvajal 2000):

$$P_h = G_2 + (1 - G_2)[(G_1\cos\alpha_h)^2 + sin^2\alpha_h/G_1]^{-3/2}$$

Where α_h denotes the acute angle in between the fibber axis direction and the scattering vector. G_1 and G_2 are the refinable parameter where G_1 refers to the X-ray powder diffractometer braggbrentano geometry for debye-scherrer while G_2 refers to the sample fracture that has not been textured yet.

If the value of G_1 is equal to 1, then there is not any preferred orientation is present, but if the $G_1<1$, then acute angle between normal to the crystallite and scattering vector is formed. It is called plarty habit. But on the contrary, if $G>1$, then angle in between the fibber axis direction and the scattering vector occurs.

• **Size-Strain Broadening**

Sample broadening and Instrumental broadening are two factors responsible for the broadening of the peaks in the X-ray pattern. A particle of the powder consists of more than one crystal with being fused together. So, in this case, a crystal may be the combination of several crystallites. Thus, during in X-Ray if the angle doesn't coincide with the bragg angle, then it would lead to the case of another lattice plane which would produce a diffracted wave with the phase having opposite nature. The production of more and more plane might produce waves which may escape from process of destructive interference occurring in the case containing angular mismatch and thereby it gives rise to peak broadening.

The sample broadening mainly occurs due to twinning, stacking faults, defects and strain, while the instrumental broadening mainly occurs due to imperfection in the monochromatic source of radiation and poor alignment between the slits and diffractometer. It is mainly given by the following formula (Rodríguez-Carvajal 2000):

$$I(2\theta) = \int_{\infty}^{-\infty} I_{instrument}(\psi) I_{sample}(2\theta - \psi) d\psi$$

FTIR PEAK DATA

Table 5-1 : Table **of Characteristics IR absorption and Functional Groups**

Frequency (cm^{-1})	Bond	Functional Group
3640–3610 (s, sh)	O–H Stretch, Free Hydroxyl	Alcohols, Phenols
3500 – 3200 (s,b)	O-H Stretch, H-Bonded	Alcohols, Phenols
3400 – 3250 (m)	N-H Stretch	10, 20 Amines, Amides
3300 – 2500 (m)	O-H Stretch	Carboxylic Acids
3330 – 3270 (n,s)	-C= C - H	Alkynes
3100 – 3000 (s)	C-H Stretch	Aromatics
3100–3000 (m)	=C–H Stretch	Alkenes
3000–2850 (m)	C–H Stretch	Alkanes
2830–2695 (m)	H–C=O: C–H Stretch	Aldehydes
2260 – 2210 (v)	C= N Stretch	Nitriles
2260 – 2100 (v)	-C=C Stretch	Alkynes
1760 – 1665 (s)	C=O Stretch	Carbonyls
1760 – 1690 (s)	C=O Stretch	Carboxylic Acids
1750 – 1735 (s)	C=O Stretch	Esters, Saturated Aliphatic
1740 – 1720 (s)	C=O Stretch	Aldehydes,Saturated Aliphatic
1730–1715 (s)	C=O Stretch	α,β Unsaturated Ester
1715 (s)	C=O Stretch	Ketones, Saturated Aliphatic
1710–1665 (s)	C=O Stretch	α,β Unsaturated Aldehydes, Ketones
1680–1640 (m)	–C=C– Stretch	Alkenes
1650- 1580 (m)	N-H Bend	10 Amines
1600 – 1585 (m)	C-C Stretch	Aromatics
1550 – 1475 (s)	N-O Asymmetric Stretch	Nitro Compounds
1500 – 1400 (m)	C-C Stretch (In Ring)	Aromatics
1470 – 1459 (m)	C-H Bend	Alkanes
1370 – 1350 (m)	C-H Rock	Alkanes
1360 – 1290 (m)	N-O Asymmetric Stretch	Nitro Compounds
1335 – 1250 (m)	C-N Stretch	Aromatic Amines
1320 – 1000 (s)	C-O Stretch	Alcohols, Carboxylic Acids,
1300 – 1150 (s)	C-H Wag	Alkyl Halides
1250 – 1020 (m)	C-N Stretch	Aliphatic Amines
1000 – 650 (s,b)	=C-H Bend	Alkenes
950 – 910 (m)	O-H Bend	Carboxylic Acids
910 – 665 (s)	N-H Wag	10, 20 Amines
900 – 675 (s)	C-H "Oop"	Aromatics
850 – 550 (m)	C-Cl Stretch	Alkyl Halides
725 – 720 (m)	C-H Rock	Alkanes
700 – 610 (b,s)	-C=C-H	Alkynes
690 – 515 (m)	C-Br	Alkyl Halides

Where, m=medium, w=weak, s=strong, n=narrow, b=broad, sh=sharp

Chen, H.-T., S. Huh, et al. (2007). Fine tuning the functionalization of mesoporous silica, CRC Press, Taylor & Francis Publishing Group: New York.

McCusker, L., R. Von Dreele, et al. (1999). "Rietveld refinement guidelines." Journal of applied Crystallography 32(1): 36-50.

Rodríguez-Carvajal, J. (2000). "An introduction to the program." Full prof.

Skoog, D. A., F. J. Holler, et al. (2017). Principles of instrumental analysis, Cengage learning.